FORGE

Fate Of Repository Gases

European Commission FP7

Final Report of FORGE WP4.1.1: The stress-path permeameter experiment conducted on Callovo-Oxfordian Claystone

FORGE Report D4.17

Keywords.

Callov-Oxfordian claystone, argillite, permeability, specific storage, modulus, capillary entry pressure, gas, TPRL.

Bibliographical reference

JF HARRINGTON, DJ NOY & RC Cuss. 2013 Callovo Oxfordian Claystone: processes governing advective gas flow. British Geological Survey Commissioned Report, CR/13/088. EU Report D5.16 82pp.

Euratom 7th Framework Programme Project: FORGE

EURATOM

Fate of repository gases (FORGE)

The multiple barrier concept is the cornerstone of all proposed schemes for underground disposal of radioactive wastes. The concept invokes a series of barriers, both engineered and natural, between the waste and the surface. Achieving this concept is the primary objective of all disposal programmes, from site appraisal and characterisation to repository design and construction. However, the performance of the repository as a whole (waste, buffer, engineering disturbed zone, host rock), and in particular its gas transport properties, are still poorly understood. Issues still to be adequately examined that relate to understanding basic processes include: dilational versus visco-capillary flow mechanisms; long-term integrity of seals, in particular gas flow along contacts; role of the EDZ as a conduit for preferential flow; laboratory to field up-scaling. Understanding gas generation and migration is thus vital in the quantitative assessment of repositories and is the focus of the research in this integrated, multi-disciplinary project. The FORGE project is a pan-European project with links to international radioactive waste management organisations, regulators and academia, specifically designed to tackle the key research issues associated with the generation and movement of repository gasses. Of particular importance are the long-term performance of bentonite buffers, plastic clays, indurated mudrocks and crystalline formations. Further experimental data are required to reduce uncertainty relating to the quantitative treatment of gas in performance assessment. FORGE will address these issues through a series of laboratory and field-scale experiments, including the development of new methods for up-scaling allowing the optimisation of concepts through detailed scenario analysis. The FORGE partners are committed to training and CPD through a broad portfolio of training opportunities and initiatives which form a significant part of the project.

Further details on the FORGE project and its outcomes can be accessed at www.FORGEproject.org.

Contact details:

J.F. Harrington

British Geological Survey
Keyworth
Nottingham
NG12 5GG
UK

Tél.: +441159363100
E-mail: rjfha@bgs.ac.uk

British Geological Survey
NATURAL ENVIRONMENT RESEARCH COUNCIL

Callovo Oxfordian Claystone: processes governing advective gas flow

Minerals and Waste Programme

Commissioned Report CR/13/088

EU Report D5.16

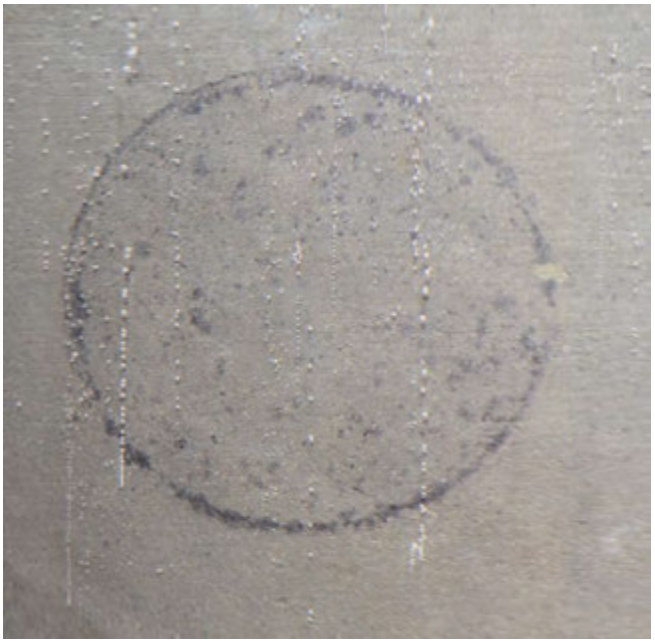

BRITISH GEOLOGICAL SURVEY

MINERALS AND WASTE PROGRAMME

COMMISSIONED REPORT CR/13/088
EU REPORT D5.16

Callovo Oxfordian Claystone: processes governing advective gas flow

JF Harrington, DJ Noy & RJ Cuss

Keywords

Callov-Oxfordian claystone, argillite, permeability, specific storage, modulus, capillary entry pressure, gas, TPRL.

Front cover

Photo of gas discharged from a laboratory sample following gas injection.

Bibliographical reference

JF HARRINGTON, DJ NOY & RC Cuss. 2013 Callovo Oxfordian Claystone: processes governing advective gas flow. *British Geological Survey Commissioned Report*, CR/13/088. EU Report D5.16 82pp.

Copyright in materials derived from the British Geological Survey's work is owned by the Natural Environment Research Council (NERC) and/or the authority that commissioned the work. You may not copy or adapt this publication without first obtaining permission. Contact the BGS Intellectual Property Rights Section, British Geological Survey, Keyworth, e-mail ipr@bgs.ac.uk. You may quote extracts of a reasonable length without prior permission, provided a full acknowledgement is given of the source of the extract.

© NERC2013. All rights reserved

Keyworth, Nottingham British Geological Survey 2013

BRITISH GEOLOGICAL SURVEY

The full range of our publications is available from BGS shops at Nottingham, Edinburgh, London and Cardiff (Welsh publications only) see contact details below or shop online at www.geologyshop.com

The London Information Office also maintains a reference collection of BGS publications, including maps, for consultation.

We publish an annual catalogue of our maps and other publications; this catalogue is available online or from any of the BGS shops.

The British Geological Survey carries out the geological survey of Great Britain and Northern Ireland (the latter as an agency service for the government of Northern Ireland), and of the surrounding continental shelf, as well as basic research projects. It also undertakes programmes of technical aid in geology in developing countries.

The British Geological Survey is a component body of the Natural Environment Research Council.

British Geological Survey offices

BGS Central Enquiries Desk

Tel 0115 936 3143 Fax 0115 936 3276

email enquiries@bgs.ac.uk

Kingsley Dunham Centre, Keyworth, Nottingham NG12 5GG

Tel 0115 936 3241 Fax 0115 936 3488
email sales@bgs.ac.uk

Murchison House, West Mains Road, Edinburgh EH9 3LA

Tel 0131 667 1000 Fax 0131 668 2683
email scotsales@bgs.ac.uk

Natural History Museum, Cromwell Road, London SW7 5BD

Tel 020 7589 4090 Fax 020 7584 8270
Tel 020 7942 5344/45 email bgslondon@bgs.ac.uk

Columbus House, Greenmeadow Springs, Tongwynlais, Cardiff CF15 7NE

Tel 029 2052 1962 Fax 029 2052 1963

Forde House, Park Five Business Centre, Harrier Way, Sowton EX2 7HU

Tel 01392 445271 Fax 01392 445371

Maclean Building, Crowmarsh Gifford, Wallingford OX10 8BB

Tel 01491 838800 Fax 01491 692345

Geological Survey of Northern Ireland, Colby House, Stranmillis Court, Belfast BT9 5BF

Tel 028 9038 8462 Fax 028 9038 8461

www.bgs.ac.uk/gsni/

Parent Body

Natural Environment Research Council, Polaris House, North Star Avenue, Swindon SN2 1EU

Tel 01793 411500 Fax 01793 411501
www.nerc.ac.uk

Website www.bgs.ac.uk
Shop online at www.geologyshop.com

Foreword

This report is the product of a study by the British Geological Survey (BGS) undertaken on behalf of the French radioactive waste management company Agence Nationale pour la Gestion des Déchets Radioactifs (Andra) and the European Union 7th framework Euratom Programme under the auspices of the Fate of repository Gases (FORGE) project, to examine the hydraulic and gas transport properties of the Callovo-Oxfordian argillite.

Acknowledgements

This study was undertaken using the facilities of the BGS Transport Properties Research Laboratory (TPRL) and the Scanning Electron Microscopy Laboratory. Funding for the study was provided by the French radioactive waste management operator, Andra, the European Union (FORGE Project) and the British Geological Survey through its well-founded laboratory programme and the Geosphere Containment project (part of the BGS core strategic programme). The authors would like to thank Dr Jeremy Rushton who undertook the petrographic analysis presented in Section 2.2.1 and Mr Humphrey Wallis and colleagues within the Research & Development Workshops at BGS.

Contents

Foreword i

Acknowledgements i

Contents i

Summary viii

1 Introduction 1
  1.1 Objective of study 1

2 Experimental system 1
  2.1 Test conditions 3
  2.2 Test material 3
  2.3 Calibration 8
  2.4 Experimental procedure 8

3 Data reduction and modelling approaches 8
  3.1 Hydraulic flow 9
  3.2 Gas flow 9

4 Provisional results and numerical modelling 10
  4.1 Callovo-Oxfordian Clay sample 1 (Cox-1) 10
  4.2 Callovo-Oxfordian Clay sample 2 (CoX-2) 43
  4.3 Callovo-Oxfordian Clay sample 3 (CoX-3) 55

5 Modelling of the gas data 64
  5.1 An initial model for sample 1 66

5.2 A model for sample 1 fitted to gas breakthrough at backpressure filter..... 66
5.3 A model for sample 1 fitted to gas outflow rates. 66
5.4 A model for sample 2 fitted to backpressure guard ring arrival time..... 72
5.5 A model for sample COx-2 fitted to injection guard ring arrival time..... 74

6 Implications for process understanding 77

7 References 81

FIGURES

Figure 2-1 Schematic diagram of the pressure vessel and sample assembly for the BGS guard-ring permeameter. The pressure vessel is a custom-built stainless steel vessel rated to 70 MPa. The cylindrical clay specimen is sandwiched between two stainless steel end-caps, each with two filters recessed into the load-bearing surface, and jacketed in heat shrink Teflon to exclude the confining fluid. 2

Figure 2-2 Discing of the core during early attempts to prepare a suitable test plug. As core preparation techniques evolved this problem was virtually eliminated. 4

Figure 2-3. Sub-sampling of the core barrel (by dry cutting using a diamond encrusted blade) prior to preparation of the specimen by diamond coring and surface grinding. 5

Figure 2-4 Photo looking longitudinally along the core showing a number of linear features crossing the core. 6

Figure 2-5 The linear feature is approximately 2mm across, dark grey in the central portion with orange-brown edges. Outside the orange-brown zone is a thin ‘bleached’ zone and outside this the sediment has a slightly darker grey colour for a further 1-2mm. Locally the edge between the dark grey interior and orange-brown zone is marked by a thin white zone. The edges of the dark grey interior are darker grey and iridescent. The box shows the area of the SEM image shown in Figure 2-6. 7

Figure 2-6 The central high brightness portion comprises finely granular iron sulphide (pyrite). The adjacent zones of intermediate brightness correspond to the orange-brown zones and record compositions rich in iron and oxygen (ED analysis), suggesting the presence of iron oxide / hydroxide. The embayment of the central portion suggests that it is the edges of the sulphide that have been altered and dissolved. The box, located on the boundary between these zones, shows the area of the SEM image shown in Figure 2-7. 7

Figure 2-7 Detail of the edge of the iron sulphide (pyrite) inner zone, showing the presence of a thin band of strontium sulphate. This has formed as <10 micron euhedral and subhedral crystals. These are scattered amongst pyrite framboids, in contrast to the densely granulated inner structure of the linear feature.....8

Figure 4-1 Flux response for backpressure and confining circuits during the initial the equilibration stage [1]. Positive flows for red and blue lines represent flux into the specimen. The negative flow for the green line denotes flux out of the pump system suggestive of time dependent swelling. 10

Figure 4-2 Cumulative flow from backpressure and confining systems from test stages [2] and [3]. The backpressure response shows well defined transients associated with drainage of the argillite as confining stress is increased. 12

Figure 4-3 Comparison on model output to test data for the first step of the consolidation test, stage [2]. 14

Figure 4-4 Comparison on model output to test data for the second step of the consolidation test, stage [3]. 14

Figure 4-5 Comparison of observed guard ring pressures with the model simulation of the hydraulic test.....15

Figure 4-6 Comparison of observed flow rates from the injection and back pressure filters with the model simulation of the hydraulic test.....15

Figure 4-7 Comparison of observed guard ring pressures with the model simulation of the hydraulic test, using a model with isotropic clay and leakage over the axial surfaces. 16

Figure 4-8 Comparison of observed flow rates from the injection and back pressure filters with the model simulation of the hydraulic test.....17

Figure 4-9 Pressure data from the injection, backpressure, and guard-ring filters during the gas injection test.....18

Figure 4-10 Gas flow rates at the injection and backpressure filters during the gas injection test. The large spikes in injection flux relate to the compression of the gas phase during constant flow rate test stages.....19

Figure 4-11 Backpressure flow rate and injection gas pressure plotted against elapsed time for test stages [6] through [9]. Note a small but measureable increase in discharge rate following the rise in gas pressure. The rapid increase in flow at around 171.5 days is indicative of major gas breakthrough. 20

Figure 4-12 Backpressure flow rate and injection gas pressure plotted against elapsed time for test stages [6] through [7]. Linear regression of the data suggests flux is decreasing during stage [7]. 21

Figure 4-13 Cross-plot of gas pressure and equivalent hydraulic conductivity versus discharge rate during test stages [6], [7] and the initial section of [9]. Projection of the flux data to the zero flow condition suggests a gas entry pressure of around 0.9 MPa (see Figure 4-14). Equivalent hydraulic conductivities are of a similar magnitude to those observed during hydraulic testing. 22

Figure 4-14 Cross-plot of IGR versus excess injection gas pressure. Extrapolation of the line suggests a gas entry pressure of approximately 1.3 MPa. 23

Figure 4-15 Pressure data from the injection, backpressure, and guard-ring filters during the stage [6]. The asymmetry of the injection guard-ring response observed during the first 12.6 days of the test is atypical of hydraulic behaviour, as is the spontaneous increase in IGR pressure at 12.6 days.....23

Figure 4-16 Pressure from the injection, backpressure, and guard-ring filters during the step-wise increase in pressure from stages [6] to [7]. The rate and shape of the IGR transient is atypical of hydraulic behaviour.....24

Figure 4-17 Evolution of IGR pressure during stage [7]. The spontaneous drops in pressure at days 57 and 78 are symptomatic of unstable pathways flow. 24

Figure 4-18 Evolution of guard-ring pressure during test stage [9]. Correlation lines [i], [ii] and [iii], indicate the start of stage [9], the initiation of the spontaneous negative pressure transient for the IGR filter and the inflection in the IGR pressure curve. 25

Figure 4-19 Evolution of guard-ring pressure during gas breakthrough. Correlation lines [i], [ii] and [iii] relate to increases in filter pressure at the injection and backpressure guard-rings and an increase in discharge rate respectively.....26

Figure 4-20 Cross-plot of flow in and out the sample plotted against excess gas pressure. The intersection of the lines provides an estimate for the gas breakthrough pressure. The hysteresis between ascending and descending flow cycles is evident in the data. 27

Figure 4-21 Flow and strain data from a triaxial test performed on COx (Cuss and Harrington 2012). Plot A shows the slow time dependent evolution in flux out of the core, while plot B, shows the sample dilating in response to changes in gas outflow....28

Figure 4-22 STP flow rate into and out of the specimen during test stage [9]. The inflow data has been cropped during the early part of the test due to problems with leakage from the injection system. 29

Figure 4-23 Evolution of guard-ring pressure during test stage [9]. The dash line indicates the point at which flux out of the specimen increases. The dynamic behaviour exhibited by the backpressure guard-ring can only be explained by the existence of highly unstable gas pathways. 30

Figure 4-24 STP flow rate into and out of the specimen and gas injection pressure plotted against elapsed time during test stage [9] through [15]. 30

Figure 4-25 STP flow rate into and out of the specimen and gas injection pressure plotted against elapsed time during test stage [16] through [19]. 31

Figure 4-26 Downstream guard-ring response during gas testing. The saw-tooth pressure response observed in later data is symptomatic of unstable gas pathways. 31

Figure 4-27 STP flow rates into and out of the sample. The red shaded areas at the beginning of each stage delineate the sections of the transient response used to estimate saturation. 33

Figure 4-28 Cross-plot of excess gas pressure against estimated water saturation based on mass balance. Estimates for the water saturation are derived from mass balance of the STP data presented in Figure 4-27. STP volumes have been corrected back to experimental conditions assuming a capillary threshold pressure of 2.0 MPa. However, the data predicts unrealistically high desaturations which cannot be reconciled with post-test measurements of sample saturation. 34

Figure 4-29 Outflow from backpressure filter and cumulative flow from confining pump (from day 322 onwards) plotted against elapsed time. While the correlation is rather crude the data suggests an underlying trend of volume increase as outflow (and pressure) increase and volume decrease when outflow (and pressure) fall. 34

Figure 4-30 Shut-in response for test COx-1. The protracted nature of the shut-in response is a function of the initial gas volume and the non-linearity in the gas flow law. However, a good numerical fit to the data is obtained allowing a prediction of the capillary threshold pressure to be made.....35

Figure 4-31 Hydraulic response following the initial gas injection cycle. Flow in asymptotes at a value very close to that of the pre-gas injection stage (red line). The offset in the outflow data probably relates to minor leakage. 36

Figure 4-32 Guard ring response during second hydraulic test. While the slow pressurisation of the injection guard ring (IGR) is caused by the presence of residual gas within the filter, the asymptote is very close to the previous value. This suggests little if any change in hydraulic anisotropy. The downstream guard ring pressure (BGR) appears insensitive to the hydraulic gradient with its response probably dominated by the presence of residual gas. 37

Figure 4-33 Comparison of observed guard ring pressures and flow rates with the model simulation of the post-gas injection hydraulic test on sample COx-1. 37

Figure 4-34 Evolution in flow into and out of sample COx-1 to examine self-sealing characteristics of the Callovo Oxfordian Clay during stage [25]. 38

Figure 4-35 Evolution in pressure within sample COx-1 following the reinjection of gas, stage [25]. The inflections in the guar ring response are symptomatic of the opening and closing of unstable gas pathways. 39

Figure 4-36 Evolution in flow into and out of the sample as gas pressure gradient is increased across the sample. 39

Figure 4-37 Evolution in pressure for sample COx-1 from 140 days onwards. Injection pressure guard ring tracks gas pressure while backpressure guard-ring appears insensitive to the change in gas pressure gradient. 40

Figure 4-38 Steady state flow rates plotted against excess gas pressure for both gas injection cycles, stage [6] to [21] and [25] to [27] respectively. 41

Figure 4-39 Out flow and volumetric strain plotted against time. Volumetric strain is estimated from the pre-test volume of the sample (Table 2-1) and the change in confining system volume. Negative strain represents dilation of the sample. 42

Figure 4-40 Volumetric strain plotted against STP flow rate for COx-1 showing a clear correlation between major gas flow and expansion (dilation) of the sample. 42

Figure 4-41 Gas discharged from sample COx-1 following submersion and gentle heating in a glycerol bath. [1] = injection face; [2] = backpressure face. 43

Figure 4-42 Cumulative flow from backpressure system from test stages [1] through [3] for sample COx-2. The backpressure response shows well defined transients associated with drainage of the argillite as confining stress is increased. The cumulative flow data has been edited between day 20 and 31 to correct for a pump problem. 44

Figure 4-43 Comparison on model output to test data for the first step of the consolidation test on sample 2. 45

Figure 4-44Figure 4-44 Comparison on model output to test data for the second step of the consolidation test on sample 2. 45

Figure 4-45 Comparison of observed guard ring pressures with the model simulation of the hydraulic test on sample 2. 46

Figure 4-46 Comparison of observed flow rates from the injection and back pressure filters with the model simulation of the hydraulic test on sample 2. 47

Figure 4-47 Comparison of observed guard ring pressures with a model simulation of the hydraulic test on sample 2 using a two layer representation of the sample. 48

Figure 4-48 Comparison of observed flow rates from the injection and back pressure filters with a two layer model simulation of the hydraulic test on sample 2. 48

Figure 4-49 Plot showing initial slug flow through specimen COx-2 during test stage [6]. 49

Figure 4-50 Plot showing the evolution in guard ring pressures and outflow due to changes in gas pressure gradient. The spike in data observed at around 257 days stems from the failure of the laboratory air conditioning system. However, it is clear from the GR response that this had no permanent effect on the behaviour of the claystone. 50

Figure 4-51 Detailed plot of guard ring and injection pressure evolution as gas begins to migrate through the sample.....50

Figure 4-52 Sample COx-2: material response during gas entry and subsequent breakthrough. Zone index: A = dewatering of IGR filter; A-B = migration of gas across the sample; C = out flow dominated by drainage of water BGR filter; D = as BGR filter is drained of water gas pressure increases; E = gas breakthrough occurs. 51

Figure 4-53 Sample COx-2: Out flow and volumetric strain plotted against time. Volumetric strain is estimated from the pre-test volume of the sample (Table 2-1) and the change in confining system volume. Negative strain represents dilation of the sample. The grey dotted line indicates the point at which confining stress was increased, stage [22]. 52

Figure 4-54 Sample COx-2: material response as gas pressure gradient and thereafter confining pressure are increased. 52

Figure 4-55 Evolution of flow and pressure after gas testing. Positive flux indicates flow out of the sample. Injection and backpressure filter pressures were maintained constant at 4.5 MPa during this stage of testing. 53

Figure 4-56 Cross plot of outflow against backpressure guard ring from day 60 to 120, showing cyclic behaviour between flow and GR pressure as the sample degasses. 54

Figure 4-57 The material components and mesh of the quarter cylinder flow model used for simulation of the hydraulic test for sample COx-3.....56

Figure 4-58 Comparison of an isotropic permeability model with flow data for sample COx-3. 56

Figure 4-59 Comparison of an isotropic permeability model with guard ring pressure data for sample COx-3. 57

Figure 4-60 Comparison of an anisotropic permeability model with flow data for sample COx-3. 57

Figure 4-61 Comparison of an anisotropic permeability model with guard ring pressures for sample COx-3. 58

Figure 4-62 Comparison of an anisotropic permeability model with end surface leakage to flow data for sample COx-3. 58

Figure 4-63 Comparison of an anisotropic permeability model with end surface leakage to guard ring pressures for sample COx-3. 59

Figure 4-64 Comparison of an isotropic permeability model with end surface leakage to flow data for sample COx-3. 59

Figure 4-65 Comparison of an anisotropic permeability model with end surface leakage to guard ring pressures for sample COx-3. 60

Figure 4-66 Evolution in pressure within sample COx-3 and outflow during test stages [6 to 10]. The small emergent flux is symptomatic of a low gas breakthrough pressure. 60

Figure 4-67 Evolution in pressure within sample COx-3 and outflow during test stages [11 to 13]. 61

Figure 4-68 Cyclic behaviour between backpressure guard ring and outflow response indicating pathways formation and closure in response to changes in local gas pressure. 62

Figure 4-69 Cross plot of outflow versus backpressure guard ring from day 225 to 260. The underlying cyclic behaviour between flow and pressure becomes clear, with the arrow indicating the direction of the response. 62

Figure 4-70 Evolution in guard ring pressure and outflow during stage [13], test COx-3. 63

Figure 5-1 The main elements and calculational mesh used for the TOUGH2 models of the gas injection test. Cylindrical symmetry about the z-axis is assumed. ...65

Figure 5-2 Relative permeability data compared to the models presented in sections 5.1, 5.2, and 5.3 below. 65

Figure 5-3 Initial model pressures compared to guard-ring data from sample 1. 67

Figure 5-4 Initial model flow rates compared to the injection and backpressure filter data from sample 1. 68

Figure 5-5 Pressures from a model fitted to the gas breakthrough time at the backpressure filter compared to test data from sample 1. 69

Figure 5-6 Flow rates at the injection and backpressure filters from a model fitted to the gas breakthrough time compared to test data from sample 1.....70

Figure 5-7 Pressures from a model fitted to the gas flow rates at the backpressure filter compared to test data from sample 1. 71

Figure 5-8 Flow rates at the backpressure filter from a model fitted to the gas flow rates compared to test data from sample 1. 72

Figure 6-1 Contour plots of gas saturation (SG) at two times from the model of Section 5.3. 78

Figure 6-2 Axial profiles of gas saturation (S_g) and relative permeability of the gas phase (k_{rg}) at two times from the model of Section 5.3.....79

Figure 6-3 Data from Angeli et al. (2009), showing a significant change in radial strain prior to and during gas breakthrough for a test performed on Draupne shale taken from the Troll East Field in the Norwegian Section of the North Sea. The change in P-wave velocity following breakthrough is symptomatic of gas penetration of the fabric due to the change in compressibility of the CO_2 compared with that of the original porewater. 80

TABLES

Table 2-1 Provisional basic physical properties of the test specimens from pre-test measurements of water content from off-cut material adjacent to the core. An assumed specific gravity for the mineral phases of 2.70 $Mg.m^{-3}$ (Zhang et al. 2007) was used in these calculations. 5

Table 4-1 Experimental history for specimens COx-1 and COx-2 showing the initial test stages. CO = consolidation stage; CPH = constant pressure hydraulic stage; PRH = pressure recovery hydraulic stage; CPG = constant pressure gas stage; CFG = constant flow rate gas stage, PDG = pressure decay gas stage. 11

Table 4-2 Provisional consolidation data for test specimen during test stages [2] and [3]. The start value for void ratio [1] is based on the pre-test measurement. Values for Young's modulus are based on a Poisson's ratio of 0.3 (Wileveau and Bernier, 2008). Values in parentheses are derived from finite element modelling.....12

Table 4-3 Summary of the steady-state gas results for test stages [9] through [27]. Analysis of the flux data indicates breakthrough pressure for initially water saturated conditions in the range 1.9 to 2.2 MPa.....33

Table 4-4 Provisional consolidation data for test specimens COx-1, -2 and -3 during test stages [2] and [3]. The start value for void ratio [1] is based on the pre-test measurement. Values for Young's modulus are based on a Poisson's ratio of 0.3 (Wileveau and Bernier, 2008). Values in parentheses are derived from finite element modelling. Data for test COx-2 and -3 are provisional as testing is on-going at the time of writing. 44

Summary

This report describes the status of an ongoing experimental study to measure the two-phase flow behaviour of the Callovo-Oxfordian argillite from the Bure underground research laboratory (URL) in France. Funding for this study has been provided by the French radioactive waste management operator, Andra, the European Union (FORGE Project) and the British Geological Survey through its well-founded laboratory programme and the Geosphere Containment project (part of the BGS core strategic programme).

The primary objectives of the study are to measure: (i) the hydraulic conductivity and intrinsic (absolute) permeability; (ii) the (threshold) capillary displacement pressure; (iii) the effective gas permeability and relative permeability to gas for a range of conditions; and (iv) the post-test gas saturation. Hydraulic testing was undertaken using a synthetic interstitial fluid. Helium was used in gas testing. Both tests described in part in this document, were performed on specimens orientation perpendicular to the bedding plane.

Cylindrical specimens of Callovo-Oxfordian clay are subject to an isotropic confining stress simulating *in situ* conditions, with fluids injected through the base of the specimen. Initial results are divided into three components: resaturation and consolidation; hydraulic properties (measured using a synthetic interstitial fluid); gas behaviour (using helium, a safe substitute for hydrogen, as the test permeant).

Analysis of the consolidation data based on the total volume of fluid expelled yields reasonable high values for the drained bulk modulus ranging from 1490 MPa to 2262 MPa. This reflects the indurated nature of the material and suggests little, if any, damage has occurred between field sampling and laboratory testing. Commensurate values for Young's modulus were found to range from 1764 MPa to 2629 MPa. Finite element coupled deformation and porewater flow modelling of the consolidation data yielded axial permeabilities ranging from 2.5 to 4.0×10^{-21} m^2, with radial permeability in the range 6.6 to 10.6×10^{-21}. It should be noted that as confining stress increased, axial and radial permeability both decreased slightly. Estimates for specific storage (based on Young's modulus and Poisson's ratio) were found to vary from 7.2×10^{-6} m^{-1} to 8.9×10^{-6} m^{-1}.

Uncoupled finite element porewater flow models were created to simulate the hydraulic tests. It was found that anomalous guard-ring pressures strongly suggest the occurrence of leakage flows across the axial surfaces. The modelling showed that in these circumstances the hydraulic anisotropy could not be reliably determined but good estimates for the axial component of permeability could be obtained. Samples COx-1 and COx-2 yielded values of 1.8×10^{-21} m^2 and 1.6×10^{-21} m^2 respectively for permeability perpendicular to bedding. Sample COx-3 gave a value of 4.5×10^{-21} m^2 for permeability parallel to bedding. Averaging the values from the first two samples gives an estimate of 2.65 for the anisotropy. Specific storage was found to range from 5.4 to 6.0×10^{-6} m^{-1}.

The gas pressure gradient across sample COx-1 was slowly increased in a step-wise manner from 6.5 MPa to 12.0 MPa over a 600 day period. A small emergent flux was noted (common to many tests) during the early stages of testing, which was found to vary with the magnitude of the gas pressure. While analysis of the data suggests this is aqueous in nature, post-test analysis of the sample indicated no measureable desaturation, indicating the fluid was not from the original porosity of the claystone. However, data from COx-2 clearly illustrates slug flow occurred at the onset of gas testing which may account for part of the emergent flux. Displacement of water by gas from the guard ring filters may also contribute to these flows. However, further work is required to differential these potential sources in order to better define the origin of the flux and the initiation of gas breakthrough.

In COx-1, estimates for the gas entry pressure close to the inlet were found to vary between 0.9 MPa and 1.3 MPa. These values are low and probably reflect localised features within the argillite. In contrast data from COx-2 yielded a high gas entry pressure of 5.6 MPa which may be more representative of intact (undamaged) COx material. However, further work is required to confirm this hypothesis. While identifying the gas entry pressure for test COx-3 was not the primary objective, data suggest the gas entry pressure was between 1 and 3 MPa.

The relatively low gas entry values of COx-1 suggest the discrete features are discontinuous and that gas is unable to propagate across the sample. Further increments in pressure were required to initiate gas breakthrough which occurred, in the case of COx-1, between 1.9 and 2.2 MPa.

In all test samples, analysis of flux and pressure data indicates dynamic flow behaviour and time-dependent propagation of gas pathways across the specimens. These pathways appear unstable, evolving both spatially and temporally within the claystone.

Increments in gas pressure clearly show the slow temporal evolution of gas permeability within the specimens, with flux taking from 20 (COx-1) to 250 days (COx-2) to attain a quasi-steady state. These differences may reflect heterogeneities within each sample with 'damaged' material/clay containing conductive features, attaining steady state more quickly than intact material. This time dependency can be explained by time-dependent drainage (porous medium concepts) or pressure induced dilatancy and accompanied drainage, depending on the mechanism invoked. However, spontaneous increases/decreases in both guard-ring pressures and downstream flux occur throughout testing and are difficult to reconcile with standard porous medium concepts and with post-test measurements of desaturation. Initial attempts to define a saturation verses gas pressure function yielded totally unrealistic data.

Triaxial measurements by Cuss and Harrington (2012) clearly measure time-dependent deformation processes occurring in COx during the onset of gas flow. Similar volumetric responses (i.e. increases in sample volume) were observed for all isotropic samples though the magnitude and detail of the response varied between specimens. In both COx-1 and COx-2 data suggests some form of stress relaxation may occur during steady-state, though the cause for this response remains unclear. However, the underlying mechanisms controlling the interaction between the stress state variable (stress, gas and porewater pressure) remains unclear and further work is required to better understand these relationships.

Preliminary mapping of the 'drainage/imbibition' response of the claystone in test COx-1 indicates hysteresis in the flow response between ascending and descending flow histories. Analysis of the post-test saturation for specimen observed no measurable desaturation. As such, the underlying cause for this apparent hysteresis is unclear but may relate to time-dependent processes associated with the creation and subsequent closure of dilatant gas pathways.

Estimates for the apparent capillary threshold value (i.e. the point at which gas ceases to be mobile within the clay), were obtained for test COx-1 by non-linear extrapolation. This yielded a value of around 1.0 MPa, close to the original gas entry pressure.

Measurement of the hydraulic properties after extensive gas testing yielded similar values for hydraulic permeability. However, specific storage was found to increase considerably, probably due to the presence of residual gas.

Repeat gas injection measurements to examine self-sealing behaviour (after hydraulic testing) indicated hysteresis between drainage/imbibition responses was almost nullified by reinjection of water and that under these conditions the previous gas injection history has little permanent impact on the structure and fabric of the clay.

Degassing experiments to examine localisation of gas flow within the core (as inferred by the flux and guard ring pressure responses), indicated a lower density of gas pathways on the injection face compared to that of the backpressure end. Intuitively, this is to be expected and is symptomatic of an expanding network of pathways which fan out as they propagate through the

core. While this method of observation is not fully quantitative, it strongly suggests gas flow is localised within the clay, an observation supported by the non-uniform distribution of flow and the anisotropy in the strain measurements reported by Cuss and Harrington (2012).

Preliminary numerical modelling of the gas data has been undertaken using TOUGH2 and a series of characteristic function parameters based on the van Genuchten formulation. However, initial attempts to model the data in its entirety, have to date, proved elusive. By alteration of the residual saturation and gas permeability functions, it is possible to fit sections of the data to the model predictions. However, this is often to the detriment of other experimental data. Consistent functional fits to the guard-ring pressure responses have not been possible, although fits to discrete sections of the data can be achieved. Following multiple simulations it can be seen that standard porous medium models that reproduce the time of gas breakthrough give flow rates much lower than that observed. In contrast, models that generate flow rates comparable with the data breakthrough much earlier than observed.

While the exact mechanism(s) controlling gas entry and the evolution of permeability within the argillite remain unclear at this stage of testing, the inability of standard porous medium models to adequately describe the data, combined with the complex and time-dependent evolution of parameters observed above, suggest that dilatancy plays a significant role in the movement of gas through the Callovo-Oxfordian argillite. Gas flow appears focused along a localised network of pathways, with no measureable water displacement. Based on the experimental observations, a new conceptual model for gas flow has been developed, where the advective movement of gas is accompanied by measurable dilation of the clay. In these experiments, gas flow is along pressure-induced preferential pathways, where permeability is a dependent variable related to the number, width and aperture distributions of these features.

1 Introduction

Movement of repository gases through argillaceous host rocks will occur by the combined processes of molecular diffusion (governed by Fick's Law) and bulk advection. In the case of a repository for radioactive waste, corrosion of ferrous materials under anoxic conditions will lead to the formation of hydrogen. Radioactive decay of the waste and the radiolysis of water will produce additional gas. If the gas production rate exceeds the rate of diffusion of gas molecules in the pores of the clay barrier, it is possible that a discrete gas phase could form (Horseman et al. 1996; Galle, 2000; Ortiz et al. 2002). Gas would continue to accumulate until its pressure becomes sufficiently large for it to enter the engineered barrier or host rock. There is now a general consensus that in the case of plastic clays and in particular bentonite, classic concepts of porous medium two-phase flow are inappropriate and continuum approaches to modelling gas flow may be questionable depending on the scale of the processes and resolution of the numerical model. The mechanisms controlling gas entry, flow and pathway sealing in general clay-rich media are not yet fully understood. The "memory" of dilatant pathways within a mudrock could impair barrier performance.

To investigate these issues the British Geological Survey (BGS), was approached by the French radioactive waste management company Agence Nationale pour la Gestion des Déchets Radioactifs (Andra), to perform a series of laboratory-scale tests on preserved samples of the Callovo-Oxfordian argillite, a candidate host rock for the storage of radiaoctive waste material in France. This work was undertaken within the auspices of the "Transfert de Gaz" initiative. Funding for the study was provided by Andra and the BGS through its well-founded laboratory programme and the Geosphere Containment project (part of the BGS core strategic programme). This programme of work has now been combined with a second study on gas transfer mechanisms funded through the European Union 7th framework Euratom Programme under the auspices of the Fate of repository Gases (FORGE) project.

1.1 OBJECTIVE OF STUDY

The objective of the proposed study is to define the conditions under which gas (present as a discrete gas-phase) will be mobile in laboratory specimens of Callovo-Oxfordian argillite and quantify the gas entry pressure and the gas permeability of the specimens using a combination of controlled flow rate and constant pressure methodologies. Intrinsic permeability (to a synthetic pore solution) will also be measured. Two flow directions will be examined: (a) parallel to bedding, and (b) normal to bedding. Each experiment will take in excess of one year to complete depending on the complexity of the planned test. A minimum of two tests will be completed during the study.

The primary objectives of this experimental study are to measure:

(a) the hydraulic conductivity and intrinsic (absolute) permeability;

(b) the (threshold) capillary displacement pressure;

(c) the effective gas permeability and relative permeability to gas for a range of conditions;

(d) the post-test gas saturation.

2 Experimental system

The basic permeameter (Figure 2-1) consists of five main components: (1) a specimen assembly, (2) a 70 MPa rated pressure vessel and associated confining pressure system, (3) a fluid injection

system, (4) a backpressure system, and (5) a PC-based data acquisition system. The specimen is subject to an isotropic confining stress, with injection platen mounted on the base of the specimen. A novel feature of the apparatus is the use of porous annular guard-ring filters around the inflow and outflow filters. The pressures in these two guard-rings can be independently monitored. The advantages of the guard-ring approach are: (a) pore pressure evolution can be studied, (b) hydraulic anisotropy can be quantified in a single test, (c) a check can be made of flow symmetry in the specimen, (d) excess gas pressure at gas entry can be determined, and (e) uncertainties associated with possible sheath leakage can be eliminated from data interpretation. Permeants (gas and water) are injected at the base of the specimen to minimise the chance of slug flow during gas testing.

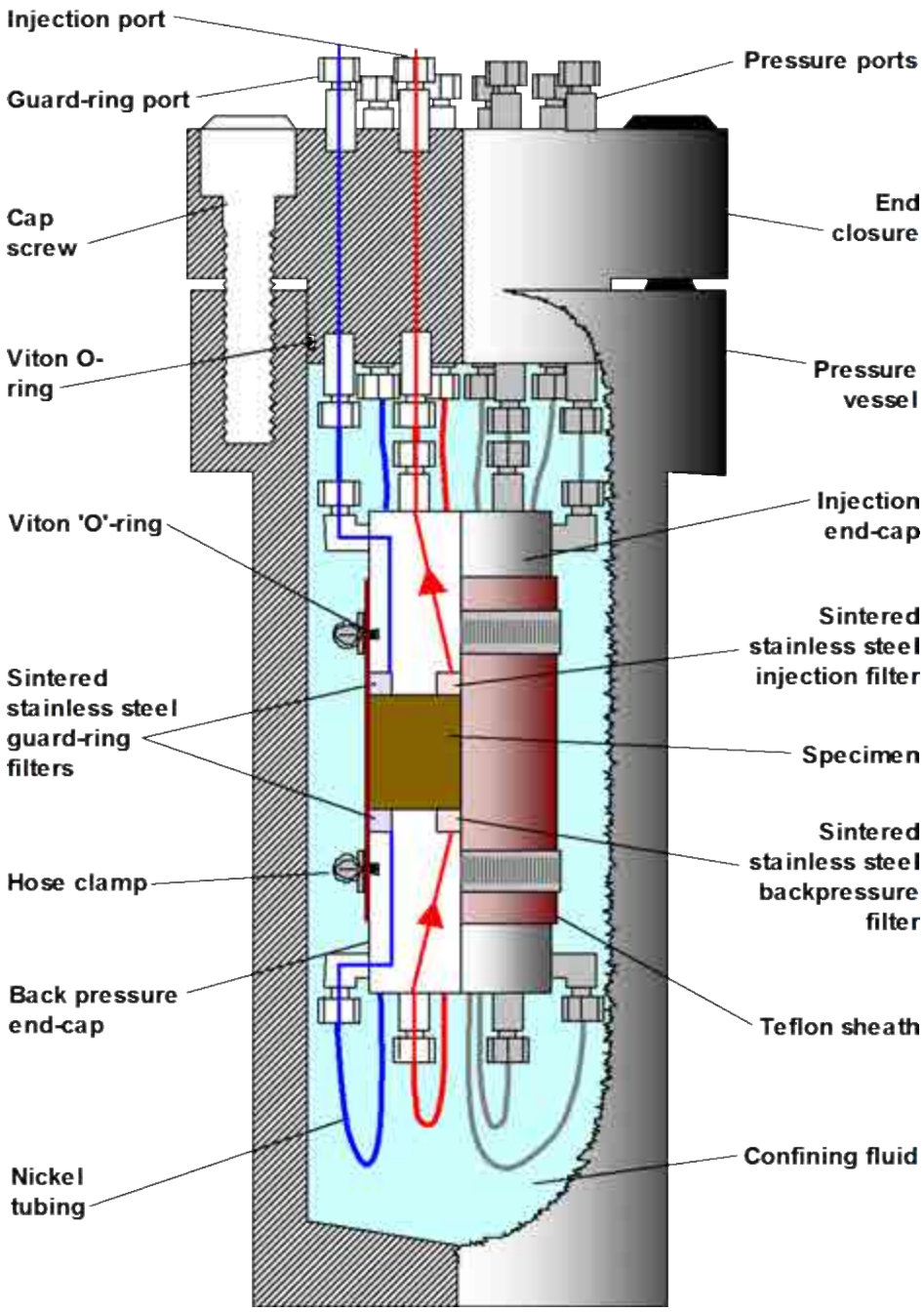

Figure 2-1 Schematic diagram of the pressure vessel and sample assembly for the BGS guard-ring permeameter. The pressure vessel is a custom-built stainless steel vessel rated to 70 MPa. The cylindrical clay specimen is sandwiched between two stainless steel end-caps, each with two filters recessed into the load-bearing surface, and jacketed in heat shrink Teflon to exclude the confining fluid.

The test specimen is sandwiched between two stainless steel end-caps and jacketed in heat-shrink Teflon to exclude confining fluid. Tapered locking rings compress the Teflon against two Viton "O"-rings in each end-cap to provide a leak-tight seal. The inlet and outlet zones for water or gas flow through the specimen are provided by porous filter discs 20 mm in diameter which are recessed into the bearing surface of the end-caps (Figure 2-1). These act as either source or sink for the injection of test permeants. Annular guard-ring filters with an internal diameter of 48.4 mm and an external diameter of 54.4 mm are recessed into the end-caps so that they completely encircle the inlet and outlet filters. A seal between the guard-ring and source/sink filters is achieved through the application of the confining stress, compressing the carefully machined surface of each platen against the clay. During hydraulic measurements, all the filters are saturated with an aqueous porewater solution.

Volumetric flow rates are controlled or monitored using a pair of ISCO-260, Series D, syringe pumps operated from a single digital control unit. The position of each pump piston is determined by an optically encoded disc graduated in segments equivalent to a change in volume of 16.6 nL. Movement of the pump piston is controlled by a micro-processor which continuously monitors and adjusts the rate of rotation of the encoded disc using a DC-motor connected to the piston assembly via a geared worm drive. This allows each pump to operate in either constant pressure or constant flow modes. A programme written in LabVIEW^{TM} elicits data from the pump at pre-set time intervals. Testing is performed in an air-conditioned laboratory at a nominal temperature of 20 ºC. A typical test history comprises a sequence of test stages, each designed to examine a particular system response, as described in Section 2.4.

2.1 TEST CONDITIONS

In order to limit osmotic swelling of the specimen, a synthetic porewater solution was prepared for use as the backpressuring fluid and permeant during hydraulic test stages. Details of the hydrochemistry of the interstitial fluid were provided by Andra. A stock solution comprised of the following components was used as the aqueous test fluid in all hydraulic and consolidation test stages: Ca^{2+} (227 mg l^{-1}); Mg^{2+} (125 mg l^{-1}); Na^{+} (1012 mg l^{-1}); K^{+} (35.7 mg l^{-1}); SO_4^{2-} (1266 mg l^{-1}); S_i (4.59 mg l^{-1}); S_iO^2 (9.83 mg l^{-1}); S_r (13.5 mg l^{-1}); total S (423 mg l^{-1}); total Fe (0.941 mg l^{-1}). ICP-AES analysis of the stock solution was undertaken to verify the fluid composition. This fluid was saturated with fluorescein prior to testing. Post-test analysis of the core will be undertaken to try and identify the location and extent of the fluorescein within the sample. Helium gas (selected as a safe substitute for hydrogen) was used to measure the gas transport properties of the argillite. *In situ* (isotropic) confining stress data was provided by Andra with the initial confining stress nominally set to 12.5 MPa with a backpressure of 4.0 MPa.

2.2 TEST MATERIAL

The composition of the Callovo-Oxfordian argillite (150-160 Ma) can be divided in to three main constituents; clay, silt and carbonate. Wenk et al. (2008) reports these constituents (at the Bure site) as follows; clay 25-55 wt%, 23-44% carbonates and 20-31% silt (essentially quartz + feldspar). Clay minerals are reported to include illite and illite-smectite with subordinate kaolinite and chlorite. In the upper half of the formation the illite-smectite is disordered and contains 50-70% smectite interlayers, whilst in the lower half the illite-smectite is ordered (R=1 type) with lower contents (20-40%) of smectite interlayers (Wenk et al., 2008). Beds can contain common organic matter.

Other authors report compositions similar to these. Wileveau and Bernier (2008) quote values for quartz (18%), calcite (25%), clay minerals (55%; illite-smectite ~65%, illite 30%) and kaolinite and chlorite (2%) with subordinate feldspars, pyrite and iron oxides (2%). Esteban et al. (2006) report 35-60% clay minerals with the remaining shared by calcite and silt. Gaucher et

al. (2004) includes highly detailed mineralogical and chemical compositions of the sequence which are again in broad agreement with the above compositions.

The argillite was deposited under marine basin conditions during a period in which the Paris Basin was variously linked to the Atlantic and Tethyan Oceans, as well as to the London Basin and North Sea (Rousset and Clauer, 2003). Clay sedimentation is therefore considered to have two primary inputs; continental and oceanic. The argillite is over- and underlain by Oxfordian and Bathonian shelf limestones. It is primarily clayey at its base, then becomes increasingly silty and then increasingly calcareous at its top (Gaucher et al., 2004). A maximum clay content zone within the clayey base has been identified; this is interpreted to mark the inflection point (and interval of maximum flooding) from a lower transgressive sequence to an upper regressive sequence (Gaucher et al., 2004).

Upon receipt of the preserved T1-cell core barrels at BGS, the material was catalogued and stored under refrigerated conditions of 4°C (to minimise biological and chemical degradation) ready for future testing. Following several unsuccessful attempts to manufacture a suitable core plug because of discing of the core (Figure 2-2), a test specimen was finally prepared following sub-sampling of the core barrel (Figure 2-3) by a combination of dry core-drilling (with gas flushing and vacuum removal of fines) and diamond slicing. The ends of the sample were then surface ground flat and parallel to minimise “end-effects” during testing. The specimen was accurately measured using a digital micrometer and weighed. The curved surfaces of the specimen were covered with a thin coat of high-purity silicone sealant, providing a good seal between the Teflon sheath and the rock surface. Off-cuts from the coring process were weighed and oven dried to obtain an estimate of moisture content. The dimensions and provisional geotechnical properties of the specimen are given in Table 2-1.

Figure 2-2 Discing of the core during early attempts to prepare a suitable test plug. As core preparation techniques evolved this problem was virtually eliminated.

The initial test specimen, designated COx-1, was cut with the flow direction perpendicular to the bedding, and was taken from drilling core EST27367, dated 10/12/07 from location PAC1011, drilling interval 10.23m to 10.55m. The torque applied to the axial confining system of the T1-cell was around 18 Nm. Table 2-1 shows the preliminary pre-test physical properties of the specimens based on the moisture content of the off-cuts and a grain density of 2.70 Mg m^{-3}

(Zhang et al. 2007). The provisional data presented in Table 2-1 is in fairly good agreement with the generic values quoted by Zhang et al.. However, on the basis of the preliminary numbers for specimen COx-1, the current test sample would appear have a slightly lower porosity than average which is also reflected in the values for dry and bulk density.

A second test specimen was prepared in a similar manner to that described above. The sample was cut perpendicular to bedding from the next 100mm core segment from drilling core EST27367 (location PAC1011). This sample was designated COx-2. A third sample, cut parallel to bedding from core EST30341, was prepared on a machine lathe. The basic geotechnical properties for the material are presented in Table 2-1. The preliminary values obtained for CoX-2 is in line with those reported by Zhang et al. 2007. The minor differences in geotechnical properties between specimens COx-1 and -2 are illustrative of the localised heterogeneity within the Callovo-Oxfordian formation. However, while these small-scale variations in geotechnical properties are of only minor interest, their importance may increase when it comes to the interpretation of hydraulic and gas data.

Figure 2-3 Sub-sampling of the core barrel (by dry cutting using a diamond encrusted blade) prior to preparation of the specimen by diamond coring and surface grinding.

Specimen		Length (mm)	Diameter (mm)	Moisture content (%)	Bulk density (Mg m^{-3})	Dry density (Mg m^{-3})	Porosity (%)	Saturation (%)
COx-1	Pre-test	53.9	54.4	6.1	2.45	2.31	14.6	97
	Post-test	54.1	54.5	6.7	2.44	2.29	15.2	100
COx-2	Pre-test	55.0	54.4	6.6	2.41	2.26	16.5	91
	Post-test	-	-	-	-	-	-	-
COx-3	Pre-test	63.7	54.5	-	-	-	-	-
	Post-test	-	-	-	-	-	-	-
Zhang et al. 2008		-	-	7.7	2.41	2.25	16.8	-

Table 2-1 Provisional basic physical properties of the test specimens from pre-test measurements of water content from off-cut material adjacent to the core. An assumed specific gravity for the mineral phases of 2.70 Mg.m^{-3} (Zhang et al. 2007) was used in these calculations.

2.2.1 Petrographic Analysis of Linear Feature on Fractured Core Surface

Initial attempts to manufacture a suitable test sample were unsuccessful. On a number of failure planes, linear features were noted running through the core (Figure 2-4). An example feature was sent for analysis and the preliminary results of the ongoing study are presented below.

The linear feature is approximately and uniformly 2mm across (Figure 2-5) with a central dark grey portion that comprises finely granular iron sulphide (pyrite). The edges of this central portion are finely embayed and marked by a line of strontium sulphate (celestine) and framboidal pyrite that corresponds to a narrow strip of white-coloured sediment. Outside this the sediment is orange-brown in colour for a thickness of 200-300 microns; this sediment is enriched with iron oxide / hydroxide (Figure 2-6). This outer portion and the sediment beyond still contain iron sulphide in the form of scattered pyrite framboids; the dissolution and alteration of some of these has left scattered rounded pores lined by iron oxide / hydroxide (Figure 2-7).

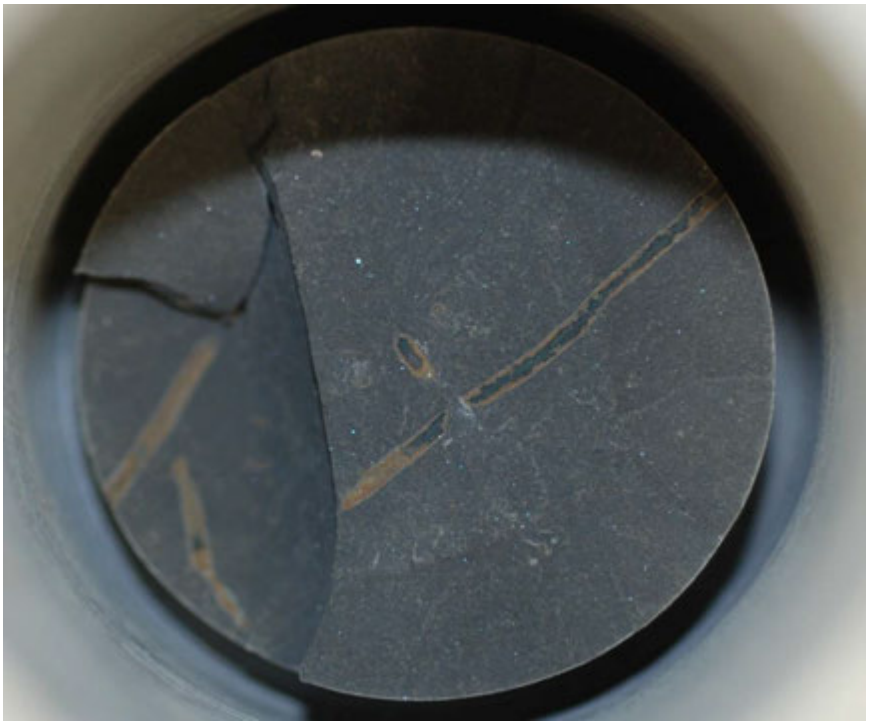

Figure 2-4 Photo looking longitudinally along the core showing a number of linear features crossing the core.

Other off-cuts from the same core contain oval features with cross-sections of 2-3mm with the same sequence of colours. These features were most likely deposited as organic matter, subsequently pyritised. The pyrite has then been partially oxidised along its margins, resulting in the formation of strontium sulphate and iron oxide / hydroxides. The features have a higher porosity than the surrounding sediment, particularly along the oxidation ‘front’ and may provide localised channels of enhanced permeability. Further work will focus on defining the vertical density of the features, on attempting to identify their typical lateral extents and to examine the origin of the oxidisation front.

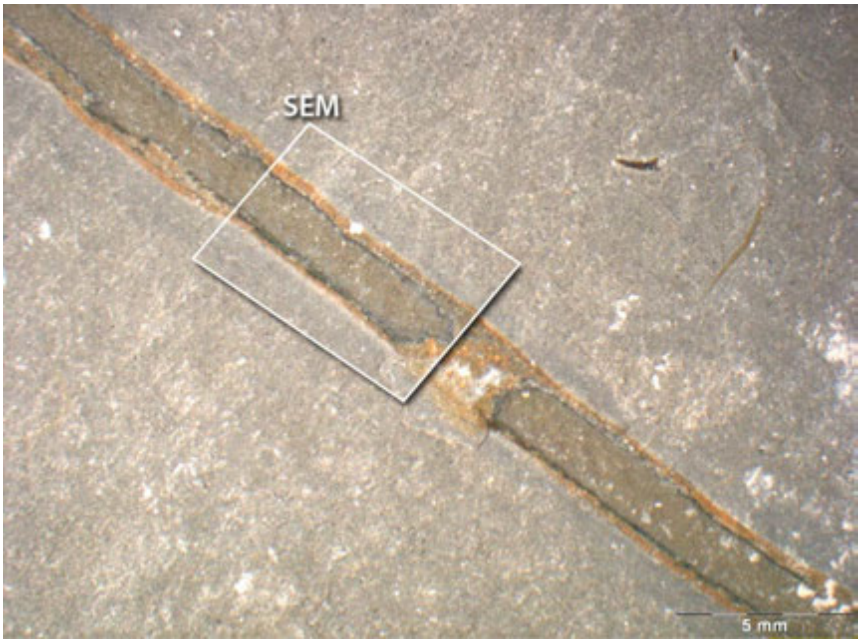

Figure 2-5 The linear feature is approximately 2mm across, dark grey in the central portion with orange-brown edges. Outside the orange-brown zone is a thin 'bleached' zone and outside this the sediment has a slightly darker grey colour for a further 1-2mm. Locally the edge between the dark grey interior and orange-brown zone is marked by a thin white zone. The edges of the dark grey interior are darker grey and iridescent. The box shows the area of the SEM image shown in Figure 2-6.

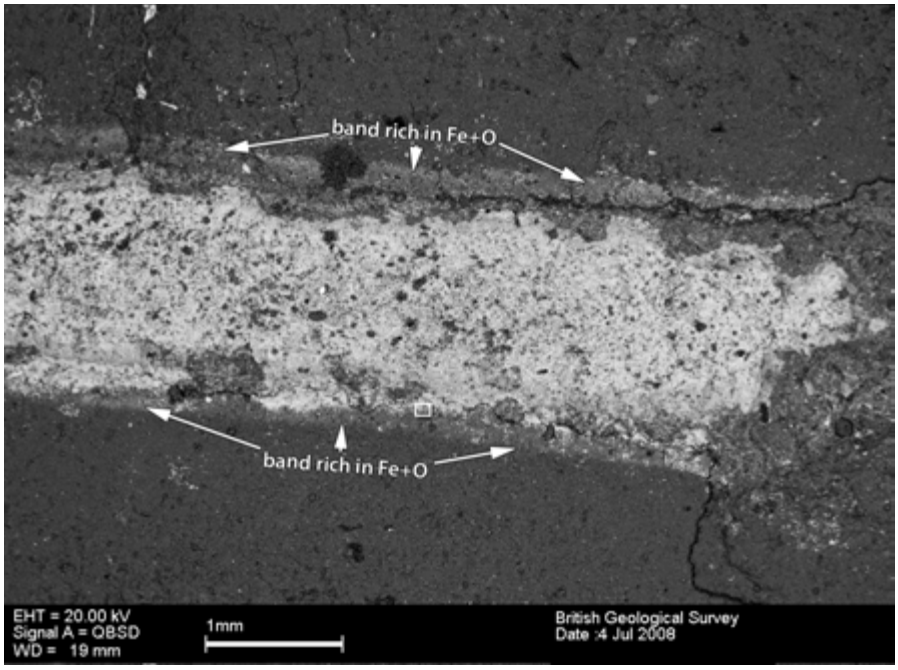

Figure 2-6 The central high brightness portion comprises finely granular iron sulphide (pyrite). The adjacent zones of intermediate brightness correspond to the orange-brown zones and record compositions rich in iron and oxygen (ED analysis), suggesting the presence of iron oxide / hydroxide. The embayment of the central portion suggests that it is the edges of the sulphide that have been altered and dissolved. The box, located on the boundary between these zones, shows the area of the SEM image shown in Figure 2-7.

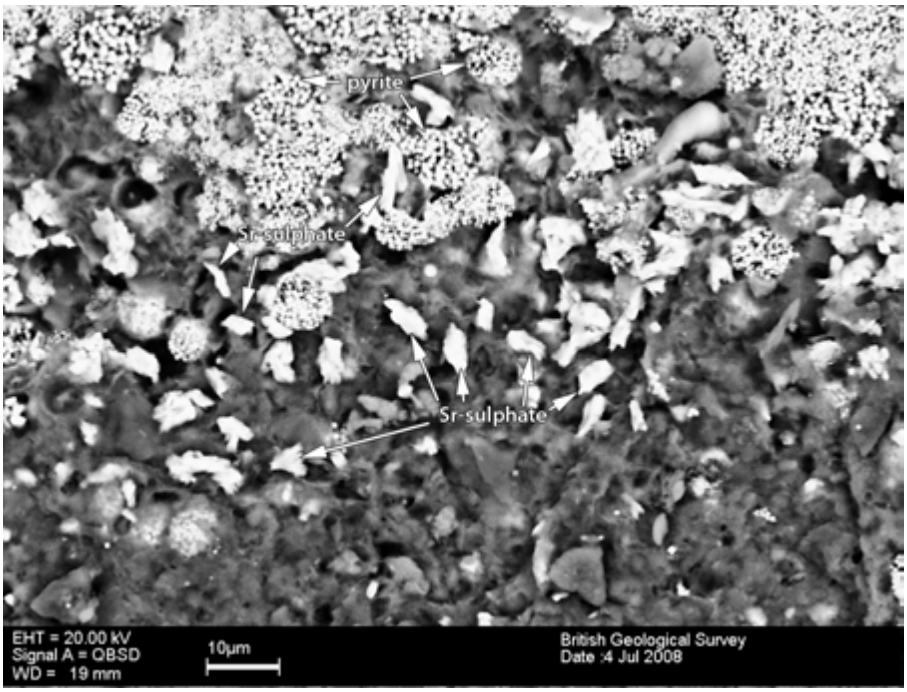

Figure 2-7 Detail of the edge of the iron sulphide (pyrite) inner zone, showing the presence of a thin band of strontium sulphate. This has formed as <10 micron euhedral and subhedral crystals. These are scattered amongst pyrite framboids, in contrast to the densely granulated inner structure of the linear feature.

2.3 CALIBRATION

All pressure sensors were calibrated against laboratory standards by applying incremental steps in pressure, from atmospheric to a pre-determined maximum value. This was followed by a descending sequence to quantify any hysteresis. Least-squares fits were calculated and the regression parameters used to correct raw data.

2.4 EXPERIMENTAL PROCEDURE

An individual test history comprises a sequence of test stages (Table 4-1). A consolidation (CO) stage involves incrementally raising confining pressure and measuring the volume of fluid displaced while backpressure (and injection pressure) are held constant. Constant pressure hydraulic (CPH) and gas (CPG) stages are used to evaluate the intrinsic permeability, specific storage, gas entry and breakthrough pressure, apparent threshold capillary pressure and gas permeability. At the end of hydraulic testing a pressure recovery stage (PRH) allows excess porewater pressures to dissipate (i.e. the injection pump is reset to the backpressure value and the flux and guard-ring pressure response monitored with time). Transient analysis of this data provides an alternative determination of the hydraulic properties. Synthetic groundwater solution is used as the backpressuring fluid in all test stages.

3Data reduction and modelling approaches

Moving average smoothing was applied to all flow data to remove background experimental noise associated with pump switching and minor diurnal variations in temperature.

3.1 HYDRAULIC FLOW

The equation of porewater flow is obtained by combining Darcy's Law with the equation of fluid mass conservation to give (de Marsily, 1986):

$$\frac{S_s}{\rho_w g}\frac{\partial p_w}{\partial t} = \nabla.\left(\frac{k_i}{\mu_w}\left(\nabla p_w + \nabla z\right)\right) + Q \tag{1}$$

where S_s is the specific storage (m^{-1}), k_i is the intrinsic permeability (m^2), ρ_w is the density of water ($kg.m^{-3}$), g is the acceleration due to gravity ($m.s^{-2}$), μ_w is the viscosity of water (Pa.s), p_w is the pore-water pressure (Pa), z is the vertical coordinate (m) and Q is the rate of fluid volume injection per unit volume of porous medium (s^{-1}). This equation is solved here by the finite element method for an axisymmetric two dimensional domain subject to specified head and specified flow boundary conditions. Hydraulic head, h (m), is related to the pore-water pressure by $p_w = \rho_w g(h-z)$.

In order to model the consolidation tests it is necessary to couple the porewater flow equation to equations for the stress-strain relationships. The porewater equation for this takes the form Huyakorn and Pinder (1983):

$$\nabla.\left(\frac{k_i}{\mu_w}\left(\nabla p_w + \rho_w g \nabla z\right)\right) = \phi\beta\frac{\partial p_w}{\partial t} + \frac{\partial}{\partial t}\left(\nabla.\mathbf{u}\right) \tag{2}$$

where ϕ is the porosity, β is the fluid compressibility (Pa^{-1}), and **u** is the vector of solid phase displacements (m). For the case of elastic plane strain, the equations for the displacements are

$$\frac{E}{2(1+\nu)}\nabla^2\mathbf{u} + \frac{E}{2(1+\nu)(1-2\nu)}\nabla\left(\nabla\cdot\mathbf{u}\right) - \nabla p_w = 0 \tag{3}$$

Here E is Young's modulus (Pa) and ν is Poisson's ratio. Equations (2) and (3) are solved using the finite element code STAFAN (Intera, 1983).

3.2 GAS FLOW

The equation for steady state flow of gas as a single phase in a porous medium may be written by combining the mass continuity equation with a generalisation of Darcy's law:

$$\nabla.\left(\frac{\rho_g k_g}{\mu_g}\nabla\left(p_g\right)\right) = 0 \tag{4}$$

where p_g is the gas pressure (Pa), ρ_g is the gas density ($kg.m^{-3}$), $k_g = k_{rg}\, k_i$ is the effective gas permeability (m^2), and μ_g is the gas viscosity (Pa.s). Assuming ideal gas behaviour and a constant value for k_g, equation (4) can be integrated along a 1D flow path to obtain an expression for the flow rate at STP, Q_{st}, in terms of the pressures at either end of the path:

$$Q_{st} = \frac{v_{mst} k_g A}{2RT\mu_g L}\left(p_{gi}^2 - p_{go}^2\right) \tag{5}$$

where v_{mst} is the molar volume of the gas at STP, A is the specimen's cross-sectional area, L is the specimen length, R is the gas constant, T is the absolute temperature, p_{gi} is the gas pressure at injection, and p_{go} the pressure at outlet. Although gas pressure p_{go} cannot be measured directly in these experiments, it can be related to the backpressure of the water at the downstream end of the specimen, p_{wo}, by the relationship $p_{go} = p_{wo} + p_{co}$, where p_{co} is the apparent capillary threshold pressure.

4 Provisional results and numerical modelling

The results and interpretation presented in the following sections are provisional and are subject to alteration once testing is complete.

4.1 CALLOVO-OXFORDIAN CLAY SAMPLE 1 (COX-1)

4.1.1 Consolidation behaviour

Following assembly of the apparatus an initial equilibration period of 15 days was applied to the specimen, with confining and backpressure both held constant at 9.5 MPa and 4.5 MPa respectively. During this time, flux into and out of the specimen were monitored to provide data on the resaturation of the clay (Figure 4-1). Simultaneously, changes in hydraulic volume of the confining system were also monitored to provide an estimate for the volume change of the specimen during hydration.

Examination of the data in Figure 4-1 clearly shows that at the onset of testing, a rapid uptake of water by the specimen is observed as the sample resaturates. This flux progressively declines with time, such that by around 12 days, the net flow of water into the specimen is practically zero. A similar, but less prominent response is also observed by the confining pressure pump, which indicates an increase in specimen volume as a result of time dependent swelling of the argillite. Comparison of the cumulative flow curves from the backpressure and confining systems indicate changes in volume of 1.72 ml and -0.56 ml respectively (the minus sign denoting swelling of the argillite). This suggests the net volume change due to resaturation of the clay is around 1.16 ml during stage [1]. This is in close agreement with pre-test measurements of saturation (Table 2-1), suggesting the bulk of the gas phase was resident in non-dilatant pores and that the specimen was in a good state of preservation at the time of emplacement.

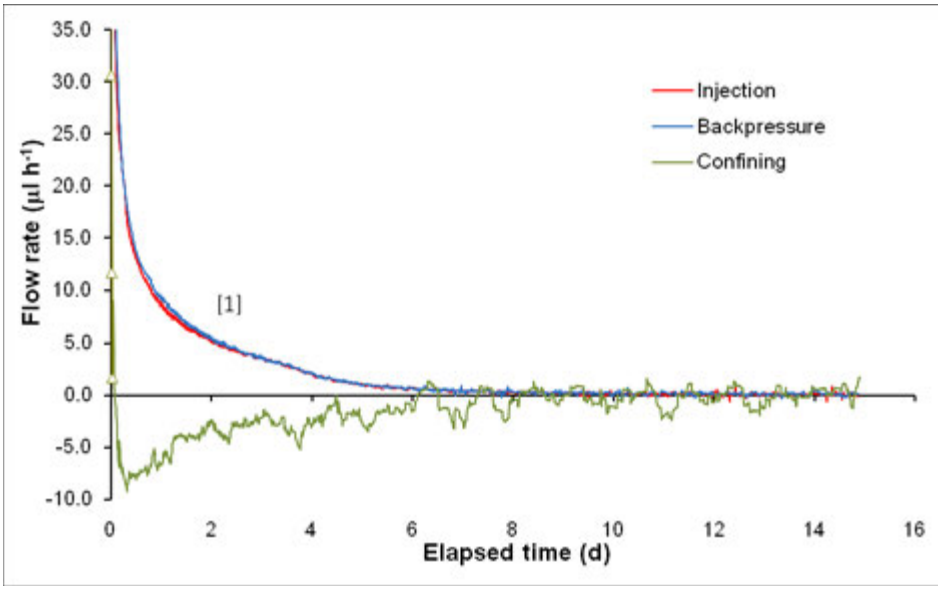

Figure 4-1 Flux response for backpressure and confining circuits during the initial the equilibration stage [1]. Positive flows for red and blue lines represent flux into the specimen. The negative flow for the green line denotes flux out of the pump system suggestive of time dependent swelling.

Stage no.	Specimen COx-1				Specimen COx-2				Specimen COx-3			
	Type	Confining pressure	Injection pressure	Back pressure	Type	Confining pressure	Injection pressure	Back pressure	Type	Confining pressure	Injection pressure	Back pressure
1	CO	9.5	4.5	4.5	CO	9.5	4.5	4.5	CO	9.5	4.5	4.5
2	CO	11.0	4.5	4.5	CO	11.0	4.5	4.5	CO	11.6	4.5	4.5
3	CO	12.5	4.5	4.5	CO	12.5	4.5	4.5	CO	12.5	4.5	4.5
4	CPH	12.5	7.5	4.5	CPH	12.5	7.5	4.5	CPH	12.5	7.5	4.5
5	PRH	12.5	4.5	4.5	PRH	12.5	4.5	4.5	PRH	12.5	4.5	4.5
6	CPG	12.5	6.5	4.5	CPG	12.5	7.5	4.5	CPG	12.5	4.5	4.5
7	CPG	12.5	7.0	4.5	CFG	12.5	7.5 to 8.0	4.5	CFG	12.5	4.5 to 5.5	4.5
8	CFG	12.5	7.0 to 7.5	4.5	CPG	12.5	8.0	4.5	CPG	12.5	5.5	4.5
9	CPG	12.5	7.5	4.5	CFG	12.5	8.0 to 8.5	4.5	CFG	12.5	5.5 to 7.5	4.5
10	CFG	12.5	7.5 to 8.0	4.5	CPG	12.5	8.5	4.5	CPG	12.5	7.5	4.5
11	CPG	12.5	8.0	4.5	CFG	12.5	8.5 to 9.0	4.5	CPG	12.5	7.5	6.5
12	CFG	12.5	8.0 to 8.5	4.5	CPG	12.5	9.0	4.5	CPG	12.5	9.5	6.5
13	CPG	12.5	8.5	4.5	CFG	12.5	9.0 to 9.5	4.5	CPG	12.5	9.5	8.5
14	CFG	12.5	8.5 to 9.0	4.5	CPG	12.5	9.5	4.5				
15	CPG	12.5	9.0	4.5	CFG	12.5	9.5 to 10.0	4.5				
16	CFG	12.5	9.0 to 10.5	4.5	CPG	12.5	10.0	4.5				
17	CPG	12.5	10.5	4.5	CFG	12.5	10.0 to 10.5	4.5				
18	CFG	12.5	10.5 to 12.0	4.5	CPG	12.5	10.5	4.5				
19	CPG	12.5	12.0	4.5	FG	12.5	10.5 to 11.3	4.5				
20	CPG	12.5	9.0	4.5	CPG	12.5	11.3	4.5				
21	CPG	12.5	7.0	4.5	CPG	12.5	12.3	4.5				
22	PDG	12.5	-	4.5	CPG	15.0	12.3	4.5				
23	CPH	12.5	7.5	4.5	CPH	15.0	4.5	4.5				
24	PRH	12.5	4.5	4.5								
25	CGP	12.5	7.5	4.5								
26	CFG	12.5	7.5 to 12.0	4.5								
27	CPG	12.5	12.0	4.5								
	Test complete											

Table 4-1 Experimental history for specimens COx-1 and COx-2 showing the initial test stages. CO = consolidation stage; CPH = constant pressure hydraulic stage; PRH = pressure recovery hydraulic stage; CPG = constant pressure gas stage; CFG = constant flow rate gas stage, PDG = pressure decay gas stage.

Once the equilibration stage was complete a two-step consolidation test was then performed. In the first step, stage [2], the confining pressure was raised to 11 MPa for 5 days and in the second step, stage [3], it was raised to 12.5 MPa for 8 days. Instantaneous flow rate and net cumulative flow volume data were collected (Figure 4-2), with the latter equating to volumetric strain. Inspection of the data show well defined transient responses for the backpressure system for each increment in confining stress. A similar response is noted for net flow out of the confining system though the transients here are less well defined, due to the mixed composition (gas and water) and large fluid volume of the confining system.

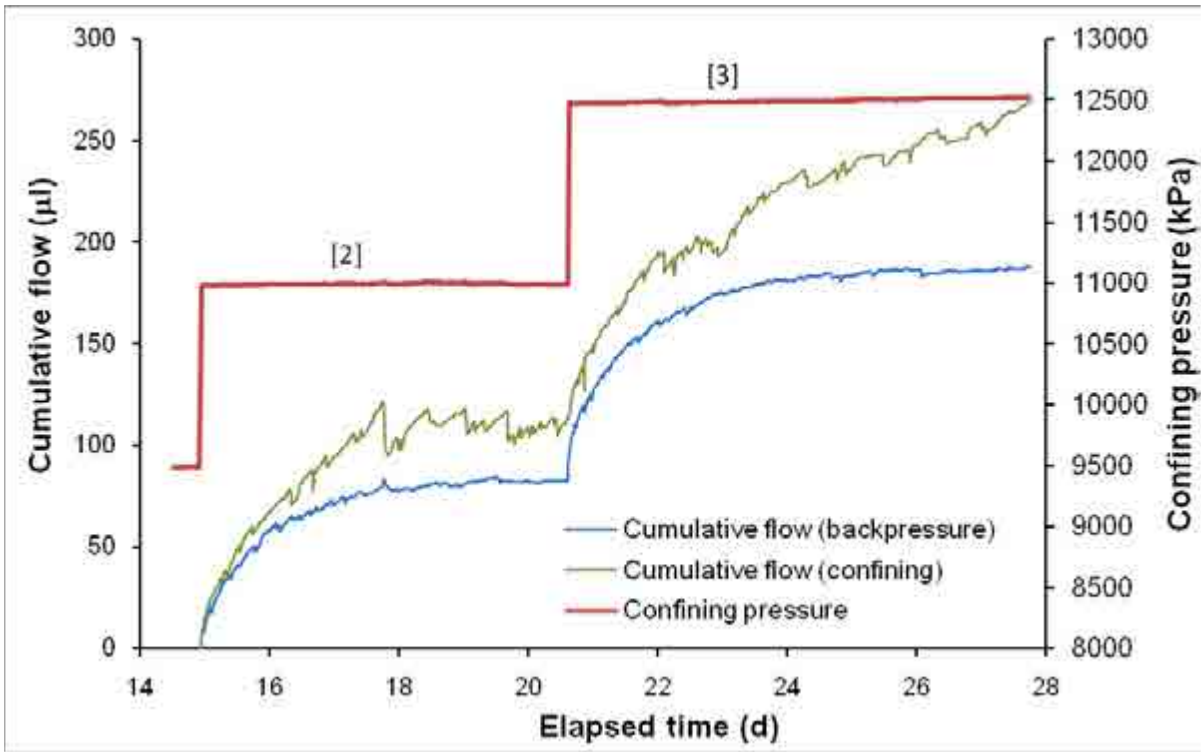

Figure 4-2 Cumulative flow from backpressure and confining systems from test stages [2] and [3]. The backpressure response shows well defined transients associated with drainage of the argillite as confining stress is increased.

Stage no.	Ave. effective stress (MPa)	Void ratio (at end of stage)	Volumetric strain (%)	Drained compressibility $\beta/10^{10}$ (Pa^{-1})	Drained bulk modulus (MPa)	Young's modulus (MPa)
1	5.0	0.175	-	-	-	-
2	6.5	0.174	0.07	4.4	2262	2629 [1825]
3	8.0	0.173	0.16	6.4	1574	1870 [1700]

Table 4-2 Provisional consolidation data for test specimen during test stages [2] and [3]. The start value for void ratio [1] is based on the pre-test measurement. Values for Young's modulus are based on a Poisson's ratio of 0.3 (Wileveau and Bernier, 2008). Values in parentheses are derived from finite element modelling.

Analysis of the consolidation data based on the total volume of fluid expelled from the specimen at the end of each step is presented in Table 4-2. Following each increment in confining stress the specimen exhibits a very small reduction in volume. Values for drained bulk modulus are therefore reasonably high, ranging from 1574 MPa to 2262 MPa, reflecting the indurated nature of the material. These values suggest that the specimen has not suffered significant damage from de-stressing during sampling, transportation and specimen preparation. Young's modulus values were found to range from 1870 MPa to 2629 MPa.

A finite element coupled deformation and porewater flow model of the experimental configuration was created to simulate the test. The two steps were found to differ slightly in the parameters required to best fit the data and so have been interpreted separately. The hydraulic anisotropy obtained from the hydraulic tests of all three samples discussed below (2.65:1 radial to axial) has been maintained for these models and a Poisson's ratio of 0.3 (Wileveau and Bernier, 2008) has been used throughout. The value of the Young's modulus was adjusted to fit to the magnitude of the net flow volume in each step whilst the permeability was adjusted to fit the transients.

The first step was fitted using an axial permeability of 4.0×10^{-21} m^2, a radial permeability of 1.06×10^{-20} m^2, and a Young's modulus of 1825 MPa. This value is significantly lower than that derived from the volumetric strain data, though the reason for this is unclear at present. It may be noted that the Young's modulus, E, and Poisson's ratio, ν, can be related to the solid phase compressibility, α, and the specific storage, S_s, by (de Marsily, 1986):

$$\alpha = \frac{3(1-2\nu)}{E} \tag{6}$$

and:

$$S_s = \rho g(\alpha + \phi\beta_l) \tag{7}$$

where ρ is the porewater density, g the acceleration due to gravity, ϕ the porosity, and β_l the compressibility of the porewater. From these equations it is found that a Young's modulus of 1825 MPa corresponds to a specific storage of 7.2×10^{-6} m^{-1}, slightly more than the value found from the hydraulic test. Figure 4-3 compares output from this model with the data from the test.

The second step was fitted using an axial permeability of 3.4×10^{-21} m^2, a radial permeability of 9.0×10^{-21} m^2, and a Young's modulus of 1700 MPa. This corresponds to a specific storage of 7.7×10^{-6} m^{-1}. Figure 4-4 compares output from this model with the data from the test. It appears that the permeability reduces slightly with the increase in confining pressure, and that there is a further small reduction when the hydraulic test is conducted.

4.1.2 Hydraulic test

For the hydraulic test the confining pressure was maintained at a constant level of 12.5 MPa whilst the porewater pressure at the back pressure filter was kept at 4.5 MPa. The pressure at the injection filter was raised to 7.5 MPa for 7.6 days after which it was returned to 4.5 MPa. Flows at injection and backpressure filters were monitored together with the pressures at the two guard rings. The pressure at the backpressure guard ring did not rise from that of the backpressure filter. This behaviour could potentially be the result of some degree of leakage across the axial surfaces of the samples during the experiment and additional models exploring this option are discussed below. A finite element porewater flow model of the experimental configuration was created to simulate the test and it was found that a good fit to the data could be obtained by setting axial permeability to 1.8×10^{-21} m^2 and radial permeability to 4.5×10^{-20} m^2. The latter value is difficult to reconcile with direct measurements of permeability parallel to bedding presented in Section 4.3.2. A specific storage of 5.4×10^{-6} m^{-1} was used to obtain a reasonable fit to the transients, although the injection guard ring pressure data just after each step change are

not well represented. Increasing the specific storage does improve these early time fits at the expense of poorer late time fits and poorer fits to the flow rate data. Figure 4-5 and Figure 4-6 show comparisons of the model output with these parameters to the data for guard ring pressures and filter flow rates respectively.

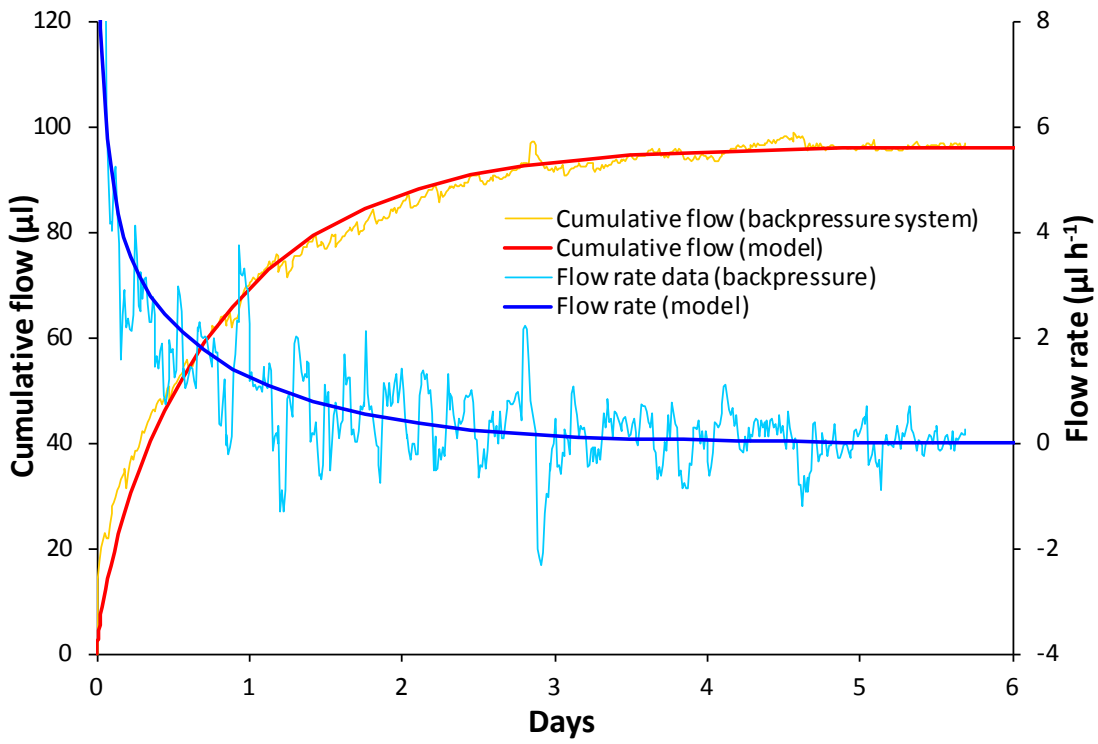

Figure 4-3 Comparison on model output to test data for the first step of the consolidation test, stage [2].

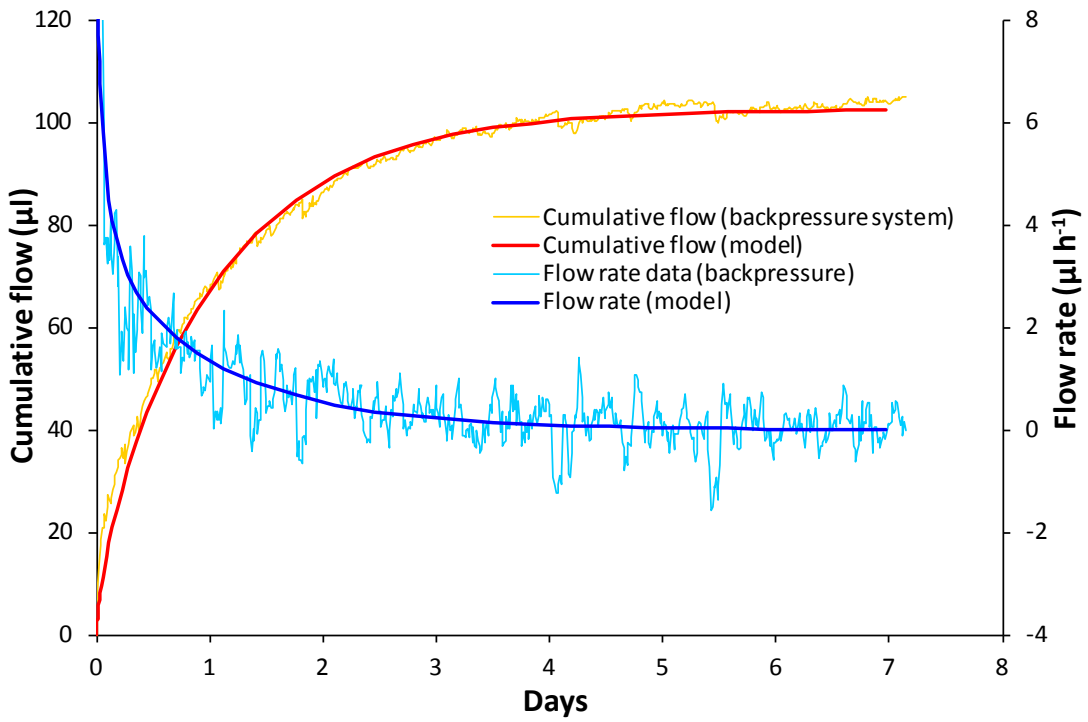

Figure 4-4 Comparison on model output to test data for the second step of the consolidation test, stage [3].

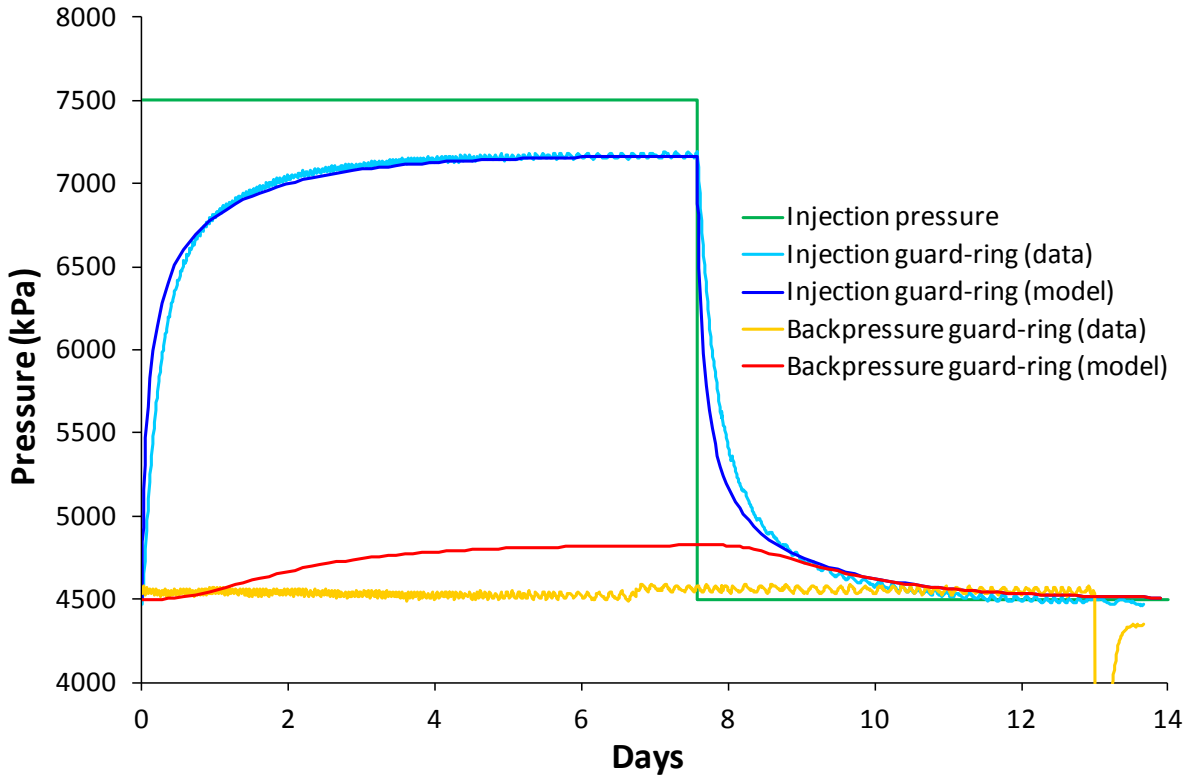

Figure 4-5 Comparison of observed guard ring pressures with the model simulation of the hydraulic test.

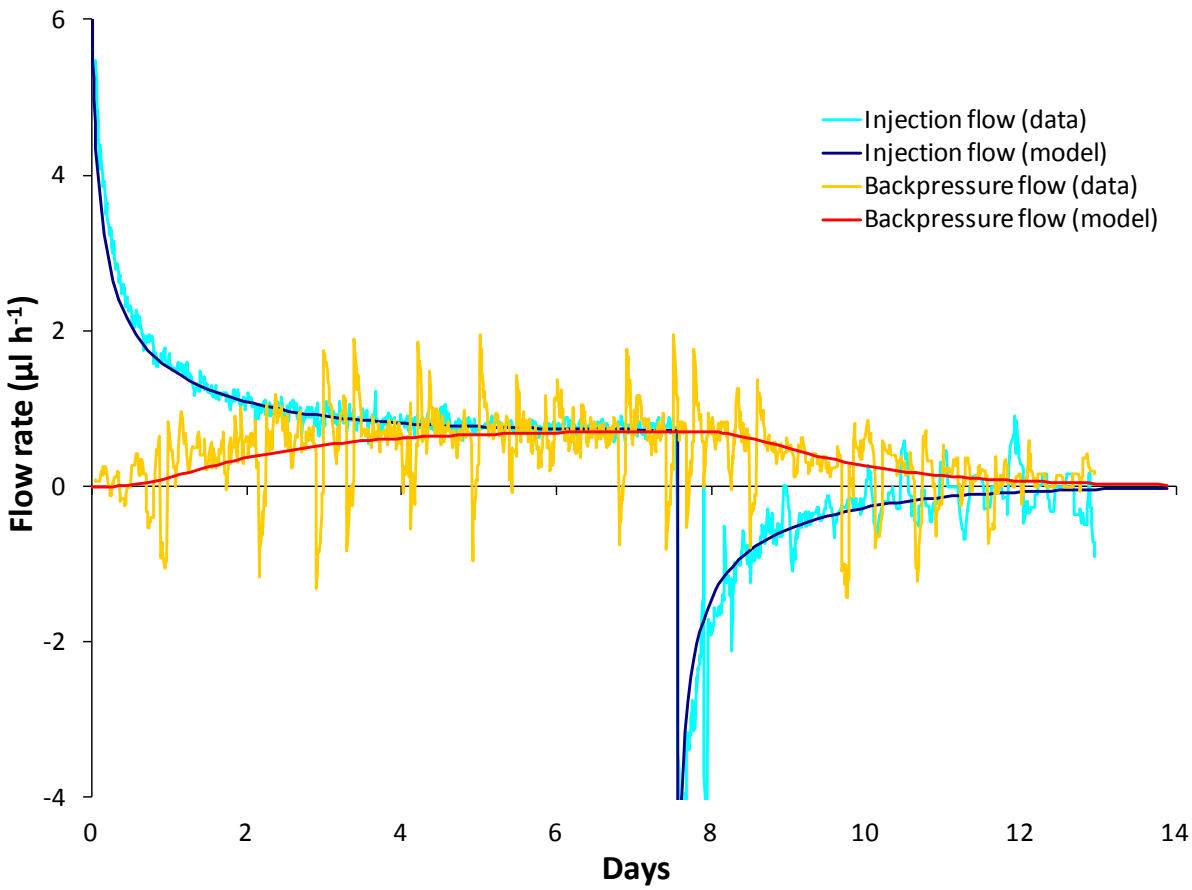

Figure 4-6 Comparison of observed flow rates from the injection and back pressure filters with the model simulation of the hydraulic test.

As noted above, the lack of any change in pressure at the backpressure guard-ring potentially indicates the occurrence of leakage over the surface of the sample. Similarly, the high degree of anisotropy required to explain the injection guard-ring pressures may also indicate some leakage over this surface too. To examine this possibility a second model was run in which elements between injection / backpressure filters and their respective guard-rings are given enhanced permeabilities, whilst the clay was set to an isotropic permeability of 1.8×10^{-21} m^2.

Figure 4-7and Figure 4-8 show that a good fit to the data, including the backpressure guard-ring pressures, can be obtained from this model. In this model the transmissivity (product of hydraulic conductivity and thickness) of the injection end surface is 5.0×10^{-16} m^2s^{-1} and of the backpressure end surface is 5.0×10^{-15} m^2s^{-1}. Further runs of this model with anisotropic permeabilities for the clay up to an anisotropy of 10 show that essentially identical results can be obtained with small adjustments to the transmissivity of the injection surface. Thus, for this model the anisotropy of the clay is undetermined in the absence of any independent information about the transmissivity of the axial surfaces. The estimate of axial permeability does appear to be robust however.

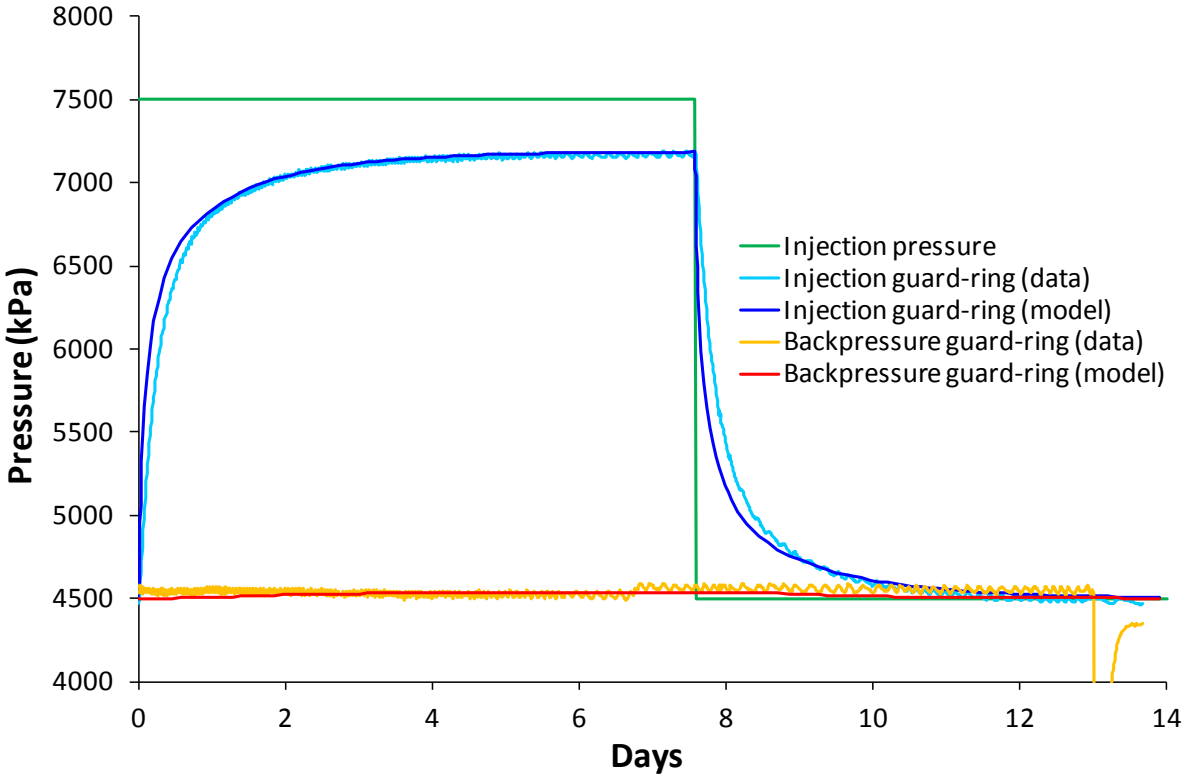

Figure 4-7 Comparison of observed guard ring pressures with the model simulation of the hydraulic test, using a model with isotropic clay and leakage over the axial surfaces.

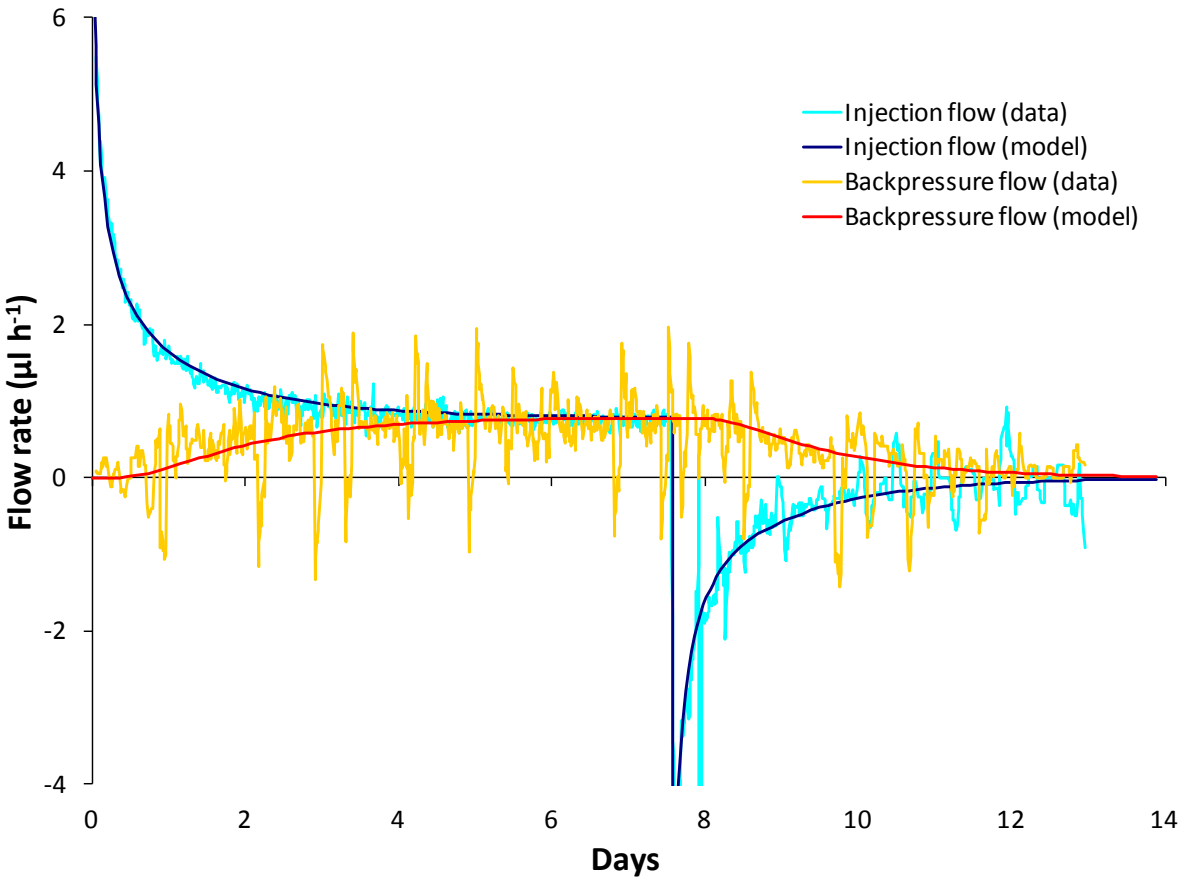

Figure 4-8 Comparison of observed flow rates from the injection and back pressure filters with the model simulation of the hydraulic test.

4.1.3 Gas injection

The gas pressure gradient across the sample has been slowly increased in a step-wise manner in order to investigate the mechanisms governing gas migration through the Callovo-Oxfordian clay. For each test stage the confining pressure and backpressure were maintained constant at values of 12.5 MPa and 4.5 MPa respectively. A list of test stages is presented inError! Reference source not found.. The pressure at the injection filter was raised from 6.5 MPa to 12 MPa in a series of 7 steps over 620 days. The first 5 steps were of 0.5 MPa and the last 2 were 1.5 MPa. The data obtained for pressures and flow rates are shown in Figure 4-9 and Figure 4-10. The data from the backpressure guard-ring is notable for the fact that it differs significantly from that of the backpressure filter only for a short period around 200 days into the test. The data from the injection guard-ring after about 180 days track the pressures at the injection filter very closely with an offset of only about 100 kPa. Before that time a number of anomalous features are seen in the injection guard-ring (Section 4.1.3.1). At the start of the test the injection guard-ring pressure declines from about 6.1 MPa to 5.0 MPa before abruptly rising again to about 5.8 MPa. That pressure is maintained until the injection pressure is stepped up to 7 MPa when the guard-ring pressure rises to about 6.5 MPa and remains at that level, with a slight decline, for the duration of the step. When the injection pressure rises to 7.5 MPa the guard-ring pressure initially follows but falls back by about 150 kPa for a period before rising again at about 180 days to a pressure that is about 100 kPa below the injection pressure. This offset remains consistent for the duration of the test, ranging from 100 to 135 kPa.

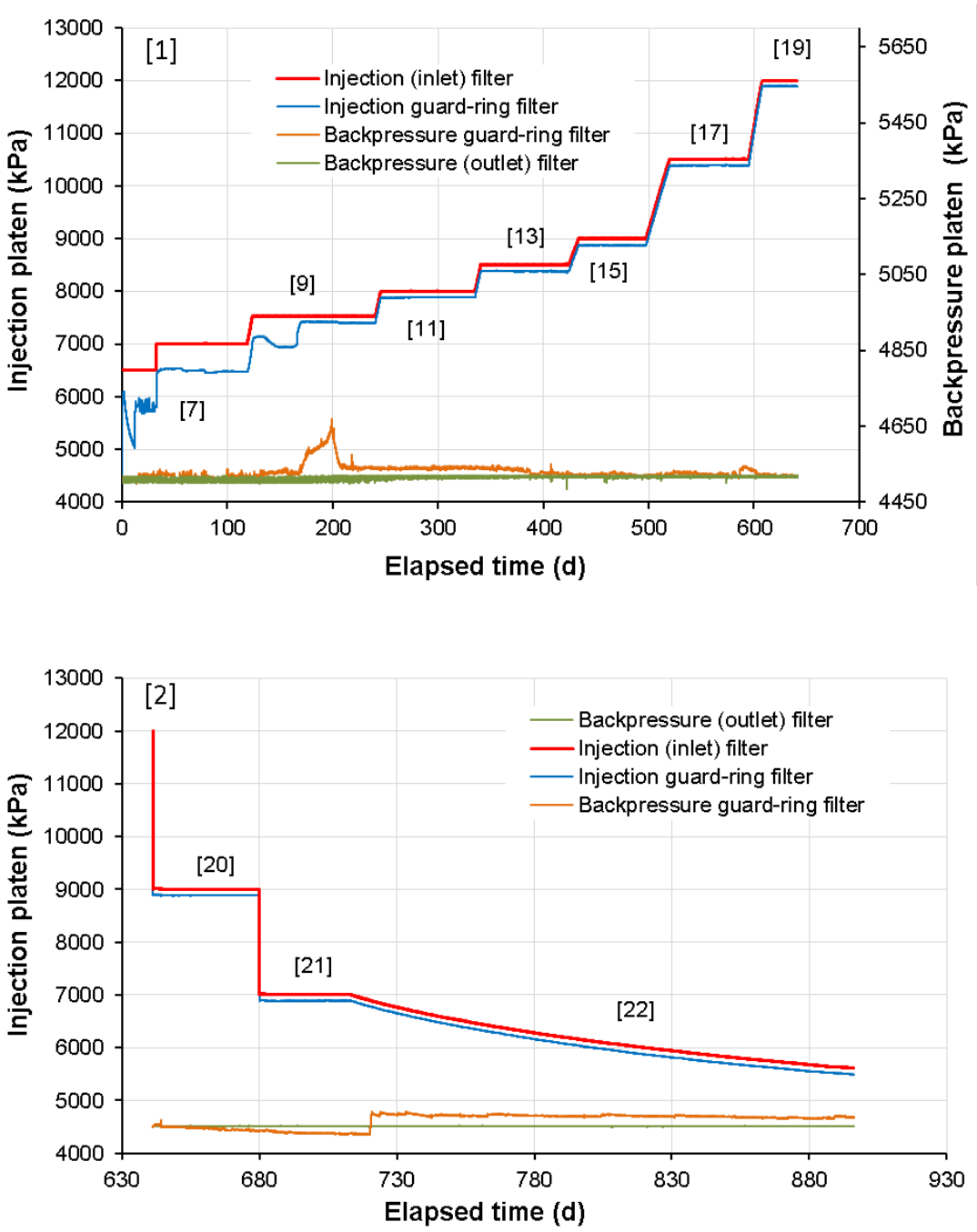

Figure 4-9 Pressure data from the injection, backpressure, and guard-ring filters during the gas injection test.

The gas outflow data show a small emergent flux until about 170 days (Section 4.1.3.1) when there is a gradually rising flow rate until an abrupt step at 200 days. Flow rate reduces again slightly at about 220 days and then follows a generally rising trend until about 430 days when the injection pressure is raised to 9 MPa. After an initial sharp rise in flow rate during this step there is a rapid decline at about 460 days and then recovery during the rest of the step. Flow rates then roughly double at the first of the 1.5 MPa steps in the injection pressure and a similarly substantial increase appears to be occurring in steps [17] and [19]. As the imposed flow rate is reduced, stages [20] and [21], the data exhibits significant hysteresis, with outflow larger during this 'imbibition' phase of the test history.

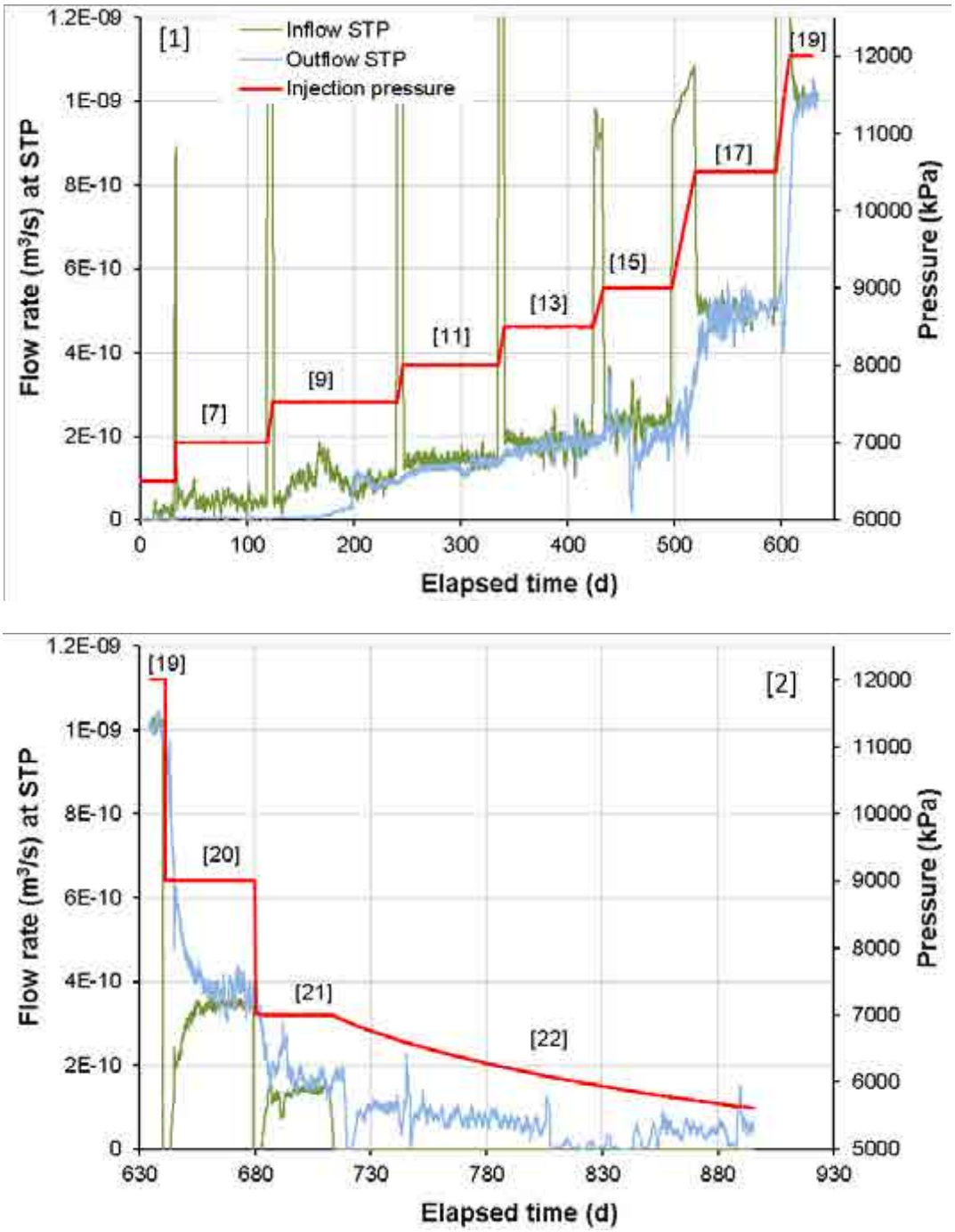

Figure 4-10 Gas flow rates at the injection and backpressure filters during the gas injection test. The large spikes in injection flux relate to the compression of the gas phase during constant flow rate test stages.

4.1.3.1 PRECURSOR FLOW

In test stages [6] through [9] gas pressure was increased in a series of steps while flux into[1] and out of the sample were monitored with time (Figure 4-11). The data clearly shows a small emergent flux discharged from the backpressure end of the specimen which begins shortly after the first increment in gas pressure is applied, test stage [6]. Flux out of the argillite remains constant at around 0.3 µl h^{-1} for the duration of the stage. Linear regression of the data (Figure

[1] Minor leakage problems with the injection pump degraded the resolution of the injection system resulting in the loss of accurate volumetric data for the first 200 days of testing.

4-12A) indicates quasi-steady state flow for the duration of the stage. After 32.8 days the increase in gas pressure, test stage [7], results in a small but measureable increase in discharge rate. This quickly plateaus at around 0.5 µl h^{-1} and remains constant for approximately 30 days (similar in length to the entire duration of stage [6]), before exhibiting a slow progressive decline to a value of around 0.4 µl h^{-1}. Linear regression of the discharge rate plotted against elapsed time yields a small negative slope symptomatic of the reduction in flux (Figure 4-12B). As before, flow out of the specimen quickly increases when gas pressure was again raised during test stage [9]. However, this time the discharge rate appears to remain in a quasi-steady state, yielding an average volumetric flow rate of approximately 0.6 µl h^{-1}. This continued for a further 47 days until the flux spontaneously increased, indicative of the start of major gas breakthrough. At this point in time the total fluid volume discharged from the specimen is around 1.87 ml. If we assume this relates purely to the displacement of water from the original porosity of the sample, then it would equate to a gas saturation of around 10%[2].

While this value outwardly appears reasonable a cross-plot of flux verses excess gas pressure (Figure 4-13) provides an initial estimate for the gas entry pressure of only 0.9 MPa. This estimate is low and is actually comparable to values reported for Boom Clay (Ortiz et al, 1997) which has a hydraulic permeability two orders of magnitude greater than the Callovo-Oxfordian argillite. Extrapolation of IGR pressure presented in Table 4-3 using a 3rd order polynomial fit to the data, Figure 4-14, provides a second estimate for the gas entry pressure. This yields a value around 1.3 MPa. We can therefore surmise that the initial gas entry pressure, close to the injection face of the clay, is in the range 0.9 to 1.3 MPa. However, it is important to recognise that these values are estimates only and relate specifically to the argillite in close proximity to the inlet filter and may relate to localised discrete features within the clay which are discontinuous within the majority of the sample.

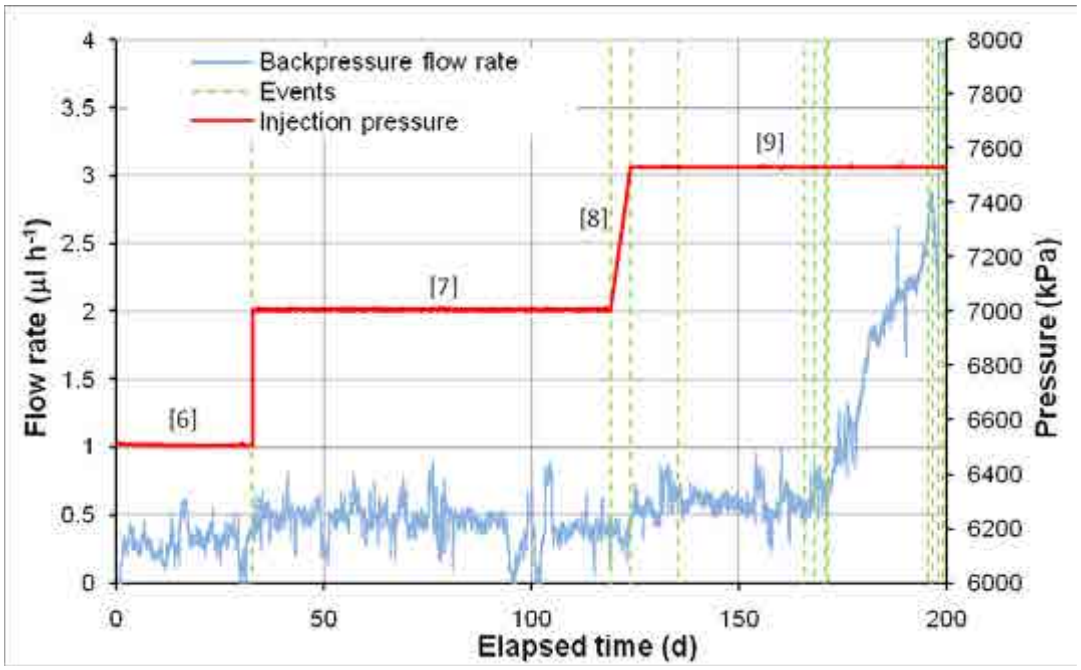

Figure 4-11 Backpressure flow rate and injection gas pressure plotted against elapsed time for test stages [6] through [9]. Note a small but measureable increase in discharge rate following the rise in gas pressure. The rapid increase in flow at around 171.5 days is indicative of major gas breakthrough.

[2] This estimate is likely to be high and may reflect a combination of processes including slug flow from residual water trapped in the injection filter at the time of gas sweeping.

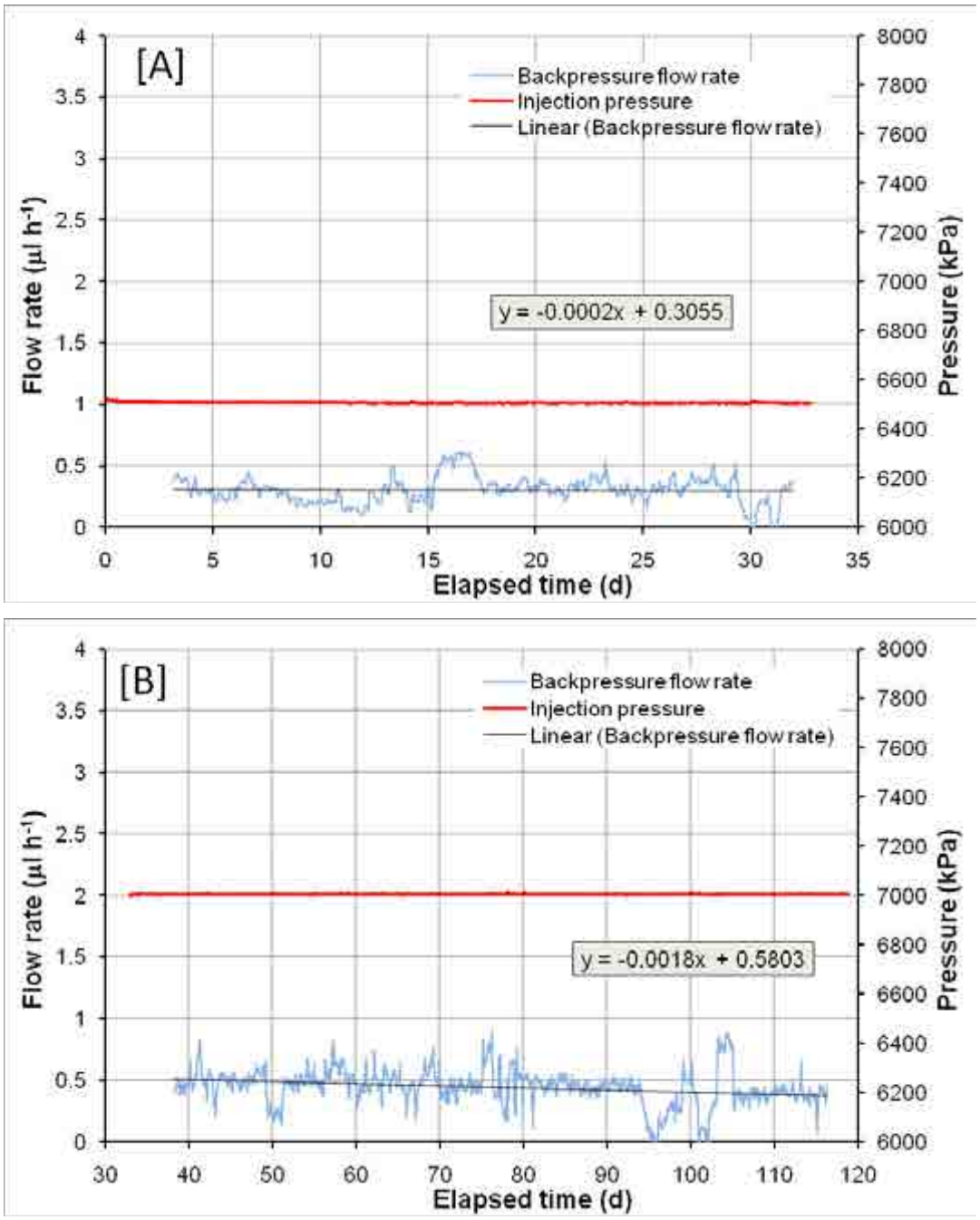

Figure 4-12 Backpressure flow rate and injection gas pressure plotted against elapsed time for test stages [6] through [7]. Linear regression of the data suggests flux is decreasing during stage [7].

While the origin of these precursor fluxes remains somewhat unclear, it is worth noting that the discharge rates are comparable to those observed during hydraulic testing, if the higher hydraulic gradient is appropriately scaled, suggesting the flux is aqueous in nature. Equivalent hydraulic conductivities calculated for these fluxes are of a similar order of magnitude to those observed during hydraulic testing (Figure 4-13). This hypothesis is supported by inspection of flux transients, which rapidly plateaus at the new steady-state value, following the change in injection pressure. This behaviour is suggestive of an incompressible response in which desaturation of the specimen plays little, if any, part. Analysis of data from the first gas stage of test COx-2 provides clear evidence for the existence of 'slug flow'. It is possible that the same applied to test COx-1 and that part or all of the observed precursor flow stems from incomplete sweeping of the injection filter and connecting pipe work. It is also possible that some of the fluid

originates from displacement of water following the early penetration of the injection guard-ring (IGR) by gas shortly after testing begins. This hypothesis is supported by the analysis of the hydraulic data in final section of 4.1.2.

However, further examination of the guard-ring data provides a useful insight into the system behaviour. As gas pressure is applied to the sample, stage [6], pressure in the injection guard-ring rapidly increases, reaching a peak value of 6095 kPa, before spontaneously declining to a minimum value of 5040 kPa. The asymmetry of this event (Figure 4-15) combined with the rapid increase in IGR pressure at day 12.6 are symptomatic of dynamic behaviour and suggests the movement of gas along unstable pathways. It is also noteworthy that following the jump in gas pressure at 12.6 days, the pressure plateaus at a significantly lower value than that observed the peak (day 1.5). This suggests that the network of conductive pathways has evolved during these events. Given the dynamic nature of this behaviour, it is highly unlikely that this relates to flow between the sample-platen interface, but rather gas movement along preferential features within the top section of the clay.

When gas pressure in the inlet filter was increased at the beginning of stage [7], the IGR pressure rapidly increased over a period of several hours, reaching a well-defined plateau. The difference in pressure between the injection inlet and guard-ring filter is around 0.7 MPa and 0.5 MPa for stages [6] and [7] respectively. The rate of IGR pressure increase and in particular, the shape of the resulting pressure transient (Figure 4-16), are atypical of the hydraulic behaviour observed in Figure 4-5 and are suggestive of gas pathway flow. Small spontaneous drops in IGR pressure at days 57 and 78 (Figure 4-17), further support this hypothesis and are highly indicative of unstable pathway flow.

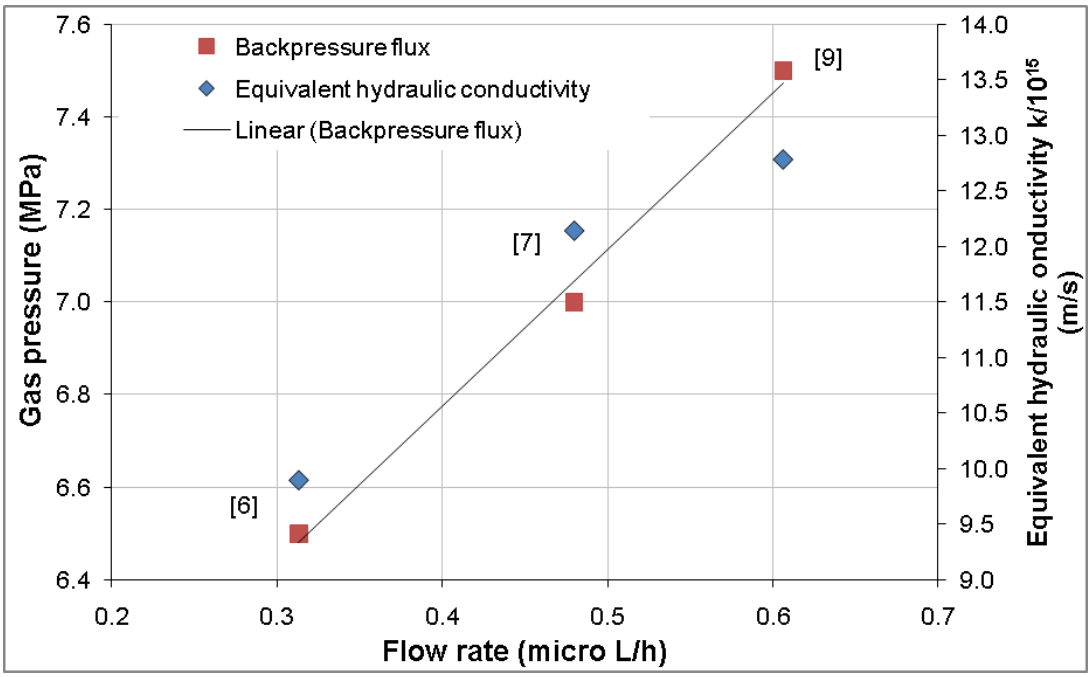

Figure 4-13 Cross-plot of gas pressure and equivalent hydraulic conductivity versus discharge rate during test stages [6], [7] and the initial section of [9]. Projection of the flux data to the zero flow condition suggests a gas entry pressure of around 0.9 MPa (see Figure 4-14). Equivalent hydraulic conductivities are of a similar magnitude to those observed during hydraulic testing.

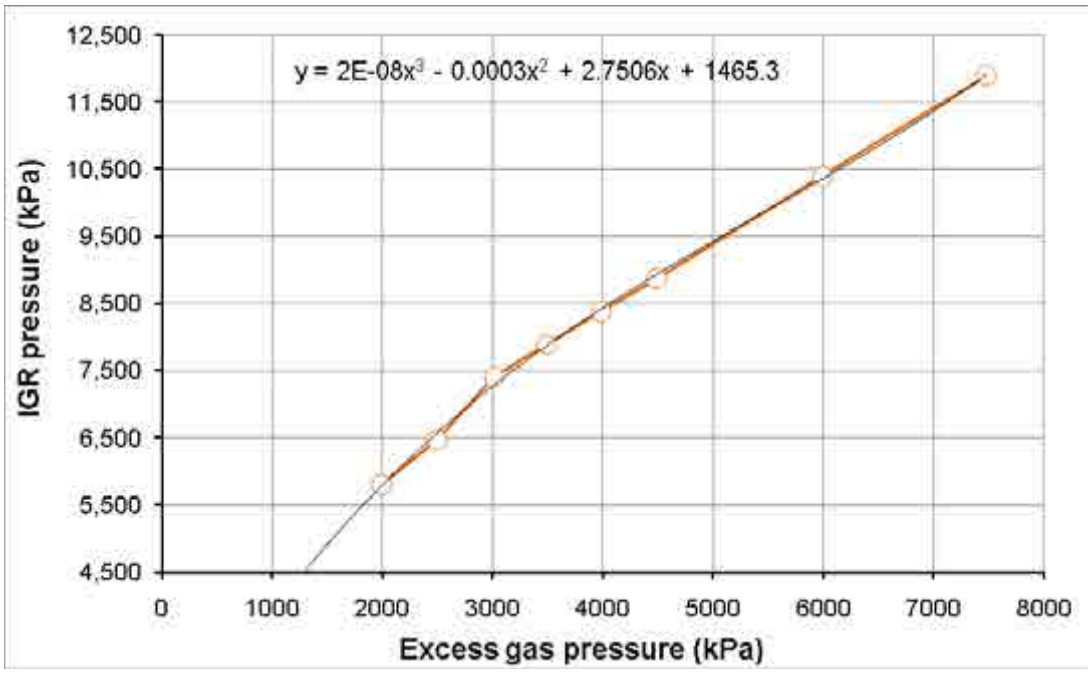

Figure 4-14 Cross-plot of IGR versus excess injection gas pressure. Extrapolation of the line suggests a gas entry pressure of approximately 1.3 MPa.

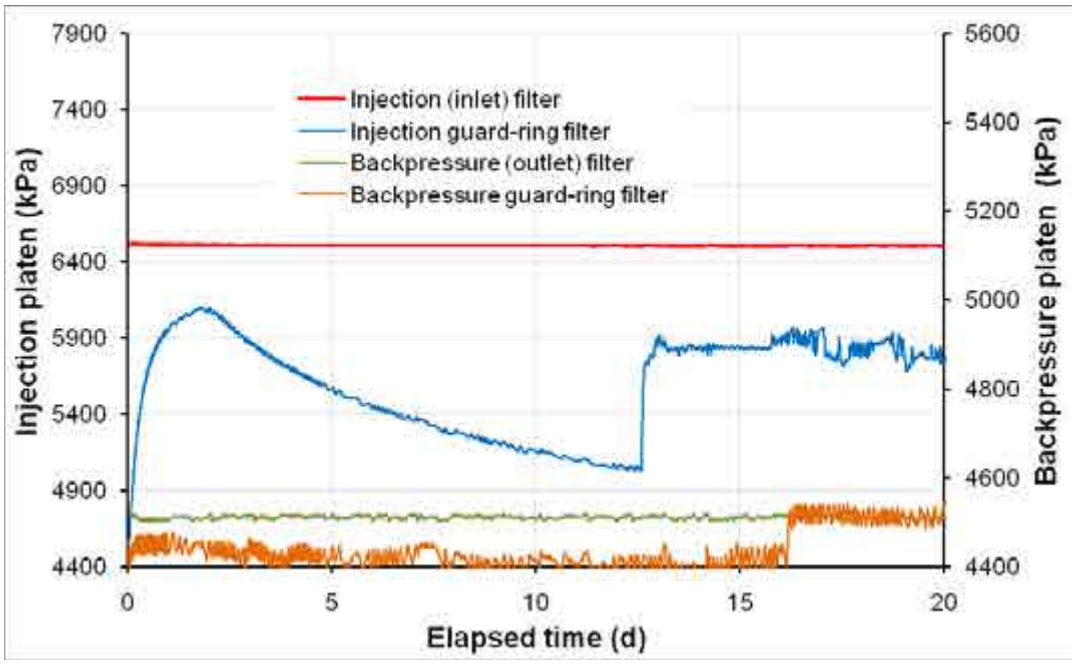

Figure 4-15 Pressure data from the injection, backpressure, and guard-ring filters during the stage [6]. The asymmetry of the injection guard-ring response observed during the first 12.6 days of the test is atypical of hydraulic behaviour, as is the spontaneous increase in IGR pressure at 12.6 days.

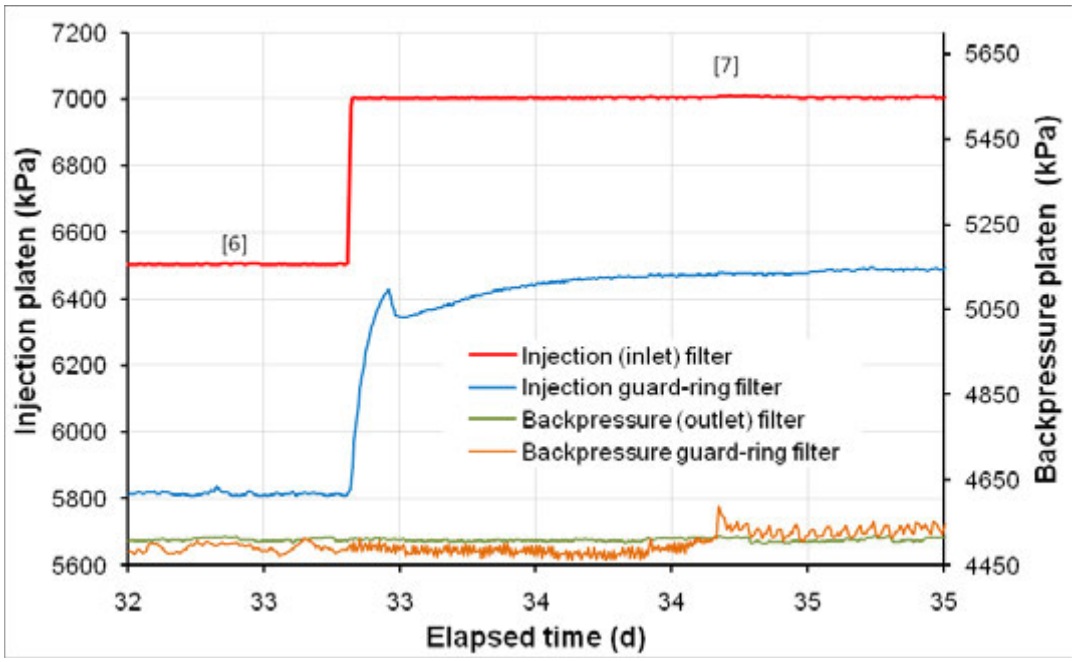

Figure 4-16 Pressure from the injection, backpressure, and guard-ring filters during the step-wise increase in pressure from stages [6] to [7]. The rate and shape of the IGR transient is atypical of hydraulic behaviour.

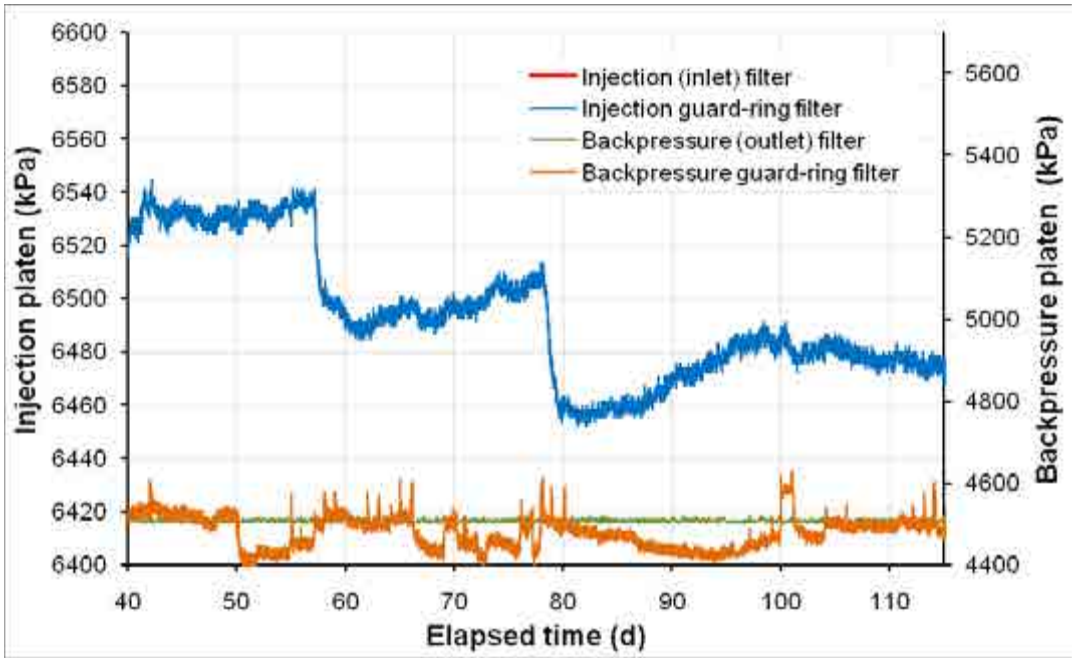

Figure 4-17 Evolution of IGR pressure during stage [7]. The spontaneous drops in pressure at days 57 and 78 are symptomatic of unstable pathways flow.

In summary, it seems clear from analysis of the data that gas penetrates the upper section of the argillite near the injection face relatively early in the test history. However, the lack of correlation between the IGR data and that of the downstream guard-ring pressures or the emergent flux, suggest that gas is unable to fully propagate across the specimen during stages [6] and [7]. While the origin of the precursor flux remains somewhat unclear, the data suggest they are predominantly aqueous in nature and do not relate to desaturation of the sample (Table 2-1). It is possible that part of this flow stems from desaturation of the argillite close to the injection The low value for the initial estimate of the gas entry pressure probably relates to localised

features within the clay close to the injection face, which may account for the initial high anisotropy observed in the hydraulic modelling (Section 4.1.2). Post-test mineralogy and petrology investigations of the sample in this zone may provide additional data with which to help to explain these observations.

4.1.3.2 BREAKTHROUGH

On day 123.9 the injection pump was switched to constant pressure mode signifying the start of test stage [9]. The inlet filter pressure was then held constant for the next 116.6 days. Analysis of the pressure data from the IGR filter exhibits a small time lag in reaching an asymptote at around 128 days (Figure 4-18). Pressure in the IGR filter then remains constant until day 135.3 when it spontaneously begins to decay even though the gas pressure gradient across the specimen remains constant. This behaviour is again symptomatic of unstable gas flow through a network of pathways between IGR and inlet filters. Gas pressure in the upstream IGR filter then begins to decay into the neighbouring clay which continues until day 146.8, at which point the pressure levels, oscillating around 6.95 MPa. Subtracting the backpressure from this value gives yields a highly tentative estimate for the capillary pressure locally within the sample of around 2.45 MPa, though this may be a somewhat arbitrary number if time dependent dilatancy plays a significant role in this behaviour. This value is significantly higher than the initial estimate for the gas entry pressure (Section 4.1.3.1) which suggests that either the gas has penetrated further into the clay, or, the network of clays pathways has evolved during the first 150 days of the test. It is also noteworthy that flux out of the specimen remains constant during this time.

However, what is clear from this data is that such dynamic responses in pressure cannot be explained by simple hydraulic flow and that gas penetration of the specimen provides the only viable mechanism to explain these observations.

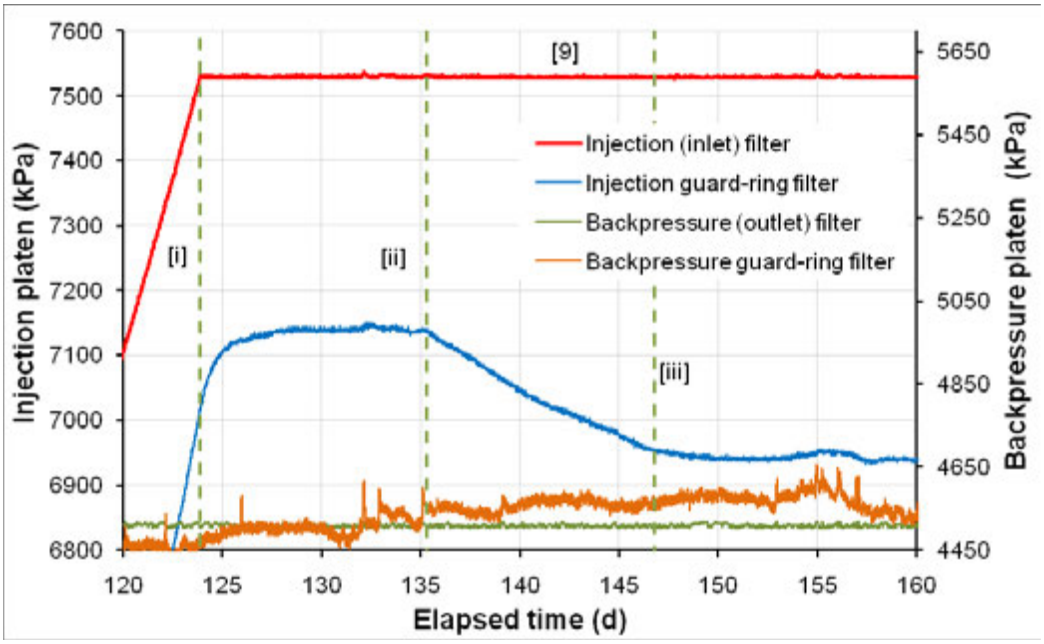

Figure 4-18 Evolution of guard-ring pressure during test stage [9]. Correlation lines [i], [ii] and [iii], indicate the start of stage [9], the initiation of the spontaneous negative pressure transient for the IGR filter and the inflection in the IGR pressure curve.

On day 165.7, pressure in the injection guard-ring spontaneously increases (Figure 4-19). On day 170.8, the backpressure guard-ring exhibits a small jump in pressure which then continues to steadily increase. This is followed on day 171.5 by a marked increase in discharge rate from the outlet filter, signifying the start of major gas breakthrough. By comparing 'breakthrough' times for the injection and backpressure guard-rings, it is possible to estimate the transit time of the gas across the specimen. Analysis of the data yields a value of around 5 days. It then takes a further 0.8 days for the gas to propagate to the outlet filter.

By cross-plotting the inflow and outflow data from stages [6] through [9] (Section 4.1.3.3, Figure 4-20) and linear regressing the data it is possible to estimate the excess gas breakthrough pressure. This value was found to be in the range 1.9 to 2.2 MPa.

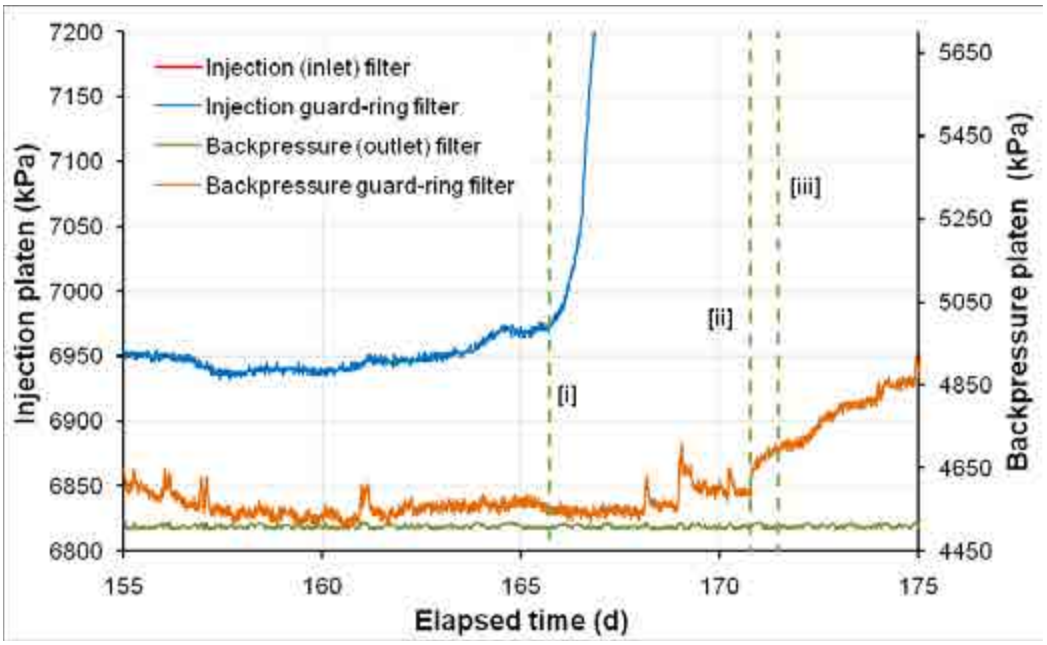

Figure 4-19 Evolution of guard-ring pressure during gas breakthrough. Correlation lines [i], [ii] and [iii] relate to increases in filter pressure at the injection and backpressure guard-rings and an increase in discharge rate respectively.

However, this raises an obvious question. Assuming these events are integrally linked, why did it apparently only takes five days for the gas phase to propagate across the specimen, given that the gas pressure gradient had remained constant for the previous 42 days? At present there is no definitive answer to this question, in part due the paucity of data from other detailed tests performed on the Callovo-Oxfordian clay. However, there is clear evidence from analysis of the guard-ring data for the existence of highly unstable gas pathways whose conductivity varies geospatially and temporally within the sample and test respectively.

Data from a triaxial test (Figure 4-21) clearly illustrates the time-dependent nature of deformation (i.e. radial displacement) within the COx during gas breakthrough (Cuss and Harrington, 2012). The change in sample volume stems from slow time-dependent deformation of the fabric. This evolution in behaviour provides an explanation for the evolution in gas flow observed across the specimen, as the gas meets and then slowly deforms its way through lower permeability or less compressible zones within the clay (see Section 6). Such a mechanism would introduce a time-dependency into the mechanisms governing gas flow in the Callovo-Oxfordian clay and would help to explain the observations seen in this experiment.

4.1.3.3 STEADY-STATE GAS FLOW

Following major gas breakthrough, flux out of the specimen again exhibits dynamic behaviour, first overshooting (Figure 4-22) then undershooting the ultimate value for steady-state[3]. This type of behaviour, observed in previous gas tests reported by Harrington and Horseman (1999; 2003), was considered to be indicative of the instability of conductive gas pathways.

[3] Even after extended periods of gas flow there is some evidence to suggest that there remains small residual slopes to a number of steady states.

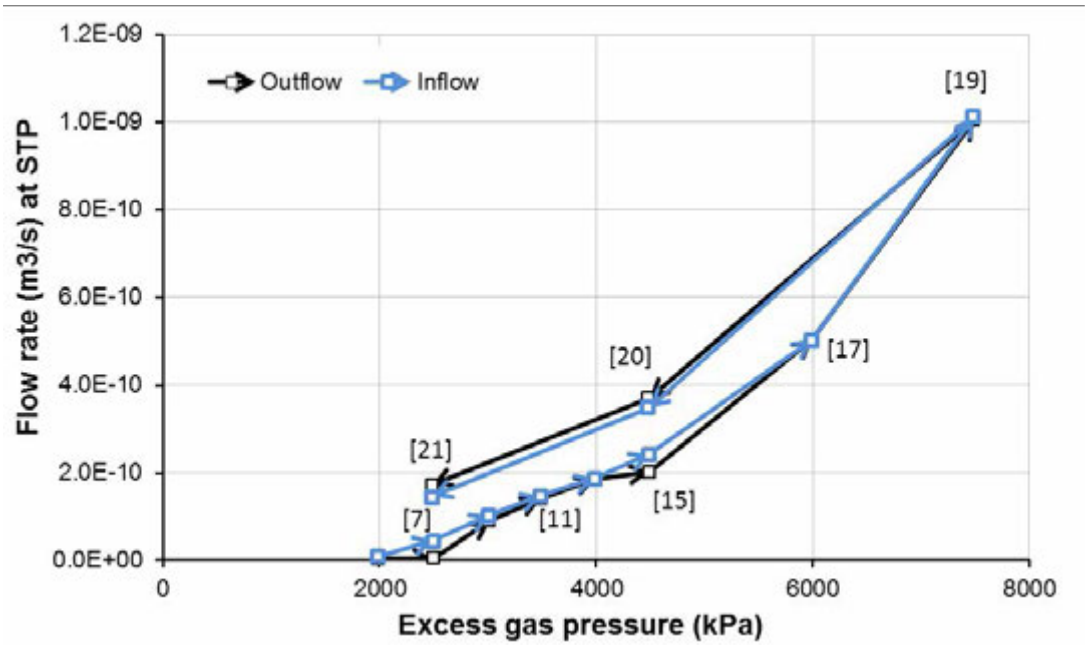

Figure 4-20 Cross-plot of flow in and out the sample plotted against excess gas pressure. The intersection of the lines provides an estimate for the gas breakthrough pressure. The hysteresis between ascending and descending flow cycles is evident in the data.

Prior to major gas breakthrough, pressure in the downstream guard-ring filter begins to increase (Figure 4-23). This continues for several days before levelling off at around 176 days. Pressure in the guard-ring then remains constant for a further 4 days, before spontaneously increasing to a peak value of 5.5 MPa. The observed inflections in slope are highly indicative of the spontaneous development of new conductive gas pathways. Following the peak, pressure in the guard-ring rapidly declines, exhibiting a sharp inflection in slope around day 210. Thereafter, gas pressure remains fairly constant for the duration of the stage. The highly dynamic nature of the guard-ring response provides conclusive proof for the existence of a network of highly unstable gas pathways. In the opinion of the authors such extreme changes in pressure are highly unlikely to occur as a result of instabilities associated with flow as embodied within classic concepts of two-phase flow, but are more likely to be symptomatic of the movement of gas along unstable, dilational gas pathways. This assertion is supported by post-test measurements of water saturation which show no discernible desaturation.

At the end of stage [9], gas pressure was gradually increased over a 5 day period to the next target value of 8.0 MPa, stage [11]. Here, gas pressure was again held constant for a further 89.4 days while flux into and out of the sample were monitored (Figure 4-24). While examination of the data in Figure 4-24 clearly shows the injection flux quickly levels, flow out of the sample lags significantly behind, taking a further 20 plus days to reach near steady-state. This time-dependent evolution in discharge rate is indicative of the slow development of conductive gas pathways, stemming from the dilation and deformation of the clay fabric. A summary of the gas data for each test stage is presented in Table 4-3.

Further examination of the data from stage [11] shows a small reduction in discharge rate around day 300. This is followed by an increase in flux from day 303 leading to a quasi steady-state where fluxes in and out closely agree. While these changes in flux are small they may reflect localised instabilities associated with the opening and closure of gas pathways.

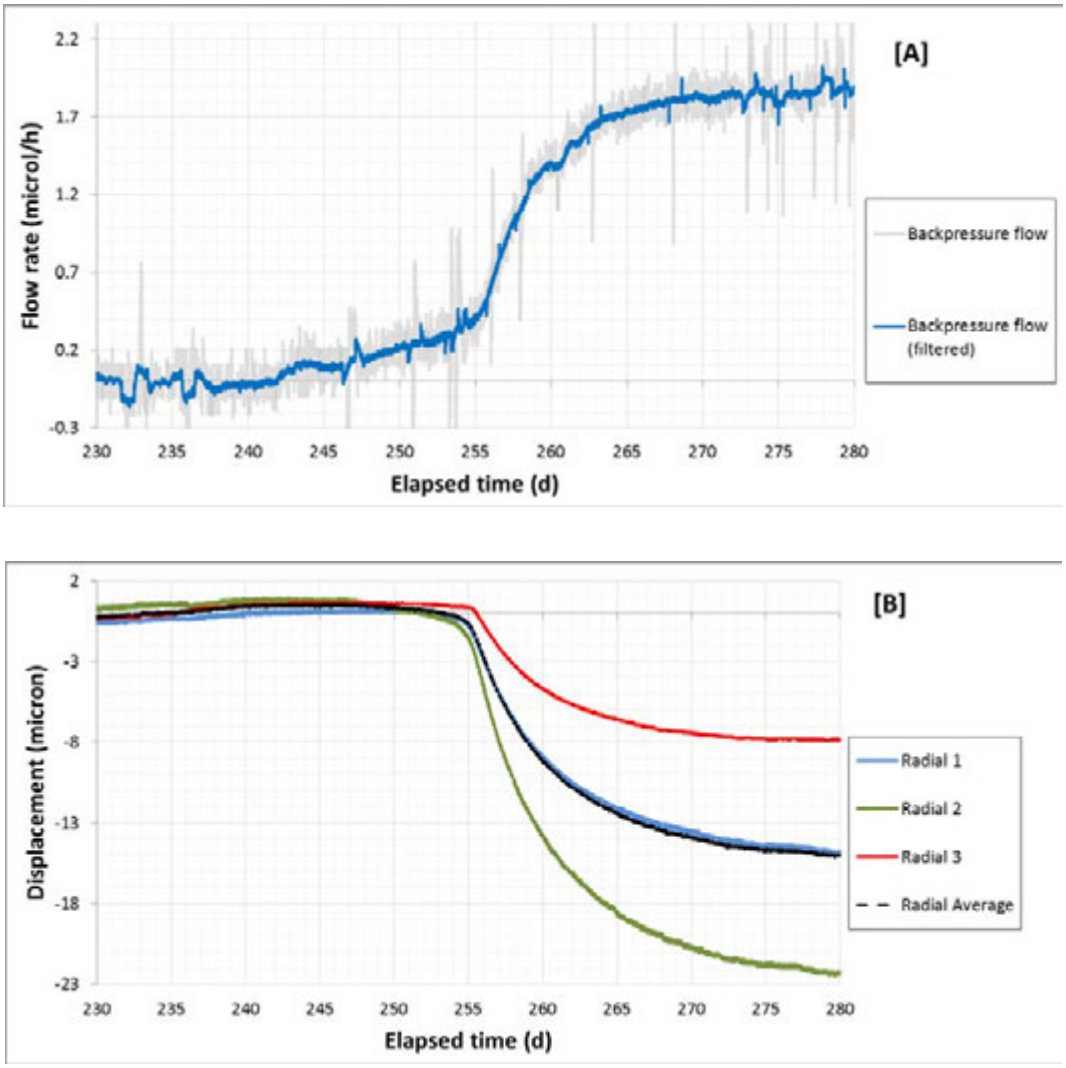

Figure 4-21 Flow and strain data from a triaxial test performed on COx (Cuss and Harrington 2012). Plot A shows the slow time dependent evolution in flux out of the core, while plot B, shows the sample dilating in response to changes in gas outflow.

The gas pressure gradient across the sample was then increased by 0.5 MPa in each of the next two increments, test stages [13] and [15]. As before, flux into and out of the specimen increased with the change in gas pressure gradient leading to quasi steady-states. Again, flux out of the sample lagged considerably behind the change in gas pressure, indicative of the time-dependent processes outlined above. Further evidence for the instability of gas pathways is seen within the data, in particular test stage [15], where outflow rapidly declines around day 459. It then takes a further 35-40 days for the flux to recover to close to the previous steady-state value.

In the final two ascending stages of the gas test, gas pressure in the inlet filter was increased to 10.5 MPa and then 12.0 MPa respectively, Figure 4-24. For each stage gas pressure was held constant for an extended period of time, yielding quasi steady-states. Comparison of data with that from Figure 4-25 shows that flux across the specimen significantly increases as the gas pressure gradient rises, approximately doubling between stages [15] and [17] and again between [17] and [19], even though the pressure gradient across the specimen has only increased by 25%. It is notable that the instability in flow apparent in the earlier data appears to reduce as the flux of gas across the specimen significantly increases. It is also notable that the time taken to reach steady-state is significantly less during these test stages. Given that the hydraulic conductivity of the intact clay remains the same as in previous stages, proportionally less, if any, desaturation of

the sample appears to occur at these higher flow rates. This suggests that dilation of the fabric plays a dominant role in the movement of gas through the argillite.

Setting aside the large obvious spike in downstream guard-ring pressure following the initial breakthrough event, it is possible through close scrutiny of the data to elicit significant detail relating to the mechanics controlling gas flow. Figure 4-26 contains a series of 30 day plots showing the downstream guard-ring response at various times during the gas injection test. From around day 245, there is a significant change in the underlying response of the pressure transducer, which begins to exhibit a 'saw tooth' type response, characterised by a rapid increase in pressure which then decays with time. Inspection of the data suggests some form of periodicity to the response though this has not been analysed as part of this report. This saw-tooth behaviour is symptomatic of unstable gas flow within the argillite, as gas pathways connect, discharge and then close. The pressurised gas trapped in the guard-ring filter then slowly decays with time as the gas moves back into the clay. However, at around day 380, the pressure in the guard-ring begins to reduce to a value roughly equal to that of the backpressure filter. Thereafter, the saw-tooth pattern is far less distinctive; suggesting gas flow to the guard ring has significantly reduced or stopped.

Hysteresis

During test stages [20] and [21], Figure 4-10 (2), the gas pressure gradient was decreased in a stepwise manner, mimicking stages [7] and [15] previous undertaken during the ascending gas history. Flux into and out of the specimen decreased with time, slowly evolving to a well-defined steady-state. In test stage [20] the asymptotic volumetric flow rate was nearly twice that of stage [15], Figure 4-20, indicating significant hysteresis in the flow response between ascending and descending flow histories. As pressure was reduced still further, stage [21], gas flow into and out of the specimen continued. This is in contrast to the equivalent stage [7], where little if any flow was observed. Analysis of the post-test saturation for specimen COx-1 suggests the sample remained fully saturated throughout the test. As such, the underlying cause for this apparent hysteresis is unclear but may relate to time-dependent processes associated with the creation and subsequent closure of dilatant gas pathways.

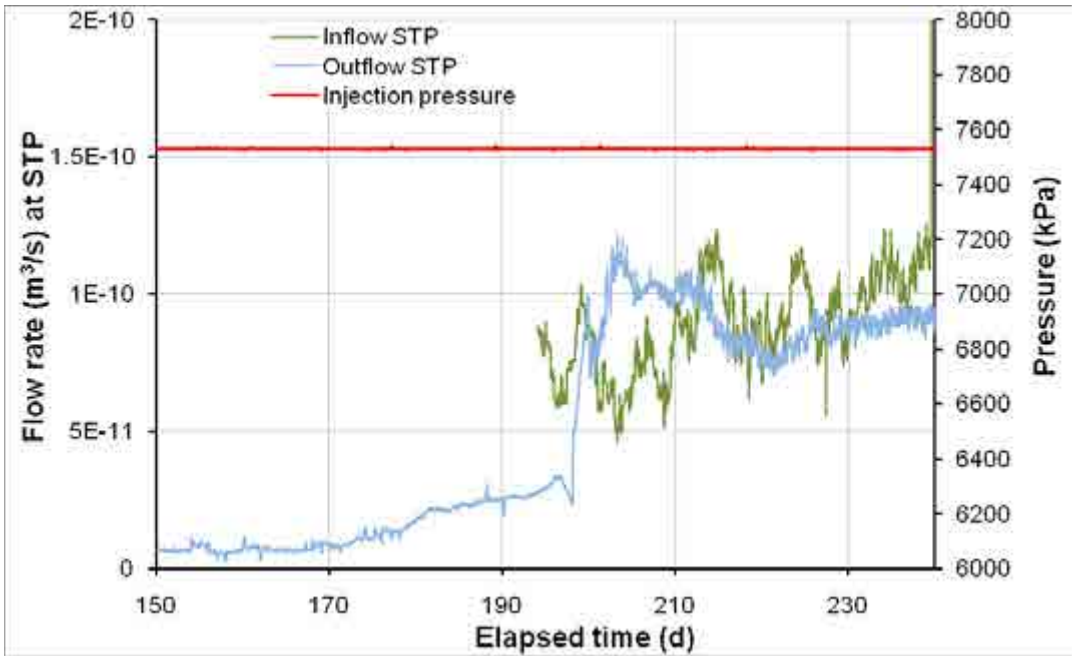

Figure 4-22 STP flow rate into and out of the specimen during test stage [9]. The inflow data has been cropped during the early part of the test due to problems with leakage from the injection system.

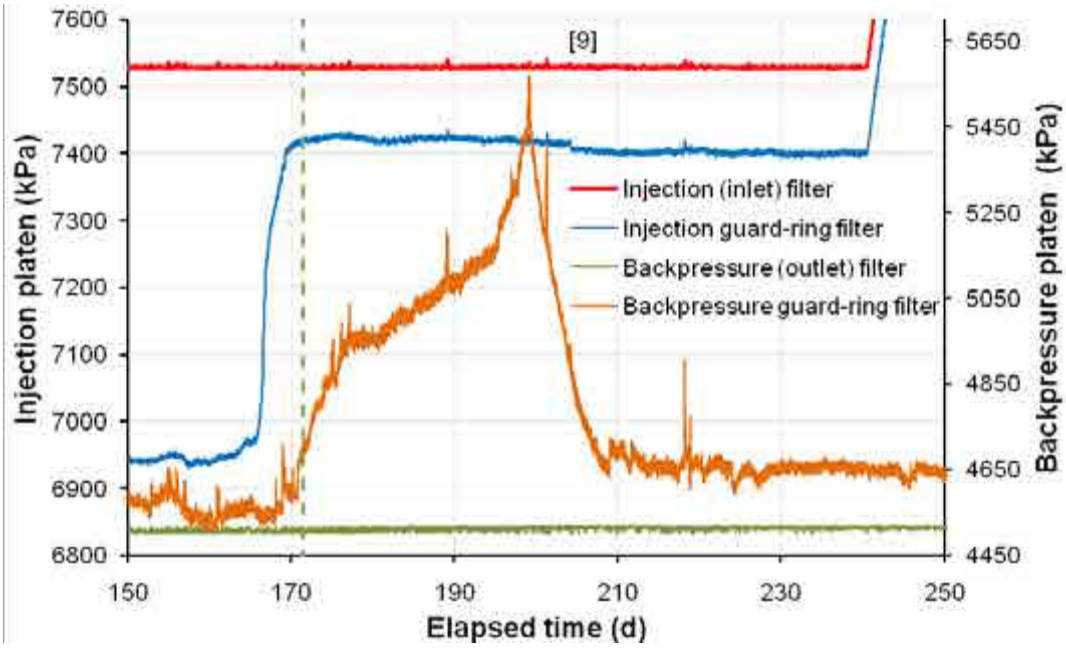

Figure 4-23 Evolution of guard-ring pressure during test stage [9]. The dash line indicates the point at which flux out of the specimen increases. The dynamic behaviour exhibited by the backpressure guard-ring can only be explained by the existence of highly unstable gas pathways.

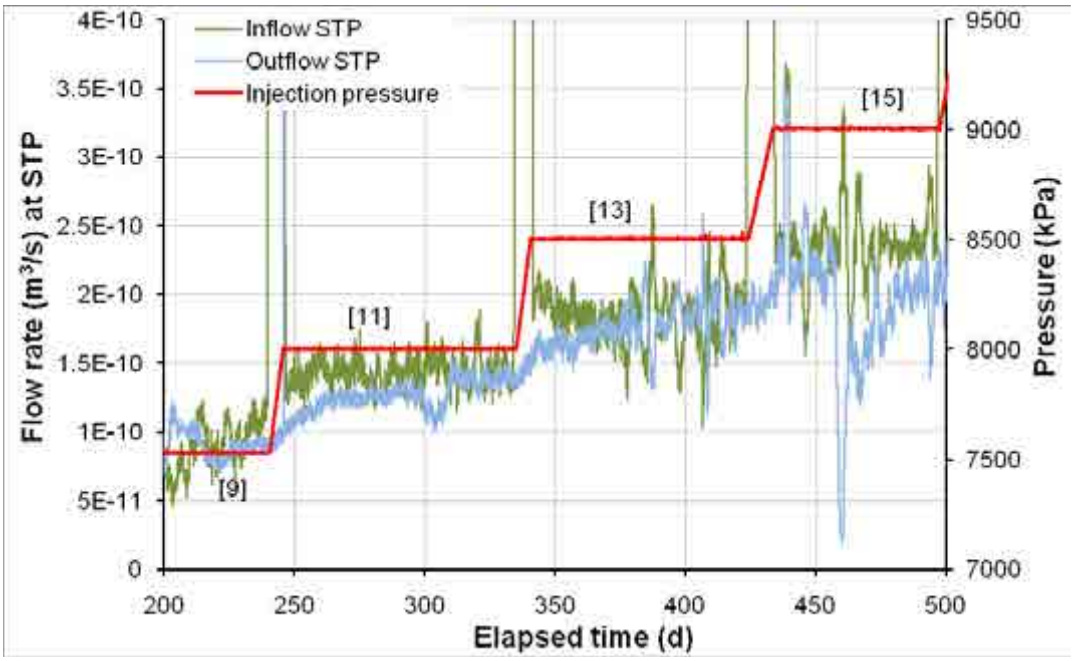

Figure 4-24 STP flow rate into and out of the specimen and gas injection pressure plotted against elapsed time during test stage [9] through [15].

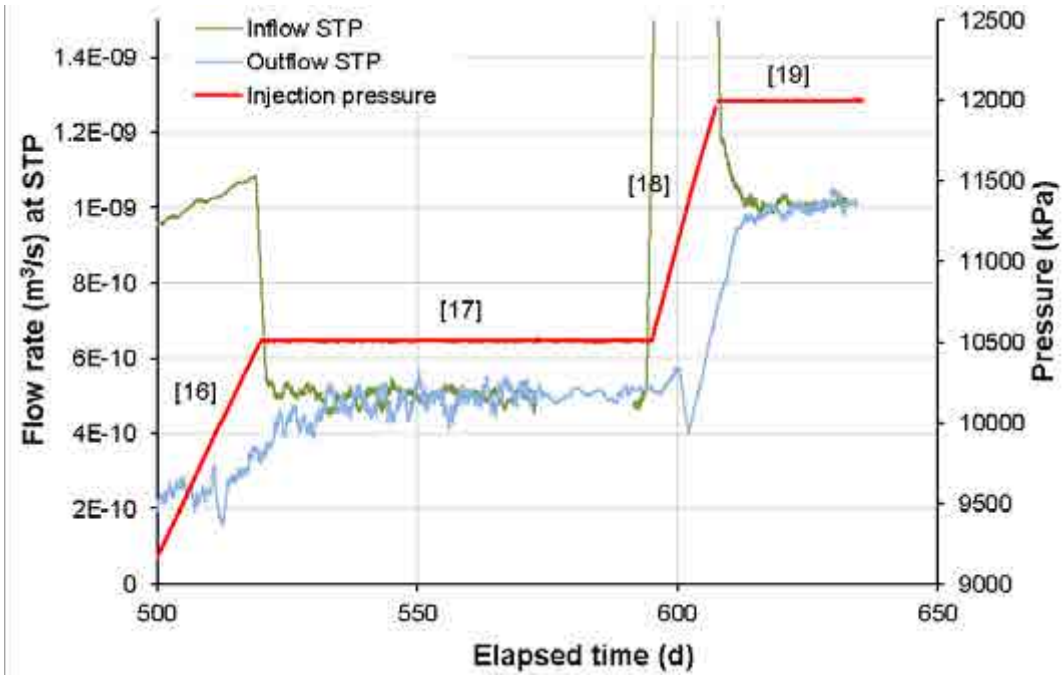

Figure 4-25 STP flow rate into and out of the specimen and gas injection pressure plotted against elapsed time during test stage [16] through [19].

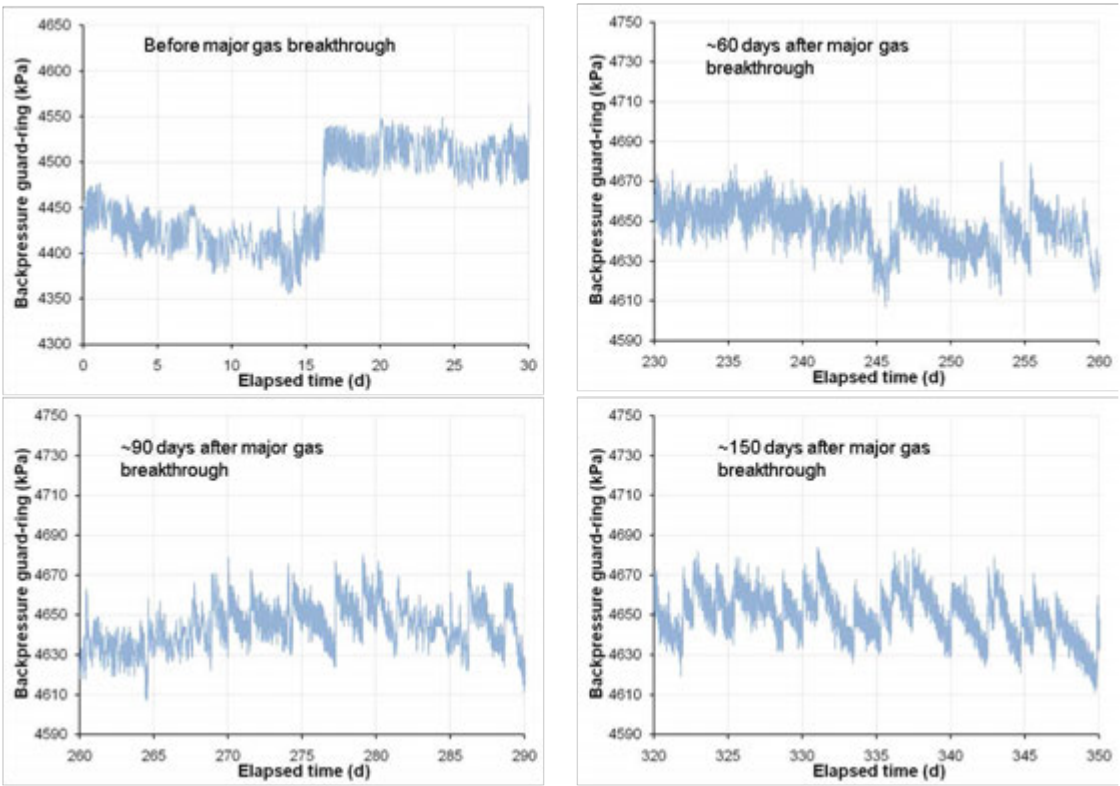

Figure 4-26 Downstream guard-ring response during gas testing. The saw-tooth pressure response observed in later data is symptomatic of unstable gas pathways.

Evidence for desaturation during gas testing

Inspection of the data from Figure 4-24 and Figure 4-25 show quasi steady-states for each test stage. By comparing mass flux into and out of the specimen, it is possible to estimate the

evolution of gas saturation associated with each increment in gas pressure (assuming standard concepts of two-phase flow apply). Figure 4-27 shows the area of flux (shaded in light red) which has been used to calculate the change in saturation for each step. As can been seen, a conservative approach to the calculation has been adopted, which should result in the prediction of minimal desaturation of the argillite for each test stage. However, a cross-plot of the data with excess gas pressure, Figure 4-28, indicates unrealistically high gas saturations for relatively minor excess gas pressures. This result, directly contradicts post-test measurements of sample desaturation (Table 2-1) which indicate no measureable desaturation of the sample, and would appear to confirm early observations suggesting dilatancy plays an important role in the movement of gas through the COx.

Analysis of volumetric data from the confining pressure pump appears to support this hypothesis showing a general trend of increasing sample volume as gas pressure increases (Figure 4-29), when gas pressure is reduced the sample volume decreases. While the correlation is rather crude more detailed measurements from a triaxial test (Figure 4-21) provide clear evidence of gas induced dilatancy (Cuss and Harrington, 2012).

Evidence for sample-sheath integrity

To address the potential for fluid flow between the sheath and sample when testing low permeability materials, the BGS developed the 'guard-ring' arrangement of filters. These provide an independent measure of pressure around the circumference of each platen which can be used to monitor the pressure evolution (and therefore interaction with the gas phase) during gas testing. While the guard-ring data clearly indicates the periodic presence of gas, it is hard from a mechanistic perspective, to see why this flow would periodically stem from flux around the sheath/sample during discrete stages of the gas test. There is no obvious correlation between upstream and downstream guard-ring pressures.

Close inspection of the data between 170 and 380 days shows that the downstream guard-ring pressure is above that of the downstream filter, indicating a small pressure drop exists between the two filters. The fact that this pressure drop remains fairly constant and doesn't vary even though discharge rate substantially increases indicates gas flow is not from the guard-ring to the outlet filter and therefore cannot be along the wall of the sheath. The fact the downstream guard-ring exhibited a maximum pressure of ~5.5 MPa indicates it was capable of supporting a significant pressure gradient to the downstream filter.

It may be that there are a number of conductive pathways near the downstream end of the sample which combine to give the results observed during hydraulic testing (which is likely to be far more uniformly distributed within the clay) but if gas flow is localised, may not interact with the downstream guard-ring during testing. This would explain the sudden peak in gas pressure near breakthrough and provide an explanation for the subsequent decay in pressure as pathway geometries evolve within the sample and the downstream guard-ring ceases to act as a significant sink. It should also be noted that if gas flow was along conductive features between sample and the wall of the sheath, the time taken to reach steady state (following an increment in pressure), should be relatively short.

However, inspection of the data clearly indicates time-dependent evolution of gas pathways even after many weeks of testing. This observation cannot be reconciled with concepts of by-pass flow.

Stage no.	Injection pressure (MPa)	Asymptotic value of guard-ring pressure (MPa)		STP conditions $Q_{st}/10^{11}$ ($m^3.s^{-1}$)	
		Upstream	Downstream	Flow in	Flow out
9	7.53	7.40	4.65	9.9	8.9
11	8.00	7.89	4.65	14.5	13.8
13	8.50	8.38	4.55	18.5	18.5
15	9.00	8.87	4.51	24.0	20.0
17	10.51	10.39	4.55	50.1	50.2
19	12.00	11.90	4.50	101.2	100.4
20	9.00	8.89	4.43	34.6	36.8
21	7.00	6.89	4.37	14.1	17.0
25	7.53	7.48	4.59	14.0	13.8
27	12.00	11.93	4.64	100.0	96.7

Table 4-3 Summary of the steady-state gas results for test stages [9] through [27]. Analysis of the flux data indicates breakthrough pressure for initially water saturated conditions in the range 1.9 to 2.2 MPa.

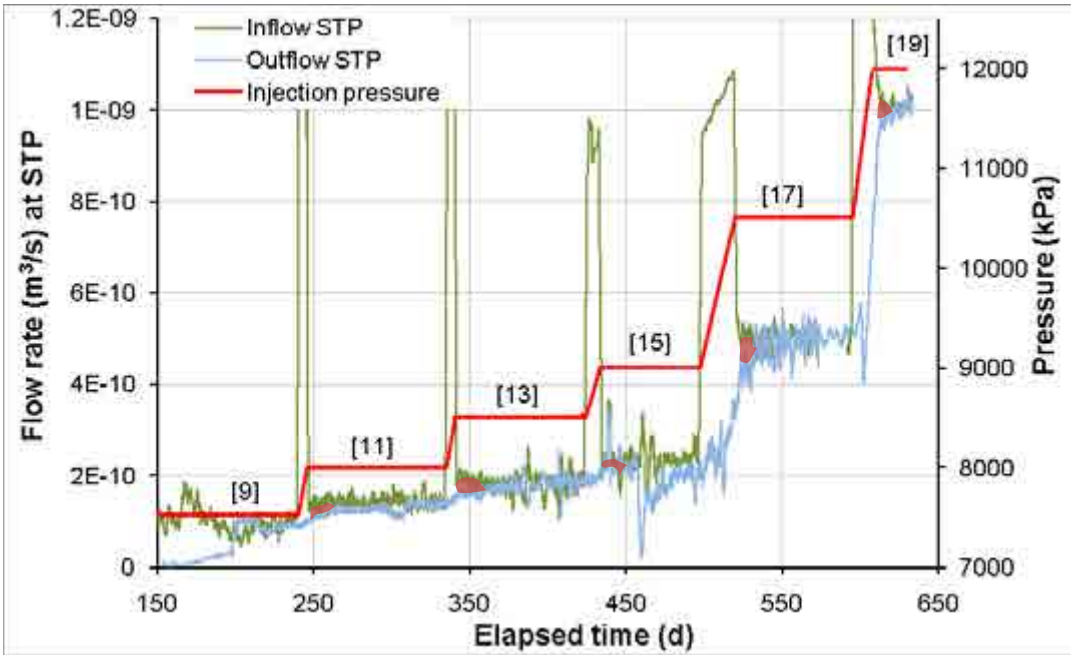

Figure 4-27 STP flow rates into and out of the sample. The red shaded areas at the beginning of each stage delineate the sections of the transient response used to estimate saturation.

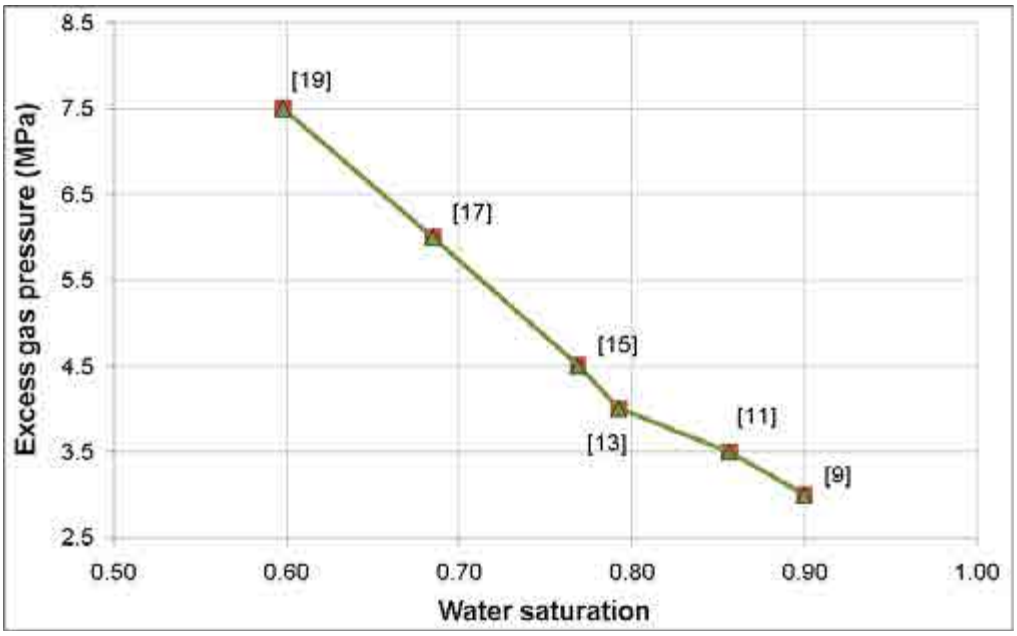

Figure 4-28 Cross-plot of excess gas pressure against estimated water saturation based on mass balance. Estimates for the water saturation are derived from mass balance of the STP data presented in Figure 4-27. STP volumes have been corrected back to experimental conditions assuming a capillary threshold pressure of 2.0 MPa. However, the data predicts unrealistically high desaturations which cannot be reconciled with post-test measurements of sample saturation.

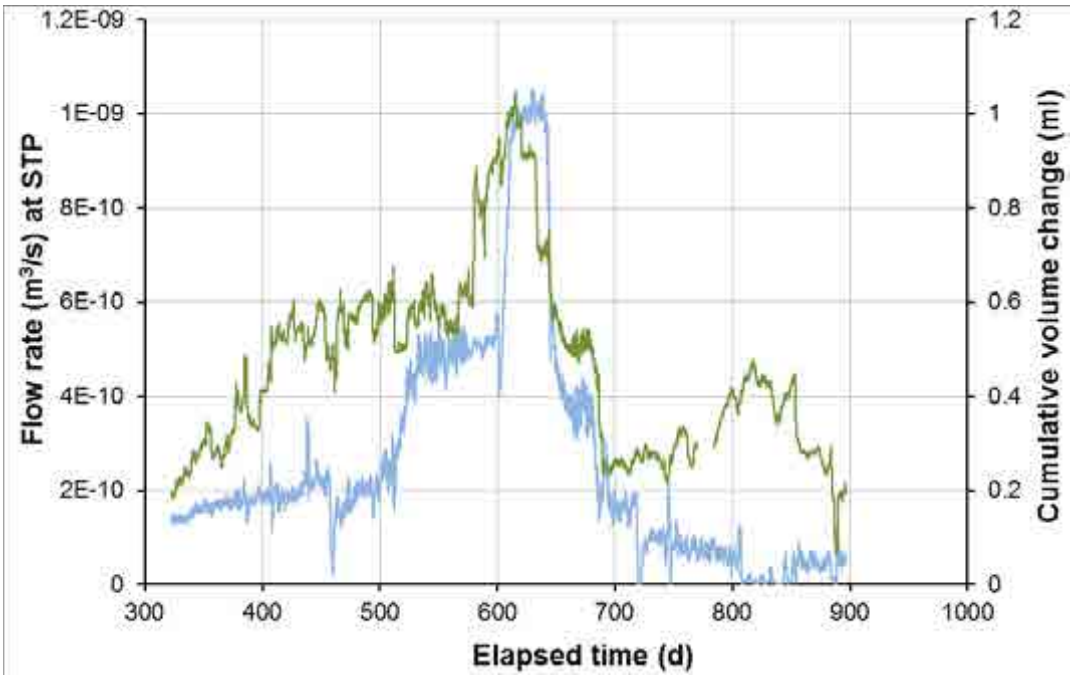

Figure 4-29 Outflow from backpressure filter and cumulative flow from confining pump (from day 322 onwards) plotted against elapsed time. While the correlation is rather crude the data suggests an underlying trend of volume increase as outflow (and pressure) increase and volume decrease when outflow (and pressure) fall.

4.1.3.4 PRESSURE DECAY (SHUT-IN)

To estimate the apparent capillary threshold value (i.e. the point at which gas ceases to be mobile within the clay), the injection pump was switched off and excess gas pressure allowed to decay.

Figure Z1 shows the slow time-dependent decrease in pressure as permeability within the sample deceases. The length of the transient is a direct consequence of the non-linearity in the gas flow law. However, an estimate of the transient length can be obtained using governing differential equation for axial flow (Harrington and Horseman, 1999)

$$V_{gi}\frac{dp_{gi}}{dt} + p_{gi}\frac{dV_{gi}}{dt} = B\left(p_{go}^2 - p_{gi}^2\right)$$

where p_{gi} and V_{gi} are the pressure and volume of gas in the injection system, p_{go} is the sum of the external water pressure (p_{wo}) and the apparent value of matric suction (p_{co}) and B is a transport variable given by

$$B = \frac{k_g A_s}{2\eta_g L_s}$$

where k_g is the effective gas permeability, A_s the cross-sectional area, η_g the viscosity of gas and L_s the length of the specimen. The solution to the governing differential equation during the shut-in stage (i.e. when the injection pump is set to zero flow rate) gives

$$p_{gi} = p_{go}\left[\frac{(p_{gi0} + p_{go})exp(Ht) + (p_{gi0} - p_{go})}{(p_{gi0} + p_{go})exp(Ht) - (p_{gi0} - p_{go})}\right]$$

where p_{gi0} is the initial pressure of gas in the injection system, *t* is the elapsed time from stopping the pump and

$$H = \frac{2Bp_{go}}{V_{gi0}}$$

where V_{gi0} is the volume of gas at the start of the shut-in. Using this solution a good fit to the data (Figure 4-30) can be achieved with the following parameters: A_s=3.142E-4 m^2 (equates to the cross-sectional area of the central injection and backpressure filters); k_g=2.55E-21 m^2; p_{co}=1x10^6 Pa. While these may not be exactly correct, we can use this technique to produce an estimate for the length of the test. Assuming conditions and material properties remain constant (which is a significant assumption) Figure 4-30 suggests stage [22] may take around 680 days to reach an asymptote.

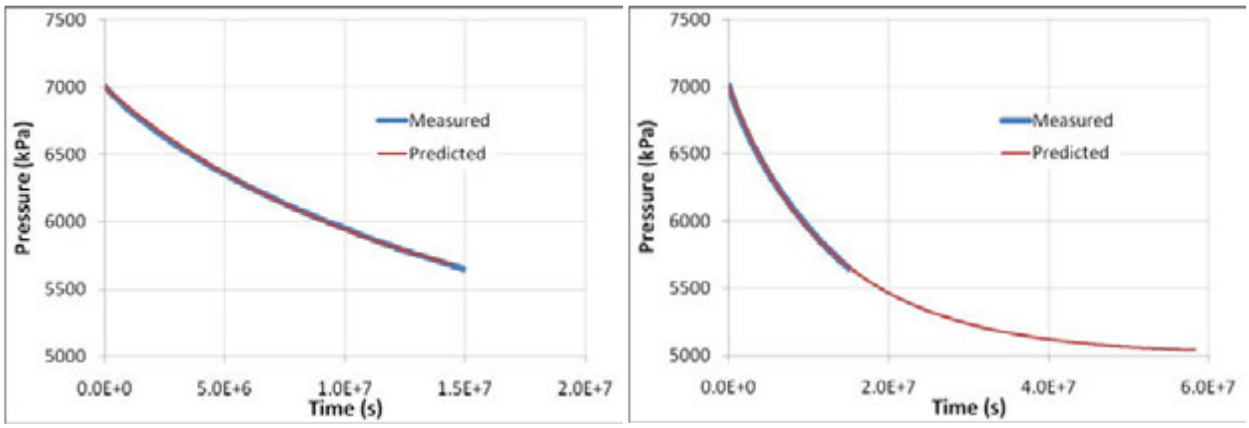

Figure 4-30 Shut-in response for test COx-1. The protracted nature of the shut-in response is a function of the initial gas volume and the non-linearity in the gas flow law. However, a good numerical fit to the data is obtained allowing a prediction of the capillary threshold pressure to be made.

4.1.4 Hydraulic test – post gas injection

Following completion of the gas injection test a second hydraulic test has been carried out and the data from which is presented in Figure 4-31 and Figure 4-32. Attempts to model this data

assuming a saturated initial state give rather poor fits, possibly due to the effects of residual gas in the system.

Figure 4-32 compares the pressure data with a model in which the axial permeability is 1.65×10^{-21} m^2, the radial permeability is 3.30×10^{-20} m^2, and the specific storage is 4.5×10^{-5} m^{-1}. It may be noted that a very similar fit can be obtained using an isotropic permeability for the clay of 1.65×10^{-21} m^2 but including surface leakage fluxes through surface zones with transmissivities of 3×10^{-16} $m^2 s^{-1}$. It can be seen that the model output does not match the data for the injection guard ring until about 25 days into the test. Similarly, during the recovery step of the test it takes about 25 days before the model again matches the injection guard ring data. The model output for the back-pressure guard ring is not at all similar to the data except for a short period around the end of the injection step and the beginning of the recovery step.

Figure 4-32 also shows the comparison of the flow rate data from the test with output from the same model. It can be seen that the model provides a good match to the inflow data after the first 20 days of the test. However, the outflow data bears almost no resemblance to the model predictions.

For comparison, the hydraulic test conducted before gas injection was found to match a model in which axial permeability is 2.0×10^{-21} m^2, radial permeability is 5×10^{-20} m^2, and specific storage is 5.4×10^{-6} m^{-1}, or, with surface leakage flow, an isotropic permeability of 1.8×10^{-21} m^2. There appear to have been small changes to the permeability, but the specific storage appears to have increased by about an order of magnitude. As indicated above, this is probably due to the effects of residual gas within the sample pore space, clearly demonstrating gas has fully penetrated the fabric of the clay.

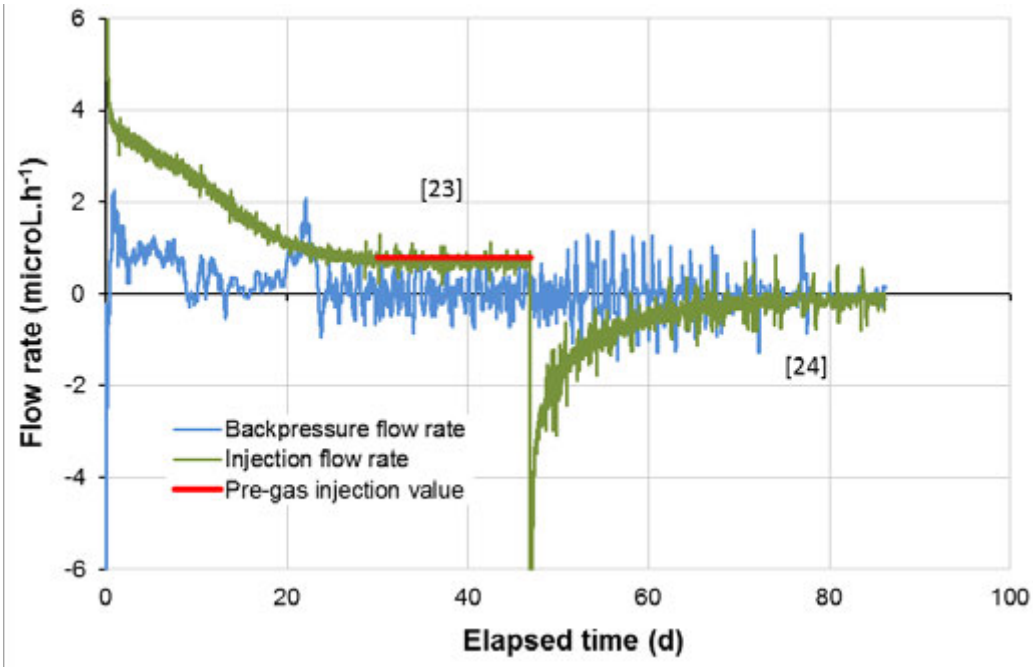

Figure 4-31 Hydraulic response following the initial gas injection cycle. Flow in asymptotes at a value very close to that of the pre-gas injection stage (red line). The offset in the outflow data probably relates to minor leakage.

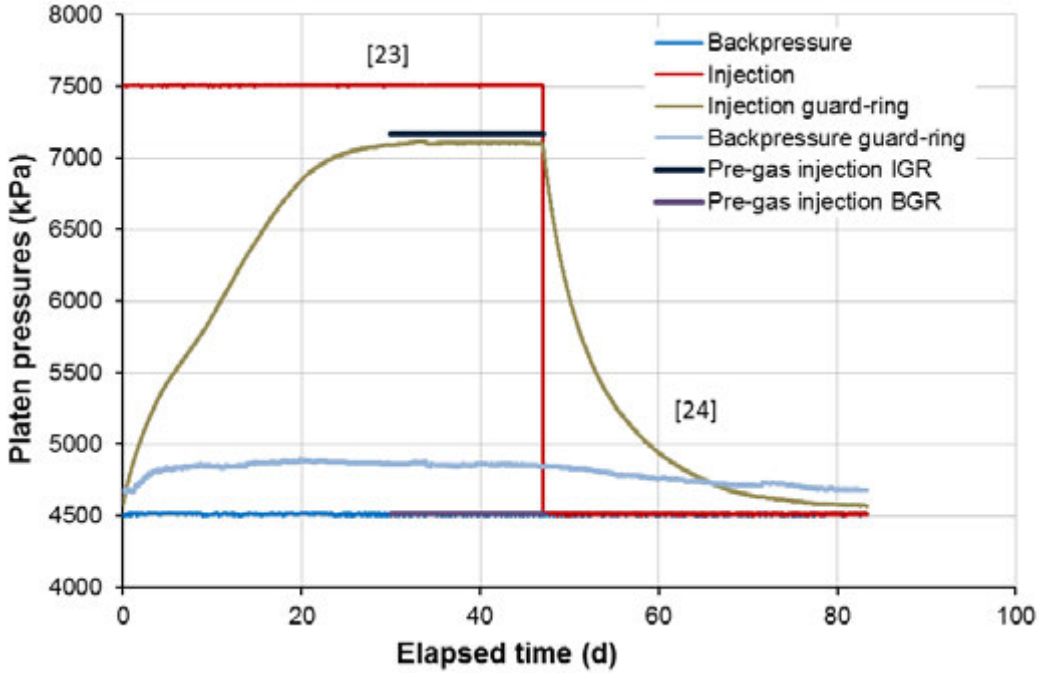

Figure 4-32 Guard ring response during second hydraulic test. While the slow pressurisation of the injection guard ring (IGR) is caused by the presence of residual gas within the filter, the asymptote is very close to the previous value. This suggests little if any change in hydraulic anisotropy. The downstream guard ring pressure (BGR) appears insensitive to the hydraulic gradient with its response probably dominated by the presence of residual gas.

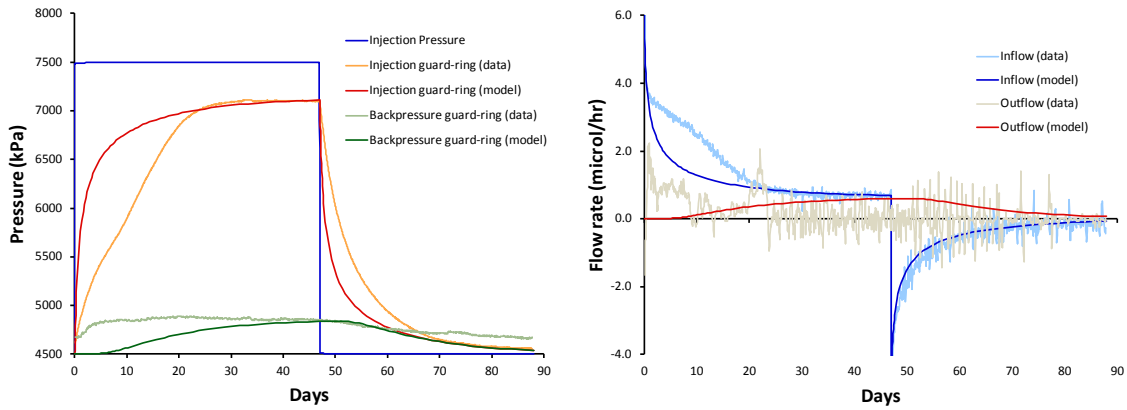

Figure 4-33 Comparison of observed guard ring pressures and flow rates with the model simulation of the post-gas injection hydraulic test on sample COx-1.

4.1.5 Second gas injection test

To examine the self-sealing capacity of the COx, it was decided to perform a second gas injection test following a simplified pressure history compared to that observed during the first gas injection cycle. Following flushing of the sintered filters with helium to try and remove the hydraulic permeant, the injection pressure was set to 7.5 MPa and flow into and out of the sample monitored with time (Figure 4-34 and Figure 4 33). Inspection of the guard-ring data shows a rapid rise in the injection guard-ring pressure (IGR) shortly after the introduction of the gas within the central injection filter. This is accompanied by a small increase in backpressure guard-ring (BGR), possibly caused by gas displacement of water from the IGR filter, and a small emergent flux of fluid out of the sample.

In total 1.38 ml of fluid was expelled from the sample during this period. As pressure was maintained constant, out flow spontaneously increased at around 82.5 days. This was accompanied by a drop in backpressure guard-ring and a subsequent increase in the injection guard ring pressure (Figure 4-35) at a slightly later time of around 83.3 days. Prior to these events, small scale changes in guard ring pressure suggests a dynamic network of gas filled pathways begin to form early in the test stage. These unstable features then continue to evolve in time and space within the sample, opening and closing depending on the localised flow of gas.

Flow into and out of the sample then evolves to 'two' apparent steady-states. The first at day 82.5 is interpreted as major gas breakthrough. This quasi-steady state lasts for around 14 days, before flux spontaneously increases. The evolution of flow during this second transient phase is markedly different to that observed during the initial event at 82.5 days. While the injection flow rate rapidly increases to a well-defined asymptote, outflow evolves much more slowly. This transient behaviour can be viewed as the time dependent development of permeability within the sample. During this time there are also a number of notable changes in guard-ring pressure. These responses are again, symptomatic of an evolving network of highly unstable gas pathways, the number and distribution of which appear to vary with time. Interestingly many of these events do not correlate with specific changes in flow, suggesting they may be relatively unimportant to the bulk movement of gas through the sample. By around day 140, the system enters a stable quasi-steady state regime with flow in and out generally equal.

While there are a number of subtle differences between the stages [25] and [9], examination of the data suggests a number of clear commonalities between the two breakthrough events. These include the time dependent development of conductive pathways, and pathways which are unstable and evolve both in time and space. While unclear at present, the origin of the initial outflow may relate to slug flow and displacement of water from the injection guard-ring filter/system. However, this phenomenon requires further investigation, what is clear, is that gas flow in the COx is a highly dynamic and coupled process.

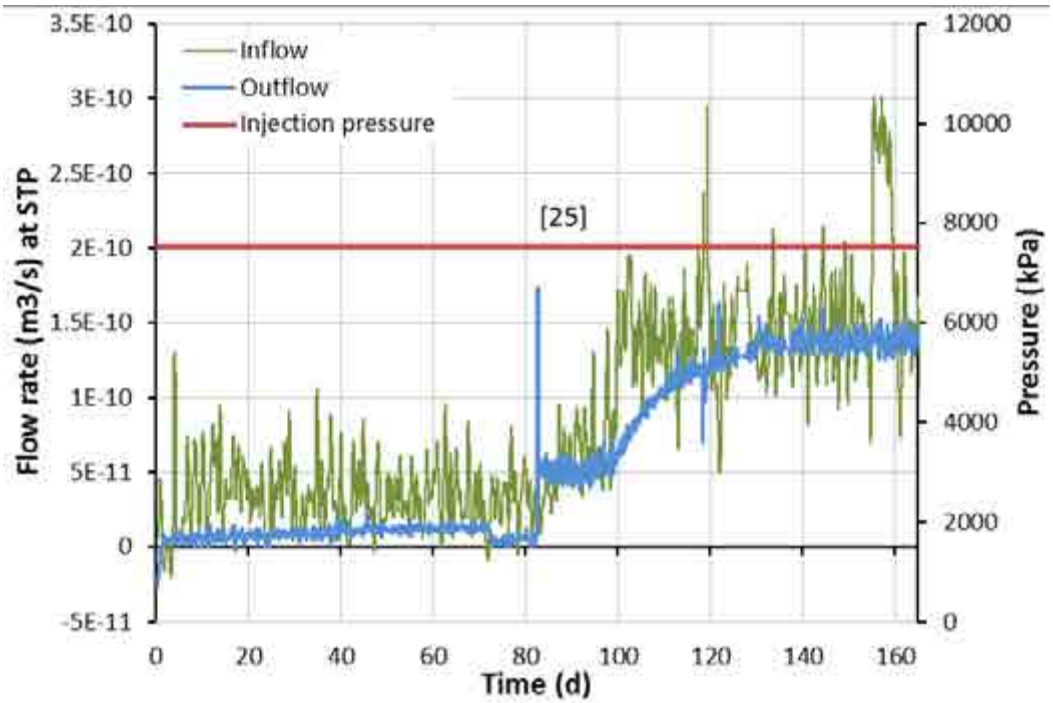

Figure 4-34 Evolution in flow into and out of sample COx-1 to examine self-sealing characteristics of the Callovo Oxfordian Clay during stage [25].

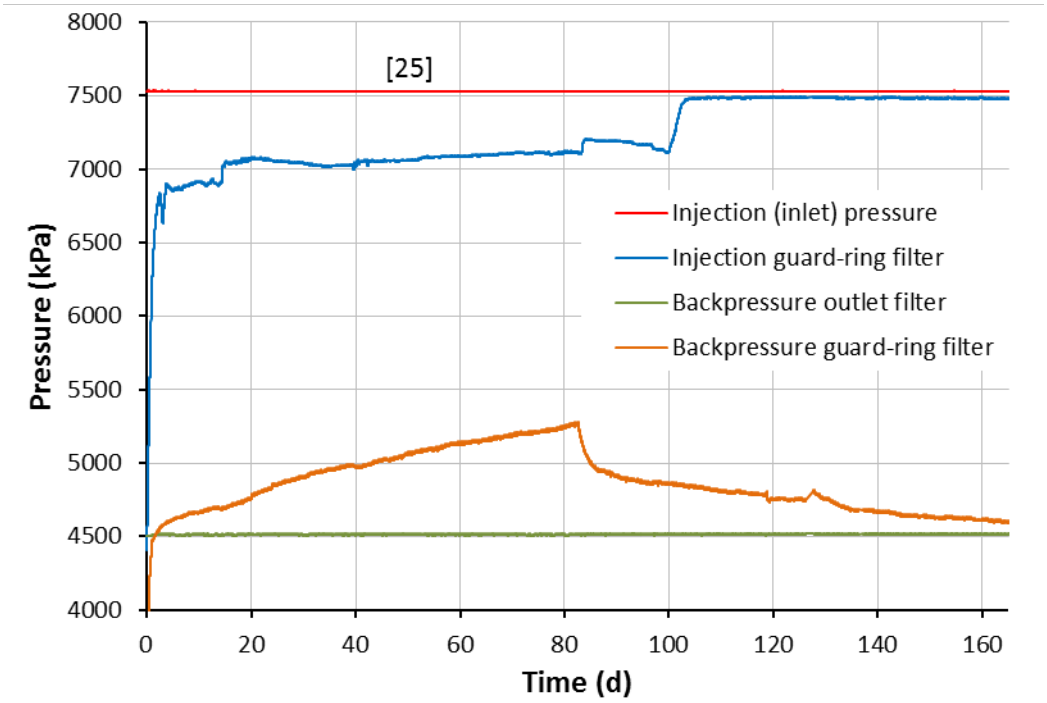

Figure 4-35 Evolution in pressure within sample COx-1 following the reinjection of gas, stage [25]. The inflections in the guar ring response are symptomatic of the opening and closing of unstable gas pathways.

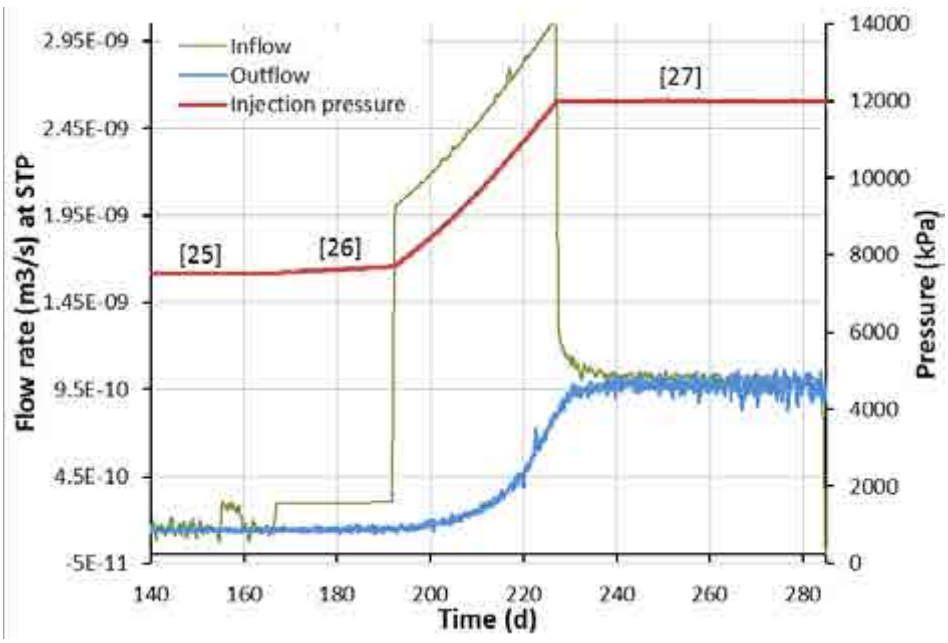

Figure 4-36 Evolution in flow into and out of the sample as gas pressure gradient is increased across the sample.

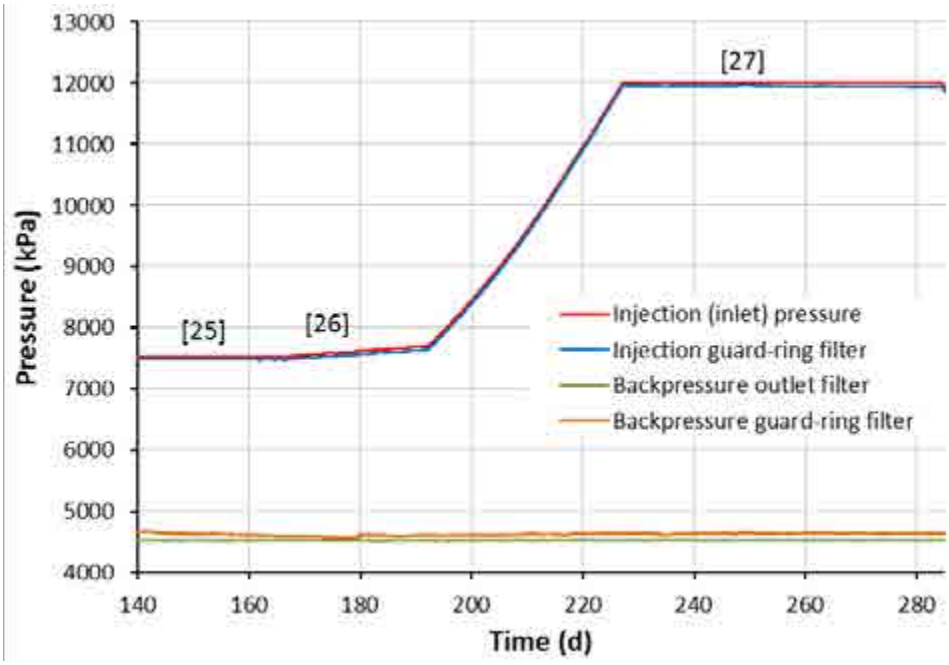

Figure 4-37 Evolution in pressure for sample COx-1 from 140 days onwards. Injection pressure guard ring tracks gas pressure while backpressure guard-ring appears insensitive to the change in gas pressure gradient.

At day 167 the injection pressure is slowly increased, over the following 60 days, to the next target value of 12.0 MPa (Figure 4-36 and Figure 4-37). During this time flux out of the specimen gradually increases approaching a well-defined asymptote at around 240 days. During this phase of gas testing the injection guard-ring closely tracks the pressure in the inlet filter, suggesting very little if any pressure drop exists between them. In contrast, the backpressure guard ring shows no sensitivity to the change in gas pressure gradient and continues the negative trend begun in Figure 4-47, reaching an asymptote value close to that of the back pressure filter. Given this filter was able to sustain a significant pressure differential and that its behaviour from day 83 exhibits no correlation to the gas pressure gradient, it provides strong evidence to confirm the sheath integrity (4.1.3.3).

The steady state data from stages [25] and [26] are presented in Table 4-3 and has been plotted against data from the first gas cycle (Figure 4-38). Inspection of the graph indicates little change in volumetric gas flow rate between test cycles, suggesting that the hysteresis observed between stages [19] and [21] has been nullified by the reinjection of water. Under these conditions, this observation suggests the gas has little permanent impact on the structure and fabric of the clay.

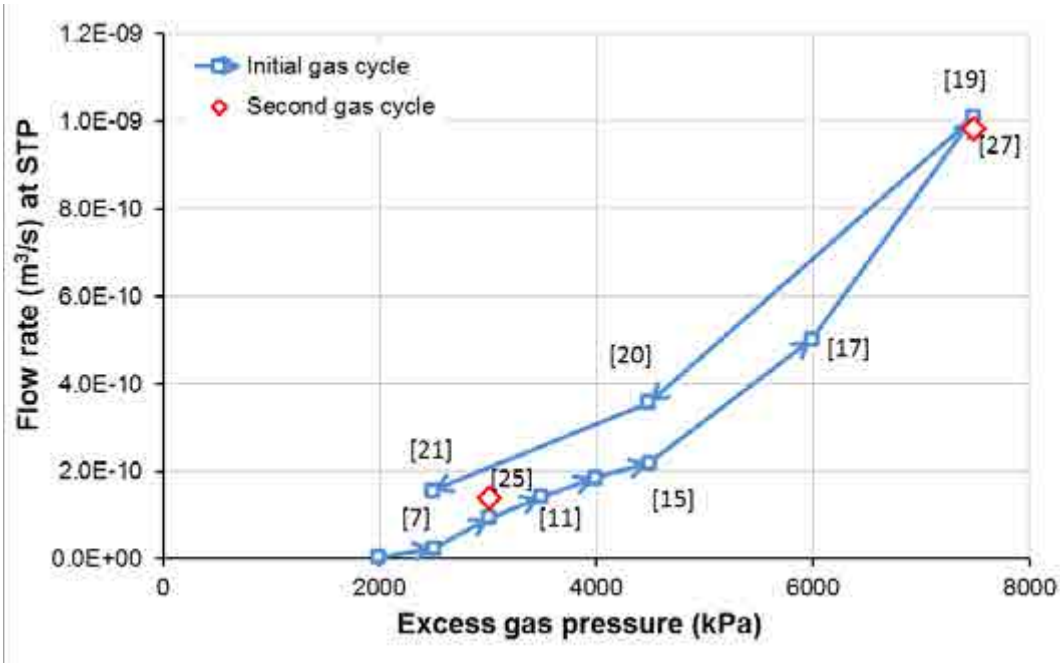

Figure 4-38 Steady state flow rates plotted against excess gas pressure for both gas injection cycles, stage [6] to [21] and [25] to [27] respectively.

4.1.5.1 Further evidence for dilatancy

Figure 4-39 shows a plot of out flow and volumetric strain plotted against time for test stages [25] to [27] inclusive. Strain is calculated based on the pre-test volume of the sample and the cumulative change in the confining system volume. While this approach is less refined than measurements from more complex triaxial systems, it can be used to identify systematic trends. The negative slope of the strain response is symptomatic of an increase in sample volume i.e. dilation. There is a clear correlation between the increase in outflow and sample volume from day 195 onwards, as gas flow out of the sample begins to increase. As outflow asymptotically approaches steady state, volumetric strain plateaus, and the system enters a quasi-steady state. These results are in general agreement with those presented in Figure 4-29 for COx-1 and the triaxial data from Figure 4-21.

By cross plotting volumetric strain against STP flow rate the correlation between flow and sample volume becomes apparent (Figure 4-40). However, the initial response at low volumetric strains suggests that for low gas entry pressure samples like COx-1, very small gas flows may be possible without significant dilation of the clay. However, the composition and limited resolution of the strain data in these tests undermines rigorous interpretation of the data during this phase of testing. As the sample approaches steady state, volumetric strains begin the plateau at an average value of around 0.5%. Interestingly, as flux across the sample remains fairly constant, the core appears to undergo some form of stress relaxation. The cause for this response remains unclear but may stem from time dependent processes related to local reorientation of the clay fabric adjacent to conductive gas pathways. Alternatively, leakage from the confining system may also play a factor though this seems unlikely as the pump piston would be traversing the same section of barrel as that experienced during the initial dilation response.

Either way, when viewed in its totality, this data provides further compelling evidence for the movement of gas by pathway dilation.

4.1.5.2 Localisation of gas flow

Upon removal from the apparatus, sample COx-1 was submerged in glycerol and gently heated to promote the release of gas. Figure 4-41 shows two images of gas evolved from the injection

and backpressure faces of the sample. Visual inspection clearly indicates a lower density of gas pathways on the inject face compared to that of the backpressure end. Intuitively, this is to be expected and is symptomatic of an expanding network of pathways which fan out as they propagate through the core. While this method of observation is not fully quantitative, it strongly suggests gas flow is localised within the clay. This observation supports the early results describing the evolution of guard ring pressures, the time dependent and non-uniform distribution of flow and the anisotropy in the strain measurements reported by Cuss and Harrington (2012). It should also be noted that no discharge of gas was observed in a control test performed on a 'fresh' section of intact core.

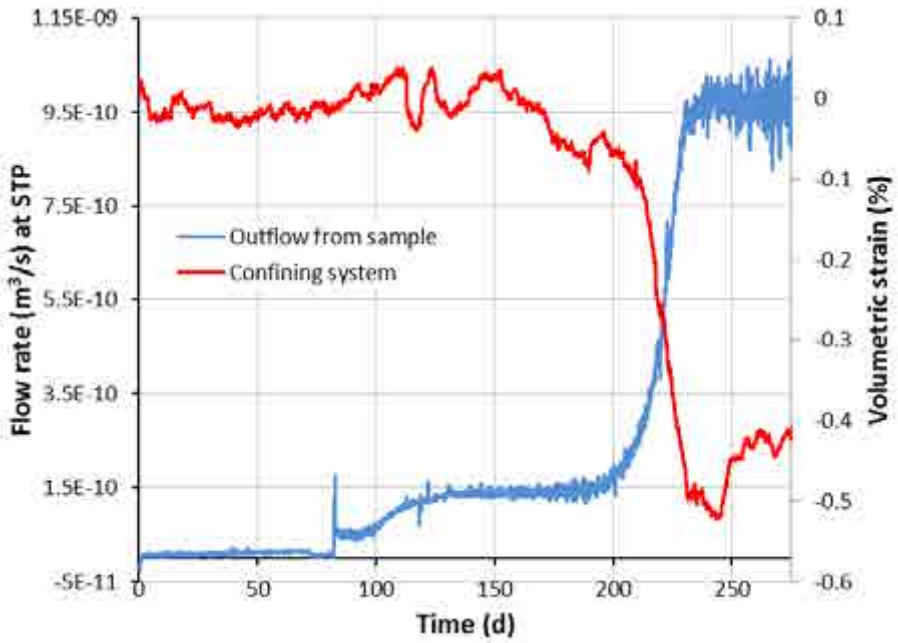

Figure 4-39 Out flow and volumetric strain plotted against time. Volumetric strain is estimated from the pre-test volume of the sample (Table 2-1) and the change in confining system volume. Negative strain represents dilation of the sample.

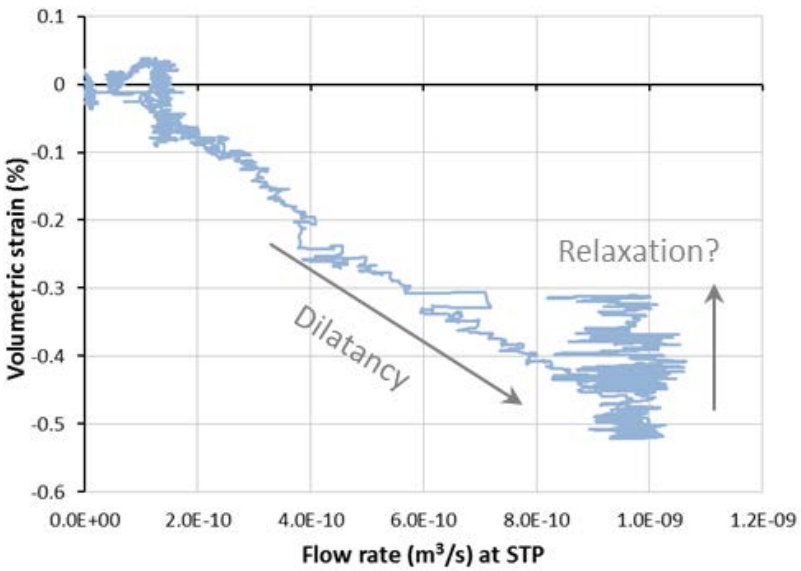

Figure 4-40 Volumetric strain plotted against STP flow rate for COx-1 showing a clear correlation between major gas flow and expansion (dilation) of the sample.

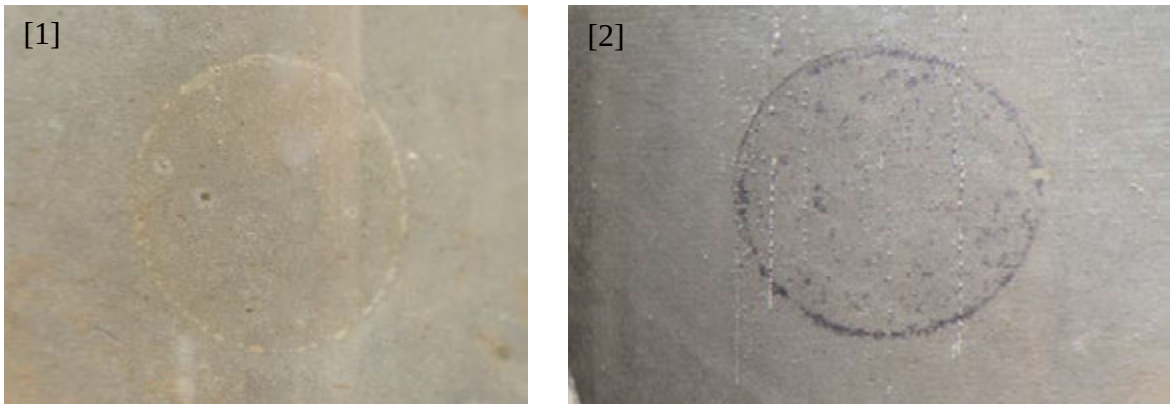

Figure 4-41 Gas discharged from sample COx-1 following submersion and gentle heating in a glycerol bath. [1] = injection face; [2] = backpressure face.

4.2 CALLOVO-OXFORDIAN CLAY SAMPLE 2 (COX-2)

4.2.1 Consolidation behaviour

A two-step consolidation test was carried out after an initial equilibration period of 31 days with the confining pressure held at 9.5 MPa. In the first step the confining pressure was raised to 11 MPa for 8 days and in the second step it was raised to 12.5 MPa for 15 days. Instantaneous flow rate and net cumulative flow volume data were collected, Figure 4-42.

Examination of the data clearly shows that at the onset of testing there is a rapid uptake of water by the specimen as it resaturates. This flux progressively declines with time, such that by around day 18, the net flow of water into the specimen is practically zero. Unlike in test COx-1, no data was available from the confining system due to a small background leak from the control pump. However, analysis of data from stage [1] indicates a net volume change of around 2.54 ml during resaturation. This is somewhat larger than the initial estimate of gas volume derived from the geotechnical data (Table 2-1), but this may in part relate to errors in the initial estimate (which is based on the moisture content of off-cut material and an assumed value for the grain density), or, more probably, reflects the fact that the sample underwent a higher degree of swelling during restauration.

Analysis of the consolidation data based on the total volume of fluid expelled from the specimen at the end of each step is presented in Table 4-4, along with the data from test COx-1 for comparison. Following each increment in confining stress specimen COx-2 exhibits a very small reduction in volume. Values for drained bulk modulus are therefore reasonably high, ranging from 1490 MPa to 1759 MPa, reflecting the indurated nature of the material. As with specimen COx-1, these values suggest that the specimen has not been subject to significant damage from de-stressing during sampling, transportation or specimen preparation. Young's modulus values were found to range from 1764 MPa to 2092 MPa.

Comparison of the data in Table 4-4 indicates specimen COx-2 is somewhat more compressible than specimen COx-1, exhibiting larger volumetric strains for a given change in confining stress. This supports the theory that COx-2 underwent a higher degree of swelling during stage [1] which would then explain the discrepancy between the measured inflow and the initial estimate for the gas saturation. While there is some degree of variance in the calculated parameters for each test specimen, the numbers are relatively similar which is to be expected since both samples came from neighbouring sections of the same core barrel.

Stage no.	Ave. effective stress (MPa)	Void ratio (at end of stage)	Volumetric strain (%)	Drained compressibility $\beta/10^{10}$ (Pa^{-1})	Drained bulk modulus (MPa)	Young's modulus (MPa)
Data for COx-1						
1	5.0	0.175	-	-	-	-
2	6.5	0.174	0.07	4.4	2262	2629 [1825]
3	8.0	0.173	0.16	6.4	1574	1870 [1700]
Data for COx-2						
1	5.0	0.193	-	-	-	-
2	6.5	0.192	0.09	5.6	1759	2092 [1600]
3	8.0	0.191	0.19	6.7	1490	1764 [1450]
Data for COx-3						
1	5.0	-	-	-	-	-
2	7.0	-		5.3	1902	2334 [-]
3	8.1	-		4.7	2133	2381 [-]

Table 4-4 Provisional consolidation data for test specimens COx-1, -2 and -3 during test stages [2] and [3]. The start value for void ratio [1] is based on the pre-test measurement. Values for Young's modulus are based on a Poisson's ratio of 0.3 (Wileveau and Bernier, 2008). Values in parentheses are derived from finite element modelling. Data for test COx-2 and -3 are provisional as testing is on-going at the time of writing.

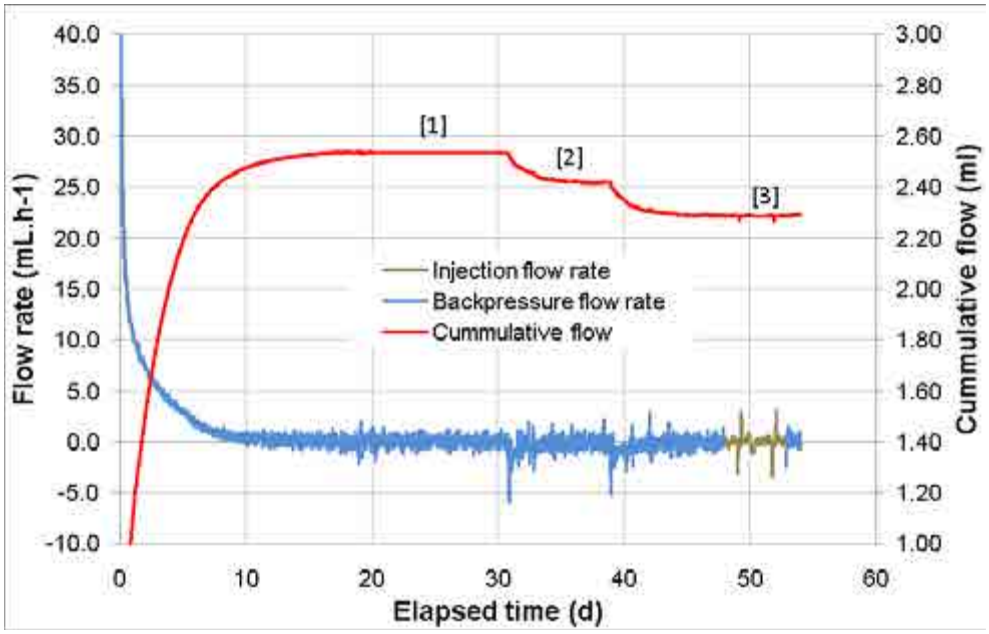

Figure 4-42 Cumulative flow from backpressure system from test stages [1] through [3] for sample COx-2. The backpressure response shows well defined transients associated with drainage of the argillite as confining stress is increased. The cumulative flow data has been edited between day 20 and 31 to correct for a pump problem.

As before, a finite element coupled deformation and porewater flow model of the experimental configuration was created to simulate test COx-2. The two steps were found to differ slightly in the parameters required to best fit the data and so have been interpreted separately. The hydraulic anisotropy derived from the values from the hydraulic tests on all three samples (2.65:1 radial to

axial) has been maintained for these models and a Poisson's ratio of 0.3 has been used throughout. The value of the Young's modulus was adjusted to fit to the magnitude of the net flow volume in each step whilst the permeability was adjusted to fit the transients.

The first step was fitted using an axial permeability of 2.5×10^{-21} m^2, a radial permeability of 6.62×10^{-21} m^2, and a Young's modulus of 1600 MPa. From equations (6) and (7) it is found that a Young's modulus of 1600 MPa corresponds to a specific storage of 8.1×10^{-6} m^{-1}. Figure 4-43 compares output from this model with the data from the test.

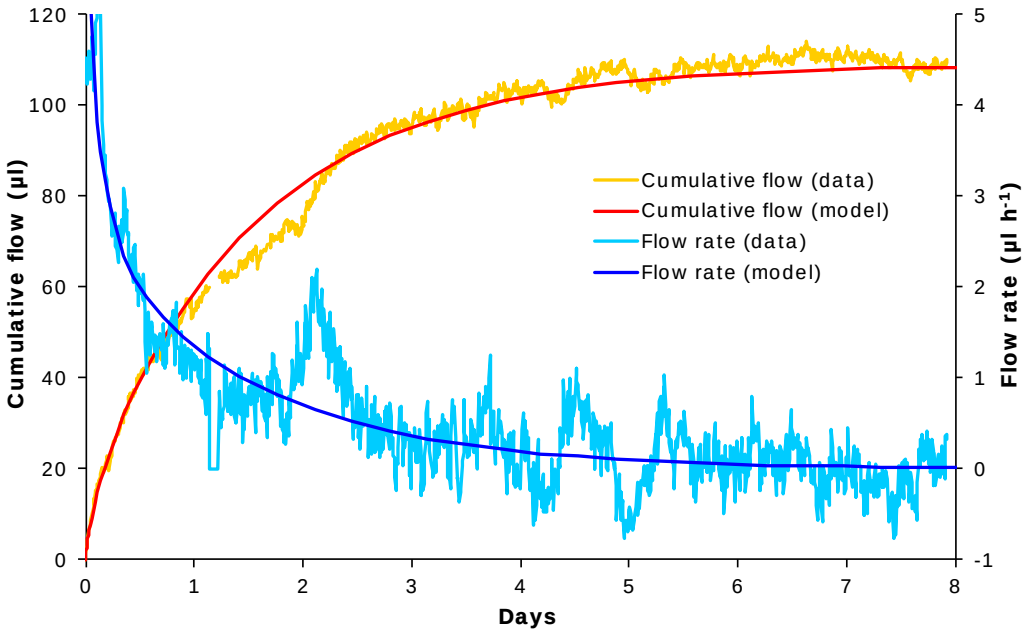

Figure 4-43 Comparison on model output to test data for the first step of the consolidation test on sample 2.

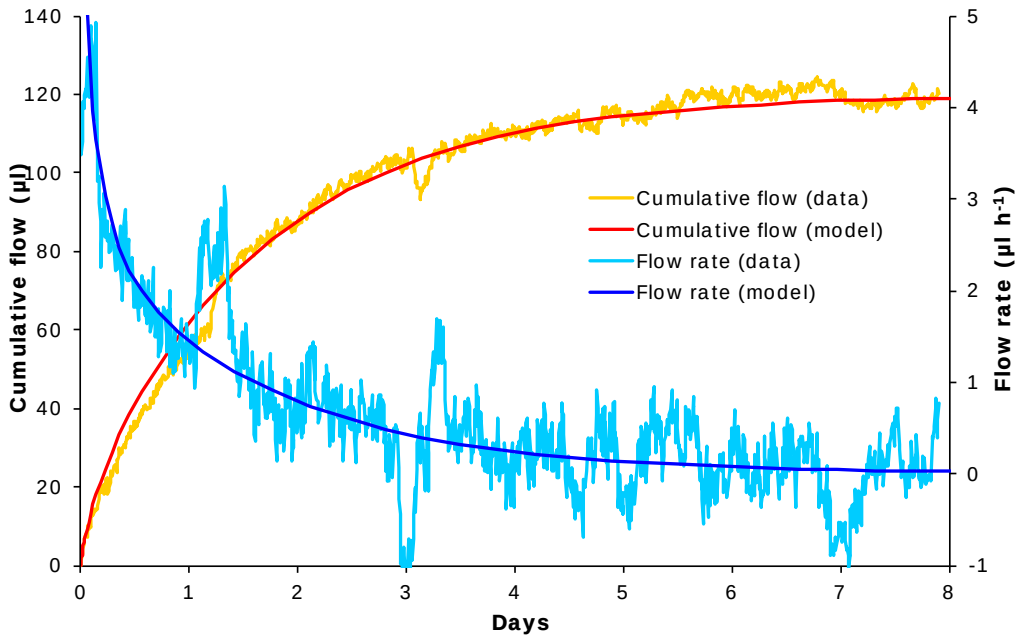

Figure 4-44Figure 4-44 Comparison on model output to test data for the second step of the consolidation test on sample 2.

The second step was fitted using an axial permeability of 2.5×10^{-21} m^2, a radial permeability of 6.62×10^{-21} m^2, and a Young's modulus of 1450 MPa, corresponding to a specific storage of 8.9×10^{-6} m^{-1}. Figure 4-44 compares output from this model with the data from the test. It appears that the permeability increases very slightly with the increase in confining pressure, but there is a small reduction when the hydraulic test is conducted. The estimates of specific storage derived

from the fitted values for Young's Modulus are slightly higher than the value found from the hydraulic test.

4.2.2 Hydraulic test

For the hydraulic test the confining pressure was maintained at a constant level of 12.5 MPa whilst the porewater pressure at the back pressure filter was kept at 4.5 MPa. The pressure at the injection filter was raised to 7.5 MPa for 21 days after which it was returned to 4.5 MPa. Flows at injection and backpressure filters were monitored together with the pressures at the two guard rings. A finite element porewater flow model of the experimental configuration was created to simulate the test and it was found that a good fit to the flow rate data could be obtained by setting axial permeability to 1.6×10^{-21} m^2 and radial permeability to 14.0×10^{-21} m^2, with a specific storage of 6.0×10^{-6} m^{-1}. Figure 4-45 and Figure 4-46 show comparisons of the model output with these parameters to the data for guard ring pressures and filter flow rates respectively. It can be seen that the model pressures are too high for both the injection and backpressure guard rings and the model parameters have been chosen as a compromise. The injection guard ring data imply a lower anisotropy in the permeability whilst the backpressure guard ring data imply a greater anisotropy.

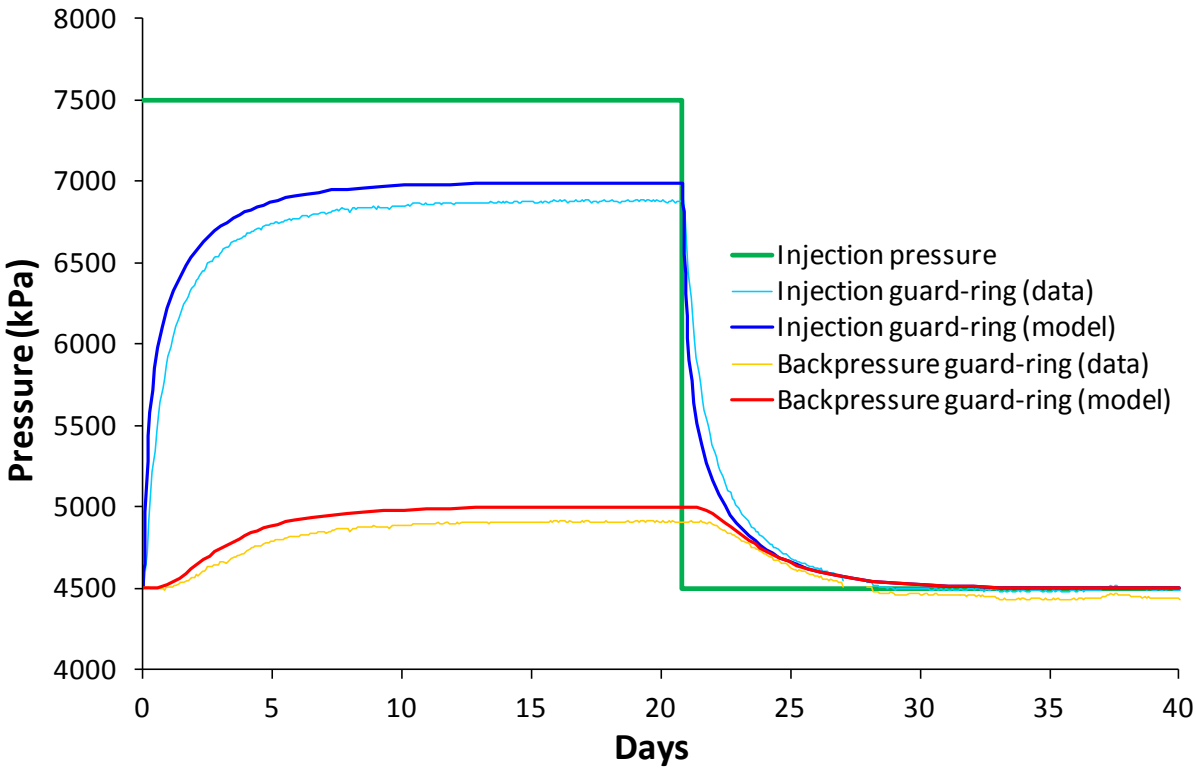

Figure 4-45 Comparison of observed guard ring pressures with the model simulation of the hydraulic test on sample 2.

The apparent differences in anisotropy of the permeability indicated by the guard ring data can be accommodated only by introducing more than a single rock type into the model. Two alternative models were constructed. In the first the sample was divided arbitrarily into separate rock layers half way along its axis. The rock properties of the two layers were set to the same values except that the radial permeability of the layer at the injection end was set to 8.8×10^{-21} m^2 and at the back pressure end to 22.4×10^{-21} m^2. This corresponds to an anisotropy in the permeability of 5.5 at the injection end and 14 at the back pressure end. The output of this model is compared to the guard ring pressure data and the flow rate data in Figure 4-47 and Figure

4-48. It can be seen that this model has a much improved fit to the guard ring data with very little change to the fit to the flow rate data.

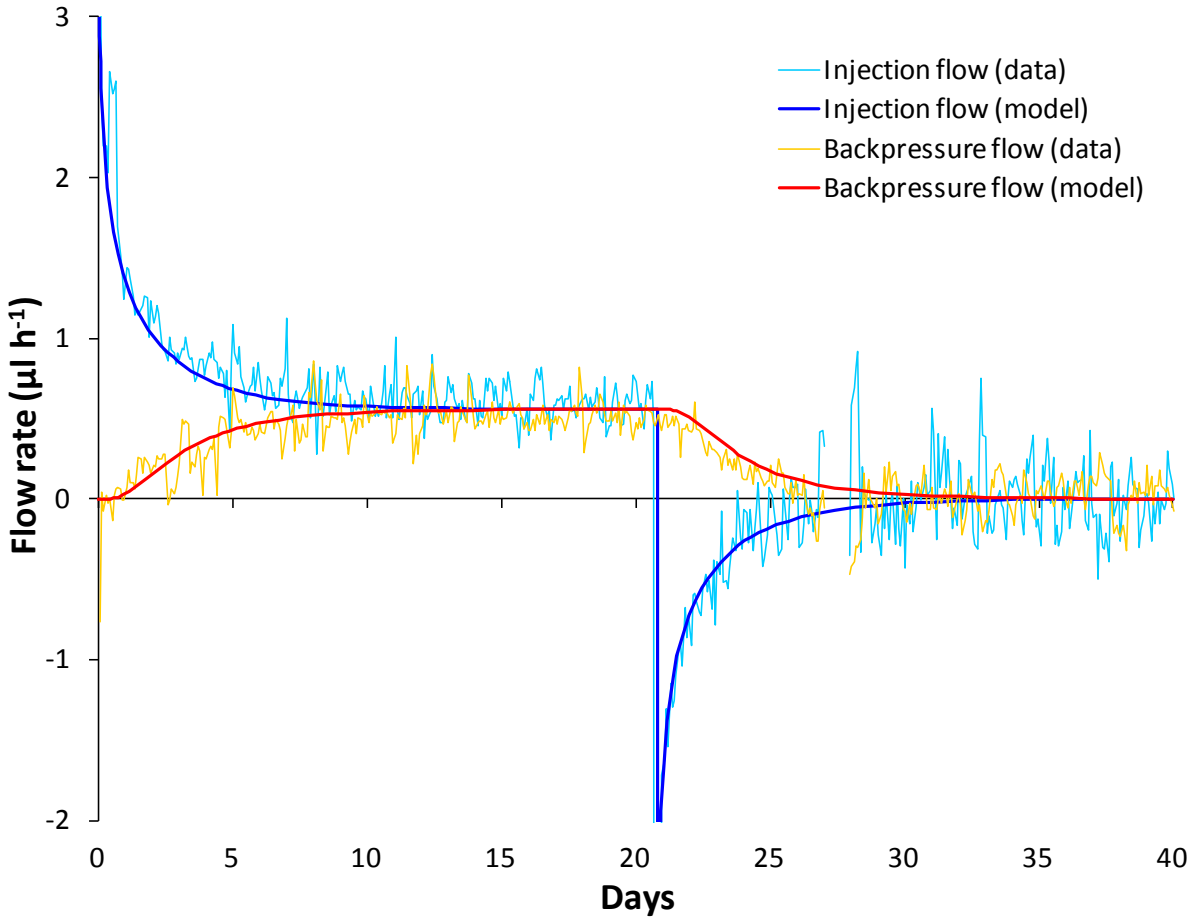

Figure 4-46 Comparison of observed flow rates from the injection and back pressure filters with the model simulation of the hydraulic test on sample 2.

The second alternative model adopted the approach of the alternative model for the first sample, having isotropic properties for the clay itself and adding thin surface leakage layers at either end of the sample. Thus the sample is given a permeability of 1.6×10^{-21} m^2 and a specific storage of 6.0×10^{-6} m^{-1}. Setting the injection surface transmissivity to 1.2×10^{-16} $m^2 s^{-1}$ and the backpressure surface transmissivity to 2.3×10^{-16} $m^2 s^{-1}$ gave fits to the data that were indistinguishable from those shown in Figure 4-47 and Figure 4-48. As for sample COx-1, with this model the anisotropy of the clay is undetermined, though with an upper limit of 5.5, since any anisotropy came be compensated for by adjustments to the surface transmissivities.

The heterogeneity introduced during the modelling exercise clearly illustrates the important role small-scale features play in determining the pressure distribution within the specimen. While this approach was not adopted for test COx-1, it may go some of the way to help explaining the low gas entry pressure and non-ideal response of the downstream guard-ring observed during gas test. It is also interesting to note, that the introduction of a bi-modal model had little effect on the advective flux.

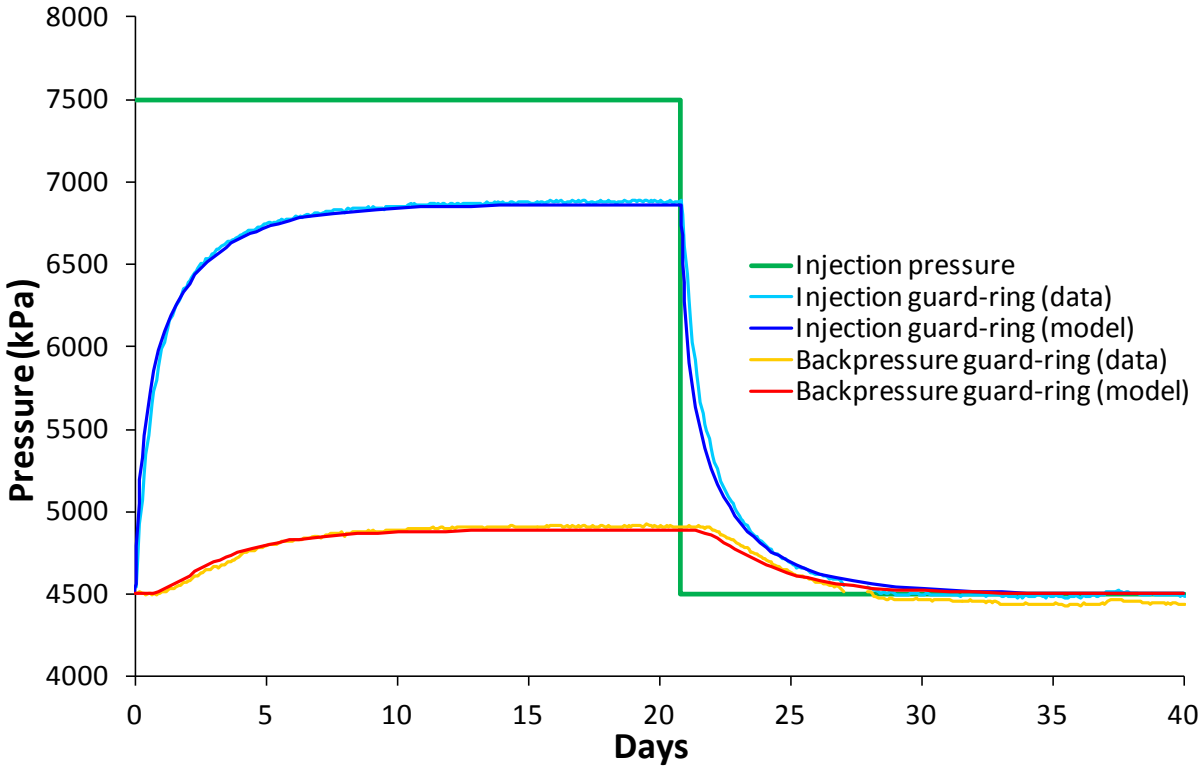

Figure 4-47 Comparison of observed guard ring pressures with a model simulation of the hydraulic test on sample 2 using a two layer representation of the sample.

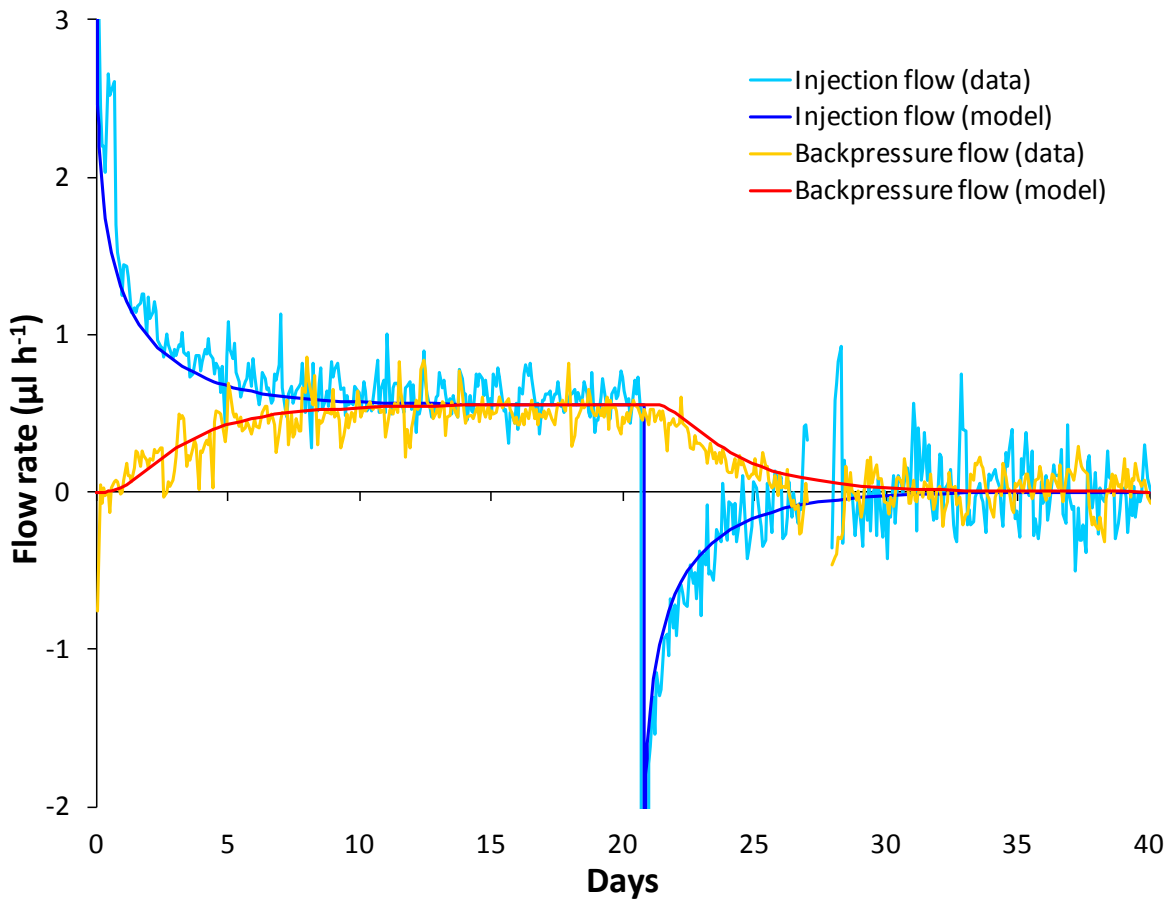

Figure 4-48 Comparison of observed flow rates from the injection and back pressure filters with a two layer model simulation of the hydraulic test on sample 2.

4.2.3 Gas injection

In a similar fashion to test COx-1, gas pressure was initially increased in a stepwise manner from 7.5 MPa, stage [6], to 11.25 MPa, stage [20], during the first 510 days of gas testing. At each stage, the injection pressure was maintained constant while flux into and out of the specimen monitored with time. During the first constant pressure gas stage [6], a small emergent flux of fluid was noted (Figure 4-49), which was also accompanied by an increase in both guard-ring pressures. This behaviour can be simply explained by the displacement of residual water, by gas, from the injection system/filter. By the end of the test stage flux and guard ring pressures all return to their original values. Gas pressure was then held constant at 7.5 MPa until day 171.8 with no obvious sign of gas flow (outflow values and guard ring pressures exhibit no conspicuous changes in behaviour).

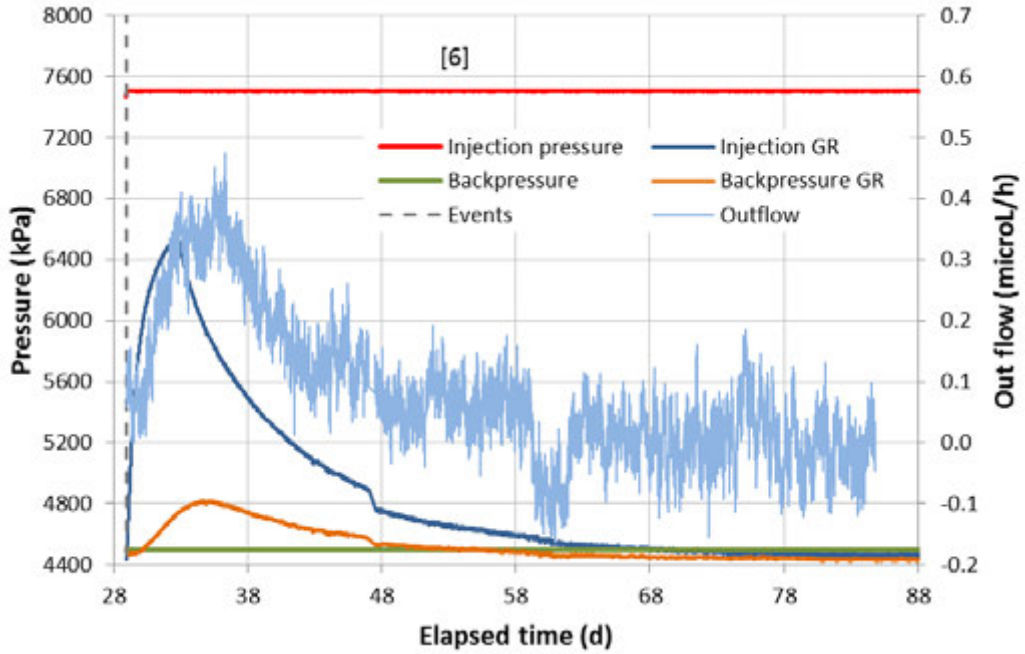

Figure 4-49 Plot showing initial slug flow through specimen COx-2 during test stage [6].

Gas pressure was then slowly increased to 8.0, 8.5, 9.0, 9.5, 10.0, 10.5 and lastly 11.25 MPa over a 338 day period. At each interval, gas pressure was held constant for between 17 and 326 days in order to observe the system response (Figure 4-50). During stages [6] through [16] there is no conspicuous sign of gas entry or breakthrough with guard ring pressures remaining fairly constant and flux out of the sample approximately equal to zero.

As gas pressure in the injection filter was then slowly increased over a 19 day period, stage [17], to the next target pressure of 10.5 MPa, the injection guard ring data (Figure 4-51) shows a conspicuous change in behaviour as the system pressure begins to increase. A similar response is observed in the backpressure guard ring a few days later. It is difficult to determine the absolute flux out of the clay during this stage due to a small leak in the backpressure pump. However, examination of the outflow data shows no conspicuous inflections or changes in response, suggesting that, if any outflow was occurring, it was fairly constant in nature. By around day 450, the leak in the back pressure pump had been fixed and a small but measurable positive flow (i.e. discharge) is observed emanating from the sample (Figure 4-50).

As seen in previous tests, inspection of the guard ring data during this phase of testing indicates underlying time dependent behaviour, with the development of conductive pathways which vary temporally and spatially within the sample (signified by changes in slope of the guard ring pressure traces). It is interesting to note that the gradual increase in IGR pressure observed from around day 418 onwards, occurs at an injection gas pressure of 10.1 MPa. This is only 0.1 MPa

larger than the previous value which was held constant for in excess of 26 days. While superposition of time dependent phenomena cannot be totally ruled out, the observation demonstrates COx is able to withstand significant gas pressure gradients for extended periods of time prior to this point of gas entry. This latter quantity is therefore estimated to be in the region of 10.1 MPa for sample COx-2. This value is in close agreement with gas entry data from the Andra/BGS triaxial test (Cuss and Harrington, 2012) which yielded a similar value of 10.2 MPa.

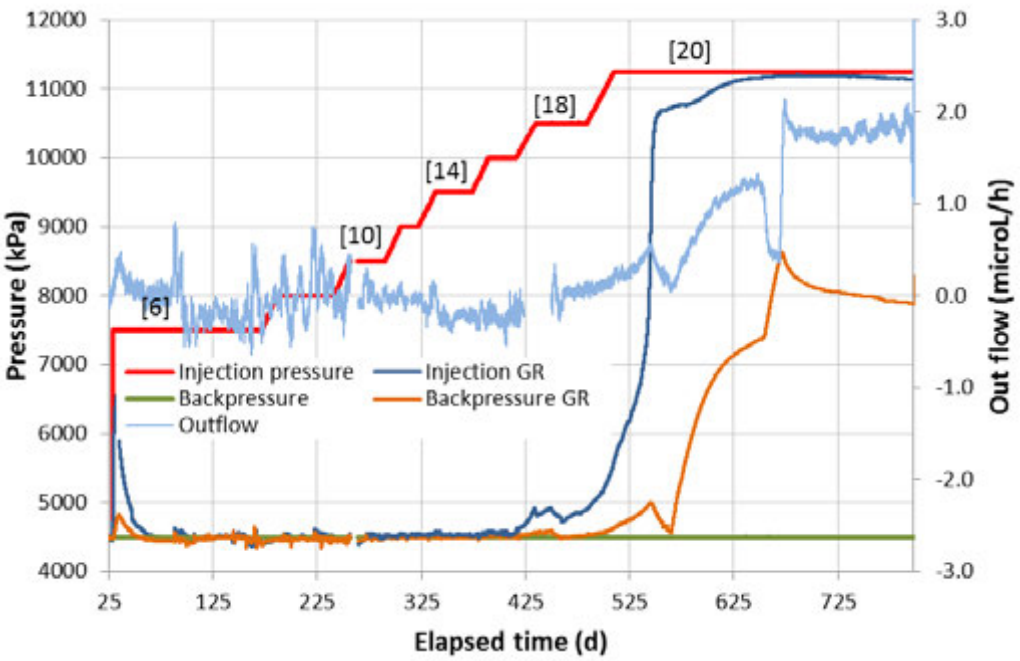

Figure 4-50 Plot showing the evolution in guard ring pressures and outflow due to changes in gas pressure gradient. The spike in data observed at around 257 days stems from the failure of the laboratory air conditioning system. However, it is clear from the GR response that this had no permanent effect on the behaviour of the claystone.

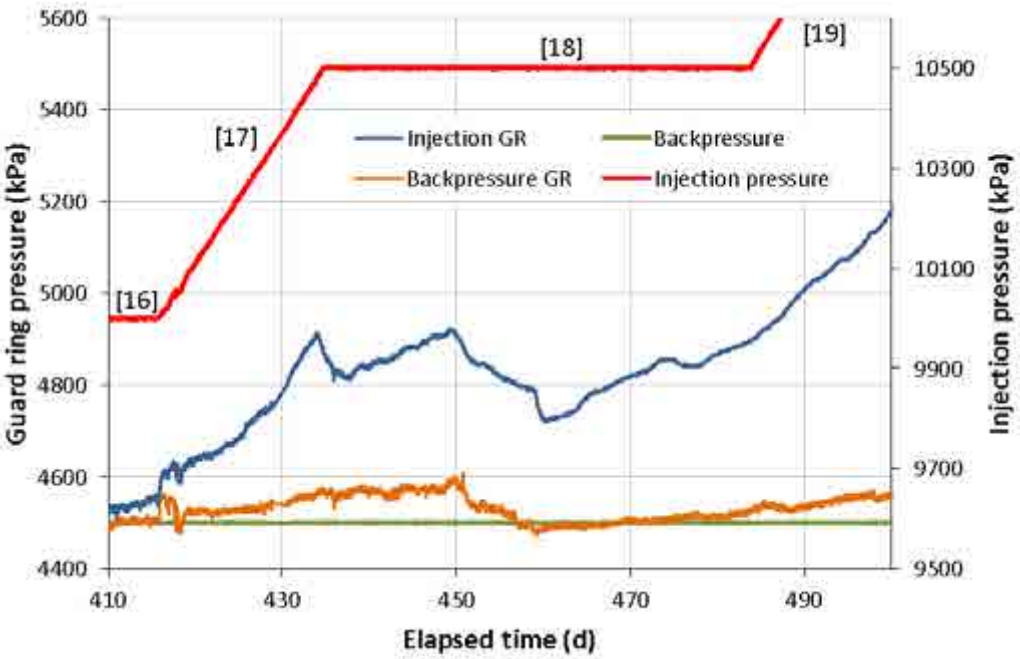

Figure 4-51 Detailed plot of guard ring and injection pressure evolution as gas begins to migrate through the sample.

By day 460, flux out of the sample asymptotes and thereafter remains fairly constant for the remainder of stage [18]. As gas pressure is then increased during stage [19], pressure in the injection guard ring filter begins to rise. This is accompanied by a much smaller increase in pressure in the backpressure guard ring. During this time out flow from the sample also begins to increase. This response is interpreted as the drainage of water displaced from the injection guard ring by the invasion of gas (Figure 4-52, zone A).

The injection pump is switched from constant flow rate to constant pressure mode (day 510) and the value maintained constant at 11.25 MPa. At around day 540 the rate of pressure increase in the IGR circuit begins to increase. This is followed 5 days later by a spontaneous reduction in both outflow and BGR pressure (Figure 4-52, zone B), suggesting most of the water from the IGR circuit has now been replaced by gas. A network of conductive gas pathways then continues to develop, reaching the BGR filter at around 565 days, inferred by the rise in filter pressure (zone C). Water then begins to drain from this circuit, resulting in a second increase in measured outflow. At around day 579, IGR pressure increases again, leading to a temporary asymptote close to the injection pressure, before declining slightly, for the remainder of the stage. These responses are symptomatic of the time-dependent increase in the number and/or conductivity of the nascent pathway network.

At around day 653, out flow decreases for a second time (zone D), thought to signify the end of water drainage from the BGR filter. Backpressure guard ring pressure then rapidly increases from day 654 onwards, reaching a peak value of 8.63 MPa at day 671, before slowly decaying to a projected asymptote of around 7.7 MPa. At day 669, out flow spontaneously increased, interpreted as the onset of major gas breakthrough (zone E). This yields a gas breakthrough pressure of 11.25 MPa. Thereafter, flux exhibited a minor peak, before entering a quasi-steady state condition.

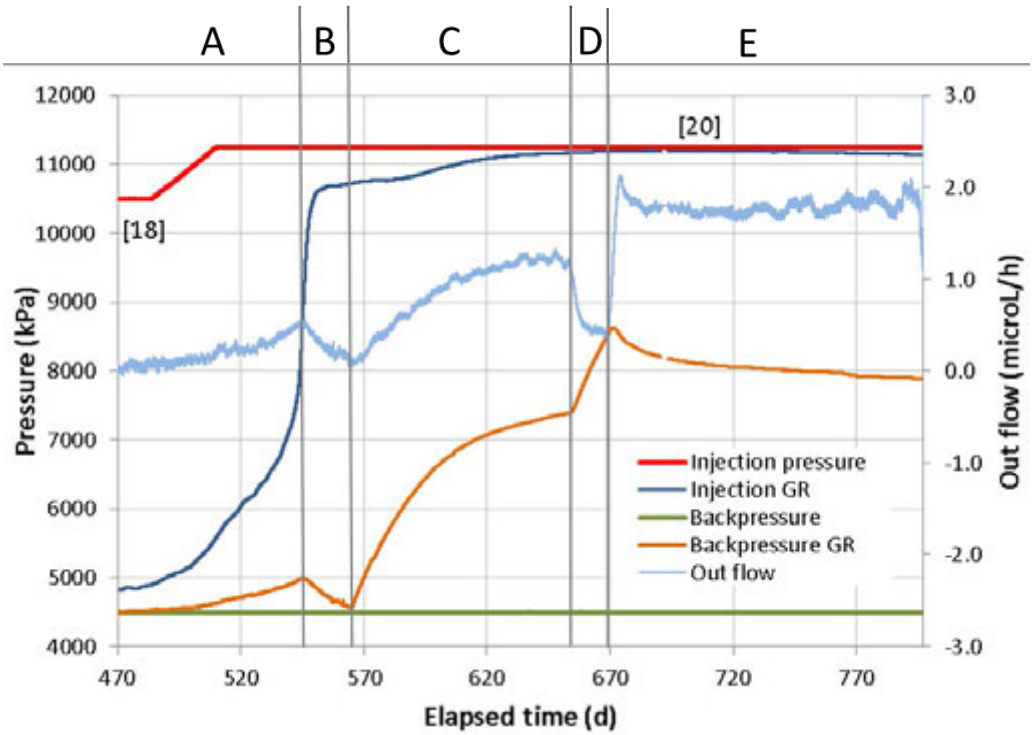

Figure 4-52 Sample COx-2: material response during gas entry and subsequent breakthrough. Zone index: A = dewatering of IGR filter; A-B = migration of gas across the sample; C = out flow dominated by drainage of water BGR filter; D = as BGR filter is drained of water gas pressure increases; E = gas breakthrough occurs.

As in previous tests, the volumetric strain before, during and after gas breakthrough has been calculated based on the pre-test volume of the sample and the change in confining pump volume (Figure 4-53). Like the data presented in Figure 4-29 and Figure 4-40, sample COx-2 shows evidence for sample dilation during the onset of gas and water flow. As with the data presented in Figure 4-40, COx-2 also appears to show some form of stress relaxation during steady-state (days 700 to 787) as volumetric strains reduce with time. This behaviour was not observed in high precision traixial tests and further work is required to better understand the coupling between gas flow and volumetric strain.

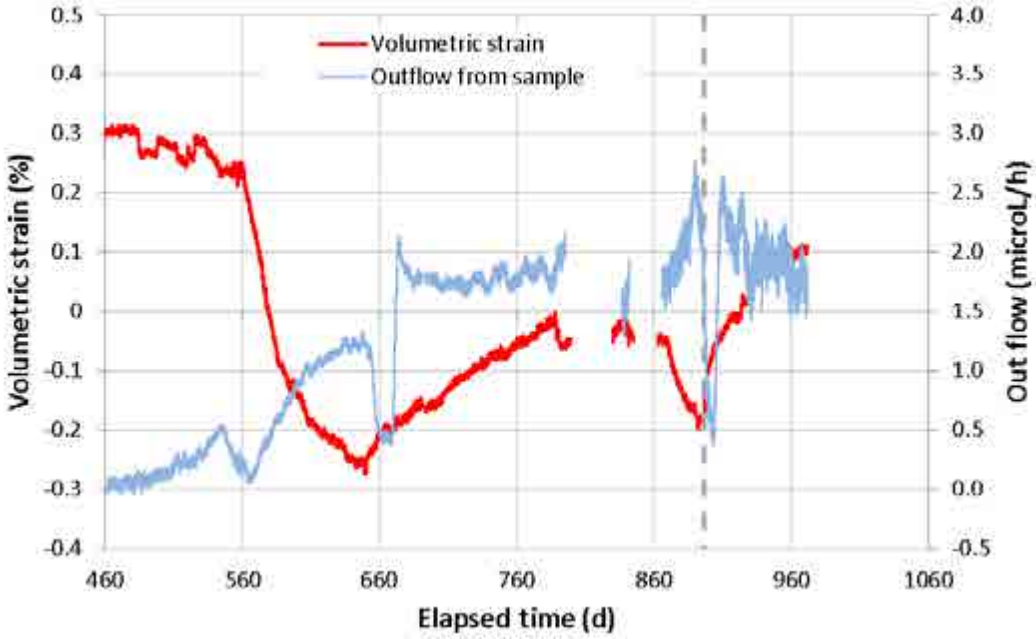

Figure 4-53 Sample COx-2: Out flow and volumetric strain plotted against time. Volumetric strain is estimated from the pre-test volume of the sample (Table 2-1) and the change in confining system volume. Negative strain represents dilation of the sample. The grey dotted line indicates the point at which confining stress was increased, stage [22].

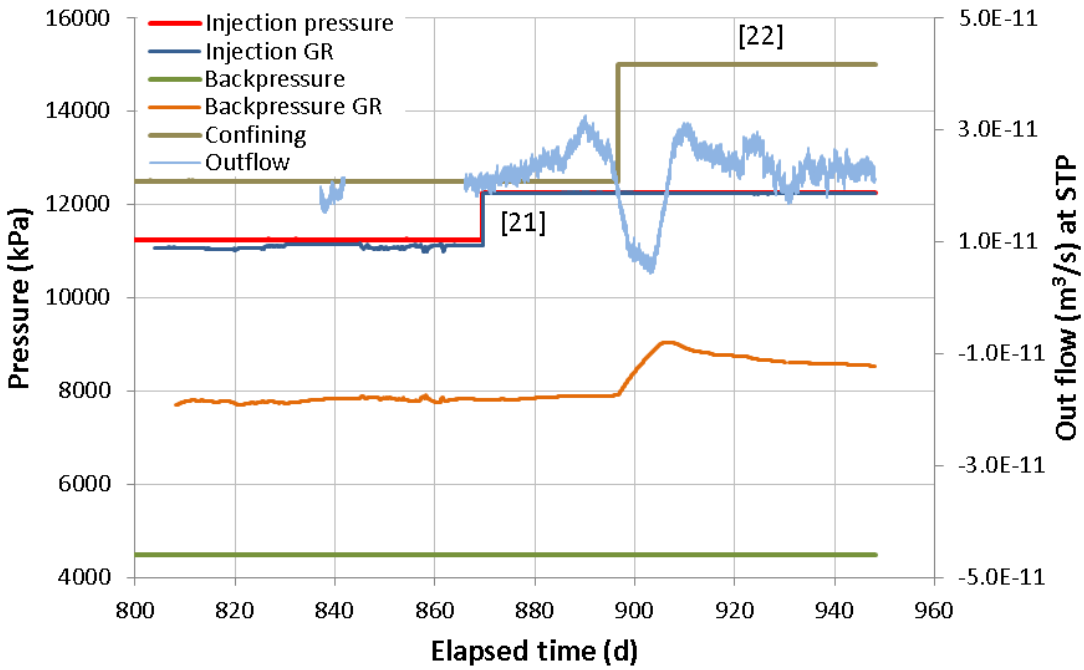

Figure 4-54 Sample COx-2: material response as gas pressure gradient and thereafter confining pressure are increased.

At the onset of stage [21], day 870, gas pressure in the inlet filter was increased to 12.25 MPa. This was followed by an increase in outflow, Figure 4-54, which peaked around day 890, before reducing to a quasi-steady state by the end of the test stage. This increase in outflow was accompanied by a second dilation event, Figure 4-53, which continued to evolve throughout the duration of the stage. At this point, confining stress was then increased to 15.0 MPa, stage [21], which, if fully transmitted to the conductive gas pathways, should be of sufficient magnitude to cause them to collapse and potentially reseal. The increase in confining stress (grey dotted line **Figure 4-53**) was accompanied by a spontaneous increase in volumetric strain (i.e. a reduction in sample volume) which continued to evolve for the following 100 days. By day 960, volumetric strain had reached an apparent asymptote of around 0.1%. During this time, outflow from the sample reduced by around 30% from 2.5 to 1.7 µl h^{-1}. While flux significantly reduced following the increment in confining stress, the data provides no clear evidence to suggest flow would ultimately asymptote at a zero flow condition. This suggests that a modest increase in confining is not sufficient to close the network of conductive gas pathways and that the interaction between gas permeability, dilatancy and confining stress is highly complex. As indicated above, further work is required to better understand these relationships.

4.2.4 Hydraulic test post gas injection

Upon completion of the gas test, all tubes and filters (including those in both guard ring circuits) were flushed with synthetic water to remove as much gas as possible. Injection and backpressure pumps were set to constant pressure mode at a calibrated value of 4.5 MPa. In/outflow and guard-ring pressure were monitored with time.

Figure 4-55 and shows the complex evolution of outflow and guard ring pressure response as sample COx-2 degasses following prolonged gas testing. While this stage is on-going, examination of the cumulative flow response exhibits a long duration transient response, suggesting an asymptote in flow at around day 250. Inspection of the guard ring data indicates rapid degassing occurs at the beginning of the stage with a higher rate of discharge at the injection end of the core (signified by a faster rate of guard ring pressurisation).

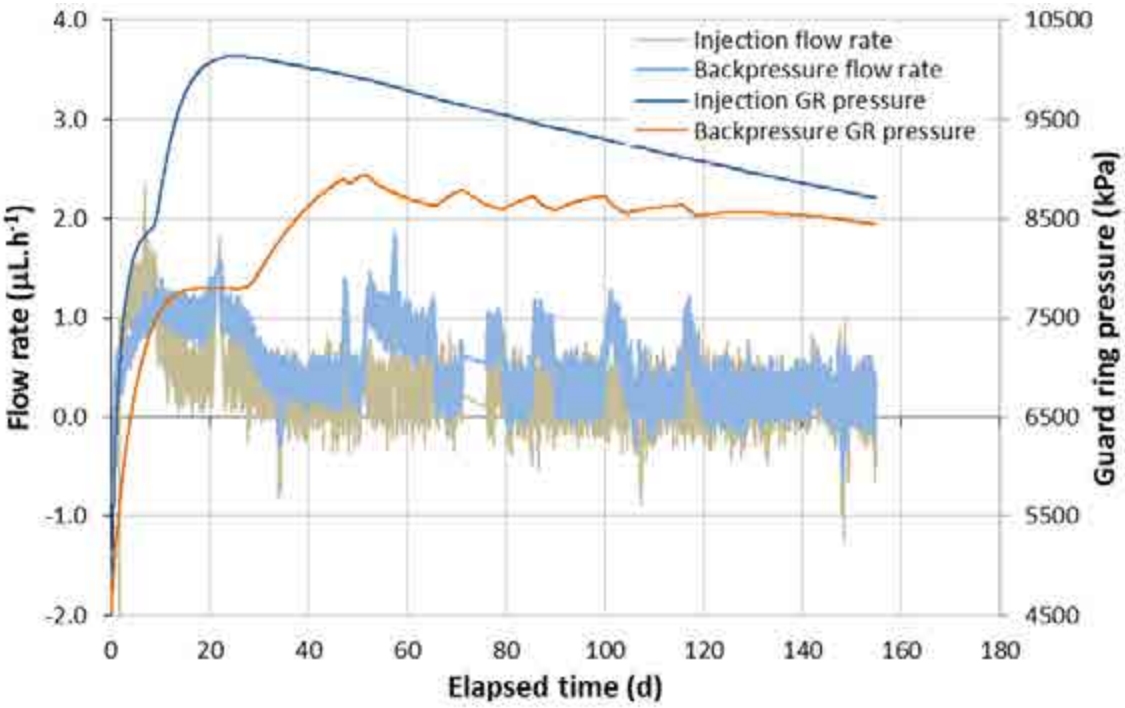

Figure 4-55 Evolution of flow and pressure after gas testing. Positive flux indicates flow out of the sample. Injection and backpressure filter pressures were maintained constant at 4.5 MPa during this stage of testing.

However, this is to be expected given the gas pressure gradient previously imposed across the sample. Around day 7 outflow to the injection filter spontaneous begins to decrease. This is accompanied by a second pressure transient resulting in a peak guard ring pressure of 10.14 MPa. Thereafter, injection GR pressure begins to decline in a linear manner which is mirrored in a small residual outflow to the injection filter.

Conversely, examination of the backpressure data clearly indicates outflow, rate of guard ring pressurisation and the absolute value of guard ring pressure are integrally linked, with changes in flow reflected in the other two responses. The asymptote in IGR pressure at around day 25 is followed by a spontaneous increase in BGR pressure, with flux out of the sample declining as gas preferentially flows to the backpressure GR filter. From day 60, the system appears to exhibit some degree of repeatability, with cyclic increases in backpressure guard ring followed by a breakthrough event, depressurisation and an increase in outflow. A cross plot of outflow to the backpressure filter versus the backpressure guard ring, Figure 4-56, illustrates this cyclic behaviour, with the plot comprised of a series of superimposed 'loops'. As gas drains to the BGR filter the pressure increases. During this time a residual outflow of gas (from background degassing of the sample) continues at a fairly constant rate. At a critical threshold pressure of around 8.72 MPa, gas begins migrates from the guard ring to the backpressure filter, resulting in a spontaneous reduction in GR pressure and an increase in outflow to the backpressure filter. As gas drains and the GR filter pressure declines, the pathways reseal (at around 8.53 MPa), flow returns to the residual degassing value, and the process begins again. The large differences in pressure between the backpressure and guard ring filters clearly demonstrates that very high gas pressure gradients exist within the clay and that much if not all of the drop in gas pressure (during advective gas flow) is within the last few millimetres (or less) of the clay.

While the test is on-going, the data indicates that advective gas transport remains possible in sample COx-2 at pressures above 8.72 MPa. While this is a little lower than the gas entry pressure quoted in Section 4.2.3 (10.1 MPa), it may reflect a range of issues associated with long term interactions between the clay and the gas phase. What is clear however is that the integrity of the seal between the platens and the sample remains intact and does not appear to act as a conduit for flow. Once testing draws to a conclusion, the asymptote of the guard ring pressures will provide important data on the anisotropy of the clay to gas flow and the distribution of gas pressure within the sample.

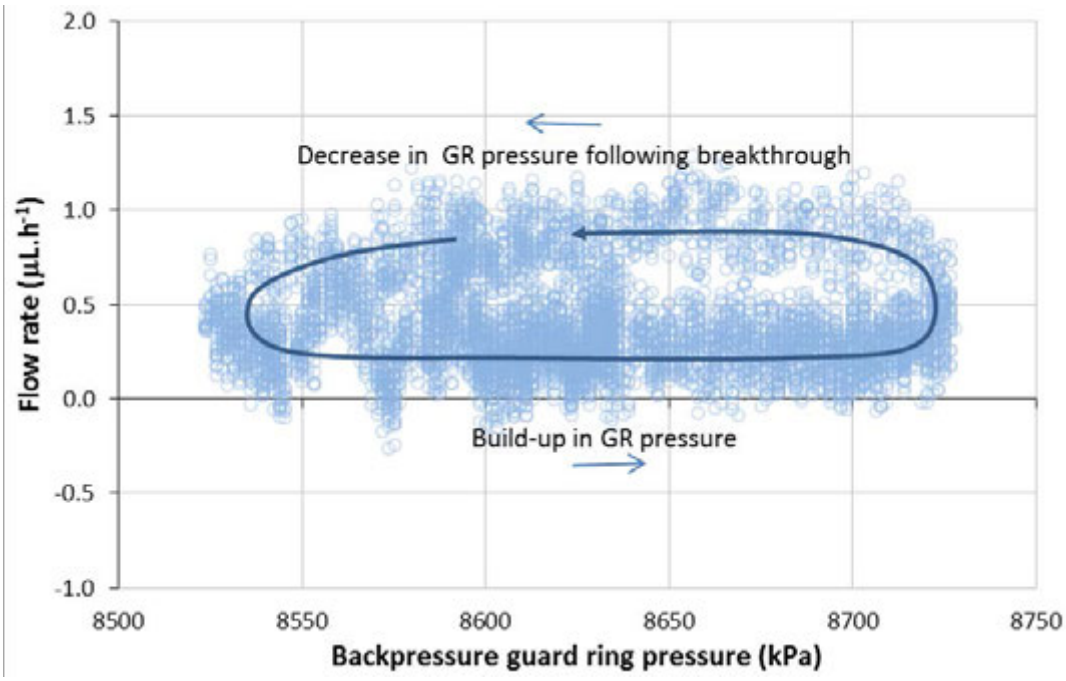

Figure 4-56 Cross plot of outflow against backpressure guard ring from day 60 to 120, showing cyclic behaviour between flow and GR pressure as the sample degasses.

4.3 CALLOVO-OXFORDIAN CLAY SAMPLE 3 (COX-3)

4.3.1 Consolidation behaviour

A two-step consolidation test was carried out after an initial equilibration period of 15 days with the confining pressure held at 9.5 MPa. In the first step the confining pressure was raised to 11.6 MPa for 6 days, test stage [2], and in the second step it was raised to 12.7 MPa for 8 days, stage [3]. Instantaneous flow rate and net cumulative flow volume data were collected.

Sample COx-3 has been taken with its cylindrical axis parallel to the bedding plane which makes the geometry of the test fully three dimensional. Unfortunately, the finite element code used for simulation of the consolidation tests on samples COx-1 and COx-2 treats only two dimensional and axisymetric problems, so it has not been possible to make a simulation of this sample. Analysis of the consolidation data based on the total volume of fluid expelled from the specimen at the end of each step is presented in Table 4-4

4.3.2 Hydraulic test

For the hydraulic test the confining pressure was maintained at a constant level of 12.5 MPa whilst the porewater pressure at the back pressure filter was kept at 4.5 MPa. The pressure at the injection filter was raised to 7.5 MPa for 16 days, stage [4], after which it was returned to 4.5 MPa, stage [5]. Flows at injection and backpressure filters were monitored together with the pressures at the two guard rings.

A 3D finite element model of porewater flow in the hydraulic test apparatus was created that included both the sample and the filters at either end. The symmetry of the experimental apparatus permits the model to consider just a quarter cylinder and flows into and out of the full system will be four times those obtained from this model. The material components and the mesh used are shown in Figure 4-57. It was assumed that the sample's bedding lay in the X-Z plane with the Y axis perpendicular to bedding. It can be seen that elements were included in the model to represent the end surfaces between the filters. These were initially given very low permeabilities so that the response of the sample alone could be considered. Further models were run with more conductive elements here to study the effects of leakages on these surfaces.

An initial model was run in which the clay sample was assumed to have an isotropic permeability and the value was adjusted to fit the data for flows into and out of the sample. The fit shown in Figure 4-58 was obtained using a permeability of 7.7×10^{-21} m^2 and a specific storage of 6×10^{-6} m^{-1}. It can be seen that a good fit has been obtained to the data. However, the model's predictions for the guard ring pressures are very poor as shown in Figure 4-59.

Since the sample is known to have bedding in the X-Z plane further models were run with the Y-axis component of permeability reduced to see if the fit of the guard ring pressure response to the data could be improved. Figure 4-60 and Figure 4-61 show results from a model with an anisotropy of 20, the X-Z plane permeability having been adjusted to fit the flow rate data. Here the X-Z plane permeability is 10^{-20} m^2 and the Y-axis permeability is 5×10^{-22} m^2. It can be seen that the guard ring pressure fit is in fact somewhat poorer than for the isotropic model.

It is apparent that the guard ring pressure data are incompatible with the models considered above and indeed the injection guard ring data in particular strongly suggest a highly permeable connection to the injection filter. To examine the effect of such connections further models were run in which the permeability of the surface zone elements was raised until improved fits to the guard ring pressures were obtained. The X-Z plane permeability of the sample was then adjusted to fit the flow data whilst maintaining the Y-axis permeability at 5×10^{-22} m^2 as in the previous model. Figure 4-62 and Figure 4-63 show the results obtained with the X-Z plane permeability at 4.5×10^{-21} m^2 after setting the injection surface zone transmissivity to 3×10^{-14} m^2s^{-1} and the backpressure surface zone to 8×10^{-16} m^2s^{-1}. Whilst this model shows a greatly improved fit to the guard ring data there remains a gradual increase in the back-pressure guard ring pressure that is

not reproduced by the model. One possible explanation would be that the back-pressure surface zone is gradually reducing in transmissivity over time.

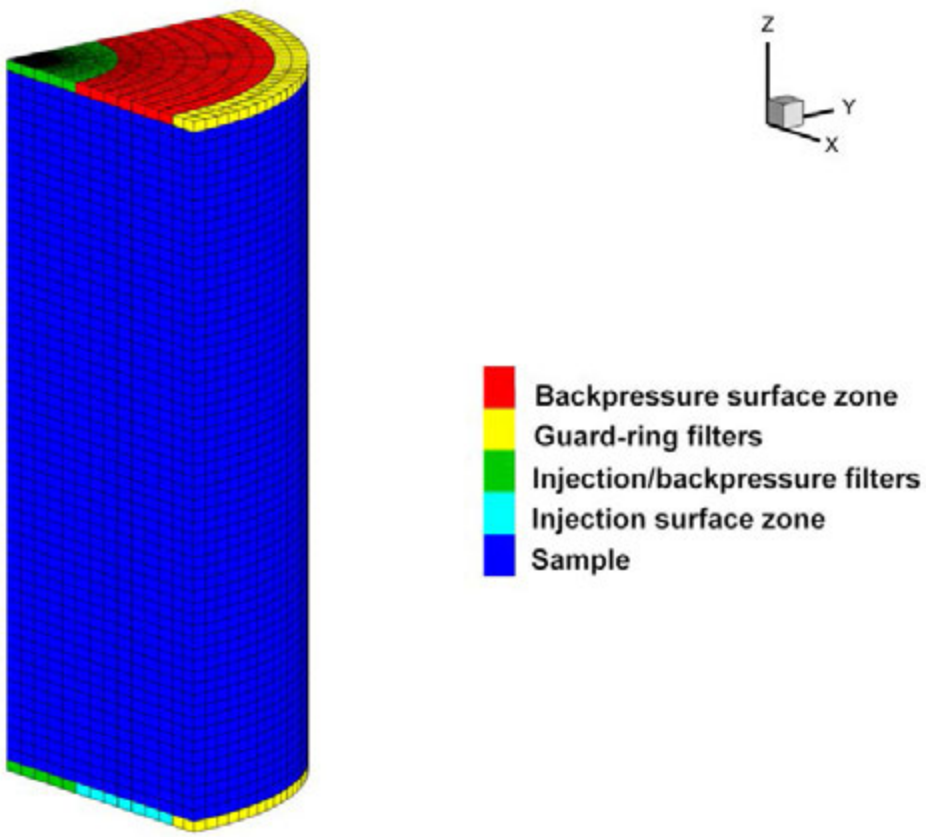

Figure 4-57 The material components and mesh of the quarter cylinder flow model used for simulation of the hydraulic test for sample COx-3.

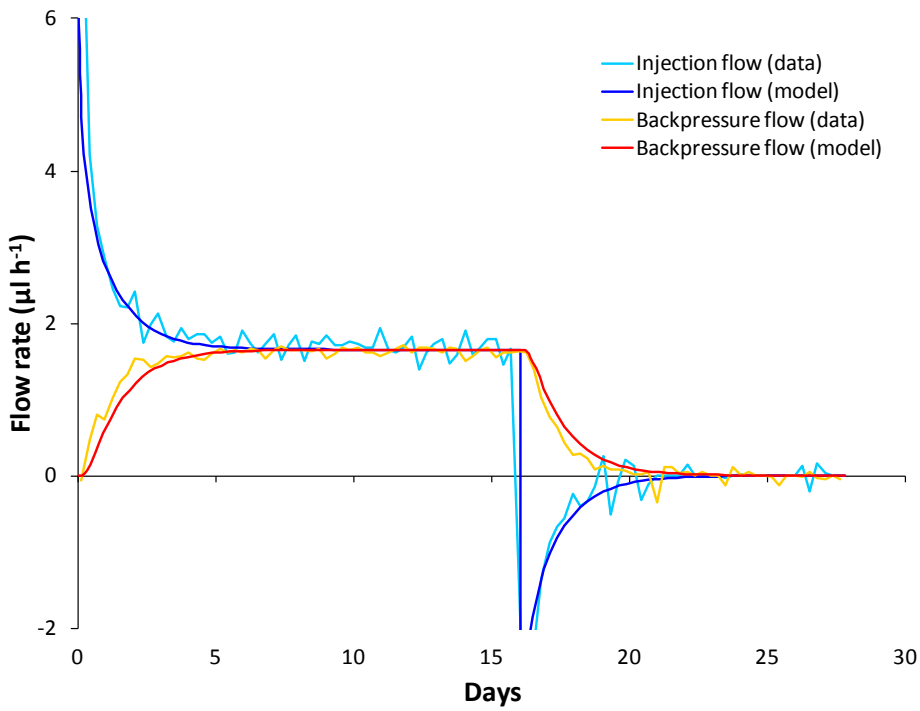

Figure 4-58 Comparison of an isotropic permeability model with flow data for sample COx-3.

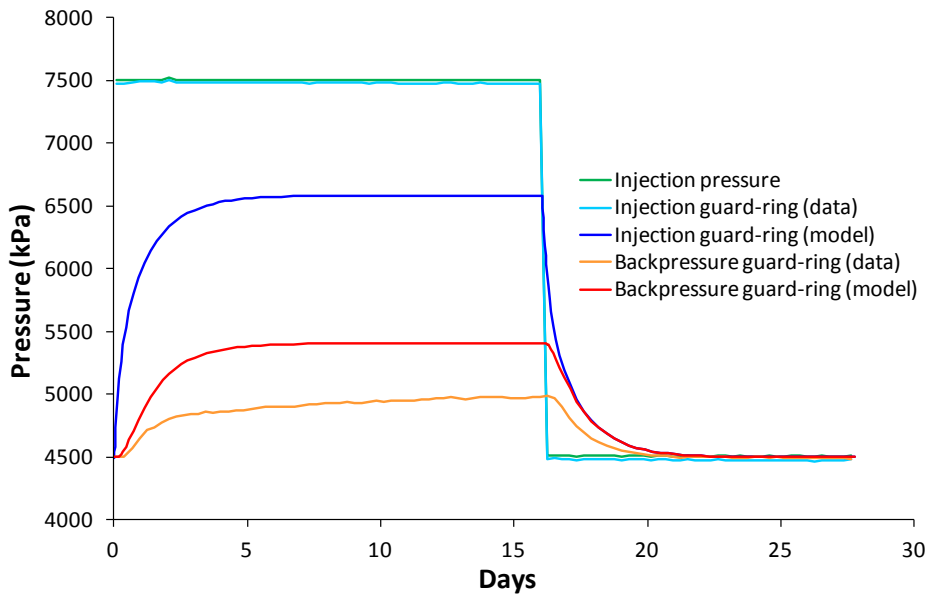

Figure 4-59 Comparison of an isotropic permeability model with guard ring pressure data for sample COx-3.

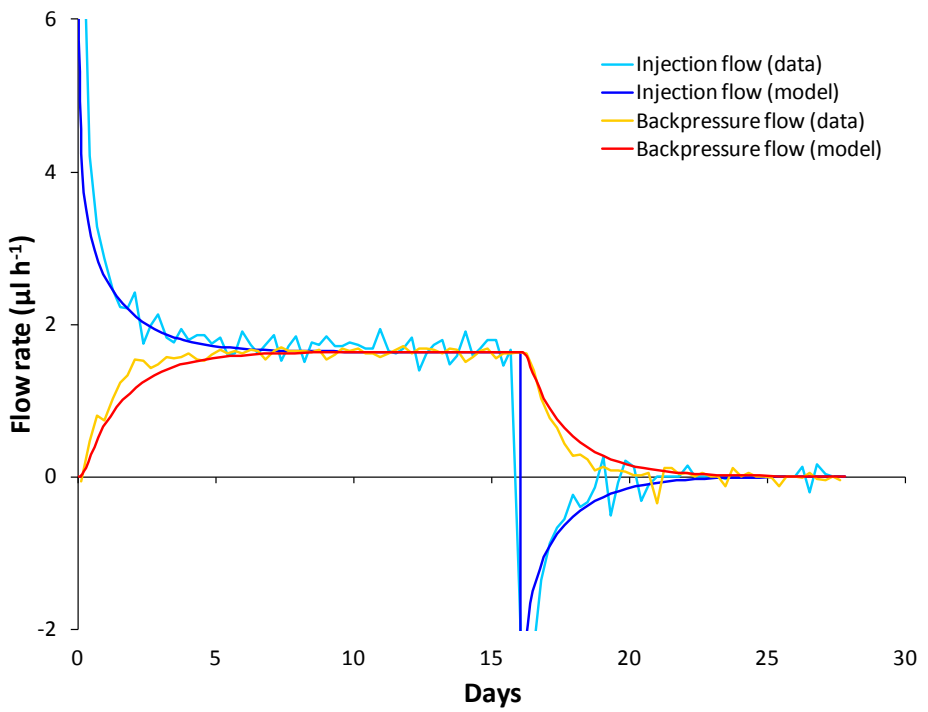

Figure 4-60 Comparison of an anisotropic permeability model with flow data for sample COx-3.

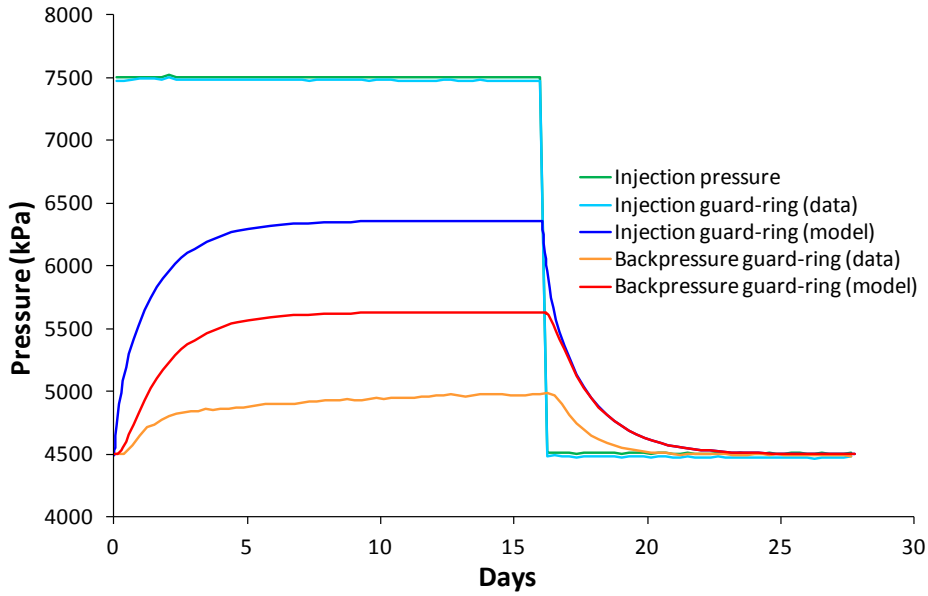

Figure 4-61 Comparison of an anisotropic permeability model with guard ring pressures for sample COx-3.

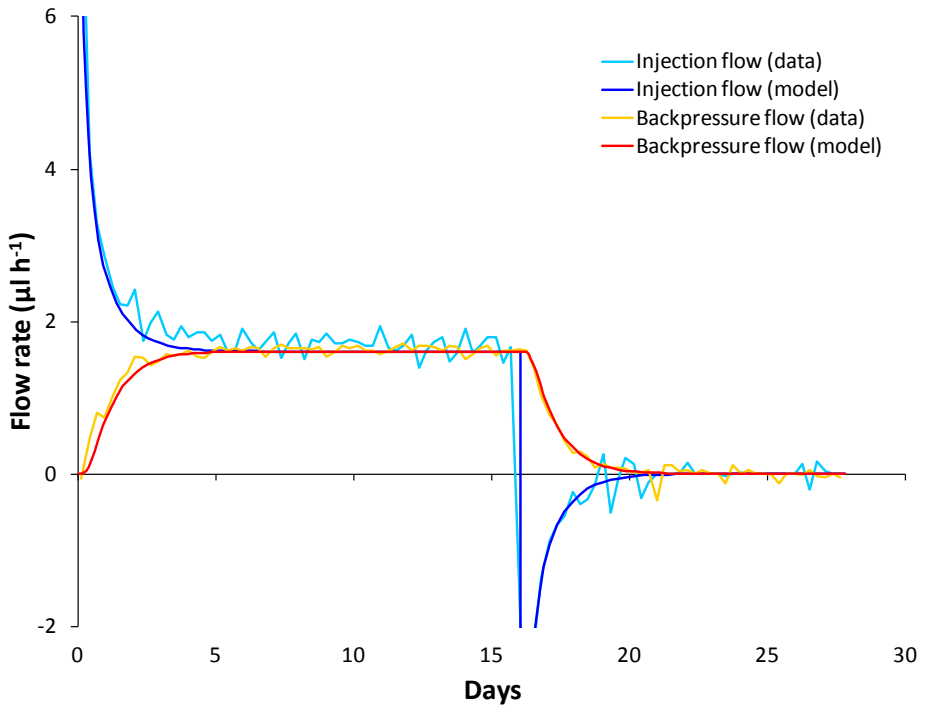

Figure 4-62 Comparison of an anisotropic permeability model with end surface leakage to flow data for sample COx-3.

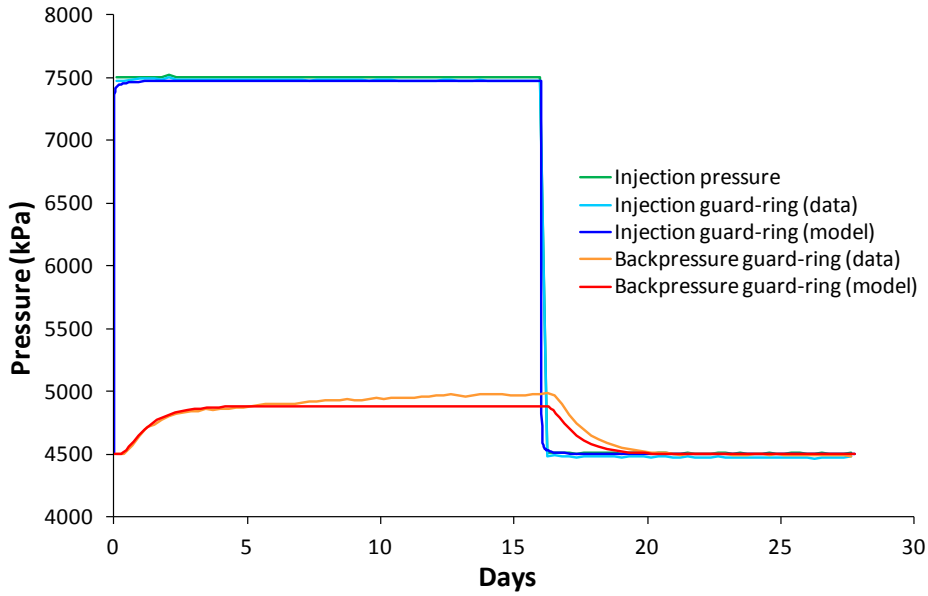

Figure 4-63 Comparison of an anisotropic permeability model with end surface leakage to guard ring pressures for sample COx-3.

One final model has been considered in which the sample has isotropic permeability. Figure 4-64 and Figure 4-65 show the results for a model in which the sample permeability on all three axies is set to 4.5×10^{-21} m^2, all other parameters being as for the previous model. It can be seen that the fit is essentially identical to that obtained before. This shows that, in the presence of these end surface leakage flows, the test is unable to make any determination of the sample anisotropy.

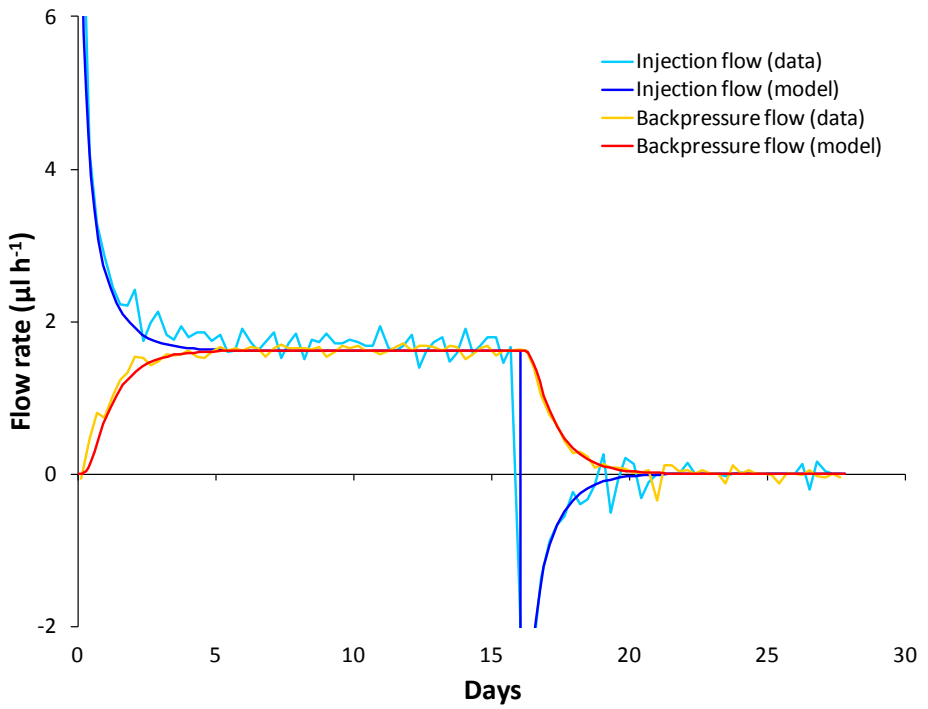

Figure 4-64 Comparison of an isotropic permeability model with end surface leakage to flow data for sample COx-3.

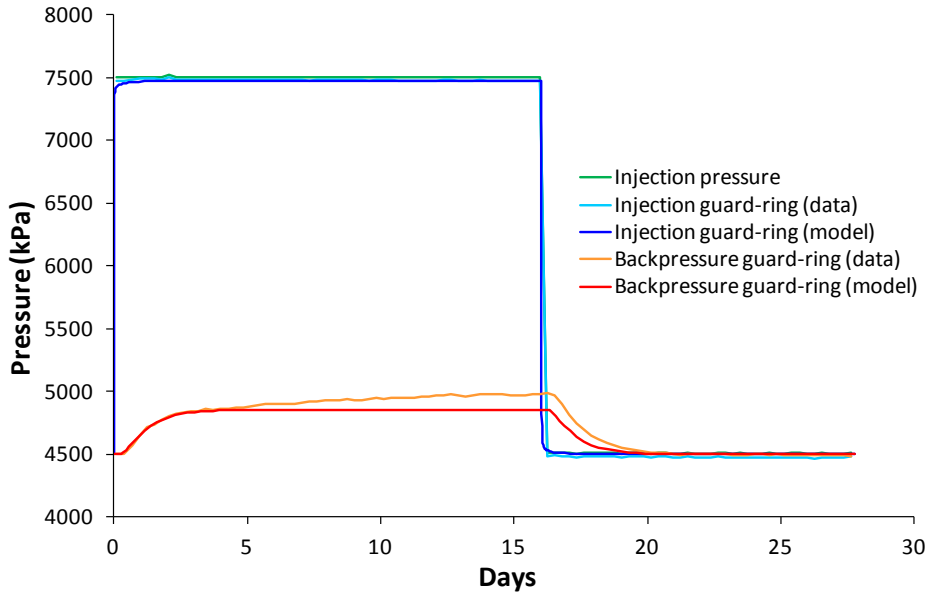

Figure 4-65 Comparison of an anisotropic permeability model with end surface leakage to guard ring pressures for sample COx-3.

4.3.3 Gas injection

The ethos behind gas test COx-3 was subtly different to that of previous experiments. Here the purpose of the test was to provide information on the stress state variables in an unsaturated medium (σ, p_g and p_w), in particular, the repeatability of the gas migration response to equal changes in gas and porewater pressure. With this in mind, helium gas was first equilibrated with the sample at the reference backpressure of 4.5 MPa, stage [6].

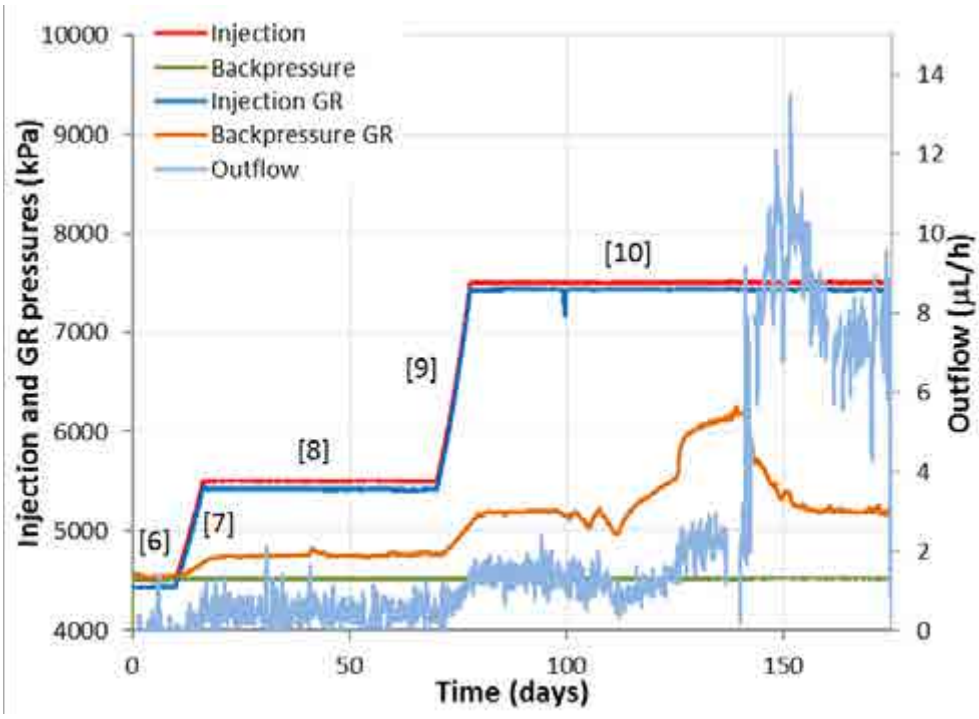

Figure 4-66 Evolution in pressure within sample COx-3 and outflow during test stages [6 to 10]. The small emergent flux is symptomatic of a low gas breakthrough pressure.

In a similar manner to previous gas tests, gas pressure was then increased in a stepwise manner from 4.5 MPa, stage [6], to 7.5 MPa, stage [10], during the first 175 days of gas testing. At each stage, the injection pressure was maintained constant while flux into and out of the specimen monitored with time. During the first constant pressure gas stage [8], a small emergent flux of fluid of around 0.5 $\mu l.h^{-1}$ was noted (Figure 4-66). By the end of the stage both guard ring pressures remained elevated and showed no sign of returning to the previous reference (backpressure) value. As the next gas pressure ramp began, stage [9], outflow and guard ring pressures began to increase. These continued to increase until the start of stage [10]. Thereafter, downstream guard ring and outflow reached an asymptote at values around 5.2 MPa and 1.4 $\mu l.h^{-1}$ respectively.

The system then remained in a quasi-steady state until day 98 when the backpressure guard ring began to fluctuate. This was accompanied by systematic changes in outflow as the pressure profile across the sample spontaneously moved into a transitory phase. Backpressure guard ring and outflow continued to evolve until major gas breakthrough occurred at day 140. This was accompanied by a sudden increase in outflow and decrease in backpressure guard ring. As permeability across the sample increased, outflow peaked before decrease to a quasi-steady state condition at around day 160. Major gas breakthrough was accompanied by a negative pressure transient in the backpressure guard ring trace, which was offset (i.e. predated the evolution in outflow) and asymptote at around 5.2 MPa, Figure 4-66. While this is very close to its the pre-major gas breakthrough value of 5.2 MPa, the offset in response strongly indicates the existence of multiple gas pathways across the sample.

To examine the sensitivity of gas flow to changes in porewater pressure, the pressure in the backpressure filter was increased to 6.5 MPa, stage [11]. This resulted in an inflow of fluid into the backpressure end of the sample, Figure 4-67. As inflow occurred, pressure in backpressure guard ring began to increase, reaching a peak value of 7.24 MPa at day 210 i.e. an excess pressure of 0.72 MPa. This value is very close to asymptote value for the guard ring during stage [10] i.e. 0.7 MPa, suggesting that conductive gas pathways connect the guard ring and backpressure filters at pressures in excess of 0.7 MPa.

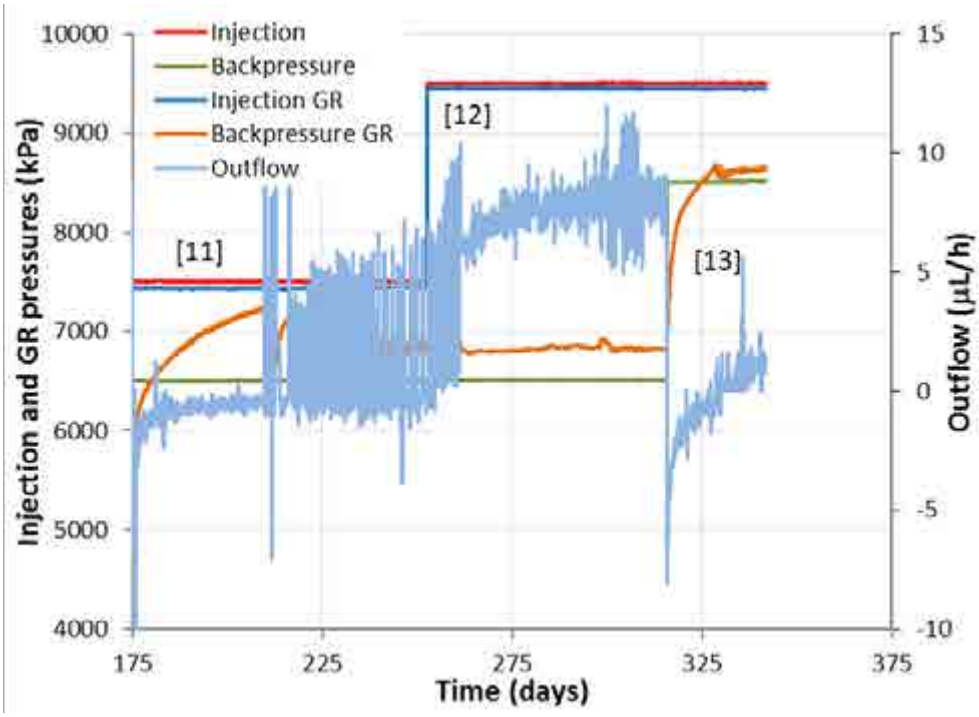

Figure 4-67 Evolution in pressure within sample COx-3 and outflow during test stages [11 to 13].

As the pathway(s) connect, pressure spontaneously decreases as permeability develops and outflow increases. The sudden increase in permeability results in a drop guard ring pressure,

which continues to fall until the pathway(s) can no longer be maintained and spontaneously close. This 'resealing' of the pathways is followed by a second pressurisation event, after which, the cycle begins anew. Figure 4-68 shows this behaviour in detail and suggests a cyclicity and repeatability to the response which lasts for the duration of stage [11]. Visual inspection of the data suggests there is a periodicity and repeatability to the response. This becomes evident in a cross plot between backpressure guard ring and outflow response from day 225 to 260, Figure 4-69, yielding a similar response to that of observed in Figure 4-56. As before the arrow denotes the direction of cycling with a small amount of noise in the plot introduced through the superposition of individual pressure cycles.

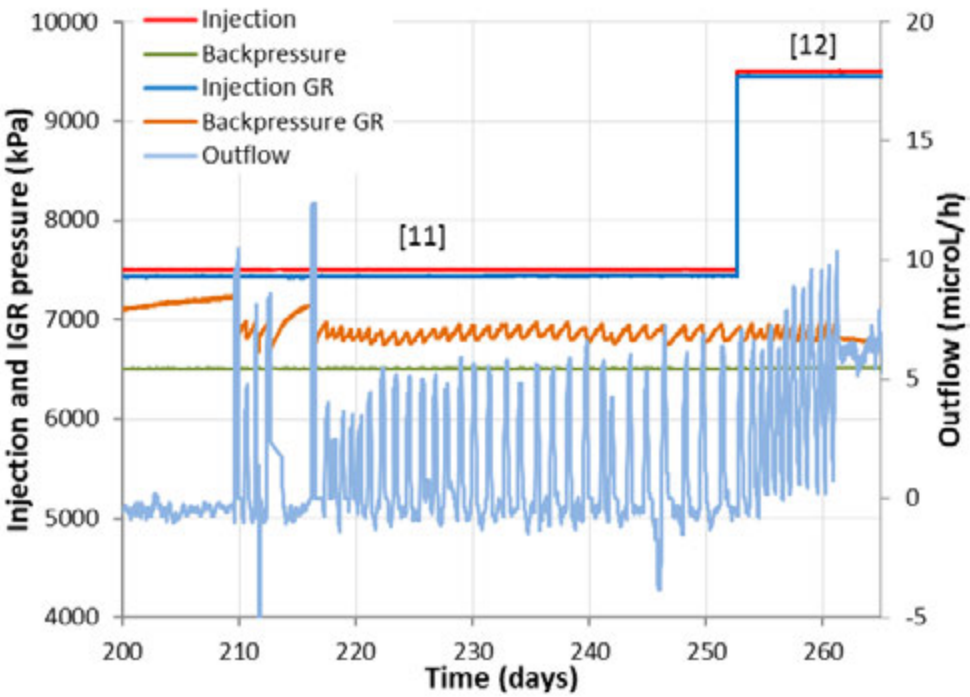

Figure 4-68 Cyclic behaviour between backpressure guard ring and outflow response indicating pathways formation and closure in response to changes in local gas pressure.

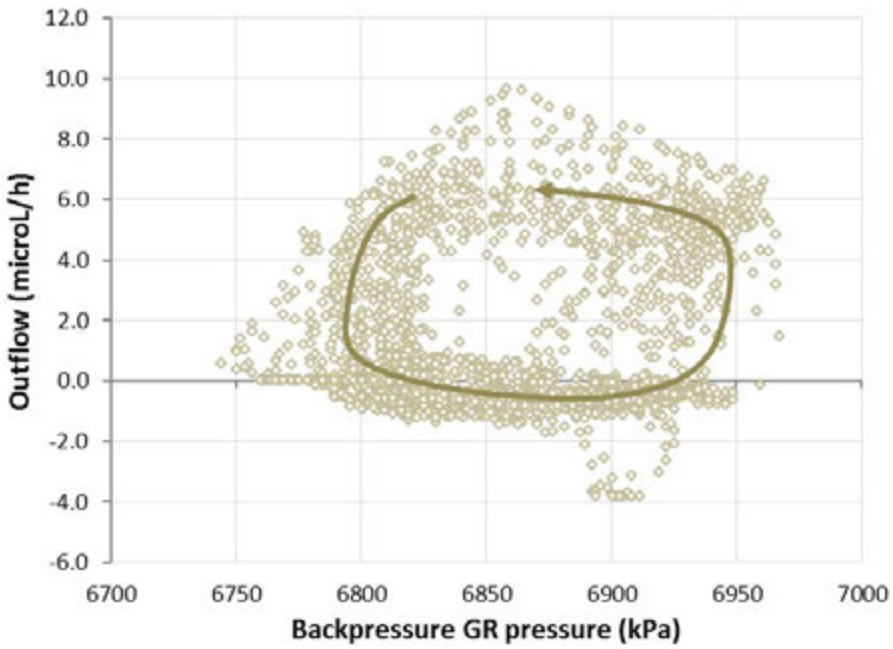

Figure 4-69 Cross plot of outflow versus backpressure guard ring from day 225 to 260. The underlying cyclic behaviour between flow and pressure becomes clear, with the arrow indicating the direction of the response.

In summary, as the gas pressure in the GR filter increased, it reached a critical value re-initiating gas outflow. However, unlike before, this outflow was highly episodic exhibiting clear burst-type behaviour. This would suggest that at very low gas pressure gradients COx does not always seal following a previous gas injection event. Interestingly this is in contrast to the triaxial test performed report by Cuss and Harrington (2012) who observed spontaneously self-sealed during advective gas flow. This difference in behaviour requires further work to better elucidate the main processes governing gas flow.

To investigate the symmetry of these processes and the validity of concepts such as axis translation, the previous gas pressure gradient was imposed across the sample on day 253, stage [12]. This was followed by a progressive increase in outflow. The burst-type behaviour noted in stage[11] continued at an increased periodicity until around day 261, then spontaneously stopped, probably when there is a sufficient number/density of pathways through the sample. Outflow is then much 'smoother' than before and the oscillation in pressure within the backpressure guard ring stops. By day 280, outflow had reached a well-defined asymptote of around 7.7 $\mu l.h^{-1}$, very close to the previous value of 7.3 $\mu l.h^{-1}$ from stage [10]. This suggests that the permeability of the sample remains approximately constant for the same gas pressure gradient as the test conditions repeatedly cycle between drainage and imbibition responses. However, the validity of this observation to COx in general requires more work to understand the differences in behaviour between this and COx-1 and COx-2.

In an attempt to better understand the relationship between gas and porewater pressure, pressure in the backpressure filter was increased to 8.5 MPa, stage [13], to apply the same excess gas pressure (and therefore driving gradient) across the sample as that imposed in stage [11]. As before, the change in boundary condition was followed by an inflow of fluid to the sample and a slow increase in backpressure guard ring Figure 4-70. As pressure in the backpressure guard ring increased above that in the reference backpressure filter, inflow reversed and a net outflow of fluid was observed. This initial change in flow direction occurred at a guard ring pressure of 8.68 MPa, an excess pressure of only 0.18 MPa. This is significantly lower than before and may reflect a change in system behaviour. As in stage [11], the guard ring pressure thereafter exhibits an episodic response, though this time with a much higher frequency. While there is some noise in the guard ring response, pressures appear to stabalise around 8.64 MPa from day 344. A slight upward trend in backpressure guard-ring is observed during the remainder of the stage which may relate to the evolution in conductive pathways. This test remains ongoing.

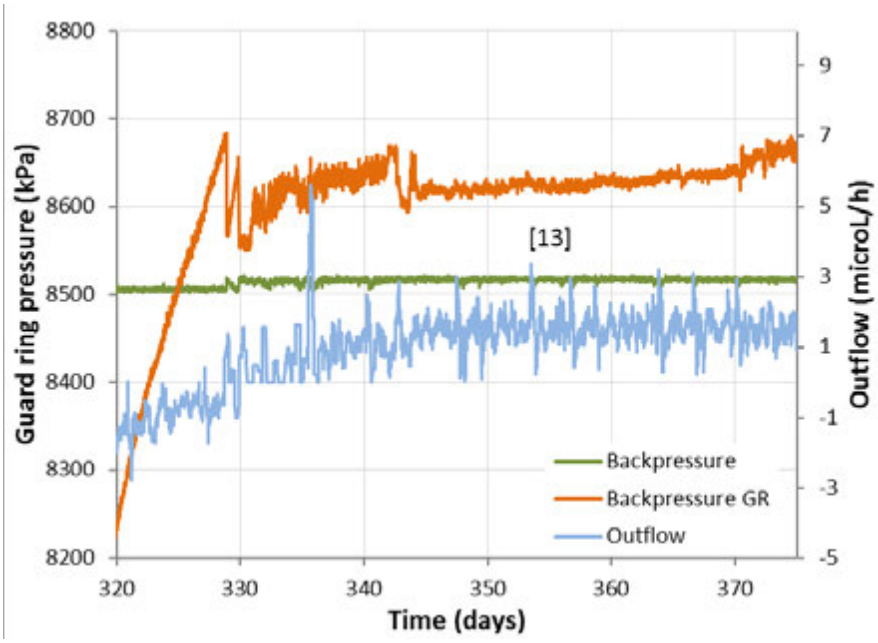

Figure 4-70 Evolution in guard ring pressure and outflow during stage [13], test COx-3.

5 Modelling of the gas data

A numerical model was set up to try to reproduce some of these features of the data and to help understand the properties of the sample. The multi-phase flow code TOUGH2 was used with the EOS3 equation of state module (Pruess et al, 1999). An axisymmetric mesh was used with some refinement towards the sample ends and including the various filters as separate elements of the model, as shown in Figure 5-1.

The clay sample 1 was assumed to have a radial permeability of $5\text{x}10^{-20}$ m^2 and an axial permeability of $2\text{x}10^{-21}$ m^2 as determined by the hydraulic test, while sample 2 was assumed to have a radial permeability of $8.8\text{x}10^{-21}$ m^2 and an axial permeability of $1.6\text{x}10^{-21}$ m^2. The porosity was set at 14.5% for both samples and their solid phase compressibilities at $4.8\text{x}10^{-10}$ Pa^{-1}. The filters were given an isotropic permeability of 10^{-16} m^2 and a porosity of 0.5.

In attempting to reproduce the test results the parameters of the relative permeability function for the clay were used as potential fitting parameters. The functions used by TOUGH2 in this study for relative permeability are slightly modified forms of the model due to van Genuchten (1980). The relative permeability for the liquid phase is given by

$$k_{rl} = \sqrt{S^*}\left\{1-\left(1-\left[S^*\right]^{1/\lambda}\right)^{\lambda}\right\}^2$$

and the relative permeability of the gas phase is given by

$$k_{rg} = 1 - k_{rl} \qquad \text{if } S_l = 0$$

$$k_{rg} = \left[\left(1-\hat{S}\right)^2\left(1-\hat{S}^2\right)\right]^n \qquad \text{if } S_{gr} > 0$$

where

$$S^* = \frac{\left(S_l - S_{lr}\right)}{\left(S_{ls} - S_{lr}\right)}$$

and

$$\hat{S} = \frac{\left(S_l - S_{lr}\right)}{\left(1 - S_{lr} - S_{gr}\right)}$$

The parameters for this model are λ a fitting parameter, S_{lr} the residual liquid saturation, S_{ls} the maximum liquid saturation, S_{gr} the residual gas saturation, and n an additional fitting parameter. In the current work, λ was set to 0.6, S_{ls} was set to 1.0, and S_{gr} was set to 0.001. Variations in S_{lr} and n were used to change the model response to compare with different aspects of the test data from sample COx-1. Figure 5-2 shows some experimental data from ANDRA (2009) together with the relative permeability curves used in the three models of sample 1 presented below. The curve labelled Model 5.1 was used for modelling sample COx-2.

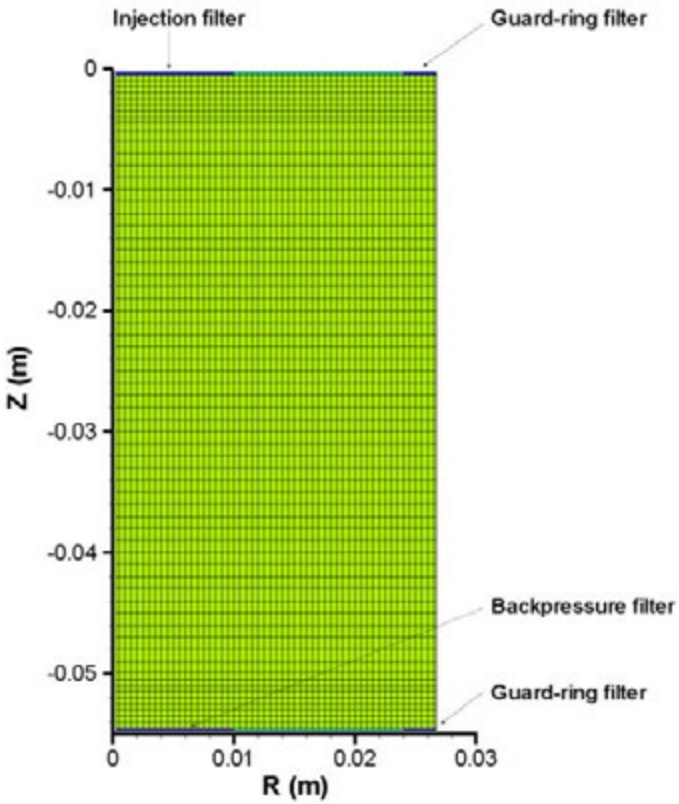

Figure 5-1 The main elements and calculational mesh used for the TOUGH2 models of the gas injection test. Cylindrical symmetry about the z-axis is assumed.

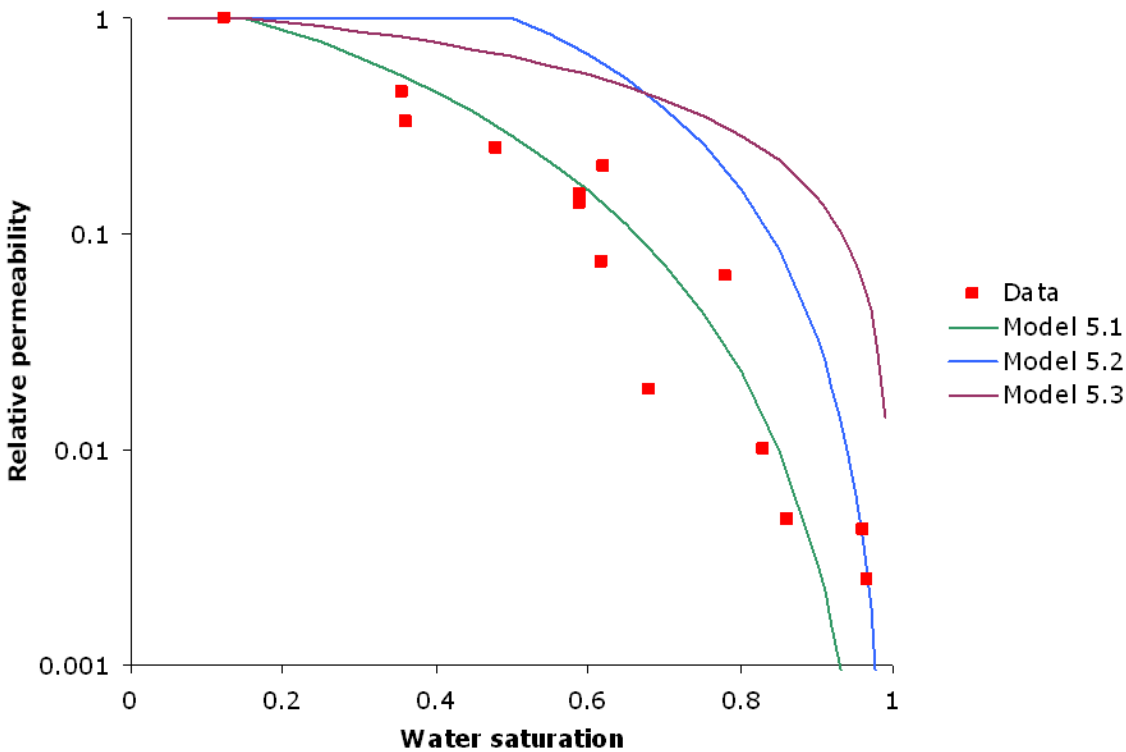

Figure 5-2 Relative permeability data compared to the models presented in sections 5.1, 5.2, and 5.3 below.

TOUGH2 also requires the definition of the capillary pressure functions and for this work the functions due to van Genuchten (1980) were also used. Thus the capillary pressure is given by

$$P_{cap} = -P_0\left(\left[S^*\right]^{-1/\lambda} - 1\right)^{1-\lambda}$$

subject to the restriction $-P_{max} \leq P_{cap} \leq 0$.

Here,

$$S^* = \frac{(S_l - S_{lr})}{(S_{ls} - S_{lr})}$$

The new parameter for this model is P_0, which is effectively the capillary entry pressure for this function. In this work the value of P_0 was set to 2 MPa for the clay sample 1 and to 20 kPa for the filters. P_0 was used as an adjustable parameter when modelling sample 2.

5.1 AN INITIAL MODEL FOR SAMPLE 1

A first model for sample 1 was obtained by setting S_{lr} to 0.15 and n to 1.0. As shown in Figure 5-2, this gives a relative permeability function that reproduces the experimental data of ANDRA (2009) quite well. The filter pressures obtained from the model are compared to the data in Figure 5-3 and the flow rate at the backpressure filter predicted by the model is compared to the data in Figure 5-4. It can be seen that this model gives a good fit to the injection guard-ring data after 170 days but there are significant differences before that time except for the initial pressure decline over the first 9 days. It may be noted that there is a step in the model pressure accompanying the arrival of gas at the injection guard-ring that is comparable in magnitude with that seen in the data, but it arrives at about day 32 instead of day 16. Modelled gas phase arrival at the backpressure filter and guard ring occurs at about 350 days whereas the data indicates its arrival at about 170 days, and the modelled inflow and outflow rates after arrival are much less than the measured values. The modelled water outflow rates before 170 days are comparable to the flow rates seen in the data at about 0.5 $\mu l.hr^{-1}$.

5.2 A MODEL FOR SAMPLE 1 FITTED TO GAS BREAKTHROUGH AT BACKPRESSURE FILTER.

One of the key features of the test that was not reproduced by the initial model was the time of first arrival of the injected gas at the backpressure filter. Adjustments to the model parameters were made to try to improve this. Figure 5-5 and Figure 5-6 show the output from a model in which S_{lr} has been increased to 0.5 and n reduced to 0.8. As shown in Figure 5-2, this gives increased gas phase relative permeabilities which allows the gas to break through at the backpressure filter earlier than in the initial model. It can be seen that the model predictions for pressures at the injection filter and injection guard-ring filter are little different from those of the earlier model. The modelled pressure at the backpressure guard ring shows a distinctive ‘double step’ in the middle of the 7.5 MPa injection pressure stage at the time of gas arrival which is similar to the shape of the test data between 170 and 200 days. However, the test data then show a steep drop back to pressures close to that of the backpressure filter, while the model predicts the pressure to continue to rise with further steps occurring in close association with those in the injection pressure. The flow rate data show that although the modelled gas breakthrough occurs at the same time as that seen in the test data, the modelled injection and outflow rates grow much more slowly than are observed.

5.3 A MODEL FOR SAMPLE 1 FITTED TO GAS OUTFLOW RATES.

As seen in the models above, predicted gas outflow rates are much lower than are seen in the test data. Further parameter changes were attempted to determine what would be required to obtain flow rates comparable to those observed. Figure 5-7 and Figure 5-8 show the results obtained

from a model with S_{lr} set to 0.15, as for the initial model, and n reduced to 0.33. It can be seen that this reduction in n, which increases the relative permeability to gas for a given gas saturation (see Figure 5-2), allows the gas to penetrate the sample more quickly and flow at a greater rate after breakthrough. Indeed, a good fit to the flow rates has been obtained between about 220 and 600 days apart from an anomalous event at about 460 days. However, this fit is obtained by allowing a gas breakthrough after only 50 days and it would appear that flow rates after the injection pressure step to 12 MPa at 600 days are again greater than predicted by the model. This model also has a poor representation of the very early pressure response at the injection guard-ring filter where the rapid gas movement has eliminated the early pressure decline seen in the data for the first 12 days.

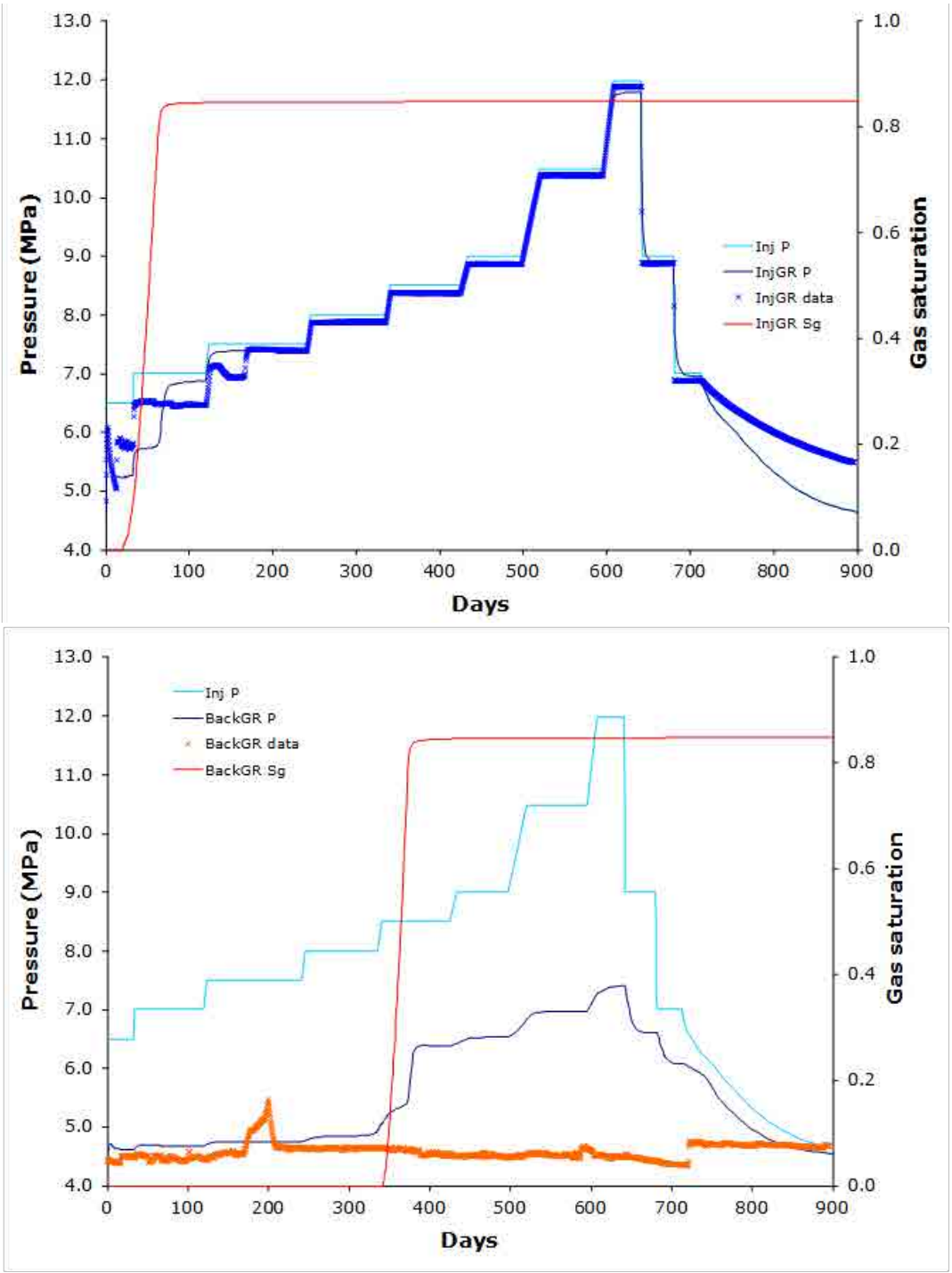

Figure 5-3 Initial model pressures compared to guard-ring data from sample 1.

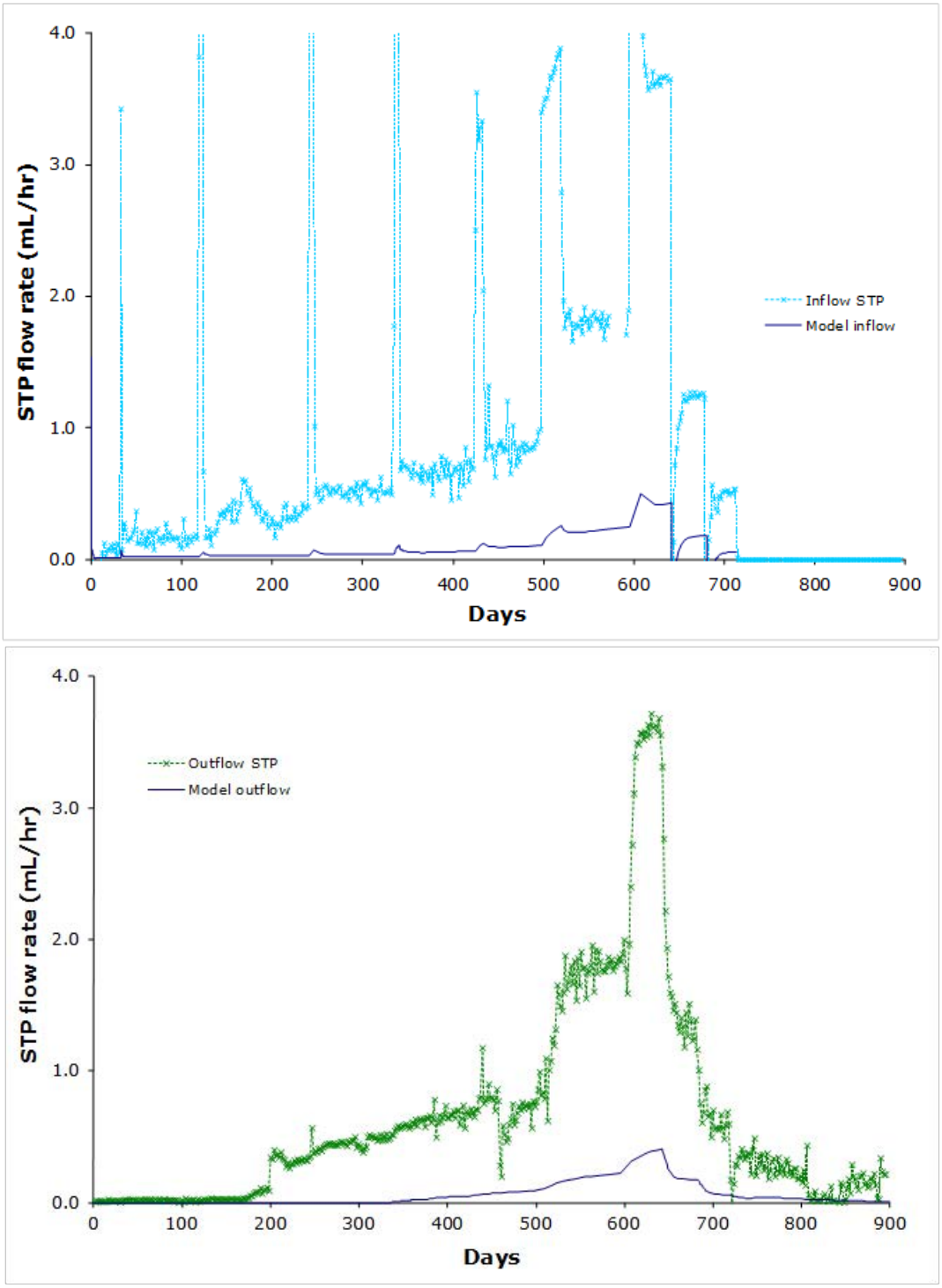

Figure 5-4 Initial model flow rates compared to the injection and backpressure filter data from sample 1.

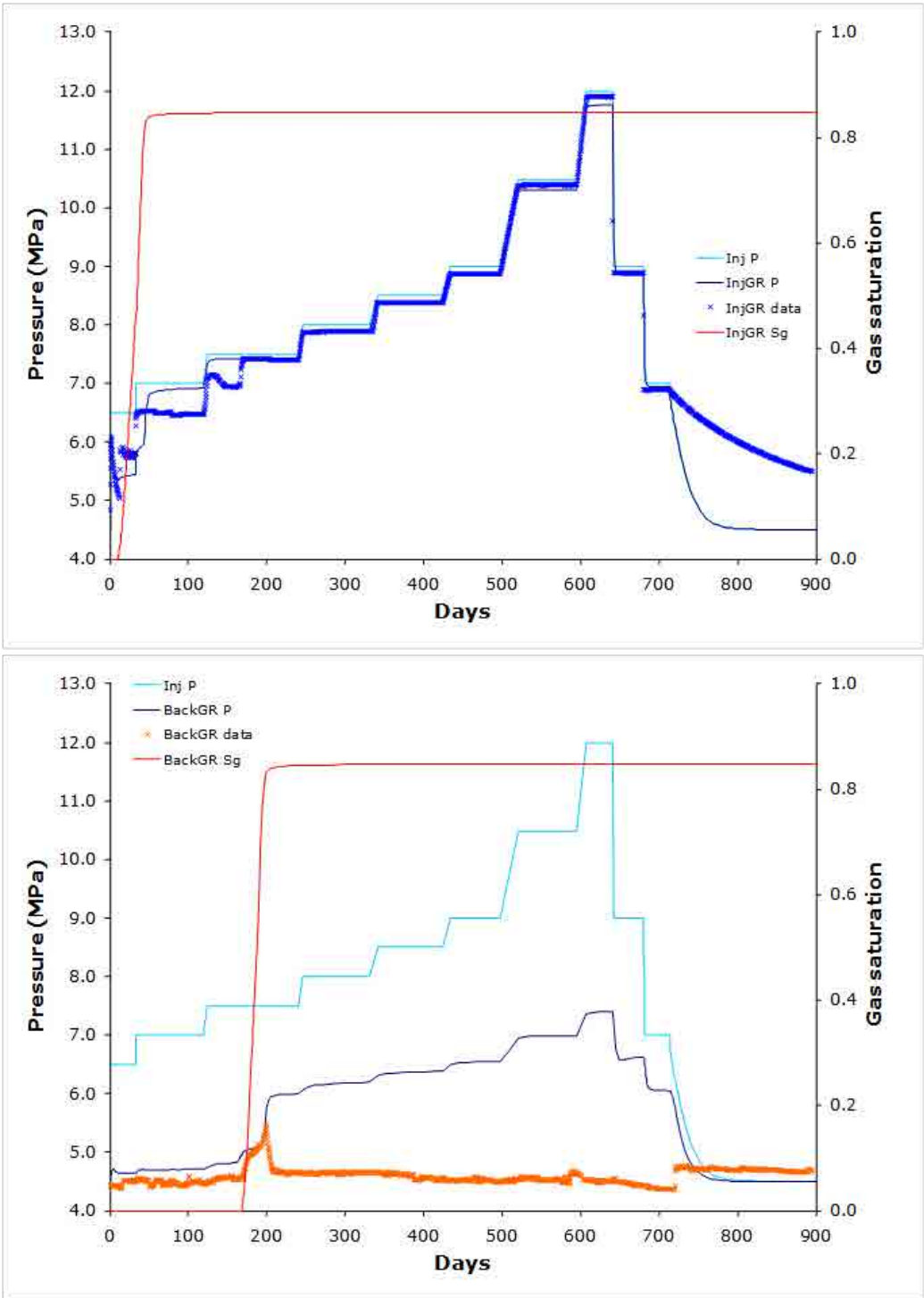

Figure 5-5 Pressures from a model fitted to the gas breakthrough time at the backpressure filter compared to test data from sample 1.

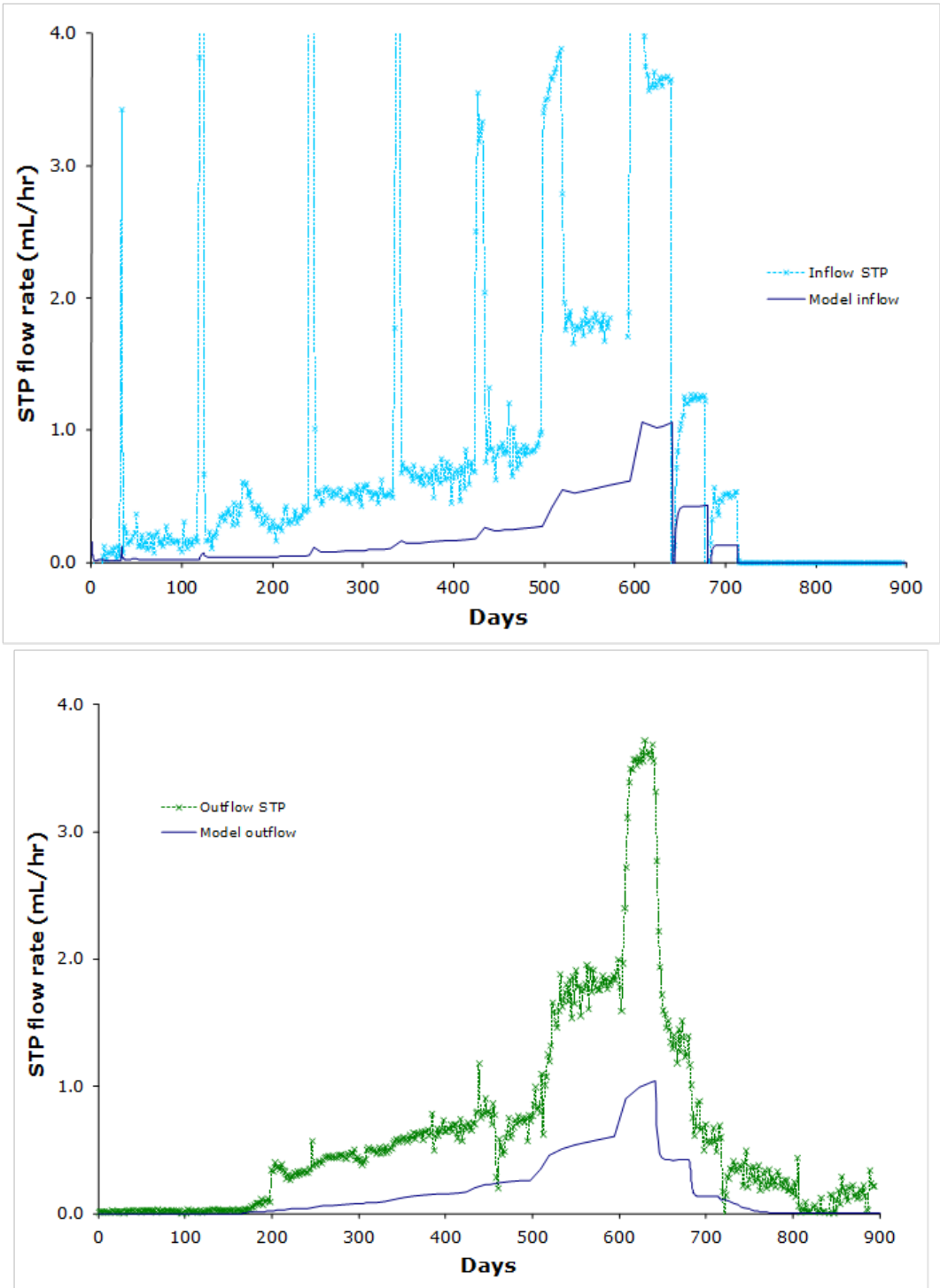

Figure 5-6 Flow rates at the injection and backpressure filters from a model fitted to the gas breakthrough time compared to test data from sample 1.

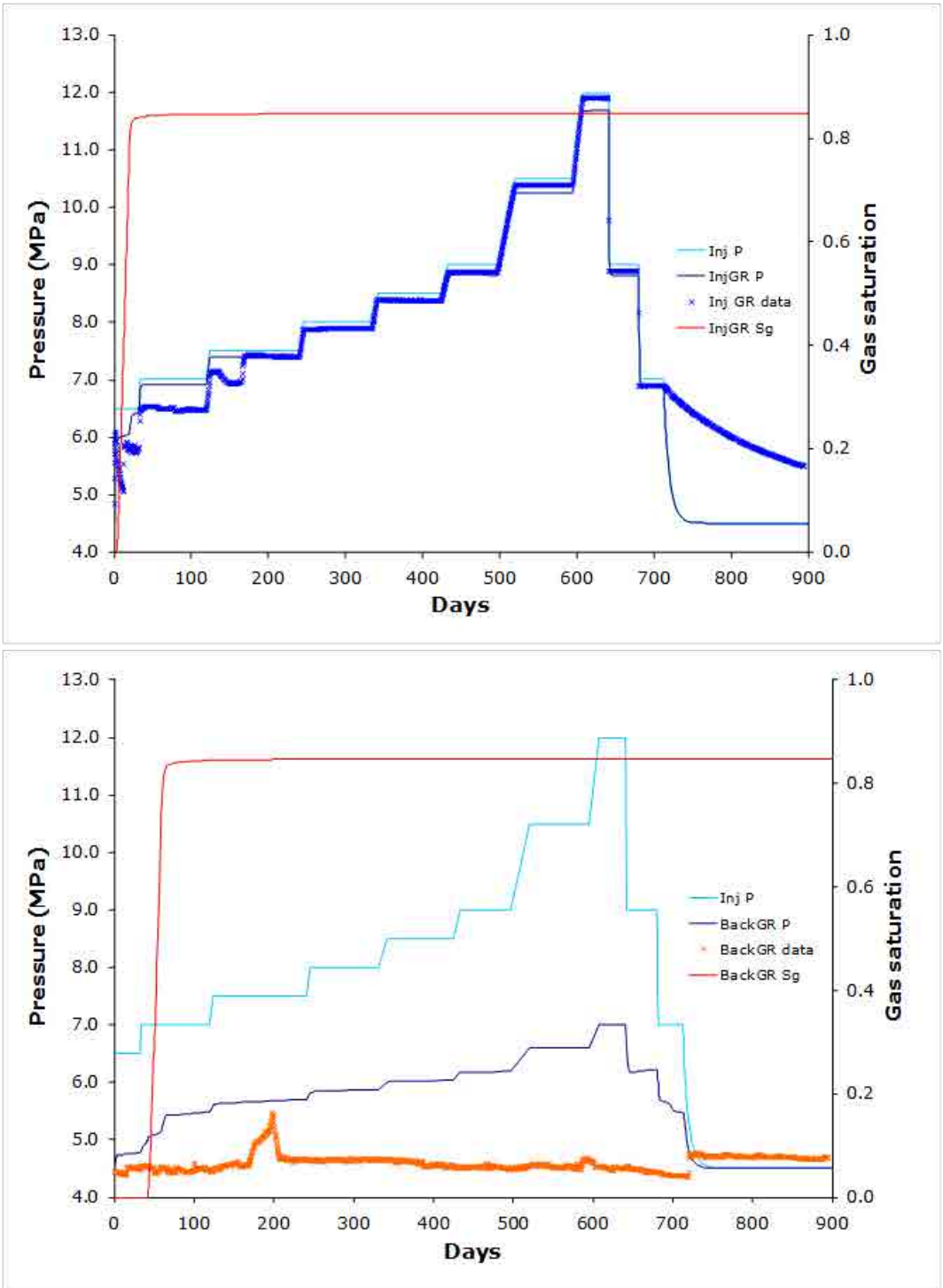

Figure 5-7 Pressures from a model fitted to the gas flow rates at the backpressure filter compared to test data from sample 1.

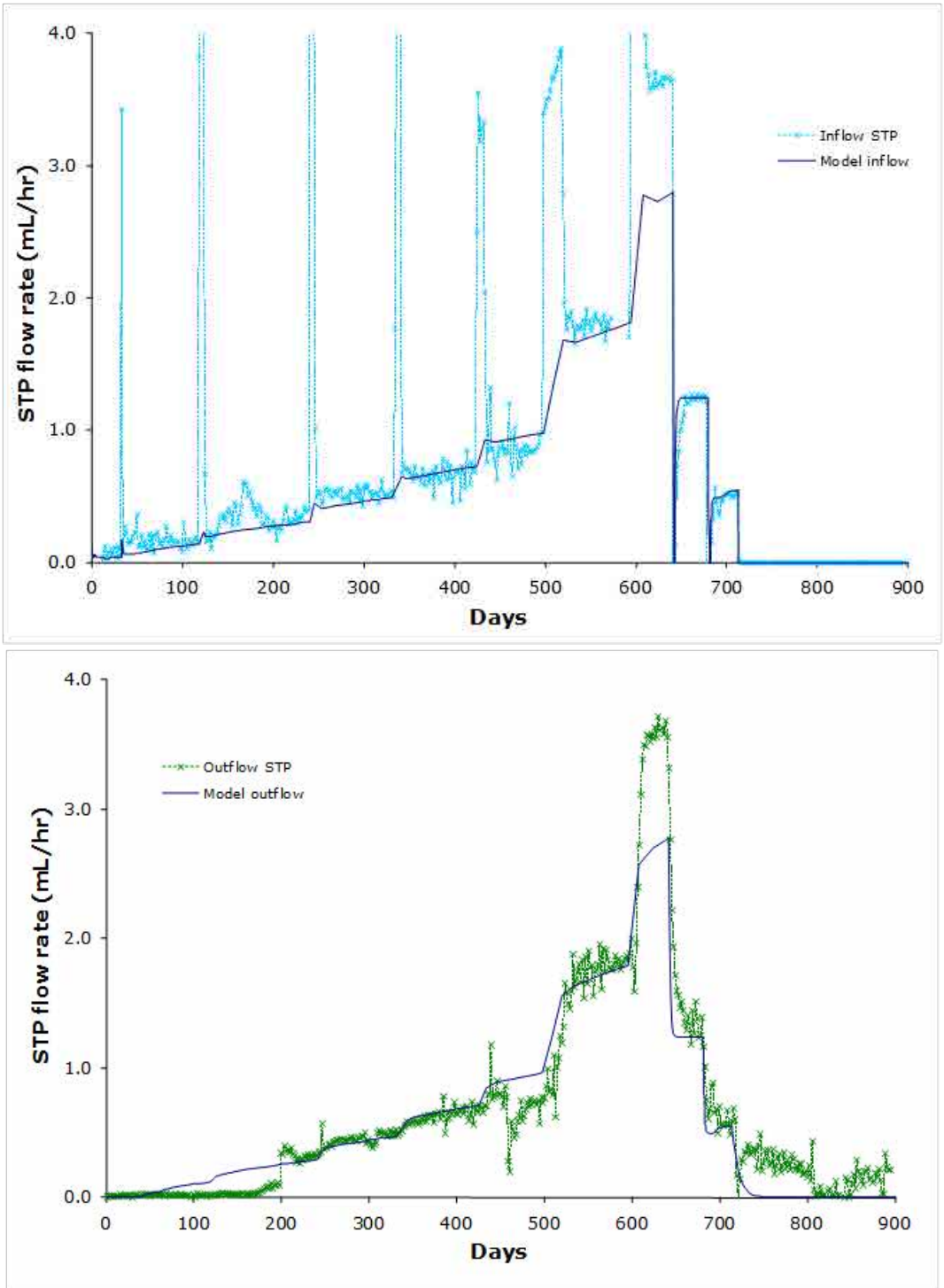

Figure 5-8 Flow rates at the backpressure filter from a model fitted to the gas flow rates compared to test data from sample 1.

5.4 A MODEL FOR SAMPLE 2 FITTED TO BACKPRESSURE GUARD RING ARRIVAL TIME

For the purposes of this modelling the multiple steps to the ramp up of the injection pressure were approximated by a single continuous rate of increase of the pressure between the initial value of 7 MPa and the final value of 11.25 MPa, as shown in Figure 5-9. It was found that setting the parameter P_0 to 5 MPa gave a good agreement between the model and the observed time of pressure change at the backpressure guard ring filter. However, as shown in Figure 5-9, this model has a very poor representation of the pressure at the injection guard ring filter.

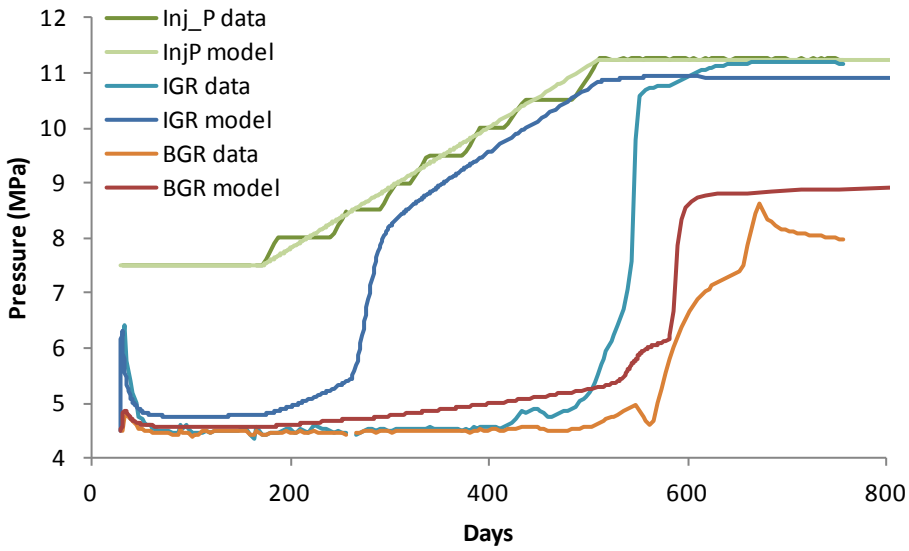

Figure 5-9 Comparison of model pressures to the data for sample 2 from the injection, injection guard ring, and backpressure guard ring filters. P_0 = 5 MPa for this model.

As shown in Figure 5-10, this model also provides quite a good representation of the gas flow rates observed at the outflow (backpressure) filter.

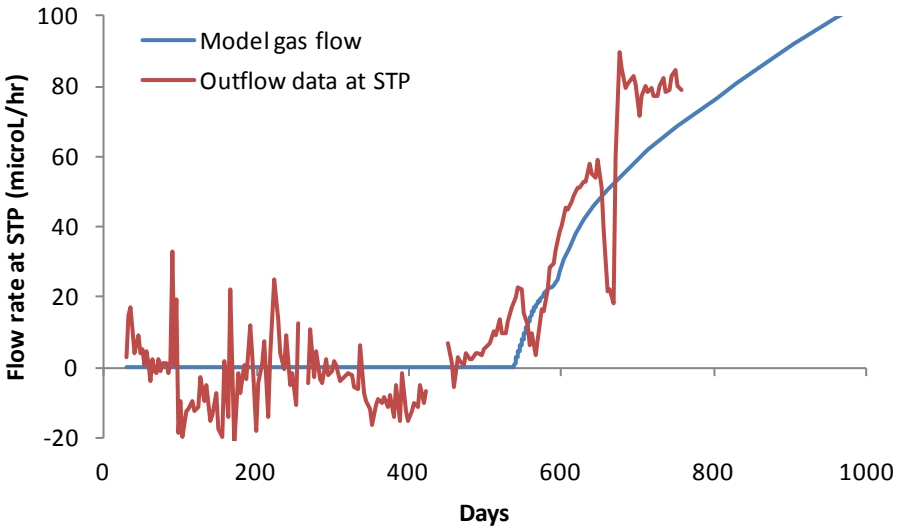

Figure 5-10 Comparison of the data for sample 2 for gas outflow rate, converted to STP, with the values calculated from the model with P_0 = 5 MPa.

The model discussed above does not include diffusion of the gas within the aqueous phase. A variation was run in which the diffusion coefficient, D, was set to 2.0×10^{-10} m^2 s^{-1}. The pressures calculated from this model are shown in Figure 5-11 and the gas outflow rates in Figure 5-12. It can be seen that some smoothing of the model curves has occurred, but otherwise the main features are much the same.

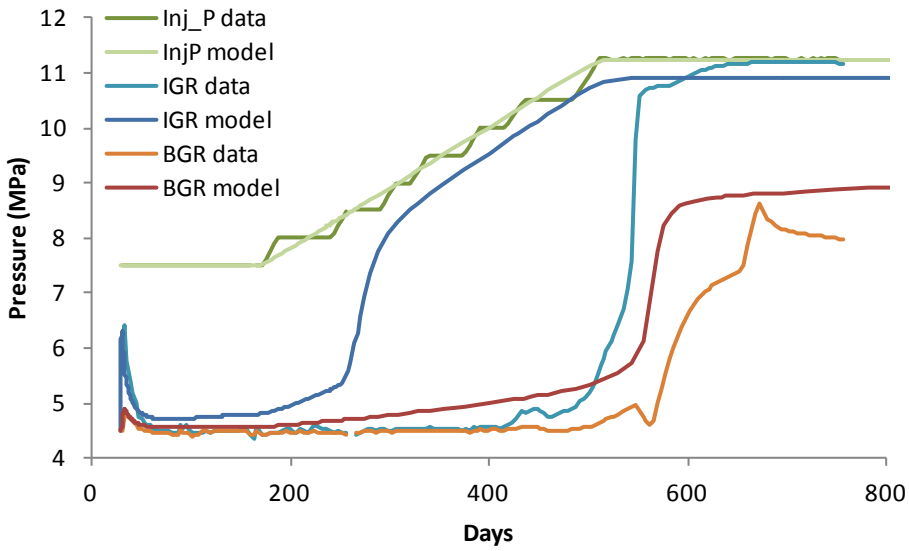

Figure 5-11 Comparison of model pressures to the data for sample 2 from the injection, injection guard ring, and backpressure guard ring filters. P_0 = 5 MPa and D = 2.0x10^{-10} m^2 s^{-1} for this model.

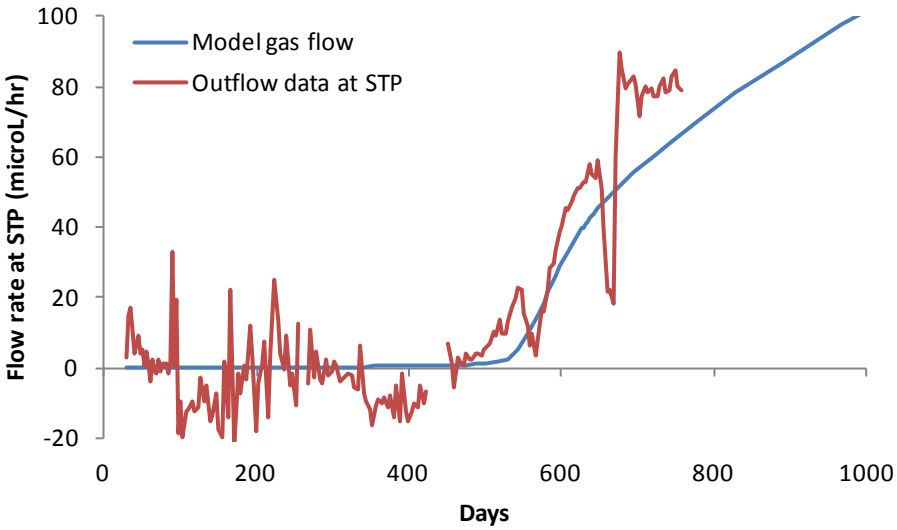

Figure 5-12 Comparison of the data from sample 2 for gas outflow rate, converted to STP, with the values calculated from the model with P_0 = 5 MPa and D = 2.0x10^{-10} m^2 s^{-1}.

5.5 A MODEL FOR SAMPLE COX-2 FITTED TO INJECTION GUARD RING ARRIVAL TIME

Further runs of the model were made to try to fit to the pressure data from the injection guard ring filter. Figure 5-13 shows the results obtained with a value of P_0 = 11 MPa. The time of arrival of the pressure step at the injection guard ring is reproduced well but the model shows no response at the backpressure guard ring within the first 800 days. Figure 5-14 shows the continued model behaviour with the backpressure guard ring responding at about 1300 days.

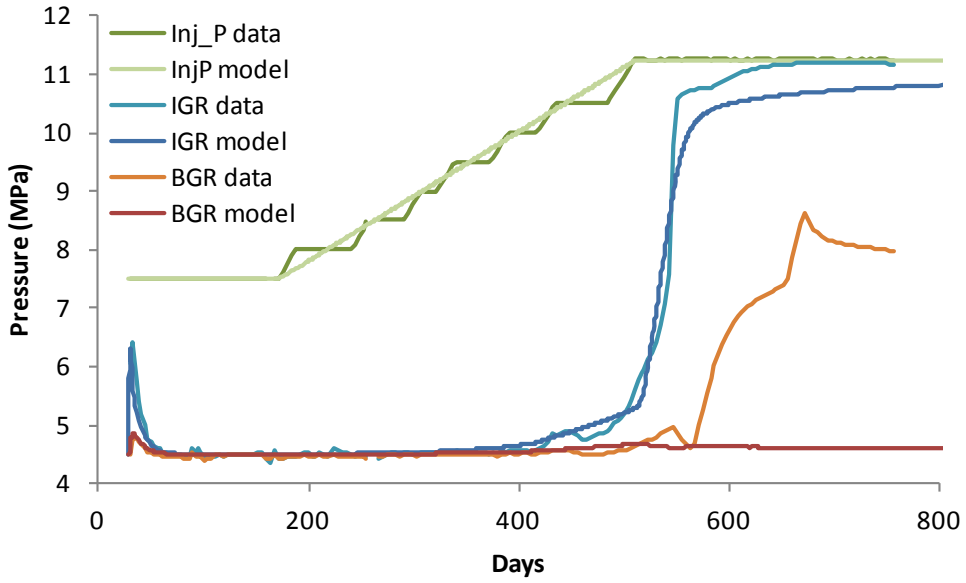

Figure 5-13 Comparison of model pressures to the data for sample 2 from the injection, injection guard ring, and backpressure guard ring filters. P_0 = 11 MPa for this model.

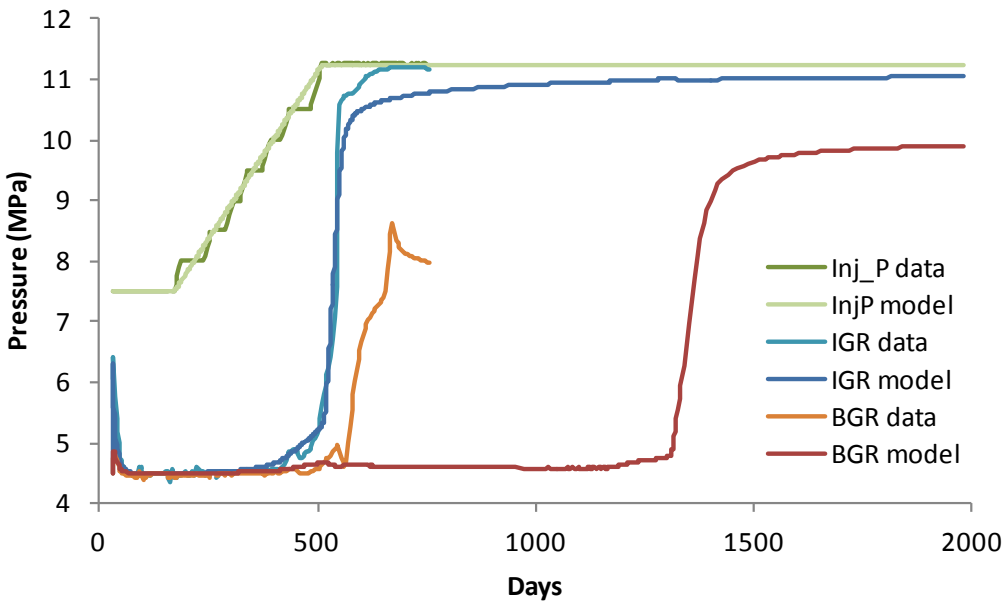

Figure 5-14 Comparison of model pressures to the data for sample 2 from the injection, injection guard ring, and backpressure guard ring filters. P_0 = 11 MPa for this model.

Similarly, the gas outflow from this model is greatly delayed, as shown in Figure 5-15. The first signs of flow from the backpressure filter occur at about 1200 days and thereafter the flow rate is approximately one tenth of the magnitude seen in the data.

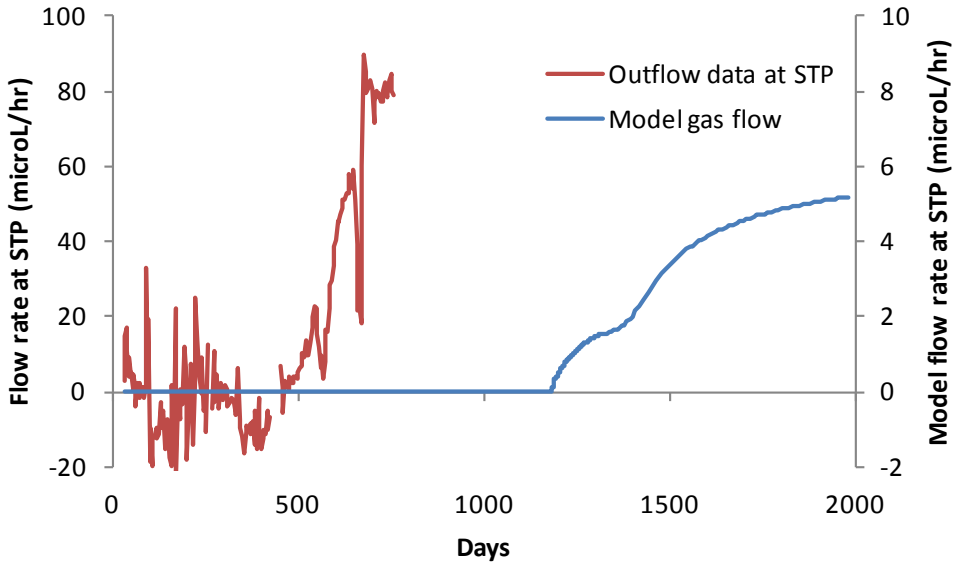

Figure 5-15 Comparison of the data from sample COx-2 for gas outflow rate, converted to STP, with the values calculated from the model with P_0 = 11 MPa.

The effect of diffusion on this model is slightly more significant than before and it was found that using a diffusion coefficient of $2x10^{-10}$ m^2 s^{-1} as before it was necessary to increase the value of P_0 to 12.5 MPa to get the good fit to the timing of the injection guard ring pressure response, as shown in Figure 5-16. Figure 5-17 shows that the response at the backpressure guard ring first occurs much earlier than before at about 800 days, but still much later than is seen in the data and the pressure build up is much more gradual.

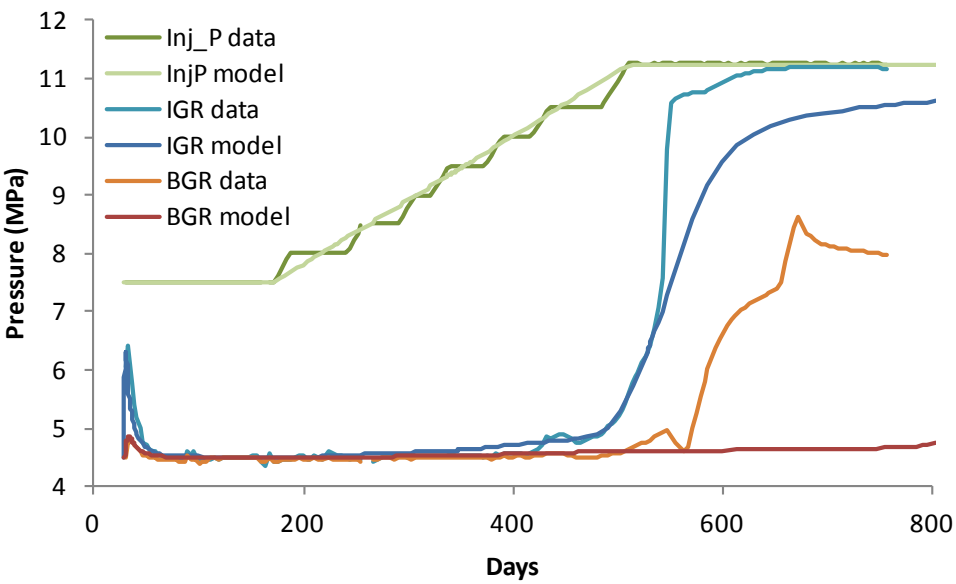

Figure 5-16 Comparison of model pressures to the data for sample 2 from the injection, injection guard ring, and backpressure guard ring filters. P_0 = 12.5 MPa and D = $2.0x10^{-10}$ m^2 s^{-1} for this model.

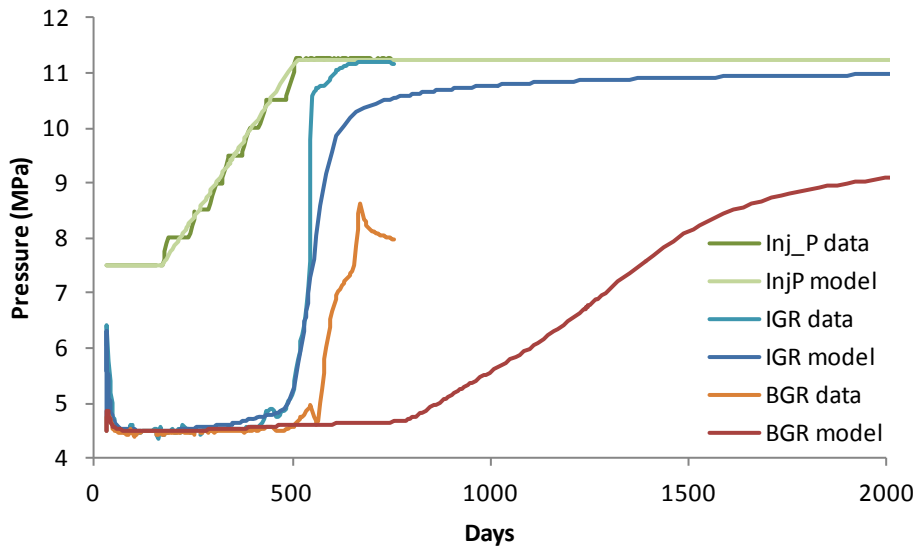

Figure 5-17 Comparison of model pressures to the data for sample COx-2 from the injection, injection guard ring, and backpressure guard ring filters. P_0 = 12.5 MPa and D = 2.0x10^{-10} m^2 s^{-1} for this model.

Figure 5-18 shows that outflow from the backpressure filter also occurs much earlier than before, at about 350 days which is comparable to that seen in the data. However, the magnitude of the flow is still much smaller than in the experimental data.

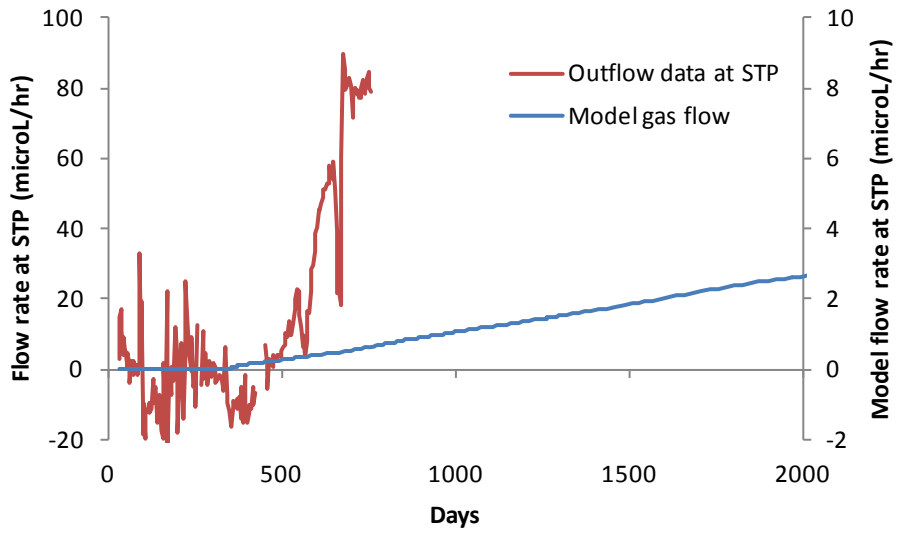

Figure 5-18 Comparison of the data from sample 2 for gas outflow rate, converted to STP, with the values calculated from the model with P_0 = 12.5 MPa and D = 2.0x10^{-10} m^2 s^{-1}.

6 Implications for process understanding

Clearly, none of the models presented in Section 5 provide a good representation of the whole data set and indeed there are some features in the data that none of the models are able to reproduce such as the pressure reduction on the injection guard-ring filter in the middle of the 7.5 MPa stage and the abrupt pressure loss on the backpressure guard-ring at 200 days. A possible explanation for the latter event could be the development of a discrete conductive flow path between the guard-ring and backpressure filters. Alternatively, the substantial increase in

the gas flow rate at the backpressure filter at the same time might indicate the development of a discrete flow path between injection and backpressure filters, by-passing the backpressure guard-ring.

Despite these indicators of discrete path flow it is notable that the growth of gas flow rates between 220 and 600 days of the test on sample Cox-1 seems to follow the form of a porous medium path, with the flow rate growing as the gas saturation increases which in turn allows the gas phase relative permeability to rise. The change in gas saturation through the sample during this period is shown in Figure 6-1 and axial profiles of gas saturation and gas phase relative permeability are given in Figure 6-2. It can be seen that in this model, which provides a good fit to the gas flow rates during this period, the gas saturations and relative permeabilities approximately double between these two dates. It should be noted that the gas saturations continue to increase during the periods when the injection pressure is held constant, and this is reflected in the gradually rising gas flow rates seen during in a number of the test stages. This has implications for any attempt to re-interpret the test data in terms of discrete path flow since it would be necessary to include a mechanism for the paths to continue to expand over the periods of constant injection pressure in such a way that the gas flow rate rises in the same way as for the porous medium model.

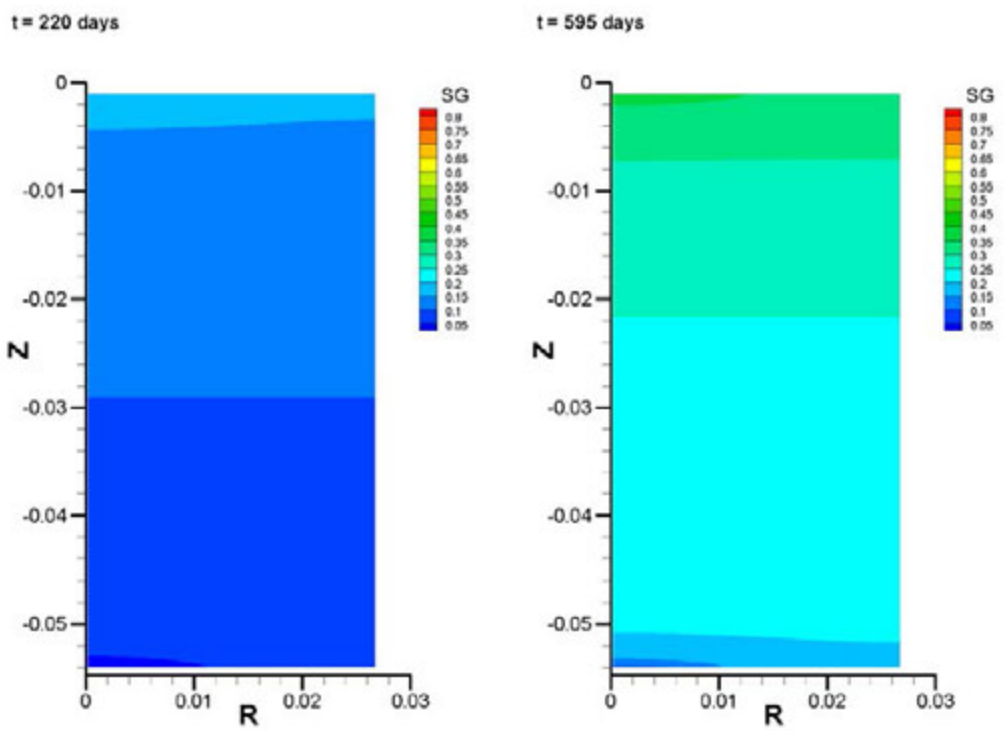

Figure 6-1 Contour plots of gas saturation (SG) at two times from the model of Section 5.3.

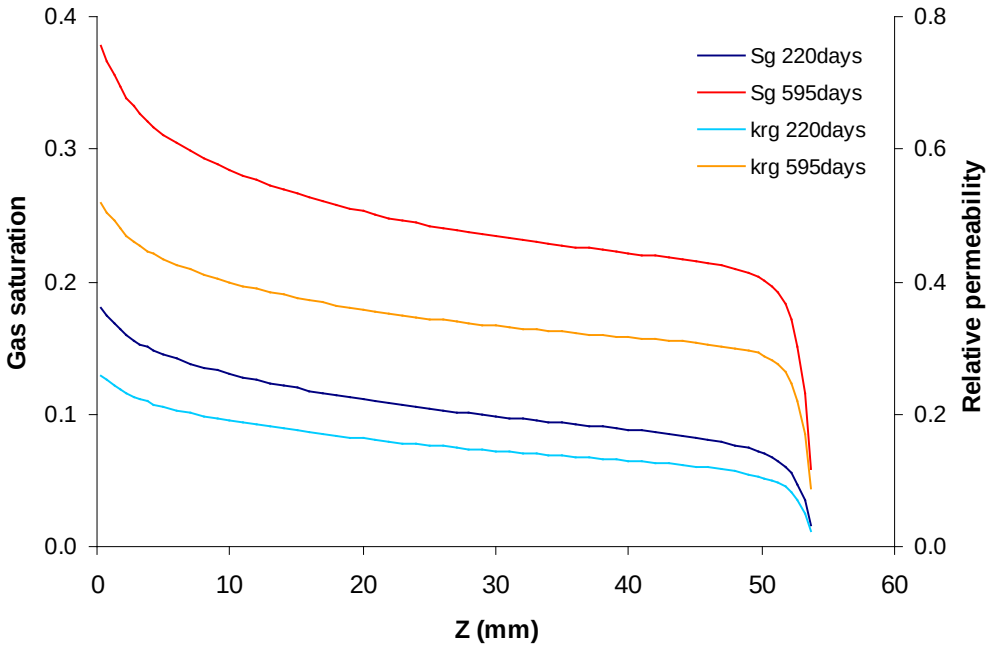

Figure 6-2 Axial profiles of gas saturation (S_g) and relative permeability of the gas phase (k_{rg}) at two times from the model of Section 5.3.

However, the existence of time-dependent discrete pathway flow coupling gas pressure gradient, porewater pressure and stress has been well documented in pure clay systems (Horseman and Harrington, 1997; Horseman et al. 1996, 1999; Harrington and Horseman, 2003; Cuss et al., 2010) and natural plastic clays (Horseman and Harrington, 1994; Ortiz et al, 1996; Sen et al., 1996; Harrington and Horseman 1999; Rodwell et al., 2000, Cuss and Harrington , 2012; Harrington et al., 2012 (i) and (ii)).

More recent work by Angeli et al. (2009) provides important new data regarding gas flow in indurated shale. These researchers performed a highly-instrumented test on a sample of Draupne shale from the Troll East Field located in the Norwegian Section of the North Sea (Figure 6-3). Inspection of the data indicates that at excess gas pressures <3.0 MPa, the sample exhibits no discernable strain or discharge from the base of the specimen[4]. However, two days after the gas pressure gradient is increased to 3.5 MPa (still well below the effective stress applied to the sample), the specimen starts to dilate, exhibiting considerable radial strain. This is then followed 5 days later by an increase in discharge rate out of the core which coincides with a reduction in radial strain of around 0.6% (the negative sign of the strain denoting an increase in sample volume), and is interpreted by the authors as the point of gas breakthrough. This is also accompanied by a notable reduction in P-wave velocity which the authors ascribe to the penetration of the sample by the carbon dioxide (which is around 2 orders of magnitude more compressible than the interstitial fluid) and to the opening of “cracks” within the shale.

From the start of dilation (day 26) to the end of the radial expansion phase (day 36) the sample undergoes a radial strain of around 1% (as a percentage of the porosity this would be significantly larger). During the following 26 days the radial strain data shows signs of time-dependent volume change with a slight reduction in value as conductive pathways within the shale are established. This mechanism may provide an explanation for the apparent over- and under-shooting of the ultimate steady-state value observed in Figure 4-22.

[4] The resolution of the second y-axis on Figure 6-3 precludes examination of the data for precursor flows.

It is also interesting to note that the evolution of strain in Figure 6-3 does not correlate with measured changes in P-wave velocity. While the authors pass no comment on this behaviour, it strongly suggests that following initial dilation and penetration of the shale by CO_2, the gas saturation within the sample continues to increase. It is unclear from the data available if this is associated with time-dependent deformation of the fabric (accompanied by drainage of interstitial fluid from the surrounding clay[5]), structural changes due to chemical alteration of the shale by the CO_2, or displacement of porewater from higher porosity zones within the shale (classic two-phase flow).

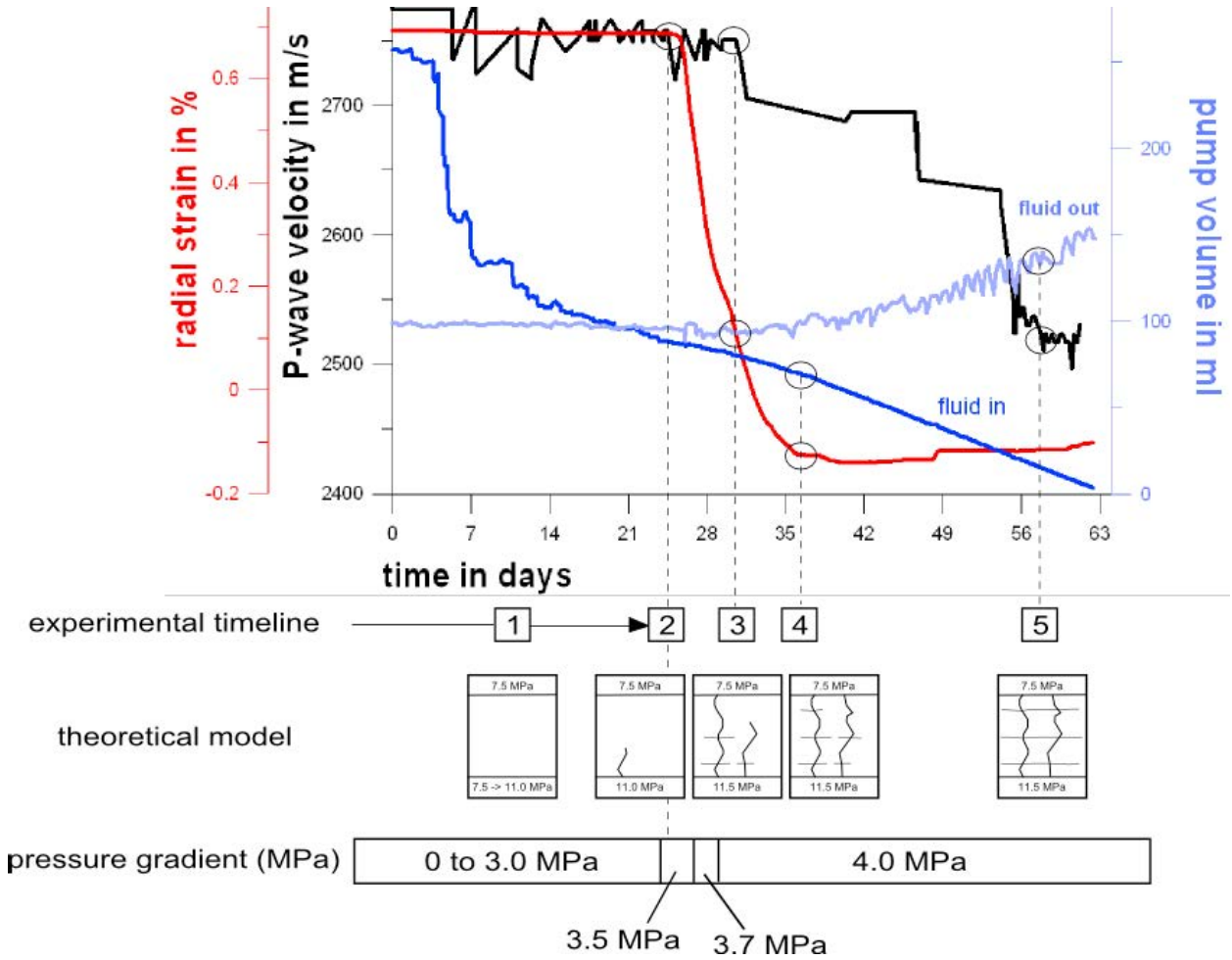

Figure 6-3 Data from Angeli et al. (2009), showing a significant change in radial strain prior to and during gas breakthrough for a test performed on Draupne shale taken from the Troll East Field in the Norwegian Section of the North Sea. The change in P-wave velocity following breakthrough is symptomatic of gas penetration of the fabric due to the change in compressibility of the CO_2 compared with that of the original porewater.

What is absolutely clear from the data is that dilatancy and time-dependent processes are key factors in the development of gas permeability within the Draupne shale. The Draupne shale has a similar clay fraction (around 40% by weight) compared to that of the Callovo-Oxfordian clay but has a significantly higher porosity (around 24%). While site specific factors will play a role in determining the multi-phase flow and hydro-mechanical behaviour of the Bure argillite, it seems highly likely that similar processes to those observed in the Draupne shale will apply. If

[5] This should not be mistaken for displacement of water through visco-capillary flow.

correct, this would explain a number of the observations reported during this experimental study and would address the apparent inability of the numerical modelling to adequately predict the system response.

7 References

British Geological Survey holds most of the references listed below, and copies may be obtained via the library service subject to copyright legislation (contact libuser@bgs.ac.uk for details). The library catalogue is available at: http://geolib.bgs.ac.uk.

ANDRA, 2009. Rapport mi-parcours pour le Groupment de Laboratoires «Transfert de Gaz». C.RP.ASCM.09.0002.

ANGELI, M., SOLDAL, M., SKURTVEIT, E. AND AKER, E., 2009. Experimental percolation of supercritical CO_2 through a caprock. *Energy Procedia* 1, 3351-3358.

CUSS, R.J., HARRINGTON, J.F. AND NOY, D.J., 2010. Large scale gas injection test (Lasgit) performed at the Äspö Hard Rock Laboratory. Summary report 2008. *Report TR-10-38*. Svensk Kärbränslehantering AB (SKB), Stockholm, Sweden.

CUSS, R.J., and HARRINGTON, J.F. (2012) Final Report of FORGE WP4.1.1: The stress path permeameter experiment conducted on Callovo-Oxfordian Claystone. *British Geological Survey Commissioned Report*, CR/12/140. 116pp.

ESTEBAN, L., BOUCHEZ, J., L. AND TROUILLER, A., 2006; The Callovo-Oxfordian argillites from the eastern Paris Basin: Magnetic data and petrofabrics, *Comptes Rendus Geosciences* **338**, pp 867-881

GALLÉ, C., 2000. Gas breakthrough pressure in compacted Fo–Ca clay and interfacial gas overpressure in waste disposal context. *Applied Clay Science*. 17 (1–2), 85–97.

GAUCHER, E., ROBELIN, C., MATRAY, J.-M., NÉGREL, G., GROS, Y., HEITZ, J.-F., VINSOT, A., REBOURS, H., CASSAGNABÈRE, A. AND BOUCHE, A. T, 2004. ANDRA underground research laboratory: interpretation of the mineralogical and geochemical data acquired in the Callovo-Oxfordian formation by investigative drilling, *Phys. Chem. Earth* **29**, pp. 55–77.

HARRINGTON, J.F. AND HORSEMAN, S.T., 1999. Gas transport properties of clays and mudrocks. In. Aplin, A.C., Fleet, A.J. and Macquaker, J.H.S. (eds) Muds and Mudstones: Physical and Fluid Flow Properties. *Geol. Soc. London, Spec. Pub.* 158, 107-124.

HARRINGTON, J.F. AND HORSEMAN, S.T., 2003. Gas migration in KBS-3 buffer bentonite: Sensitivity of test parameters to experimental boundary conditions. *Report TR-03-02*. Svensk Kärbränslehantering AB (SKB), Stockholm, Sweden.

HARRINGTON, J.F. MILODOWSKI, A.E., GRAHAM, C.C., RUSHTON, J.C. and CUSS, R.J. (2012 (i)). Evidence for gas-induced pathways in clay using a nanoparticle injection technique. Mineralogical Magazine, Vol. 76(8), pp3327-3336.

HARRINGTON, J.F., de La VAISSIERE, R., NOY, D.J., CUSS, R.J. and TALANDIER, J. (2012 (ii)). Gas flow in Callovo-Oxfordian Clay (COx): Results from laboratory and field-scale measurements. Mineralogical Magazine, Vol. 76(8), pp. 3303-3318.

HORSEMAN, S.T. AND HARRINGTON, J.F., 1994. Migration of repository gases in an overconsolidated clay. *British Geological Survey, British Geological Survey*, Technical report WE/94/7.

HORSEMAN, S.T., HIGGO, J.J.W., ALEXANDER, J. AND HARRINGTON, J.F., 1996. Water, gas and solute movement in argillaceous media. Rept. No. CC-96/1 to OECD/NEA Working Group on Measurement and Physical Understanding of Groundwater Flow through Argillaceous Media. Nuclear Energy Agency, OECD, Paris.ISBN 92-64-1488-1.

HORSEMAN, S.T., HARRINGTON, J.F. AND SELLIN, P., 1996. GAS migration in Mx80 buffer bentonite. In: Symposium on the Scientific Basis for Nuclear Waste Management XX (Boston), *Materials Research Society*, Vol. 465. 1003-1010.

HORSEMAN, S.T. AND HARRINGTON, J.F., 1997. Study of gas migration in Mx80 buffer bentonite. British Geological Survey, Technical Report WE/97/7.

HORSEMAN, S.T., HARRINGTON, J.F. AND SELLIN, P., 1999. Gas migration in clay barriers. In: Pusch, R. and Yong, R.N. (eds) Microstructural Modelling of Natural and Artificially Prepared Clay Soils with Special Emphasis on the Use of Clays for Waste Isolation (1999 Special Edition), *Engineering Geology*, Vol 54, pp 139-149, Elsevier, Amsterdam.

HUYAKORN, P.S. AND G.F. PINDER, 1983, Computational methods in subsurface flow. Academic Press.

INTERA ENVIRONMENTAL CONSULTANTS INC., 1983, STAFAN: A Two-Dimensional Code for Fluid Flow and the Interaction of Fluid Pressure and Stress in Fractured Rock for Repository Performance Assessment. *Office of Nuclear Waste Isolation Report ONWI 427*.

MARSILY, G. DE, 1986, Quantitative Hydrogeology for Engineers, *Academic Press*.

Ortiz, L., Volckaert, G., Mallants, D., 2002. Gas generation and migration in Boom Clay, a potential host rock formation for nuclear waste storage. *Engineering Geology* 64 (2–3), 287–296.

ORTIZ, L., VOLCHARET, G., DE CANNIERE, P., AERTSENS, M., HORSEMAN, S.T., HARRINGTON, J.F., IMPEY, M., AND EINCHCOMB, S. (1996). MEGAS - Modelling and Experiments on Gas Migration in Repository Host-rocks. Proc. EU PEGASUS Meeting at Rapolina-Terme, Italy, 14-15 June 1995. *Nuclear Science and Technology Series*, EUR 16746 EN, Luxembourg, 127-147.

PRUESS K., OLDENBURG C., MORIDIS G., 1999. TOUGH2 user's guide, version 2.0. *Lawrence Berkeley National Laboratory report* LBNL-43134.

RODWELL, W.R. (ED.), 2000, Research into Gas Generation and Migration in Radioactive Waste Repository Systems (PROGRESS Project). *Nuclear Science and Technology* EUR 19133 EN, European Commission, Luxembourg.

ROUSESET, D. AND CLAUER, N., 2003; Discrete Clay Diagenesis in a Very Low-Permeable Sequence Constrained by an Isotopic (K-Ar and Rb-Sr) Study, *Contributions to Mineralogy and Petrology*, **145**, pp 182-198.

SEN, M.A., HORSEMAN, S.T. AND HARRINGTON, J.F., 1996. Further studies on the movement of gas and water in an overconsolidated clay: Contribution to MEGAS Phase 2 Report (PEGASUS Project). *British Geological Survey, Technical Report* WE/96/8 To: Commission of European Communities (CEC), Brussels.

VAN GENUCHTEN M.TH., 1980. A Closed-Form Equation for Predicting the Hydraulic Conductivity of Unsaturated Soils, *Soil Sci. Soc*., Vol. 44, pp. 892 – 898.

WENK, H.-R., VOLTOLINI, M., MAZUREK, M., VAN LOON, L.R. AND VINSOT, A., 2008, Preferred Orientations and Anisotropy in Shales: Callovo-Oxfordian Shale (France) and Opalinus Caly (Switzerland), *Clays and Clay Minerals*, **56**, pp 285-306.

WILEVEAU, Y., AND BERNIER, F. 2008. Similarities in the hydromechanical response of Callovo-Oxfordian clay and Boom Clay during gallery excavation. *Physics and Chemistry of the Earth*, 33, S343–S349.

ZHANG, C-L, ROTHFUCHS, T., SU, K., AND HOTEIT, N. 2007. Experimental study of the thermo-hydro-mechanical behaviour of indurated clays. *Physics and Chemistry of the Earth*, 32, 957–965.

.

FORGE

Fate Of Repository Gases

European Commission FP7

Summary Report of FORGE WP4.1.2: Verification of critical stress theory applied to repository concepts

FORGE Report D4.17 pt 2

Keywords.

Critical stress theory, fracture transmissivity, fracture flow, kaolinite, shear testing..

Bibliographical reference

CUSS, R.J., HARRINGTON, J.F., SATHAR. S., and REEVES, H.J. 2012. Summary Report of FORGE WP4.1.2: Verification of critical stress theory applied to repository concepts.

FORGE Report D4.17 pt 2. 27pp.

Euratom 7th Framework Programme Project: FORGE

EURATOM

Fate of repository gases (FORGE)

The multiple barrier concept is the cornerstone of all proposed schemes for underground disposal of radioactive wastes. The concept invokes a series of barriers, both engineered and natural, between the waste and the surface. Achieving this concept is the primary objective of all disposal programmes, from site appraisal and characterisation to repository design and construction. However, the performance of the repository as a whole (waste, buffer, engineering disturbed zone, host rock), and in particular its gas transport properties, are still poorly understood. Issues still to be adequately examined that relate to understanding basic processes include: dilational versus visco-capillary flow mechanisms; long-term integrity of seals, in particular gas flow along contacts; role of the EDZ as a conduit for preferential flow; laboratory to field up-scaling. Understanding gas generation and migration is thus vital in the quantitative assessment of repositories and is the focus of the research in this integrated, multi-disciplinary project. The FORGE project is a pan-European project with links to international radioactive waste management organisations, regulators and academia, specifically designed to tackle the key research issues associated with the generation and movement of repository gasses. Of particular importance are the long-term performance of bentonite buffers, plastic clays, indurated mudrocks and crystalline formations. Further experimental data are required to reduce uncertainty relating to the quantitative treatment of gas in performance assessment. FORGE will address these issues through a series of laboratory and field-scale experiments, including the development of new methods for up-scaling allowing the optimisation of concepts through detailed scenario analysis. The FORGE partners are committed to training and CPD through a broad portfolio of training opportunities and initiatives which form a significant part of the project.

Further details on the FORGE project and its outcomes can be accessed at www.FORGEproject.org.

Contact details:

R.J. Cuss

British Geological Survey
Keyworth
Nottingham
NG12 5GG
UK

Tél.: +441159363100
E-mail: rjcu@bgs.ac.uk

British Geological Survey
NATURAL ENVIRONMENT RESEARCH COUNCIL

Summary Report of FORGE WP4.1.2: Verification of critical stress theory applied to repository concepts

Minerals and Waste Programme

Commissioned Report CR/12/146

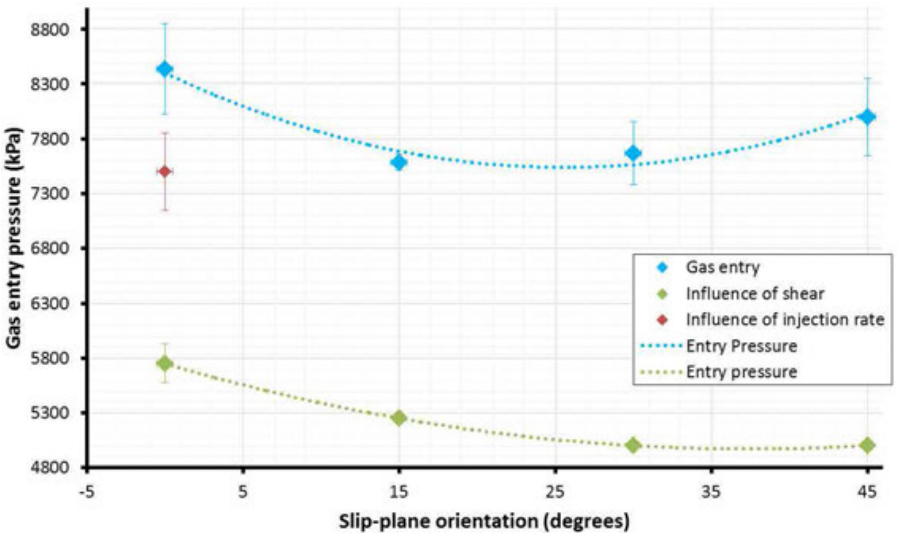

BRITISH GEOLOGICAL SURVEY

MINERALS AND WASTE PROGRAMME

COMMISSIONED REPORT CR/12/146

Summary Report of FORGE WP4.1.2: Verification of critical stress theory applied to repository concepts

R.J. Cuss, J.F. Harrington, S. Sathar, and H.J. Reeves

Keywords

Critical stress theory, fracture transmissivity, fracture flow, kaolinite, shear testing.

Front cover

Gas entry pressure for all tests showing the influence of gas injection rate, active shear, and feature orientation. This plot validates the critical stress theory

.

Bibliographical reference

CUSS, R.J., HARRINGTON, J.F., SATHAR. S., and REEVES, H.J. 2012. Summary Report of FORGE WP4.1.2: Verification of critical stress theory applied to repository concepts. *British Geological Survey Commissioned Report*, CR/12/146. 27pp.

Copyright in materials derived from the British Geological Survey's work is owned by the Natural Environment Research Council (NERC) and/or the authority that commissioned the work. You may not copy or adapt this publication without first obtaining permission. Contact the BGS Intellectual Property Rights Section, British Geological Survey, Keyworth, e-mail ipr@bgs.ac.uk. You may quote extracts of a reasonable length without prior permission, provided a full acknowledgement is given of the source of the extract.

© NERC 2012. All rights reserved

Keyworth, Nottingham British Geological Survey 2012

BRITISH GEOLOGICAL SURVEY

The full range of our publications is available from BGS shops at Nottingham, Edinburgh, London and Cardiff (Welsh publications only) see contact details below or shop online at www.geologyshop.com

The London Information Office also maintains a reference collection of BGS publications, including maps, for consultation.

We publish an annual catalogue of our maps and other publications; this catalogue is available online or from any of the BGS shops.

The British Geological Survey carries out the geological survey of Great Britain and Northern Ireland (the latter as an agency service for the government of Northern Ireland), and of the surrounding continental shelf, as well as basic research projects. It also undertakes programmes of technical aid in geology in developing countries.

The British Geological Survey is a component body of the Natural Environment Research Council.

British Geological Survey offices

BGS Central Enquiries Desk

Tel 0115 936 3143 Fax 0115 936 3276

email enquires@bgs.ac.uk

Kingsley Dunham Centre, Keyworth, Nottingham NG12 5GG

Tel 0115 936 3241 Fax 0115 936 3488
email sales@bgs.ac.uk

Murchison House, West Mains Road, Edinburgh EH9 3LA

Tel 0131 667 1000 Fax 0131 668 2683
email scotsales@bgs.ac.uk

London Information Office at the Natural History Museum (Earth Galleries), Exhibition Road, South Kensington, London SW7 2DE

Tel 020 7589 4090 Fax 020 7584 8270
Tel 020 7942 5344/45 email bgslondon@bgs.ac.uk

Columbus House, Greenmeadow Springs, Tongwynlais, Cardiff CF15 7NE

Tel 029 2052 1962 Fax 029 2052 1963

Forde House, Park Five Business Centre, Harrier Way, Sowton EX2 7HU

Tel 01392 445271 Fax 01392 445371

Maclean Building, Crowmarsh Gifford, Wallingford OX10 8BB

Tel 01491 838800 Fax 01491 692345

Geological Survey of Northern Ireland, Colby House, Stranmillis Court, Belfast BT9 5BF

Tel 028 9038 8462 Fax 028 9038 8461

www.bgs.ac.uk/gsni/

Parent Body

Natural Environment Research Council, Polaris House, North Star Avenue, Swindon SN2 1EU

Tel 01793 411500 Fax 01793 411501
www.nerc.ac.uk

Website www.bgs.ac.uk
Shop online at www.geologyshop.com

Foreword

This report is the product of a study by the British Geological Survey (BGS) undertaken on behalf of the Nuclear Decommissioning Authority – Radioactive Waste Management Directorate (NDA-RWMD) and the European Union 7th Framework Euratom Programme under the auspices of the Fate of repository Gases (FORGE) project, to examine the validation of critical stress theory applied to repository concept and the influence of fracture/fault angle on gas flow properties. This report represents the contribution to the Work Package 4 summary report. The full experimental report is given in Cuss *et al.*, 2013.

Acknowledgements

The study was undertaken by staff of the Minerals and Waste Programme of the BGS using the experimental facilities of the Transport Properties Research Laboratory (TPRL). Funding for the study was provided by the Nuclear Decommissioning Authority – Radioactive Waste Management Directorate (NDA-RWMD), the European Union (FORGE Project) and the British Geological Survey through its well-founded laboratory programme. The authors would like to thank the skilled staff of the Research & Development Workshops at the BGS, in particular Humphrey Wallis, for their design and construction of the experimental apparatus.

Contents

Foreword **2**

Acknowledgements **2**

Contents **3**

Executive summary **5**

1 Introduction **6**
1.1 Rationale 6
1.2 Objectives 7

2 Experimental set-up **8**

3 Results **9**
3.1 Loading-unloading tests 10
3.2 Gas breakthrough experiments 16
3.3 General observations 21

4 Conclusions **22**

References **23**

FIGURES

Figure 1-1 - Critical stress hypothesis 7

Figure 2-1 – Schematic of the Angled Shear Rig (ASR). 8

Figure 3-1 – Example of hysteresis seen in water flow during a loading/unloading experiment on a 30° slip-plane. 10

Figure 3-2 – Example of loading-unloading cycle seen during a gas injection tests on a 30° slip-plane. 11

Figure 3-3 – Fracture width recorded during a loading-unloading experiment. 12

Figure 3-4 – Shear displacement caused as the result of loading-unloading. 12

Figure 3-5 – The hysteresis observed in horizontal stress during loading-unloading experiments 13

Figure 3-6 – The variation of the ratio of horizontal stress to vertical stress seen during loading-unloading experiments 14

Figure 3-7 – Comparing results for water and gas injection during loading and unloading experiments 15

Figure 3-8 – Results from ASR_Tau06_30gGI showing different gas breakthrough indicating fault-valve behaviour 17

Figure 3-9 – Repeatability of gas injection tests; a) pressure response, b) flow results. 18

Figure 3-10 – Gas injection pressure variation with discontinuity orientation. 19

Figure 3-11 – Comparing gas entry pressure with normal load on the fracture. 19

Figure 3-12 – Gas injection pressure variation with discontinuity orientation and the influence of shear and injection rate. 20
Figure 3-13 – The influence of gas pressurisation rate. 20
Figure 3-14 – Photo showing the escape of gas into from the slip-plane. 21
Figure 3-15 – Example of pressure recorded on the slip-plane..... 22

Executive summary

This report outlines the major conclusions from an experimental study of 48 separate experiments with the primary aim to verify critical stress theory. Two main types of experiment were conducted: 1). Loading-unloading tests, where fracture flow was monitored at constant injection pressure as normal load was increased in steps to a given level and then reduced back to the starting stress state; 2). Gas breakthrough experiments, where gas injection pressure was increased in a pressure ramp at constant vertical load. These were conducted with and without active shear. It was found that critical stress theory is valid in predicting the preferential flow of gas in relation to the orientation of the fracture plane with respect to the maximum horizontal stress direction. However, loading unloading experiments showed that understanding the stress history of the rocks is of paramount importance and a mere knowledge of the current stress state is insufficient in accurately predicting the nature of fluid flow.

1 Introduction

1.1 RATIONALE

Discontinuities (fracture, faults, joints, interfaces, etc) play a pivotal role in controlling the movement of water and gas around an underground disposal facility (GDF) for radioactive waste. According to the current concepts, high level and long lived radioactive waste and spent fuel are intended to be stored/disposed of in a GDF within a stable geological formations (host rock) at depth (usually ~50-800 meters) beneath the ground surface. Hence, the radioactive waste is securely isolated and contained. At depth the rock mass may be a naturally fractured environment, such is the case for a GDF in crystalline rock, and the excavation of the GDF galleries is recognised to induce additional fractures (Bossart *et al.*, 2002; Rutqvist *et al.*, 2009). Therefore, all current concepts of disposal, be these in argillaceous, crystalline or salt rocks, will have a multitude of discontinuities as part of the engineered environment within the EDZ. Depending on the *in situ* stress conditions, preferential pathways may form along any, or all, of these discontinuities.

Fluids, such as gases and water, are expected to play a role in the transport of radionuclides away from the GDF. The conductivity of fluids through discontinuities is understood to be controlled by the interplay of their orientation and stress tensor direction (Barton *et al.*, 1995; Finkbeiner *et al.*, 1997). Around the GDF there are two distinct zones with differing discontinuity orientation, discontinuity densities, and fluid flow properties; (a) the EDZ where an intricate range of discontinuity (fracture) orientations are present in a complex localised-stress field, and (b) the far field zone where discontinuous (pre-fractured/faulted) host rock may be present.

It has been proposed that discontinuities that are oriented parallel to the maximum horizontal stress orientation (σ_H) experience the lowest normal stresses acting across them and therefore will undergo the least amount of closure and will thus be the most permeable (Heffer & Lean, 1993). This is based on the assumption that discontinuities experiencing the least amount of stress will offer minimum resistance to flow and therefore will have relatively high permeability. However, observations by Laubach *et al.* (2004) on a number of sedimentary basins in the western United States using core permeability, stress measurements, and fluid flow datasets showed that at a depth of >3 km, the open discontinuities were not aligned parallel to σ_H as previously understood. Hence, *in situ* stress orientations cannot be realistically used as an indicator for predicting fluid flow in fractured rocks.

Barton *et al.* (1995) proposed that discontinuities whose state of stress are close to the failure criterion are more likely to be conductive because of the localised failure as a consequence of the large shear component acting along the discontinuity surface. Such features are termed "critically stressed" and are oriented approximately 30 degrees to σ_H (Rogers, 2003; Rogers & Evans, 2002). In order to apply the critical stress theory to the study of flow, the *in situ* stress field acting along all discontinuities in a volume of rock can be resolved into shear and normal stress components. When the magnitude and direction of the stress field has been constrained, the shear stress (τ) and normal stress (σ_n) acting on a discontinuity can be expressed by (Jaeger *et al.*, 2007):

$$\tau = \beta_{11}\beta_{21}\sigma_1 + \beta_{12}\beta_{22}\sigma_2 + \beta_{13}\beta_{23}\sigma_3 \qquad \text{and} \qquad \sigma_n = \beta_{11}{}^2\sigma_1 + \beta_{12}{}^2\sigma_2 + \beta_{13}{}^2\sigma_3$$

where, β_{ij} = directional cosines between the discontinuity and the stress tensor, σ_1, σ_2, and σ_3 = magnitude of the maximum, intermediate, and minimum principal stresses respectively.

When the shear stress and normal stress on the discontinuities are plotted with respect to the *in situ* stress field in a Mohr space, the faults and fractures that are scattered above the Mohr-Coulomb failure criterion are termed critically stressed and hence expected to be conductive

(Figure 1-1). Critically stressed discontinuities are expected to be present amongst the numerous complex fracture networks within and around the EDZ and in the far field around the GDF.

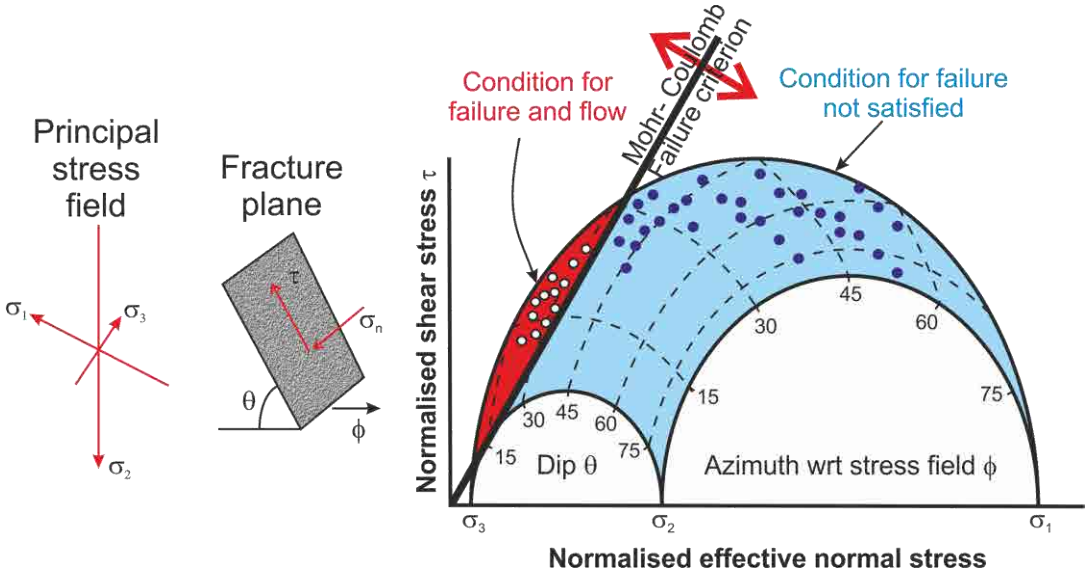

Figure 1-1 - Critical stress hypothesis (adopted from Barton *et al.*, 1995; Jaeger *et al.*, 2007; Rogers, 2003). The three-dimensional Mohr diagram represents the shear stress and normal stress acting along a fracture in response to the *in situ* stress field. The open circles represent fractures experiencing state of stress above the failure criterion and therefore subject to shear failure. The closed circles represent fractures whose stress state is insufficient to induce shear failure and hence stable.

1.2 OBJECTIVES

Whilst there is considerable field evidence for the applicability of the critical stress approach from many sedimentary basins worldwide, the theory has been found to be lacking in describing the flow regime in the Sellafield area, UK (Reeves 2002). This previous research explained the discrepancy by considering the techtonic history of the region. Sellafield has undergone uplift and the stress acting on the faulted bedrock is now lower than at the time of their formation. Therefore, this study showed that the flow regime of discontinuities is more complex than the simple critical state approach would predict.

The objective of this experimental programme was to examine the relationship between the stress tensor direction and discontinuity orientation, as well as examining the conditions under which discontinuities become conductive. In doing this experimentation it will validate the critical stress theory, which could be used to understand the reasons why some fractures in the EDZ are conductive and hence aid performance assessment. Specific objectives were:

(i) perform and interpret small scale experiments to investigate relationship between the stress tensor direction and fracture orientations, as well as examining the conditions under which fractures become conductive,

(ii) provide high-quality experimental data to test/validate the critical stress theory in relation to repository condition for the first time.

Previous work at BGS on fracture transmissivity in Opalinus clay (Cuss *et al.*, 2011) designed an effective apparatus and showed that flow is a complex, focused, transient property that is dependent upon normal stress, shear displacement, fracture topology, fluid composition, and swelling characteristics of the material. The current experimental programme aimed to extend this knowledge by investigating the influence of discontinuity orientation. The programme was not proscribed and investigation of other factors influencing flow were explored. However, some

elements of discontinuity flow were only "identified" and will require follow-up work in order to describe fully their influence.

2 Experimental set-up

All experiments were performed using the bespoke Angled Shear Rig (ASR, Figure 2-1) designed and built at the British Geological Survey. Experiments conducted on Opalinus clay (Cuss *et al.*, 2011) have shown that fracture topology is a key parameter in controlling fluid flow along fractures. In order to reduce the number of variables required to fully understand discontinuity flow, a "generic" discontinuity was investigated. The ASR comprised of two stainless steel blocks with a clay gouge of saturated kaolinite (gravimetric water content of 80%) of 60mm × 60 mm × 50 µm sandwiched between them. This allows the pure mechanical influence of discontinuity orientation to be investigated in a simplified system. Results are also applicable to clay-rich and crystalline disposal concepts in the numerous discontinuities seen.

The ASR comprised 6 main components:

1. Rigid frame that has been designed to deform as little as possible during the experiment;
2. Vertical load system comprising an Enerpac hydraulic ram that is controlled using an ISCO 260D syringe pump, a rigid loading frame and an upper thrust block (up to 20 MPa normal stress, 72 kN force);
3. Shear force actuator designed to drive shear as slow as 14 microns a day at a constant rate (equivalent to 1 mm in 69 days);
4. Pore pressure system comprising an ISCO 500D syringe pump that can deliver either water or gas through the centre of the top block directly to the fracture surface;
5. A state-of-the-art custom designed data acquisition system using National Instruments LabVIEW™ software facilitating the remote monitoring and control of all experimental parameters.
6. The experimental slip plane assembly consisting of precision machined 316 stainless steel top and bottom blocks with dips of 0, 15, 30, and 45 degrees forming fault plane. The top block was connected to the vertical loading mechanism by means of a swivel mechanism which was engaged to the shoulders on either side of the top block.

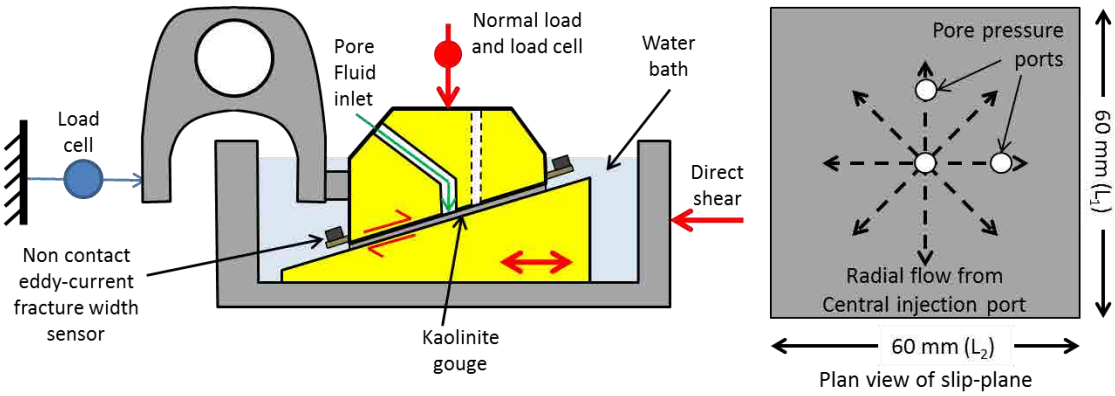

Figure 2-1 – Schematic of the Angled Shear Rig (ASR).

Unlike standard direct shear experiments, the top and bottom blocks could be oriented at different angles to the vertical load/horizontal displacement. Experiments were conducted on horizontal blocks and angles of 0, 15, 30, and 45 degrees. Vertical load was applied using a servo controlled Teledyne ISCO-260D syringe pump pressurising an Enerpac single acting hydraulic ram connected to a rigid loading frame. The Enerpac ram had a stroke of 105 mm, which meant

that the ram could easily accommodate the vertical displacement of the top block as it rode up the fracture surface at constant vertical load. Pore fluid (water or helium) was introduced through the centre of the top block by means of a Teledyne ISCO 500D syringe pump connected in series to a gas-water interface vessel. Pore pressure transducers, attached to ports which were positioned orthogonally to each other at 15 mm from the central pore fluid inlet allowed measurement of pore pressures within the slip plane (see Figure 2-1). The shear-force actuator was comprised of an ISCO 500 series D syringe pump, which was modified by mounting horizontally. The ISCO pump was designed to push a syringe through a barrel to deliver pressure. In the current setup, the barrel had been removed and the drive-train directly connected to the sample assembly, itself mounted on a low friction bearing. Horizontal load was measured using a load cell fitted laterally to the top-block.

The upper and lower thrust blocks of the apparatus were made out of stainless steel with a contact area of 60 mm × 60 mm. The lower thrust block was longer than the top one so that the contact area was maintained constant throughout the test. Vertical travel of the thrust block (giving gouge dilation) was measured by a high precision non-contact capacitance displacement transducer, which had a full range of ± 0.5 mm and an accuracy of 0.06 µm. Following early testing, it was necessary to add two high precision Eddy current non-contact displacement transducers to either end of the top thrust block in order to record gouge thickness directly and to determine non-parallel alignment of the two thrust blocks. These submersible devices had a full range of ± 1 mm and an accuracy of 0.2 µm. Lateral movement was measured using a high precision linear variable differential transformer (LVDT), which had a full range of ± 25 mm and an accuracy of 0.5 µm

3 Results

The complete experimental programme conducted 48 separate experiments. All experimental results are described in Cuss *et al.* (2013). Two main types of experiment were conducted: 1). Loading-unloading tests, where fracture flow was monitored at constant injection pressure as vertical load was increased in steps to a given level and then reduced back to the starting stress state; 2). Gas breakthrough experiments, where gas injection pressure was increased in a pressure ramp at constant vertical load. These were conducted with and without active shear. In additional, a number of other experiments were conducted. The main conclusions from this study are summarised below:

3.1 Loading-unloading tests:

3.1.1 During a loading (vertical stress) and unloading cycle considerable hysteresis in flow was observed signifying the importance of stress history on fracture flow.

3.1.2 For the case of gas injection the change in flow was chaotic at low vertical loads, whereas for water injection the flow reduced smoothly with increased vertical load.

3.1.3 Hysteresis in horizontal stress observed during unloading demonstrated the importance of the ratio between horizontal stress and vertical stress and its control on flow.

3.1.4 Differences have been observed between injection fluids (water and helium), especially the hysteresis observed in flow. For water injection flow was only partially recovered during unloading, whereas for gas enhanced flow was seen at low vertical loads.

3.2 Gas breakthrough experiments:

3.2.1 During gas breakthrough experiments episodic flow/fault valve behaviour was seen with a decrease in subsequent peak pressures and the form of the pressure response was different during subsequent breakthrough events.

3.2.2 Repeat gas injection testing has shown a consistent gas entry pressure but considerably different, non-repeatable, gas peak pressures.

3.2.3 Differences in gas entry pressure were seen dependent on the orientation of the fracture.

3.2.4 Active shear reduced the gas entry pressure, which is contrary to observations seen in Opalinus clay.

3.3 General observations:

3.3.1 The results showed that the flow of gas through clay filled fractures was non-uniform and occurred via localised preferential pathways.

3.3.2 The pressure recorded within the slip-plane showed a negligible fracture pressure and did not vary much in all tests.

Each finding is discussed in more detail below.

3.1 LOADING-UNLOADING TESTS

A total of 17 loading-unloading experiments were conducted, all on a 30° slip-plane. Nine tests were conducted without a permeant in order to understand the behaviour of the kaolinite gouge whilst loading/unloading, five tests were conducted with water as the injection fluid, whilst three gas flow experiments were conducted.

3.1.1 During a loading (vertical stress) and unloading cycle considerable hysteresis in flow was observed signifying the importance of stress history on fracture flow.

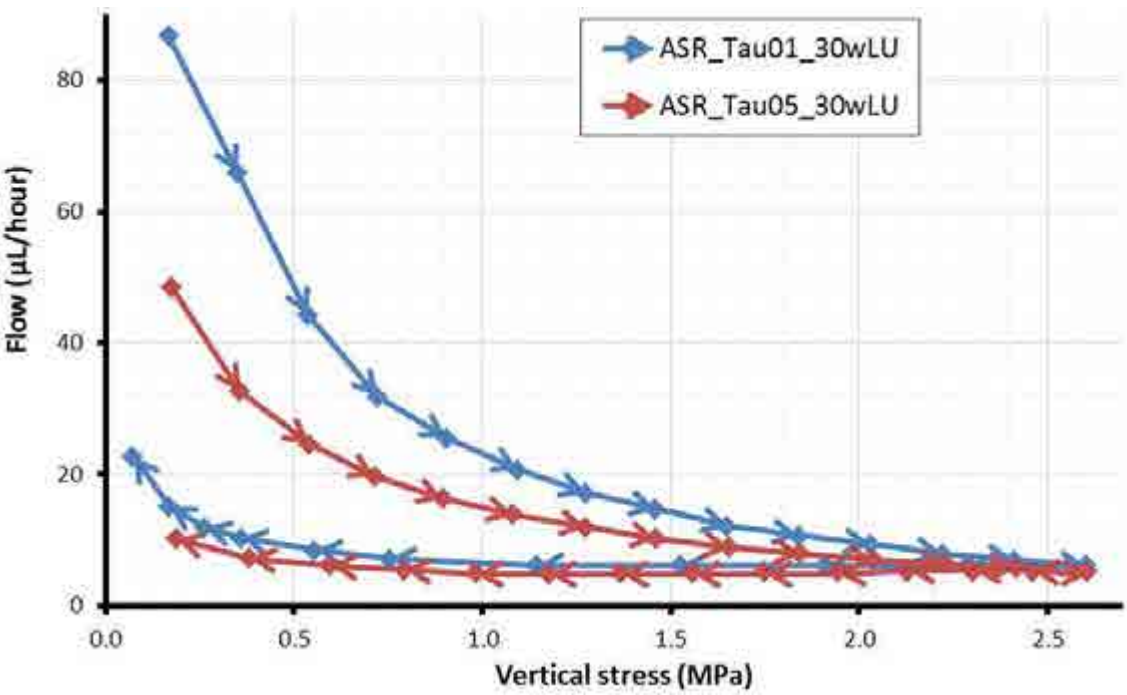

Figure 3-1 – Example of hysteresis seen in water flow during a loading/unloading experiment on a 30° slip-plane.

Figure 3-1 shows the results of flow achieved for two tests conducted injecting water into a 30° discontinuity during loading from 0.1 to 2.6 MPa and unloading from 2.6 to 0.2 MPa. As can be seen, the starting flow rate of the two tests were different by nearly a factor of 5. Both tests were setup in identical ways using the same pre-mixed weight of kaolinite and deionised water. This difference may have derived from variations of gouge thickness and as a result the experimental system was modified in order to measure the starting gouge thickness.

As normal load was increased in steps, the flow along the slip plane steadily reduced. In both expereiments, although starting from dissimilar flow rates, both achieved a flow rate of approximately 6 µl/h by 2.6 MPa vertical load. On unloading, this flowrate did not significantly alter until vertical loads of approximately 0.75 MPa. Therefore it can be noted that the "memory" of the maximum load experienced was retained. This illustrates the importance of stress history on predicting flow along discontinuities and has been used to explain the non-applicability of the critical stress approach in its simple form at the Sellafield site in the UK (Sathar *et al.*, 2012).

All loading-unloading experiments showed marked hysteresis in flow.

3.1.2 For the case of gas injection the change in flow was chaotic at low vertical loads, whereas for water injection the flow reduced smoothly with increased vertical load.

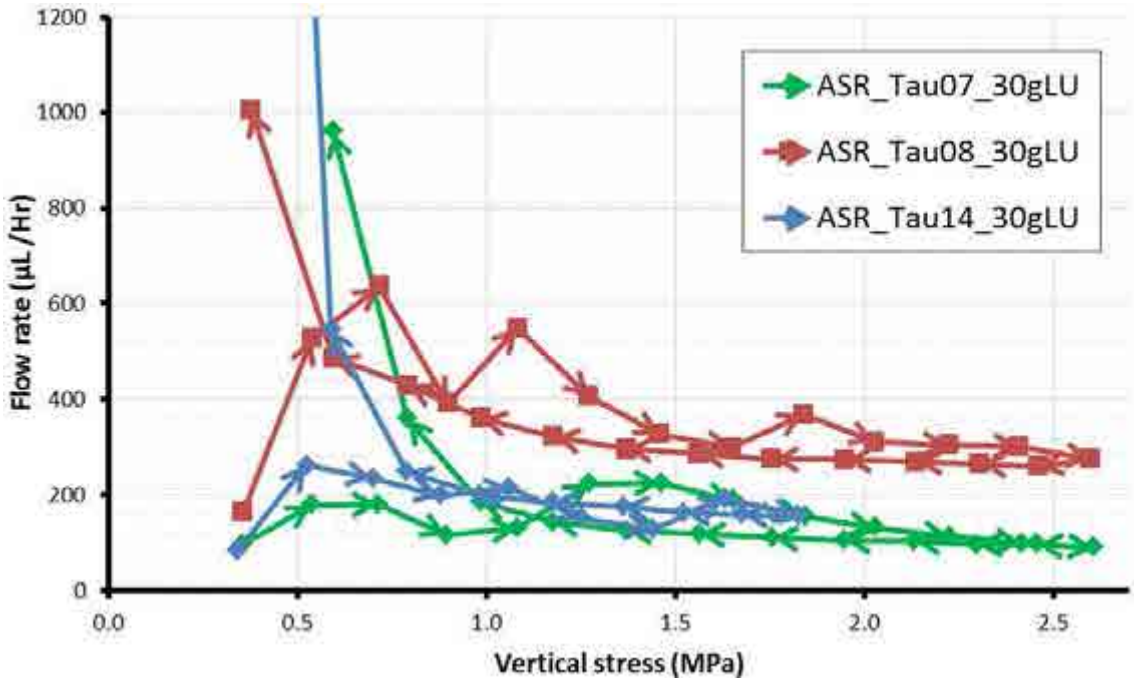

Figure 3-2 – Example of loading-unloading cycle seen during a gas injection tests on a 30° slip-plane.

Figure 3-2 shows the results for three loading-unloading experiments with gas as the injection medium. Considerable differences are seen between the loading and unloading cycles. On loading the progression of flow was chaotic. In all three tests, once vertical load was increased from the starting value of approximately 0.3 to 0.5 MPa flow increased. All three tests showed that increased vertical load resulted in episodes of increasing and decreasing flow. This could be explained by 3 possible mechanisms:

1. Gas flow was highly sensitive to water content of the gouge and the duration of the experiment meant that full drainage was not possible;
2. The gougue was not remaining even in thickness along the complete length, i.e. increased load was resulting in a wedge shaped gouge;
3. Shear movement was occuring along the 30° slope as vertical load wais increased and there was some form of stick-slip, which meant that the movement was uneven between steps.

It is difficult to rule out scenario (1) as this had not been investigated fully. However, wide variation in flow rates have not been observed, which suggests that a fairly homogenous paste of gouge had been created and that subtle, localised changes in saturation (caused by uneven drainage) was unlikely to be the main cause of this effect.

The second scenario (2) is not supported by the measurement of the gouge thickness during experimentation, as seen in Figure 3-3. Even reduction in gouge thickness was observed, with

more chaotic variations in thickness seen during unloading. This is contrary to the flow data, where chaotic flow was seen during loading and even variaion seen during unloading. Therefore this effect was unlikely to be caused by uneven thicknesses of gouge.

The third scenario (3) is also not supported by experimental observations. Figure 3-4 shows that there was shear movement as a result of only increasing vertical load. However, this increased relatively evenly and suggests that changes in load have resulted in the gouge moving evenly.

Observations of localised flow suggests that gas exploits sub-micronscale features within the clay, similar to features observed in bentonite. The exact cause of the chaotic behaviour has not been determined due to the macro-scale of measurement and the likely microscopic origin of this behaviour. However, the chaotic behaviour was repeatable and suggests that gas flow predictions of transmissivity are problematic. The "even" reduction in flow on unloading supports the "memory" effect of the clay introduced in the previous section.

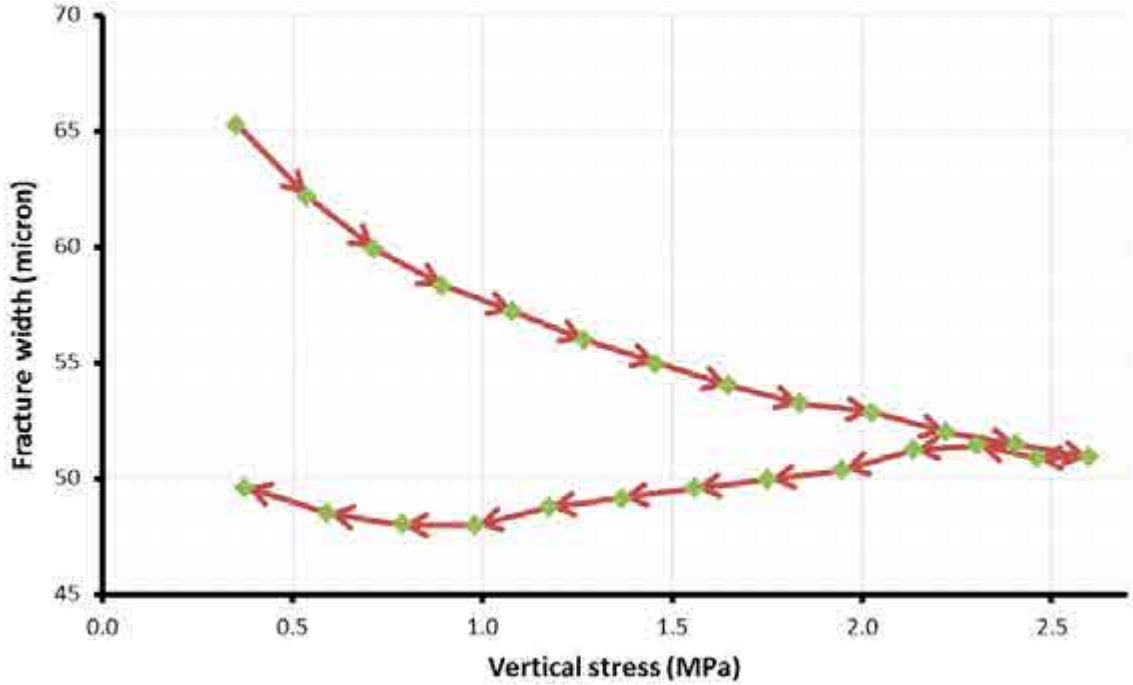

Figure 3-3 – Fracture width recorded during a loading-unloading experiment.

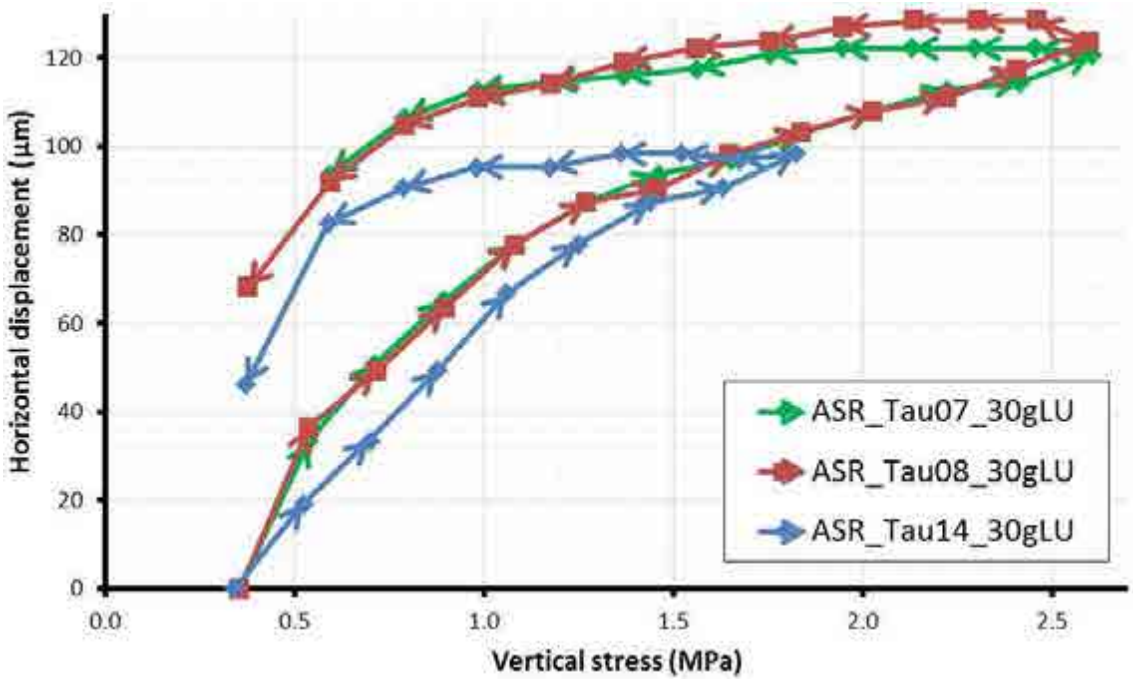

Figure 3-4 – Shear displacement caused as the result of loading-unloading.

3.1.3 Hysteresis in horizontal stress observed during unloading demonstrates the importance of the ratio between horizontal stress and vertical stress and its control on flow.

Figure 3-5 shows that considerable hysteresis was observed in horizontal stress during loading-unloading experiments for both water and gas injection. The repeatability of the results showed that free movement of the gouge was achieved. The hysteresis in horizontal stress during unloading may be attributed to the cohesive strength of the kaolinite clay gouge. Figure 3-6 shows how the ratio of horizontal stress to vertical stress varied during the experiment. Here, subtle variation between water and gas injection experiments was seen during unloading once the ratio exceeded unity. Significant gas flow rate increase occurred when the horizontal stress to vertical stress ratio increased above unity during unloading.

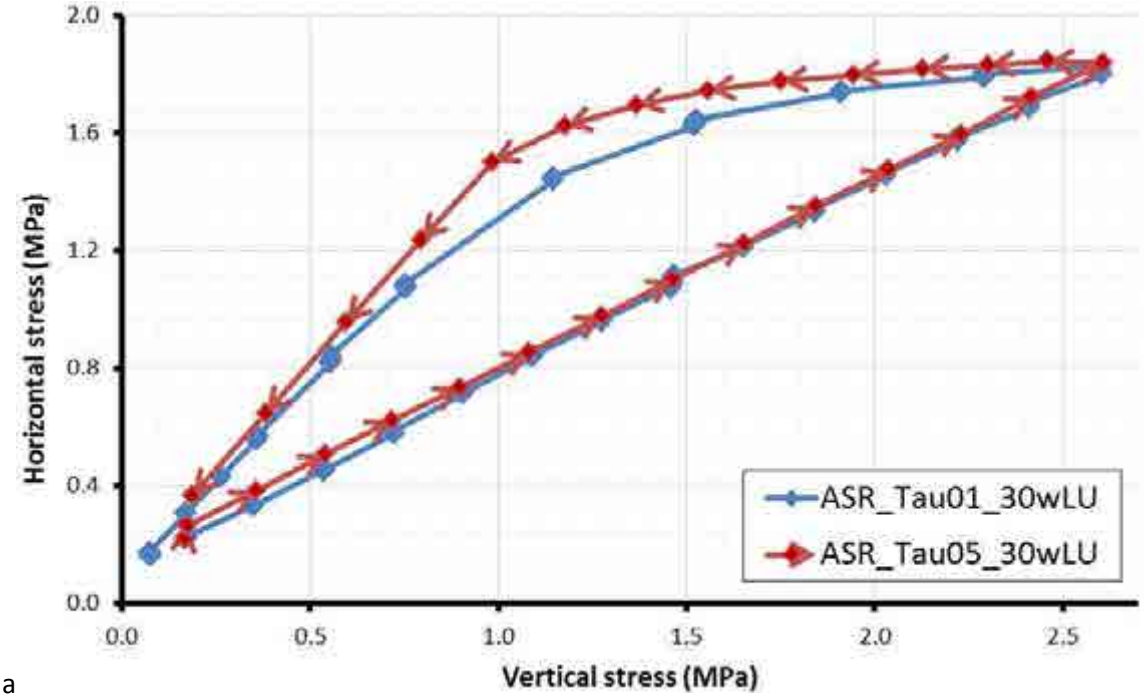

a

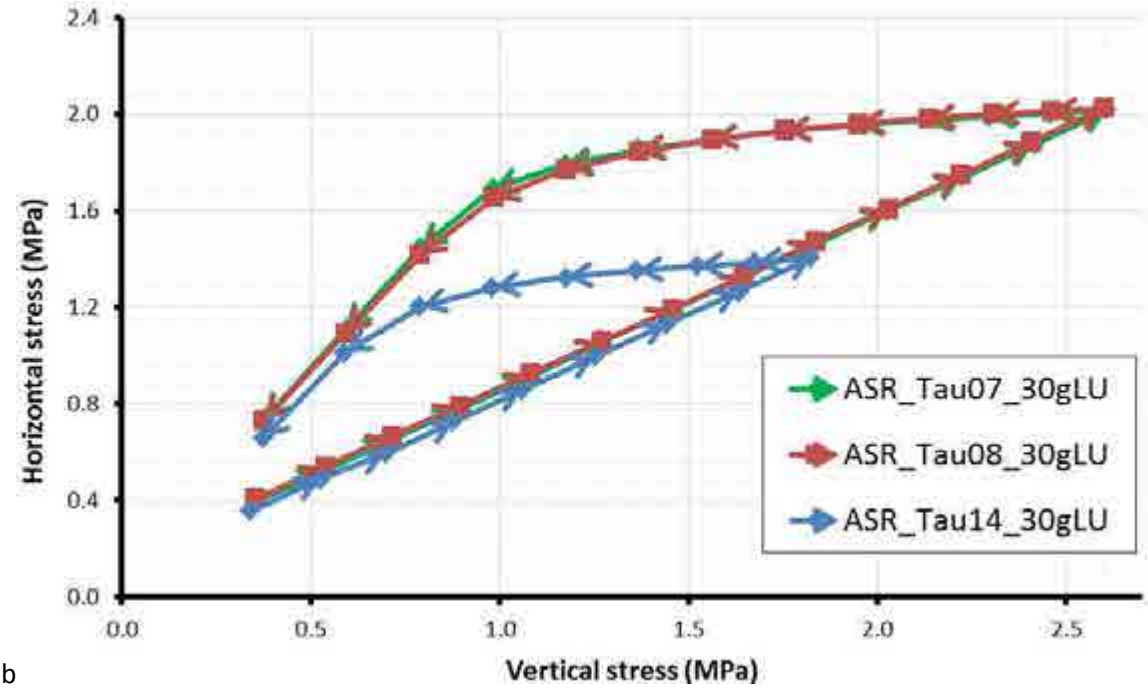

b

Figure 3-5 – The hysteresis observed in horizontal stress during loading-unloading experiments; a) water injection; b) gas injection.

Zoback *et al.* (1985) and Brudy *et al.* (1997) have shown that the ratio of shear stress to normal stress is crucial in controlling permeability and in the movement of gas through fractures. The close relationship between fracture flow and the horizontal to vertical stress ratio during the unloading stages in the present experiments also points towards its significance in understanding the flow of fluid through discontinuities. In the case of a fractured rock formation undergoing uplift stress relaxation is likely to result in a high horizontal stress to vertical stress ratio.

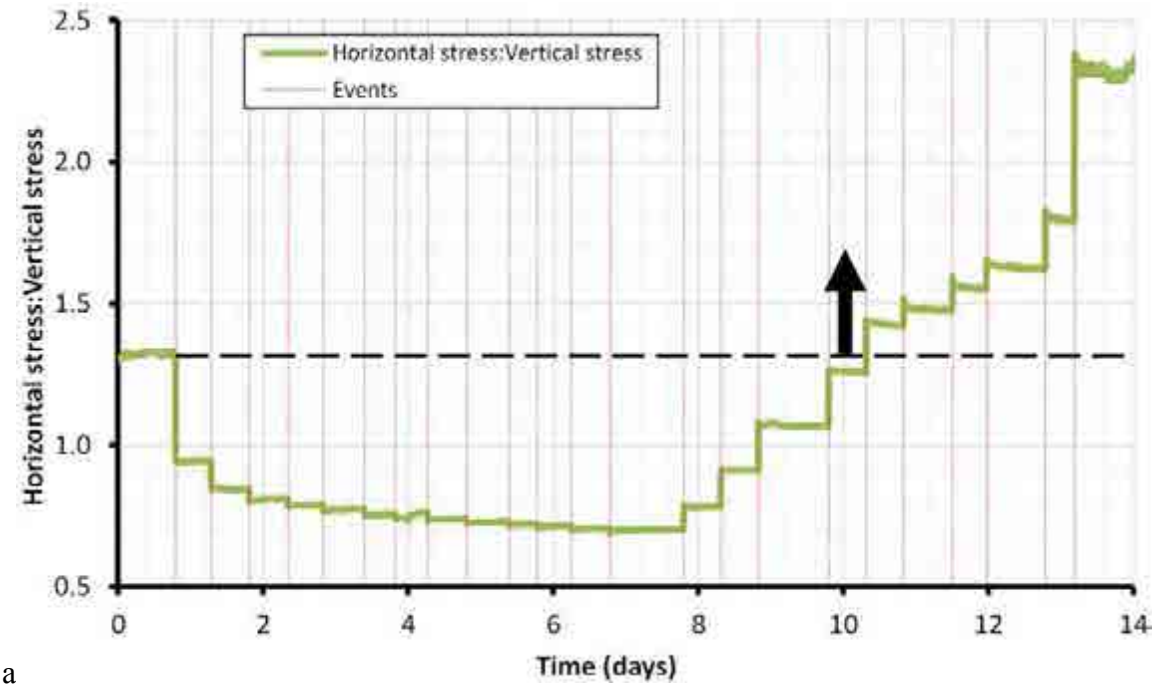

a

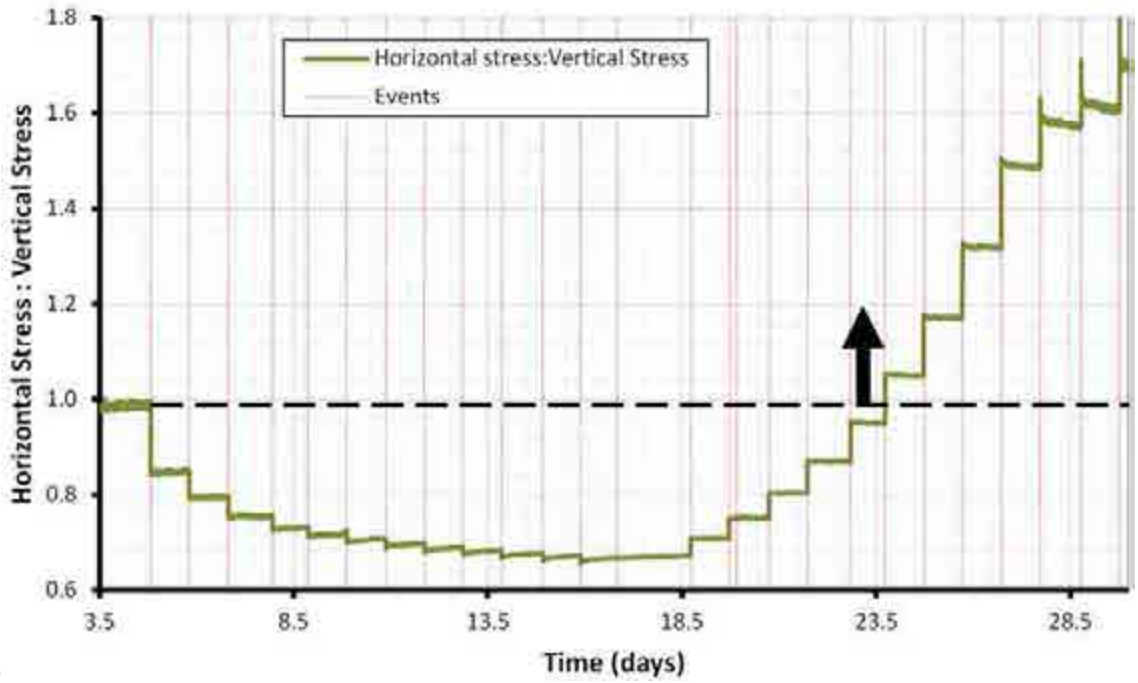

b

Figure 3-6 – The variation of the ratio of horizontal stress to vertical stress seen during loading-unloading experiments; a) water injection; b) gas injection. The arrows indicate horizontal stress to vertical stress ratios during unloading which are greater than the initial values and indicate an enhancement in flow rate.

Understanding the horizontal to vertical stress ratio is important in predicting the flow properties of discontinuities. Features experiencing high horizontal to vertical stress ratios are expected to be more conductive. High horizontal to vertical stress scenarios are likely to be more prevalent in regions experiencing stress relaxation due to structural uplift or removal of the overburden.

Again, this highlights that an understanding of the stress history of a discontinuity is essential to effectively predict the present fluid flow properties of those features.

3.1.4 Differences have been observed between injection fluids (water and helium), especially the hysteresis observed in flow. For water injection flow was only partially recovered during unloading, whereas for gas enhanced flow was seen at low normal loads.

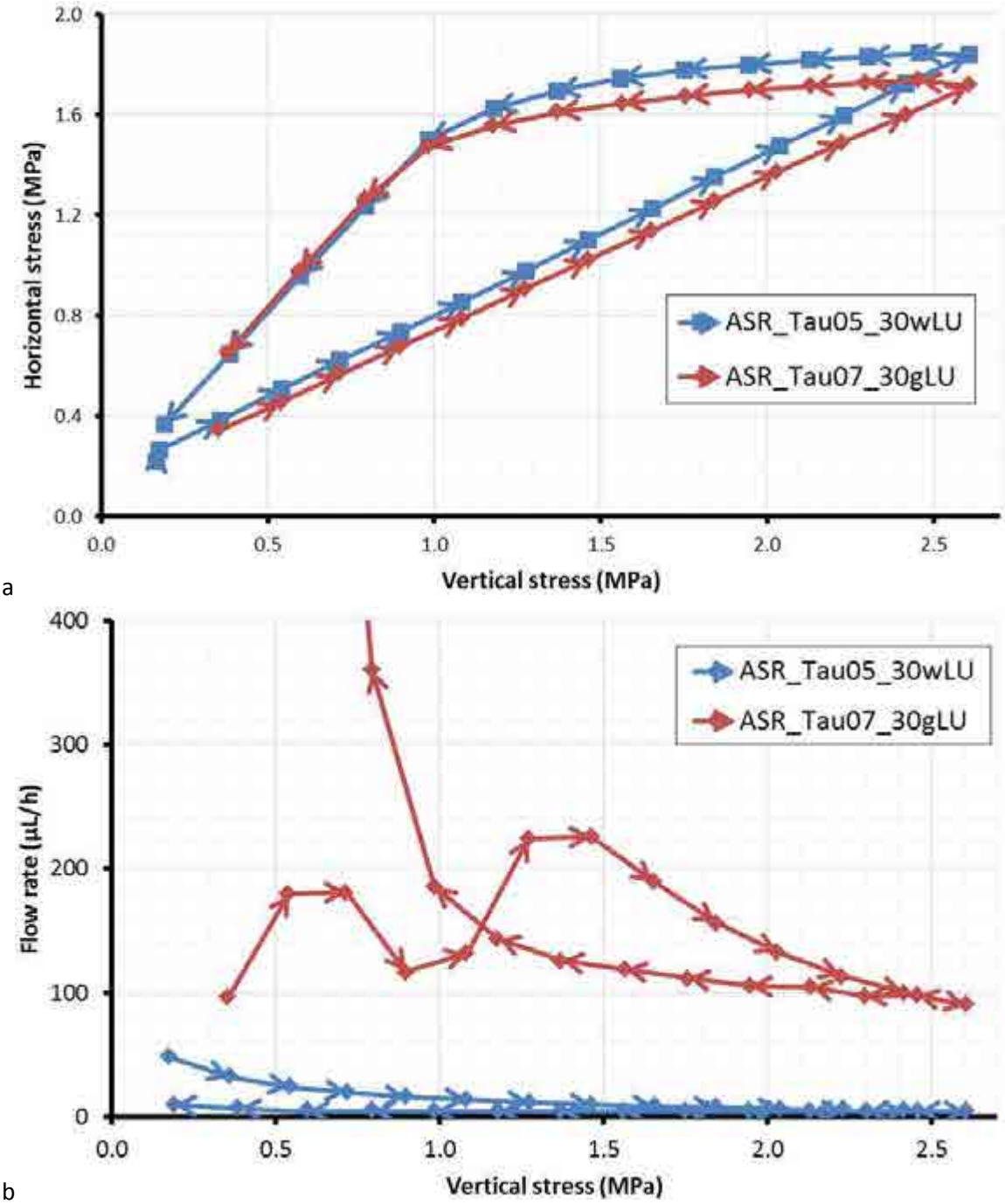

Figure 3-7 – Comparing results for water and gas injection during loading and unloading experiments; a) horizontal stress; b) flow response.

Figure 3-7a shows a comparison of the horizontal stress response during a loading-unloading experiment conducted using water and gas as the injection medium. There is agreement between the data recorded, which demonstrates that the gouge mechanically behaved the same way if water or gas was injected into a saturated kaolinite gouge. The similarities suggest that the gouge

was neither hydrated by water injection (as it is already fully saturated), nor was it desaturated by gas injection.

However, considerable differences were seen in flow behaviour. For water injection, a pore pressure of 1 MPa was sufficient to initiate flow, whereas a gas pressure in excess of 3.5 MPa was required. This resulted in much lower flow rates observed in water injection tests, as seen in Figure 3-7b. The differences suggest that the governing physics controlling gas movement is dissimilar to that controlling water movement.

As previously introduced, there was also considerable difference in the progression of flow during the loading cycle. At low vertical loads this behaviour was chaotic in gas injection, whereas it was smooth for water injection. By 1.5 MPa vertical load the two behaviours are similar, both decaying evenly with increasing vertical load.

Differences were also seen during the unloading cycle. Both injection fluids showed a similar initial response with considerable hysteresis seen and the slow recovery of flow. Dissimilarity was seen as vertical load reduced below approximately 1 MPa. For the case of water injection, flow was always only partially recovered. For gas injection, at low vertical loads flow increased to high levels much greater than that recorded at the corresponding vertical load on the loading cycle. The enhanced flow became catastrophic and at low vertical loads all gas in the gas reservoir was expelled through the slip-plane. Such catastrophic failure during water injection was not seen. This may in part be due to the expansion of gas as it propagated along the slip-plane as pressure reduced.

3.2 GAS BREAKTHROUGH EXPERIMENTS

A total of 26 gas breakthrough experiments were conducted on 0°, 15°, 30°, and 45° discontinuities; both with and without active shear. All tests were conducted in an identical manner with a known starting volume of 200 ml of helium at 4 MPa and a pressure ramp created by constant flow displacement of the ISCO syringe pump by 700 µl/h.

3.2.1 During gas breakthrough experiments episodic flow/fault valve behaviour was seen with a decrease in subsequent peak pressures and the form of the pressure response was different during subsequent breakthrough events.

A single test was conducted (ASR_Tau06) for a prolonged gas injection ramp to see if there was repeat gas entry. A total of seven steps were conducted, as seen in Figure 3-8. The exact detail of this particular test is complicated due to need to refill the gas reservoir several times and is described in detail in Cuss *et al.* (2013). However, general observations are introduced below.

It can be seen that the first gas breakthrough at 0.2 MPa vertical load resulted in the sudden catastrophic loss of gas pressure at 3.2 MPa as the gas reservoir was emptied through the slip-plane. Vertical load was increased to 1.85 MPa to see if a secondary breakthrough could be initiated following fracture sealing due to increased vertical load. This resulted in a distinct peak in gas pressure at 1.9 MPa, which was followed by a decay to 1.2 MPa and then slow recovery of gas pressure to another breakthrough at 1.6 MPa. Pressure dropped to 0.5 MPa and again recovered to another breakthrough event at about 1 MPa. This partial breakthrough was followed by pressure recovery to a plateau of 1.1 MPa. Vertical load was increased to 2.25 MPa and a fifth breakthrough occurred at 1.8 MPa.

The form of the breakthrough event changed during the experiment. The first event was a catastrophic total loss of pressure. The second event was a peak and trough, similar in form to that seen during gas injection in bentonite. The third event was a sudden drop in pressure by 1 MPa, and the fourth event could be described as the system reaching equilibrium and the attainment of a plateau.

These observations suggest that “fault-valve behaviour” had been demonstrated in the laboratory and the magnitude of subsequent break-through events reduced (at constant vertical load) and the

"form" of the breakthrough events changes with each successive feature. It also demonstrated that an increase in vertical load resulted in a degree of self-sealing, although the "memory" of previous breakthrough events may still be apparent.

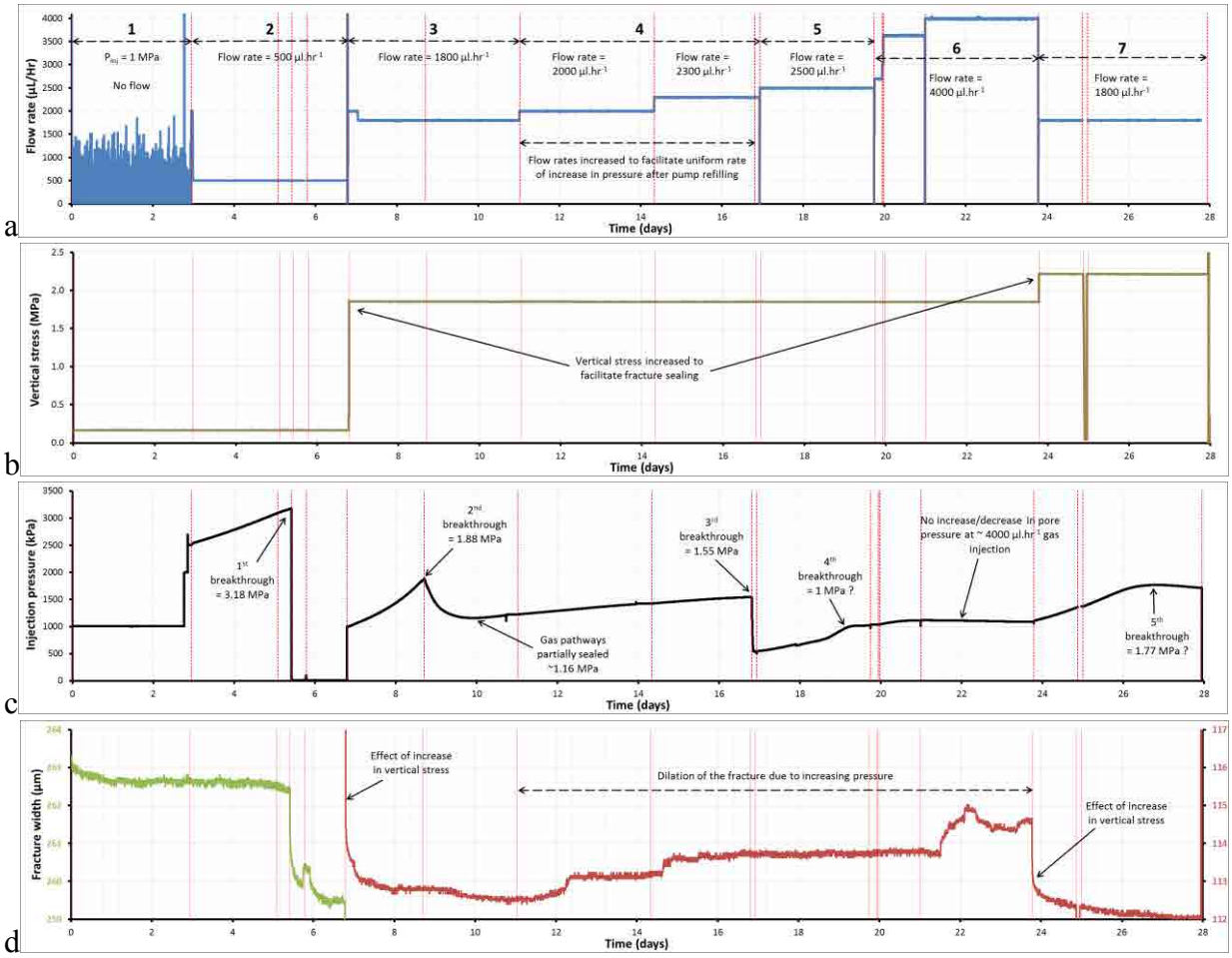

Figure 3-8 – Results from ASR_Tau06_30gGI showing different gas breakthrough indicating fault-valve behaviour. a) Flow rate versus time plot showing the gas injection rates used in different stages (indicated as numerals) of the experiment. b) Vertical stress versus time graph showing the vertical stresses applied on to the slip plane. c) Gas injection pressure versus time plot showing the evolution of injection pressure before and after each breakthrough event. d) The variations in fracture width during various gas injection stages.

3.2.2 Repeat gas injection testing has shown a consistent gas entry pressure but considerably different, non-repeatable, gas peak pressures.

Figure 3-9 shows an example of the repeatability of experimental results for four tests conducted on a discontinuity oriented at 30°. Gas entry pressure has been determined by comparing the gas pressure recorded with that predicted at the given pressure (Figure 3-9b). Three tests showed similar gas entry of approximately 8 MPa, with test ASR_Tau07 showing an anomalously low entry pressure of 5.5 MPa. This suggested that test ASR_Tau07 had gas entry at a much lower pressure for an unknown reason. Similar anomalously low gas entry pressures were seen on other orientations, suggesting that gas was able to exploit a "defect" of some form at a low pressure and the experiment was unable to be perfectly reproducible.

Whilst three of the four tests showed a similar gas entry pressure, these tests showed considerably different peak pressures of 10.8, 13.5, and 15.5 MPa (test ASR_Tau07 achieved a peak pressure of only 8.2 MPa). One test catastrophically broke-through at 10.8 MPa.

These observations suggest that the physical control on gas entry was repeatable, although in the presence of any form of imperfection gas was able to enter at lower pressures. Once gas started to move within the slip-plane the progression of pressure was less predictable and depended on whether the evolving gas network located an exit from the system. Similar results were seen for all discontinuity orientations.

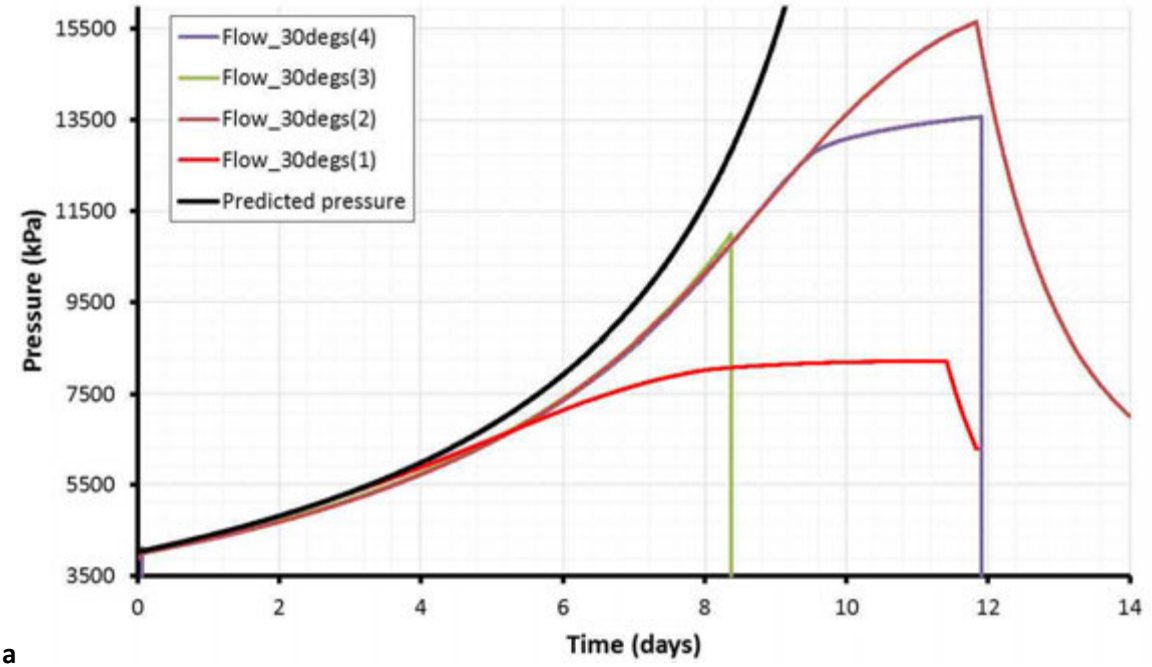

a

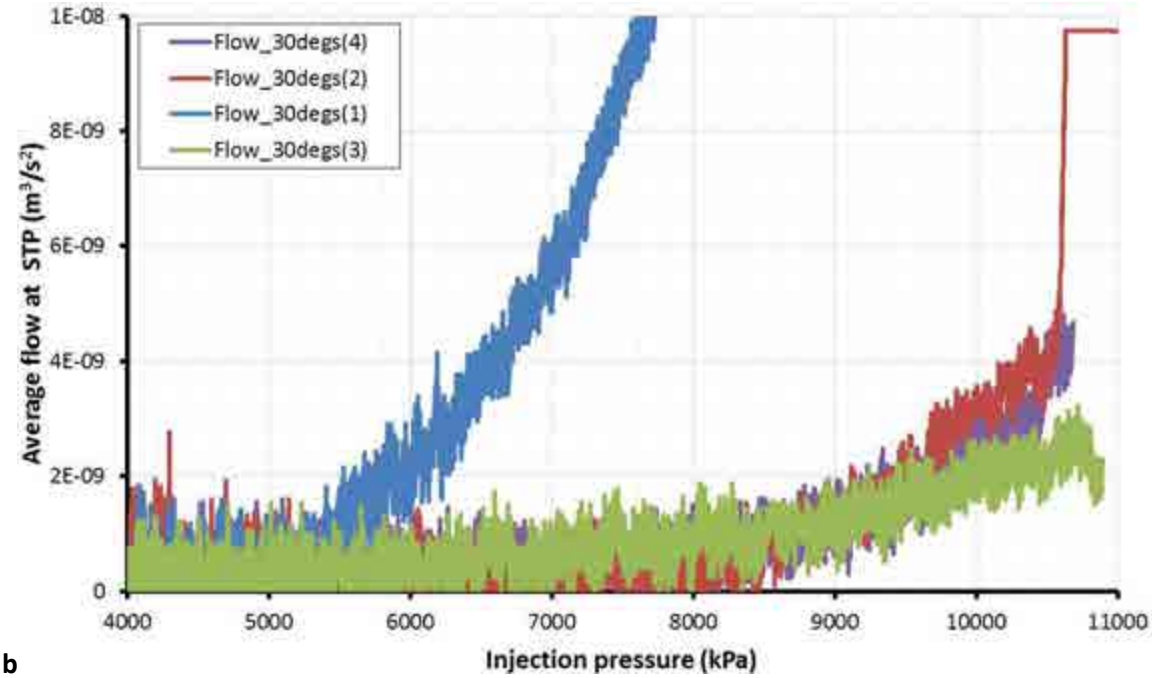

b

Figure 3-9 – Repeatability of gas injection tests; a) pressure response, b) flow results.

3.2.3 Differences in gas entry pressure are seen dependent on the orientation of the fracture.

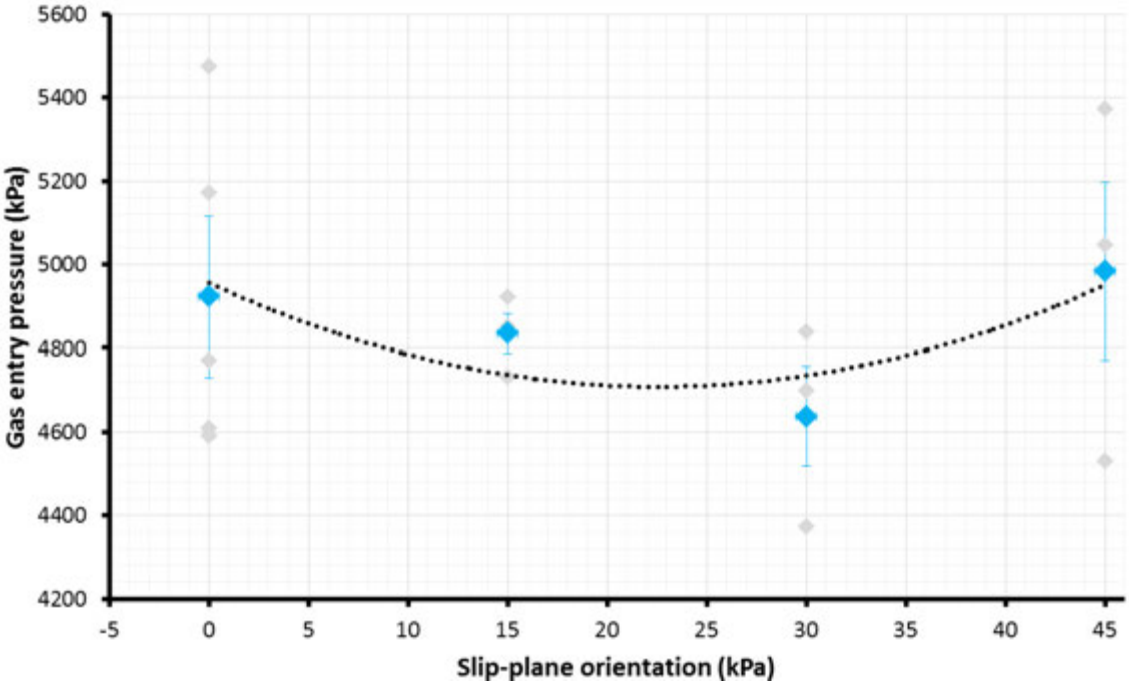

Figure 3-10 – Gas injection pressure variation with discontinuity orientation.

Although some tests have shown anomalously low gas entry pressures, Figure 3-10 shows a general variation of gas entry pressure with discontinuity orientation. The highest gas entry pressure, as expected, is seen on a flat slip-plane with an entry pressure of 8.5 MPa. The lowest gas entry pressure was recorded at 15° of 7.75 MPa. Generally, the results suggest that the lowest gas entry pressure would be observed at 22.5°.

All tests have been conducted at identical vertical loads. As discontinuity orientation varies, the load acting normal to the slip-plane will vary. Taking this geometrical effect into account, the variation seen in gas entry pressure is more complex than a simple stress rotation about the slip-plane, as shown in Figure 3-11.

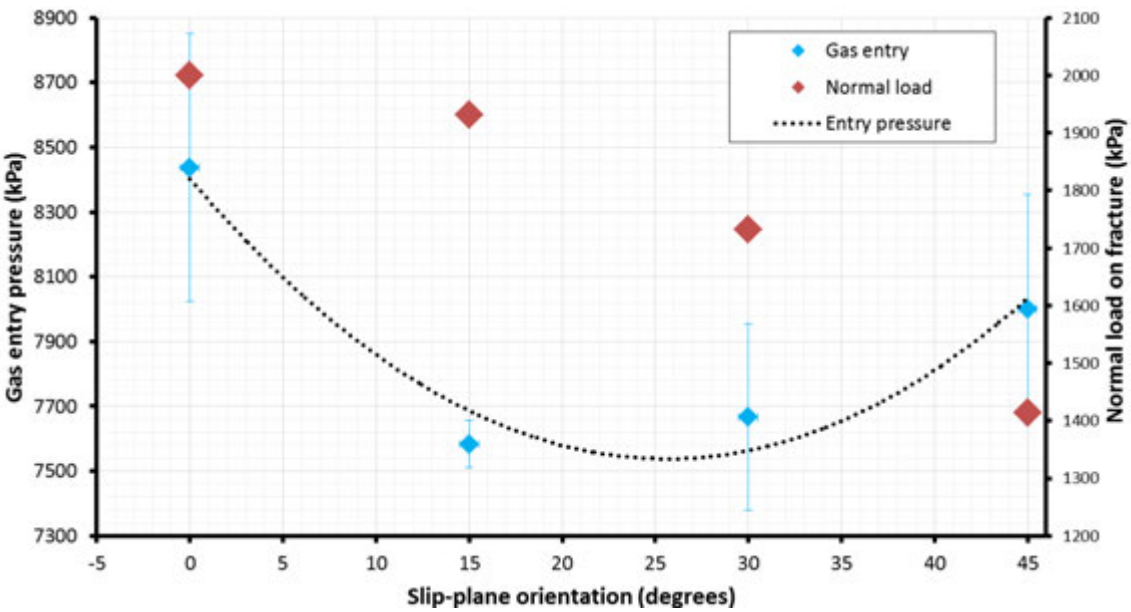

Figure 3-11 – Comparing gas entry pressure with normal load on the fracture.

The experimental study has clearly demonstrated a variation in fracture transmissivity with discontinuity orientation. This experimental study demonstrates that the critical stress theory is applicable in the absence of stress relaxation.

3.2.4 Active shear reduced the gas entry pressure; therefore in kaolinite shear has the opposite of self-sealing.

Figure 3-12 shows that tests conducted on slip-planes oriented to the direction of active shear showed a lower gas entry pressure for kaolinite and a rotation of gas entry pressure minimum to 38°. For water injection fracture transmissivity was seen to reduce due to self-sealing as a result of shearing. Therefore the reduction in gas entry pressure and observed increase in flow (as postulated from a reduced peak pressure) suggests that shearing in kaolinite has the opposite effect of self-sealing to gas.

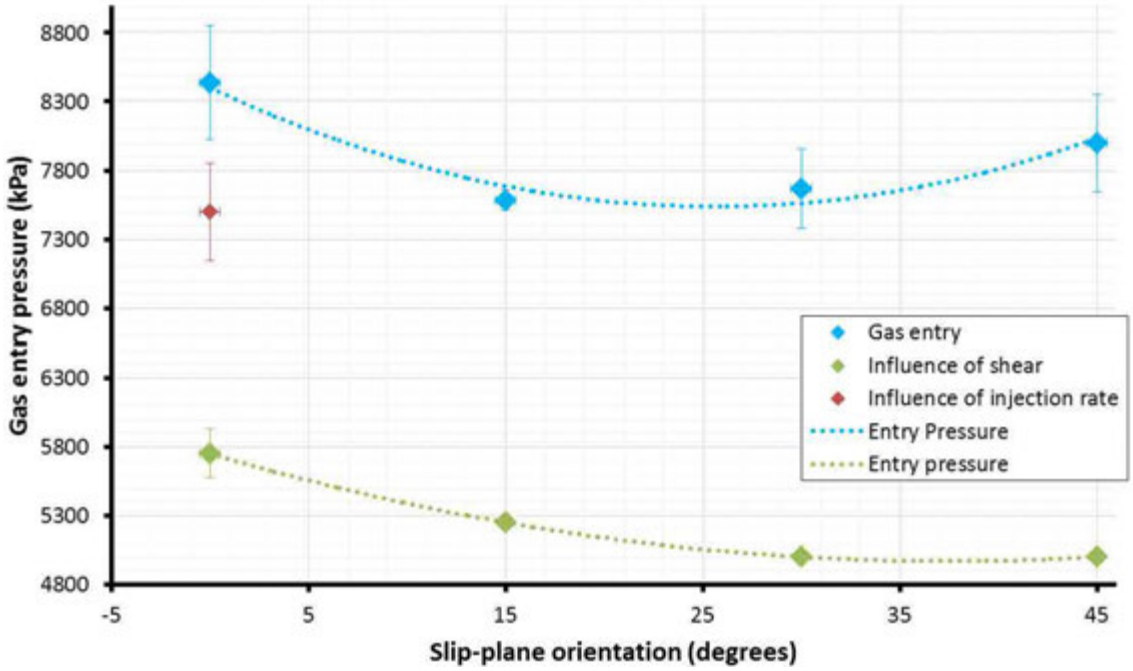

Figure 3-12 – Gas injection pressure variation with discontinuity orientation and the influence of shear and injection rate.

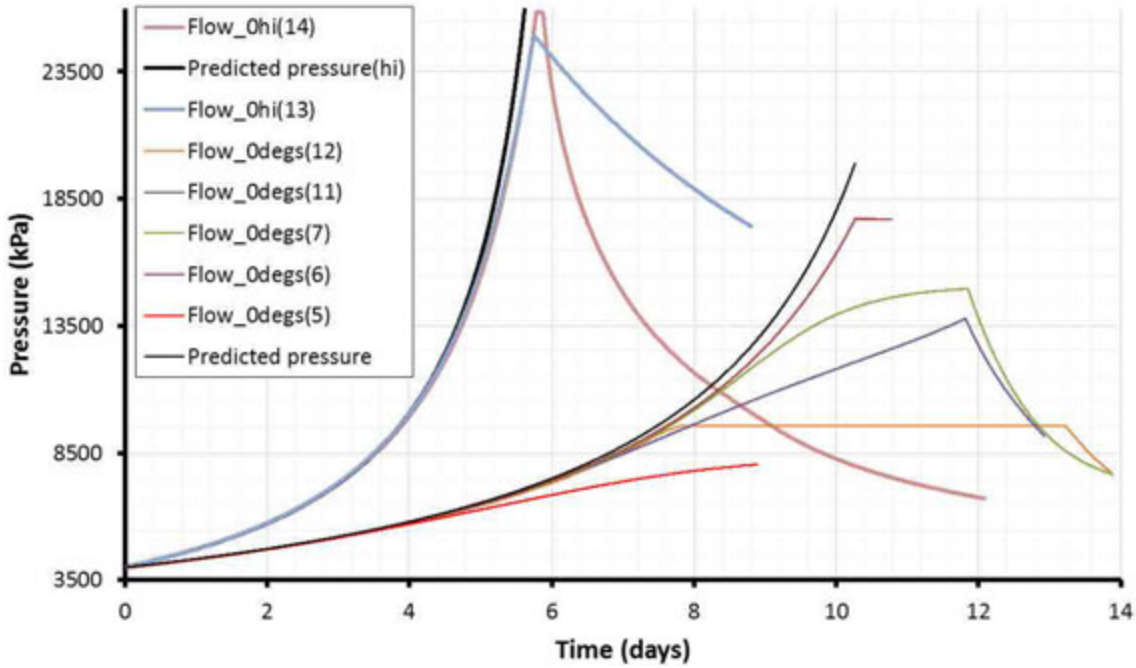

Figure 3-13 – The influence of gas pressurisation rate.

3.2.5 The response of the kaolinite gouge was rate dependent, with a change in entry pressure and peak pressure response.

Figure 3-12 and Figure 3-13 show that the test results were rate dependent. Two tests were conducted with an increased gas injection rate and both tests showed similar general results. An increased gas injection rate significantly altered the gas response of the gouge (Figure 3-13); with significantly higher gas pressure achieved in excess of 24 MPa. Neither test showed signs of reaching peak pressure behaviour.

Both tests had similar gas entry pressure when determined from STP flow, which was marginally lower than the gas entry pressure for all other tests conducted (Figure 3-12). This suggested that the rate of pressurisation had only a small effect on gas entry, but once gas was mobile within the kaolinite gouge it had a significant influence.

3.3 GENERAL OBSERVATIONS

3.3.1 The results showed that the flow of fluids through clay filled fractures was non-uniform and occurred via localised preferential pathways.

Three tests were conducted and recorded using time-lapse photography to observe the escape of gas from the slip-plane into the bath of the apparatus.

All three of these experiments showed that a small, isolated stream of bubbles escaped from a single location. In all tests a single stream of bubble was created, i.e. a single pathway and a second pathway either had not formed or did not reach the edge of the slip-plane. However, one test showed two exit points from the gouge and evidence of pathway evolution once gas was able to escape. In all tests the frequency of escaping bubbles increased, as did their size.

Fracture width data were inconsistent in recording dilation events at the onset of gas flow. However, some tests clearly showed dilation. This observation combined with the isolated single bubble stream show that gas propagated by means of a dilatant process.

Figure 3-14 – Photo showing the escape of gas into from the slip-plane.

3.3.2 The pressure recorded within the slip-plane showed a negligible fracture pressure and did not vary much in all tests.

In all tests, the two pressure ports located within the slip-plane registered pressure less than 50 kPa, effectively close to zero (see Figure 3-15). Little variation was seen, although some changes

occurred during loading-unloading experiments as a result of consolidation. However, no evidence of elevated gas pressures were seen during any experiment. This strengthens the observation of localised dilatant pathways as opposed to a distributed radial migration of gas.

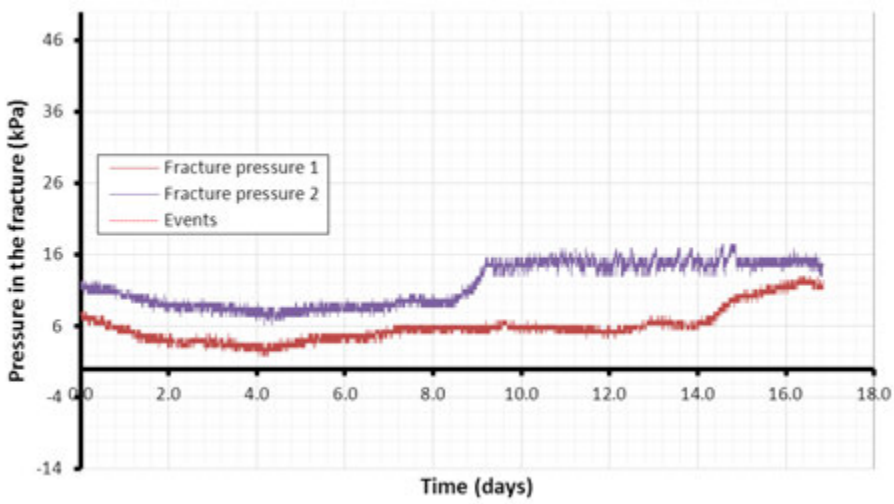

Figure 3-15 – Example of pressure recorded on the slip-plane. A low pressure of less than 20 kPa is observed. Little variation is seen, with no correlation with other data identified. Compare this data with the gas injection pressure seen in Figure 3-14.

4 Conclusions

This report describes an experimental study of 48 separate experiments with the primary aim to verify critical stress theory. Two main types of experiment were conducted: 1). Loading-unloading tests, where fracture flow was monitored at constant injection pressure as normal load was increased in steps to a given level and then reduced back to the starting stress state; 2). Gas breakthrough experiments, where gas injection pressure was increased in a pressure ramp at constant vertical load. These were conducted with and without active shear. It was found that critical stress theory is valid in predicting the preferential flow of gas in relation to the orientation of the fracture plane with respect to the maximum horizontal stress direction. However, loading unloading experiments showed that understanding the stress history of the rocks is of paramount importance and a mere knowledge of the current stress state is insufficient in accurately predicting the nature of fluid flow.

A total of 17 loading-unloading experiments were conducted, all on a 30° slip-plane. The main conclusions of this part of the study were; a). During a loading (vertical stress) and unloading cycle considerable hysteresis in flow was observed signifying the importance of stress history on fracture flow; b). For the case of gas injection the change in flow is chaotic at low normal loads, whereas for water injection the flow reduces smoothly with increased normal load; c). Hysteresis in horizontal stress observed during unloading demonstrates the importance of the ratio between horizontal stress and vertical stress and its control on flow; d). Differences have been observed between injection fluids (water and helium), especially the hysteresis observed in flow. For water injection flow is only partially recovered during unloading, whereas for gas enhanced flow is seen at low normal loads.

A total of 26 gas breakthrough experiments were conducted on 0°, 15°, 30°, and 45° discontinuities; both with and without active shear. All tests were conducted in an identical manner. The main conclusions of this part of the study were; a). During gas breakthrough experiments episodic flow/fault valve behaviour was seen with a decrease in subsequent peak pressures and the form of the pressure response was different during subsequent breakthrough events; b). Repeat gas injection testing had shown a consistent gas entry pressure but

considerably different, non-repeatable, gas peak pressures; c). Differences in gas entry pressure were seen dependent on the orientation of the fracture; d). Shear can be seen to reduce the gas entry pressure, suggesting that shearing in kaolinite has the opposite effect of self-sealing to gas.

Other general observations of gas flow along fractures included; a). The flow of fluids through clay filled fractures is non-uniform and occurs via localised preferential pathways; b). The pressure recorded within the slip-plane showed a negligible fracture pressure and did not vary much in all tests.

References

British Geological Survey holds most of the references listed below, and copies may be obtained via the library service subject to copyright legislation (contact libuser@bgs.ac.uk for details). The library catalogue is available at: http://geolib.bgs.ac.uk.

Barton, C. A., Zoback, M. D., and Moos, D. (1995) Fluid flow along potentially active faults in crystalline rock. *Geology*, **23**, no. 8, pp. 683-686.

Bossart, P., Meier, P. M., Moeri, A., Trick, T., and Mayor, J.-C. (2002) Geological and hydraulic characterisation of the excavation disturbed zone in the Opalinus Clay of the Mont Terri Rock Laboratory. *Engineering Geology*, **66**, no. 1-2, p. 19-38.

Brudy, M., Zoback, M. D., Fuchs, K., Rummel, F., and Baumgärtner, J. (1997) Estimation of the complete stress tensor to 8 km depth in the KTB scientific drill holes: Implications for crustal strength. *Journal of Geophysical Research-Solid Earth*, **102**, no. B8, p. 18453-18475.

Cuss, R.J., Sathar, S., and Harrington, J.F. (2013) Validation of critical stress theory applied to repository concepts. *British Geological Survey Commissioned Report*, **CR/13/001**. 1059pp.

Cuss, R.J., Milodowski, A., and Harrington, J.F. (2011) Fracture transmissivity as a function of normal and shear stress: first results in Opalinus clay. *Physics and Chemistry of the Earth*. **36**, pp.1960-1971.

Cuss, R.J., Sathar, S., and Harrington, J.F. (2012) Fracture transmissivity test in Opalinus Clay. *British Geological Survey Commissioned Report*, **CR/12/132**. 63pp.

Finkbeiner, T., Barton, C. A., and Zoback, M. D. (1997) Relationships Among In-Situ Stress, Fractures and Faults, and Fluid Flow, Monterey, Formation, Santa Maria Basin, California. *AAPG Bulletin*, **81**, p. 1975-1999.

Heffer, K., and Lean, J. (1993) Earth stress orientation - a control on, and guide to, flooding directionality in a majority of reservoirs, Tulsa, PennWell Books, *Reservoir Characterization III*, 799-822 p.:

Jaeger, J. C., Cook, N. G. W., and Zimmerman, R. W. (2007) *Fundamentals of rock mechanics*, Wiley-Blackwell.

Laubach, S. E., Olson, J. E., and Gale, J. F. W. (2004) Are open fractures necessarily aligned with maximum horizontal stress? *Earth and Planetary Science Letters*, **222**, no. 1, p. 191-195.

Reeves, H. (2002) *The effect of stress and fractures on fluid flow in crystalline rocks, Cumbria*, PhD Thesis, University of Durham, 239 p.

Rogers, S. F. (2003) Critical stress-related permeability in fractured rocks. *Fracture and in-Situ Stress Characterization of Hydrocarbon Reservoirs*, **209**, p. 7-16.

Rogers, S. F., and Evans, C. J. (2002) Stress-dependent Flow in Fractured Rocks at Sellafield, United Kingdom. *AAPG Special Volumes, v. AAPG Methods in Exploration No. **13**: Geological Applications of Well Logs*, p. 241-250.

Rutqvist, J., Börgesson, L., Chijimatsu, M., Hernelind, J., Jing, L., Kobayashi, A., and Nguyen, S. (2009) Modeling of damage, permeability changes and pressure responses during excavation of the TSX tunnel in granitic rock at URL, Canada. *Environmental Geology*, **57**, no. 6, p. 1263-1274.

Sathar, S., Reeves, H.J., Cuss, R.J., and Harrington, H.J. (2012) Critical stress theory applied to repository concepts; the importance of stress tensor and stress history in fracture flow. *Mineralogical Magazine*.

Zoback, M. D., Moos, D., Mastin, L., and Anderson, R. N. (1985) Well bore breakouts and in situ stress. *Journal of Geophysical Research-Solid Earth*, **90**(B7), p. 5523-5530.

FORGE

Fate Of Repository Gases

European Commission FP7

Final Report of FORGE WP4.1.2: Verification of critical stress theory applied to repository concepts

FORGE Report D4.17 pt 3

Keywords.

fracture, transmissivity, permeability, kaolinte, critical stress theory.*Bibliographical reference*

CUSS, R.J., SATHAR, S., and HARRINGTON, J.F. 2013. Final Report of FORGE WP4.1.2: Verification of critical stress theory applied to repository concepts

FORGE Report D4.17 pt 3**.** 105pp.

Euratom 7th Framework Programme Project: FORGE

EURATOM

Fate of repository gases (FORGE)

The multiple barrier concept is the cornerstone of all proposed schemes for underground disposal of radioactive wastes. The concept invokes a series of barriers, both engineered and natural, between the waste and the surface. Achieving this concept is the primary objective of all disposal programmes, from site appraisal and characterisation to repository design and construction. However, the performance of the repository as a whole (waste, buffer, engineering disturbed zone, host rock), and in particular its gas transport properties, are still poorly understood. Issues still to be adequately examined that relate to understanding basic processes include: dilational versus visco-capillary flow mechanisms; long-term integrity of seals, in particular gas flow along contacts; role of the EDZ as a conduit for preferential flow; laboratory to field up-scaling. Understanding gas generation and migration is thus vital in the quantitative assessment of repositories and is the focus of the research in this integrated, multi-disciplinary project. The FORGE project is a pan-European project with links to international radioactive waste management organisations, regulators and academia, specifically designed to tackle the key research issues associated with the generation and movement of repository gasses. Of particular importance are the long-term performance of bentonite buffers, plastic clays, indurated mudrocks and crystalline formations. Further experimental data are required to reduce uncertainty relating to the quantitative treatment of gas in performance assessment. FORGE will address these issues through a series of laboratory and field-scale experiments, including the development of new methods for up-scaling allowing the optimisation of concepts through detailed scenario analysis. The FORGE partners are committed to training and CPD through a broad portfolio of training opportunities and initiatives which form a significant part of the project.

Further details on the FORGE project and its outcomes can be accessed at www.FORGEproject.org.

Contact details:

R.J. Cuss

British Geological Survey
Keyworth
Nottingham
NG12 5GG
UK

Tél.: +441159363100
E-mail: rjcu@bgs.ac.uk

British Geological Survey
NATURAL ENVIRONMENT RESEARCH COUNCIL

Final Report of FORGE WP4.1.2: Verification of critical stress theory applied to repository concepts

Minerals and Waste Programme

Commissioned Report CR/13/001

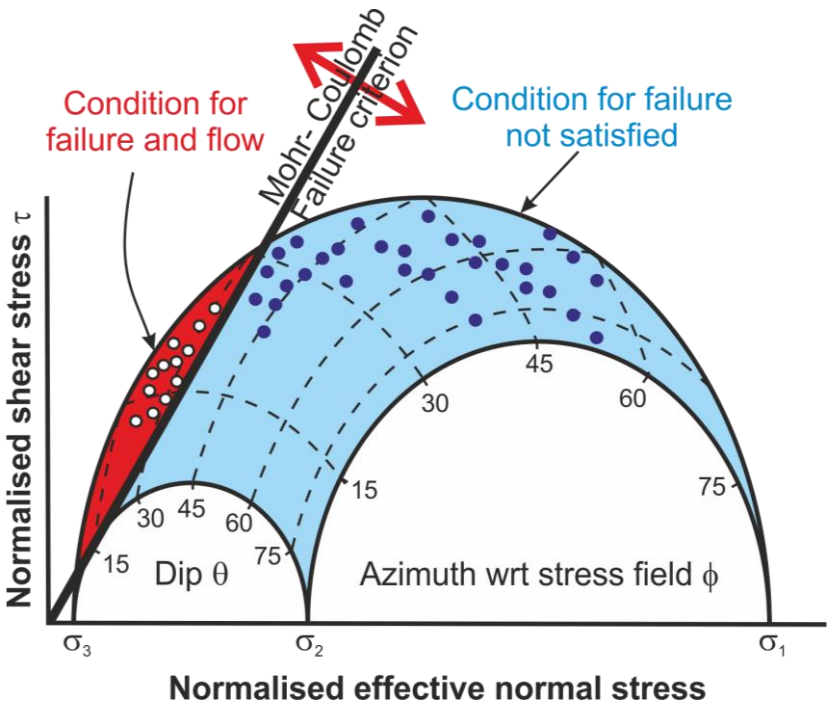

BRITISH GEOLOGICAL SURVEY

MINERALS AND WASTE PROGRAMME

COMMISSIONED REPORT CR/13/001

Final Report of FORGE WP4.1.2: Verification of critical stress theory applied to repository concepts

R.J. Cuss, S. Sathar, and J.F. Harrington

Keywords

fracture, transmissivity, permeability, kaolinte, critical stress theory.

Front cover

The three-dimensional Mohr diagram displaying the horizontal stress and normal stress on faults and fracture surface with respect to the in situ stress field.

Bibliographical reference

CUSS, R.J., SATHAR, S., AND Harrington, J.F. 2013. Final Report of FORGE WP4.1.2: Verification of critical stress theory applied to repository concepts. *British Geological Survey Commissioned Report*, CR/13/001. 105pp.

Copyright in materials derived from the British Geological Survey's work is owned by the Natural Environment Research Council (NERC) and/or the authority that commissioned the work. You may not copy or adapt this publication without first obtaining permission. Contact the BGS Intellectual Property Rights Section, British Geological Survey, Keyworth, e-mail ipr@bgs.ac.uk. You may quote extracts of a reasonable length without prior permission, provided a full acknowledgement is given of the source of the extract.

© NERC 2013. All rights reserved

Keyworth, Nottingham British Geological Survey 2013

BRITISH GEOLOGICAL SURVEY

The full range of our publications is available from BGS shops at Nottingham, Edinburgh, London and Cardiff (Welsh publications only) see contact details below or shop online at www.geologyshop.com

The London Information Office also maintains a reference collection of BGS publications, including maps, for consultation.

We publish an annual catalogue of our maps and other publications; this catalogue is available online or from any of the BGS shops.

The British Geological Survey carries out the geological survey of Great Britain and Northern Ireland (the latter as an agency service for the government of Northern Ireland), and of the surrounding continental shelf, as well as basic research projects. It also undertakes programmes of technical aid in geology in developing countries.

The British Geological Survey is a component body of the Natural Environment Research Council.

British Geological Survey offices

BGS Central Enquiries Desk

Tel 0115 936 3143 Fax 0115 936 3276

email enquires@bgs.ac.uk

Kingsley Dunham Centre, Keyworth, Nottingham NG12 5GG

Tel 0115 936 3241 Fax 0115 936 3488
email sales@bgs.ac.uk

Murchison House, West Mains Road, Edinburgh EH9 3LA

Tel 0131 667 1000 Fax 0131 668 2683
email scotsales@bgs.ac.uk

London Information Office at the Natural History Museum (Earth Galleries), Exhibition Road, South Kensington, London SW7 2DE

Tel 020 7589 4090 Fax 020 7584 8270
Tel 020 7942 5344/45 email bgslondon@bgs.ac.uk

Columbus House, Greenmeadow Springs, Tongwynlais, Cardiff CF15 7NE

Tel 029 2052 1962 Fax 029 2052 1963

Forde House, Park Five Business Centre, Harrier Way, Sowton EX2 7HU

Tel 01392 445271 Fax 01392 445371

Maclean Building, Crowmarsh Gifford, Wallingford OX10 8BB

Tel 01491 838800 Fax 01491 692345

Geological Survey of Northern Ireland, Colby House, Stranmillis Court, Belfast BT9 5BF

Tel 028 9038 8462 Fax 028 9038 8461

www.bgs.ac.uk/gsni/

Parent Body

Natural Environment Research Council, Polaris House, North Star Avenue, Swindon SN2 1EU

Tel 01793 411500 Fax 01793 411501
www.nerc.ac.uk

Website www.bgs.ac.uk
Shop online at www.geologyshop.com

Foreword

This report is the product of a study by the British Geological Survey (BGS) undertaken on behalf of the Nuclear Decommissioning Authority – Radioactive Waste Management Directorate (NDA-RWMD) and the European Union 7th Framework Euratom Programme under the auspices of the Fate of repository Gases (FORGE) project, to examine the validation of critical stress theory applied to repository concept and the influence of fracture/fault angle on gas flow properties.

Acknowledgements

The study was undertaken by staff of the Minerals and Waste Programme of the BGS using the experimental facilities of the Transport Properties Research Laboratory (TPRL). Funding for the study was provided by the Nuclear Decommissioning Authority – Radioactive Waste Management Directorate (NDA-RWMD), the European Union (FORGE Project) and the British Geological Survey through its well-founded laboratory programme. The authors would like to thank the skilled staff of the Research & Development Workshops at the BGS, in particular Humphrey Wallis, for their design and construction of the experimental apparatus.

Contents

Foreword ..... **i**

Acknowledgements ..... **i**

Contents ..... **i**

Executive summary ..... **vi**

1 Introduction **1**

1.1 Common host rock types chosen for subsurface radioactive waste disposal 1

1.2 State of stress and distribution of fractures around the excavation tunnels in the EDZ 3

1.3 Critical Stress Theory and related fluid flow 5

2 Experimental apparatus and methodology **9**

2.1 Angled Shear Rig (ASR) 9

2.2 Sample preparation and experiment assembly 12

2.3 Experimental procedure 12

2.4 Calculation of fracture transmissivity 15

2.5 Note on stress convention 16

3 Observations and results **17**

3.1 Fracture transmissivity evolution during variations in vertical load 17

3.2 Fracture transmissivity evolution during shear 31

3.3 Investigation of fault-valve behaviour during gas flow 35

4 The effect of slip-plane orientations on gas flow through gouge-filled fractures. **40**

4.1 Experimental methodology ... 40
4.2 Gas breakthrough experiments on a slip plane orientation of 0° ... 41
4.3 Gas breakthrough experiments on a slip plane orientation of 15° ... 48
4.4 Gas breakthrough experiments on a slip plane orientation of 30° ... 53
4.5 Gas breakthrough experiments on a slip plane orientation of 45° ... 59
4.6 Results and discussion for tests conducted at different orientations ... 64
4.7 The effect of shear displacement on gas entry and subsequent gas flow ... 68
4.8 Comparing results for tests conducted on a slip plane orientation of 0° with and without active shear ... 71
4.9 The effect of rate of pressurisation on gas entry and subsequent gas flow ... 79
4.10 Results for tests conducted at increased injection rate ... 81
4.11 Is gas entry at different angles simply related to normal load? ... 84

5 Time-lapse study of fracture flow ... 85
5.2 Discussion on time-lapse observations ... 87

6 Water content of the gouge material ... 88

7 Conclusions ... 89
7.1 Loading-unloading tests ... 89
7.2 Gas breakthrough experiments ... 91
7.3 General observations ... 92

8 References: ... 93

9 Appendix I ... 95

FIGURES

Figure 1 - Stress trajectories around a non-hydrostatically loaded circular opening, such as a tunnel, demonstrating the prevailing stress inhomogeneity adjacent to the tunnel wall (from Cuss, 1999) ... 4

Figure 2 - Complex network of fractures in the EDZ. The density of fractures decreases away from the tunnel opening (from Bossart *et al.*, 2002; Bossart *et al.*, 2004) ... 4

Figure 3 - Distribution of permeability in a tunnel at Mont Terri URL. Zones within 10 – 20 cm of the tunnel exhibited high permeability (1×10^{-14} m^2) (from Bossart *et al.*, 2004). ... 5

Figure 4 - The three-dimensional Mohr diagram displaying the horizontal stress and normal stress on faults and fracture surface with respect to the *in situ* stress field ... 6

Figure 5 - Detailed *in situ* stress data from the Sellafield area illustrating that none of the fractures are critically stressed at the present time. ... 7

Figure 6 - Common friction test arrangements. ... 9

Figure 7 - Angled shear rig (ASR). ... 10

Figure 8 - Components of the top block. ... 11

Figure 9 - Fluid injection circuit displaying the servo-controlled ISCO™ injection pump and the gas-water interface vessel used to inject helium into the idealised slip plane. ... 11

Figure 10 - Plan-view of the slip plane with fluid injection port in the centre and two orthogonally located pore pressure sensor ports. 15
Figure 11 - Results from test ASR_Tau01_30wLU 19
Figure 12 - Results from test ASR_Tau05_30wLU 21
Figure 13 –Detail of effect of temperature fluctuations during the unloading stages in experiment ASR_Tau05_30wLU 22
Figure 14 – Comparison of results from experiments ASR_Tau01_30wLU and ASR_Tau05_30wLU 23
Figure 15 – Results from experiment ASR_Tau07_30gLU 26
Figure 16 – Results from experiment ASR_Tau08_30gLU 27
Figure 17 – Results from experiment ASR_Tau14_30gLU 28
Figure 18 – Comparison of results from tests ASR_Tau07_30gLU, ASR_Tau08_30gLU, and ASR_Tau14_30gLU 29
Figure 19 – Comparison of the hydraulic and gas injection experiments during loading and unloading 31
Figure 20 - Results from stages 1 to 3 of test ASR_Tau02_30wLUS 32
Figure 21 - Results from stages 4 to 9 of the ASR_Tau02_30wLUS experiment 33
Figure 22 - Results from stages 8 and 9 of the ASR_Tau02_30wLUS experiment 33
Figure 23 – Summary of observations for test ASR_Tau02_30wLUS 34
Figure 24 - The effect of shearing on hydraulic flow, resulting in a 40% reduction in flow. 35
Figure 25 - Results from the fault-valve behaviour test (ASR_Tau06_30gGI) 36
Figure 26 – Stage 1 – 2 of the fault-valve behaviour test (ASR_Tau06_30gGI) 36
Figure 27 – Stage 3 of the fault-valve behaviour test (ASR_Tau06_30gGI) 38
Figure 28 - Stage 4 – 5 of the fault-valve behaviour test (ASR_Tau06_30gGI) 38
Figure 29 – Stage 6 – 7 of the fault-valve behaviour test (ASR_Tau06_30gGI) 39
Figure 30 – Evolution of pore pressure within the slip plane during the fault-valve behaviour test (ASR_Tau06_30gGI) 39
Figure 31 – Results for gas injection test 5 / ASR_Tau15_00gGI 42
Figure 32 – Results for gas injection test 6 / ASR_Tau16_00gGI 43
Figure 33 – Results for gas injection test 7 / ASR_Tau17_00gGI 44
Figure 34 – Results for gas injection test 11 / ASR_Tau21_00gGI 45
Figure 35 – Results for gas injection test 12 / ASR_Tau22_00gGI 46
Figure 36 – Results for five gas injection tests conducted on a fracture oriented 0° to the slip plane 47
Figure 37 – Gas entry pressure predicted from the average flow at STP for five gas injection tests conducted on a fracture oriented 0° to the slip plane 48
Figure 38 – Results for gas injection test 8 / ASR_Tau18_15gGI 49
Figure 39 – Results for gas injection test 9 / ASR_Tau19_15gGI 50
Figure 40 – Results for gas injection test 10 / ASR_Tau20_15gGI 51

Figure 41 –Results for three gas injection tests conducted on a fracture oriented 15° to the slip plane 52
Figure 42 –Gas entry pressure predicted from the average flow at STP for three gas injection tests conducted on a fracture oriented 15° to the slip plane 53
Figure 43 – Results for gas injection test 1 / ASR_Tau09_30gGI 54
Figure 44 – Results for gas injection test 2 / ASR_Tau11_30gGI 55
Figure 45 – Results for gas injection test 3 / ASR_Tau12_30gGI 56
Figure 46 – Results for gas injection test 4 / ASR_Tau13_30gGI 57
Figure 47 –Results for four gas injection tests conducted on a fracture oriented 30° to the slip plane 58
Figure 48 – Gas entry pressure predicted from the average flow at STP for four gas injection tests conducted on a fracture oriented 30° to the slip plane 58
Figure 49 – Results for gas injection test 15 / ASR_Tau25_45gGI 60
Figure 50 – Results for gas injection test 16 / ASR_Tau26_45gGI 61
Figure 51 – Results for gas injection test 17 / ASR_Tau27_45gGI 62
Figure 52 –Results for three gas injection tests conducted on a fracture oriented 45° to the slip plane 63
Figure 53 – Gas entry pressure predicted from the average flow at STP for three gas injection tests conducted on a fracture oriented 45° to the slip plane 63
Figure 54 – Relationship of gas entry pressure determined from STP gas flow into the fracture for all tests 65
Figure 55 – Relationship of gas entry pressure determined from the ideal gas law for all tests... 66
Figure 56 – Comparison of results from the two methods used to determine gas entry pressure 67
Figure 57 – Results for gas injection test 18 / ASR_Tau28_00gGIS 69
Figure 58 – Results for gas injection test 19 / ASR_Tau29_00gGIS 70
Figure 59 – Comparing results for gas injection tests conducted on a fracture oriented 0° to the slip plane with and without active shear 71
Figure 60 – Comparing results for gas entry pressure predicted from the average flow at STP for gas injection tests conducted on a fracture oriented 0° to the slip plane with and without active shear 72
Figure 61 – Results for gas injection test 20 / ASR_Tau30_30gGIS 73
Figure 62 – Results for gas injection test 21 / ASR_Tau31_45gGIS 75
Figure 63 – Results for gas injection test 22 / ASR_ Tau32_15gGIS 76
Figure 64 –Results for five gas injection tests conducted with active shear 77
Figure 65 – Gas entry pressure for all tests showing the influence of shear 78
Figure 66 – Results for gas injection test 13 / ASR_Tau23_00gGI 80
Figure 67 – Results for gas injection test 14 / ASR_Tau24_00gGI 81
Figure 68 – Results for two gas injection tests conducted at higher gas injection rates, compared with five tests conducted on a fracture oriented 0° to the slip plane..... 82

Figure 69 – Gas entry pressure predicted from the average flow at STP for two tests conducted at higher gas injection rate, compared with five gas injection tests conducted on a fracture oriented 0° to the slip plane 83

Figure 70 – Gas entry pressure for all tests showing the influence of gas injection rate 83

Figure 71 – Comparing gas entry pressure with normal load on the fracture 84

Figure 72 – Time-lapse results for gas injection test 10 / ASR_Tau20_15gGI. 85

Figure 73 – Time-lapse results for gas injection test 11 / ASR_Tau21_00gGI. 86

Figure 74 – Time-lapse results for gas injection test 12 / ASR_Tau22_00g GI 86

Figure 75 – Time-lapse results for gas injection test 13 / ASR_Tau23_00g GI 87

Figure 76 – Time-lapse results for gas injection test 12 / ASR_Tau22_00g GI 87

Figure 77 – Water content of the kaolinite gouge material measured at five locations on the sample surface. 88

TABLES

Table 1 – List of all experiments undertaken as part of the current study. 13

Table 2 - Variation in load cell reading during variation in ISCO syringe pump pressure. 14

Table 3 - The loading and unloading stages in test ASR_Tau01_30wLU. 18

Table 4 - The loading and unloading stages in test ASR_Tau05_30wLU. 20

Table 5 – Loading and unloading stages during gas injection loading/unloading experiments ASR_Tau07_30gLU, ASR_Tau08_30gLU, and ASR_Tau14_30gLU. 25

Table 6 – Experimental stages of test ASR_Tau02_30wLUS. 31

Table 7 – The normal stress acting on the experimental slip plane at different orientations. The normal stress decreases as the slip plane orientation increases. 40

Table 8 – List of gas-injection experiments conducted. 41

Table 9 – Results for gas entry pressure for the five gas injection experiments conducted on a fracture oriented 0° to the slip-plane 48

Table 10 – Results for gas entry pressure for three gas injection experiments conducted at an angle of 15° 53

Table 11 – Results for gas entry pressure for four gas injection experiments conducted at an angle of 30° 59

Table 12 – Results for gas entry pressure for three gas injection experiments conducted at an angle of 45° 64

Table 13 – Results for gas entry pressure for all gas injection experiments 67

Table 14 – Results for gas entry pressure for all gas injection experiments conducted at 0º. @ with shear 72

Table 15 – Results for gas entry pressure for all gas injection experiments 77

Table 16 – Results for gas entry pressure for all gas injection experiments 82

Table 17 – Results for gas entry pressure for all gas injection experiments 95

Executive summary

This report describes an experimental study of 48 separate experiments examining the validity of critical stress theory. Two main types of experiment were conducted: 1). Loading-unloading tests, where fracture flow was monitored at constant injection pressure as normal load was increased in steps to a given level and then reduced back to the starting stress state; 2). Gas breakthrough experiments, where gas injection pressure was increased in a pressure ramp at constant vertical load. These were conducted with and without active shear. It was found that critical stress theory is valid in predicting the preferential flow of gas in relation to the orientation of the fracture plane with respect to the maximum horizontal stress direction. However, loading unloading experiments showed that understanding the stress history of the rocks is of paramount importance and a mere knowledge of the current stress state is insufficient in accurately predicting the nature of fluid flow.

A total of 17 loading-unloading experiments were conducted, all on a 30° slip-plane. The main conclusions of this part of the study were; a). During a loading (vertical stress) and unloading cycle considerable hysteresis in flow was observed signifying the importance of stress history on fracture flow; b). For the case of gas injection the change in flow is chaotic at low normal loads, whereas for water injection the flow reduces smoothly with increased normal load; c). Hysteresis in horizontal stress observed during unloading demonstrates the importance of the ratio between horizontal stress and vertical stress and its control on flow; d). Differences have been observed between injection fluids (water and helium), especially the hysteresis observed in flow. For water injection flow is only partially recovered during unloading, whereas for gas enhanced flow is seen at low normal loads.

A total of 26 gas breakthrough experiments were conducted on 0°, 15°, 30°, and 45° discontinuities; both with and without active shear. All tests were conducted in an identical manner. The main conclusions of this part of the study were; a). During gas breakthrough experiments episodic flow/fault valve behaviour was seen with a decrease in subsequent peak pressures and the form of the pressure response was different during subsequent breakthrough events; b). Repeat gas injection testing had shown a consistent gas entry pressure but considerably different, non-repeatable, gas peak pressures; c). Differences in gas entry pressure were seen dependent on the orientation of the fracture; d). Shear can be seen to reduce the gas entry pressure, suggesting that shearing in kaolinite has the opposite effect of self-sealing to gas.

Other general observations of gas flow along fractures included; a). The flow of fluids through clay filled fractures is non-uniform and occurs via localised preferential pathways; b). The pressure recorded within the slip-plane showed a negligible fracture pressure and did not vary much in all tests.

1 Introduction

Deep geological disposal is being widely considered as a viable option for the safe storage of high level radioactive waste. Safe management and disposal of radioactive waste in an isolated sub-surface setting is necessary to minimize the long term effects of radioactive waste on the biosphere. Deep geological disposal is currently the only available pragmatic solution for the storage and safe disposal of radioactive waste in Europe.

According to the current concepts, high level and long lived radioactive waste and spent fuel are intended to be stored/disposed of in a geological disposal facility (GDF) within a stable geological formation (host rock) at depth (typically ~50 – 800 m) beneath the ground surface. Hence, the radioactive waste is securely isolated and contained. At depth the rock mass may be a naturally fractured environment and the excavation of underground repositories is recognized to induce additional fractures (Bossart *et al.*, 2002; Rutqvist *et al.*, 2009). The zone of the host rock in the vicinity of the underground opening whose hydromechanical properties are modified as a consequence of excavation activities are referred to as excavation damaged zones (EDZ)[1]. The interplay of existing fractures and newly formed fractures in the EDZ will result in a complex array of fractures around the GDF. Depending on the in situ stress conditions, preferential pathways may form along faults, joints and the EDZ. Understanding the significance of such fractures and their connectivity in the transmission of repository fluids is of paramount importance in the long term storage of radioactive waste in the repository.

This study aimed to experimentally understand the dependence of different fracture orientations and stress states on the transmissivity of repository fluids through both natural and induced EDZ fractures. Furthermore, this study attempted to experimentally validate the critical stress theory proposed by Barton *et al.* (1995).

1.1 COMMON HOST ROCK TYPES CHOSEN FOR SUBSURFACE RADIOACTIVE WASTE DISPOSAL

The host rock formations considered for radioactive waste disposal can be broadly classified into crystalline rock, rock salt, indurated clay, and plastic clay formations. The rock salt, indurated clay, and plastic clay formations may self-heal and self-seal with time whereas crystalline formations may not do so. However, excavation of repositories in a crystalline formation is relatively stable when compared to those of rock salt, indurated clay, or plastic clay. Different host rocks behave in diverse ways during the various stages of repository development. During the excavation stage construction damage may lead to enhanced flow properties and result in stress redistribution. During the open-drift stage ventilation of the repository may modify the sealing properties of EDZ considerably. During the course of the early closure stage the effect of backfilling, resaturation and heating from waste canisters are likely to modify the properties of host rock and the EDZ. The degree of cooling, support degradation and self-sealing will influence the flow properties of an EDZ in the late closure stage. An extensive comparison of processes and issues associated with different EDZ host rock formations can be found in Tsang *et al.* (2005). A brief summary of different processes and factors affecting the EDZ in different host rock types is presented below.

---

[1] The term EDZ has been used interchangeably in scientific literature to denote either Excavation Disturbed Zone or the Excavation Damaged Zone. The definitions of these zones differ for specific host rock types such as crystalline rock, rock salt, indurated clay, and plastic clay. Detailed discussion about the terminology and characteristics of the Excavation Disturbed Zone or the Excavation Damaged Zone are presented in Tsang *et al.* (2005). In the present study we have adopted the definition of EDZ proposed by Bäckblom *et al.* (2004) where EDZ is defined as "the part of the rock mass closest to the underground opening that has suffered irreversible deformation where shearing of existing fractures as well as propagation or development of new fractures has occurred".

1.1.1 Crystalline rock

In crystalline rocks the type of excavation method used can have a profound influence on the thickness of the EDZ and the resulting change in permeability. Excavation by drill-and-blast can lead to approximately 2 – 3 orders of magnitude increase in permeability with an EDZ thickness of between 10 and 150 cm; whereas the use of a tunnel boring machine will result in only one order of magnitude increase in permeability and the thickness of the damage zone is likely to be of the order of 1 cm. Stress redistribution following the excavation results in different parts of the drift experiencing either tension, compression, or shear. The extent of this stress anisotropy may extend up to 2 – 3 meters beyond the wall of the drift. In the open-drift stage, the EDZ may dehydrate and the air flow through the shafts may lead to oxidizing conditions and potential chemical and biological activities. In the early closure stage, the presence of faults within the EDZ control the swelling pressure imparted by the wetting and swelling of a bentonite buffer and bentonite/sand mixture backfill material. During the late closure stage of a repository, the inability of the fractures in crystalline rocks to self-seal may cause problems in containing radionuclides. However, over a period of thousands of years, clay minerals are expected to migrate into the fractures as a consequence of long-term heating and thermohydrologic effects and are expected to offer a suitable seal. Moreover, parameters such as *in situ* stress, density of fractures, orientation of fractures, rock strength, and the orientation of the drift with respect to the principal stress field needs to be taken into consideration. The Äspö Hard Rock Laboratory (Sweden) and the Underground Research Laboratory at Pinawa, Manitoba (Canada) are examples of research laboratories which have been studied to experimentally assess the viability of radioactive waste disposal in crystalline host rocks.

1.1.2 Rock salt

Dilatancy, healing and creep properties of rock salt help minimise the effect of excavation on the fluid flow properties in the EDZ during the excavation stage. Ventilation and salt dehydration may affect salt creep properties whilst the drift is open. In the early closure stage, the increase in humidity is likely to affect the EDZ properties. The heating from the canisters will induce high temperature gradients which will in turn affect the creep properties of the salt. During the late closure stage self-healing of the fractures and microcracks will occur by means of viscoplastic deformation and recrystallization in the presence of brine which will reduce the permeability of the rock salt. Irrespective of its excellent self-healing and sealing properties, excavation of repositories in rock salt may require the installation of a stiff liner during or immediately after excavation which may be problematic. The Asse Mines (Germany) and the Waste Isolation Pilot Plant (New Mexico, USA) are examples of research laboratories which have been studied to experimentally assess the viability of radioactive waste disposal in rock salt.

1.1.3 Indurated clay

In the case of indurated clays, the stress redistribution that results from excavation may give rise to strongly anisotropic, deviatoric compression and/or tensile stresses; these result in: a) tensile and shear fracturing along bedding planes, and b) vertical extensional or tensile fracturing in rock adjoining side walls. Similar to crystalline rocks, rock property parameters, *in situ* stress state, drift orientation relative to bedding plane direction, moisture content of rocks, and drift shape play a crucial role in controlling the properties of the EDZ. During the open-drift stage, rock creep may result in gallery wall convergence. Dehydration of the host rock due to ventilation may result in rock strengthening and contraction. Potential microbiological processes may also operate under these conditions. In the early closure stage of the repository, humidity increase during resaturation may weaken the rock, enhance creep, and induces closure of fractures and faults formed during excavation. However, the influence of transient and spatially varying temperature and water-saturation on rock properties is crucial in the early closure stage. In the late closure stage self-sealing of fractures may occur via precipitation of infill minerals. The Mont Terri Rock Laboratory (Switzerland) and the Laboratory Souterrain Meuse/Haute

Marne (Bure, France) are examples of research laboratories which have been studied to experimentally assess the viability of radioactive waste disposal in indurated clay rocks.

1.1.4 Plastic clay

During the excavation of drifts in plastic clay formations, stress redistributions may result in contractant and dilatant processes with induced fracturing. During the open-drift stage of the repository, the drift wall moves towards the support offered by the liner. The hydromechanical properties of the clay are likely to be modified by drift ventilation and rock dehydration with ventilation leading to retardation in self-sealing capability of the rock. The effect of oxidation is usually limited to around 1 m into the rock. In the early closure stage, the effect of heating from the canister will result in a varying degree of saturation and thermal expansion/contraction and is likely to modify the rock properties. The creep rate of plastic clays will be boosted under increasing temperature conditions and open fractures are expected to heal. Piezometric studies in natural analogues have indicated that open fractures do not extend beyond a metre of the drift during simulated heating experiments. In the late closure stage, slow healing of fractures may take place during consolidation due to swelling and creep. Ensuing transport of radionuclides is likely to occur via diffusion mechanism. The Hades Underground Research Laboratory (Mol, Belgium) is an example of a research laboratory which has been studied to experimentally assess the viability of radioactive waste disposal in plastic clays.

1.2 STATE OF STRESS AND DISTRIBUTION OF FRACTURES AROUND THE EXCAVATION TUNNELS IN THE EDZ

The removal of rock mass during underground tunnel excavation significantly alters the local stress field (Figure 1). As a result of the redistribution of the *in-situ* stresses, the rock in the vicinity of the EDZ has to accommodate the stress borne earlier by the excavated rock mass. Tunnelling methodologies, such as drill & blasting or use of a tunnel boring machine, tends to damage the host rock which in combination with the inhomogeneous distribution of stress field results in the creation of complex fracture networks around the EDZ (Figure 2). Bossart *et al.* (2004) identified two distinct zones within the EDZ in Opalinus Clay of the Mont Terri Underground Research Laboratory (URL). The inner zone extends a metre from the tunnel wall made up of interconnected fracture network connected to the tunnel. The outer zone extends from the inner zone boundary to approximately 2 m from the tunnel wall and comprises non-connected unloading fractures (Figure 2). The fracture density decreases away from the tunnel wall with the inner zone containing many more fractures than the outer zone.

The hydromechanical and geochemical modification in the EDZ during excavation may lead to one or more orders of magnitude increase in permeability (Tsang *et al.*, 2005). However, the extent of this hydromechanical and geochemical modification will be determined by the nature of the host rock and the associated physicochemical conditions. Studies by Bossart *et al.* (2004) on the permeability distribution around a test tunnel at the Mont Terri URL on Opalinus Clay have shown zones of high permeability located within the first 10 – 20 cm within the inner zone of the EDZ with permeability values in the range of 10^{-11} to 10^{-13} m^2 (Figure 3). However, between 40 and 100 cm from the tunnel permeability values were up to two orders of magnitude lower than in the previous case with typical permeability values in the range of 10^{-15} to 10^{-16} m^2 (Figure 3) .

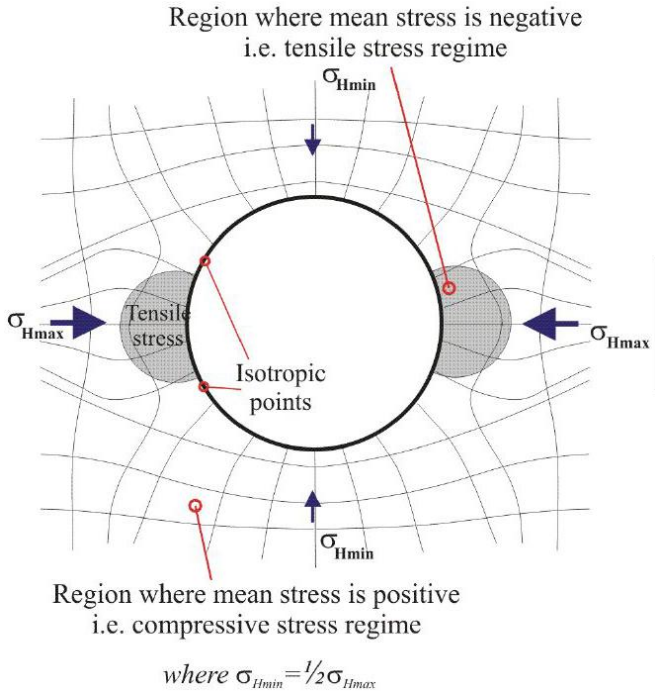

Figure 1 - Stress trajectories around a non-hydrostatically loaded circular opening, such as a tunnel, demonstrating the prevailing stress inhomogeneity adjacent to the tunnel wall (from Cuss, 1999).

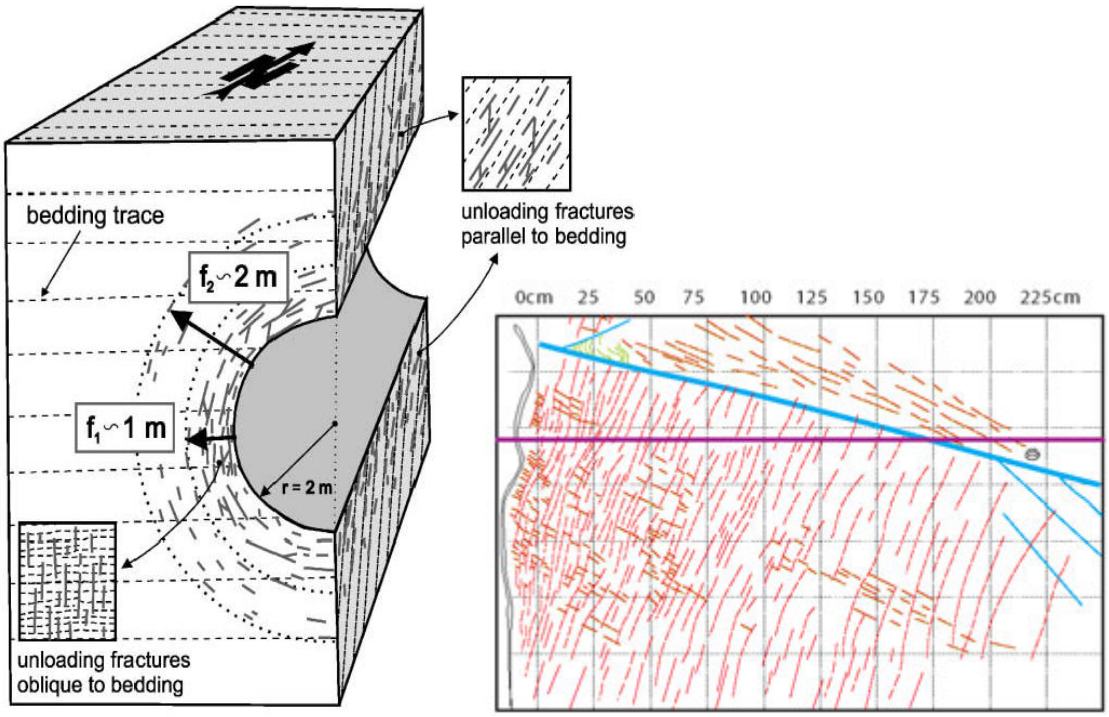

Figure 2 - Complex network of fractures in the EDZ. The density of fractures decreases away from the tunnel opening (from Bossart *et al.*, 2002; Bossart *et al.*, 2004).

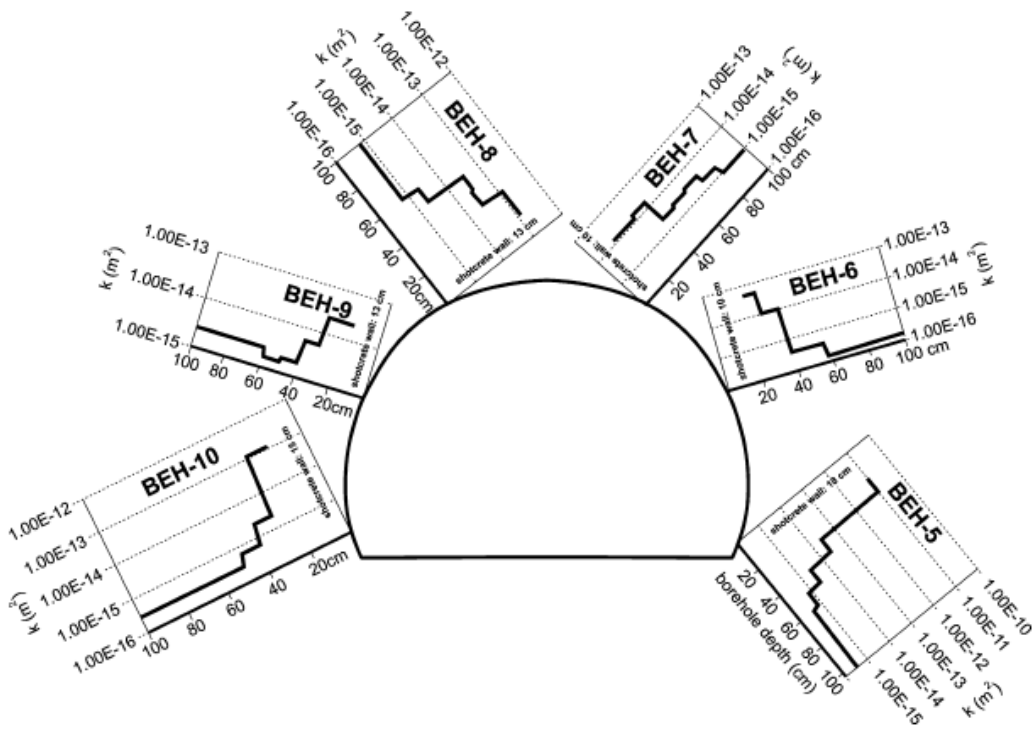

Figure 3 - Distribution of permeability in a tunnel at Mont Terri URL. Zones within 10 – 20 cm of the tunnel exhibited high permeability (1×10^{-14} m^2) (from Bossart *et al.*, 2004).

1.3 CRITICAL STRESS THEORY AND RELATED FLUID FLOW

The formation of fractures during tunnel excavation provides preferential pathways for fluids within the EDZ. The flow of repository fluids (water and/or gas) away from the repository along the fracture network will be determined by the fracture density, aperture of the fracture, extent of the fracturing, connectivity of the fractures, permeability through the fracture planes, and the orientation of the fractures (Barton *et al.*, 1997; Barton *et al.*, 1995; Finkbeiner *et al.*, 1997; Rogers, 2003). Previous studies have shown that only some fractures within a fractured system act as conduits for fluid movement whereas other fractures do not contribute towards fluid movement. Critical stress theory has been proposed to explain these differences in fracture conductivities.

It has been proposed that fractures and faults that are oriented parallel to σ_{Hmax} have the lowest normal stresses acting across them and therefore will undergo the least amount of closure and hence will be the most permeable (Heffer & Lean, 1993). Fractures and faults experiencing the least amount of stress will offer minimum resistance to flow and therefore will have relatively high permeability. Studies by Laubach *et al.* (2004) on a number of sedimentary basins in the western United States using core permeability datasets, stress measurements, and fluid flow data have shown that at a depth greater than three kilometres the open fractures do not parallel the σ_{Hmax} direction. Hence, *in situ* stress direction cannot be used as an indicator for predicting maximum permeability directions.

Barton *et al.* (1995) suggested that fractures whose state of stress is close to the failure criterion are likely to be more conductive because of the localised failure as a consequence of large shear component acting along the fracture. Such fractures were termed to be critically stressed. To apply the critical stress theory for fracture flow, the *in situ* stress field acting along all the faults and fractures are resolved into shear and normal stress components. When the magnitude and direction of the stress field has been constrained, the horizontal stress (τ) and normal stress (σ_n) acting on a fracture surface can be given by (Jaeger *et al.*, 2007):

$$\tau = \beta_{11}\,\beta_{21}\,\sigma_1 + \beta_{12}\,\beta_{22}\,\sigma_2 + \beta_{13}\,\beta_{23}\,\sigma_3 \text{ and}$$

$$\sigma_n = \beta_{11}^2\,\sigma_1 + \beta_{12}^2\,\sigma_2 + \beta_{13}^2\,\sigma_3$$

Where; β_{ij} = directional cosines between the fracture surface and the stress tensor; σ_1, σ_2, and σ_3 = magnitude of the maximum, intermediate, and minimum principal stresses respectively.

A three dimensional Mohr diagram (Figure 4) is commonly used to display the stress and orientation data. Since the magnitudes of the stresses increase with depth in a borehole all the data are normalised with respect to the vertical stress component to facilitate plotting of all data points within the same Mohr circle space. The Mohr-Coulomb failure criterion can be used to recognize whether a fracture or fault surface is expected to shear under the prevailing stress conditions (Figure 4). Assuming conditions of effective stress, the Coulomb failure criterion in given as:

$$\tau = \mu\,(\sigma_n - P_p)$$

Where; μ = coefficient of friction; P_p = pore pressure.

Later studies by Byerlee (1978) proposed that up to normal stresses of 200 MPa, the horizontal stress required to cause frictional sliding can be given by the equation:

$$\tau = 0.85\,\sigma_n$$

and for normal stresses above 200 MPa, the horizontal stresses required for sliding can be given by the equation:

$$\tau = 50 + 0.6\,\sigma_n$$

The intrinsic shear strength or cohesion of rocks is assumed to be negligible under the crustal stress conditions and hence neglected. Critical stress theory proposes that fractures with their horizontal stress and normal stress data that fall above the Mohr-Coulomb failure criterion are in a critically stressed state and therefore are likely to exhibit enhanced permeability.

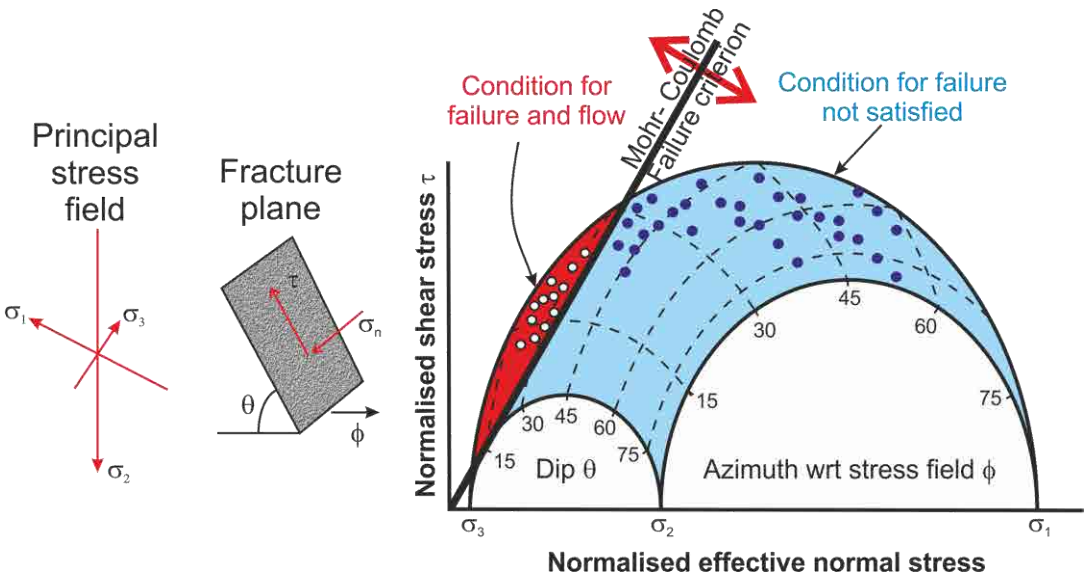

Figure 4 - The three-dimensional Mohr diagram displaying the horizontal stress and normal stress on faults and fracture surface with respect to the *in situ* stress field. The points lying above the Mohr-Coulomb failure criterion are critically stressed and are likely to be conductive. Conversely, the points lying below the Mohr-Coulomb failure criterion have not reached the condition for failure and hence will be impermeable to fluid flow (from Rogers, 2003).

Based on field observations in the Sellafield area, Cumbria, UK, Rogers (2003) suggested that maximum flow is unlikely to occur along the σ_{Hmax} direction and is more likely to occur along a direction ± 30 degree to the σ_{Hmax} direction (Figure 4). However, detailed studies of the *in situ*

stress distribution at Sellafield confirmed that a majority of fractures lie below the Mohr-Coulomb failure criterion and are not critically stressed (Reeves, 2002; Figure 5). Experimental understanding of critical stress behaviour and variations in fracture orientation in assisting fluid (water and gas) flow through discontinuities become important in the light of these uncertainties in field observations.

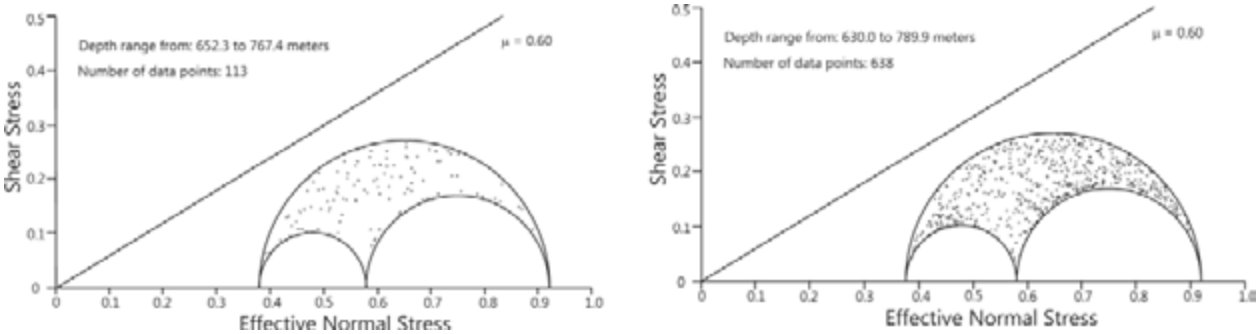

Figure 5 - Detailed *in situ* stress data from the Sellafield area illustrating that none of the fractures are critically stressed at the present time. Flowing fractures are plotted on the left and the non-flowing fractures are plotted on the right.

Analysis of fracture permeability and *in situ* stress by Ito & Zoback (2000) for fractures in the depth range of 3 to 7 km in the KTB scientific drillhole have shown that the permeable faults and fracture were aligned close to the Mohr-Coulomb failure envelope for a coefficient of friction of 0.6. They concluded that critically stressed fractures in the crust are the most conductive to fluid flow and non-critically stressed fractures are least conductive.

Berge *et al.* (1999) modelled the geomechanical behaviour of the Topopah Springs tuff, Yucca Mountain, Nevada by applying the concept of critical stress theory. The zones of enhanced permeability were determined following the work of Barton *et al.* (1995; 1997). Their Thermo-hydro-mechanical (THM) modelling showed a factor of two increase in permeability for vertical fractures and up to a factor of four increase in permeability for fractures with slip movement.

Analysis of fracture and fluid flow datasets from the geothermal reservoir at Dixie Valley by Barton *et al.* (1998) indicated that the majority of fractures with high permeability were critically stressed for frictional failure. However, many non-flowing but critically stressed fractures were also encountered in the same area. They concluded that in the Dixie Valley high fault zone high permeability was observed only when the individual fractures along with the Stillwater fault zone within the area were optimally oriented and critically stressed for frictional failure.

A review of the role of hydro-mechanical (HM) coupling in fractured rock engineering by Rutqvist & Stephansson (2003) concluded that stress-dependant permeability plays a major role in rocks containing flat microcracks and macrofractures. They suggested that the fracture permeability under varying stress conditions depends on hydraulic properties such as fracture permeability and connectivity of the fracture network, and also on mechanical parameters such as fracture normal stiffness and fracture shear strength. Additionally, they ascribed the enhancement of permeability during shear slip on a critically stressed fracture to mechanisms such as brecciation, surface roughness, and breakdown of seals as proposed by Barton *et al.* (1995).

Talbot & Sirat (2001) studied the hydraulic conductivity in highly fractured granitoid bedrock with large range of orientations and complicated deformation histories exposed in the Äspö Hard Rock Laboratory in Sweden. Out of ~ 11,000 documented fractured in the locality, only 8 % of those fractures appeared to be conductive during initial excavation. The majority of the wet fractures were either sub-horizontal, which were prone to thrusting, or sub-vertical with an underlying stress regime susceptible to wrench faulting. They concluded that faults favourably oriented for slip or dilation in the ambient stress field were most conductive to fluid flow. Similar observations were reported in the case of groundwater flow in Monterey Formation,

Santa Maria Basin, California by Finkbeiner *et al.* (1997) and in the vicinity of Yucca mountain, Nevada by Ferrill *et al.* (1999).

Evans (2005) evaluated the fluid flow properties of critically stressed fractures in a 3.5 km deep borehole in granite at the Soultz-sous-Forets Hot Dry Rock (HDR) project site in the Rhinegraben area in France. He observed that all 18 naturally flowing fractures were critically stressed. Nonetheless, a significant number (~ 500) of fractures were non-flowing irrespective of fulfilling the critical stress criterion. He concluded that being critical stressed is a necessary condition for fracture flow but not a sufficient criteria for identifying flowing fractures.

Rutqvist *et al.* (2009) presented numerical modelling of excavation-induced damage, permeability changes and fluid pressure responses during the excavation of a test tunnel in Lac du Bonnet granite as part of the tunnel sealing experiment (TSX) at the URL, Canada. They observed that the permeability changes during excavation are related to the combined effects of disturbance induced by stress redistribution around the tunnel and by the drill-and-blast-operation. The decrease in mean effective stress at the side of the tunnel and the high horizontal stress and strain at the top of the tunnel resulted in permeability increase. The increase in permeability at the top of the tunnel was ascribed to the formation of fractures as a consequence of a series of microseismic events during excavation.

An investigation into the stress controlled fluid flow in fractures within the crystalline basement of Fennoscandian shield in the Olkiluoto Island (Finland) by Matilla & Tammisto (2012) showed that the critical stress theory could not predict which of the fractures were conducting or not. The study involved the analysis of fluid flow properties of 38,703 fractures. They observed that between a depth range of 0 to 300 metres the majority of the conductive fractures were critically stressed. However, at depths of 300 to 800 metres almost all conductive fractures lay well below the critical stress criterion. They concluded that the transmissivity of fluids along fractures is determined by the normal traction acting across the fractures and suggested the integrated use of contemporary stress state in addition to slip & dilation tendency analysis of the fractures to predict fluid flow.

The concept of critical stress has been widely applied in predicting and modelling the fluid flow through fractures under *in situ* stress conditions under many geological settings. The relationship between critically stressed fractures and fluid flow from field studies has been inconclusive. Moreover, the occurrence of flowing fractures in non-critically stressed rocks, and conversely, the presence of non-flowing fractures in critically stressed rocks call for an experimental investigation into the conductivity of critically stressed fractures. In order to experimentally validate the critical stress theory under controlled hydromechanical conditions, a series of experiments were planned and performed using the bespoke Angled Shear Rig at the Transport Properties Research Laboratory (TPRL) of the British Geological Survey (BGS).

2 Experimental apparatus and methodology

A variety of different experimental geometries have been employed in the laboratory simulation of shear deformation. Different methods have distinct advantages and disadvantages. The most commonly used methods in laboratory fracture studies are (after Mogi, 2007):

A) Conventional direct shear test;

B) Conventional double-shear test;

C) Biaxial compression shear test;

D) Conventional triaxial compression test.

Schematic representations of the different experimental setups are shown in Figure 6. The conventional direct shear test can be used to study large samples with large shear planes. The major disadvantage with this kind of experimental setup is that large contact area between the top and bottom blocks can result in non-uniform distribution of normal stresses along the experimental slip plane. Moreover, larger contact surface area implies that the maximum stresses that can be applied to the slip plane are relatively low. In the conventional double-shear test, two sliding surfaces are present; this setup also results in inhomogeneous distribution of stresses along the slip planes. In a biaxial compression shear test, uniform normal stresses could be applied but constant normal stresses cannot be maintained for stick-slip and the stresses that can be achieved are quite low. Conventional triaxial compression tests are employed in studies where higher stresses are required. The contact area of the slip plane is small and the contact area changes with shearing leading to variation in normal stress values. Apart from these fundamental shear apparatuses, rotary shear (ring-shear) apparatus are also employed where large displacements of the gouge can be achieved by rotary movement of the blocks.

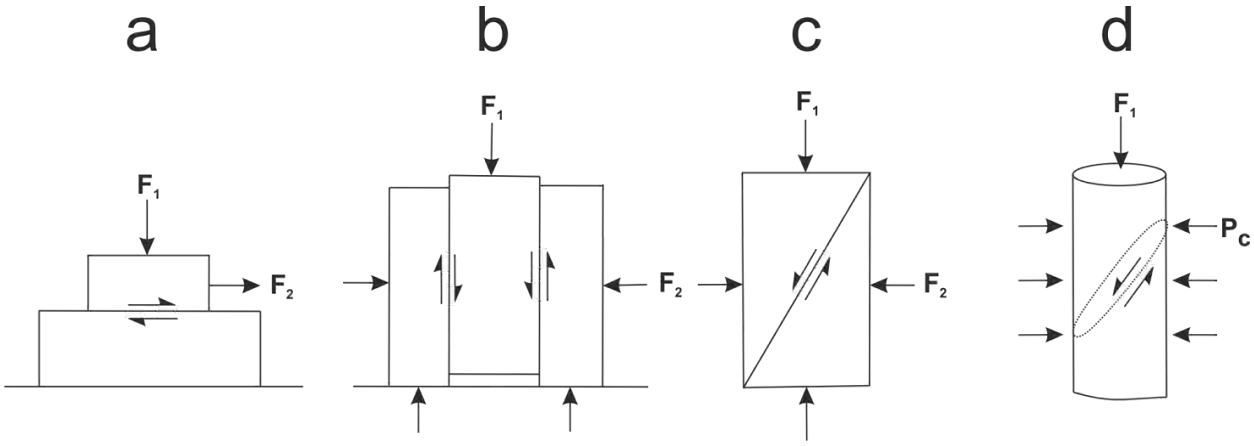

Figure 6 - Common friction test arrangements. a) Conventional shear test. b) Conventional double shear test. c) Biaxial test. d) Conventional triaxial test (from Mogi, 2007).

In order to achieve the objective of the present study, conventional direct shear was adopted. A bespoke Angled Shear Rig (ASR) was built at the Transport Properties Research Laboratory (TPRL), British Geological Survey (BGS), and was employed to validate the applicability of critical stress theory in repository scenarios.

2.1 ANGLED SHEAR RIG (ASR)

The ASR (Figure 7) used in the present study is a custom-modified form of the standard soil-shear apparatus (conventional direct shear apparatus) as outlined by Gutierrez *et al.* (2000). The ASR facilitated independent control of the slip plane orientation, vertical and horizontal stresses,

pore pressure, and horizontal displacement (shear) rate. This assisted in experimentally understanding the relationship of fracture conductivity and the combined effect of variations in fracture orientation and stress conditions. The core components of the ASR are listed below:

1. Rigid frame that has been designed to withstand the applied vertical and horizontal stresses.
2. Vertical loading system comprised of a rigid loading beam, a rigid loading frame, two load cells, and a hydraulic jack controlled by a servo controlled ISCO syringe pump.
3. Horizontal force actuator connected in parallel with a load cell. The force actuator was capable of a linear horizontal movement as slow as 14 µm a day along a low friction bearing.
4. Pore pressure system comprised of an ISCO syringe pump connected to a water/gas interface vessel that could be used to inject either water or gas at a constant rate or at a constant pressure. A schematic of the fluid injection system is shown in Figure 9.
5. Data acquisition system connected to the pressure transducers, load cells, thermocouples by means of acquisition software written in National Instruments LabVIEW™ environment. This software also allowed remote monitoring and control of all experimental parameters.
6. The experimental slip plane assembly consisting of precision machined 316 stainless steel top and bottom blocks with dips of 0º, 15º, 30º, and 45º. The top block was connected to the vertical loading mechanism by means of a swivel mechanism which was engaged to the shoulders on either side of the top block (Figure 8a).

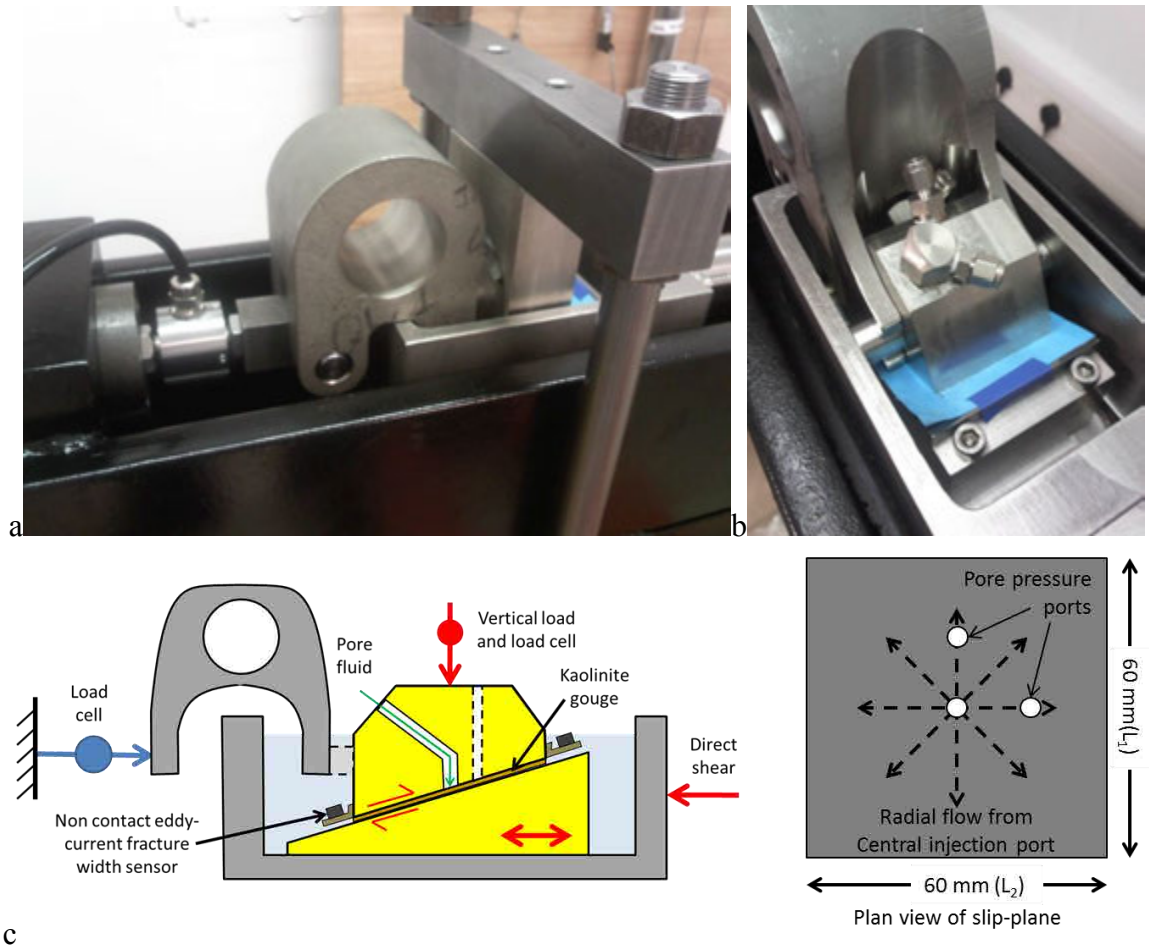

Figure 7 - Angled shear rig (ASR). a) Photograph of the vertical and horizontal loading system. b) Photograph of the angled shear block and the upper platen arrangement. c) Schematic of the ASR.

A fully saturated kaolinite clay sample (80 % gravimetric water content) was placed between two stainless-steel blocks forming a 60 × 60 mm slip plane surface and was deformed by applying a vertical load and/or horizontal displacement which resulted in a gouge thickness of

approximately 70 ± 10 µm. The kaolinite paste was selected for two reasons; firstly it prevented cold-welding of the steel blocks, and secondly kaolinite is a low swelling clay which is commonly found as fracture fill.

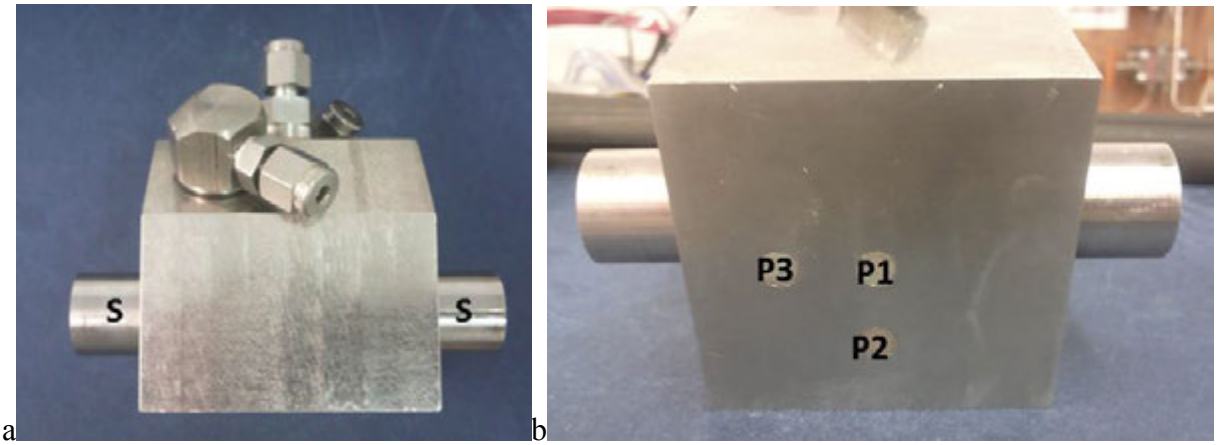

Figure 8 - Components of the top block. a) Frontal-view of top block. "S" depicts the shoulders that are engaged to the loading mechanism to impart uniform normal stress along the slip plane. b) The bottom-view of the top block showing the central pore fluid injection port (P1) and the two orthogonally spaced pore pressure ports (P2 & P3) to monitor the pore pressure within the slip plane during the course of the experiment.

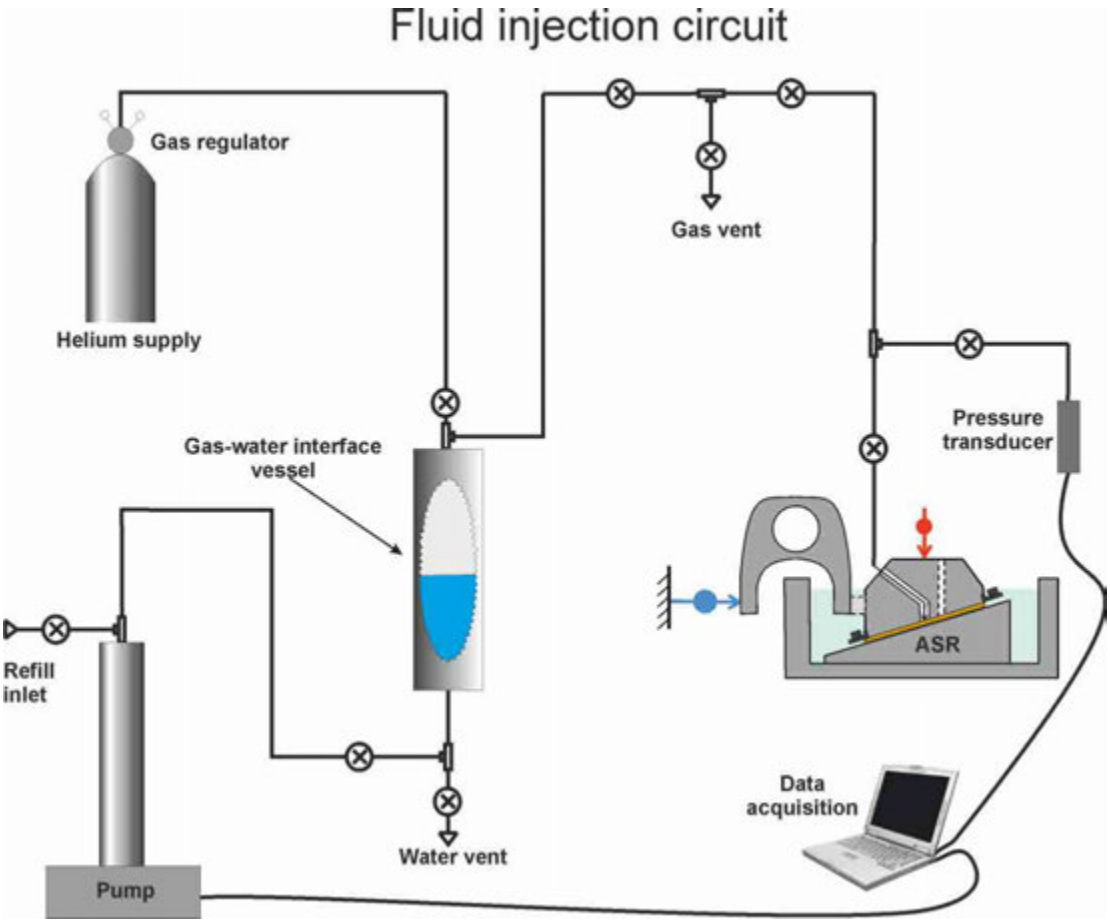

Figure 9 - Fluid injection circuit displaying the servo-controlled ISCO^{TM} injection pump and the gas-water interface vessel used to inject helium into the idealised slip plane.

2.2 SAMPLE PREPARATION AND EXPERIMENT ASSEMBLY

The powdered kaolinite (Echantillon Sample – Supreme Powder) used in the present study was acquired from ECC International (presently known as Imerys Minerals Ltd.). Kaolinite paste was prepared by adding 16 g of de-ionised water to 20 g of kaolinite powder. The water and kaolinite powder were then meticulously stirred for about five minutes giving a kaolinite paste with a gravimetric water content of 80 ± 1 %. The paste was smeared uniformly onto the surface of the top block, which was then carefully lowered onto the bottom block thus forming a kaolinite paste gouge. The initial thickness of the gouge was measured to be 1 – 2 mm. However, with loading the gouge thickness decreased to approximately 70 ± 10 microns.

The experiments were conducted after carefully setting the load frame of the vertical loading system in order to ensure even loading across the width of the slip plane. The pore fluid was injected into the centre of the slip plane by means of an injection port (P1) in the top block and the distribution of fluid pressures within the slip plane was monitored using two orthogonally spaced ports (P2 and P3) positioned 1cm away from P1 (Figure 8b). Whilst setting the experiment the pipework and pressure transducers were filled with de-ionised water to ensure air volumes in P2 and P3 were minimised.

2.3 EXPERIMENTAL PROCEDURE

A series of experiments (Table 1) were performed to study the fluid flow properties through experimental slip planes under different stress conditions. Experiments were performed on slip plane orientations of 0º, 15º, 30º, and 45º relative to the maximum horizontal stress direction. All the experiments can be broadly categorised into two types:

1. Loading-Unloading (LU) Experiments
2. Gas Injection (GI) Experiments

In a few selected experiments, the effect of shear on fluid flow was investigated in both LU and GI experiments. In such cases, the bottom block attached to a servo controlled shear mechanism was allowed to move at a fixed rate to induce horizontal movement whereas the top block was locked into stationary position.

2.3.1 Loading-Unloading (LU) Experiments

In loading-unloading (LU) experiments the vertical stress acting across the slip plane was increased and decreased in stages and the corresponding response of flow-rate was monitored. As previously stated, vertical load was applied to the slip plane by means of a ISCO syringe pump connected to a hydraulic jack. The pressure of the syringe pump was increased in steps of 1 MPa from 1 MPa up to 14 MPa and subsequently decreased in steps to 1 MPa. As shown in Table 2, a 1 MPa increase in pump pressure resulted in a force of 73.95 kg, or a stress of 172 kPa. The vertical load was controlled within ± 1 kg.f throughout each stage. In the case of LU experiments with water, the injection pressure was maintained at 1 MPa. In the case of LU experiments with helium a gas pressure in excess of the gas breakthrough pressure was used. Gas breakthrough was achieved by systematically increasing the gas injection pressure in steps of 50 kPa until significant gas flow was detected; gas pressure was then maintained constant and the normal load was varied accordingly to test the effect of normal load variation on gas flow. The list of LU experiments using water and gas injection fluids are given in Table 1.

	Experiment	Start date	Sample Material	Type of test	Pore fluid	Slip-plane orientation	Gas Injection test number
1	ASR_Cal01_30	26-Jan-10	None	Calibration	He		
2	ASR_Cal02_30			Calibration			
3	ASR_Cal03_30			Calibration			
4	ASR_Cal04_30			Calibration			
5	ASR_Tau01_30wLU	09-Nov-10	Kaolinite	LU	H_2O		
6	ASR_Tau02_30wLUS	10-Dec-10	Kaolinite	LU + shear			
7	ASR_Cal05_30xLU	26-Apr-11	Dry kaolin	LU	None		
8	ASR_Cal06_30xLU	04-May-11	Kaolinite				
9	ASR_Cal07_30xLU	09-May-11					
10	ASR_Cal08_30xLU	12-May-11	None	Leak test			
11	ASR_Cal09_30xLU	12-May-11	Kaolinite	LU			
12	ASR_Cal10_30xLU	17-May-11	Dry				
13	ASR_Cal11_30xLU	19-May-11					
14	ASR_Cal12_30xLU	20-May-11	Kaolinite				
15	ASR_Tau03_30wLU	24-May-11	Kaolinite (100%)	Pore fluid permeability test	H_2O	30°	
16	ASR_Tau04_30wLU	25-May-11					
17	ASR_Tau05_30wLU	27-May-11	Kaolinite (80% saturated)				
18	ASR_Tau06_30gGI	24-Jun-11			Helium		A
19	ASR_Tau07_30gLU	22-Jul-11		Flow test			
20	ASR_Tau08_30gLU	22-Aug-11		Helium gas permeability (GI)			
21	ASR_Tau09_30gGI	27-Sep-11					1
22	ASR_Tau10_30gGI	10-Oct-11					
23	ASR_Tau11_30gGI	11-Oct-11					2
24	ASR_Tau12_30gGI	09-Nov-11					3
25	ASR_Tau13_30gGI	18-Nov-11					4
26	ASR_Cal13_30xLU	08-Dec-11					
27	ASR_Tau14_30gLU	12-Dec-11					
28	ASR_Tau15_00gGI	14-Feb-12				0°	5
29	ASR_Tau16_00gGI	23-Feb-12					6
30	ASR_Tau17_00gGI	05-Mar-12					7
31	ASR_Tau18_15gGI	22-Mar-12				15°	8
32	ASR_Tau19_15gGI	03-Apr-12					9
33	ASR_Tau20_15gGI	18-Apr-12					10
34	ASR_Tau21_00gGI	01-May-12				0°	11
35	ASR_Tau22_00gGI	14-May-12					12
36	ASR_Tau23_00gGI	28-May-12					13
37	ASR_Tau24_00gGI	06-Jun-12					14
38	ASR_Tau25_45gGI	19-Jun-12				45°	15
39	ASR_Tau26_45gGI	03-Jul-12					16
40	ASR_Tau27_45gGI	13-Jul-12					17
41	ASR_Tau28_00gGIS	25-Jul-12				0°	18
42	ASR_Tau29_00gGIS	06-Aug-12					19
43	ASR_Cal14_30x	20-Aug-12				30°	
44	ASR_Tau30_30gGIS	29-Aug-12					20
45	ASR_Tau31_45gGIS	10-Sep-12				45°	21
46	ASR_Tau32_15gGIS	25-Sep-12				15°	22

Table 1 – List of all experiments undertaken as part of the current study.

	ASR_Tau05_30wLU		ASR_Tau07_30gLU	
	ISCO Pump Pressure (MPa)	Load cell (kg.f)	ISCO Pump Pressure (MPa)	Load cell (kg.f)
LOADING	1	73.95	-	-
	2	151.40	2	149.18
	3	229.19	3	227.42
	4	304.00	4	302.69
	5	380.46	5	378.97
	6	458.59	6	458.74
	7	538.37	7	538.33
	8	615.83	8	617.43
	9	700.60	9	700.53
	10	781.22	10	779.96
	11	863.66	11	859.56
	12	944.27	12	940.16
	13	1022.89	13	1021.09
	14	1106.15	14	1103.36
UNLOADING	13	1044.49	13	1042.03
	12	977.68	12	974.56
	11	904.55	11	903.93
	10	826.42	10	830.81
	9	741.49	9	751.04
	8	663.86	8	666.79
	7	579.92	7	596.83
	6	498.64	6	499.29
	5	417.68	5	417.86
	4	336.74	4	336.77
	3	255.45	3	254.01
	2	164.37	2	162.62
	1	79.42	-	-

Table 2 - Variation in load cell reading during variation in ISCO syringe pump pressure.

2.3.2 Gas Injection (GI) Experiments

All the GI experiments reported here (Table 1) were performed at a pressure of 10 MPa in the controlling ISCO syringe pump, giving a load of 782 kg.f (2 MPa vertical load). The gas injection rate was controlled using a second ISCO pump as shown in Figure 9. All the GI experiments were started at a gas pressure of 4 MPa. It should be noted that the starting volume of gas within the water/gas interface vessel was 200 ± 0.2 cc in all GI experiments. Gas injection was performed by injecting water into the gas/water interface vessel at a flow rate of 700 $\mu l.h^{-1}$ using the ISCO pump. This increased the gas pressure within the interface vessel at a steady rate. Boyle's law allowed gas pressure to be predicted knowing the initial volume and change in volume. Gas entry could be determined by carefully comparing the recorded pressure with the predicted pressure. When the two values begin to differ it showed that gas was moving into the clay gouge. The pressure at which gas entry occurred provided valuable information about the dependence of gas flow on the orientation of the slip plane along with the evolution of gas pressure after gas breakthrough and the evolution of fluid.

2.4 CALCULATION OF FRACTURE TRANSMISSIVITY

Assuming radial flow of injection fluids (gas or water) from the central injection port (Figure 10), transmissivity of fluid was determined from flow rate using the equation:

$$Q = \frac{2\pi TH}{\ln(r_2 / r_1)} \qquad \textbf{Equation 1}$$

where, Q = flow rate of the fluid ($m^3.s^{-1}$); T = transmissivity ($m^2.s^{-1}$); H = pressure head (m); r_1 = radius of the injection tube (m); $r_2 = \sqrt{(L_1 L_2)/\pi}$ = equivalent outer radius of the slip plane surface (m).

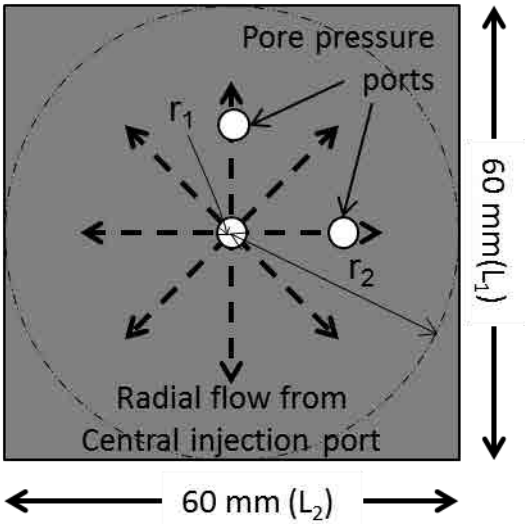

Figure 10 - Plan-view of the slip plane with fluid injection port in the centre and two orthogonally located pore pressure sensor ports. The parameters L_1, L_2, r_1, and r_2 are also depicted.

Equation 1 can be rewritten as:

$$T = \frac{Q\ln(r_2 / r_1)}{2\pi H} \qquad \textbf{Equation 2}$$

since,

$$H = \frac{P_i}{\rho_f g} \qquad \textbf{Equation 3}$$

where; P_i = fluid injection pressure (Pa); ρ_f = density of the fluid ($kg.m^{-3}$); g = acceleration due to gravity ($m.s^{-2}$).

Substituting H in Equation 2 with Equation 3, transmissivity can be determined from the following:

$$T = \frac{Q\rho_f g \ln(r_2 / r_1)}{2\pi P_i} \qquad \textbf{Equation 4}$$

Hydraulic conductivity can be determined from T by the relation:

$$K = \frac{T}{e} = \frac{Q\rho_f g \ln(r_2 / r_1)}{2\pi e P_i} \qquad \textbf{Equation 5}$$

Where; K= hydraulic conductivity ($m.s^{-1}$); e = conducting aperture of the slip plane (m)

Permeability can then be determined by the relation:

$$k = \frac{K\mu_f}{\rho_f g} = \frac{Q\mu_f \ln(r_2/r_1)}{2\pi e H \rho_f g} = \frac{Q\mu_f \ln(r_2/r_1)}{2\pi e P_i} \qquad \textbf{Equation 6}$$

Where; k = permeability (m^2); μ_f = dynamic viscosity of the fluid ($kg.s^{-1}.m^{-1}$).

2.5 NOTE ON STRESS CONVENTION

Stress is described in this report with reference to the experimental apparatus; i.e. stress is horizontal (parallel with movement direction of the apparatus) and vertical. Stresses have not been converted to normal and shear directions parallel with and perpendicular to the fracture orientation. This approach has been adopted as the boundary condition of vertical stress is constant in different experiments with fractures at varying angles. Therefore variations observed in flow are in part due to differences in normal and horizontal stress at different fracture orientation, but illustrate the differences that would be seen in a similar location where multiple fracture directions are observed.

3 Observations and results

3.1 FRACTURE TRANSMISSIVITY EVOLUTION DURING VARIATIONS IN VERTICAL LOAD

The effect of loading and unloading on fracture transmissivity was studied by sequentially loading and unloading an idealised kaolinite gouge filled slip plane (fracture plane) oriented at an angle of 60º to the vertical stress direction by means of a bespoke shear apparatus (Figure 7). Both water (de-ionised) and gas (helium) were used as permeants (pore fluids) in order to understand the differences in behaviour of water and gas transmissivity.

3.1.1 Hydraulic flow during loading and unloading through an idealised slip plane

Two experiments (ASR_Tau01_30wLU and ASR_Tau05_30wLU) were conducted to understand the effect of loading and unloading on hydraulic fracture transmissivity. Test ASR_Tau01_30wLU was a short duration experiment where vertical load was varied a couple of times a day whereas in test ASR_Tau05_30wLU the vertical load was varied once every day.

3.1.1.1 RESULTS

Test ASR_Tau01_30wLU comprised of a quick loading-unloading test devised to assess the experimental apparatus and to understand how the hydraulic flow along the slip plane was affected during variations in vertical load (Figure 11). The kaolinite gouge filled slip plane was loaded in stages of 0.2 MPa from 0 to 2.6 MPa and unloaded from 2.6 to 0 MPa in similar 0.2 MPa steps (Figure 11b). The loading-unloading stages and their respective durations are listed in Table 3. The temperature fluctuation during the entire duration of the experiment is shown in Figure 11a. An abrupt drop in temperature from 21.4 °C to 20.5 °C was observed around Day 9. The variation in flow rate at an injection pressure of 1 MPa in response to variations in vertical load was analysed. Flow rate decreased from 87 $\mu l.h^{-1}$ at 0.2MPa to 5 $\mu l.h^{-1}$ at 2.6MPa (Figure 11c&d). During unloading a partial recovery of flow rate to 22 $\mu l.h^{-1}$ was observed. An abrupt increase in flow from 10 $\mu l.h^{-1}$ to 30 $\mu l.h^{-1}$ was recorded at Day 9. Similarly, transmissivity decreased from 9.3×10^{-14} $m^2.s^{-1}$ to 7×10^{-15} $m^2.s^{-1}$ during loading. Unloading of the slip plane surface from 2.6 to 0 MPa resulted in an increase in transmissivity from 7×10^{-15} $m^2.s^{-1}$ to 2.3×10^{-14} $m^2.s^{-1}$ (Figure 11f). Horizontal stress increased linearly with each vertical load increase during loading. However, during unloading considerable hysteresis was observed in horizontal stress (Figure 11e). The pore pressures within the slip plane remained low (23 kPa and 15 kPa) and unchanged irrespective of the high injection pressures of 1 MPa applied approximately 1 cm away from the slip plane pressure sensors (Figure 11g).

In order to understand the effect of loading and unloading on hydraulic flow in more detail, a longer duration repeat experiment ASR_Tau05_30wLU was performed (Table 4). Vertical stress was sequentially increased in stages of 0.2 MPa per day to a maximum vertical stress of 2.6 MPa (Figure 12). The pore fluid injection pressure was maintained at a constant value of 1 MPa. Although no horizontal stress was applied, the increase in horizontal stress as a consequence of vertical stress increase was logged throughout the duration of the experiment (Figure 12b). During the unloading stage, the vertical stress was decreased in steps of 0.2 MPa from 2.6 MPa to 0.2 MPa.

	Stage	Vertical stress (MPa)	Time (days)
LOADING	1	0.2	0.0
	2	0.4	0.8
	3	0.6	1.3
	4	0.8	1.8
	5	1.0	2.3
	6	1.3	2.8
	7	1.5	3.4
	8	1.7	3.8
	9	1.9	4.3
	10	2.1	4.8
	11	2.3	5.4
	12	2.6	5.8
	13	2.8	6.2
	14	3.0	6.8
UNLOADING	15	2.6	7.8
	16	2.2	8.3
	17	1.8	8.8
	18	1.3	9.8
	19	0.9	10.3
	20	0.6	10.8
	21	0.4	11.5
	22	0.3	12.0
	23	0.2	12.8
	24	0.1	13.2

Table 3 - The loading and unloading stages in test ASR_Tau01_30wLU.

Temperature remained uniform at 20.5 ± 0.1 °C throughout the entire duration of the experiment, with a few fluctuations of 0.2 °C at Day 17, 18, and 21 (Figure 12a). During loading (stages 1 to 14), a linear increase of horizontal stress was observed with increase in vertical stress whereas during unloading (stages 15 to 27), the horizontal stress showed considerable hysteresis (Figure 12b,e). The flow rate decreased an order of magnitude from 50 $\mu l.h^{-1}$ to 5 $\mu l.h^{-1}$ during loading from 0 to 2.6 MPa. During unloading from 2.6 to 0.2 MPa, flow rate doubled from 5 $\mu l.h^{-1}$ to 10 $\mu l.h^{-1}$. Also from 2.6 MPa to 1.0 MPa vertical stress, the flow rate remained more or less constant at 5 $\mu l.h^{-1}$ irrespective of the significant reduction in vertical load (Figure 12c,d). Pore pressure within the slip plane recorded much lower pressures (50 – 80 kPa and 5 – 25 kPa) than the injection pressure (1 MPa) (Figure 12f). Vertical stress to normal stress ratio decreased from 1.6 to a minimum value of 0.7 during loading and increased to 1.9 during unloading (Figure 12g). Moreover, a close correlation between the horizontal stress to vertical stress ratio and flow rate was observed in the unloading phase particularly when the initial horizontal stress to vertical stress ratio of 1.5 was exceeded and the flow rate doubled from 5 $\mu l.h^{-1}$ to 10 $\mu l.h^{-1}$. During loading, transmissivity decreased from 5×10^{-14} $m^2.s^{-1}$ to 0.6×10^{-14} $m^2.s^{-1}$. However, during unloading transmissivity recovered to only 1.1×10^{-14} m^2s^{-1} (Figure 12h). The thickness of the kaolinite gouge decreased with loading from 54 µm at a vertical stress of 0.2 MPa to 42 µm at a vertical stress of 2.6 MPa. During unloading slip plane width continued to decrease further to 40 µm before finally recovering to 43 µm after full unloading.

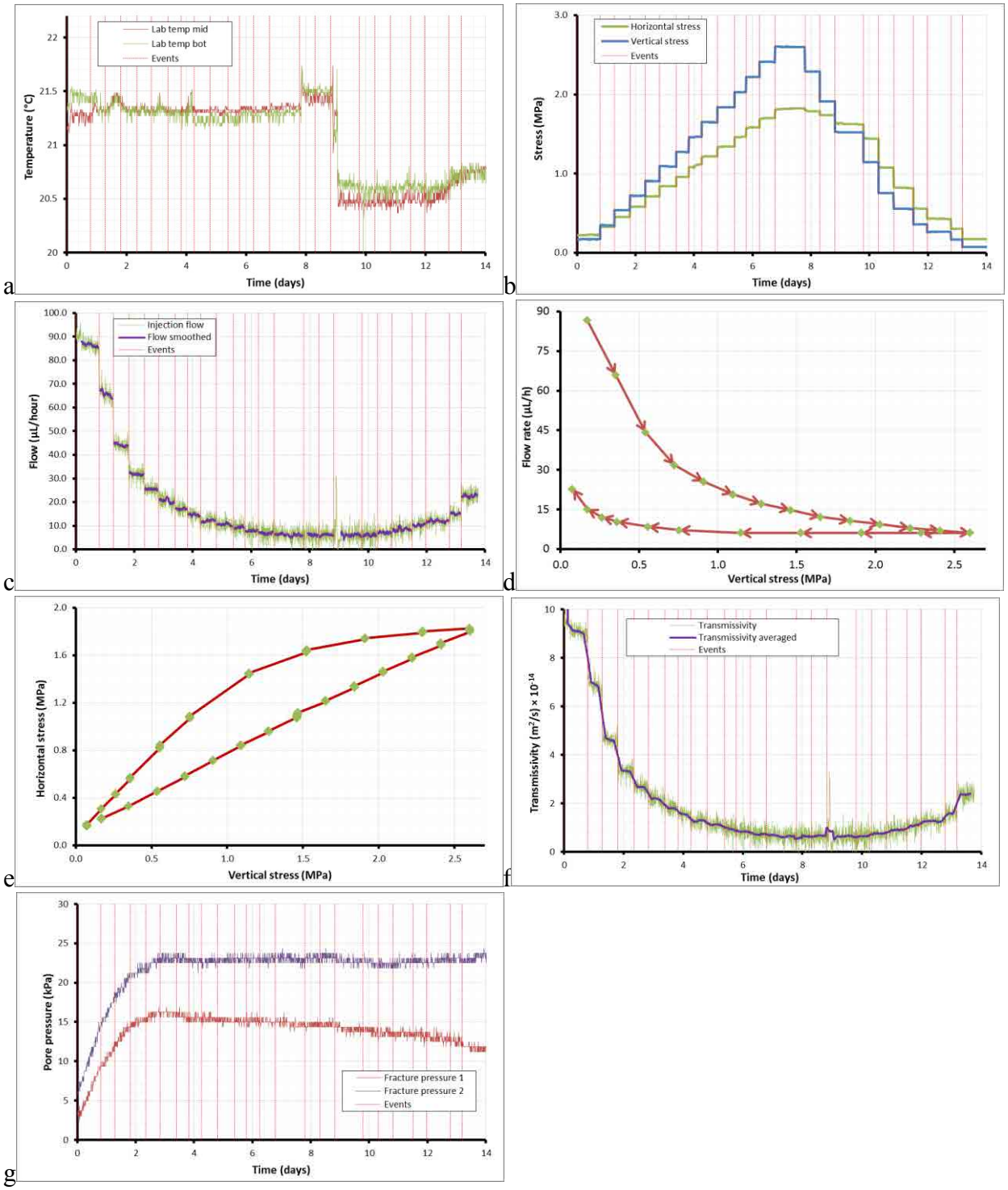

Figure 11 - Results from test ASR_Tau01_30wLU: a) Temperature; b) Loading and unloading steps showing the stepwise variation in vertical stress and corresponding variations in horizontal stress; c) Hydraulic flow with time; d) Hydraulic flow variation with vertical stress; e) Horizontal stress versus vertical stress plot showing hysteresis; f) Hydraulic transmissivity; g) Pore pressures within the slip plane.

	Stage	Vertical stress (MPa)	Time (days)
LOADING	1	0.2	0
	2	0.4	1
	3	0.5	2
	4	0.7	3
	5	0.9	4
	6	1.1	5
	7	1.3	6
	8	1.5	7
	9	1.7	8
	10	1.8	9
	11	2.0	10
	12	2.2	11
	13	2.4	12
	14	2.6	13
UNLOADING	15	2.5	14
	16	2.3	15
	17	2.1	16
	18	1.9	17
	19	1.8	18
	20	1.6	19
	21	1.4	20
	22	1.2	21
	23	1.0	22
	24	0.8	23
	25	0.6	24
	26	0.4	25
	27	0.2	26

Table 4 - The loading and unloading stages in test ASR_Tau05_30wLU.

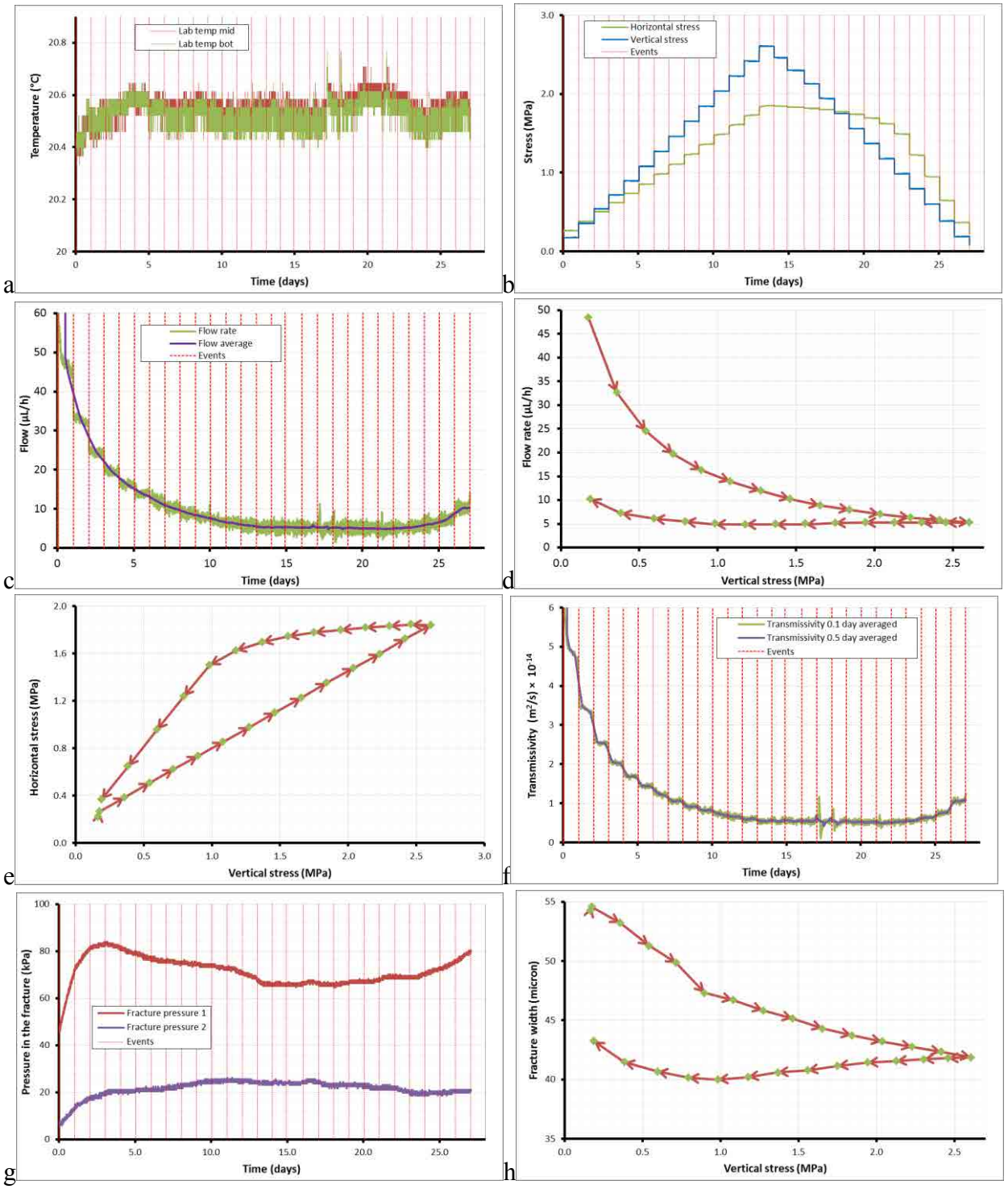

Figure 12 - Results from test ASR_Tau05_30wLU: a) Temperature; b) Loading and unloading steps showing the stepwise variation in vertical stress and corresponding variations in horizontal stress; c) Hydraulic flow with time; d) Hydraulic flow variation with vertical stress; e) Horizontal stress versus vertical stress plot showing hysteresis; f) Hydraulic transmissivity; g) Pore pressures within the slip plane; h) Fracture width variation. Since only one eddy-current sensor was used in this experiment the decrease in fracture width during unloading might have been a result of the tilting of the top block when the vertical stress was decreased.

The abrupt increase in laboratory temperature during unloading is presented in additional detail in Figure 13a. Abrupt increases in temperature were detected at Days 17, 18 and 21.

Corresponding increase in flow rate and transmissivity were also observed (Figure 13 b&c). Figure 13d shows the increase in horizontal stress to vertical stress ratio during unloading.

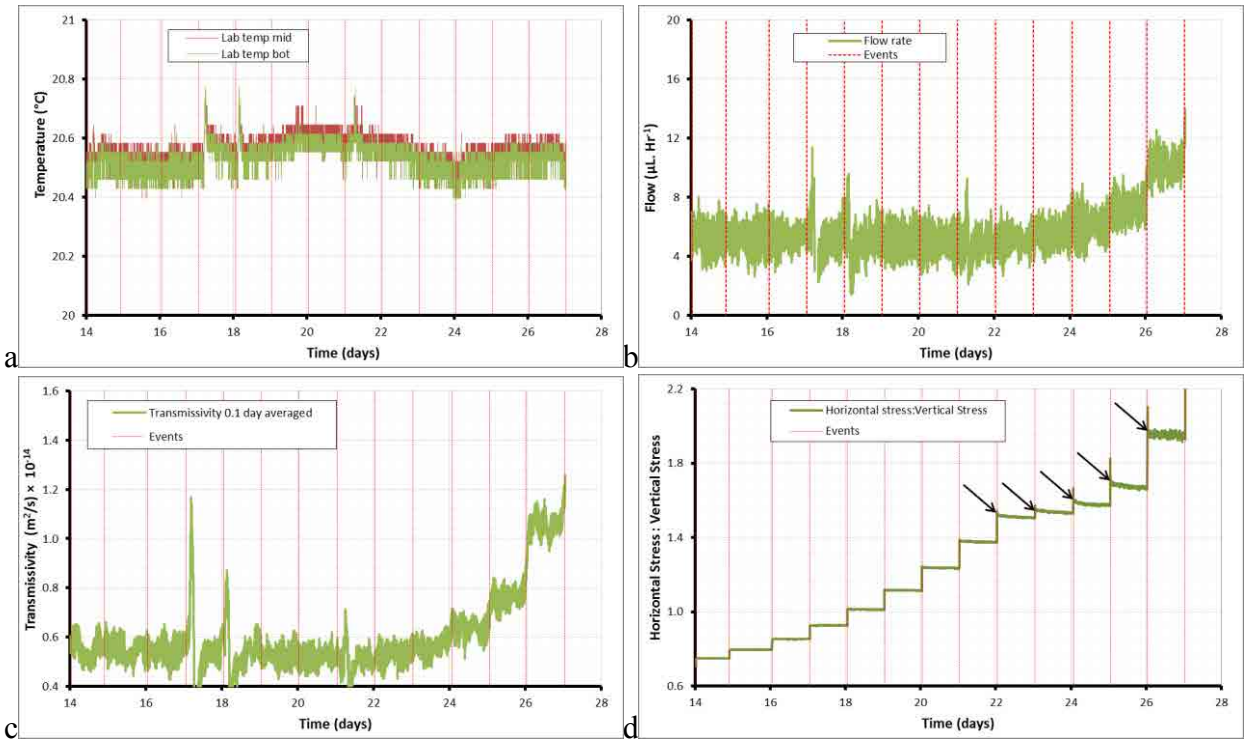

Figure 13 –Detail of effect of temperature fluctuations during the unloading stages in experiment ASR_Tau05_30wLU. a) Temperature; b) Flow rate; c) Transmissivity; d) Horizontal stress to vertical stress ratio. The arrows indicate the initial increase in horizontal stress to vertical stress ratio during unloading which might be due to the movement of the top block during each stepwise decrease in vertical stress. These steps also mark the stages where horizontal stress decreases rapidly during unloading as shown in Figure 12e.

3.1.1.2 Discussion

A comparison of results from experiments ASR_Tau01_30wLU and ASR_Tau05_30wLU (Figure 14) shows that an increase in vertical stress resulted in a corresponding linear increase in horizontal stress during loading. The hysteresis in horizontal stress observed during unloading may be attributed to the cohesive strength of the clay as a result of hydrogen bonding between adsorbed water molecules and atomically charged clay mineral surfaces (Ikari & Kopf, 2011; Marry *et al.*, 2008). The decrease in flow rate and transmissivity during loading suggests the progressive constriction of fluid pathways during loading. The initial dissimilarities in flow rate during loading between ASR_Tau01_30wLU and ASR_Tau05_30wLU might have been due to the initial packing of the clay platelets and the geometry of the initial pathways formed. However, at a vertical stress of 2.6 MPa, flow decreased to a uniform value of 5 $\mu l.h^{-1}$ irrespective of the initial flow rates. After complete unloading, flow increased uniformly in both tests ASR_Tau01_30wLU and ASR_Tau05_30wLU to 12 ± 2 $\mu l.h^{-1}$ (Figure 14). The hysteresis in flow rate and horizontal stress during a loading and unloading cycle suggests that understanding the complete stress history rather than the current stress state is of paramount importance in predicting the flow of fluids through fractures. Heterogeneous distribution of pore pressures away from the central pore fluid injection port within the idealised slip plane suggests that the hydraulic flow through clays occurs via localised channel/s within the slip plane. Fluctuations in laboratory temperatures during the course of the experiments revealed an inexplicit relationship to fluid flow rates. In ASR_Tau01_30wLU an abrupt decrease in temperature of 1 °C on Day 9 from 21.5 °C to 20.5 °C resulted in the flow rate increasing from 5 $\mu l.h^{-1}$ to 30 $\mu l.h^{-1}$ and transmissivity values increasing from 0.3×10^{-14} $m^2.s^{-1}$ to 3.3×10^{-14}

$m^2.s^{-1}$ (Figure 11 c & f). An increase in temperature in ASR_Tau05_30wLU of 0.2 °C resulted in a flow rate increase from 4 $\mu l.h^{-1}$ to 11 $\mu l.h^{-1}$ and a corresponding doubling of transmissivity from 0.6×10^{-14} $m^2.s^{-1}$ to 1.2×10^{-14} $m^2.s^{-1}$ (Figure 13 a-c). This short-term increase in flow rate and transmissivity may be attributed to the thermal expansion and/or contraction of water or stainless steel pore fluid pump reservoir and pipe networks with rise or fall in laboratory temperature respectively. The exact process responsible for this anomalous observation is unclear from the present dataset. The diverse differences in the injection pressure and the pressure within the slip plane (Figure 11g & Figure 12g) suggests that the concept of effective stress (total stress minus pore fluid pressure) cannot be applied consistently to clays with the same assurance as it has been applied in the study of more porous and permeable rocks such as sandstones and fractured crystalline rocks (Cuss *et al.*, 2011).

Kaolinite being a non-swelling clay might behave differently to other swelling clays such as montmorillonite, illite and smectite during hydraulic flow. The flow rates in fault gouges filled with swelling-clays is expected to be significantly lower compared to that of a non-swelling clay. The process of swelling is likely to constrict any open pathways. Additional experiments with swelling clays are necessary to completely understand the hydraulic flow properties through a slip plane containing a mixture of swelling and non-swelling clays.

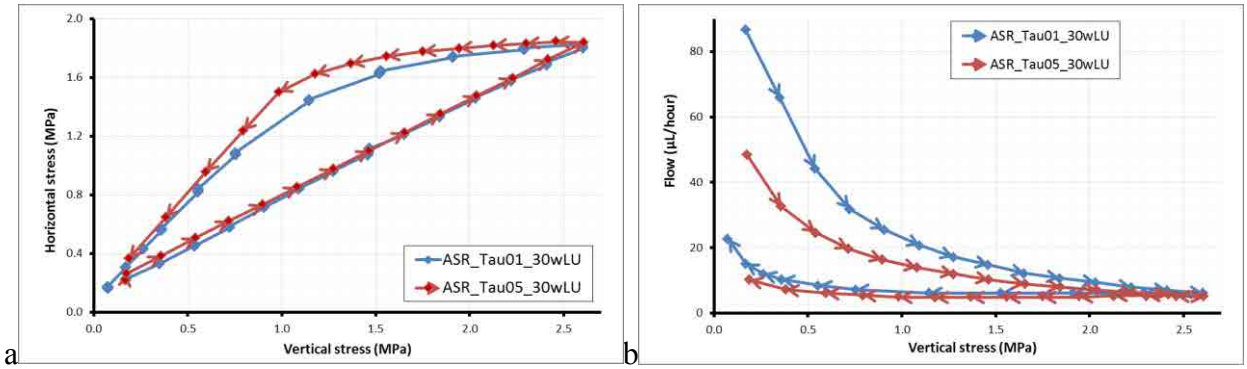

Figure 14 – Comparison of results from experiments ASR_Tau01_30wLU and ASR_Tau05_30wLU. a) Horizontal stress versus vertical stress plot. Similar results are seen during loading, with only marginally differences seen during unloading; b) Flow versus vertical stress. During loading the initial flow rate in ASR_Tau01_30wLU were higher (90 $\mu l.h^{-1}$) than the initial flow rate observed in ASR_Tau05_30wLU (50 $\mu l.h^{-1}$) during the initial part of the loading cycle. After loading to 2.6 MPa flow rate decreased to 5 $\mu l.h^{-1}$ for tests. Both tests also followed a similar unloading path.

3.1.2 Gas flow during loading and unloading through an idealised slip plane

Three loading and unloading experiments (ASR_Tau07_30gLU, ASR_Tau08_30gLU, and ASR_Tau14_30gLU) were conducted with gas injection to understand the effect of stress on gas flow through fractures. In all the experiments, vertical load was varied in steps of 0.2 – 0.3 MPa per day. These experiments were performed at gas injection pressures equivalent to the pressure at which gas flow was detected (gas breakthrough pressures) which were different in each experiment. The injection pressures used were 3.55, 4.95, and 4.45 MPa for ASR_Tau07_30gLU, ASR_Tau08_30gLU, and ASR_Tau14_30gLU respectively. The experimental stages are listed in Table 5.

3.1.2.1 RESULTS

In ASR_Tau07_30gLU, the experimental slip plane was loaded and unloaded in steps at a constant gas injection pressure of 3.55 MPa (Figure 15). The temperature within the laboratory was maintained at 20 ± 0.25 °C throughout the test (Figure 15a). The vertical stress was increased in steps of 0.2 – 0.3 MPa per day up to a maximum stress of 2.6 MPa and decreased in

similar steps to 0.4 MPa and the corresponding variations in gas flow rate were recorded (Table 5, Figure 15b). As stated earlier, vertical load was varied only after gas flow through the slip plane had been achieved. During the loading stages of the experiment, flow rate increased and decreased randomly from 100 $\mu l.h^{-1}$ at 0.4 MPa through 80 $\mu l.h^{-1}$ at 0.5 – 0.7 MPa and 117 $\mu l.h^{-1}$ at 0.9 – 1.1 MPa to 225 $\mu l.h^{-1}$ at a normal stress of 1.3 MPa (see Figure 15 c&d). Subsequent loading of the slip plane to a maximum stress of 2.6 MPa resulted in a steady decrease in flow rate from 225 $\mu l.h^{-1}$ to 90 $\mu l.h^{-1}$. During unloading, gas flow rate increased slowly from 90 $\mu l.h^{-1}$ at 2.6 MPa to 144 $\mu l.h^{-1}$ at 1.2 MPa. Significant increase in flow rate was observed during further unloading with flow rate increasing to 186 $\mu l.h^{-1}$, 360 $\mu l.h^{-1}$, and 961 $\mu l.h^{-1}$ at 1.0 MPa, 0.8 MPa, and 0.6 MPa respectively (Figure 15d). Horizontal stress increased linearly during loading and hysteresis was observed during the unloading stages (Figure 15e). The significant increase in flow rate on Day 27 during unloading appears to be related to the corresponding rapid decrease in horizontal stress as shown in Figure 15c,e. Pore pressure within the slip plane remained more or less unchanged during the entire duration of the experiment irrespective of the high injection pressure around 1cm away from the pore pressure sensors (Figure 15f). Horizontal stress to vertical stress ratio decreased during loading from 1 to 0.7 and during unloading increased remarkably to 1.6 (Figure 15g). Horizontal stress to vertical stress ratios above 1.5 corresponded to abrupt increases in flow rate as observed in Figure 15c,d. Similar to fluid flow, transmissivity increased and decreased during the initial loading stages up to 1.3 MPa. However, with further loading, transmissivity decreased from 1.2×10^{-17} $m^2.s^{-1}$ at 1.3 MPa to 4×10^{-18} $m^2.s^{-1}$ at a maximum vertical stress of 2.6 MPa (Figure 15h). During unloading, transmissivity increased gradually from 4×10^{-18} $m^2.s^{-1}$ to 7×10^{-18} $m^2.s^{-1}$ at 1.2 MPa vertical stress. With further unloading transmissivity of gas increased by up to an order of magnitude to 5.1×10^{-17} $m^2.s^{-1}$ at a vertical stress of 0.6 MPa. The thickness of the gouge within the slip plane decreased from 48.1 µm to 34.5 µm, and during unloading decreased further to 34.1 µm (Figure 15i).

In experiment ASR_Tau08_30gLU, the kaolinite gouge-filled slip plane was subjected to a loading and unloading cycle and the effect of variations in load on gas flow was studied. The results are presented in Figure 16. Random increase and decrease in flow rate was observed during the initial part of the loading cycle (Figure 16 c&d) as observed in previously. The flow rate fluctuated between 165 $\mu l.h^{-1}$ and 550 $\mu l.h^{-1}$ during stepwise loading from 0.4 MPa to 1.1 MPa. Further loading resulted in more or less steady decrease in flow rate from 550 $\mu l.h^{-1}$ at 1.1 MPa to 276 $\mu l.h^{-1}$ at 2.6 MPa. During unloading, flow rate increased gradually from 276 $\mu l.h^{-1}$ at 2.6 MPa to 298 $\mu l.h^{-1}$ at 1.4 MPa. The final unloading step at 0.4 MPa saw a considerable increase in flow resulting in approximately 1000 $\mu l.h^{-1}$. Horizontal stress increased linearly with loading and displayed hysteresis during unloading (Figure 16e). The pressure within the gouge remained approximately zero throughout the entire duration of the loading and unloading stages (Figure 16f). Horizontal stress to vertical stress ratio decreased during loading from 1.0 to 0.7 and during unloading significantly increased to 1.8 (Figure 16g). The transmissivity of gas through the slip plane fluctuated between 6×10^{-18} $m^2.s^{-1}$ and 2×10^{-17} $m^2.s^{-1}$ during the initial loading stages and decreased to 1×10^{-17} $m^2.s^{-1}$ (Figure 16h). During unloading of the slip plane gas transmissivity increased to 3.8×10^{-17} $m^2.s^{-1}$ at 0.4 MPa vertical stress. Fracture width decreased with loading from 65µm to 51µm and during unloading remained relatively constant (Figure 16i).

A third experiment (ASR_Tau14_30gLU) was performed at identical test conditions (Figure 17), with the slip plane loaded in steps to a maximum vertical stress of 1.8 MPa followed by unloading (Figure 17b). Flow rate fluctuated during the loading stages as observed in the previous experiments. The experiment was commenced at a flow rate of 85 $\mu l.h^{-1}$ at an injection pressure of 4.45 MPa and a vertical stress of 0.3 MPa (Figure 17c,d). However, an increase in vertical stress to 0.5 MPa resulted in a remarkable increase in flow rate from 85 $\mu l.h^{-1}$ to 262 $\mu l.h^{-1}$. Even though the flow rate fluctuated during loading, the general trend shows a decrease in flow rate during loading (Figure 17d). Flow at the maximum vertical stress of 1.8 MPa was 158 $\mu l.h^{-1}$. With unloading flow rate increased to 548 $\mu l.h^{-1}$ at a vertical stress of 0.6 MPa. Hysteresis

in horizontal stress was observed during the unloading stages and the pore pressures within the fracture remained relatively unaffected during the course of the experiment (Figure 17e,f). Horizontal stress to vertical stress ratio decreased from 0.9 to 0.7 during loading and subsequently increased to 1.5 during unloading (Figure 17g). Transmissivity of gas through the slip plane increased from 3.8×10^{-18} $m^2.s^{-1}$ to 1×10^{-17} $m^2.s^{-1}$ during a slight increase in vertical stress from 0.3 MPa to 0.5 MPa (Figure 17h). Further loading resulted in the gas transmissivity to decrease randomly to 5.9×10^{-18} $m^2.s^{-1}$ at a vertical stress of 1.8 MPa. During the unloading stage, transmissivity increased gradually to 8.4×10^{-18} $m^2.s^{-1}$ at a vertical stress of 1.0 MPa followed by an abrupt increase to 2.3×10^{-17} $m^2.s^{-1}$ at a low stress of 0.6 MPa. When vertical stress was decreased further to 0.2 MPa, transmissivity increased by an order of magnitude to 1.8×10^{-16} $m^2.s^{-1}$. Contrary to ASR_Tau07_30gLU and ASR_Tau08_30gLU where only one fracture width measuring eddy-current sensor was employed, ASR_Tau14_30gLU used two fracture-width sensors. The fracture width measured by one sensor showed a decrease in fracture width with loading from 10 µm to -9 µm whereas the second sensor showed a corresponding increase in from 28 µm to 75 µm (Figure 17i). The opposite behaviour in fracture width evolution was observed during the unloading stage. The average fracture width showed unexpected increase from 22 µm to 32 µm during loading. However, during unloading the fracture width remained constant at 33 ± 1 µm (Figure 17i).

	ASR_Tau07_30gLU			ASR_Tau08_30gLU			ASR_Tau14_30gLU		
	Stage	Vertical Stress (MPa)	Time (Days)	Stage	Vertical Stress (MPa)	Time (Days)	Stage	Vertical Stress (MPa)	Time (Days)
Loading	1	0.4	3	1	0.4	11	1	0.3	28
	2	0.5	5	2	0.5	12	2	0.5	29
	3	0.7	6	3	0.7	13	3	0.7	30
	4	0.9	7	4	0.9	14	4	0.9	31
	5	1.1	8	5	1.1	15	5	1.1	32
	6	1.3	9	6	1.3	16	6	1.3	33
	7	1.5	10	7	1.5	17	7	1.4	35
	8	1.7	11	8	1.6	18	8	1.6	36
	9	1.8	12	9	1.8	19	9	1.8	37
	10	2.0	13	10	2.0	20	–	–	–
	11	2.2	14	11	2.2	21	–	–	–
	12	2.4	15	12	2.4	22	–	–	–
	13	2.6	16	13	2.6	23	–	–	–
Unloading	14	2.5	19	14	2.5	24	–	–	–
	15	2.3	20	15	2.3	25	–	–	–
	16	2.1	21	16	2.1	26	–	–	–
	17	1.9	22	17	1.9	27	–	–	–
	18	1.8	23	18	1.8	28	10	1.7	38
	19	1.6	24	19	1.6	29	11	1.5	39
	20	1.4	25	20	1.4	30	12	1.4	40
	21	1.2	26	21	1.2	31	13	1.2	41
	22	1.0	27	22	1.0	32	14	1.0	42
	23	0.8	28	23	0.8	33	15	0.8	43
	24	0.6	29	24	0.6	34	16	0.6	44
	25	0.4	30	25	0.4	35	17	0.4	45

Table 5 – Loading and unloading stages during gas injection loading/unloading experiments ASR_Tau07_30gLU, ASR_Tau08_30gLU, and ASR_Tau14_30gLU.

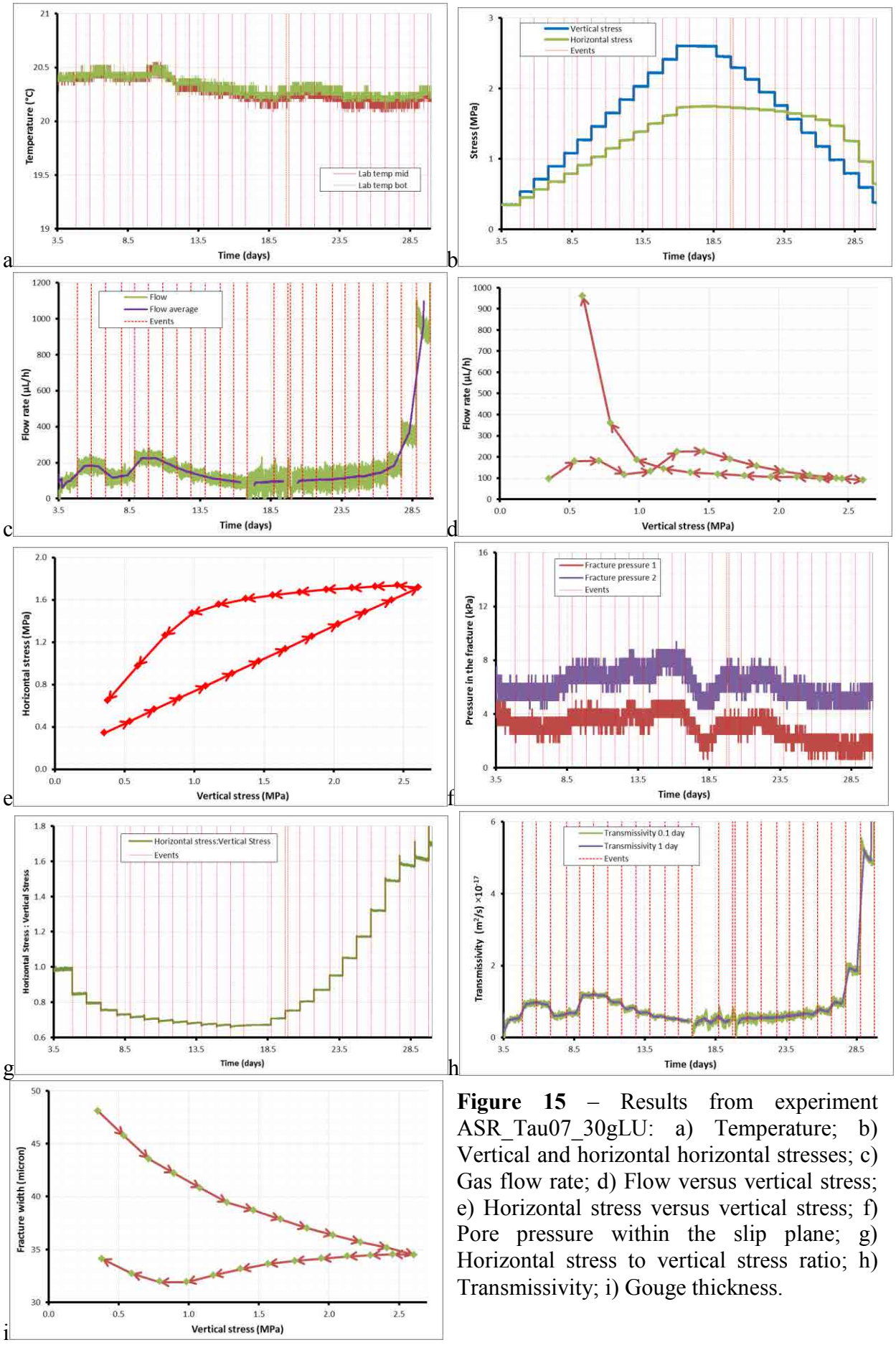

Figure 15 – Results from experiment ASR_Tau07_30gLU: a) Temperature; b) Vertical and horizontal horizontal stresses; c) Gas flow rate; d) Flow versus vertical stress; e) Horizontal stress versus vertical stress; f) Pore pressure within the slip plane; g) Horizontal stress to vertical stress ratio; h) Transmissivity; i) Gouge thickness.

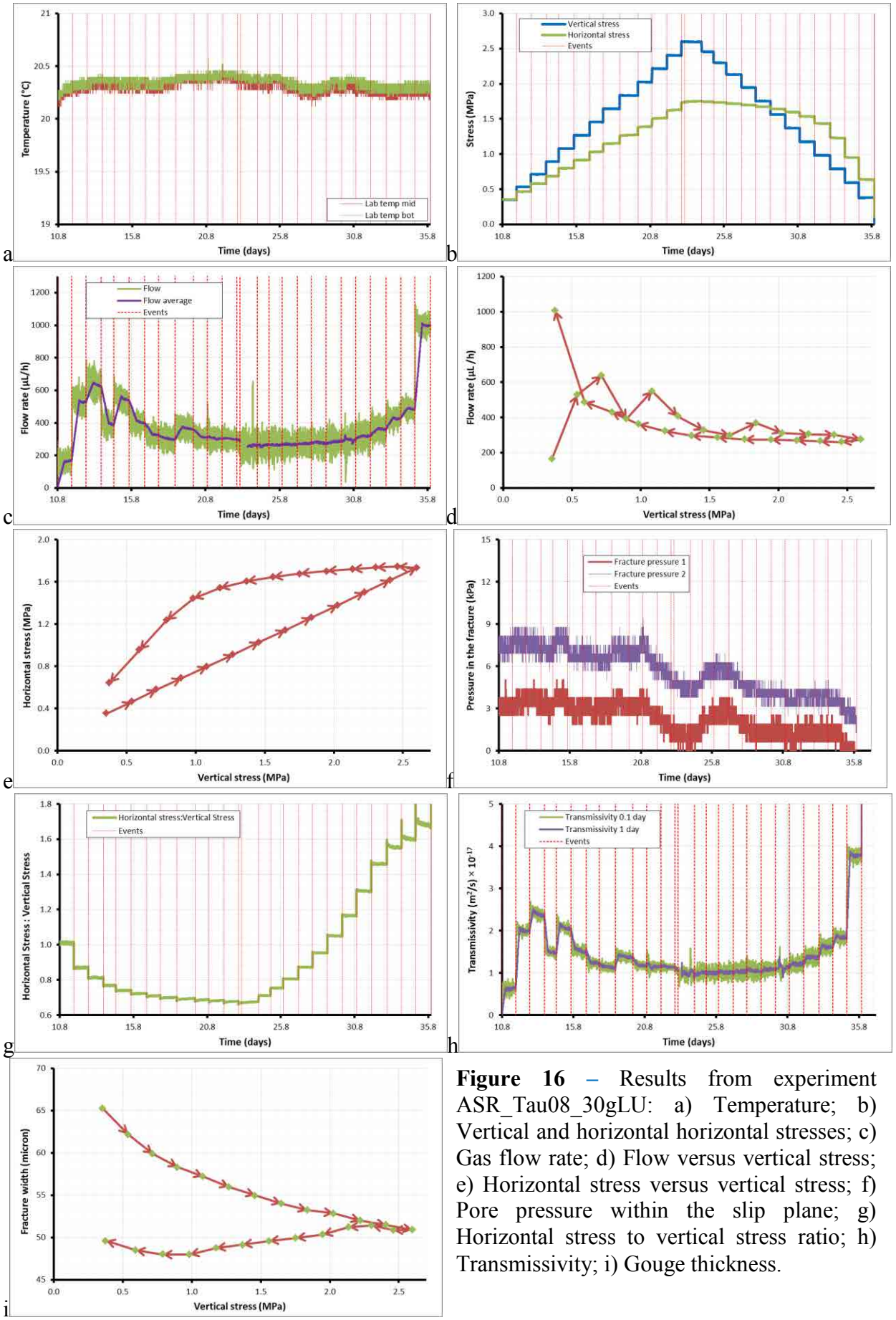

Figure 16 – Results from experiment ASR_Tau08_30gLU: a) Temperature; b) Vertical and horizontal horizontal stresses; c) Gas flow rate; d) Flow versus vertical stress; e) Horizontal stress versus vertical stress; f) Pore pressure within the slip plane; g) Horizontal stress to vertical stress ratio; h) Transmissivity; i) Gouge thickness.

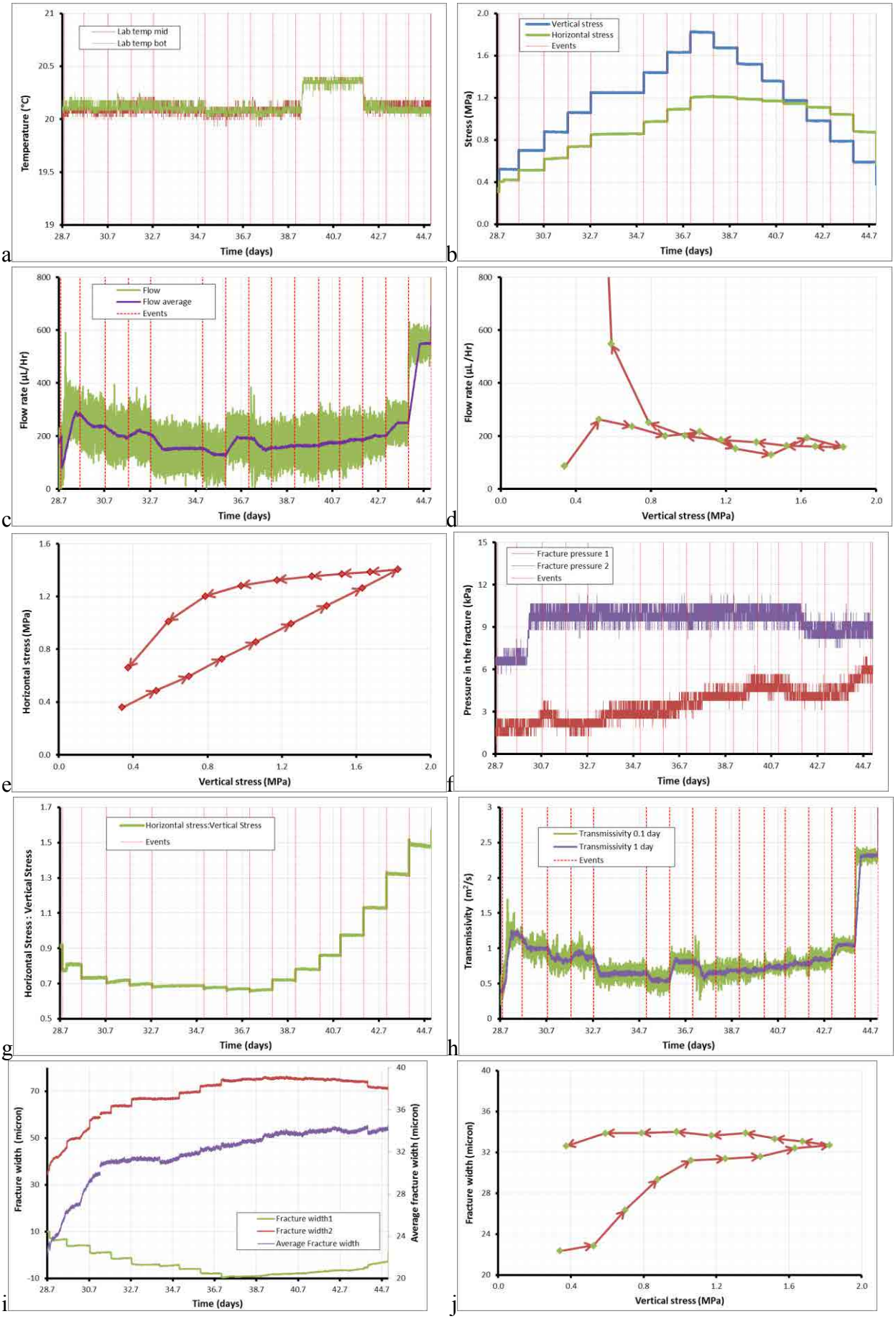

Figure 17 – Results from experiment ASR_Tau14_30gLU: a) Temperature; b) Vertical and horizontal horizontal stresses; c) Gas flow rate; d) Flow versus vertical stress; e) Horizontal stress versus vertical stress; f) Pore pressure within the slip plane; g) Horizontal stress to vertical stress ratio; h) Transmissivity; i) Gouge thickness; j) Gouge thickness with vertical load.

3.1.2.2 Discussion on gas injection loading-unloading experiments

The three gas injection loading-unloading experiments were initiated at dissimilar injection pressures of 3.55, 4.95, and 4.45 MPa. The injection pressures in these experiments corresponded to the pressures at which gas breakthrough was detected. Gas breakthrough pressure varied irrespective of identical sample preparation and sample assembly routines. This might be attributed to the formation of preferential pathways which exploited a multitude of inherent weaknesses within the gouge matrix which may have varied in each experiment. The flow rate of gas fluctuated seemingly in a random manner during the initial loading stages of the experiments (Figure 18a). However, during further loading a decrease in flow rate was observed. The random nature of flow rate variation during the initial loading stages may be due to the horizontal movement of the steel blocks during each step wise increase in load which in turn affected the geometry and nature of the gas flow-pathways. Flows observed during almost total unloading of the fracture were an order of magnitude higher than flow observed during the initial loading stages. The significant enhancement of flow during the unloading stages of the experiments may also be ascribed to the effect of movement of the steel blocks on the gas flow-pathways with each stepwise decrease in normal stress. Since different injection pressures were applied in each experiment, direct comparisons of the variations in flow rates between the different experiments were not attempted here. However, the flow rate of gas has been observed to be directly proportional to the injection pressure applied with higher injection pressures resulting in higher flow rates and vice versa. In experiment ASR_Tau07_30gLU run at an injection pressure of 3.55 MPa, the flow rate recorded at 1.8 MPa normal stress was 112 $\mu l.h^{-1}$. In ASR_Tau14_30gLU performed at an injection pressure of 4.45 MPa, flow rate of 158 $\mu l.h^{-1}$ was recorded. In the case of ASR_Tau08_30gLU performed at the uppermost injection pressures amongst the experiments reported here, a flow rate of 276 $\mu l.h^{-1}$ was recorded at a normal stress of 1.8 MPa.

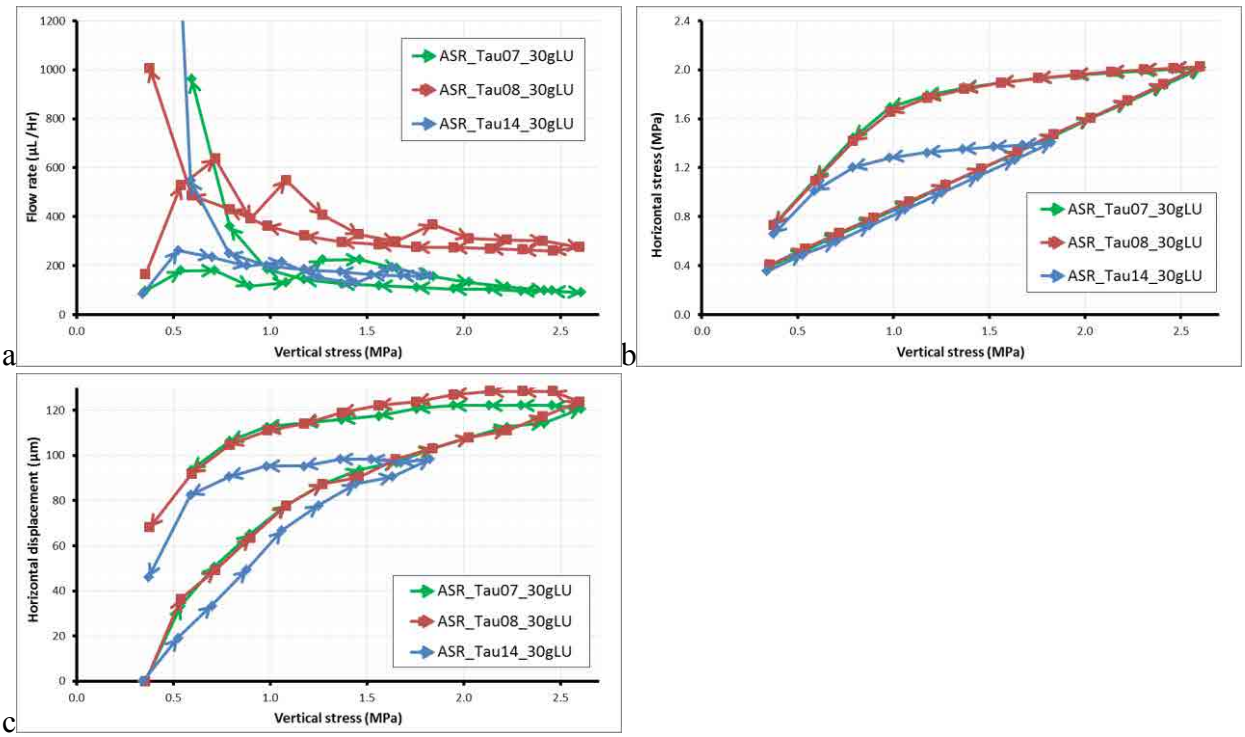

Figure 18 – Comparison of results from tests ASR_Tau07_30gLU, ASR_Tau08_30gLU, and ASR_Tau14_30gLU. a) Flow rate versus vertical stress; b) Horizontal stress versus vertical stress showing hysteresis during unloading; c) Horizontal displacement with vertical stress.

Horizontal stress increased linearly with step wise increase in vertical stress during loading. However, prominent hysteresis was observed in horizontal stress during the unloading stages of

the experiment (Figure 18b). As discussed earlier, this hysteresis may be attributed to the cohesive strength of the clay as a result of hydrogen bonding between adsorbed water molecules and atomically charged clay mineral surfaces (Ikari & Kopf, 2011; Marry *et al.*, 2008). Even though horizontal movement of the top block was prevented as much as possible during the course of the experiment by securing the movement of the force actuator, horizontal displacements of 100 – 120 μm were recorded in all the experiments. The amount of horizontal displacement appear to be linearly proportional to the degree of vertical loading with ASR_Tau14_30gLU which was subjected to a maximum vertical stress of 1.8 MPa recorded a horizontal displacement of 98 μm whereas ASR_Tau07_30gLU and ASR_Tau08_30gLU which were subjected to a maximum vertical stress of 2.6 MPa underwent horizontal displacements of 120 μm and 125μm respectively (Figure 18c). Since different gas injection pressures were employed in these experiments, the accurate determination of the effect of above mentioned horizontal displacement in decreasing the overall transmissivity of gas was not possible. However, shear displacement is a well-established self-sealing mechanism and would have contributed to some decrease in gas transmissivity and the contribution of shear mechanism in the decrease in gas transmissivity observed in these present experiments cannot be entirely ruled out.

3.1.3 Comparison of hydraulic flow and gas flow during loading and unloading

A direct comparison of the effect of water and gas transmissivity during loading and unloading was not feasible because of the different injection pressures used. Irrespective of these differences, a general decrease in flow rate was observed during loading in the case of both water and gas injection experiments (Figure 19a). Hydraulic flow through the gouge-filled slip plane decreased with corresponding increase in normal stress. In the case of gas injection, the flow rate through the slip plane decreased and increased with corresponding normal load increase suggesting that new gas flow-pathways were being formed during the initial loading stages. In the case of water injection experiments, flow rates increased to only 0.25 of the starting flow rate during unloading (Figure 14b). However, in the case of gas injection, the flow rates observed during the unloading stages were up to an order of magnitude higher than that observed during the loading stages (Figure 18a). These observations suggest that the mechanism of gas flow and water flow through a gouge filled fracture during loading and stress-relaxation are significantly different. The gas flow properties through fractures are likely to be severely influenced by stress relaxation during tectonic uplift compared to that of hydraulic flow. Moreover, the pore pressures within the experimental slip plane recorded via two orthogonally located pore pressure ports located 10 mm from the central injection port remained unchanged throughout the duration of the experiment irrespective of the high injection pressure (Figure 8b). This inhomogeneous distribution of pore pressures within the slip plane indicates that the fluid flow must have occurred via localised fluid pathways within the fracture plane as reported by Cuss *et al.* (2012).

In both water and gas injection experiments, horizontal stress increased linearly during loading (Figure 14a, Figure 19b). A close correlation between the horizontal stress to vertical stress ratio and increase in flow rate was observed during the unloading stage with manifest increase in flow rate during unloading occurring when the horizontal stress to vertical stress ratio values were above the starting ratio prior to loading. The present observations indicate the importance of horizontal stress to vertical stress ratio in determining the rate of fluid flow through fractures as reported by Zoback *et al.* (1985) and Brudy *et al.* (1997). Prominent hysteresis in horizontal stress was observed during the unloading stage and implies that understanding the stress history of the fractured rocks is of paramount importance in predicting the fluid flow behaviour. Complex stress histories are common for fractured crystalline bedrock which may have undergone complex subsidence and uplift histories, with multiple stressing and stress-relaxation events. Hence the predictions of fluid flow behaviour through fractures based on mere datasets of present-day stress regimes are insufficient and are likely to result in erroneous predictions of fluid flow behaviour.

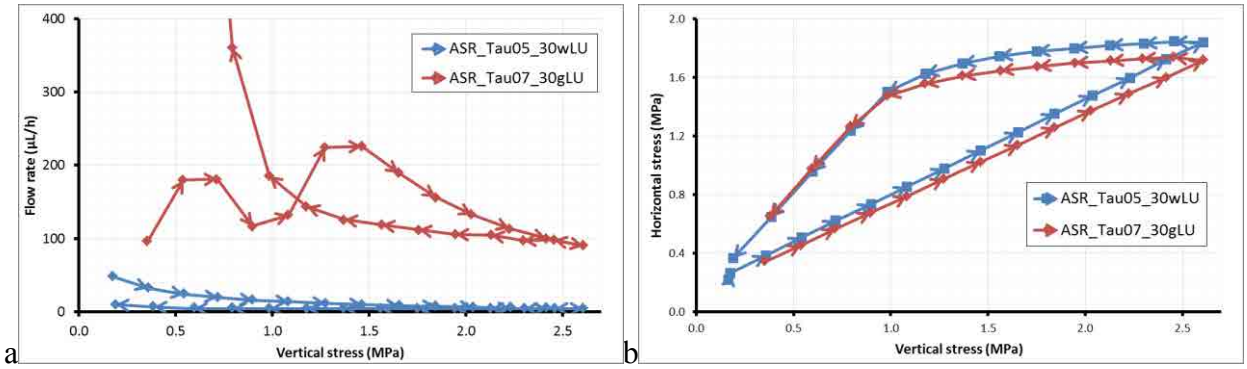

Figure 19 – Comparison of the hydraulic and gas injection experiments during loading and unloading. a) Flow rate versus vertical stress plot for water injection experiment ASR_Tau05_30wLU and gas injection experiment ASR_Tau07_30gLU. b) Horizontal stress versus vertical stress plot showing identical hysteresis in horizontal stress in the case of water and gas injection experiments.

3.2 FRACTURE TRANSMISSIVITY EVOLUTION DURING SHEAR

Test ASR_Tau02_30wLUS was carried out to understand the influence of shear on fracture fluid flow.

3.2.1 Experimental methodology

The experiment was performed using water as the permeant. The kaolinite gouge filled slip plane was subjected to independent variations in vertical load, horizontal displacement rate, and injection pressure while keeping other parameters constant. The different stages involved in ASR_Tau02_30wLUS experiment are listed in Table 6.

Stage	Pore pressure (kPa)	Vertical load pump (kPa)	Horizontal displacement rate (mm.day^{-1})	TIME (days)
1	1000	5000	0	0.0
2	1000	10000	0	5.8
3	1000	1000	0	12.1
4	1000	1000	0.3	14.2
5	1000	2000	0.3	17.8
6	1000	3000	0.3	27.0
7	1000	3000	0.9	33.9
8	1000	3000	0	38.1
9	2000	3000	0	39.8
10	2000	3000	0	40.1

Table 6 – Experimental stages of test ASR_Tau02_30wLUS.

Stages 1 to 3 aimed to understand the effect of vertical stress variation on fluid flow through the gouge. In stage 1 the vertical stress was increased to 0.96 MPa while the injection pressure was maintained constant at 1 MPa and the resulting flow rate was monitored. In stage 2 at day 5.8, the vertical stress was increased from 0.96 MPa to 1.86 MPa while maintaining other parameters constant. In Stage 3 the vertical stress was reduced to 0.15 MPa and the effect on flow rate was monitored. Stages 3 to 7 were carried out to understand the effect of shearing and vertical load on fluid flow through the gouge. In stage 4 the slip plane was displaced horizontally at a rate of 0.3 mm.day^{-1}. In stage 5 the vertical stress was increased from 0.17 MPa to 0.37 MPa and the corresponding variation in flow rate was analysed. In stage 6 the vertical stress was increased

from 0.37 MPa to 0.56 MPa whilst the sample still underwent shear. The horizontal displacement rate was increased from 0.3 mm.day^{-1} to 0.9 mm.day^{-1} in stage 7. Shearing was stopped in stage 8 and the hydraulic flow rate was monitored. In stage 9 the pore fluid injection pressure was increased from 1 MPa to 2 MPa and stage 10 signifies the end of the test. The time duration of each stage in ASR_Tau02_30wLUS and the boundary conditions of each stage are listed in Table 6.

3.2.2 Results and discussion

The results from stages 1 to 3 are shown in Figure 20. In stage 1 at a vertical stress of 0.96 MPa and a pore fluid injection pressure of 1 MPa an initial flow rate of 20 µl.h^{-1} was recorded. However the flow rate decreased rapidly from to 8 µl.h^{-1} within 7 hours. Subsequently, the flow rate further decreased gradually to 2.8 µl.h^{-1} at Day 6. The initial sharp decline in flow rate may be attributed to the healing or the blocking of the fluid pathways. Since the pathways constantly evolved with time, no steady state flow was reached. The flow rate decreased marginally to 1.4 µl.h^{-1} when the vertical stress acting on the slip plane was doubled in stage 2 from 0.96 MPa to 1.86 MPa. Data acquisition problems resulted in a loss of data from days 8.6 to 9.8. However, when the vertical stress was decreased in stage 3 from 1.86 MPa to 0.15 MPa, the hydraulic flow rate increased from 1.4 µl.h^{-1} to 50 µl.h^{-1}. As discussed in section 3.1.1, the hydraulic flow rate decreased during an increase in vertical stress and vice versa.

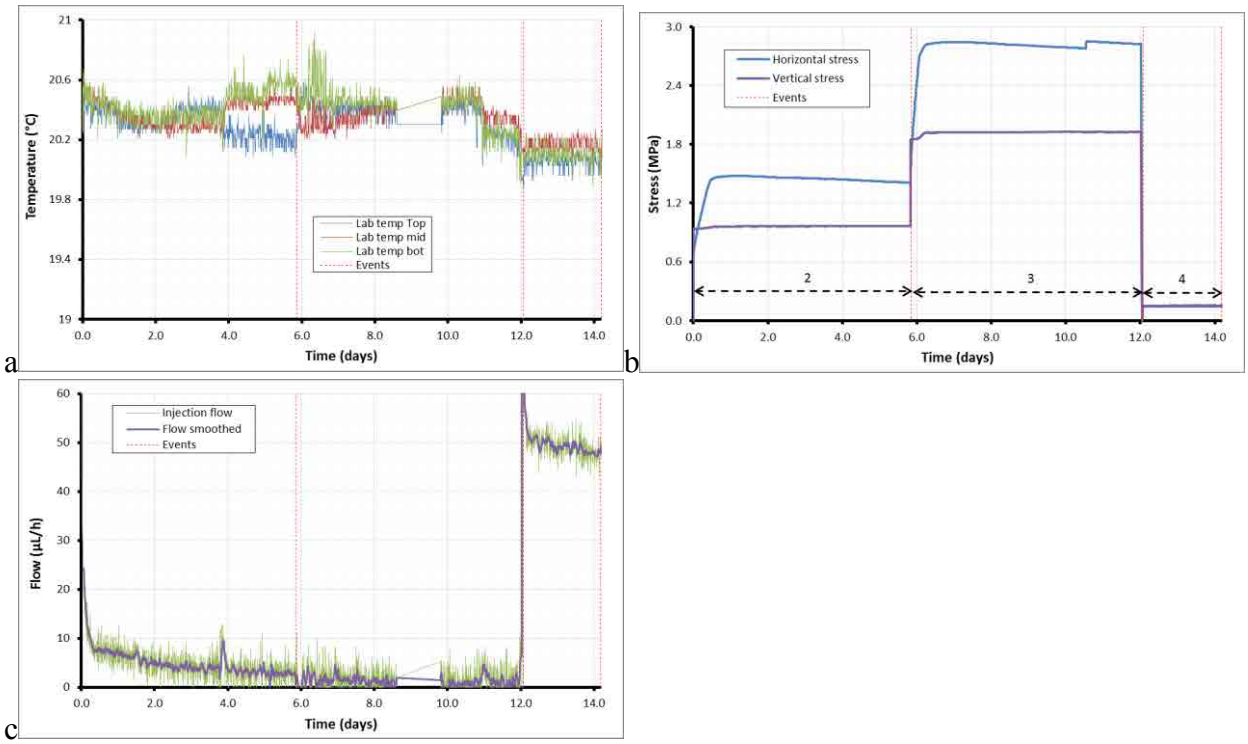

Figure 20 - Results from stages 1 to 3 of test ASR_Tau02_30wLUS. a) Temperature; b) Vertical and horizontal stress; c) Hydraulic flow.

The hydraulic flow rate under conditions of shear from stage 4 to 8 is shown in Figure 21. The temperature of the laboratory remained constant at 20 ± 0.2 °C until day 32.1 when an abrupt increase of 0.5 °C occurred. Spikes in hydraulic flow were observed during the temperature fluctuation. However the effect of the temperature perturbations was negligible on the overall flow rate. At stage 4, the slip plane was subjected to horizontal movement at a rate of 0.3 mm.day^{-1}. As a result of horizontal movement, the hydraulic flow rate decreased significantly from 50 µl.h^{-1} to 29 µl.h^{-1}. This suggests that shearing is an effective self-sealing mechanism and hence fractures undergoing shear are likely to be less conductive to hydraulic flow than fractures which are not experiencing any horizontal movement. An increase in vertical stress from 0.17 MPa to 0.37 MPa in stage 5 with simultaneous horizontal displacement rate of 0.3 mm.day^{-1}

resulted in a further reduction in hydraulic flow from 29 µl.h^{-1} to 15 ± 5 µl.h^{-1}. The flow rate failed to attain steady state conditions even after 10 days (stage 5). An increase in vertical stress from 0.37 MPa in stage 5 to 0.56 MPa in stage 6 led to a gradual decrease in flow rate from 15 ± 5 µl.h^{-1} to 9 ± 1 µl.h^{-1}. The horizontal displacement rate was increased from 0.3 mm.day^{-1} to 0.9mm.day^{-1} during stage 7 resulting in a decrease in flow from 9 ± 1 µl.h^{-1} to 5 ± 1 µl.h^{-1}.

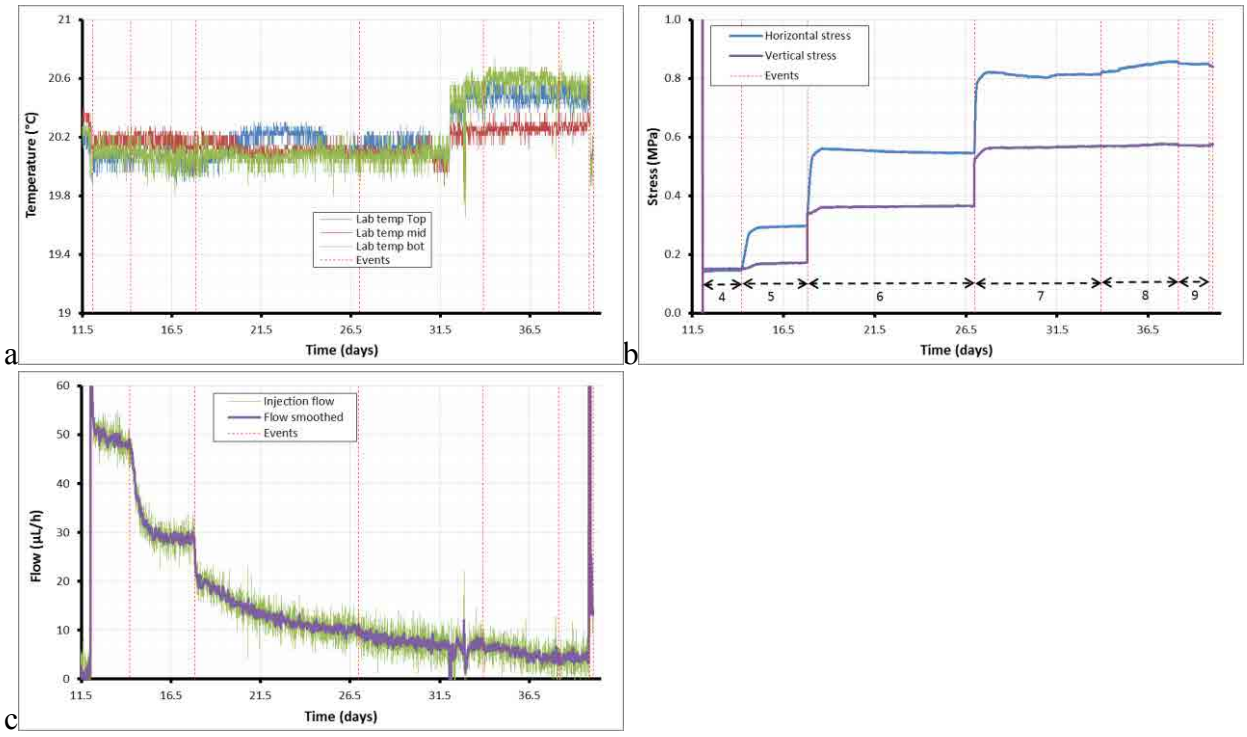

Figure 21 - Results from stages 4 to 9 of the ASR_Tau02_30wLUS experiment. a) Temperature; b) Horizontal and vertical stress; c) Flow.

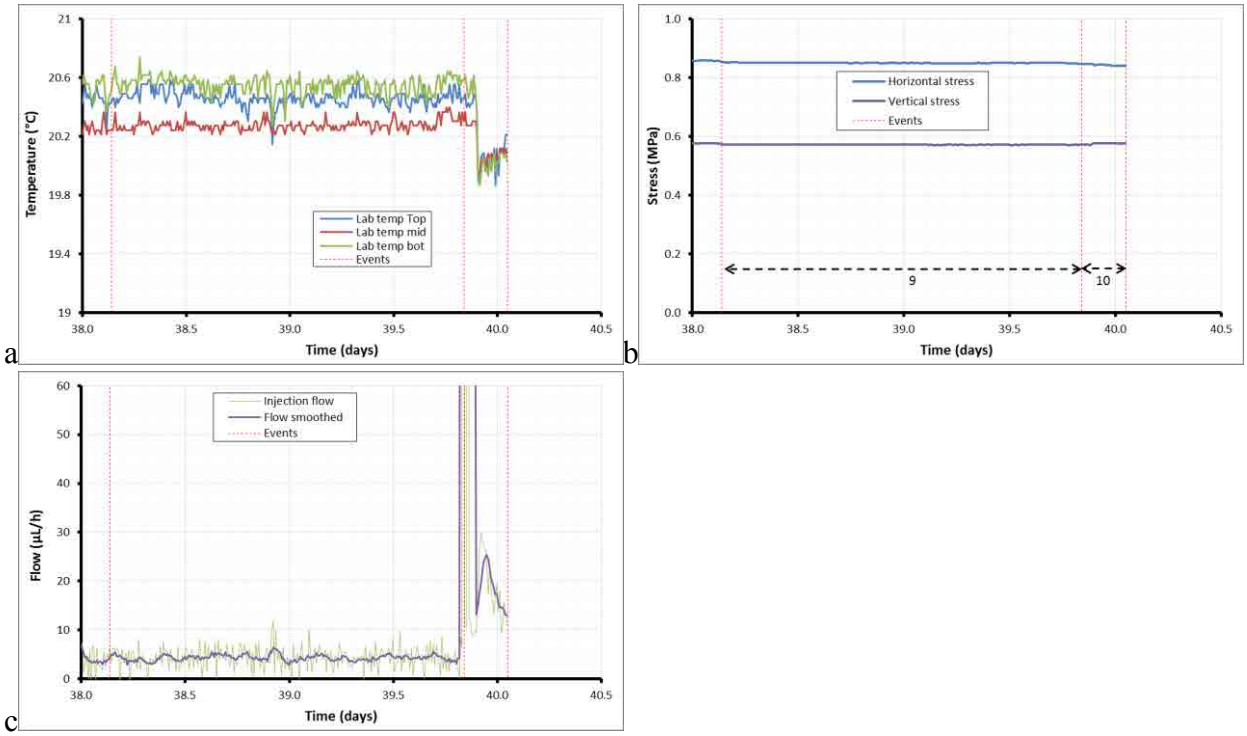

Figure 22 - Results from stages 8 and 9 of the ASR_Tau02_30wLUS experiment. a) Temperature; b) Horizontal and vertical stress; c) Flow rate.

Flow rate remained virtually unchanged at 5 ± 1 µl.h^{-1} when the horizontal movement was stopped in stage 8 (Figure 22). This observation suggests that the sealing of fluid flow-pathways achieved as a result of shear displacement is perpetual and is not likely to be affected by the ending of any shear displacement that the rocks have undergone. The decrease in hydraulic flow-rate through the kaolinite gouge observed in the present experiment might be due to the stacking of individual kaolinite clay platelets in an orientation parallel to its c-axis thus forming a dense framework of clay material and concomitant reduction in bulk porosity of the gouge. However, shear experiments on intact Opalinus Clay by Cuss *et al.* (2011) have shown evidence of enhanced flow as a result of the formation of new fractures during shearing. An increase in hydraulic injection pressure from 1 MPa to 2 MPa during stage 9 resulted in an increase in hydraulic flow from 5 ± 1 µl.h^{-1} to 20 ± 7 µl.h^{-1} even though steady state flow was not attained.

Flow progressively decrease form 50 µl.h^{-1} at a vertical stress of 0.15 MPa to 7 µl.h^{-1} at a vertical stress of 0.56 MPa (Figure 23a). From the results presented in Figure 20, Figure 21, and Figure 22 along with the results presented in Figure 23b, we conclude that an increase in vertical stress and shear rate leads to a general decrease in hydraulic flow rate and on the other hand an increase in hydraulic injection pressure results in an increase in hydraulic flow rate.

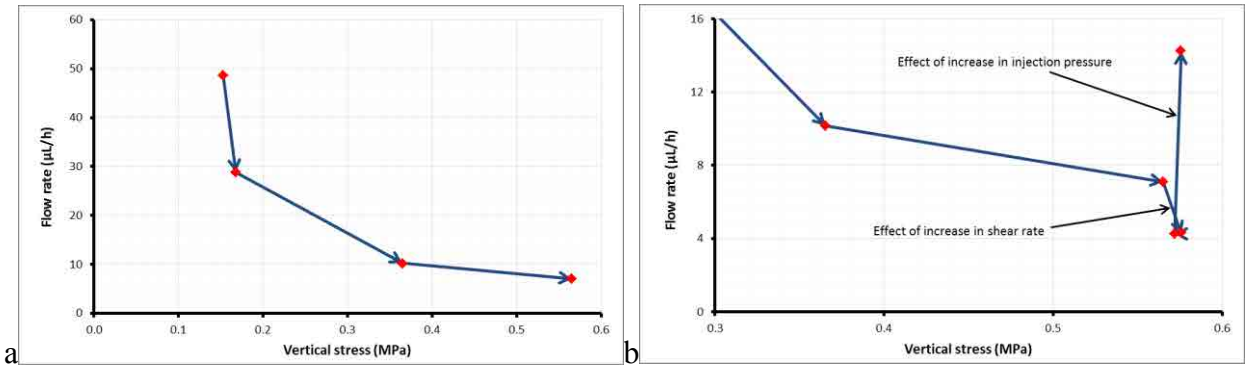

Figure 23 – Summary of observations for test ASR_Tau02_30wLUS. a) Variation in flow rate with increasing vertical stress; b) Effect of increase in shear rate and increase in injection pressure on hydraulic flow rate.

3.2.3 The effect of shearing on hydraulic flow rate

In order to understand the magnitude of flow rate reduction during shearing, a comparison of hydraulic flow rate evolution during loading-unloading experiments with horizontal movement (ASR_Tau02_30wLUS) and without horizontal movement (ASR_Tau05_30wLU) was done. The results are presented in Figure 24. The initial hydraulic flow rates recorded in the experiments ASR_Tau05_30wLU and ASR_Tau02_30wLUS were similar at 49 µl.h^{-1}. However, in ASR_Tau02_30wLUS the slip plane was subjected to shear at a rate of 0.3 mm.day^{-1} and the horizontal movement resulted in approximately 40% reduction in hydraulic flow rate (Figure 24). With progressive loading of the slip plane under conditions of shear resulted in a flow rate of 7 µl.h^{-1} at a vertical stress of 0.56 MPa. On the other hand, under conditions of no horizontal movement, vertical stress as high as 2.04 MPa was required to reduce the hydraulic flow rate to 7 µl.h^{-1}. These observations suggest that shear displacement along a fracture plane is an efficient sealing mechanism and the effect of shear on sealing is considerably more pronounced than that of the effect of an increase in vertical stress.

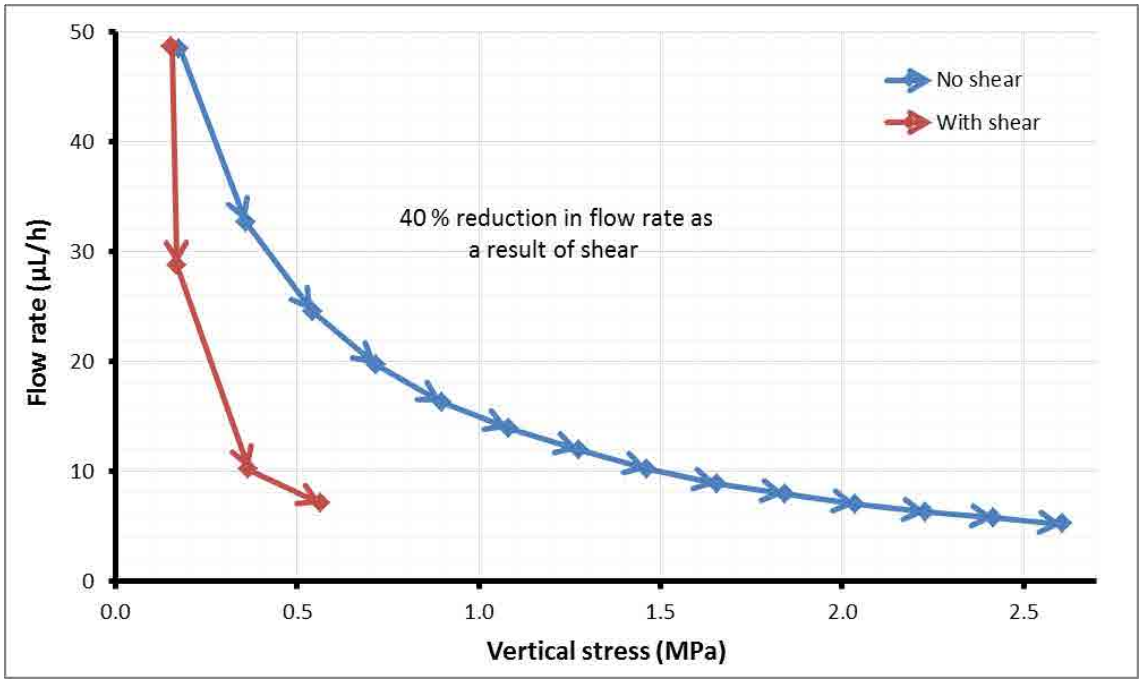

Figure 24 - The effect of shearing on hydraulic flow, resulting in a 40% reduction in flow.

3.3 INVESTIGATION OF FAULT-VALVE BEHAVIOUR DURING GAS FLOW

Experiment ASR_Tau06_30gGI was initially planned to understand the effect of loading and unloading on the rate of flow of helium gas through a kaolinite gouge-filled experimental slip plane. A comparison with the observations of hydraulic flow (test ASR_Tau05_30wLU) could then be made. However, the injection pressure of 1 MPa applied was far below the gas entry/breakthrough pressures required for gas flow through the slip plane. Consequently it was decided to test for gas entry pressures in the current experimental setup and investigate the likelihood of studying the fault-valve behaviour during gas flow through fractures.

3.3.1 Experimental methodology

Experiment ASR_Tau06_30gGI included 7 stages lasting 28 days in total. Stage 1 was performed at a vertical stress of 0.17 MPa and a constant gas injection pressure of 1 MPa, with gas flow monitored. Since no gas flow was detected, constant gas injection rate was commenced. In stage 2, gas was injected into the slip plane at a constant injection rate of 500 $\mu l.h^{-1}$ and the corresponding increase in gas pressure was monitored. As the gas entry/breakthrough pressure was reached an abrupt drop in gas pressure was anticipated. Stages 3 to 7 represent stages of discrete gas injection rate where multiple gas breakthrough events occurred. The gas injection rates employed in the different stages in ASR_Tau06_30gGI are shown in Figure 25a.

3.3.2 Results and discussion

Results for the entire duration of the fault-valve behaviour test (ASR_Tau06_30gGI) are presented in Figure 25. Detailed descriptions of the results from each stage of the experiment are given below.

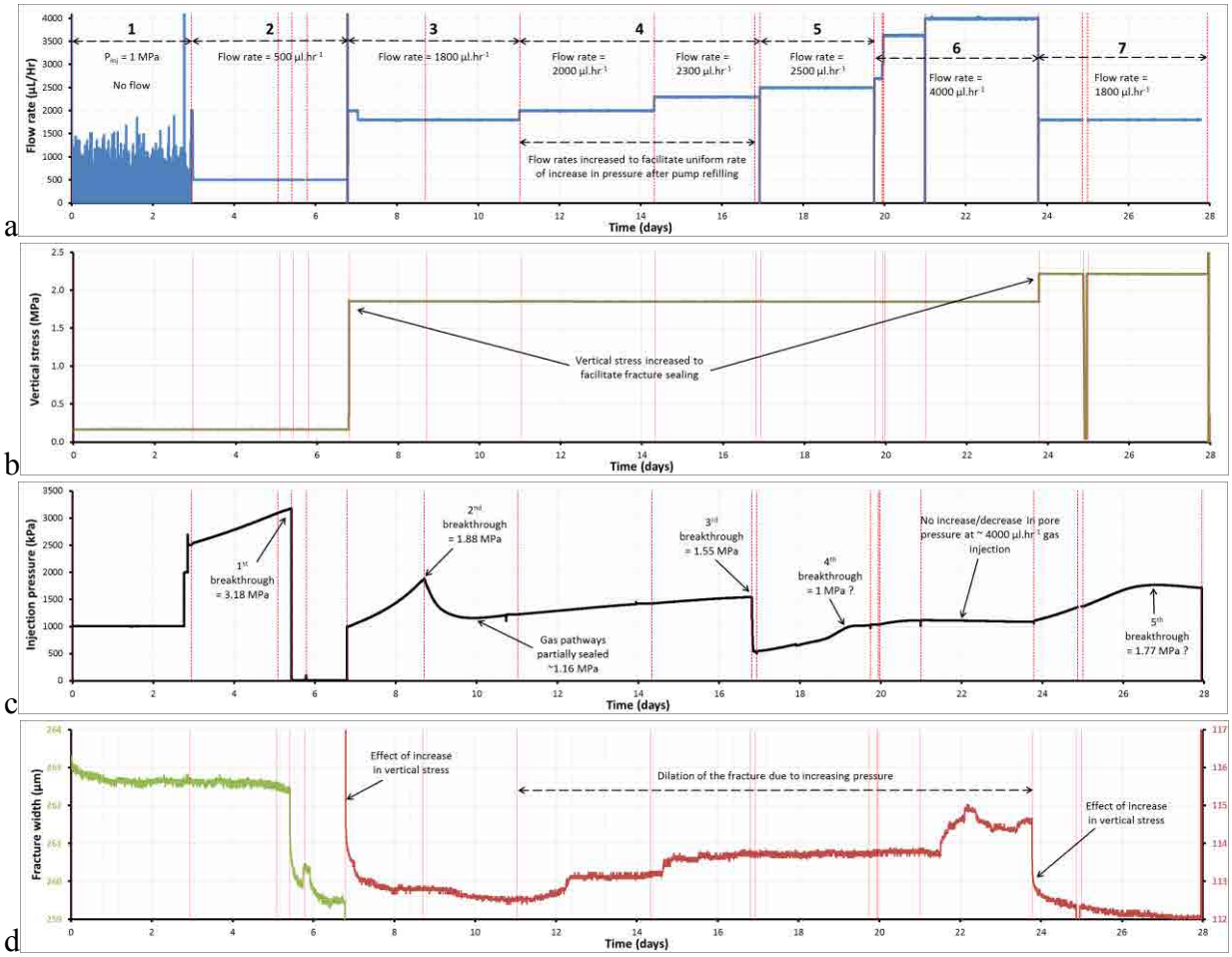

Figure 25 - Results from the fault-valve behaviour test (ASR_Tau06_30gGI). a) Flow rate; b) Vertical stress; c) Gas injection pressure; d) Fracture width.

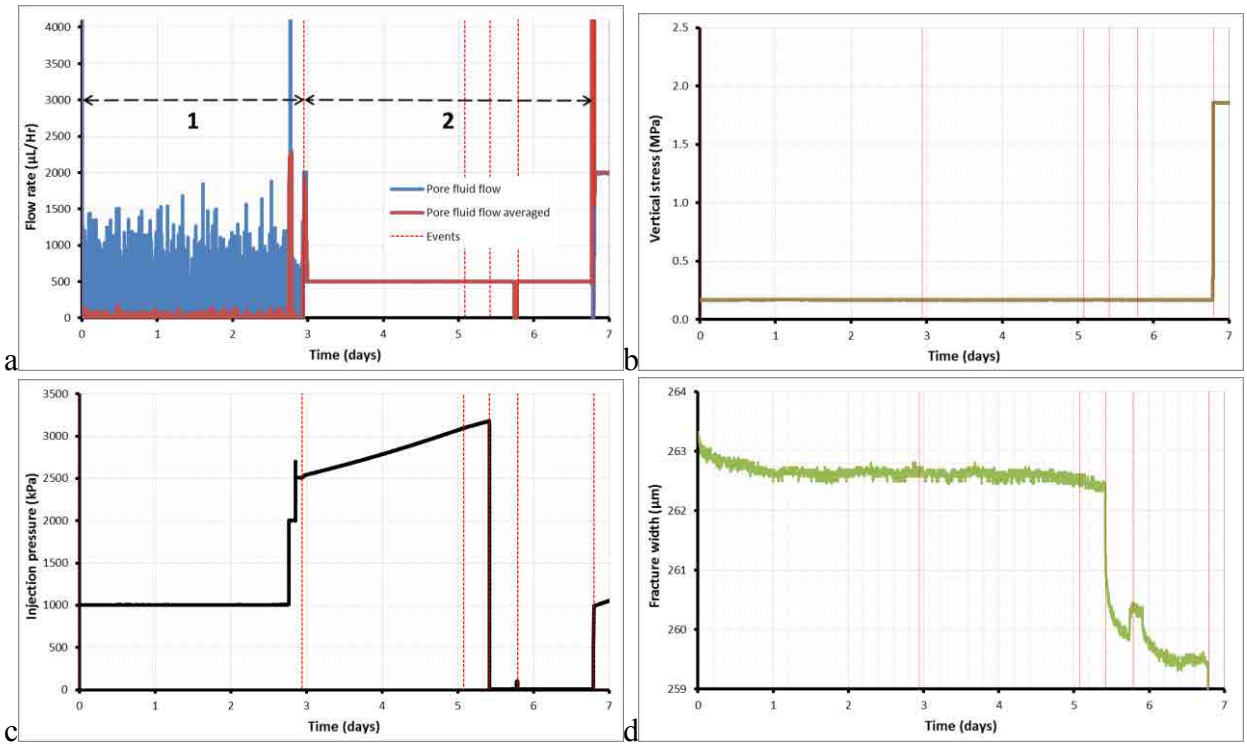

Figure 26 – Stage 1 – 2 of the fault-valve behaviour test (ASR_Tau06_30gGI). a) Flow rate. In stage 1, no flow was detected. Stage 2 was conducted as a constant flow gas injection test; b) Vertical stress; c) Injection pressure; d) Fracture width showing an abrupt decrease in gouge thickness after the gas breakthrough event.

In stage 1 the gas injection pressure was maintained constant at 1 MPa and resulting flow of gas through the slip plane was monitored. No flow of gas was detected and hence it was concluded that gas injection pressure had to be increased so as to achieve gas entry and subsequent gas flow. Vertical stress was maintained constant at 0.17 MPa and the thickness of the gouge material was 262.6 microns. Maintaining the vertical stress at 0.17 MPa, stage 2 was commenced by increasing the gas injection pressure to 2.5 MPa followed by a constant gas injection rate of 500 $\mu l.h^{-1}$. The constant gas injection rate resulted in an increase in gas pressure from 2.5 MPa at day 2.9 to 3.18 MPa at day 5.4. Subsequently gas entry and breakthrough occurred and the gas pressure dropped from 3.18 MPa to 0 MPa. The gas breakthrough event was associated with removal of gouge material from the slip plane as displayed by the abrupt decrease in gouge thickness from 262.6 microns to 260.7 microns during the gas breakthrough event. Flow rate was kept constant for an additional period of time (from day 5.4 to day 6.8) to test whether the formed gas pathway(s) had self-sealed. The gouge could not sustain any pressure and showed that the pathway(s) had not self-sealed and was still conductive. Subsequently it was decided to increase the vertical stress so as to facilitate sealing.

Stage 3 started at Day 6.8 with an injection rate at 2000 $\mu l.h^{-1}$ (Figure 27). However, at day 7 the gas injection rate was reduced from 2000 $\mu l.h^{-1}$ to 1800 $\mu l.h^{-1}$. The gas pressure increased gradually with gas injection from 1 MPa at day 6.8 to 1.84 MPa at day 8.7. Gas breakthrough occurred at day 8.7 and as a result gas pressure dropped from 1.84 MPa to 1.16 MPa. Constant gas injection rate of 1800 $\mu l.h^{-1}$ was maintained in stage 3 after gas breakthrough to test the sealing of the gas pathway(s) (Figure 27). By Day 10 the pressure reduction had stabilised and resulted in a slow increase in gas pressure. An increase in gas pressure will be observed when the rate of injection of gas into the system is greater than the rate at which the gas escapes through the gas pathways. The gradual sealing of the gas pathways can be deciphered easily from the gas pressure versus time curve in Figure 27c. After the gas breakthrough event new gas flow pathways formed and the rate of gas escaping through the pathways was more than the gas being injected into the slip plane. As the gas pathways gradually sealed the rate of decline in gas pressure decreased up until between days 9.8 and 10 when no decrease or increase in gas pressure was observed. The steady state in gas pressure between days 9.8 and 10 marks the stage when the rate of gas injection was equal to the rate of gas leakage. With time, the gas pathway(s) exhibited improved sealing and the gas pressure started to increase with continued gas injection. The thickness of the gouge (fracture width) remained constant at 113 microns after the gas breakthrough event which suggests that the gas breakthrough event between stage 3 and 4 might have occurred as a result of the reopening of the pre-existing gas pathway(s) which formed during the first gas breakthrough event reported in stage 2 (Figure 26c).

Satge 4 was conducted with a continuous gas injection at a rate of 2000 $\mu l.h^{-1}$ resulting in a steady rate of increase in gas pressure from day 11 to 14 until steady state gas pressure was observed between day 13.89 and 14.33 (Figure 28). The gas injection rate was increased from 2000 $\mu l.h^{-1}$ to 2300 $\mu l.h^{-1}$ and led to a steady increase in gas pressure until the third breakthrough event occurred at day 16.8 at a gas pressure of 1.54 MPa. After the breakthrough event, gas pressure dropped to 0.57 MPa. In stage 5, the water-gas interface vessel was refilled with 200cc of helium gas at 0.57 MPa and the constant gas injection rate experiment was resumed at an injection rate of 2500 $\mu l.h^{-1}$. With continued gas injection the gas pressure increased from 0.57 MPa to 1.0 MPa. The inhomogeneous evolution of the gas flow-pathways can be deciphered from the variation in slope of the gas pressure curve in Figure 28c. An obvious variation in slope was observed at day 18.6 indicating that the pathways had undergone some kind of modification which has resulted in enhanced sealing. The fourth gas breakthrough event occurred at a gas pressure of 1.0 MPa. Moreover, after the gas breakthrough event the gas pressure remained more or less steady at 1.0 MPa indicating that the breakthrough event was associated with the gradual opening of the pre-existing gas pathways. With continuous gas injection, fracture width increased from 112.5 μm to 113.7 μm. This increase in fracture width may be due to the minute dilation of the slip plane as a result of the formation of gas pathways and/or due to the heave

resulting from the excess gas pressure at the centre of the slip plane. Following the fourth gas breakthrough event, the flow of gas occurred at a steady rate as observed by no increase in gas pressure irrespective of a gas injection rate of 2500 µl.h^{-1}.

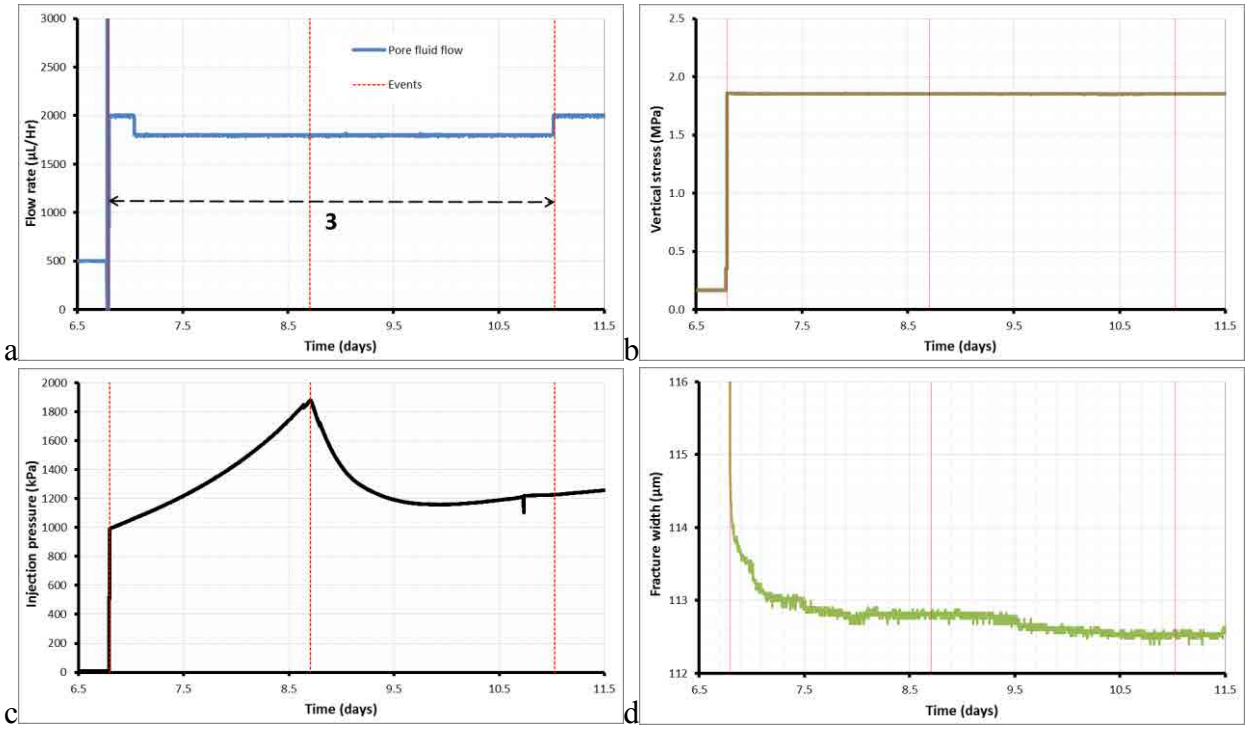

Figure 27 – Stage 3 of the fault-valve behaviour test (ASR_Tau06_30gGI). a) Flow rate; b) Vertical stress. In order to facilitate sealing, the vertical stress was increased from 0.17 MPa to 1.86 MPa at the beginning of stage 3. c) Gas pressure with continuous gas injection at a rate of 1800 µl.h^{-1}; d) Fracture width.

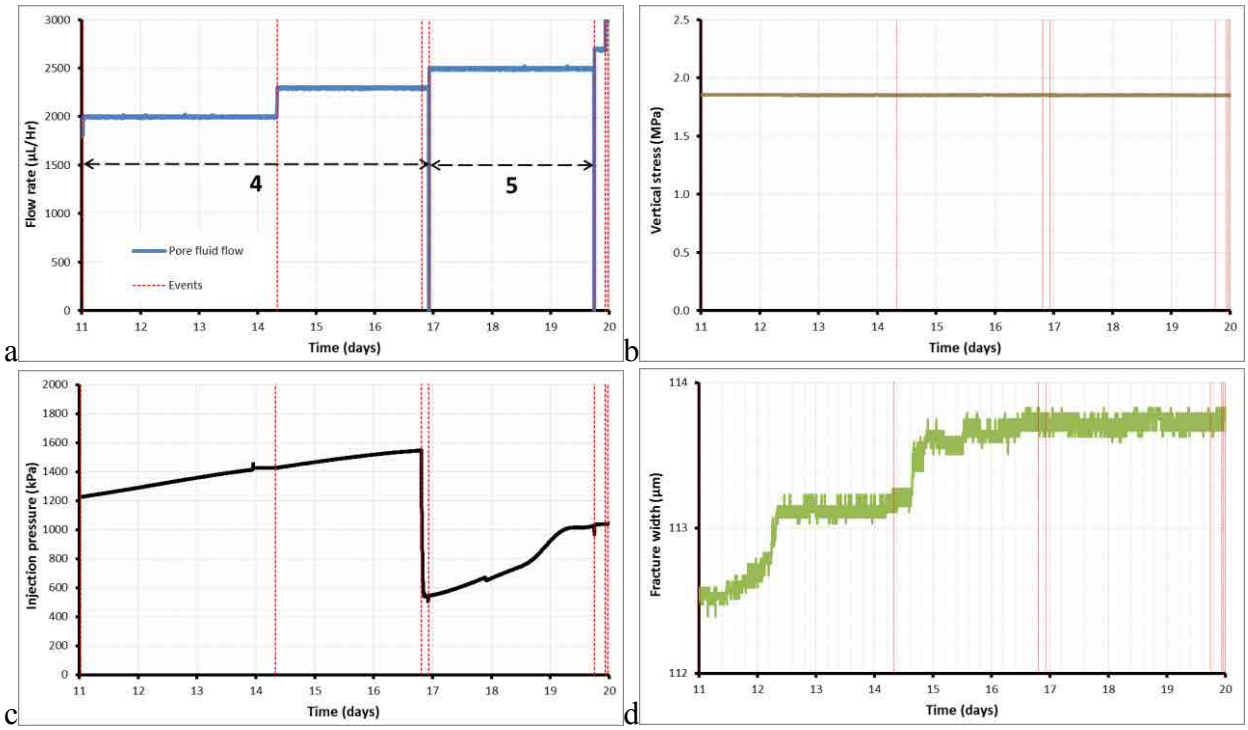

Figure 28 - Stage 4 – 5 of the fault-valve behaviour test (ASR_Tau06_30gGI). a) Flow rate; b) Vertical stress; c) Gas pressure; d) Fracture width.

The gas injection rate was increased to 4000 µl.h^{-1} in stage 6. This increase in gas injection rate resulted in only a trivial increase in gas pressure as the gas flow through the pathways remained

under steady state from day 21 to day 24 (Figure 29). An increase in fracture width from 113.6 µm to 115 µm was observed suggesting that the gas flow was accompanied by dilation of the gouge. In stage 7 the vertical stress was increased from 1.8 MPa to 2.2 MPa to facilitate sealing of the fractures. An abrupt decrease in fracture width from 114.6 µm to 112.8 µm resulted and the flow rate was reduced to 1800 µl.h^{-1}. The gas pressure increased at a steady rate until the fifth gas breakthrough event occurred at a pressure of 1.77 MPa at day 26.4.

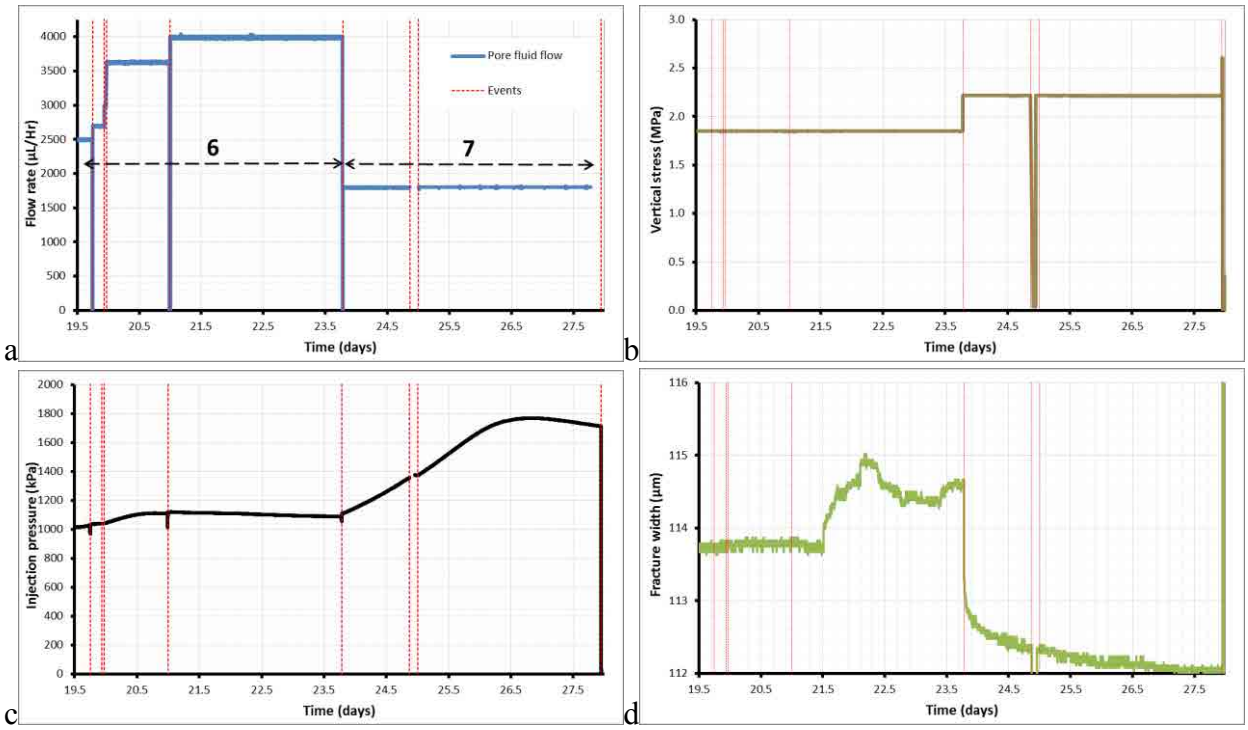

Figure 29 – Stage 6 – 7 of the fault-valve behaviour test (ASR_Tau06_30gGI). a) Flow rate; b) Vertical stress; c) Gas pressure; d) Fracture width.

3.3.3 Conclusions

The results from the seven stages of the ASR_Tau06_30gGI experiment demonstrate the fault valve behaviour associated with the flow of fluids (gases and water) through fractures under natural conditions. The first gas breakthrough event was associated with the formation of the gas pathways and associated expulsion of gouge material from the experimental slip plane. No significant variations in pore pressures were observed within the slip plane throughout the full duration of the experiment (Figure 30) suggesting that the gas migration occurred via localised channels formed as a result of dilation of the kaolinite clay gouge.

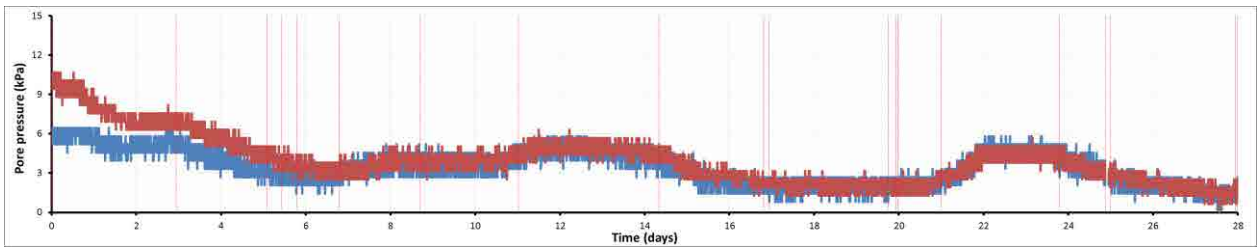

Figure 30 – Evolution of pore pressure within the slip plane during the fault-valve behaviour test (ASR_Tau06_30gGI). No significant increase in pore pressure was observed.

The pressure at which gas breakthrough occurred decreased with each subsequent gas breakthrough event. This decrease in gas breakthrough pressure suggests that each gas

breakthrough event occurs via the opening and closing of the pre-existing gas pathway(s). An increase in vertical stress has been observed to facilitate the sealing of the flow pathways. The results suggests that a close relationship exists between the vertical stress acting on the slip plane, gas injection rate and the gas breakthrough pressures observed. An increase in vertical stress or an increase in gas injection rate results in higher breakthrough pressures. In exceptional circumstances, steady state flow may be achieved when the rate of gas inflow equals the rate of gas outflow from the fracture plane as observed in stage 6 following the fourth gas breakthrough event. The occurrence of natural fractures with steady state flow is likely provided constant gas generation rates can be achieved either by the maturation of kerogens in an oil reservoir or as a result of various chemical processes (corrosion, radiolysis etc.) occurring within a radioactive waste repository.

4 The effect of slip-plane orientations on gas flow through gouge-filled fractures.

A series of experiments were performed to understand the effect of different slip plane orientations on gas entry/breakthrough and subsequent gas flow. Gas injection experiments were performed at a constant injection rate on experimental slip planes with orientations of 0°, 15°, 30°, and 45° with respect to maximum horizontal stress σ_{Hmax} direction.

4.1 EXPERIMENTAL METHODOLOGY

Kaolinite paste was prepared following the methodology elaborated in Section 2.2. The paste was uniformly smeared on the surface of the top block and the top block was aligned over the bottom block. The axial loading system was engaged using a hydraulic jack connected to a syringe pump set at a pressure of 10 MPa. This imparted a constant vertical stress on the slip plane, the magnitude of which was determined by the orientation of the slip plane with respect to horizontal as shown in Table 7. The gas injection system was fitted with a water-gas interface vessel as mentioned in Section 2.3.2. During the gas injection experiments, the volume of gas in the interface vessel at the beginning of the experiment was maintained at a constant volume of 200 cc at 4 MPa gas pressure. The experiment was commenced by the injection of water into the interface vessel at a constant rate of 700 $\mu l.h^{-1}$. As a result, the pressure of the helium gas within the interface vessel gradually increased until gas pressure reached the gas breakthrough pressure and gas entered the gouge filled slip plane. The evolution of gas pressure with constant injection of water was predicted using the Boyles law and the number of moles of gas entering the slip plane was estimated using the ideal gas law.

Slip plane orientation (degrees)	Pressure on Hydraulic jack (MPa)	Normal stress on the slip plane (MPa)
0	10	2.13
15	10	2.06
30	10	1.84
45	10	1.50

Table 7 – The normal stress acting on the experimental slip plane at different orientations. The normal stress decreases as the slip plane orientation increases.

A total of 22 gas-injection experiments were conducted, as shown in Table 8. Due to repeatability issues, a minimum of three tests were conducted at each angle. Due to time limitations, it was not possible to perform multiple testing at different fracture angles during active shearing.

	Experiment	Start date	Slip-plane orientation	Gas Injection test number
2	ASR_Tau09_30gGI	27-Sep-11	30°	1
4	ASR_Tau11_30gGI	11-Oct-11		2
5	ASR_Tau12_30gGI	09-Nov-11		3
6	ASR_Tau13_30gGI	18-Nov-11		4
9	ASR_Tau15_00gGI	14-Feb-12	0°	5
10	ASR_Tau16_00gGI	23-Feb-12		6
11	ASR_Tau17_00gGI	05-Mar-12		7
12	ASR_Tau18_15gGI	22-Mar-12	15°	8
13	ASR_Tau19_15gGI	03-Apr-12		9
14	ASR_Tau20_15gGI	18-Apr-12		10
15	ASR_Tau21_00gGI	01-May-12	0°	11
16	ASR_Tau22_00gGI	14-May-12		12
17	ASR_Tau23_00gGI	28-May-12		13
18	ASR_Tau24_00gGI	06-Jun-12		14
19	ASR_Tau25_45gGI	19-Jun-12	45°	15
20	ASR_Tau26_45gGI	03-Jul-12		16
40	ASR_Tau27_45gGI	13-Jul-12		17
41	ASR_Tau28_00gGIS	25-Jul-12	0°	18
42	ASR_Tau29_00gGIS	06-Aug-12		19
44	ASR_Tau30_30gGIS	29-Aug-12	30°	20
45	ASR_Tau31_45gGIS	10-Sep-12	45°	21
46	ASR_Tau32_15gGIS	25-Sep-12	15°	22

Table 8 – List of gas-injection experiments conducted.

The following sections are discussed in terms of similar test protocols, i.e. for each fracture angle, as opposed to chronological order. As all tests were conducted as close to identical conditions as possible no influence of time was seen in the test results.

4.2 GAS BREAKTHROUGH EXPERIMENTS ON A SLIP PLANE ORIENTATION OF 0°

A total of five gas injection experiments were conducted on a flat slip plane, i.e. at an orientation of 0° with respect to the slip direction. As stated previously, each test was performed as identical as possible, with identical water content of gouge produced, similar vertical load, similar volumes of gas, and identical gas injection rates. The only parameter that is likely to have varied between tests was the thickness of the gouge at the start of the experiment. However, as best as could be established, this did not vary significantly between tests as the gouge became very thin in all tests.

4.2.1 Test ASR_Tau15_00gGI (Gas test 5)

Test ASR_Tau15_00gGI was the fifth gas injection test conducted and was performed on a fracture oriented 0° to the slip plane direction. The results of the test are summarised in Figure 31. As can be seen in Figure 31a, the gas injection experiment resulted in a maximum gas pressure of approximately 8 MPa, although peak pressure was not achieved due to limited volumes of helium. In the early stages of the test, the fracture could be seen to compress (Figure 31c). However, the capacitance sensor used to measure vertical movement of the apparatus malfunctioned at about Day 1.8. The dilation data is viewed as secondary to the main objectives of the experiment and therefore the test was continued. A secondary measurement system also gives information about the fracture thickness (Figure 31d). A pair of fracture width eddy current sensors similarly showed that the fracture compressed. At the time when the capacitance sensor failed, the fracture width sensors show that the fracture began to dilate; this corresponded with the onset of pressure deviation from the ideal gas law prediction and is likely to signify gas entry. Approximately Day 2.8, the fracture width sensors also malfunctioned.

Figure 31b shows the difference between the gas pressure observed and the predicted pressure from the ideal gas law. As seen, this data suggests that gas started to enter the fracture at around Day 2.2 when the gas pressure was 4,770 kPa. Figure 31e shows the average flow at STP into the fracture, with gas entry inferred to be approximately 5,000 kPa. Both methods used to predict gas entry gave similar results.

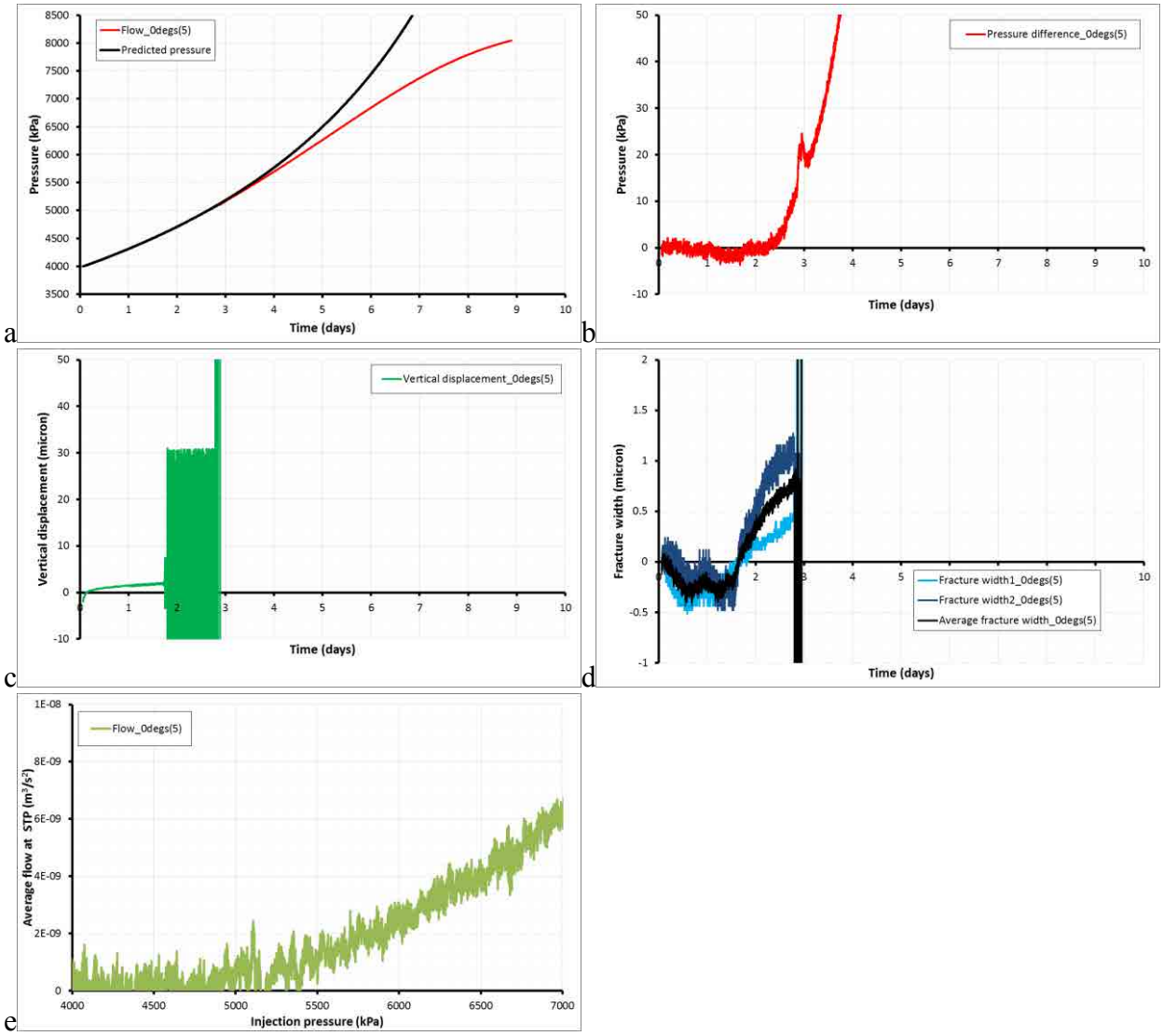

Figure 31 – Results for gas injection test 5 / ASR_Tau15_00gGI. a) Gas injection pressure compared with prediction from ideal gas law; b) comparison of gas injection and ideal gas law as a way of predicting gas entry pressure; c) normal displacement [note malfunctioned]; d) fracture width [note malfunctioned]; e) flow into the slip plane as a way of predicting gas entry pressure.

4.2.2 Test ASR_Tau16_00gGI (Gas test 6)

The second test conducted on a fracture oriented 0° to the slip-plane was ASR_Tau16_00gGI; the sixth gas injection test conducted. The results of the test are summarised in Figure 32. As can be seen in Figure 32a, the gas injection experiment resulted in a maximum gas pressure of approximately 17.5 MPa, although peak pressure was not achieved due to limited volumes of helium. This was significantly higher than the gas pressure seen in test ASR_Tau15_00gGI. In the early stages of the test, the fracture could be seen to compress approximately 20 µm (Figure 32c), much more than in the previous test. The compression can be seen to be non-uniform, with minor dilational events seen at Day 1 and Day 3.5. At Day 5 the sensor showed significant dilation. The pair of eddy current fracture width sensors showed a complex history (Figure 32d). One sensor shows simple compression throughout the test history. The other showed much

greater compression, with significant dilation events; one of these clearly corresponded with the dilation seen in the normal displacement and the other corresponds with a minor normal load dilational event. One eddy current sensor was mounted either end of the top-block, therefore the data suggest that only one end of the fracture was significantly compressing or dilating.

Figure 32b shows the difference between the gas pressure observed and the predicted pressure from the ideal gas law. As seen, this data suggests that gas started to enter the fracture at around Day 1.8 when the gas pressure was 4,600 kPa. Figure 32e shows the average flow at STP into the fracture, with gas entry inferred to be approximately 7,000 kPa. In contrast to test ASR_Tau15_00gGI, the methods used to predict gas entry gave dissimilar results.

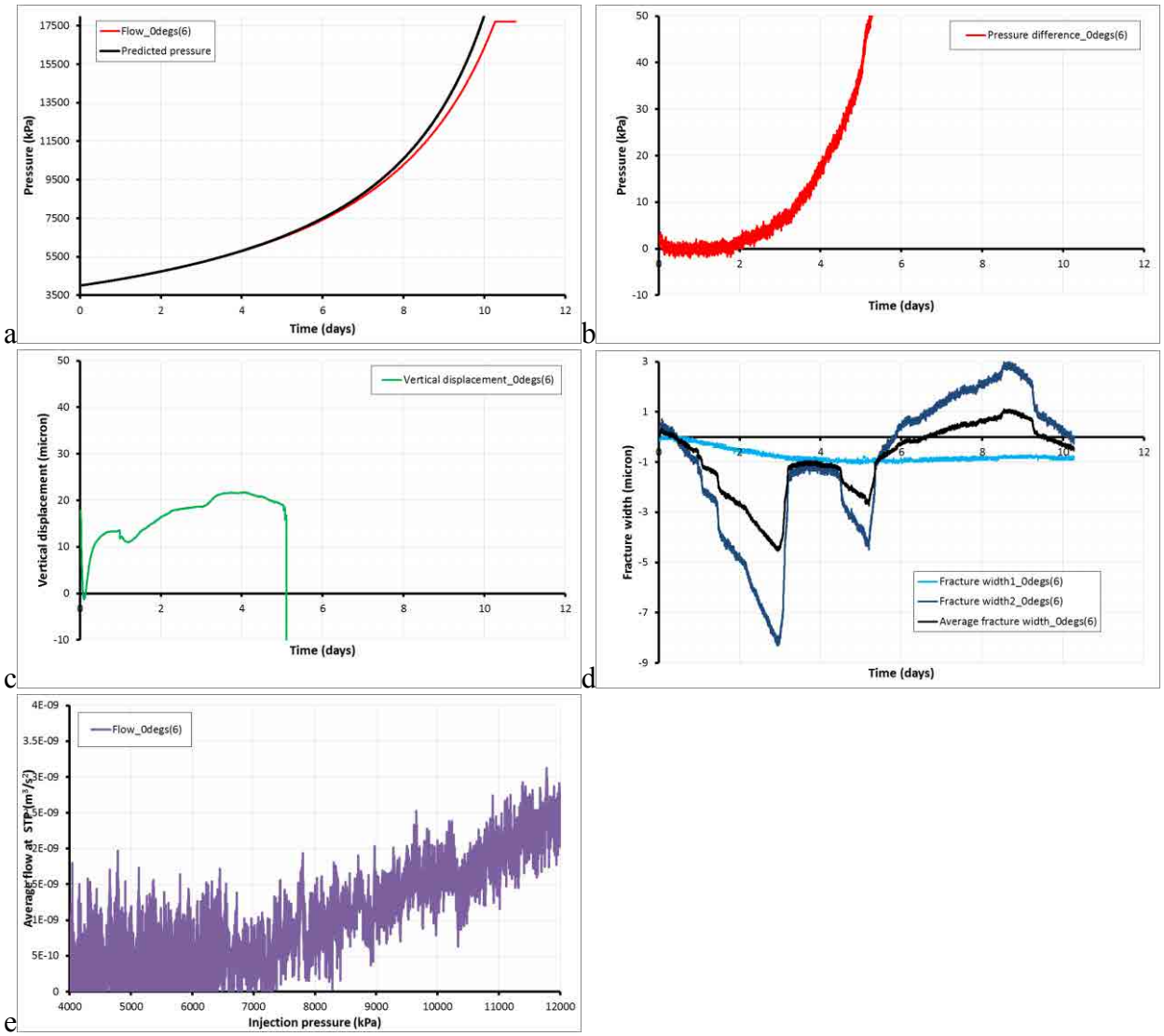

Figure 32 – Results for gas injection test 6 / ASR_Tau16_00gGI. a) Gas injection pressure compared with prediction from ideal gas law; b) comparison of gas injection and ideal gas law as a way of predicting gas entry pressure; c) normal displacement; d) fracture width; e) flow into the slip plane as a way of predicting gas entry pressure.

4.2.3 Test ASR_Tau17_00gGI (Gas test 7)

The third test conducted on a fracture oriented 0° to the slip-plane was test ASR_Tau17_00gGI; the seventh gas injection test conducted. The results of the test are summarised in Figure 33. As can be seen in Figure 33a, the gas injection experiment resulted in a maximum gas pressure of approximately 14.5 MPa, with peak pressure nearly achieved. Following the cessation of gas injection on Day 12, a gas shut-in stage was conducted for two days. An asymptote of pressure

would have taken a significant amount of time and so the experiment was halted. Throughout the test history the fracture could be seen to dilate by only 1 µm (Figure 33c). The eddy current sensors showed a complex history (Figure 33d). One sensor showed no change for 1.5 days, followed by dilation throughout the remaining test history. The other showed much greater changes in fracture width, with significant compression and dilation events. One eddy current sensor was mounted either end of the top-block, therefore the data suggest that the fracture width was not constant throughout the test history. It should be noted that the same sensor was showing complex behaviour as in test ASR_Tau16_00gGI. This may suggest that the sensor was behaving in a non-ideal way.

Figure 33b shows the difference between the gas pressure observed and the predicted pressure from the ideal gas law. As seen, this data suggested that gas started to enter the fracture at around Day 2 when the gas pressure was 4,590 kPa. Figure 33e shows the average flow at STP into the fracture, with gas entry inferred to be approximately 8,000 kPa. In contrast to test ASR_Tau15_00gGI, the methods used to predict gas entry gave significantly dissimilar results.

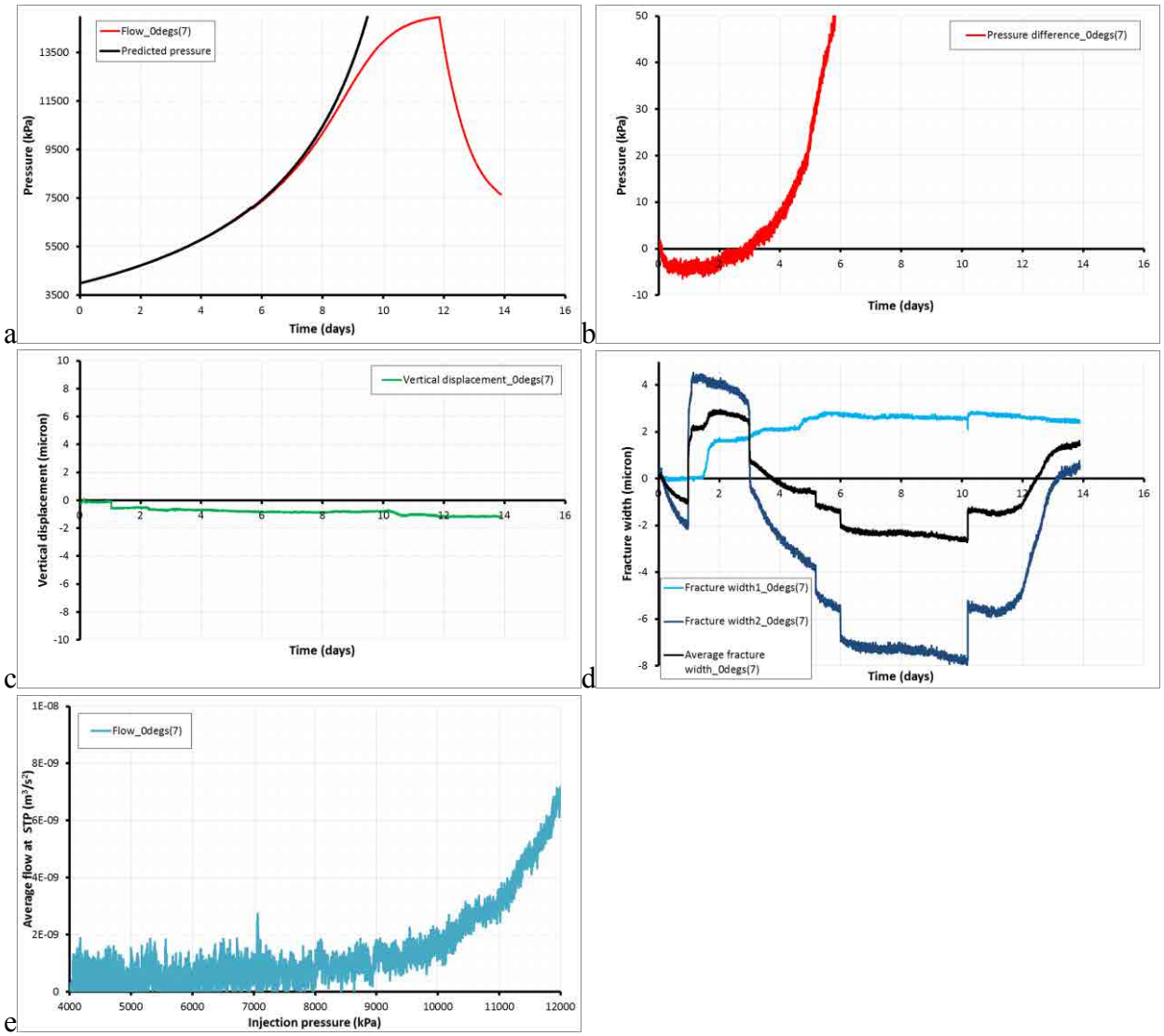

Figure 33 – Results for gas injection test 7 / ASR_Tau17_00gGI. a) Gas injection pressure compared with prediction from ideal gas law; b) comparison of gas injection and ideal gas law as a way of predicting gas entry pressure; c) normal displacement; d) fracture width; e) flow into the slip plane as a way of predicting gas entry pressure.

4.2.4 Test ASR_Tau21_00gGI (Gas test 11)

The fourth test conducted on a fracture oriented 0° to the slip-plane was test ASR_Tau21_00gGI; the eleventh gas injection test conducted. The results of the test are summarised in Figure 34. As can be seen in Figure 34a, the gas injection experiment resulted in a maximum gas pressure of approximately 12.5 MPa, with peak pressure not achieved. Following the cessation of gas injection on Day 12, a gas shut-in stage was conducted for one day. An asymptote of pressure would have taken a significant amount of time and so the experiment was halted. The normal displacement data (Figure 34c) suggested that the induction sensor malfunctioned. The eddy current sensors showed a complex history (Figure 34d). One sensor shows minor dilation of approximately 1 µm, whilst the other shows compression of 1 µm. It can be seen that a compressional event corresponds with the onset of gas flow inferred from the ideal gas law (Figure 34b). The data suggest that the top-block was "rocking" about the central loading point.

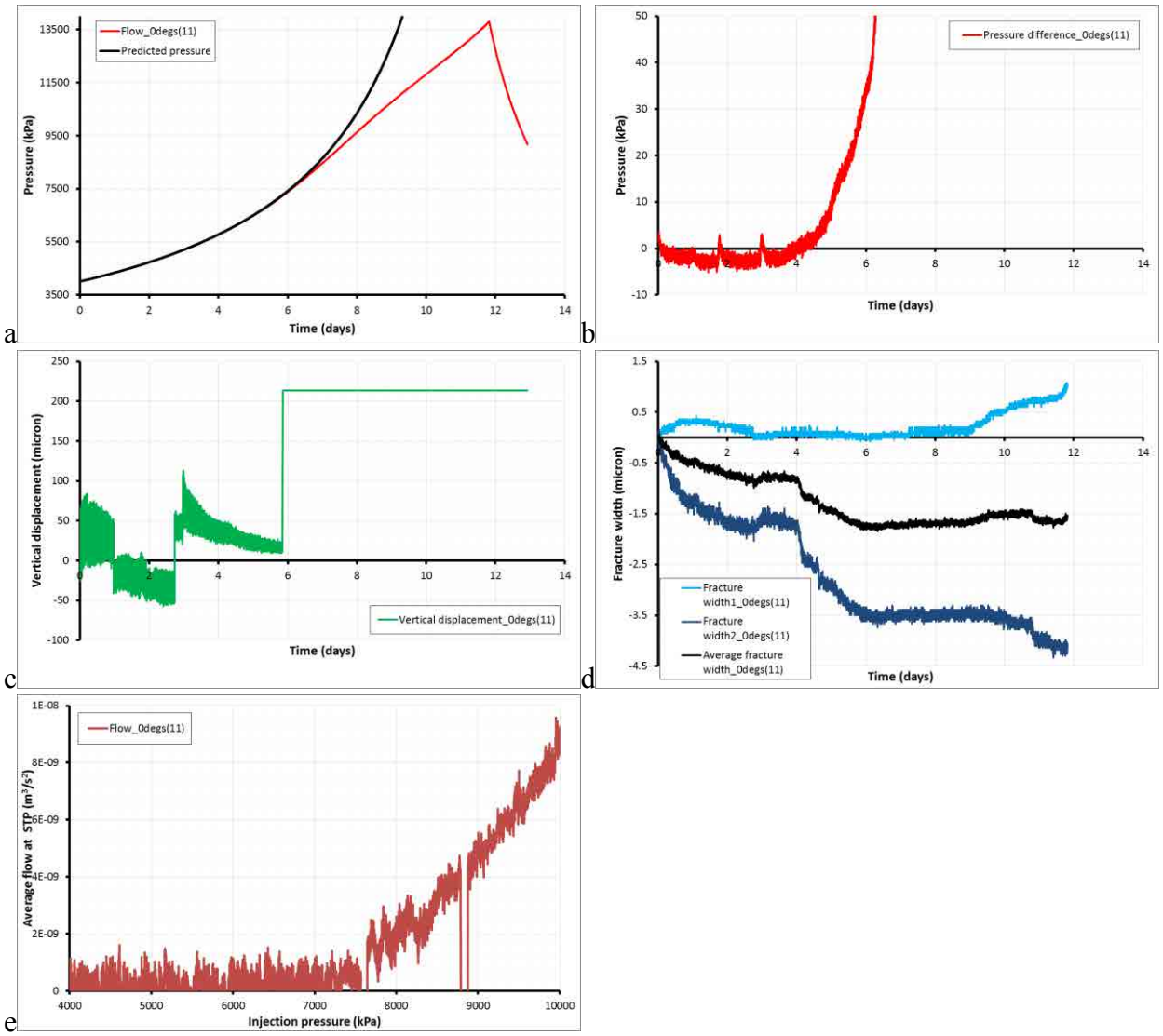

Figure 34 – Results for gas injection test 11 / ASR_Tau21_00gGI. a) Gas injection pressure compared with prediction from ideal gas law; b) comparison of gas injection and ideal gas law as a way of predicting gas entry pressure; c) normal displacement [note malfunctioned]; d) fracture width; e) flow into the slip plane as a way of predicting gas entry pressure.

Figure 34b shows the difference between the gas pressure observed and the predicted pressure from the ideal gas law. As seen, this data suggested that gas started to enter the fracture at around Day 3.5 when the gas pressure was 5,475 kPa. Figure 34e shows the average flow at STP into the

fracture, with gas entry inferred to be approximately 7,500 kPa. In contrast to test ASR_Tau15_00gGI, the methods used to predict gas entry gave dissimilar results.

4.2.5 Test ASR_Tau22_00gGI (Gas test 12)

The fifth test conducted on a fracture oriented 0° to the slip-plane was test ASR_Tau22_00gGI; the twelfth gas injection test conducted. The results of the test are summarised in Figure 35. As can be seen in Figure 35a, a logging error occurred between Day 7.5 and Day 13.5. This means that it is unclear what maximum pressure was achieved and only data for gas entry can be achieved from this experiment. Throughout the test history the induction sensor measuring normal displacement was not registering any data; therefore this sensor had malfunctioned. The eddy current sensors showed a complex history (Figure 35d). One sensor showed compression, whilst the other showed dilation. However, the sensor showing dilation had considerable numbers of steps within the data, suggesting that some form of malfunction had occurred. It can be seen that the sensor that initially showed compression had a dilational event that corresponded with the onset of gas entry as predicted from the ideal gas law.

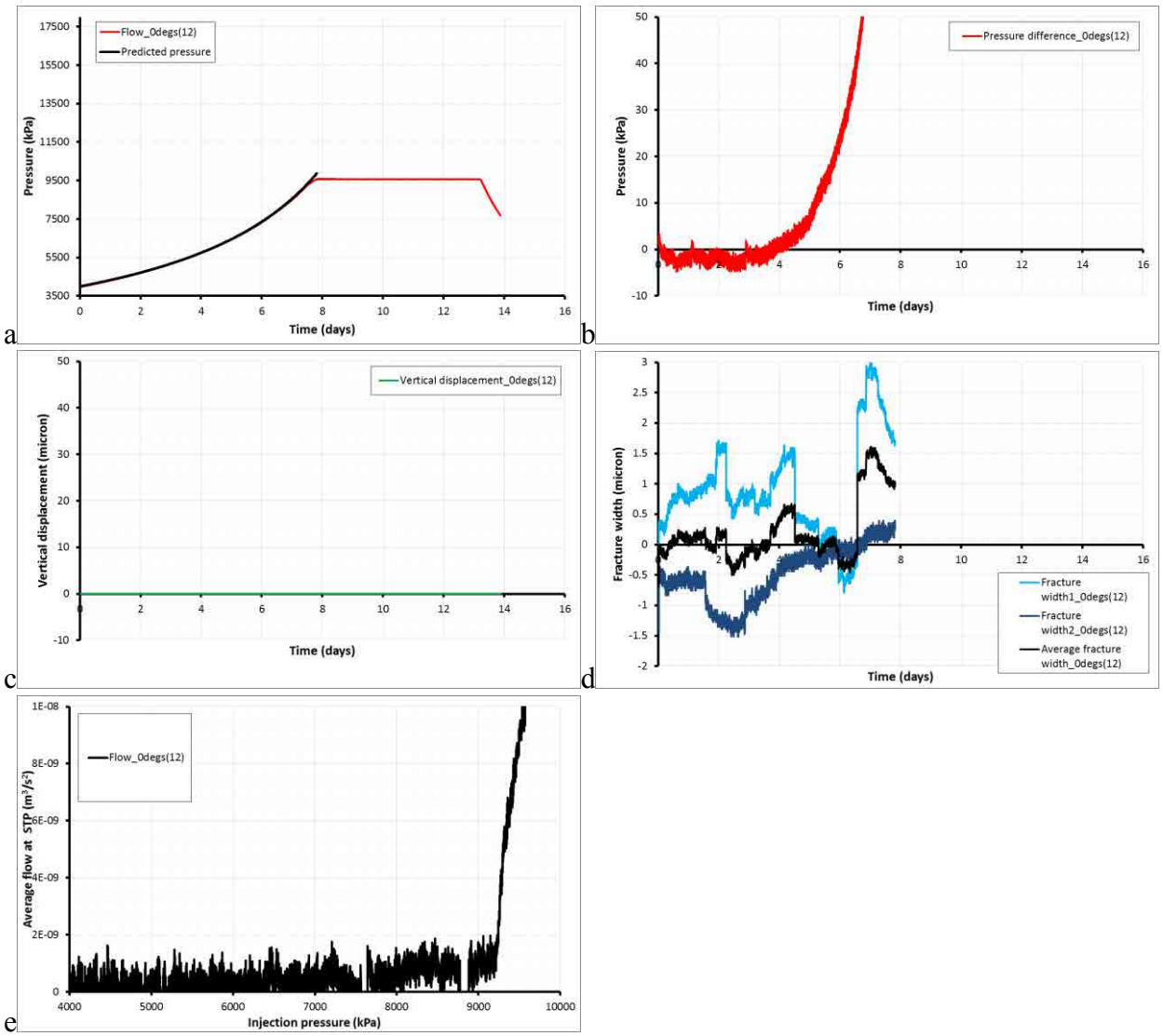

Figure 35 – Results for gas injection test 12 / ASR_Tau22_00gGI. a) Gas injection pressure compared with prediction from ideal gas law; b) comparison of gas injection and ideal gas law as a way of predicting gas entry pressure; c) normal displacement [note malfunctioned]; d) fracture width; e) flow into the slip plane as a way of predicting gas entry pressure.

Figure 35b shows the difference between the gas pressure observed and the predicted pressure from the ideal gas law. As seen, this data suggested that gas started to enter the fracture at around Day 3 when the gas pressure was 5,170 kPa. Figure 35e shows the average flow at STP into the fracture, with gas entry inferred to be approximately 9,250 kPa. In contrast to test ASR_Tau15_00gGI, the methods used to predict gas entry gave significantly dissimilar results.

4.2.6 Results for tests conducted in a slip plane orientation of 0°

Figure 36 shows the gas pressure for all five of the gas injection tests conducted on a fracture oriented 0° to the slip-direction. As clearly seen, there is little repeatability in the gas pressures achieved with pressures between 8 and 18 MPa achieved. However, close examination of the data showed that gas entry pressure had a much better repeatability. As described above, two methods were employed for estimating the gas entry pressure; the first compared the gas pressure result with the predicted pressure from the ideal gas law and the second calculated average flow at STP into the fracture. All results are summarised in Table 9, with the results from flow into the fracture shown in Figure 37. As seen in Figure 37, four tests showed similar gas entry pressures of between 7.5 and 9 MPa, whilst one test had an anomalously low gas entry pressure of 5 MPa.

The repeatability seen in gas entry pressure and not peak pressure suggests that the physics governing the onset of flow was maintained for all tests; however, once gas started to be mobile the permeability of the kaolinite filled fracture plane was inconsistent, resulting in variations of behaviour post gas entry. This may be due to differences in the number of pathways formed.

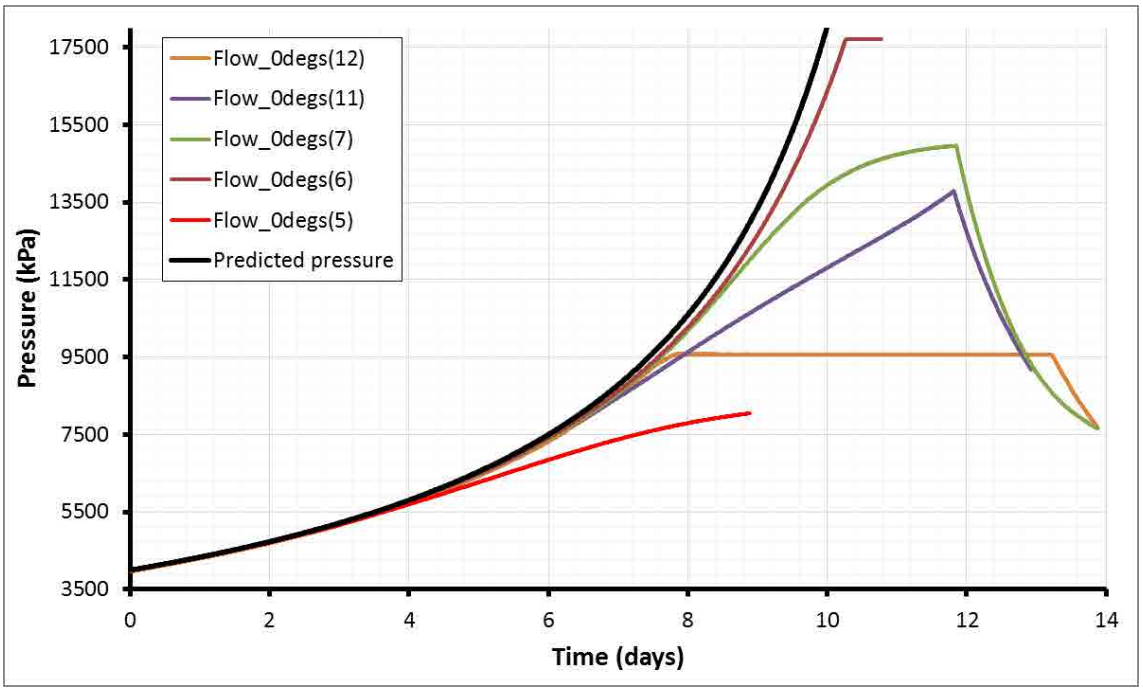

Figure 36 – Results for five gas injection tests conducted on a fracture oriented 0° to the slip plane. As can be seen, considerable differences are seen in peak pressure and form of the curve indicating that fracture transmissivity is not repeatable.

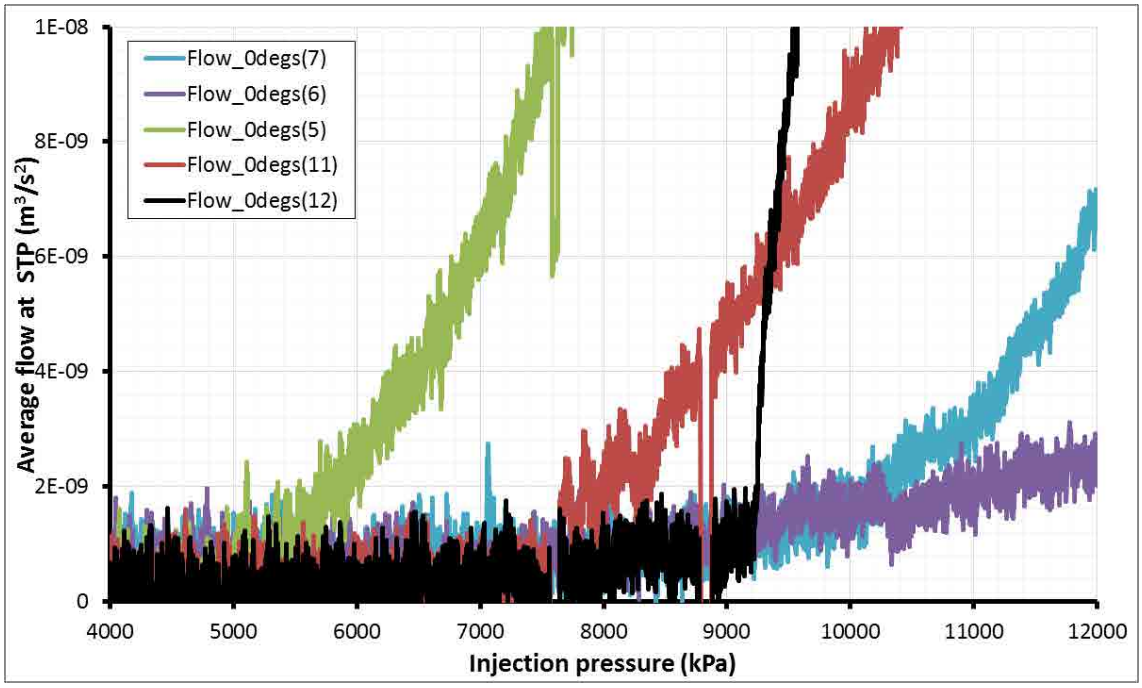

Figure 37 – Gas entry pressure predicted from the average flow at STP for five gas injection tests conducted on a fracture oriented 0° to the slip plane. As can be seen, repeatable gas entry pressure is seen for four of the five tests, with one test (5) showing a considerably lower gas entry pressure.

Test	Fracture angle	+/-	Method 1			Method 2		
			Gas entry pressure (kPa)	Average entry pressure	+/-	Gas entry pressure (kPa)	Average entry pressure	+/-
0degs(5)	0°	0.5°	*5000*	8440	413	4772	4920	193
0degs(6)			8000			4610		
0degs(7)			9000			4590		
0degs(11)			7500			5475		
0degs(12)			9250			5170		

Table 9 – Results for gas entry pressure for the five gas injection experiments conducted on a fracture oriented 0° to the slip-plane. Method 1 = gas entry determined from STP gas flow into the fracture; Method 2 = entry pressure inferred from comparing pressure curve with ideal gas law.

4.3 GAS BREAKTHROUGH EXPERIMENTS ON A SLIP PLANE ORIENTATION OF 15°

A total of three gas injection experiments were conducted on a fracture oriented 15° with respect to the slip direction. As stated previously, each test was performed as identical as possible, with identical water content of gouge produced, similar normal load, similar volumes of gas, and identical gas injection rates. The only parameter that was likely to have varied between tests was the thickness of the gouge at the start of the experiment. However, as best as could be established, this did not vary significantly between tests as the gouge became very thin in all tests.

4.3.1 Test ASR_ Tau18_15gGI (Gas test 8)

The first test conducted on a fracture oriented 15° to the slip-plane was test ASR_Tau18_15gGI; the eighth gas injection test conducted. The results of the test are summarised in Figure 38. As can be seen in Figure 38a, the gas injection experiment resulted in a maximum gas pressure of approximately 12 MPa, with peak pressure achieved. The normal displacement data (Figure 38c) suggested that the gouge compressed a few micron throughout the test history. The eddy current sensors showed a complex history (Figure 38d). One sensor showed minor dilation of approximately 2 µm, whilst the other showed compression of 5 µm, followed by dilation of approximately 25 µm. It can be seen that the dilational event at approximately Day 3 corresponded with the onset of gas flow inferred from the ideal gas law (Figure 38b).

Figure 38b shows the difference between the gas pressure observed and the predicted pressure from the ideal gas law. As seen, this data suggested that gas started to enter the fracture at around Day 3.5 when the gas pressure was 4,850 kPa. Figure 38e shows the average flow at STP into the fracture, with gas entry inferred to be approximately 7,500 kPa. The two methods used for determining gas entry therefore gave significantly dissimilar results.

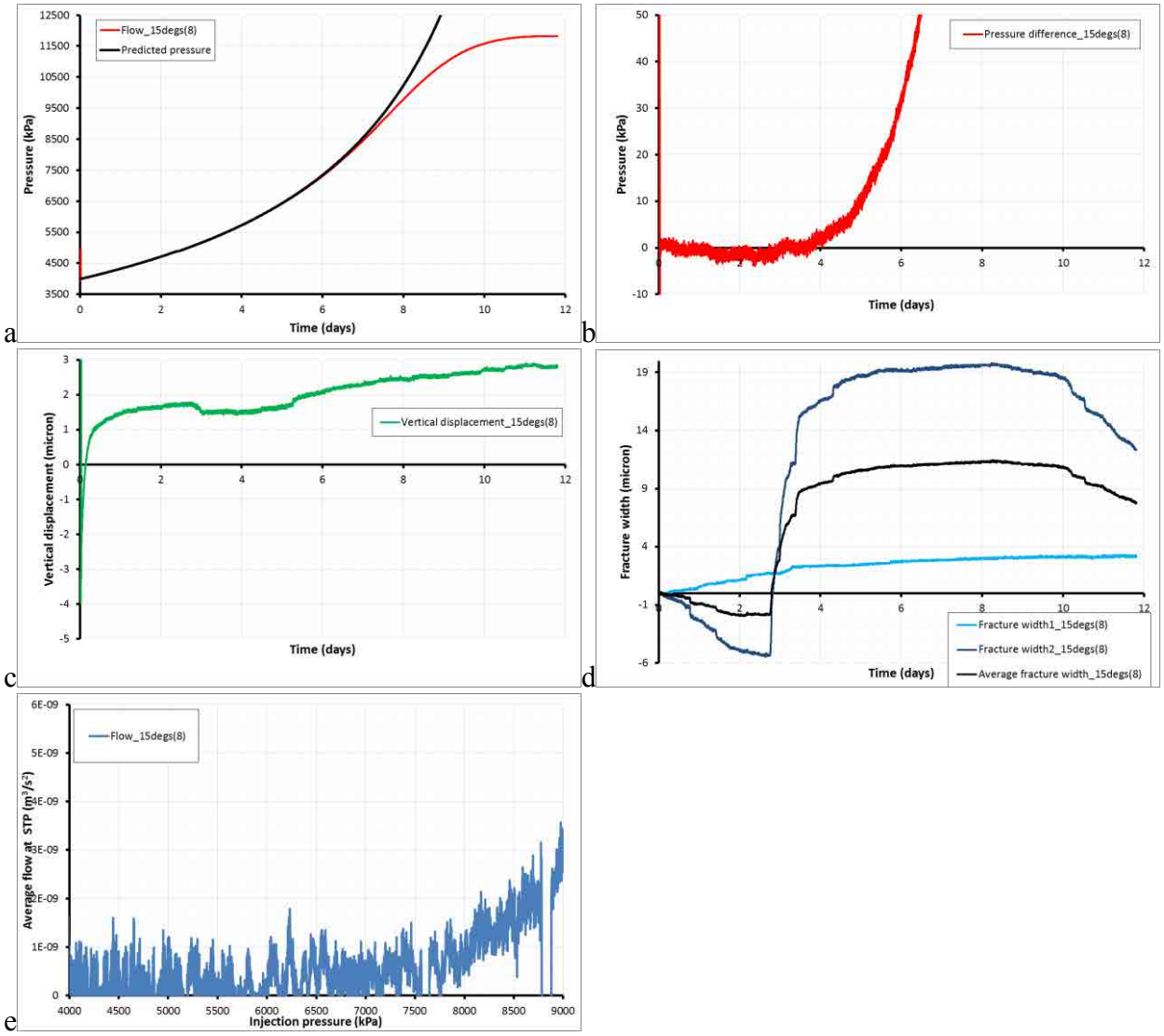

Figure 38 – Results for gas injection test 8 / ASR_Tau18_15gGI. a) Gas injection pressure compared with prediction from ideal gas law; b) comparison of gas injection and ideal gas law as a way of predicting gas entry pressure; c) normal displacement; d) fracture width; e) flow into the slip plane as a way of predicting gas entry pressure.

4.3.2 Test ASR_Tau19_15gGI (Gas test 9)

The second test conducted on a fracture oriented 15° to the slip-plane was test ASR_Tau19_15gGI; the ninth gas injection test conducted. The results of the test are summarised in Figure 39. As can be seen in Figure 39a, the gas injection experiment resulted in a maximum gas pressure of approximately 8 MPa, with peak pressure achieved and significant decrease in gas pressure post peak. Following the cessation of gas injection on Day 11, a gas shut-in stage was conducted for one day. An asymptote of pressure would have taken a significant amount of time and so the experiment was halted. The normal displacement data (Figure 39c) suggests that fracture compressed throughout the entire test history. Both eddy current sensors showed the fracture was compressing, although one sensor showed a small amount of compression of less than 1 µm (Figure 39d). The other sensor showed greater compression of 14 µm. Little correlation is seen between normal displacement or fracture width with the onset of gas entry. No significant change is seen at the peak pressure.

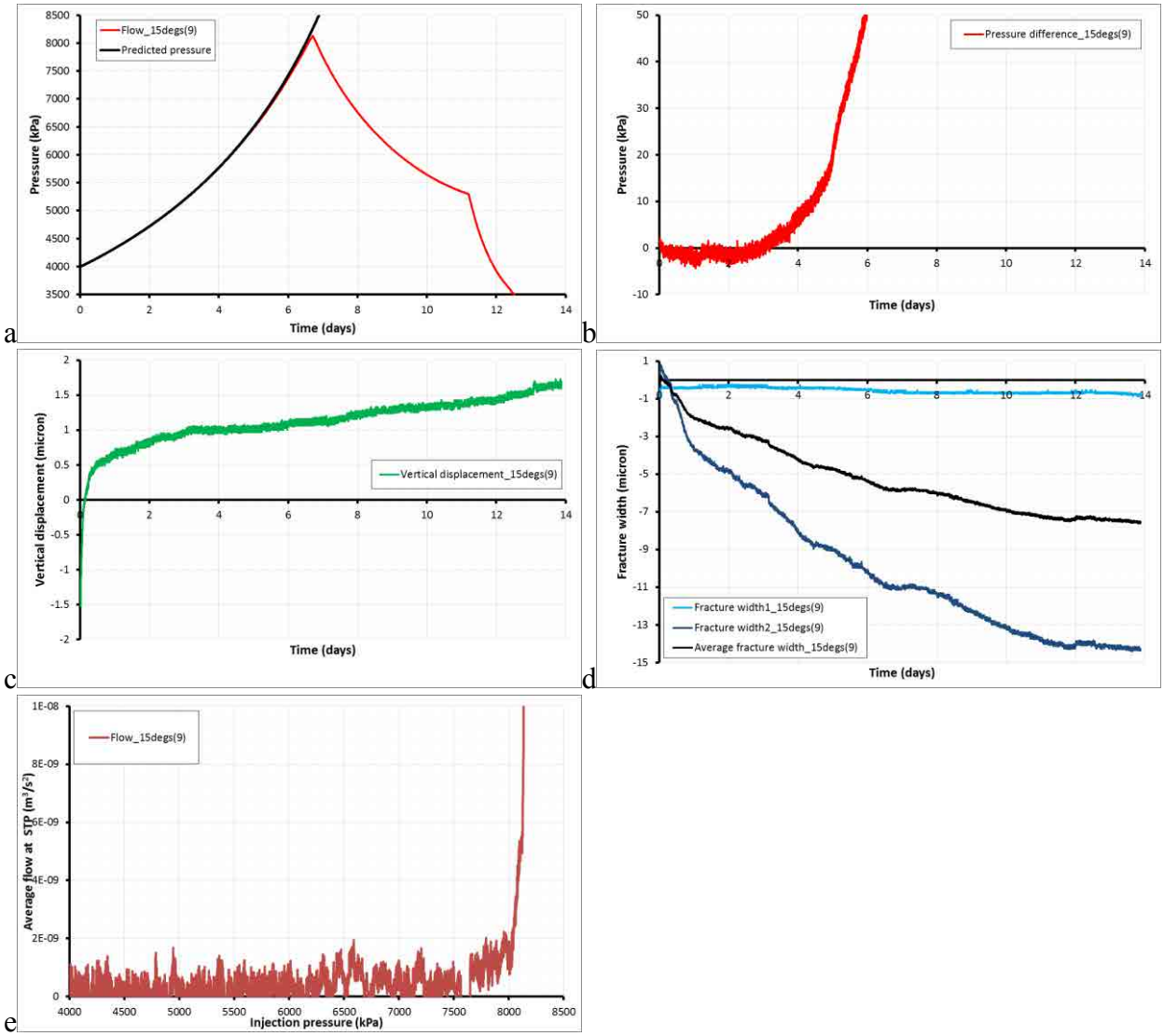

Figure 39 – Results for gas injection test 9 / ASR_Tau19_15gGI. a) Gas injection pressure compared with prediction from ideal gas law; b) comparison of gas injection and ideal gas law as a way of predicting gas entry pressure; c) normal displacement; d) fracture width; e) flow into the slip plane as a way of predicting gas entry pressure.

Figure 39b shows the difference between the gas pressure observed and the predicted pressure from the ideal gas law. As seen, this data suggests that gas started to enter the fracture at around Day 3 when the gas pressure was 4,750 kPa. Figure 39e shows the average flow at STP into the

fracture, with gas entry inferred to be approximately 7,500 kPa. The two methods used for determining gas entry therefore gave significantly dissimilar results.

4.3.3 Test ASR_Tau20_15gGI (Gas test 10)

The third test conducted on a fracture oriented 15° to the slip-plane was test ASR_Tau20_15gGI; the tenth gas injection test conducted. The results of the test are summarised in Figure 40. As can be seen in Figure 40a, the gas injection experiment resulted in a maximum gas pressure of approximately 13 MPa, with peak pressure not achieved. Following the cessation of gas injection on Day 12, a gas shut-in stage was conducted for one day. An asymptote of pressure would have taken a significant amount of time and so the experiment was halted. The normal displacement data (Figure 40c) showed that the fracture compressed throughout the entire test history; although on Day 8 there was evidence for small amounts of dilation. The eddy current sensors showed a complex history (Figure 40d). One sensor showed no variation for over 5 days and then showed dilation of 2.5 1 µm, whilst the other sensor showed dilation and compression in a complex way. It can be seen that a dilational event corresponds with the onset of gas flow inferred from the ideal gas law (Figure 40b).

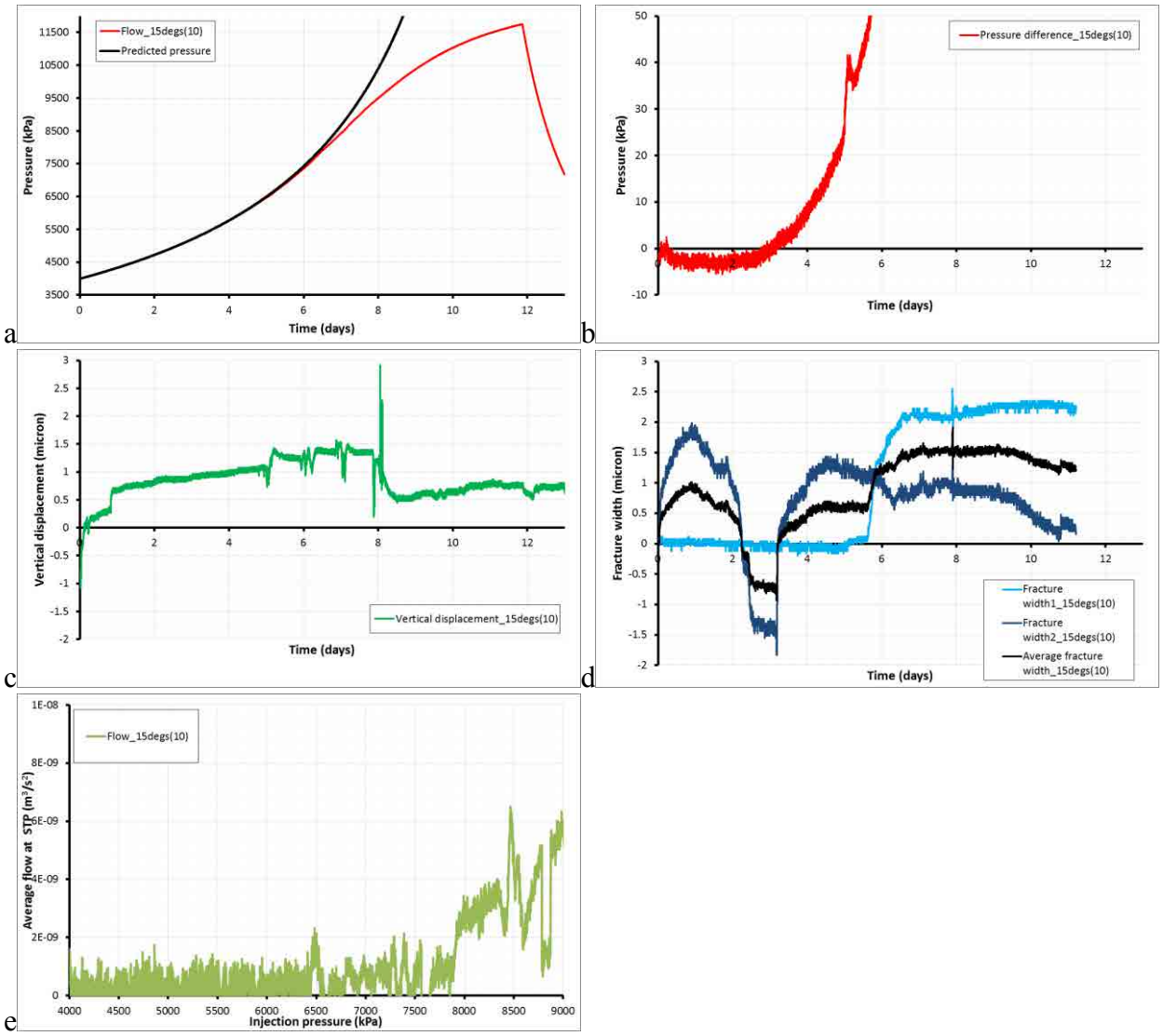

Figure 40 – Results for gas injection test 10 / ASR_Tau20_15gGI. a) Gas injection pressure compared with prediction from ideal gas law; b) comparison of gas injection and ideal gas law as a way of predicting gas entry pressure; c) normal displacement; d) fracture width; e) flow into the slip plane as a way of predicting gas entry pressure.

Figure 40b shows the difference between the gas pressure observed and the predicted pressure from the ideal gas law. As seen, this data suggests that gas started to enter the fracture at around Day 3 when the gas pressure was 4,925 kPa. Figure 40e shows the average flow at STP into the fracture, with gas entry inferred to be approximately 7,750 kPa. The two methods used for determining gas entry therefore gave significantly dissimilar results.

4.3.4 Results for tests conducted in a slip plane orientation of 15°

Figure 41 shows the gas pressure for all three of the gas injection tests conducted on a fracture oriented 15° to the slip-direction. As clearly seen, there is little repeatability in the gas pressures achieved with pressures between 8 and 12 MPa achieved. However, close examination of the data showed that gas entry pressure had a much better repeatability. As described above, two methods were employed for estimating the gas entry pressure; the first compared the gas pressure result with the predicted pressure from the ideal gas law and the second calculated average flow at STP into the fracture. All results are summarised in Table 10, with the results from flow into the fracture shown in Figure 42. As seen in Figure 42, all three tests had gas entry between 7,500 and 7,750 kPa.

As stated previously, the repeatability seen in gas entry pressure and not peak pressure suggests that the physics governing the onset of flow was maintained for all tests; however, once gas started to be mobile the permeability of the kaolinite filled fracture plane was inconsistent, resulting in variations of behaviour post gas entry.

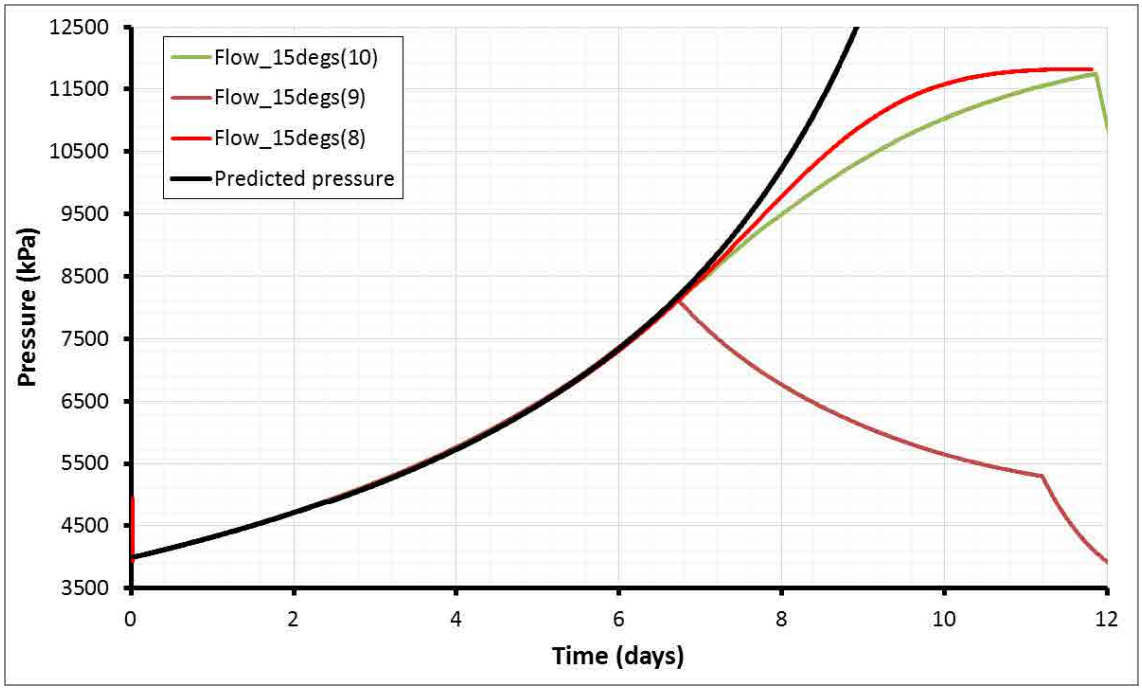

Figure 41 –Results for three gas injection tests conducted on a fracture oriented 15° to the slip plane. As can be seen, considerable differences are seen in peak pressure and form of the curve indicating that fracture transmissivity is not repeatable.

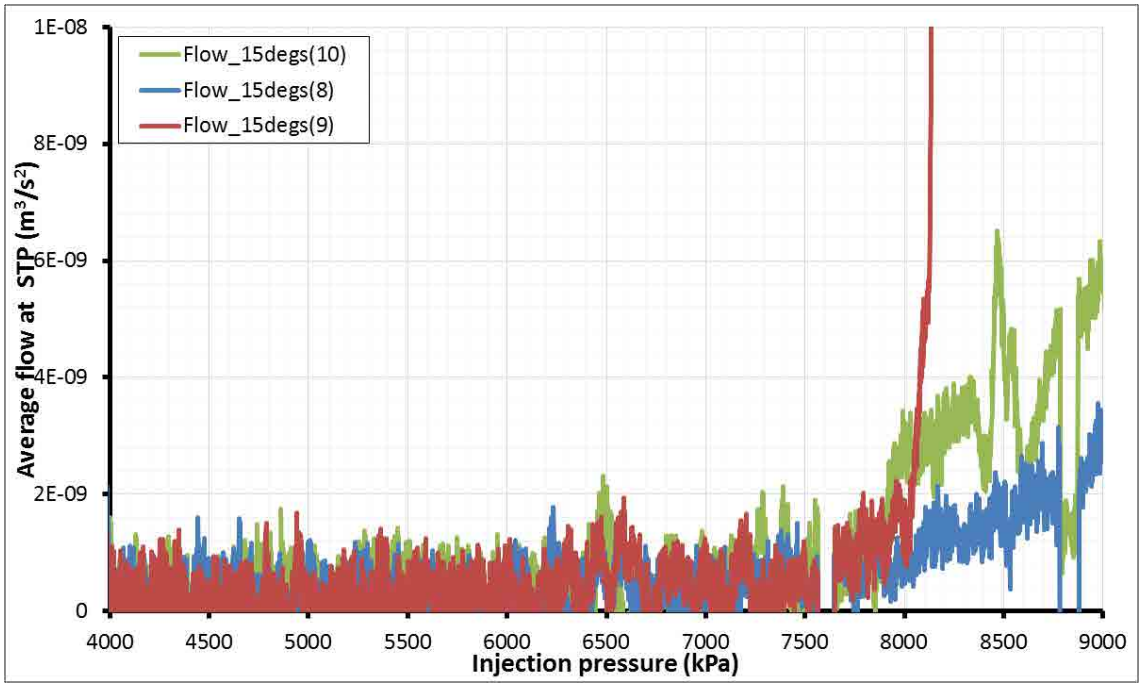

Figure 42 –Gas entry pressure predicted from the average flow at STP for three gas injection tests conducted on a fracture oriented 15° to the slip plane. As can be seen, repeatable gas entry pressure is seen for all three tests.

Test	Fracture angle	+/-	Method 1			Method 2		
			Gas entry pressure (kPa)	Average entry pressure	+/-	Gas entry pressure (kPa)	Average entry pressure	+/-
15degs(8)	15°	0.5°	7500	7580	72	4850	4840	48
15degs(9)			7500			4732		
15degs(10)			7750			4922		

Table 10 – Results for gas entry pressure for three gas injection experiments conducted at an angle of 15°. Method 1 = gas entry determined from STP gas flow into the fracture; Method 2 = entry pressure inferred from comparing pressure curve with ideal gas law

4.4 GAS BREAKTHROUGH EXPERIMENTS ON A SLIP PLANE ORIENTATION OF 30°

A total of four gas injection experiments were conducted on a fracture oriented 30° with respect to the slip direction. As stated previously, each test was performed as identical as possible, with identical water content of gouge produced, similar normal load, similar volumes of gas, and identical gas injection rates. The only parameter that is likely to have varied between tests was the thickness of the gouge at the start of the experiment. However, as best as could be established, this did not vary significantly between tests as the gouge became very thin in all tests.

4.4.1 Test ASR_Tau09_30gGI (Gas test 1)

The first test conducted on a fracture oriented 30° to the slip-plane was test ASR_Tau09_30gGI; the first gas injection test conducted. The results of the test are summarised in Figure 43. As can be seen in Figure 43a, the gas injection experiment resulted in a maximum gas pressure of approximately 8 MPa, with peak pressure achieved. The normal displacement data (Figure 43c) showed that the fracture compressed through-out the test history. The step in the data at Day 8

does not correlate with any other response and therefore this is inferred to be a system error. The angled shear rig (ASR) was originally designed with only a single eddy current sensor and this showed a complex history (Figure 43d). Compression was generally seen, with dilation beginning at Day 7. This may correspond with a change in slope of the gas pressure curve and indicate enhanced flow into the fracture.

Figure 43b shows the difference between the gas pressure observed and the predicted pressure from the ideal gas law. As seen, this data suggests that gas started to enter the fracture at around Day 1 when the gas pressure was 4,375 kPa. Figure 43e shows the average flow at STP into the fracture, with gas entry inferred to be approximately 5,200 kPa.

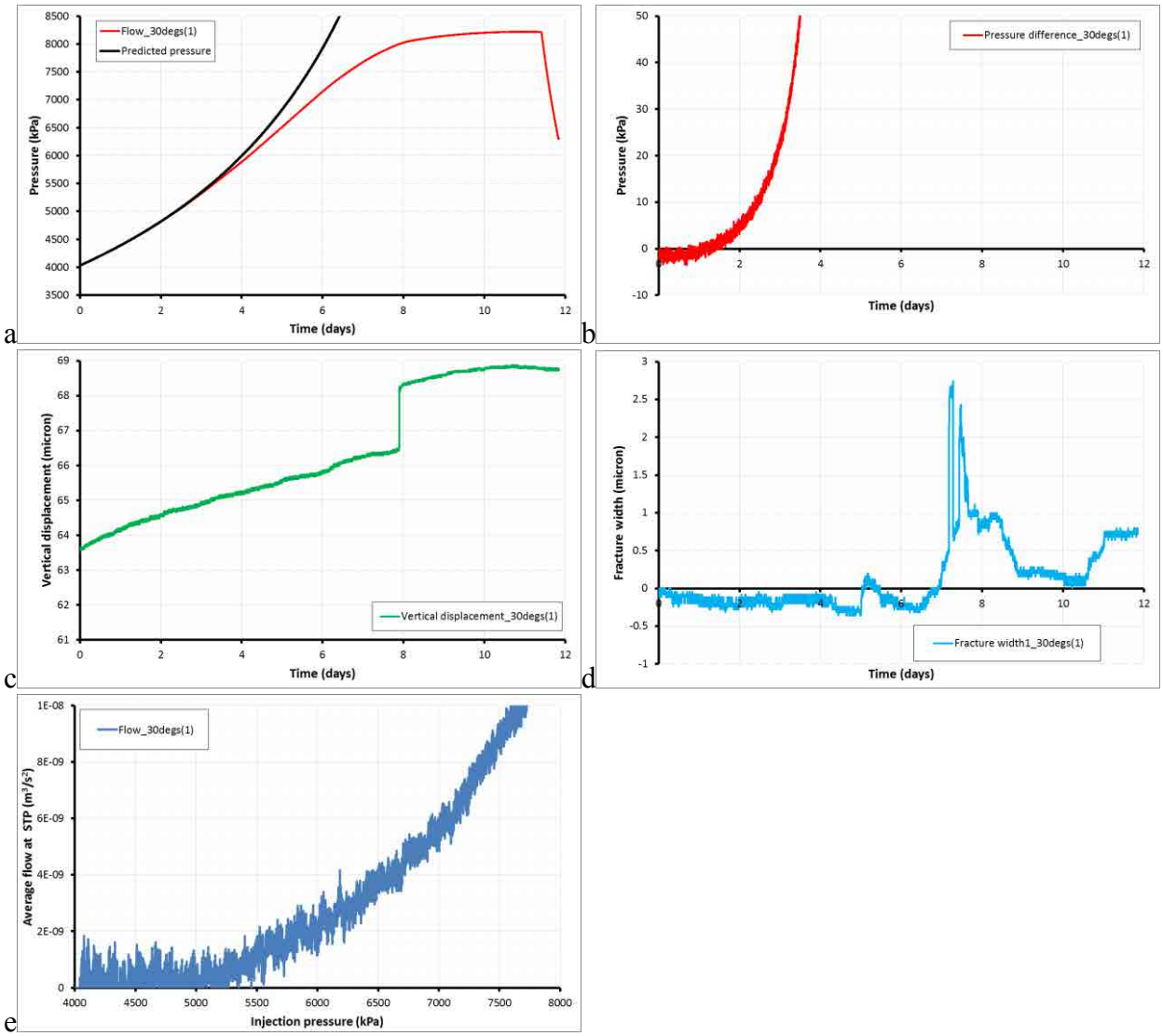

Figure 43 – Results for gas injection test 1 / ASR_Tau09_30gGI. a) Gas injection pressure compared with prediction from ideal gas law; b) comparison of gas injection and ideal gas law as a way of predicting gas entry pressure; c) normal displacement; d) fracture width; e) flow into the slip plane as a way of predicting gas entry pressure.

4.4.2 Test ASR_Tau11_30gGI (Gas test 2)

The second test conducted on a fracture oriented 30° to the slip-plane was test ASR_Tau11_30gGI; the second gas injection test conducted. The results of the test are summarised in Figure 44. As can be seen in Figure 44a, the gas injection experiment resulted in a maximum gas pressure of approximately 15.5 MPa, with peak pressure not achieved. Following the cessation of gas injection on Day 12, a gas shut-in stage was conducted for three days. The

normal displacement data (Figure 44c) showed that the fracture compressed through-out the test history. The angled shear rig (ASR) was originally designed with only a single eddy current sensor and this showed a complex history (Figure 44d). Compression was initially seen, with dilation events that may be system errors. The dilation initiated approximately Day 6 corresponded with the onset of gas flow inferred from the ideal gas law (Figure 40b).

Figure 44b shows the difference between the gas pressure observed and the predicted pressure from the ideal gas law. As seen, this data suggests that gas started to enter the fracture at around Day 6 when the gas pressure was 7,380 kPa. Figure 43e shows the average flow at STP into the fracture, with gas entry inferred to be approximately 8,000 kPa.

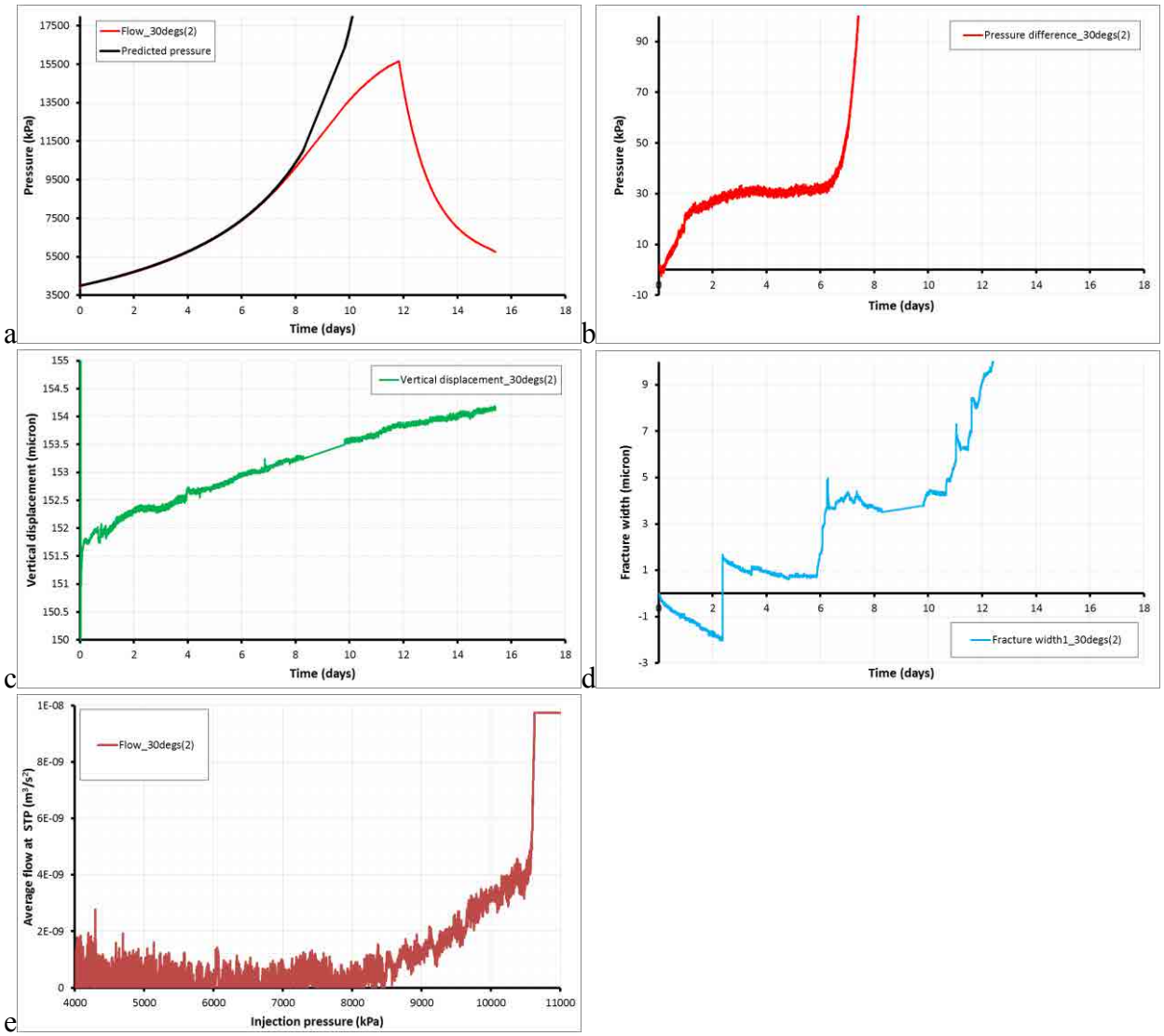

Figure 44 – Results for gas injection test 2 / ASR_Tau11_30gGI. a) Gas injection pressure compared with prediction from ideal gas law; b) comparison of gas injection and ideal gas law as a way of predicting gas entry pressure; c) normal displacement; d) fracture width; e) flow into the slip plane as a way of predicting gas entry pressure.

4.4.3 Test ASR_Tau12_30gGI (Gas test 3)

The third test conducted on a fracture oriented 30° to the slip-plane was test ASR_Tau12_30gGI; the third gas injection test conducted. The results of the test are summarised in Figure 45. As can be seen in Figure 45a, the gas injection experiment resulted in a maximum gas pressure of approximately 11 MPa, with peak pressure achieved and a loss of gas pressure as the fracture became highly conductive. The normal displacement data (Figure 45c) showed that the fracture

dilated initially and following this compressed through-out the rest of the test history. As can be seen, a significant dilation event is seen at the time of the gas breakthrough. The angled shear rig (ASR) was originally designed with only a single eddy current sensor and this showed a complex history (Figure 45d). Dilation was initially seen, followed by compression, with dilatant episodes beginning around Day 5.

Figure 45b shows the difference between the gas pressure observed and the predicted pressure from the ideal gas law. As seen, this data suggests that gas started to enter the fracture at around Day 1.5 when the gas pressure was 4,700 kPa. Figure 45e shows the average flow at STP into the fracture, with gas entry inferred to be approximately 7,000 kPa.

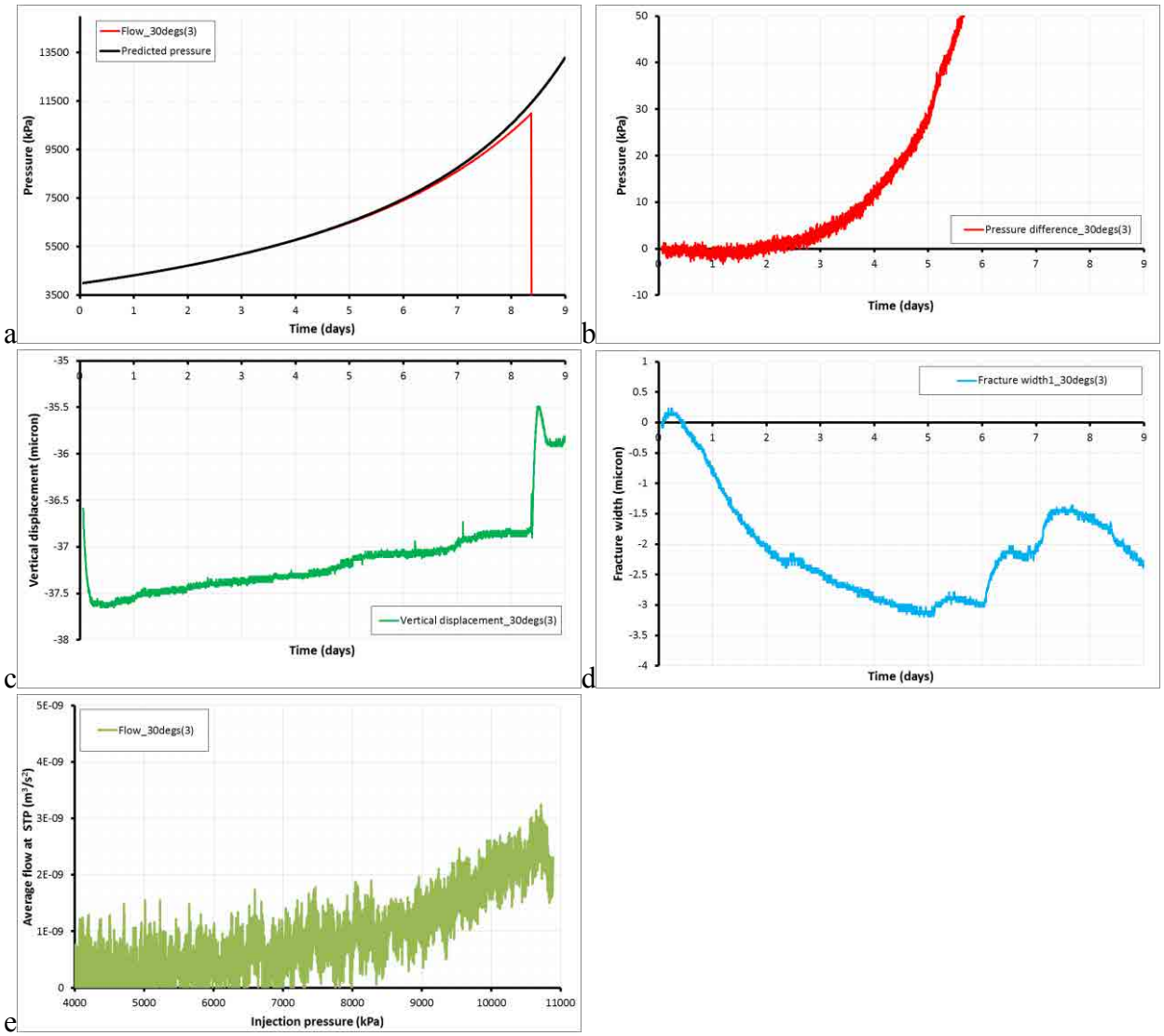

Figure 45 – Results for gas injection test 3 / ASR_Tau12_30gGI. a) Gas injection pressure compared with prediction from ideal gas law; b) comparison of gas injection and ideal gas law as a way of predicting gas entry pressure; c) normal displacement; d) fracture width; e) flow into the slip plane as a way of predicting gas entry pressure.

4.4.4 Test ASR_Tau13_30gGI (Gas test 4)

The fourth test conducted on a fracture oriented 30° to the slip-plane was test ASR_Tau13_30gGI; the fourth gas injection test conducted. The results of the test are summarised in Figure 46. As can be seen in Figure 46a, the gas injection experiment resulted in a maximum gas pressure of approximately 14 MPa, with peak pressure not achieved and a loss of gas pressure as the fracture became highly conductive. The normal displacement data (Figure

46c) showed that the fracture dilated initially and following this dilated through-out the rest of the test history. Dissimilar to test ASR_Tau12_30gGI, no dilation was seen at the time of gas pressure loss. The single eddy current sensor showed a complex history (Figure 46d). Dilation was initially seen, followed by compression, with dilatant episodes beginning about Day 6. At the time of gas pressure loss, the eddy current sensor was showing that the fracture was compressing.

Figure 46b shows the difference between the gas pressure observed and the predicted pressure from the ideal gas law. As seen, this data suggests that gas started to enter the fracture at around Day 4 when the gas pressure was 4,840 kPa. Figure 46e shows the average flow at STP into the fracture, with gas entry inferred to be approximately 8,000 kPa.

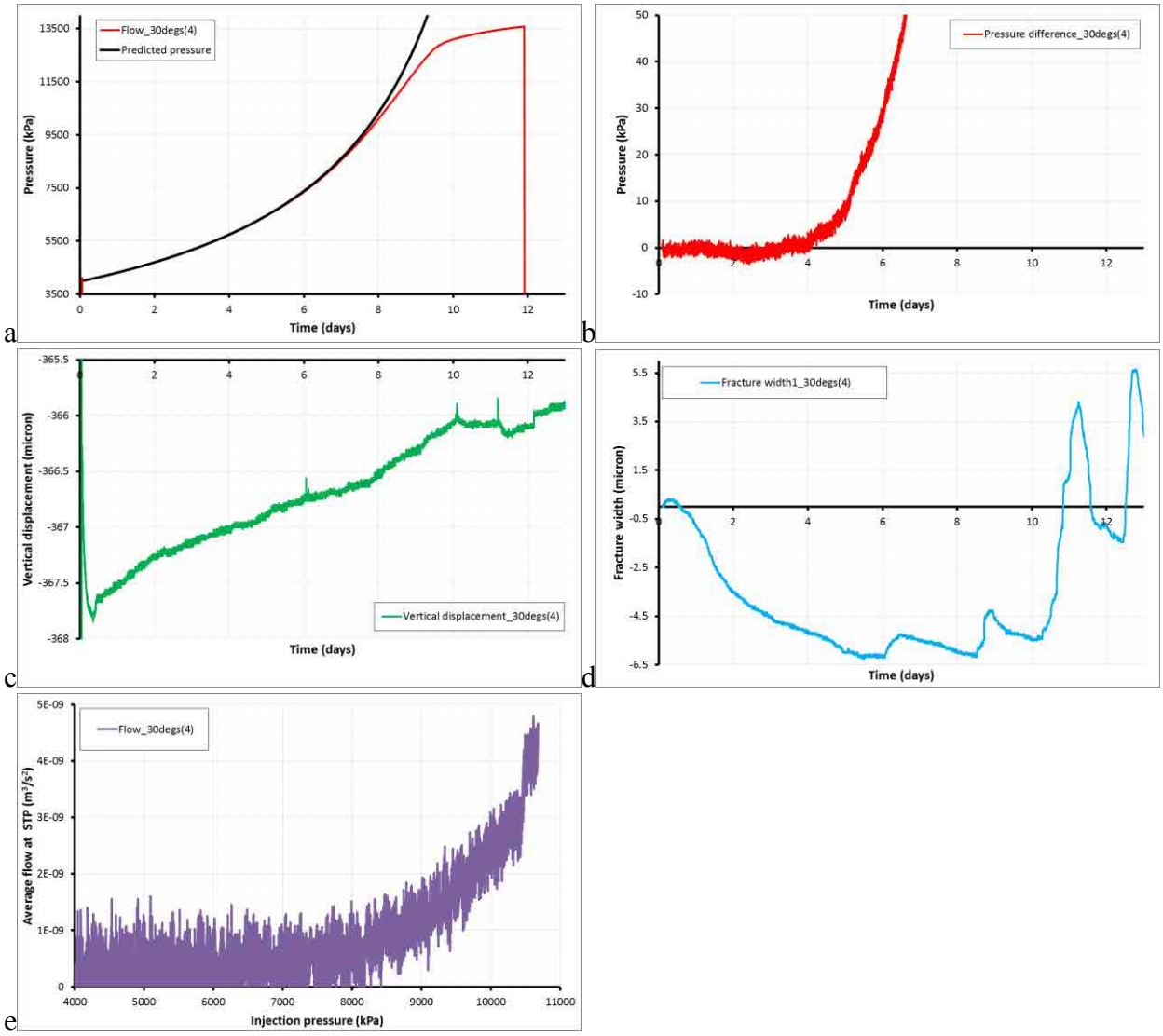

Figure 46 – Results for gas injection test 4 / ASR_Tau13_30gGI. a) Gas injection pressure compared with prediction from ideal gas law; b) comparison of gas injection and ideal gas law as a way of predicting gas entry pressure; c) normal displacement; d) fracture width; e) flow into the slip plane as a way of predicting gas entry pressure.

4.4.5 Results for tests conducted in a slip plane orientation of 30°

Figure 47 shows the gas pressure for all five of the gas injection tests conducted on a fracture oriented 30° to the slip-direction. As clearly seen, there is little repeatability in the gas pressures achieved with pressures between 8 and 16 MPa achieved. However, close examination of the data showed that gas entry pressure had a much better repeatability. As described above, two

methods were employed for estimating the gas entry pressure; the first compared the gas pressure result with the predicted pressure from the ideal gas law and the second calculated average flow at STP into the fracture. All results are summarised in Table 11, with the results from flow into the fracture shown in Figure 48. As seen in Figure 48, three tests showed similar gas entry pressures of between 7 and 8 MPa, whilst one test had an anomalously low gas entry pressure of 5.2 MPa.

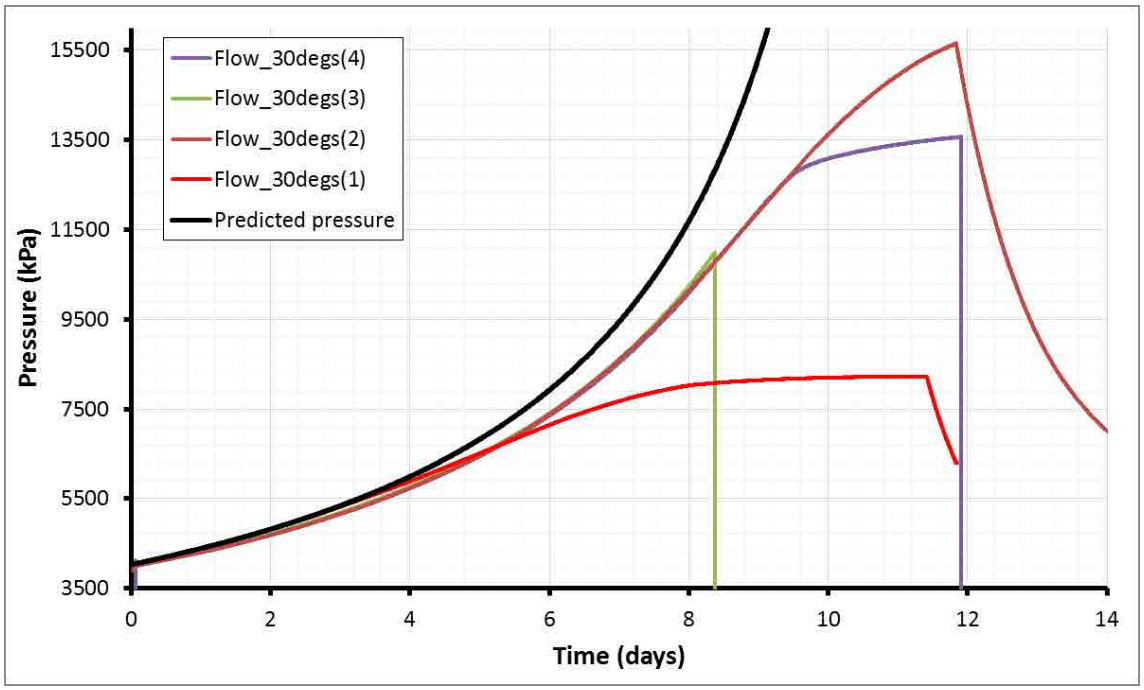

Figure 47 –Results for four gas injection tests conducted on a fracture oriented 30° to the slip plane. As can be seen, considerable differences are seen in peak pressure and form of the curve indicating that fracture transmissivity is not repeatable.

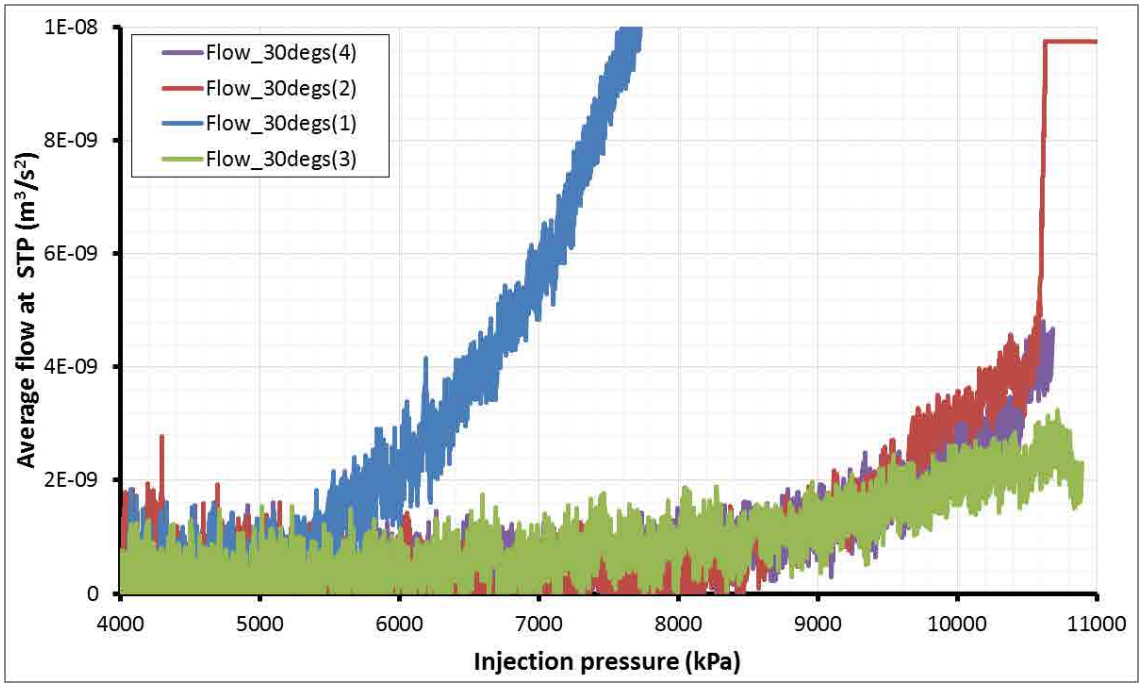

Figure 48 – Gas entry pressure predicted from the average flow at STP for four gas injection tests conducted on a fracture oriented 30° to the slip plane. As can be seen, repeatable gas entry pressure is seen for three of the four tests, with one test (1) showing a considerably lower gas entry pressure.

Test	Fracture angle	+/-	Method 1			Method 2		
			Gas entry pressure (kPa)	Average entry pressure	+/-	Gas entry pressure (kPa)	Average entry pressure	+/-
30degs(1)	30°	0.5°	*5200*	7670	289	4373	4640	120
30degs(2)			8000			*7380*		
30degs(3)			7000			4700		
30degs(4)			8000			4839		

Table 11 – Results for gas entry pressure for four gas injection experiments conducted at an angle of 30°. Method 1 = gas entry determined from STP gas flow into the fracture; Method 2 = entry pressure inferred from comparing pressure curve with ideal gas law

4.5 GAS BREAKTHROUGH EXPERIMENTS ON A SLIP PLANE ORIENTATION OF 45°

A total of three gas injection experiments were conducted on a fracture oriented 45° with respect to the slip direction. As stated previously, each test was performed as identical as possible, with identical water content of gouge produced, similar normal load, similar volumes of gas, and identical gas injection rates. The only parameter that is likely to have varied between tests was the thickness of the gouge at the start of the experiment. However, as best as could be established, this did not vary significantly between tests as the gouge became very thin in all tests.

4.5.1 Test ASR_Tau25_45gGI (Gas test 15)

The first test conducted on a fracture oriented 45° to the slip-plane was test ASR_Tau25_45gGI; the fifteenth gas injection test conducted. The results of the test are summarised in Figure 49. As can be seen in Figure 49a, the gas injection experiment resulted in a maximum gas pressure of approximately 15 MPa, with peak pressure not achieved. Following the cessation of gas injection on Day 12, a gas shut-in stage was conducted for two days. An asymptote of pressure would have taken a significant amount of time and so the experiment was halted. The normal displacement data (Figure 49c) showed that the fracture compressed throughout the entire test history. The eddy current sensors showed a complex history (Figure 49d). Initially one sensor showed compression, whilst the other showed dilation. At the onset of gas flow inferred from the ideal gas law (Figure 49b), the fracture was seen to dilate. The complexity of the fracture width data suggest that the top-block was “rocking” about the central loading point and did move when gas became mobile.

Figure 49b shows the difference between the gas pressure observed and the predicted pressure from the ideal gas law. As seen, this data suggests that gas started to enter the fracture at around Day 3.5 when the gas pressure was 5,050 kPa. Figure 49e shows the average flow at STP into the fracture, with gas entry inferred to be approximately 8,500 kPa. Considerable difference was therefore seen in gas entry pressure predicted from the two employed methods.

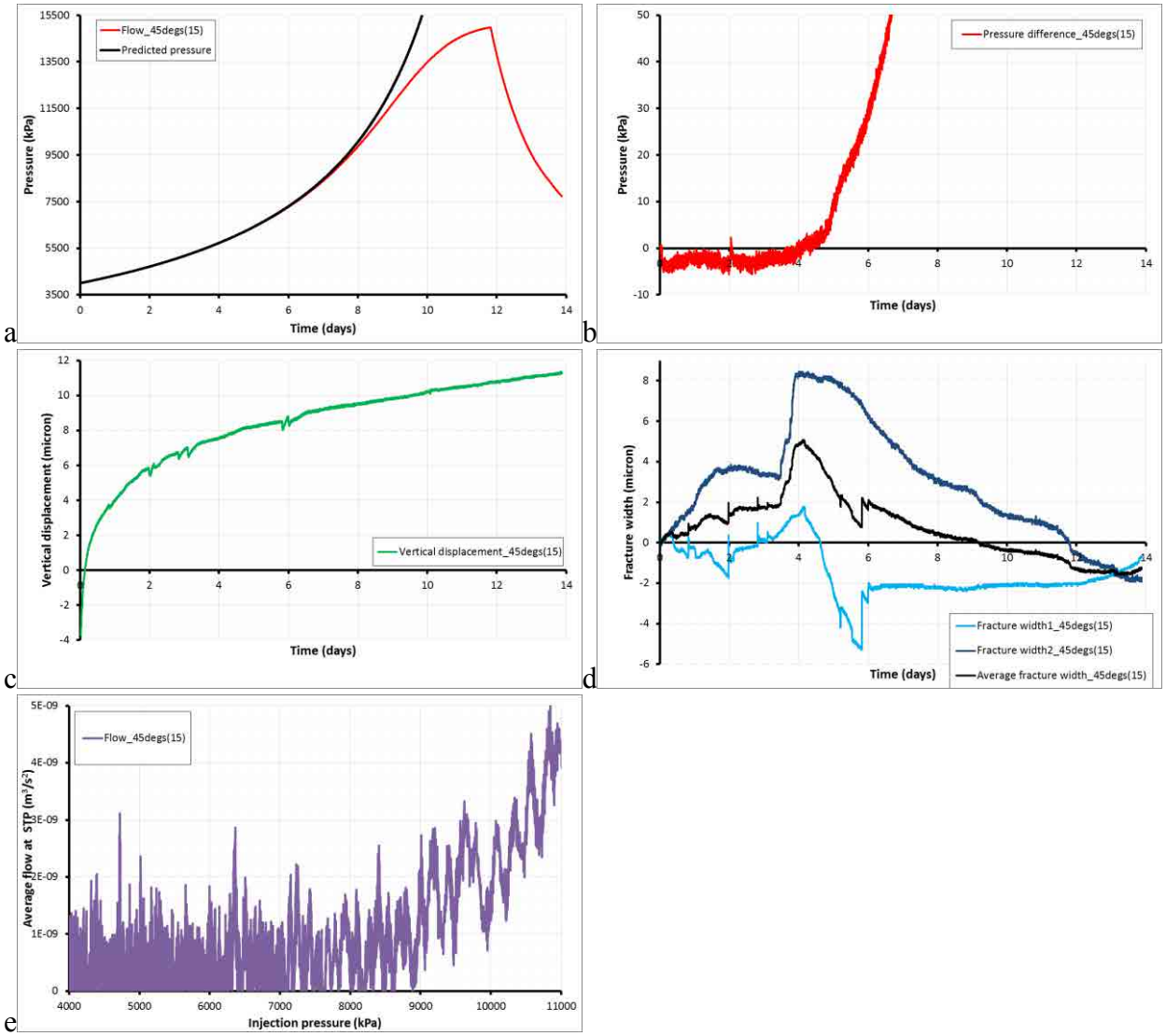

Figure 49 – Results for gas injection test 15 / ASR_Tau25_45gGI. a) Gas injection pressure compared with prediction from ideal gas law; b) comparison of gas injection and ideal gas law as a way of predicting gas entry pressure; c) normal displacement; d) fracture width; e) flow into the slip plane as a way of predicting gas entry pressure.

4.5.2 Test ASR_Tau26_45gGI (Gas test 16)

The second test conducted on a fracture oriented 45° to the slip-plane was test ASR_Tau26_45gGI; the sixteenth gas injection test conducted. The results of the test are summarised in Figure 50. As can be seen in Figure 50a, the gas injection experiment resulted in a maximum gas pressure of approximately 9.5 MPa, with peak pressure not achieved. The normal displacement data (Figure 50c) showed that the fracture compressed throughout the entire test history. The eddy current sensors showed a complex history (Figure 50d). Initially one sensor showed compression, whilst the other showed dilation. Unlike in the previous test (ASR_Tau25_45gGI), at the onset of gas flow inferred from the ideal gas law (Figure 49b), no dilation or compression was seen of the fracture. A later dilation was seen at Day 6 in one sensor, which could signify the onset of enhanced gas flow.

Figure 50b shows the difference between the gas pressure observed and the predicted pressure from the ideal gas law. As seen, this data suggests that gas started to enter the fracture at around Day 3.5 when the gas pressure was 5,375 kPa. Figure 50e shows the average flow at STP into the fracture, with gas entry inferred to be approximately 7,500 kPa. Considerable difference was therefore seen in gas entry pressure predicted from the two employed methods.

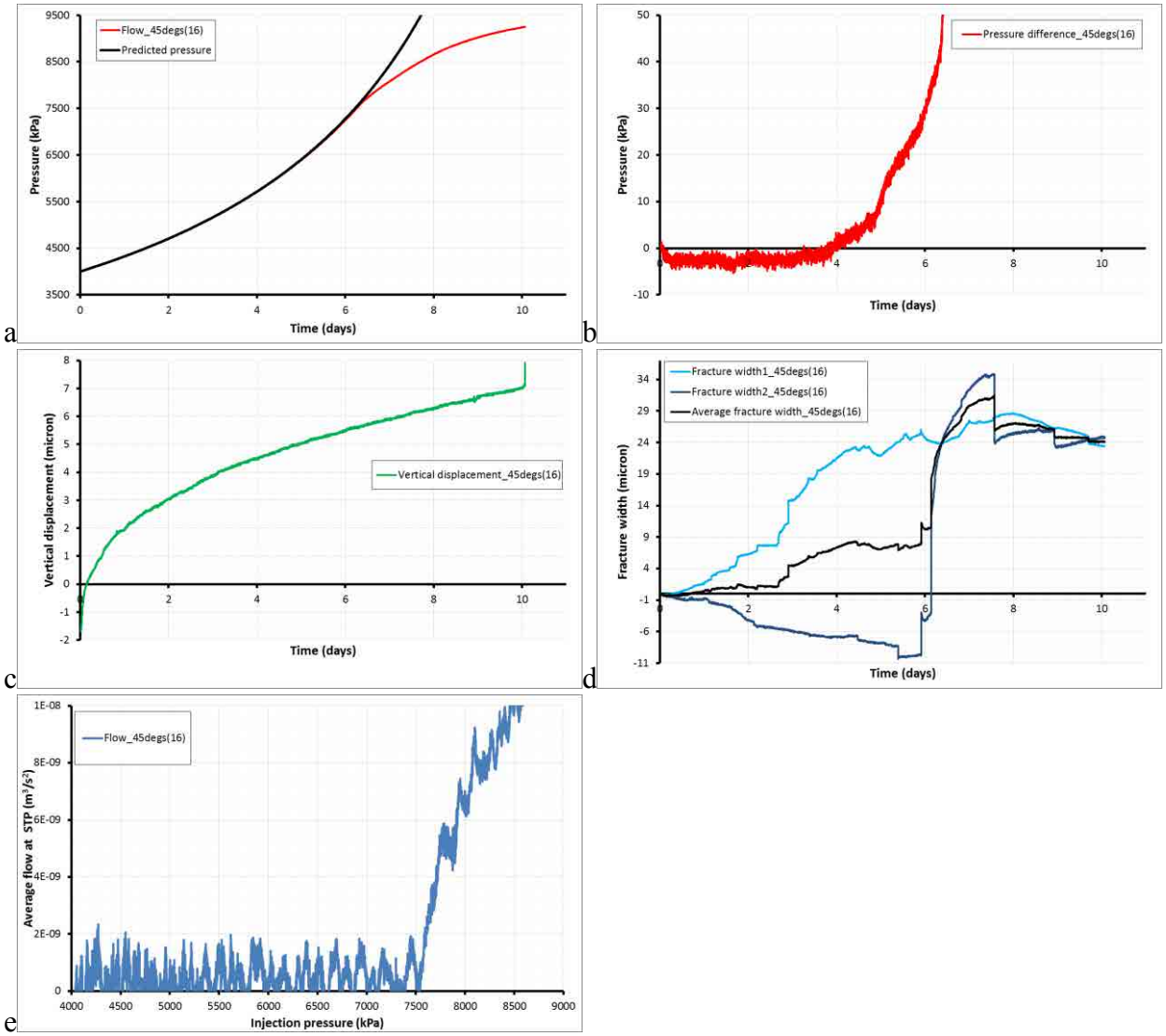

Figure 50 – Results for gas injection test 16 / ASR_Tau26_45gGI. a) Gas injection pressure compared with prediction from ideal gas law; b) comparison of gas injection and ideal gas law as a way of predicting gas entry pressure; c) normal displacement; d) fracture width; e) flow into the slip plane as a way of predicting gas entry pressure.

4.5.3 Test ASR_Tau27_45gGI (Gas test 17)

The third test conducted on a fracture oriented 45° to the slip-plane was test ASR_Tau27_45gGI; the seventeenth gas injection test conducted. The results of the test are summarised in Figure 51. As can be seen in Figure 51a, the gas injection experiment resulted in a maximum gas pressure of approximately 8.2 MPa, with peak pressure not achieved. The normal displacement data (Figure 51c) showed that the fracture compressed throughout the entire test history. The eddy current sensors showed a complex history (Figure 51d). Both sensors initially showed dilation, quickly followed after Day 1 by compression. The complexity of the fracture width data suggest that the top-block was "rocking" about the central loading point, but did not move when gas became mobile.

Figure 51b shows the difference between the gas pressure observed and the predicted pressure from the ideal gas law. As seen, this data suggests that gas started to enter the fracture at around Day 1.8 when the gas pressure was 4,550 kPa. Figure 51e shows the average flow at STP into the fracture, with gas entry inferred to be approximately 5,000 kPa. For test ASR_Tau27_45gGI there is agreement in the prediction of gas entry pressure from the two methods employed.

However, the estimate from STP flow into the fracture is considerably lower when compared with the other two tests conducted on the same orientation of fracture.

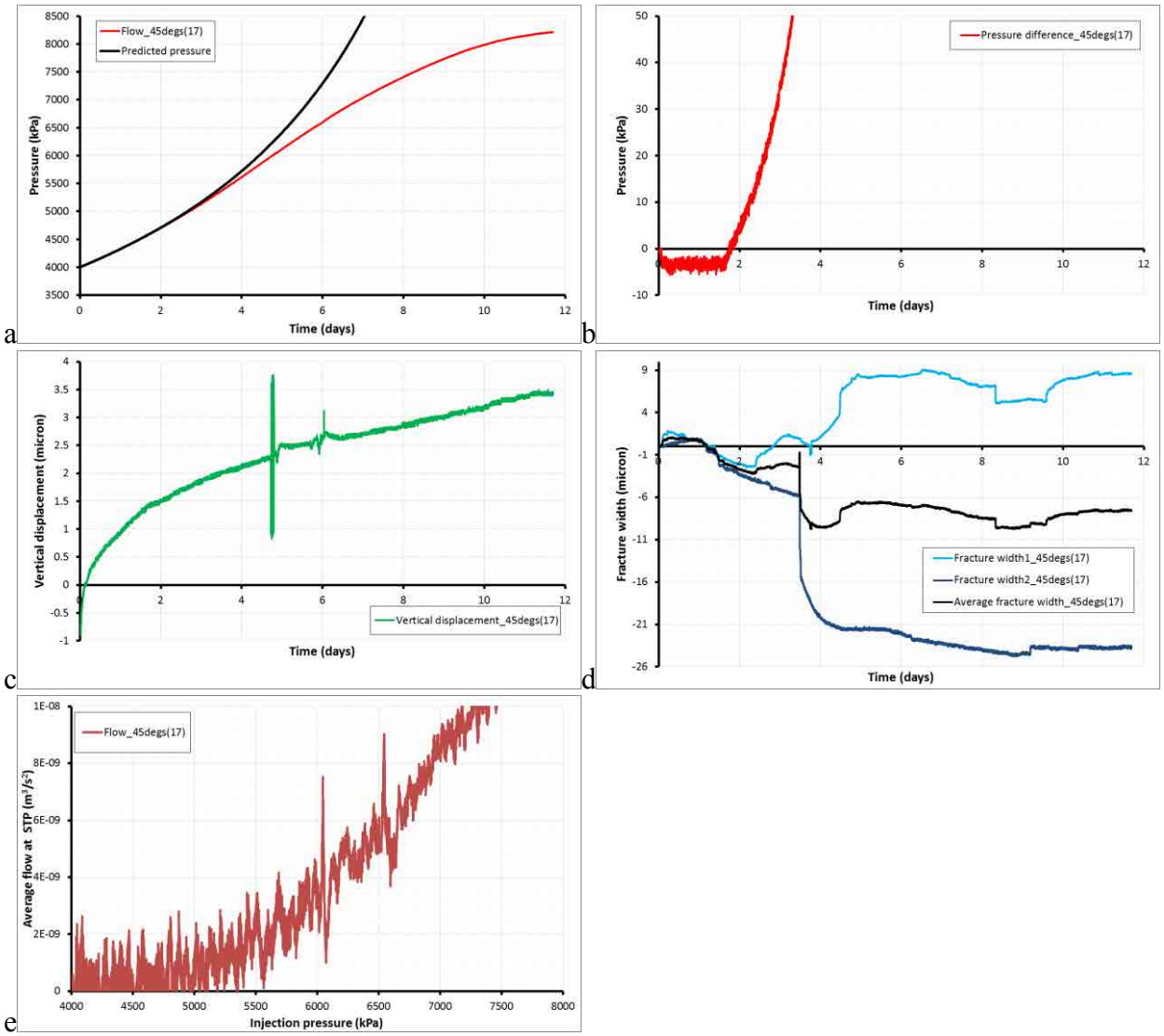

Figure 51 – Results for gas injection test 17 / ASR_Tau27_45gGI. a) Gas injection pressure compared with prediction from ideal gas law; b) comparison of gas injection and ideal gas law as a way of predicting gas entry pressure; c) normal displacement; d) fracture width; e) flow into the slip plane as a way of predicting gas entry pressure.

4.5.4 Results for tests conducted on a slip plane orientation of 45°

Figure 52 shows the gas pressure for all three of the gas injection tests conducted on a fracture oriented 45° to the slip-direction. As clearly seen, there is little repeatability in the gas pressures achieved with pressures between 8 and 15 MPa achieved. However, close examination of the data showed that gas entry pressure had a much better repeatability. As described above, two methods were employed for estimating the gas entry pressure; the first compared the gas pressure result with the predicted pressure from the ideal gas law and the second calculated average flow at STP into the fracture. All results are summarised in Table 12, with the results from flow into the fracture shown in Figure 53. As seen in Figure 53, two tests showed similar gas entry pressures of between 7.5 and 8.5 MPa, whilst one test had an anomalously low gas entry pressure of 5 MPa.

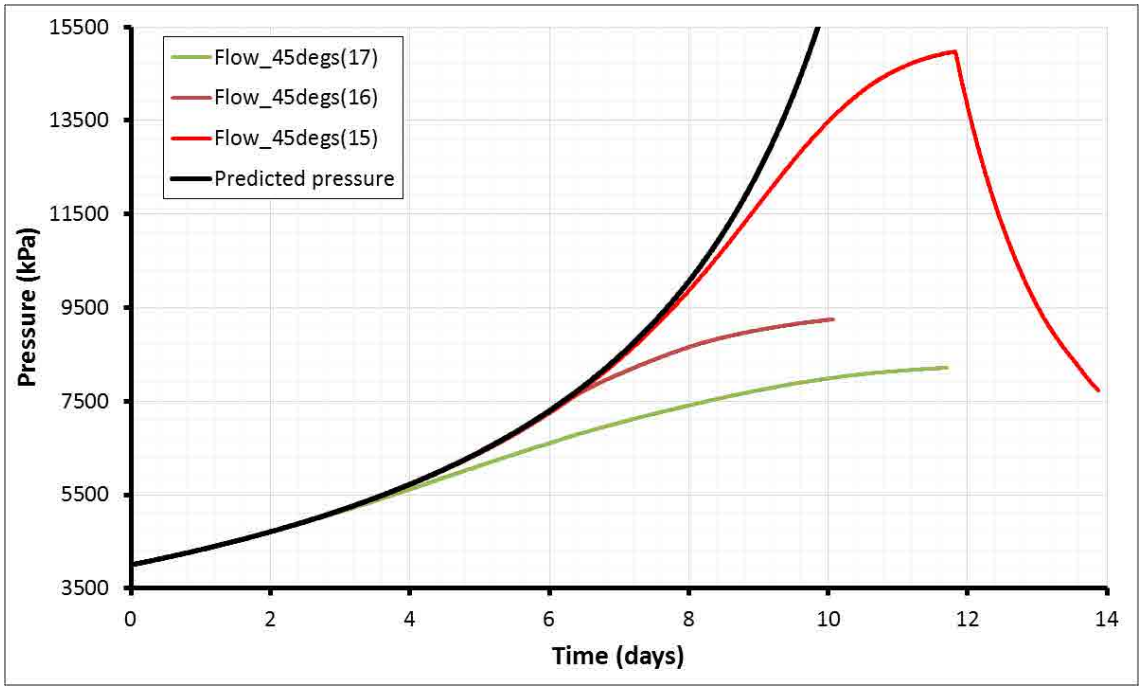

Figure 52 –Results for three gas injection tests conducted on a fracture oriented 45° to the slip plane. As can be seen, considerable differences are seen in peak pressure and form of the curve indicating that fracture transmissivity is not repeatable.

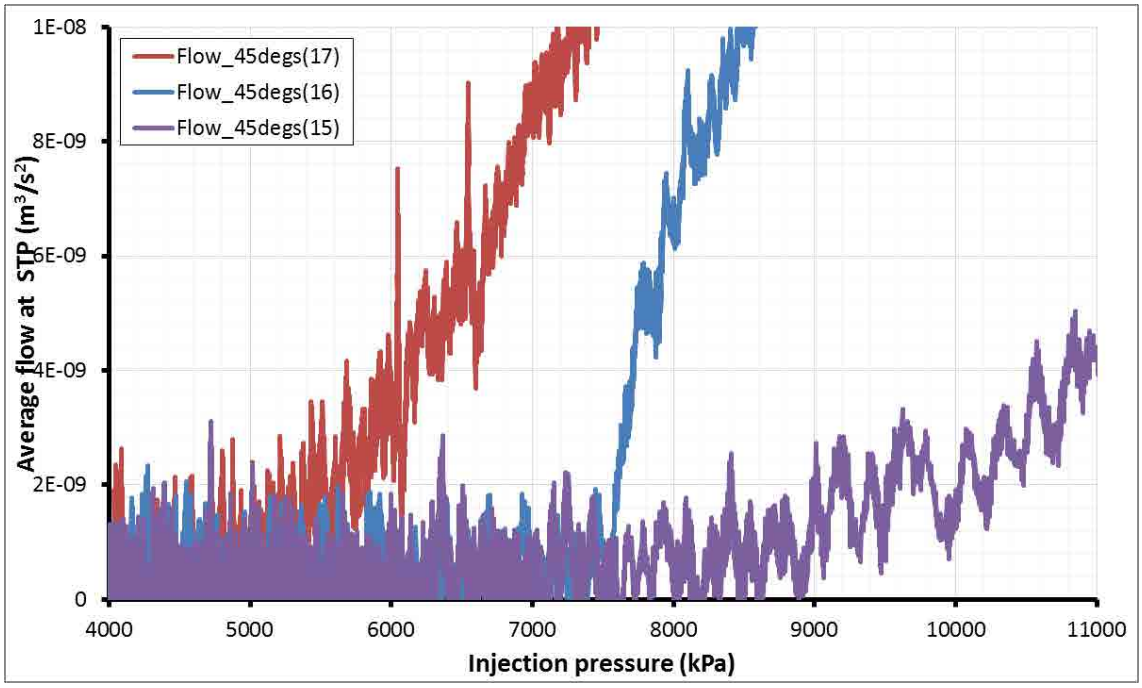

Figure 53 – Gas entry pressure predicted from the average flow at STP for three gas injection tests conducted on a fracture oriented 45° to the slip plane. As can be seen, repeatable gas entry pressure is seen for two of the three tests, with one test (17) showing a considerably lower gas entry pressure.

Test	Fracture angle	+/-	Method 1			Method 2		
			Gas entry pressure (kPa)	Average entry pressure	+/-	Gas entry pressure (kPa)	Average entry pressure	+/-
45degs(15)	45°	0.5°	8500	8000	354	5046	4980	212
45degs(16)			7500			5373		
45degs(17)			*5000*			4531		

Table 12 – Results for gas entry pressure for three gas injection experiments conducted at an angle of 45°. Method 1 = gas entry determined from STP gas flow into the fracture; Method 2 = entry pressure inferred from comparing pressure curve with ideal gas law

4.6 RESULTS AND DISCUSSION FOR TESTS CONDUCTED AT DIFFERENT ORIENTATIONS

All test results are summarised in Table 13. Figure 54 and Figure 55 show the gas entry pressure for all fifteen of the gas injection tests conducted on fractures oriented 0°, 15°, 30°, and 45° to the slip-direction. The data in Figure 54 was determined from average flow at STP into the fracture. The data in Figure 55 was determined from the ideal gas law. As can be clearly seen, both methods of determining gas entry pressure showed variation with respect to fracture orientation. It has to be noted that Figure 54a and Figure 55a both show considerable spread in the data achieved at each of the four fracture orientations. However, even taking into account this spread in result it is clear that a relationship exists between gas entry pressure and fracture orientation. Both methods suggest that the minimum gas entry pressure occurs when the fracture orientation is approximately 25º to the shear direction. Kaolinite has a reported friction angle of 15º (Waltham, 1994), therefore the prediction from the parabolic fit of the data is not related to friction angle. However, STP flow predicts a gas entry pressure minimum on a fracture oriented at 15º; therefore gas entry pressure may to be related to friction angle.

Figure 56 shows the average data for gas entry pressure at the different fracture orientations for both methods of predicting gas entry pressure. As can be seen, a similar relationship of variation of gas entry pressure with fracture orientation was seen. However, greater variability is seen in the prediction from STP flow, which also predicts an entry pressure approximately 3 MPa greater than the prediction from the ideal gas flow.

The repeatability seen in gas entry pressure and not peak pressure suggests that the physics governing the onset of flow was maintained for all tests; however, once gas started to be mobile the permeability of the kaolinite filled fracture plane was inconsistent, resulting in variations of behaviour post gas entry. This may relate to the number of pathways that form.

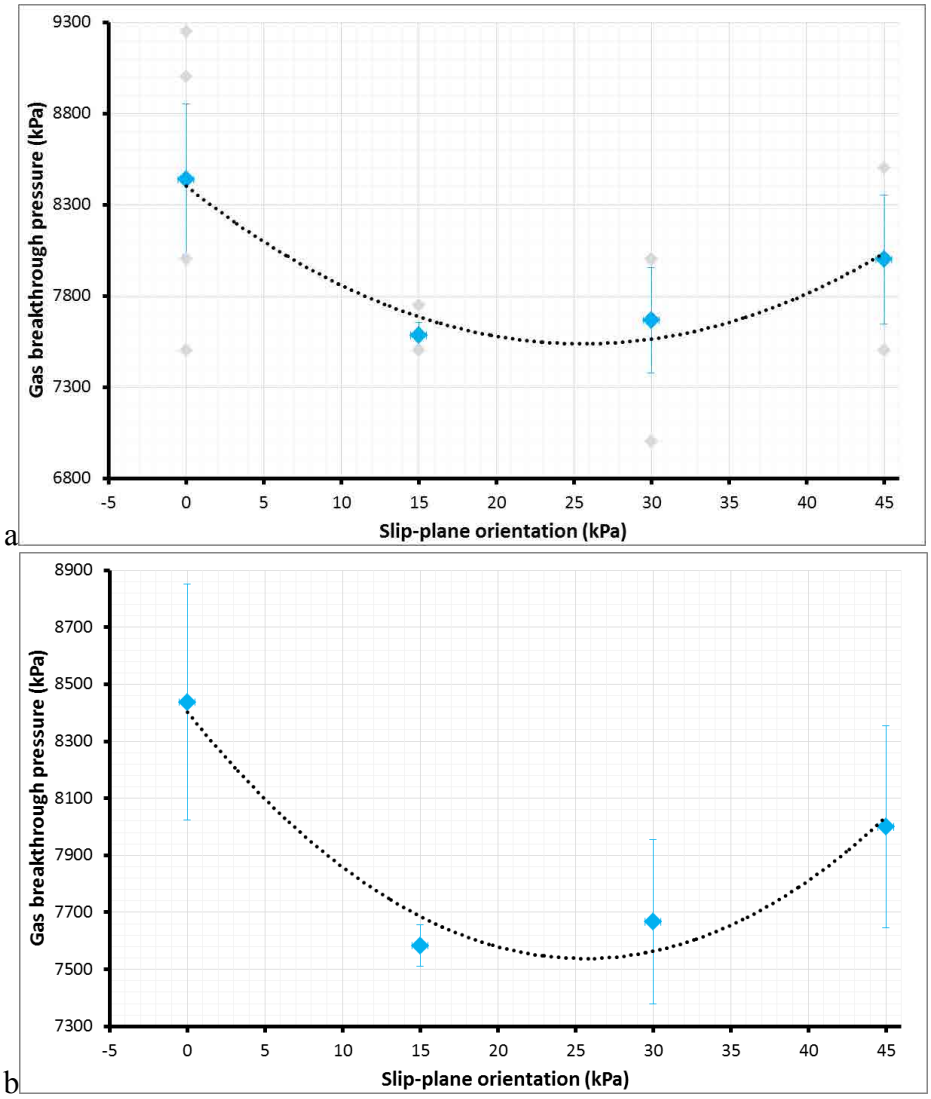

Figure 54 – Relationship of gas entry pressure determined from STP gas flow into the fracture for all tests. a) all test data and average results; b) average data.

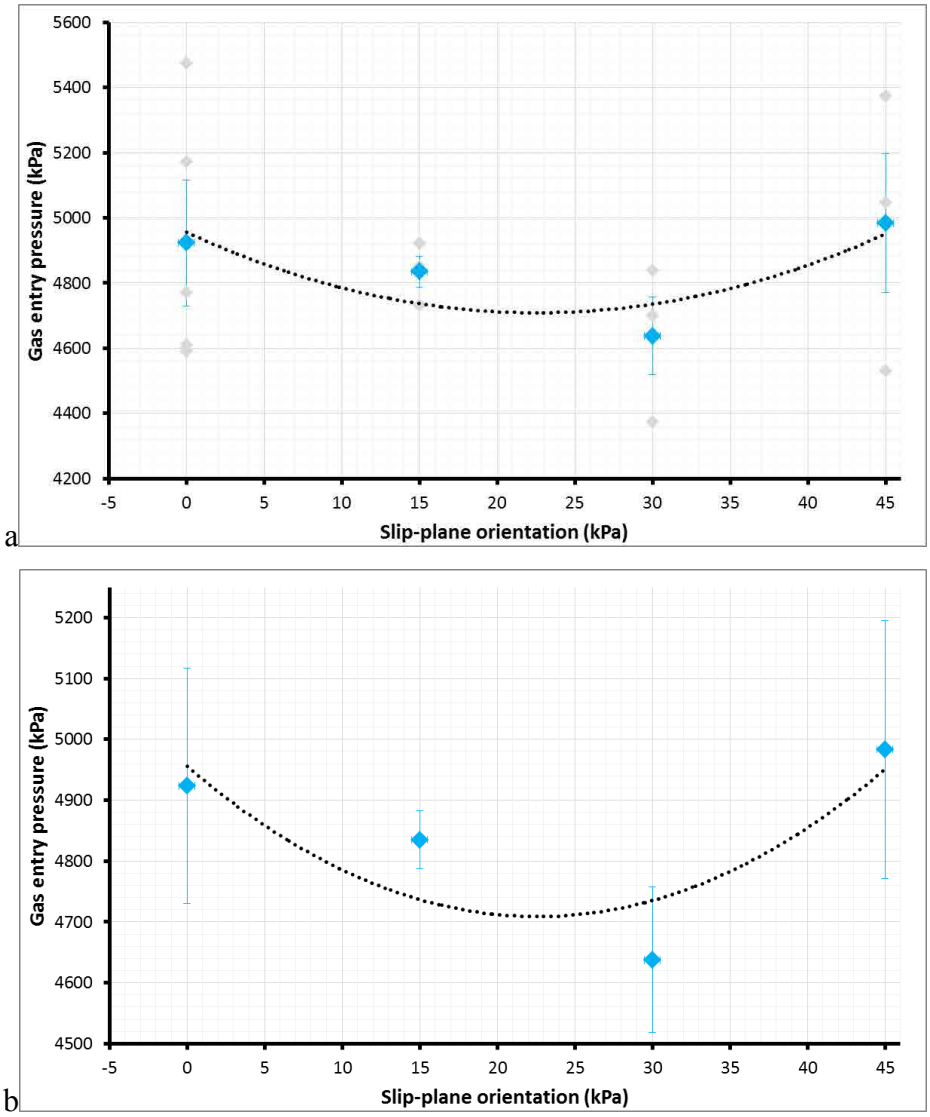

Figure 55 – Relationship of gas entry pressure determined from the ideal gas law for all tests. a) all test data and average results; b) average data.

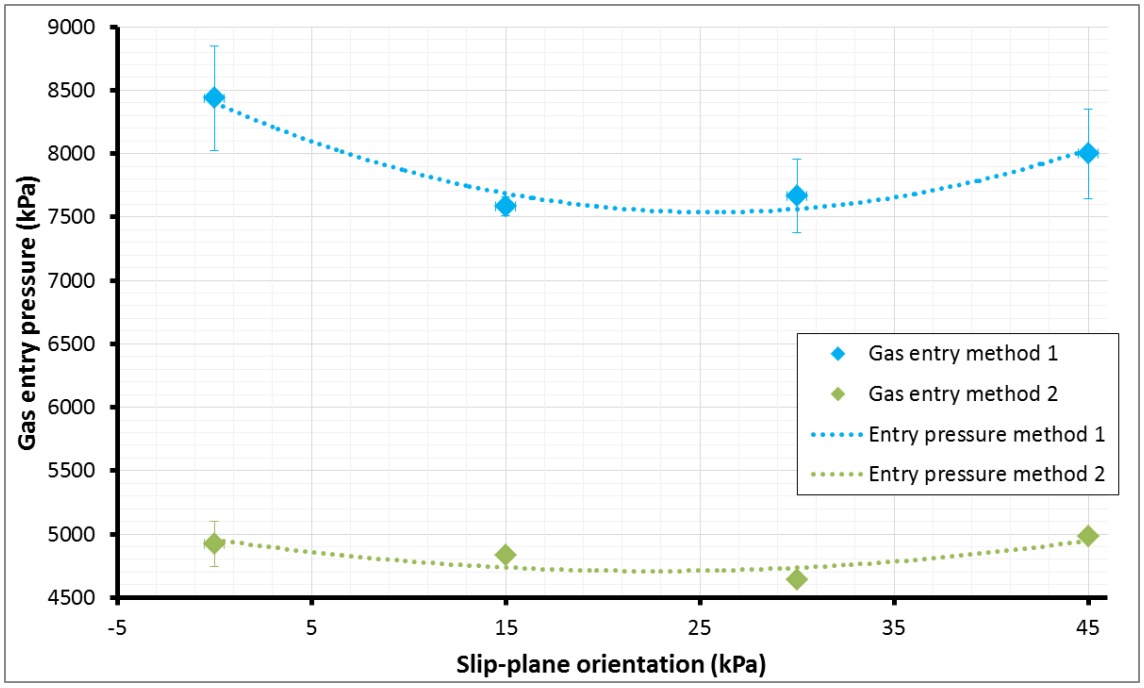

Figure 56 – Comparison of results from the two methods used to determine gas entry pressure. Both methods show that gas entry pressure alters with fracture orientation, with entry pressure determined from STP flow into the fracture predicting higher pressures.

Test	Fracture angle	+/-	Method 1			Method 2		
			Gas entry pressure (kPa)	Average entry pressure	+/-	Gas entry pressure (kPa)	Average entry pressure	+/-
0degs(5)	0°	0.5°	*5000*	8440	413	4772	4920	193
0degs(6)			8000			4610		
0degs(7)			9000			4590		
0degs(11)			7500			5475		
0degs(12)			9250			5170		
15degs(8)	15°	0.5°	7500	7580	72	4850	4840	48
15degs(9)			7500			4732		
15degs(10)			7750			4922		
30degs(1)	30°	0.5°	*5200*	7670	289	4373	4640	120
30degs(2)			8000			*7380*		
30degs(3)			7000			4700		
30degs(4)			8000			4839		
45degs(15)	45°	0.5°	8500	8000	354	5046	4980	212
45degs(16)			7500			5373		
45degs(17)			*5000*			4531		

Table 13 – Results for gas entry pressure for all gas injection experiments. Method 1 = gas entry determined from STP gas flow into the fracture; Method 2 = entry pressure inferred from comparing pressure curve with ideal gas law

4.7 THE EFFECT OF SHEAR DISPLACEMENT ON GAS ENTRY AND SUBSEQUENT GAS FLOW

A total of five gas injection experiments were conducted with the addition of active shear. Two tests were conducted on a flat slip plane, i.e. at an orientation of 0° with respect to the slip direction in order to look at repeatability. A further three tests were conducted at orientations of 15°, 30° and 45° in order to investigate the relationship between active shear and gas entry pressure at different angles. As stated previously, each test was performed as identical as possible, with identical water content of gouge produced, similar normal load, similar volumes of gas, and identical gas injection rates. The only parameter that is likely to have varied between tests was the thickness of the gouge at the start of the experiment. However, as best as could be established, this did not vary significantly between tests as the gouge became very thin in all tests. In all shear tests the sample began shear at the same time as the constant flow pressure ramp was started.

4.7.1 Test ASR_Tau28_00gGIS (Gas test 18)

The first test conducted with active shear was performed on a fracture oriented 0° to the slip-plane was ASR_Tau28_00gGIS; the eighteenth gas injection test conducted. The results of the test are summarised in Figure 57. As can be seen in Figure 57a and Figure 57f, the sample was started to shear at the same time as the constant flow pressure ramp. The gas injection experiment resulted in a maximum gas pressure of approximately 7.3 MPa, with peak pressure achieved. Following the cessation of gas injection on Day 12, a gas shut-in stage was conducted for two days. An asymptote of pressure would have taken a significant amount of time and so the experiment was halted. The normal displacement data (Figure 57c) suggest that the induction sensor malfunctioned. The eddy current sensors showed a complex history (Figure 57d). One sensor showed minor dilation of approximately 1 µm followed by compression of 6 µm, whilst the other showed compression of 3 µm followed by dilation of over 20 µm. No correlation was seen between the fracture width sensor and gas flow inferred from the ideal gas law (Figure 57b). The data suggest that the top-block was “rocking” about the central loading point. Figure 57e shows the horizontal stress data; this indicated that peak and residual strength correspond and was achieved about Day 4 with a magnitude of 0.9 MPa.

Figure 57b shows the difference between the gas pressure observed and the predicted pressure from the ideal gas law. As seen, this data suggests that gas started to enter the fracture at around Day 2 when the gas pressure was 4,620 kPa. Figure 57g shows the average flow at STP into the fracture, with gas entry inferred to be approximately 5,500 kPa. The two estimates are approximately in agreement.

4.7.2 Test ASR_Tau29_00gGIS (Gas test 19)

The second test conducted with active shear was conducted on a fracture oriented 0° to the slip-plane was ASR_Tau29_00gGIS; the nineteenth gas injection test conducted. The results of the test are summarised in Figure 58. As can be seen in Figure 58a, the gas injection experiment resulted in a maximum gas pressure of approximately 8.25 MPa. Peak pressure was achieved and considerable pressure drop was experienced by the time that gas entry was halted; over 2.5 MPa pressure drop. This degree of pressure drop had not previously been observed and indicated that the slip-plane had become highly conductive. Following the cessation of gas injection on Day 11, a gas shut-in stage was conducted for half a day. An asymptote of pressure would have taken a significant amount of time and so the experiment was halted. The normal displacement data (Figure 58c) suggested that the induction sensor malfunctioned. The eddy current sensors showed a complex history (Figure 58d). Both sensors showed general dilation, with episodes of compression. It is possible that the onset of gas flow inferred from the ideal gas law (Figure 58b) was showing as enhanced dilation in one sensor and compression in the other, suggesting that the top-block “rocked” about the central loading point as gas started to move. Figure 57e shows the

horizontal stress data; this indicated that peak and residual strength correspond and was achieved about Day 3 with a magnitude of 0.9 MPa. However, at peak stress the horizontal stress started to increase until the end of the experiment.

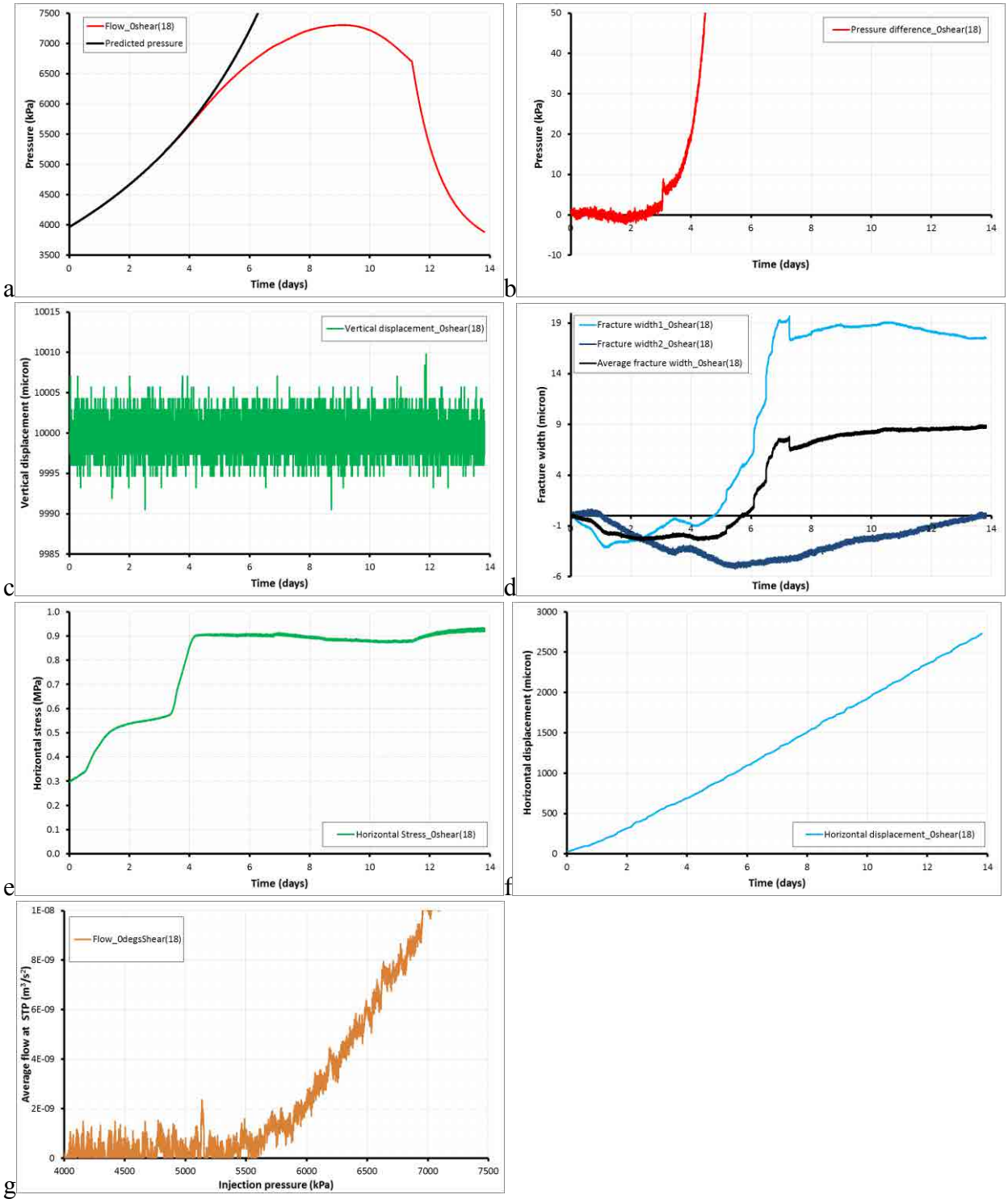

Figure 57 – Results for gas injection test 18 / ASR_Tau28_00gGIS. a) Gas injection pressure compared with prediction from ideal gas law; b) comparison of gas injection and ideal gas law as a way of predicting gas entry pressure; c) normal displacement; d) fracture width; e) horizontal stress; f) shear displacement; g) flow into the slip plane as a way of predicting gas entry pressure.

Figure 58b shows the difference between the gas pressure observed and the predicted pressure from the ideal gas law. As seen, this data suggests that gas started to enter the fracture at around Day 2 when the gas pressure was 4,700 kPa. Figure 58e shows the average flow at STP into the

fracture, with gas entry inferred to be approximately 6,000 kPa. In contrast to test ASR_Tau28_00gGIS, the methods used to predict gas entry gave dissimilar results.

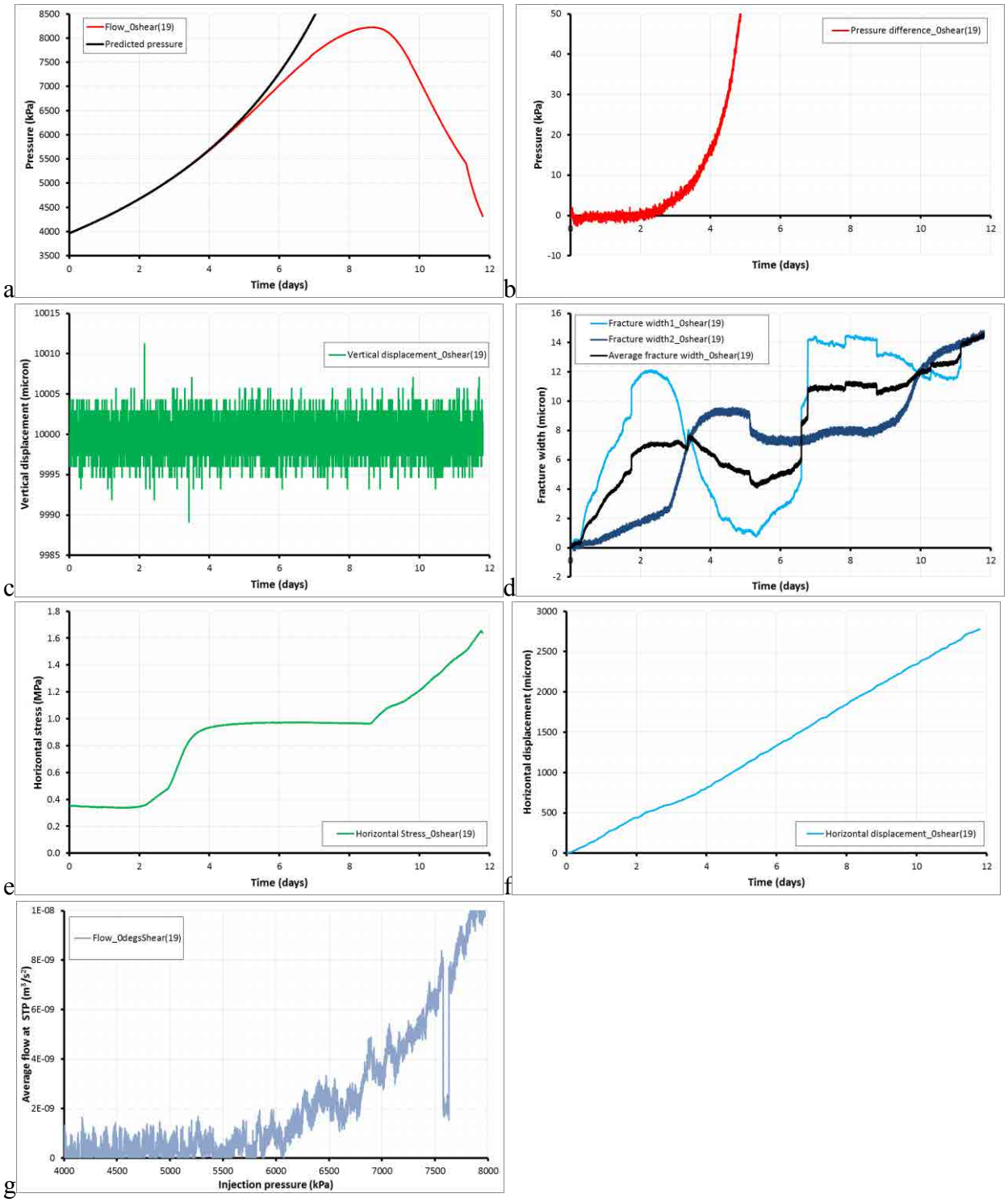

Figure 58 – Results for gas injection test 19 / ASR_Tau29_00gGIS. a) Gas injection pressure compared with prediction from ideal gas law; b) comparison of gas injection and ideal gas law as a way of predicting gas entry pressure; c) normal displacement; d) fracture width; e) horizontal stress; f) shear displacement; g) flow into the slip plane as a way of predicting gas entry pressure.

4.8 COMPARING RESULTS FOR TESTS CONDUCTED ON A SLIP PLANE ORIENTATION OF 0° WITH AND WITHOUT ACTIVE SHEAR

A total of seven gas injection experiments were conducted on a flat slip plane, with two of these being conducted with active shear. As stated previously, each test was performed as identical as possible, with identical water content of gouge produced, similar normal load, similar volumes of gas, and identical gas injection rates. The only parameter that is likely to have varied between tests was the thickness of the gouge at the start of the experiment. However, as best as could be established, this did not vary significantly between tests as the gouge became very thin in all tests.

The results conducted on a slip plane oriented 0º to the shear direction are shown in Figure 59, Figure 60 and Table 14. As seen in Figure 59, horizontal movement had a strong influence on gas transport along the gouge. Both tests conducted during shear reach peak pressure conditions at relatively low pressures compared with non-sheared tests. This suggests that the process of shear enhances transmissivity of the slip-plane. Both tests reached peak pressure and decayed, whereas without shear no pressure decay was observed. Figure 60 and Table 14 show that horizontal movement also reduced the gas entry pressure on average over 2.5 MPa from the estimate determined from STP flow. However, a lesser reduction in gas entry pressure of 0.3 MPa was seen from the estimate of gas entry pressure determined from the ideal gas law. In both methods for determining gas entry pressure a reduction was seen. It was expected that active shear would result in self-sealing. This would result in a raised gas entry pressure and a reduced transmissivity along the slip-plane. The current test results show the opposite with a reduced gas entry pressure and enhanced fracture transmissivity. This suggests that shear is not an effective self-sealing mechanism to gas in kaolinite fault gouges.

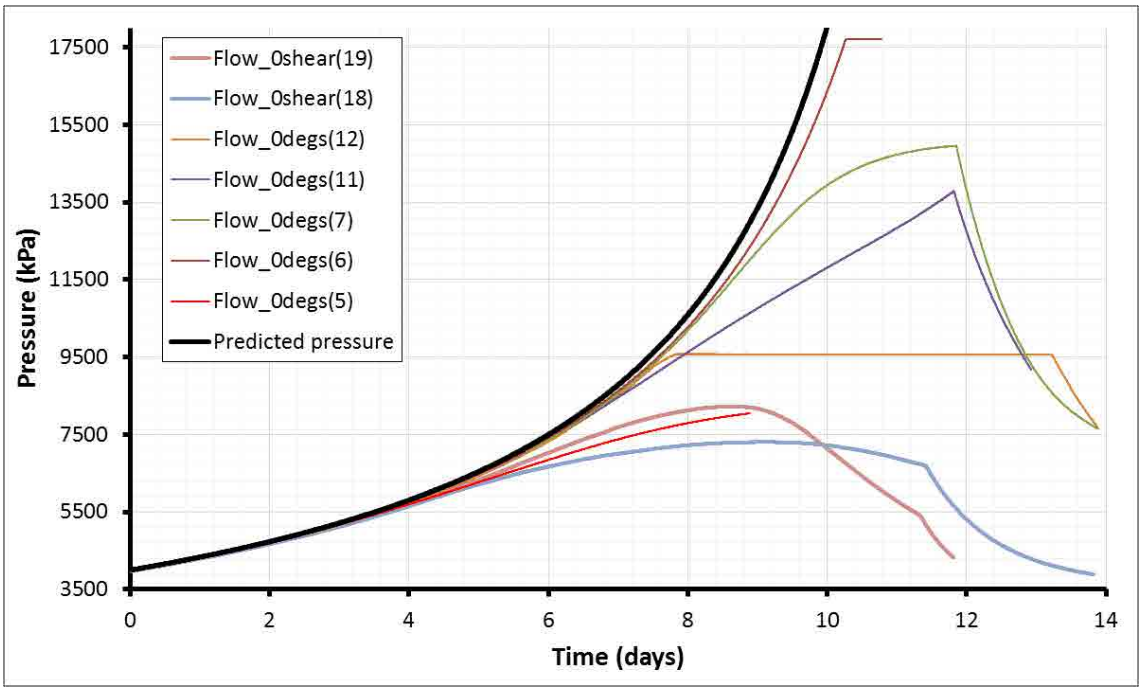

Figure 59 – Comparing results for gas injection tests conducted on a fracture oriented 0° to the slip plane with and without active shear. Due to the variability seen in gas fracture transmissivity, it is unclear if shear has significantly altered behaviour. It can be seen that the peak pressure appears to be lower.

Test	Fracture angle	+/-	Method 1			Method 2		
			Gas entry pressure (kPa)	Average entry pressure	+/-	Gas entry pressure (kPa)	Average entry pressure	+/-
0degs(5)	0°	0.5°	*5000*	8440	413	4772	4920	193
0degs(6)			8000			4610		
0degs(7)			9000			4590		
0degs(11)			7500			5475		
0degs(12)			9250			5170		
0Shear(18)	0°@	0.5°	5500	5750	177	4620	4660	28
0Shear(19)			6000			4700		

Table 14 – Results for gas entry pressure for all gas injection experiments conducted at 0º. @ with shear; Method 1 = gas entry determined from STP gas flow into the fracture; Method 2 = entry pressure inferred from comparing pressure curve with ideal gas law.

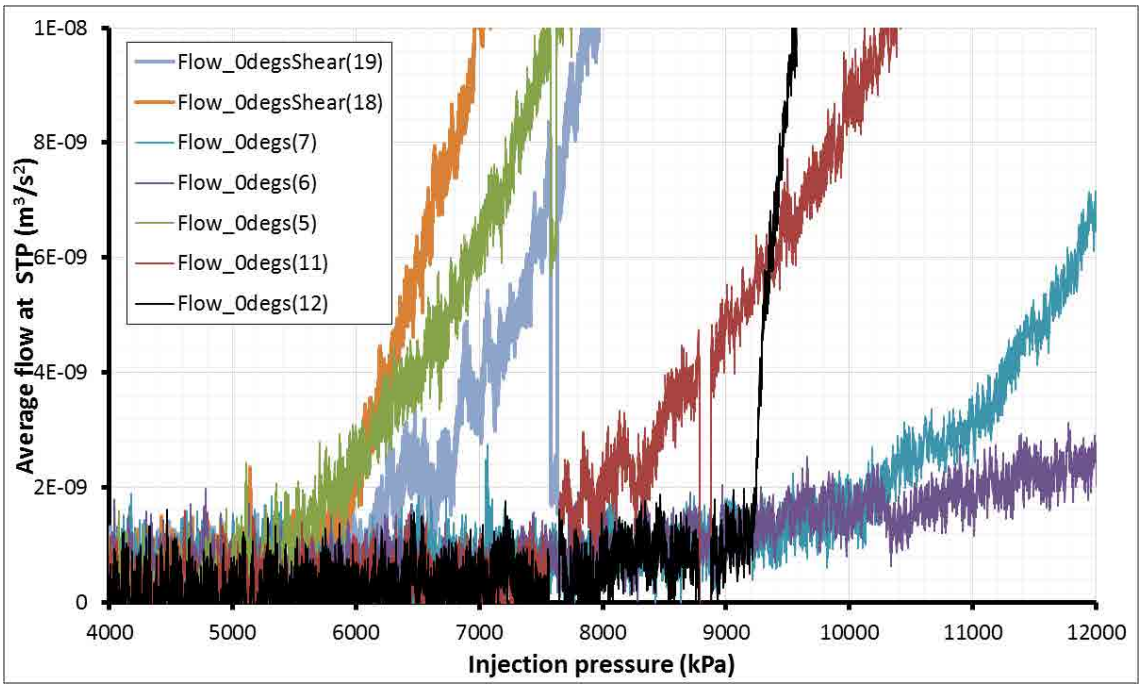

Figure 60 – Comparing results for gas entry pressure predicted from the average flow at STP for gas injection tests conducted on a fracture oriented 0° to the slip plane with and without active shear. It can be seen that shear has reduced the gas entry pressure, although this is similar in magnitude to the anomalously low entry pressure test (5).

4.8.1 Test ASR_Tau30_30gGIS (Gas test 20)

One test was conducted on a fracture oriented 30° to the slip-plane with the addition of shear, namely test ASR_Tau30_30gGI; the twentieth gas injection test conducted. The results of the test are summarised in Figure 61. As can be seen in Figure 61a, the gas injection experiment resulted in a maximum gas pressure of approximately 13.5 MPa, with peak pressure not achieved. Following the cessation of gas injection on Day 11, a gas shut-in stage was conducted for one day. An asymptote of pressure would have taken a significant amount of time and so the experiment was halted. The normal displacement data (Figure 61c) suggest that the induction sensor malfunctioned. The eddy current sensors showed a complex history (Figure 61d). Both sensors initially showed dilation, although by day 1 one sensor compressed to about -5 µm and did not change for over 8 days. The other sensor showed continued dilation throughout the test

history. Figure 61e shows the horizontal stress data; this indicated that peak and residual strength correspond and was achieved about Day 3 with a magnitude of 3.5 MPa.

Figure 61b shows the difference between the gas pressure observed and the predicted pressure from the ideal gas law. As seen, this data suggests that gas started to enter the fracture at around Day 3 when the gas pressure was 4,700 kPa. Figure 61e shows the average flow at STP into the fracture, with gas entry inferred to be approximately 7,000 kPa.

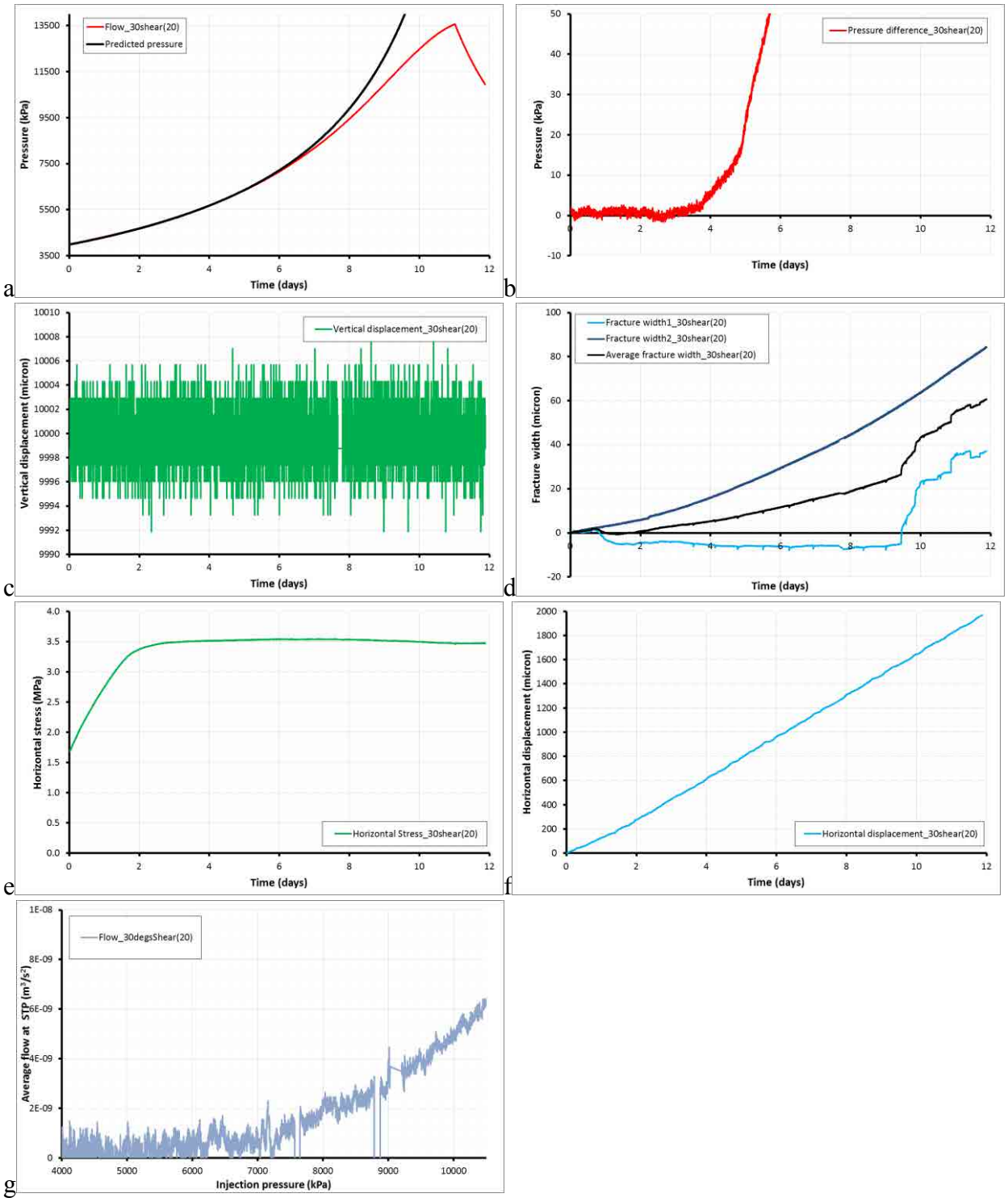

Figure 61 – Results for gas injection test 20 / ASR_Tau30_30gGIS. a) Gas injection pressure compared with prediction from ideal gas law; b) comparison of gas injection and ideal gas law as a way of predicting gas entry pressure; c) normal displacement; d) fracture width; e) horizontal stress; f) shear displacement; g) flow into the slip plane as a way of predicting gas entry pressure.

4.8.2 Test ASR_Tau31_45gGIS (Gas test 21)

One test was conducted on a fracture oriented 45° to the slip-plane with the addition of shear, namely test ASR_Tau31_45gGI; the twenty-first gas injection test conducted. The results of the test are summarised in Figure 62. As can be seen in Figure 62a, the gas injection experiment resulted in a maximum gas pressure of approximately 8.5 MPa, with peak pressure achieved and a drop of approximately 1 MPa by the time shear was stopped on Day 10. Following the cessation of gas injection the pressure was allowed to decay and suggests that pressure would asymptote at approximately 4 MPa. The normal displacement data (Figure 62c) suggest that the induction sensor malfunctioned. The eddy current sensors showed a complex history (Figure 62d). One sensor showed small (< 2 μm) dilation, with compression occurring approximately day 9 when peak pressure was achieved. The other sensor showed considerable compression of about 50 μm with dilation occurring the time of peak pressure. Therefore at peak gas pressure the top block "rocked" and gas migrated along the slip-plane. Figure 62e shows the horizontal stress data and indicates that something was faulty with the shear load cell.

Figure 62b shows the difference between the gas pressure observed and the predicted pressure from the ideal gas law. As seen, this data suggests that gas started to enter the fracture at around Day 2 when the gas pressure was 4,450 kPa. Figure 62e shows the average flow at STP into the fracture, with gas entry inferred to be approximately 5,000 kPa.

4.8.3 Test ASR_Tau32_15gGIS (Gas test 22)

One test was conducted on a fracture oriented 15° to the slip-plane with the addition of shear, namely test ASR_Tau32_15gGI; the twenty-second gas injection test conducted. The results of the test are summarised in Figure 63. As can be seen in Figure 63a, the gas injection experiment resulted in a maximum gas pressure of approximately 11 MPa. Shear was stopped on Day 12 soon after peak pressure had been achieved and a drop of about 0.5 MPa to a residual pressure of approximately 10 MPa occurred. However, approximately Day 14 all gas pressure was lost in an instantaneous enhanced gas breakthough event. The normal displacement data (Figure 63c) suggests that the induction sensor malfunctioned. The eddy current sensors showed a complex history (Figure 63d). One sensor initially showed dilation, followed on Day 1 by compression of approximately 5 μm. The other sensor showed much greater compression of about 27 μm. No correlation is seen in the flow data and the eddy current sensor data. Figure 63e shows the horizontal stress data and indicates that the shear load cell was faulty.

Figure 63b shows the difference between the gas pressure observed and the predicted pressure from the ideal gas law. As seen, this data suggests that gas started to enter the fracture at around Day 2.5 when the gas pressure was 4,830 kPa. Figure 63e shows the average flow at STP into the fracture, with gas entry inferred to be approximately 5,250 kPa.

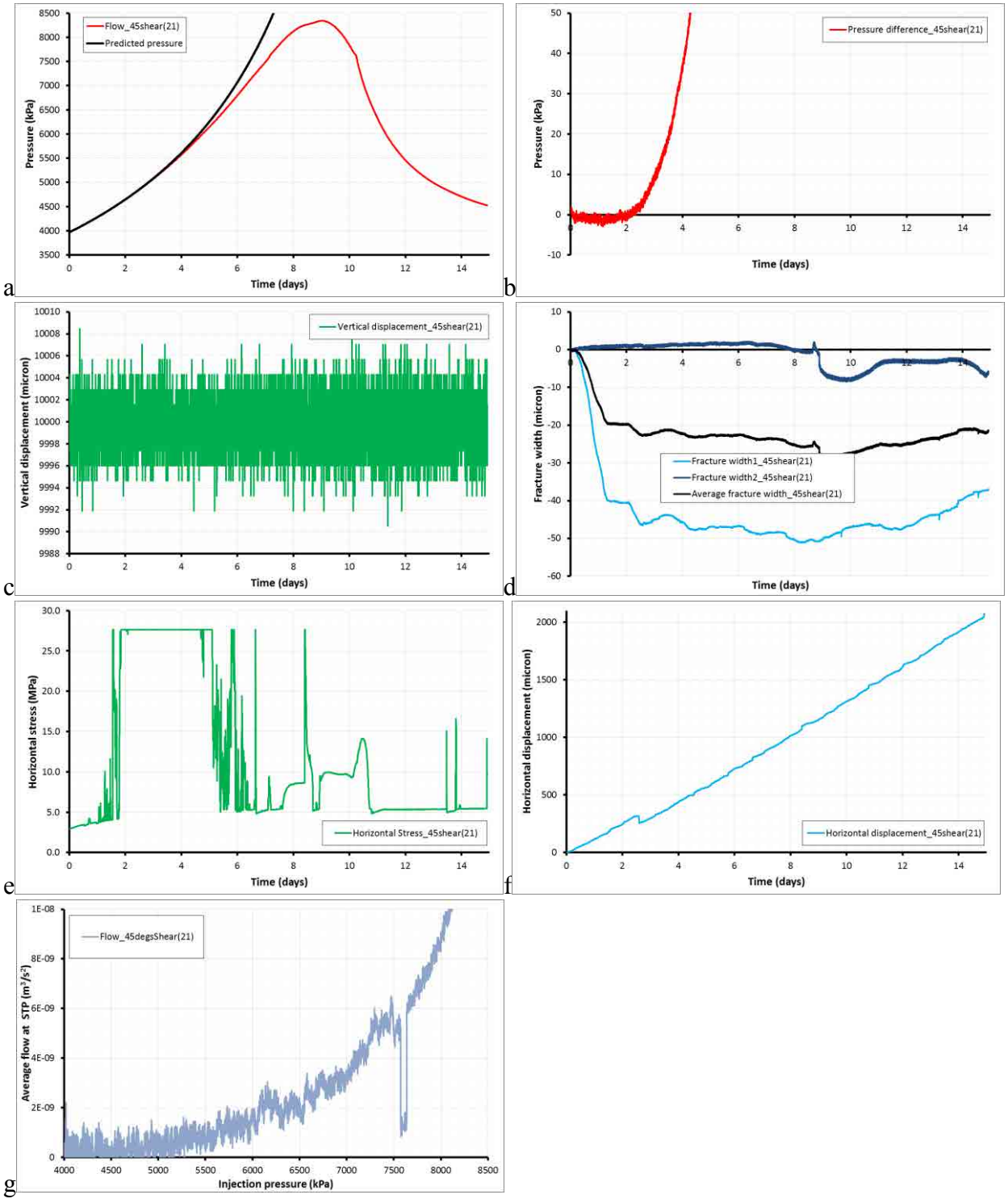

Figure 62 – Results for gas injection test 21 / ASR_Tau31_45gGIS. a) Gas injection pressure compared with prediction from ideal gas law; b) comparison of gas injection and ideal gas law as a way of predicting gas entry pressure; c) normal displacement; d) fracture width; e) horizontal stress [note malfunction]; f) shear displacement; g) flow into the slip plane as a way of predicting gas entry pressure.

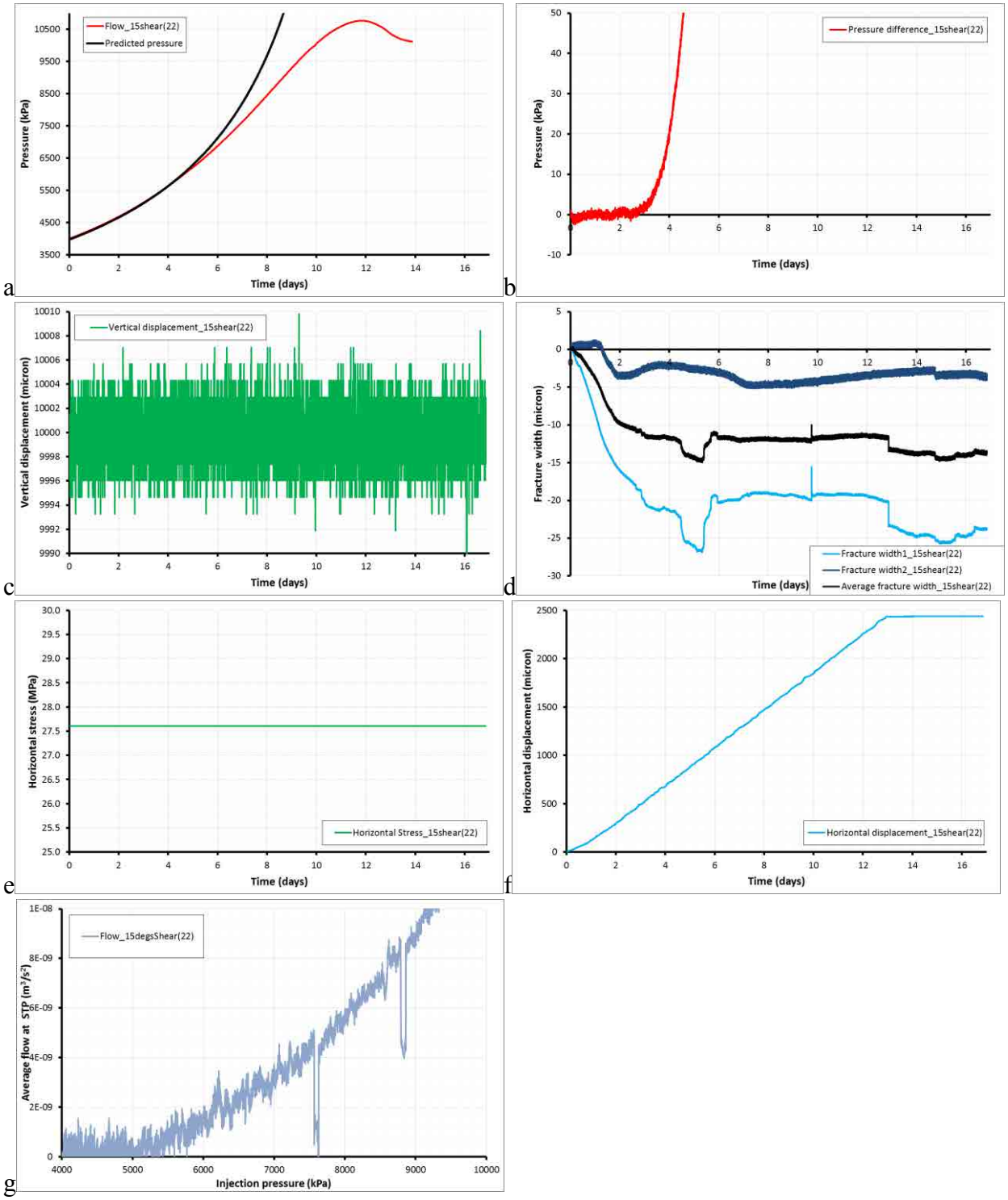

Figure 63 – Results for gas injection test 22 / ASR_ Tau32_15gGIS. a) Gas injection pressure compared with prediction from ideal gas law; b) comparison of gas injection and ideal gas law as a way of predicting gas entry pressure; c) normal displacement; d) fracture width; e) horizontal stress [note malfunction]; f) shear displacement; g) flow into the slip plane as a way of predicting gas entry pressure.

4.8.4 Results for tests conducted with active shear

A total of five gas injection experiments were conducted at different angles with active shear. As stated previously, each test was performed as identical as possible, with identical water content of gouge produced, similar normal load, similar volumes of gas, and identical gas injection rates. The only parameter that is likely to have varied between tests was the thickness of the gouge at

the start of the experiment. However, as best as could be established, this did not vary significantly between tests as the gouge became very thin in all tests.

The results conducted on a slip planes oriented between 0º and 45º to the shear direction are shown in Figure 64, Figure 65 and Table 15. As seen in Figure 64, horizontal movement has resulted in all bar one test to achieve gas peak pressure. Figure 65 shows the influence of shear on the gas entry pressure at different fracture angles. As can be seen in Figure 65a, gas entry pressure ranges from 5 to 5.8 MPa. The polynomial fit achieved by the data suggest that a minimum in gas entry pressure occurred at approximately 37º; therefore shear has resulted in the minimum gas pressure orientation increasing. Figure 65b shows the influence of shear on the gas entry pressure. As can be seen, shear has generally resulted in a 2.5 MPa reduction in gas entry pressure. It was expected that shear would have been an effective self-sealing mechanism and that gas entry pressure would increase. However, the data show that gas finds it easier to enter a slip-plane that is shearing and is more mobile. Figure 65c shows the data for gas entry pressure determined from the ideal gas law. This has a dissimilar form with a maximum gas entry pressure at 15º and a minimum at 45º. This may reflect the difficulty in determining gas entry pressure from this method.

Test	Fracture angle	+/-	Method 1			Method 2		
			Gas entry pressure (kPa)	Average entry pressure	+/-	Gas entry pressure (kPa)	Average entry pressure	+/-
0Shear(18)	0°@	0.5°	5500	5750	177	4620	4660	28
0Shear(19)			6000			4700		
30Shear(20)	30°@	0.5°	7000	7000	100	4700	4700	100
45Shear(21)	45°@	0.5°	5000	5000	100	4450	4450	100
15Shear(22)	15°@	0.5°	5250	5200	100	4830	4830	100

Table 15 – Results for gas entry pressure for all gas injection experiments. # high pressurisation rate; @ with shear; Method 1 = gas entry determined from STP gas flow into the fracture; Method 2 = entry pressure inferred from comparing pressure curve with ideal gas law.

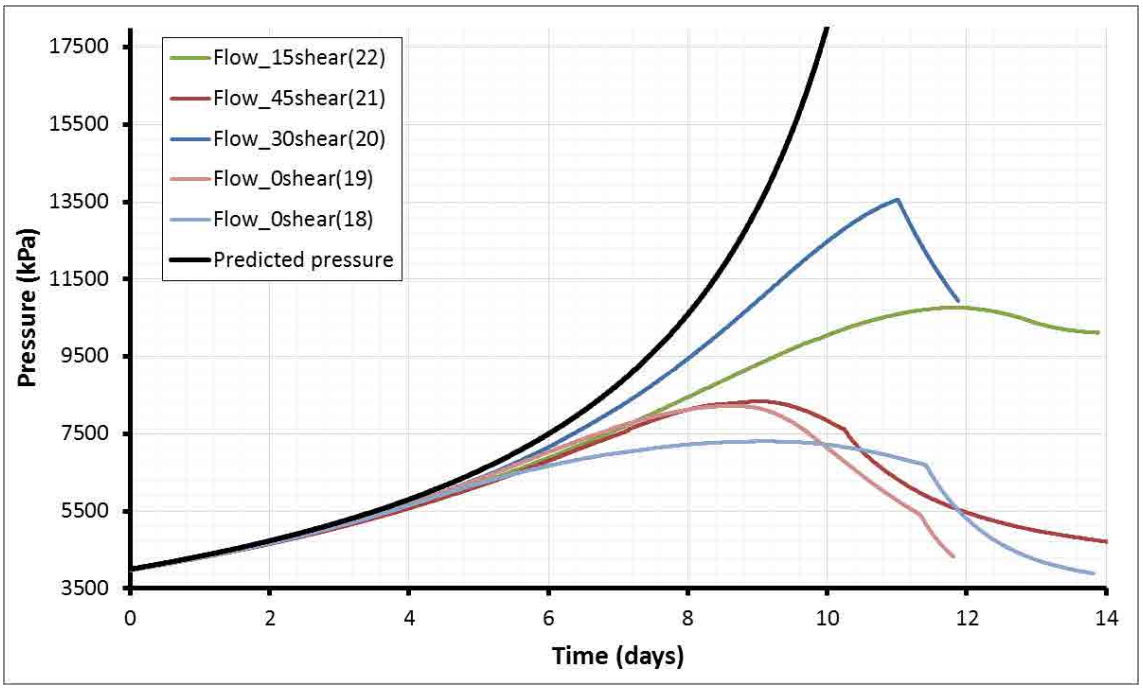

Figure 64 –Results for five gas injection tests conducted with active shear. As can be seen, considerable differences are seen in peak pressure and form of the curve indicating that fracture transmissivity is not repeatable.

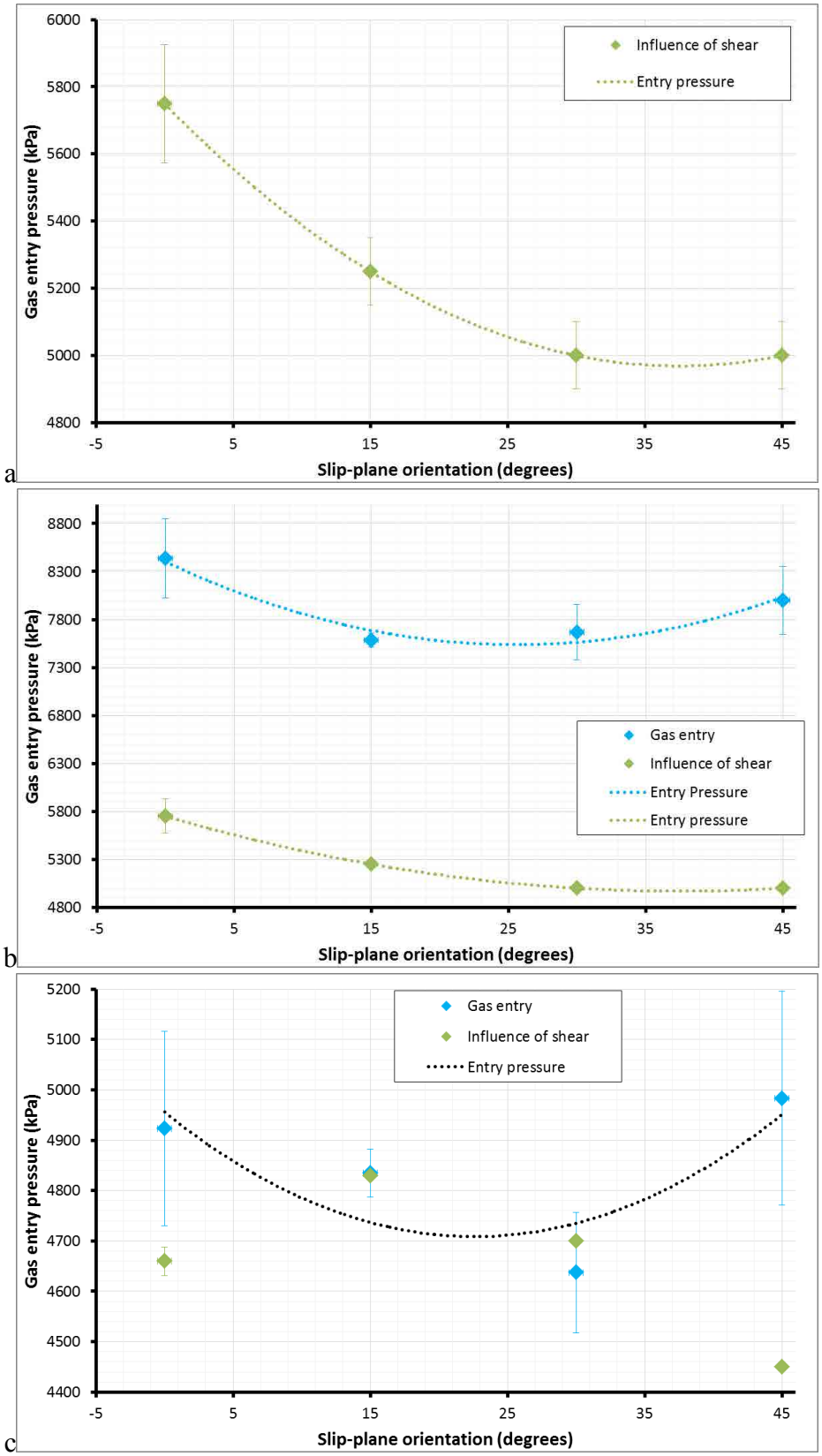

Figure 65 – Gas entry pressure for all tests showing the influence of shear. a) gas entry determined from the STP gas flow into the fracture. This shows that shear greatly reduces entry pressure; b) gas entry determined from comparing pressure response with ideal gas law. This suggests that shear does not significantly alter entry pressure.

4.9 THE EFFECT OF RATE OF PRESSURISATION ON GAS ENTRY AND SUBSEQUENT GAS FLOW

Two gas injection experiments were conducted with an increased rate of pressurisation in order to investigate whether gas entry pressure and gas peak pressure are rate dependent. As stated previously, each test was performed as identical as possible, with identical water content of gouge produced, similar normal load, and similar volumes of gas. The only parameter that is likely to have varied between tests was the thickness of the gouge at the start of the experiment. However, as best as could be established, this did not vary significantly between tests as the gouge became very thin in all tests. Therefore the two experiments conducted only varied by their pressurisation rate.

4.9.1 Test ASR_Tau23_00gGI (Gas test 13)

The first gas injection test conducted at an increased gas injection rate was test ASR_Tau23_00gGI; the thirteenth gas injection test conducted. The results of the test are summarised in Figure 66. As can be seen in Figure 66a, the gas injection experiment resulted in a maximum gas pressure in excess of 24 MPa, the limit of the gas injection ISCO syringe pumps. Following the cessation of gas injection on Day 5, a gas shut-in stage was conducted for three days. An asymptote of pressure would have taken a significant amount of time and so the experiment was halted. The normal displacement data (Figure 66c) suggest that the induction sensor malfunctioned. The eddy current sensors showed a complex history (Figure 66d). One sensor showed no variation for one day, followed by slow dilation that reached a maximum of 4.8 μm by Day 9. It has to be noted that no change was seen to the change in dilation when gas injection was stopped. The other eddy-current sensor showed an initial dilation of 2 μm, followed by a contraction between Day 2 and 3, followed by dilation. No correlation could be seen between the eddy current sensor data and the onset of gas flow inferred from the ideal gas law (Figure 66b).

Figure 66b shows the difference between the gas pressure observed and the predicted pressure from the ideal gas law. As seen, these data suggests that gas started to enter the fracture at around Day 1.5 when the gas pressure was 4,845 kPa. Figure 66e shows the average flow at STP into the fracture, with gas entry inferred to be approximately 7,000 kPa.

4.9.2 Test ASR_Tau24_00gGI (Gas test 14)

The second gas injection test conducted at an increased gas injection rate was test ASR_Tau24_00gGI; the fourteenth gas injection test conducted. The results of the test are summarised in Figure 67. As can be seen in Figure 67a, the gas injection experiment resulted in a maximum gas pressure in excess of 24 MPa, the limit of the gas injection ISCO syringe pumps. Following the cessation of gas injection on Day 5, a gas shut-in stage was conducted for six days. An asymptote of pressure was nearly achieved and suggests an asymptote at 4 MPa. The normal displacement data (Figure 67c) suggest that the induction sensor malfunctioned. The eddy current sensors showed a complex history (Figure 67d). Both sensors generally showed dilation with episodes of contraction. No correlation could be seen between the eddy current sensor data and the onset of gas flow inferred from the ideal gas law (Figure 67b).

Figure 67b shows the difference between the gas pressure observed and the predicted pressure from the ideal gas law. As seen, these data suggests that gas started to enter the fracture at around Day 2.5 when the gas pressure was 6,000 kPa. Figure 67e shows the average flow at STP into the fracture, with gas entry inferred to be approximately 8,000 kPa.

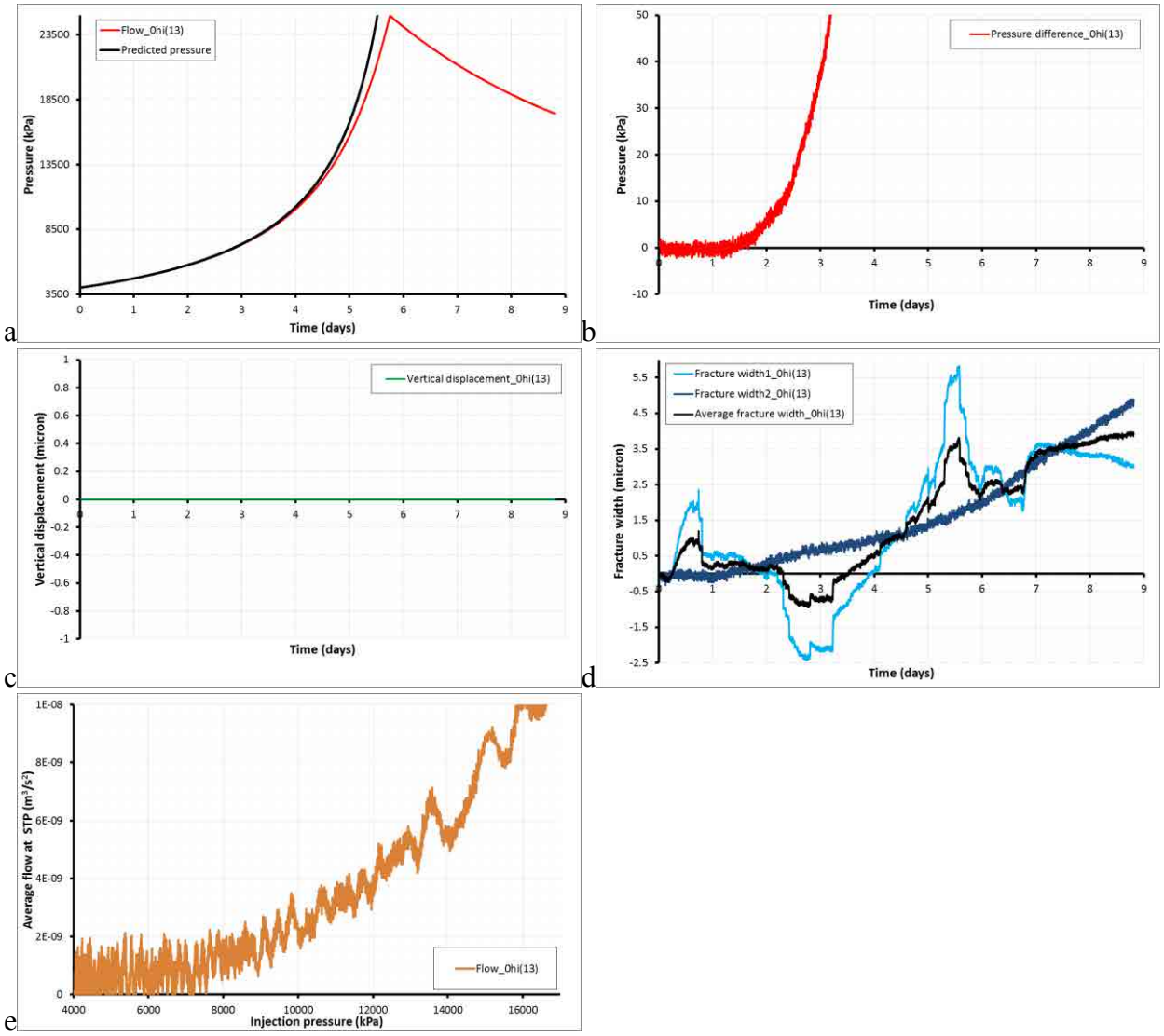

Figure 66 – Results for gas injection test 13 / ASR_Tau23_00gGI. a) Gas injection pressure compared with prediction from ideal gas law; b) comparison of gas injection and ideal gas law as a way of predicting gas entry pressure; c) normal displacement [note malfunction]; d) fracture width; e) flow into the slip plane as a way of predicting gas entry pressure.

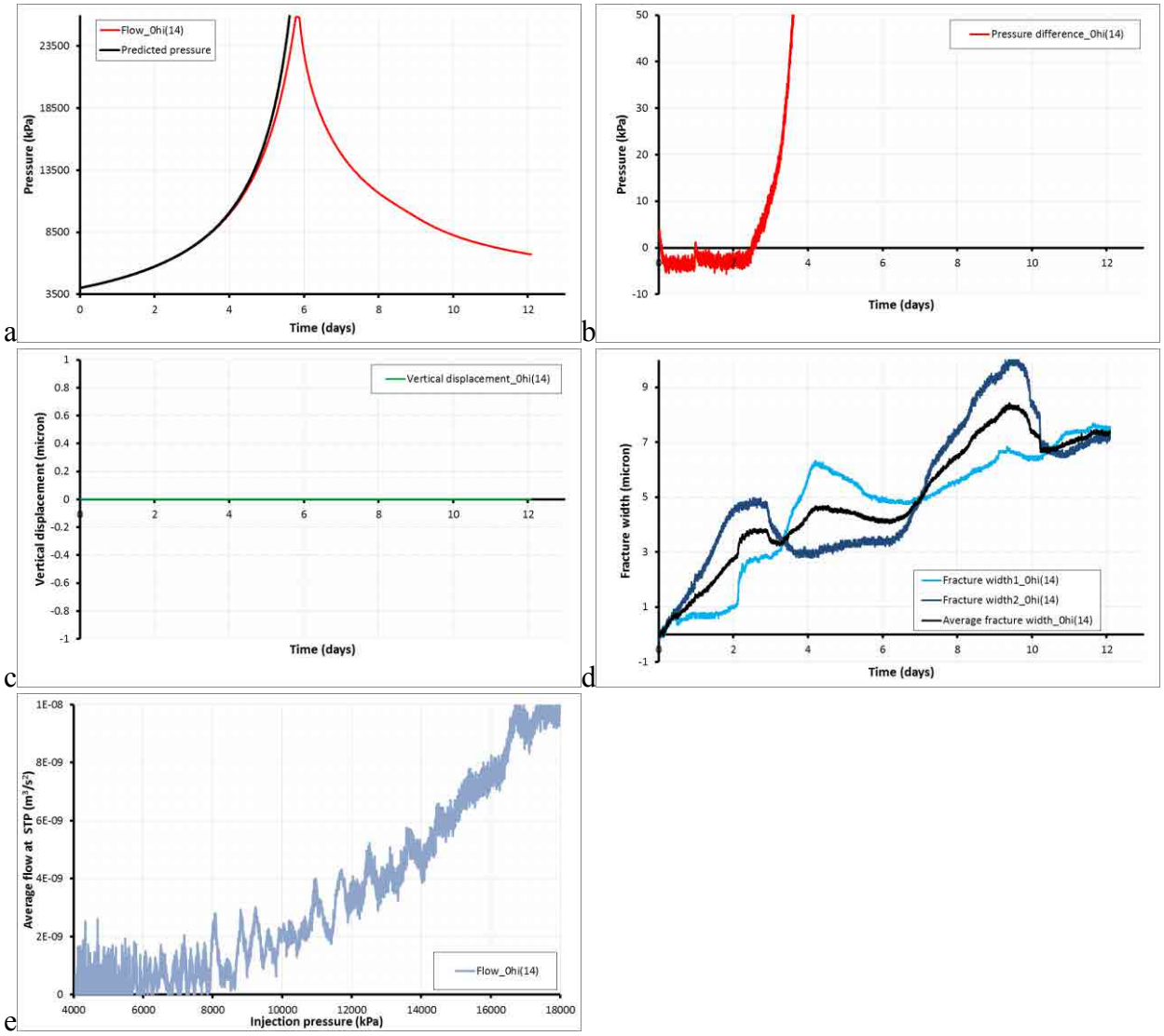

Figure 67 – Results for gas injection test 14 / ASR_Tau24_00gGI. a) Gas injection pressure compared with prediction from ideal gas law; b) comparison of gas injection and ideal gas law as a way of predicting gas entry pressure; c) normal displacement [note malfunction]; d) fracture width; e) flow into the slip plane as a way of predicting gas entry pressure.

4.10 RESULTS FOR TESTS CONDUCTED AT INCREASED INJECTION RATE

Only two tests were conducted with an increased gas injection rate and both tests showed similar general results. As stated previously, each test was performed as identical as possible, with identical water content of gouge produced, similar normal load, and similar volumes of gas. The only parameters that were likely to have varied between tests were the thickness of the gouge at the start of the experiment and the change in gas injection rate. However, as best as could be established, gouge thickness did not vary significantly between tests as the gouge became very thin in all tests.

The results conducted on a slip planes oriented at 0º with an increased gas injection rate are shown in Figure 68, Figure 69, and Table 16. As seen in Figure 68, an increased gas injection rate significantly altered the gas response of the gouge; with significantly higher gas pressure achieved in excess of 24 MPa. Neither test showed signs of reaching peak pressure behaviour.

Figure 69 and Table 16 show that both tests had similar gas entry pressure when determined from STP flow, which also corresponded with the gas entry pressure for all other tests conducted. This suggests that the rate of pressurisation was not influencing gas entry pressure.

However, the entry pressure determined from the ideal gas law for one test suggests that gas entry pressure was slightly raised. Given the significant change in peak pressure achieved, no significant change in gas entry pressure occurred. Figure 70 and Table 16 show the influence of increased gas pressurisation on the gas entry pressure. As can be seen in Figure 70a, gas entry pressure results in a minor reduction in gas entry pressure from 8.4 to 7.5 MPa when estimated from STP gas flow into the fracture. However, as seen in Figure 70b, determining gas entry pressure from the ideal gas law showed an increase in gas entry pressure from 4.9 to 5.4 MPa. Therefore it is concluded that gas entry pressure is not a rate dependent variable.

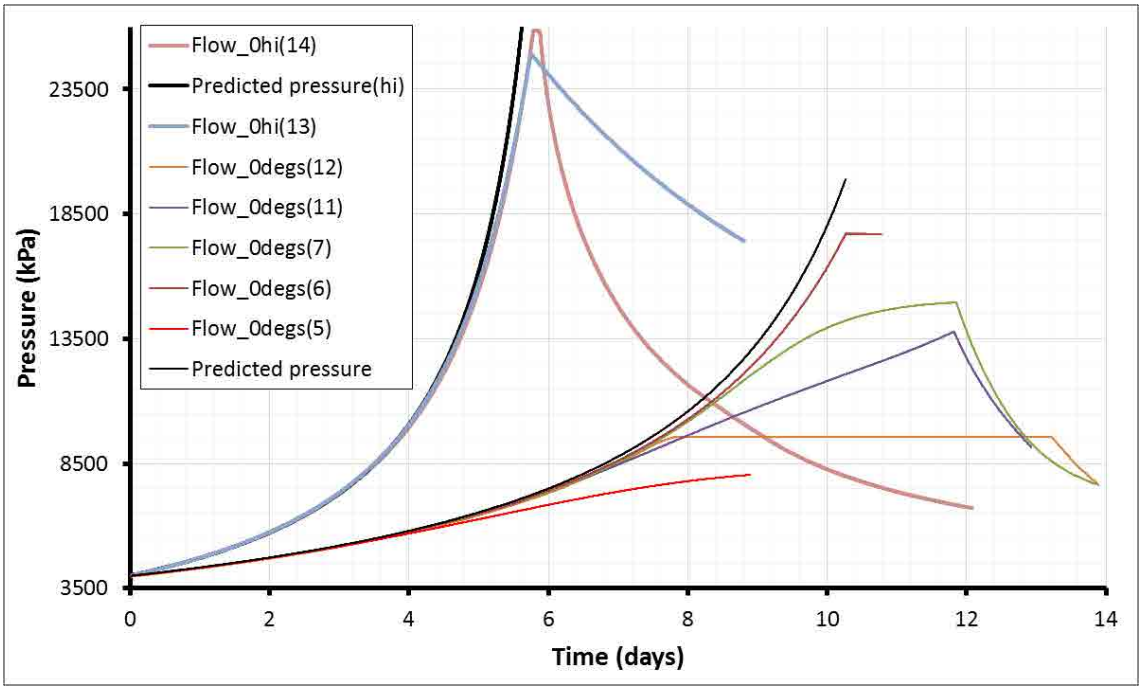

Figure 68 – Results for two gas injection tests conducted at higher gas injection rates, compared with five tests conducted on a fracture oriented 0° to the slip plane. As can be seen, considerable higher gas pressures were achieved.

Test	Fracture angle	+/-	Method 1			Method 2		
			Gas entry pressure (kPa)	Average entry pressure	+/-	Gas entry pressure (kPa)	Average entry pressure	+/-
0degs(5)	0°	0.5°	*5000*	8440	413	4772	4920	193
0degs(6)			8000			4610		
0degs(7)			9000			4590		
0degs(11)			7500			5475		
0degs(12)			9250			5170		
0hi(13)	0°#	0.5°	7000	7500	354	4845	5420	408
0hi(14)			8000			6000		

Table 16 – Results for gas entry pressure for all gas injection experiments. # high pressurisation rate; @ with shear; Method 1 = gas entry determined from STP gas flow into the fracture; Method 2 = entry pressure inferred from comparing pressure curve with ideal gas law.

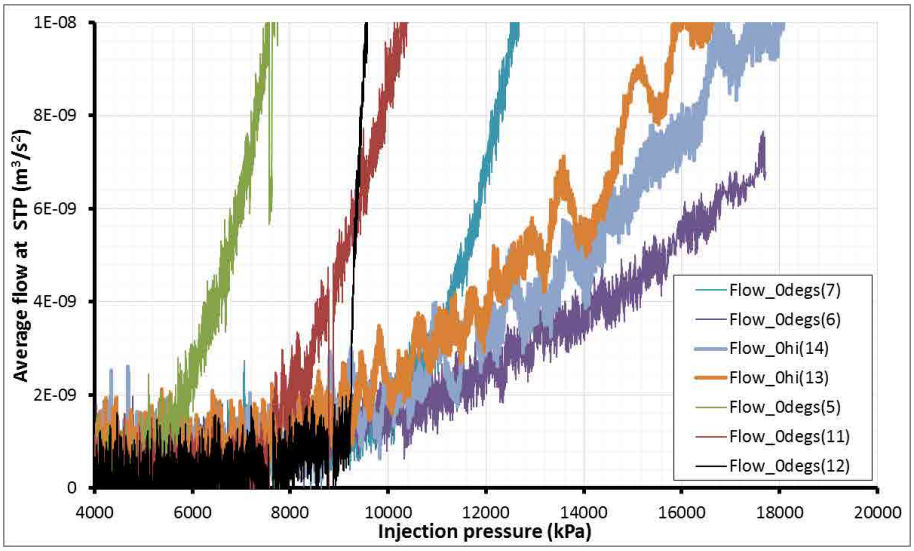

Figure 69 – Gas entry pressure predicted from the average flow at STP for two tests conducted at higher gas injection rate, compared with five gas injection tests conducted on a fracture oriented 0° to the slip plane. As can be seen, repeatable gas entry pressure is seen for all tests, suggesting that injection rate does not alter gas entry pressure.

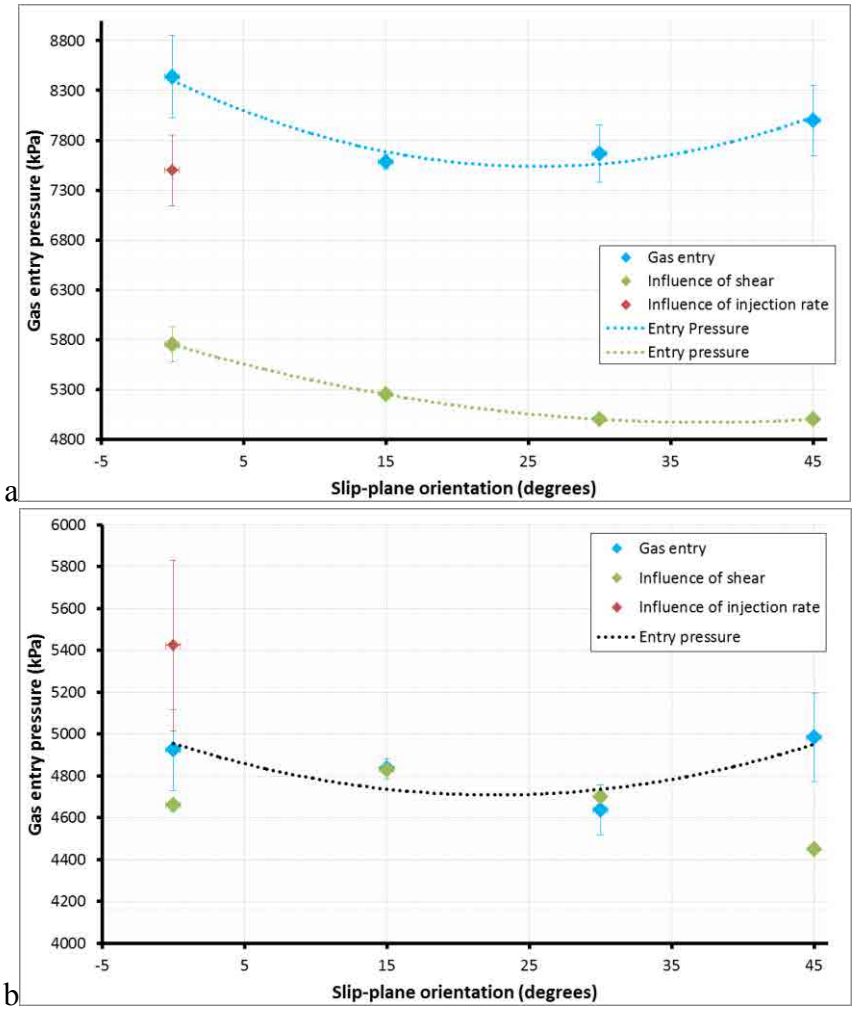

Figure 70 – Gas entry pressure for all tests showing the influence of gas injection rate. a) gas entry determined from the STP gas flow into the fracture; b) gas entry determined from comparing pressure response with ideal gas law.

4.11 IS GAS ENTRY AT DIFFERENT ANGLES SIMPLY RELATED TO NORMAL LOAD?

As shown in Section 3.1, fracture transmissivity is a function of vertical load. All gas injection experiments were conducted with identical boundary conditions with the loading system set to give 2 MPa on the fracture oriented at 0º to the slip-plane. However, the loading of the gouge perpendicular to the fracture angle would therefore differ depending on the fracture angle. As can be seen in Figure 71, the loading frame results in a normal load on the fracture of 2 MPa when the fracture if flat, reducing to a low of about 1.4 MPa when the fracture is 45º. If the change in gas entry pressure seen was simply due to changes in normal load on the fracture as a result of fracture angle it would be expected that a similar form would be seen in the relationship of both normal load and flow; which is clearly not the case in Figure 71a and Figure 71b. Therefore, although fracture transmissivity was seen to be a function of vertical load, the variation seen in gas entry pressure is not as a result of simple stress rotation about the fracture and must therefore be related to the horizontal stress generated within the fault gouge.

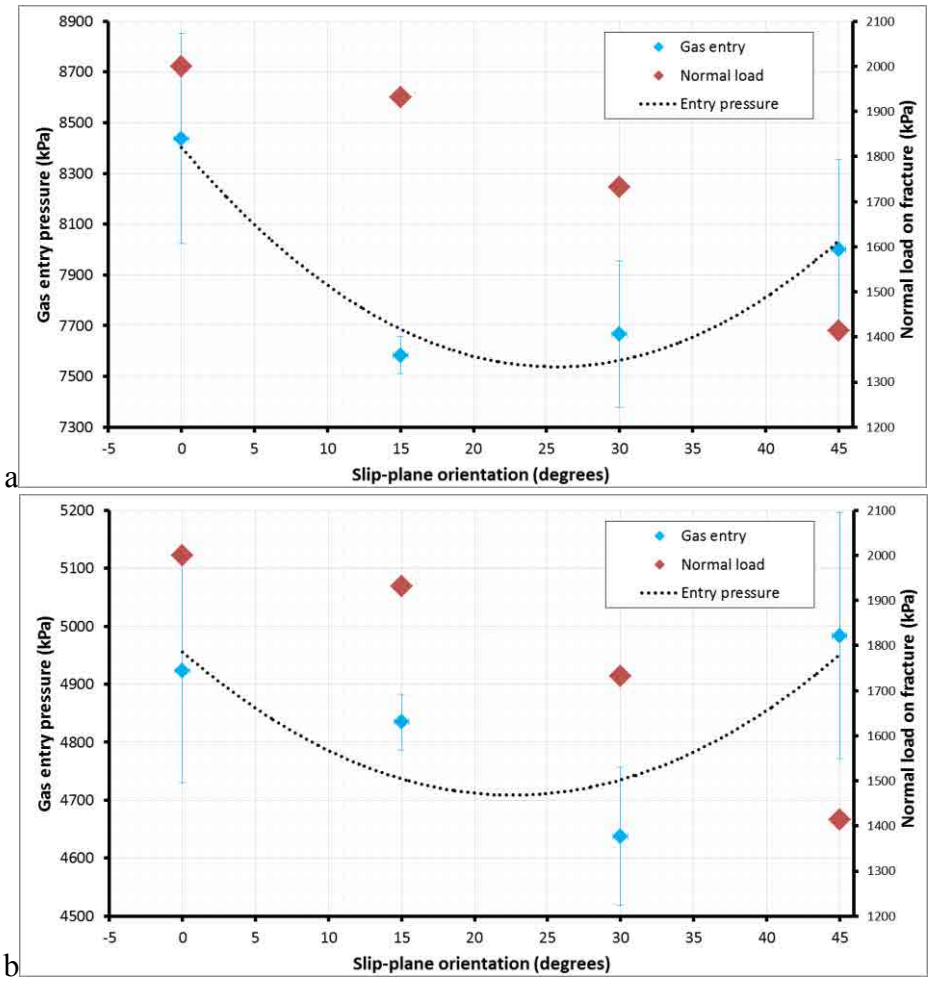

Figure 71 – Comparing gas entry pressure with normal load on the fracture; a) gas entry pressure determined from STP flow into the fracture; b) gas entry pressure determined from ideal gas law. As can be seen, the variation in gas entry pressure cannot be explained from the variation of normal load with fracture orientation alone.

5 Time-lapse study of fracture flow

Five gas injection tests were conducted with the addition of time-lapse photography in order to identify the time of gas escaping the kaolinite gouge. Two GoPro HD Hero2 cameras were mounted on the apparatus and set to take a photograph every 30 seconds during the gas injection test. The photographs were assembled into time-lapse films, allowing an approximate time of bubbles appearing to be identified. The jpeg images were then examined in order to get a better time for the first appearance of gas bubbles.

5.1.1 Time-lapse test 1 (Test ASR_Tau20_15gGI; Gas test 10)

Close examination of the time-lapse images did not show any bubbles escaping the kaolinite gouge. The first time-lapse test was conducted with a single GoPro HD Hero 2 camera and it was decided to perform all subsequent tests using two cameras in order to observe more of the kaolinite gouge area. Figure 40 shows that gas peak pressure was close to being achieved and therefore gas was mobile within the gouge. Therefore it is possible that gas was escaping from a location not covered by the camera.

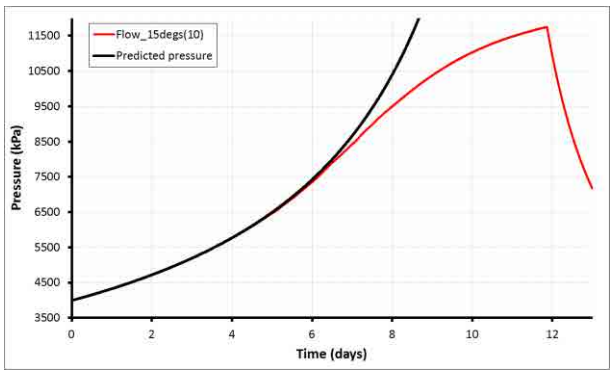

Figure 72 – Time-lapse results for gas injection test 10 / ASR_Tau20_15gGI.

5.1.2 Time-lapse test 2 (Test ASR_Tau21_00gGI; Gas test 11)

Gas bubbles were identified in the second time-lapse test conducted. Gas initially started as isolated bubbles from a single exit point, which in time developed into a large stream of gas by the end of the test. The first identifiable bubble was seen at 20:12 on the 7/5/2012 when gas pressure was at 7,500 kPa (see Figure 73). This corresponds with the gas entry pressure identified from average flow at STP into the fracture (7,500 kPa), but is higher than the gas entry pressure predicted from the ideal gas law (5,475 kPa).

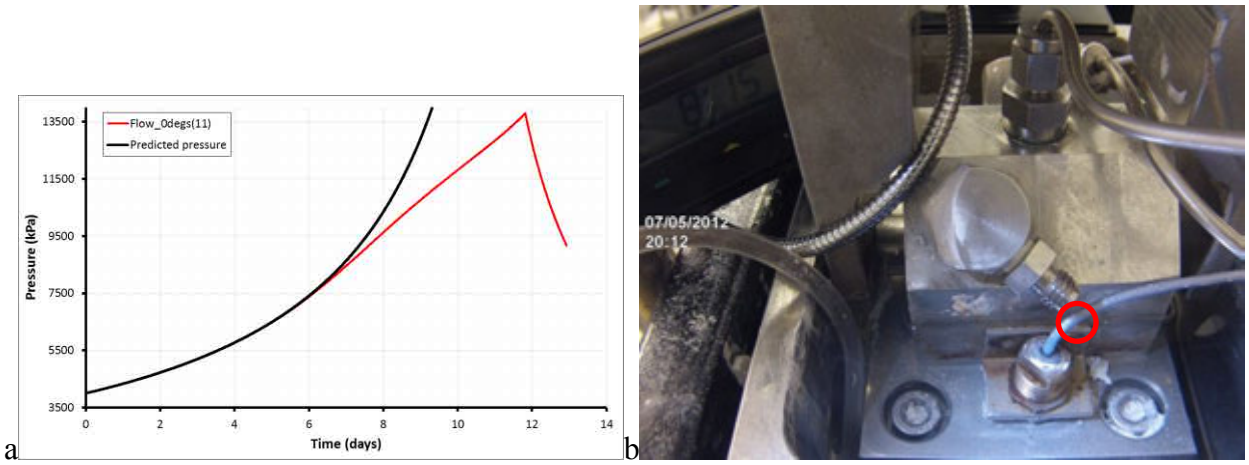

Figure 73 – Time-lapse results for gas injection test 11 / ASR_Tau21_00gGI. a) Gas injection pressure compared with prediction from the ideal gas law; b) Photo showing first identifiable bubble coming from the kaolinite gouge.

5.1.3 Time-lapse test 3 (Test ASR_Tau22_00gGI; Gas test 12)

Gas bubbles were identified in the third time-lapse test conducted. This initially started as bubbles from a single exit point, which developed into a large stream of gas by the end of the test. The first identifiable bubble was seen at 02:51 on the 22/5/2012 when gas pressure was at 9,200 kPa (see Figure 74). This corresponds with the gas entry pressure identified from average flow at STP into the fracture (9,250 kPa), but is higher than the gas entry pressure predicted from the ideal gas law (5,170 kPa).

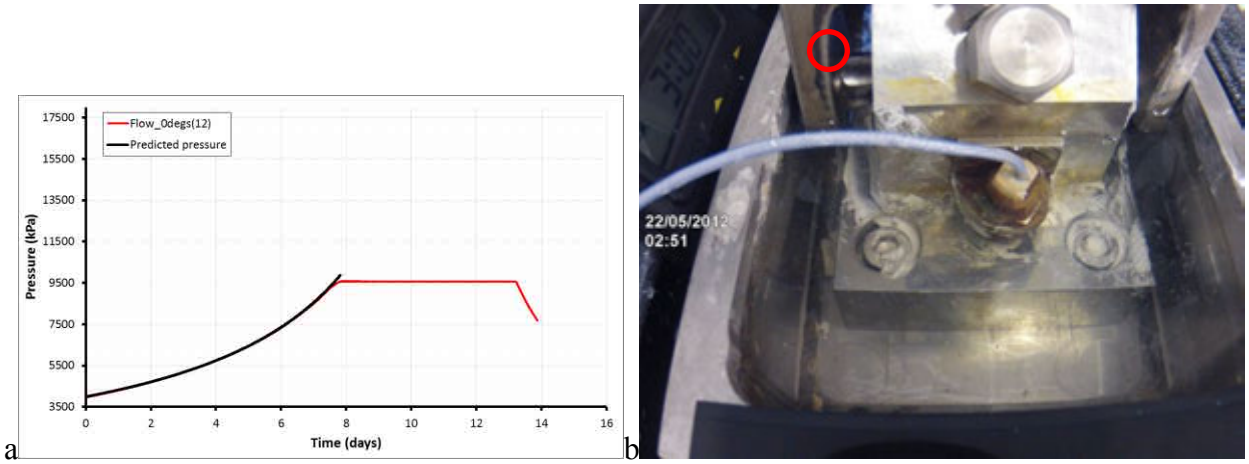

Figure 74 – Time-lapse results for gas injection test 12 / ASR_Tau22_00g GI. a) Gas injection pressure compared with prediction from ideal gas law; b) Photo showing first identifiable bubble coming from the kaolinite gouge.

5.1.4 Time-lapse test 4 (Test ASR_Tau23_00gGI; Gas test 13)

Gas bubbles were not observed in the fourth time-lapse test conducted, despite near full coverage of the kaolinite gouge by the time-lapse cameras. It is possible that gas may have been escaping out of camera view. However, no signs of bubbles disturbing the water surface were seen. Figure 75 shows that by the end of the test the observed gas pressure was close to the predicted gas pressure. This suggests that little gas had been mobilised and may explain why no gas bubbles were observed. Therefore it is concluded that gas was only mobile within the gouge and had failed to exit the test sample.

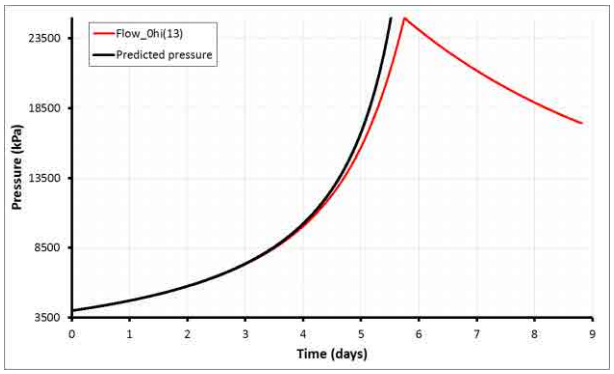

Figure 75 – Time-lapse results for gas injection test 13 / ASR_Tau23_00g GI. Gas injection pressure compared with prediction from ideal gas law.

5.1.5 Time-lapse test 5 (Test ASR_Tau24_00gGI; Gas test 14)

Gas bubbles were identified in the fifth time-lapse test conducted. This initially started as bubbles from a single exit point, which developed into a large stream of gas from two separate locations. The first identifiable bubble was seen at 21:05 on the 11/6/2012 when gas pressure was at 17,000 kPa (see Figure 76). This pressure was significantly higher than the gas entry pressure identified from average flow at STP into the fracture (8,000 kPa) and the gas entry pressure predicted from the ideal gas law (6,000 kPa).

a 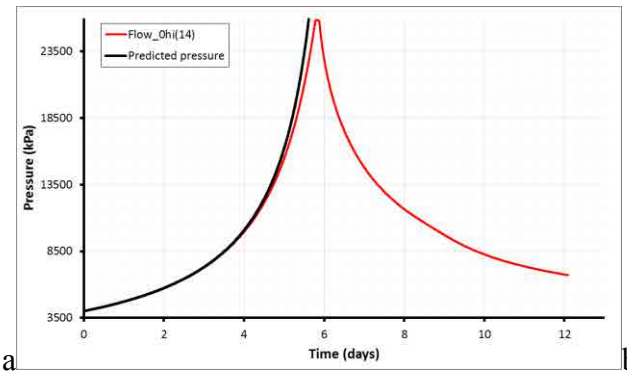

b 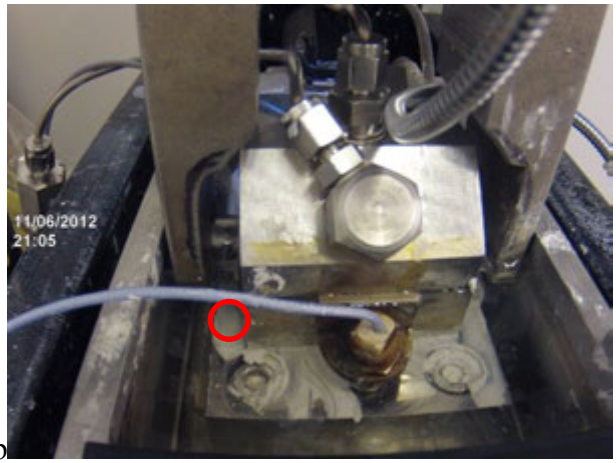

Figure 76 – Time-lapse results for gas injection test 12 / ASR_Tau22_00g GI. a) Gas injection pressure compared with prediction from ideal gas law; b) Photo showing first identifiable bubble coming from the kaolinite gouge.

5.2 DISCUSSION ON TIME-LAPSE OBSERVATIONS

Of the five time-lapse tests conducted only three had observable gas bubbles escaping the kaolinite gouge. For two of these tests the pressure at which the first bubble was identified corresponds closely with the gas entry pressure predicted from average flow at STP into the fracture. Therefore it is possible that this technique identifies the gas breakthrough pressure (the pressure when gas is sufficient to allow escape from the sample). However, one test showed gas bubbles did not appear until a pressure greatly in excess of predicted gas entry. This test showed that observed gas pressure was close to predicted gas pressure, suggesting that little gas had entered the gouge.

Two tests did not observe gas bubbles. The first test may be as a result of limited camera coverage of the kaolinite gouge. The second test displayed a gas pressure close to the predicted pressure, indicating that little gas had entered the gouge and by the end of the test this gas had not migrated as far as the outside of the kaolinite gouge.

Two tests showed that gas migrated and exited the gouge at a single point, suggesting only one pathway had allowed gas escape. However, one test showed that gas initially escaped from a single location, which soon sealed and gas then escaped from two other locations diametrically opposed on the loading platen. This suggests that multiple pathways formed and continued to evolve even once gas was able to escape the system.

6 Water content of the gouge material

During the decommissioning of test ASR_Tau08_30gLU, five sub-samples of kaolinite gouge were taken and water content was determined. This was performed by weighing the samples before and after oven drying for 24 hours. All test materials were started with an initial water content of 80%. As shown in Figure 77, water content was greatly reduced. It is likely that water would have been driven off during normal loading. It can be seen that variation is seen in the final water content. Along the centre of the sample water content appears more reduced than on the left or right of the slip-plane. However, only small quantities of kaolinite were recovered, typically 0.01 – 0.02 g for each sample and therefore considerable error could be introduced by measuring such small samples.

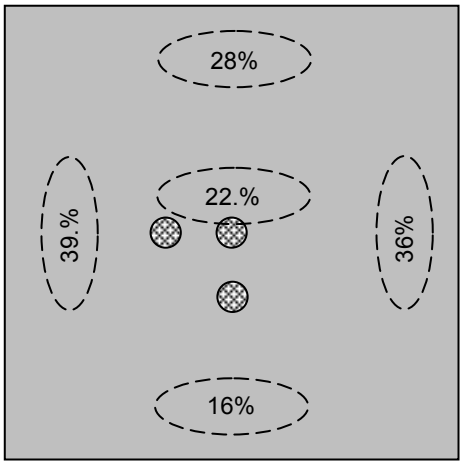

Figure 77 – Water content of the kaolinite gouge material measured at five locations on the sample surface.

7 Conclusions

The complete experimental programme conducted 48 separate experiments. Two main types of experiment were conducted: 1). Loading-unloading tests, where fracture flow was monitored at constant injection pressure as normal load was increased in steps to a given level and then reduced back to the starting stress state; 2). Gas breakthrough experiments, where gas injection pressure was increased in a pressure ramp at constant normal load. These were conducted with and without active shear. In additional, a number of other experiments were conducted. The main conclusions from this study are summarised below:

7.1 LOADING-UNLOADING TESTS

A total of 17 loading-unloading experiments were conducted, all on a 30° slip-plane. Nine tests were conducted without a permeant in order to understand the behaviour of the kaolinite gouge whilst loading/unloading, five tests were conducted with water as the injection fluid, whilst three gas flow experiments were conducted.

During a loading (vertical stress) and unloading cycle considerable hysteresis in flow was observed signifying the importance of stress history on fracture flow.

As normal load was increased in steps, the flow along the slip plane steadily reduced. Tests initially may have had dissimilar flow rates to start, but generally achieved a similar flow rate of by 2.6 MPa normal load. On unloading, this flowrate did not significantly alter until normal loads of approximately 0.75 MPa. Therefore it can be noted that the "memory" of the maximum load experienced is retained. This illustrates the importance of stress history on predicting flow along discontinuities and has been used to explain the non-applicability of the critical stress approach in its simple form at the Sellafield site in the UK (Sathar *et al.*, 2012). All loading-unloading experiments showed marked hysteresis in flow.

For the case of gas injection the change in flow is chaotic at low normal loads, whereas for water injection the flow reduces smoothly with increased normal load.

Considerable difference is seen between the loading and unloading cycles during gas flow. On loading the progression of flow is chaotic. In all three tests, once normal load was increased from the starting value of approximately 0.3 to 0.5 MPa flow increases. All three tests show that increased normal load results in episodes of increasing and decreasing flow. This could possibly be explained by 3 possible mechanisms:

1. Gas flow is highly sensitive to water content of the gouge and the duration of the experiment means that full drainage is not possible;
2. The gouge is not remaining even in thickness along the complete length, i.e. increased load is resulting in a wedge shaped gouge;
3. Horizontal movement is occuring along the 30° slope as normal load is increased and there is some form of stick-slip, which means that the movement is uneven between steps.

It is difficult to rule out scenario (1) as this has not been investigated fully. However, wide variation in flow rates have not been observed, which suggests that a fairly homogenous paste of gouge has been created and that subtle, loacalised changes in saturation (caused by uneven drainage) is unlikely to be the main cause of this effect.

The second scenario (2) is not supported by the measurement of the gouge thickness during experimentation. Even reduction in gouge thickness was observed, with more chaotic variations in thickness seen during unloading. This is contrary to the flow data, where chaotic flow is seen during loading and even variaion seen during unloading. Therefore this effect is unlikely to be caused by uneven thicknesses of gouge.

The third scenario (3) is also not supported by experimental observations. Horizontal movement occurred as a result of only increasing normal load. However, this increases relatively evenly and suggests that changes in normal load have resulted in the gouge moving evenly.

Observations of loaclised flow suggests that gas exploits sub-micronscale features within the clay, similar to features observed in bentonite. The exact cause of the chaotic behaviour has not been determined due to the macro-scale of measurement and the likely microscopic origin of this behaviour. However, the chaotic behaviour is repeatable and suggests that gas flow predictions of transmissivity are problematic. The "even" reduction in flow on unloading supports the "memory" effect of the clay introduced in the previous section.

Hysteresis in horizontal stress observed during unloading demonstrates the importance of the ratio between horizontal stress and vertical stress and its control on flow.

Considerable hysteresis was also observed in horizontal stress during loading-unloading experiments for both water and gas injection. The repeatability of the results shows that free movement of the gouge was achieved. The hysteresis in horizontal stress during unloading may be attributed to the cohesive strength of the kaolinite clay gouge. The ratio of horizontal stress to vertical stress also showed hysteresis. Subtle variation between water and gas injection experiments was seen during unloading once the ratio exceeded unity. Significant gas flow rate increase occurred when the horizontal stress to vertical stress ratio increased above unity during unloading.

Zoback *et al.* (1985) and Brudy *et al.* (1997) have shown that the ratio of horizontal stress to vertical stress is crucial in controlling permeability and in the movement of gas through fractures. The close relationship between fracture flow and the horizontal stress to vertical stress ratio during the unloading stages in the present experiments also points towards its significance in understanding the flow of fluid through discontinuities. In the case of a fractured rock formation undergoing uplift stress relaxation is likely to result in a high horizontal stress to vertical stress ratio.

Understanding the horizontal stress to vertical stress ratio is important in predicting the flow properties of discontinuities. Features experiencing high horizontal stress to vertical stress ratios are expected to be more conductive. High horizontal stress to vertical stress scenarios are likely to be more prevalent in regions experiencing stress relaxation due to structural uplift or removal of the overburden. Again, this highlights that an understanding of the stress history of a discontinuity is essential to effectively predict the present fluid flow properties of those features.

Differences have been observed between injection fluids (water and helium), especially the hysteresis observed in flow. For water injection flow is only partially recovered during unloading, whereas for gas enhanced flow is seen at low normal loads.

Observations of shear stress during loading-unloading experiments show that the gouge mechanically behaves the same way if water or gas is injected into a saturated kaolinite gouge. The similarities suggest that the gouge is neither hydrated by water injection (as it is already fully saturated), nor is it desaturated by gas injection.

However, considerable differences are seen in flow behaviour. For water injection, a pore pressure of 1 MPa is sufficient to initiate flow, whereas a gas pressure in excess of 3.5 MPa is required to initiate flow. This results in much lower flow rates observed in water injection tests. The differences suggest that the governing physics controlling gas movement is dissimilar to that controlling water movement.

As previously introduced, there is also considerable difference in the progression of flow during the loading cycle. At low normal loads this behaviour is chaotic in gas injection, whereas it is smooth for water injection. By 1.5 MPa normal load the two behaviours are similar, both decaying evenly with increasing normal load.

Differences are also seen during the unloading cycle. Both injection fluids show a similar initial response with considerable hysteresis seen and the slow recovery of flow. Dissimilarity is seen as normal load reduces below approximately 1 MPa. For the case of water injection, flow is always only partially recovered. For gas injection, at low normal loads flow increases to high levels much greater than that recorded at the corresponding normal load on the loading cycle. The enhanced flow becomes catastrophic and at low normal loads all gas in the gas reservoir is expelled through the slip-plane. Such catastrophic failure during water injection was not seen. This may in part be due to the expansion of gas as it propagates along the slip-plane as pressure reduces.

7.2 GAS BREAKTHROUGH EXPERIMENTS

A total of 26 gas breakthrough experiments were conducted on 0°, 15°, 30°, and 45° discontinuities; both with and without active shear. All tests were conducted in an identical manner with a known starting volume of 200 ml of helium at 4 MPa and a pressure ramp created by constant flow displacement of the ISCO syringe pump by 700µl/h.

During gas breakthrough experiments episodic flow/fault valve behaviour was seen with a decrease in subsequent peak pressures and the form of the pressure response was different during subsequent breakthrough events.

A single test was conducted (ASR_Tau06) for a prolonged gas injection ramp to see if there was repeat gas entry with a total of seven steps conducted. The exact detail of this particular test is complicated due to need to refill the gas reservoir several times.

The first gas breakthrough at 0.2 MPa normal load resulted in the sudden catastrophic loss of gas pressure at 3.2 MPa as the gas reservoir was emptied through the slip-plane. Normal load was increased to 1.85 MPa to see if a secondary breakthrough could be initiated following fracture sealing due to increased normal load. This resulted in a distinct peak in gas pressure at 1.9 MPa, which was followed by a decay to 1.2 MPa and then slow recovery of gas pressure to another breakthrough at 1.6 MPa. Pressure dropped to 0.5 MPa and again recovered to another breakthrough event at about 1 MPa. This partial breakthrough was followed by pressure recovery to a plateau of 1.1 MPa. Normal load was increased to 2.25 MPa and a fifth breakthrough was initiated at 1.8 MPa.

The form of the breakthrough event changed during the experiment. The first event was a catastrophic total loss of pressure. The second event was a peak and trough, similar in form to that seen during gas injection in bentonite. The third event was a sudden drop in pressure by 1 MPa, and the fourth event could be described as the system reaching equilibrium and the attainment of a plateau.

These observations suggest that “fault-valve behaviour” has been demonstrated in the laboratory and the magnitude of subsequent break-through events reduced (at constant normal load) and the “form” of the breakthrough events changed with each successive feature. It also demonstrates that an increase in normal load resulted in a degree of self-sealing, although the “memory” of previous breakthrough events may still be apparent.

Repeat gas injection testing has shown a consistent gas entry pressure but considerably different, non-repeatable, gas peak pressures.

For all fracture orientations, considerable non-repeatability was seen in the gas pressure response during repeat testing. Two methods were used to determine gas entry pressure. The first compared the observed gas pressure with the ideal gas law, whereas the second was calculated from the average flow at STP into the fracture. For most tests there was considerable difference between the two estimates. However, time-lapse photography suggests that the method used for average flow at STP into the fracture is closely determining the gas breakthrough pressure, whereas comparing the recorded gas pressure with the ideal gas law determines the gas entry

pressure. For both methods of determining the gas entry pressure there was repeatability in the results, with occasional anomalously low entry pressures.

Repeat gas injection testing has suggested that the physical control on gas entry is repeatable, although in the presence of any form of imperfection gas is able to enter at lower pressures. Once gas starts to move within the slip-plane the progression of pressure is less predictable and depends on whether the evolving gas network locates an exit from the system. Similar results are seen for all discontinuity orientations. Time-lapse photography has shown that gas pathways continue to evolve even after an exit has been established from the gouge.

Differences in gas entry pressure are seen dependent on the orientation of the fracture.

Although some tests have shown anomalously low gas entry pressures, a general variation of gas entry pressure with discontinuity orientation was observed. The highest gas entry pressure, as expected, was seen on a flat slip-plane with an entry pressure of 8.5 MPa. The lowest gas entry pressure was recorded at 15° of 7.75 MPa. Generally, the results suggest that the lowest gas entry pressure would be observed at 25°.

All tests have been conducted at identical vertical loads. As discontinuity orientation varies, the load acting normal to the slip-plane will vary. Taking this geometrical effect into account, the variation seen in gas entry pressure is more complex than a simple stress rotation about the slip-plane.

The experimental study has clearly demonstrated a variation in fracture transmissivity with discontinuity orientation. This experimental study demonstrates that the critical stress theory is applicable in the absence of stress relaxation.

Shear can be seen to reduce the gas entry pressure.

Tests conducted on slip-planes oriented to the direction of active shear showed a lower gas entry pressure for kaolinite and a rotation of gas entry pressure minimum to 38°. For water injection fracture transmissivity was seen to reduce due to self-sealing as a result of shearing. Therefore the reduction in gas entry pressure and observed increase in flow (as postulated from a reduced peak pressure) suggests that shearing in kaolinite has the opposite effect of self-sealing to gas.

7.3 GENERAL OBSERVATIONS

The results show that the flow of fluids through clay filled fractures is non-uniform and occurs via localised preferential pathways.

Five tests were conducted and recorded using time-lapse photography to observe the escape of gas from the slip-plane into the bath of the apparatus. These showed that a small, isolated stream of bubbles escaped from a single location. In most tests a single stream of bubble was created, i.e. a single pathway and a second pathway either had not formed or did not reach the edge of the slip-plane. In all tests the frequency of escaping bubbles increased, as did the size of the bubbles.

Fracture width data were inconsistent in recording dilation events at the onset of gas flow. However, some tests clearly showed dilation. This observation combined with the isolated single bubble stream show that gas propagated by means of a dilatant process.

The pressure recorded within the slip-plane showed a negligible fracture pressure and did not vary much in all tests.

In all tests, the two pressure ports located within the slip-plane registered pressure less than 50 kPa, effectively close to zero. Little variation was seen, although some changes occurred during loading-unloading experiments as a result of consolidation. However, no evidence of elevated gas pressures were seen during any experiment. This strengthens the observation of localised dilatant pathways as opposed to a distributed radial migration of gas.

8 References:

British Geological Survey holds most of the references listed below, and copies may be obtained via the library service subject to copyright legislation (contact libuser@bgs.ac.uk for details). The library catalogue is available at: http://geolib.bgs.ac.uk.

BÄCKBLOM, G, CHRISTIANSSON, R, and LAGERSTEDT, L. 2004. *Choice of rock excavation methods for the Swedish deep repository for spent nuclear fuel*. (SKB.)

BARTON, C A, HICKMAN, S, MORIN, R, ZOBACK, M D, and BENOIT, D. 1998. Reservoir-scale fracture permeability in the Dixie Valley, Nevada, geothermal field. *SPE/ISRM Rock Mechanics in Petroleum Engineering*, Stanford University, Stanford, California, 299-306.

BARTON, C A, HICKMAN, S, MORIN, R H, ZOBACK, M D, FINKBEINER, T, SASS, J, and BENOIT, D. 1997. Fracture permeability and its relationship to in-situ stress in the Dixie Valley, Nevada, geothermal reservoir. *Twenty-Second Workshop on Geothermal Reservoir Engineenng*, January 27-29, Stanford Unlverslty, Stanford, California.

BARTON, C A, ZOBACK, M D, and MOOS, D. 1995. Fluid flow along potentially active faults in crystalline rock. *Geology*, Vol. 23, 683-686.

BERGE, P A, BLAIR, S C, and WANG, H F. 1999. Thermomechanical effects on permeability for a 3-D model of YM rock. *Rock Mechanics for Industry, Vols 1 and 2*, 729-734.

BOSSART, P, MEIER, P M, MOERI, A, TRICK, T, and MAYOR, J-C. 2002. Geological and hydraulic characterisation of the excavation disturbed zone in the Opalinus Clay of the Mont Terri Rock Laboratory. *Engineering Geology*, Vol. 66, 19-38.

BOSSART, P, TRICK, T, MEIER, P M, and MAYOR, J-C. 2004. Structural and hydrogeological characterisation of the excavation-disturbed zone in the Opalinus Clay (Mont Terri Project, Switzerland). *Applied Clay Science*, Vol. 26, 429-448.

BRUDY, M, ZOBACK, M D, FUCHS, K, RUMMEL, F, and BAUMGÄRTNER, J. 1997. Estimation of the complete stress tensor to 8 km depth in the KTB scientific drill holes: Implications for crustal strength. *Journal of Geophysical Research-Solid Earth*, Vol. 102, 18453-18475.

BYERLEE, J. 1978. Friction of Rocks. *Pure and Applied Geophysics*, Vol. 116, 615-626.

CUSS, R J. 1999. An experimental investigation of the mechanical behaviour of sandstones with reference to borehole stability. PhD thesis, University of Manchester.

CUSS, R J, HARRINGTON, J F, GRAHAM, C C, SATHAR, S, and MILODOWSKI, A E. 2012. Observations of heterogeneous pore pressure distributions in clay-rich materials. *Mineralogical Magazine*, Vol. Geological Disposal of Radioactive Waste: Underpinning Science and Technology.

CUSS, R J, MILODOWSKI, A E, and HARRINGTON, J F. 2011. Fracture transmissivity as a function of normal and horizontal stress: First results in Opalinus Clay. *Physics and Chemistry of the Earth, Parts A/B/C*, in press.

EVANS, K F. 2005. Permeability creation and damage due to massive fluid injections into granite at 3. 5 km at Soultz: 2. Critical stress and fracture strength. *Journal of Geophysical Research. B. Solid Earth*, Vol. 110.

FERRILL, D A, WINTERLE, J, WITTMEYER, G, SIMS, D, COLTON, S, ARMSTRONG, A, and MORRIS, A P. 1999. Stressed rock strains groundwater at Yucca Mountain, Nevada. *GSA Today*, Vol. 9, 1-8.

FINKBEINER, T, BARTON, C A, and ZOBACK, M D. 1997. Relationships Among In-Situ Stress, Fractures and Faults, and Fluid Flow, Monterey, Formation, Santa Maria Basin, California. *AAPG Bulletin*, Vol. 81, 1975-1999.

GUTIERREZ, M, ØINO, L E, and NYGÅRD, R. 2000. Stress-dependent permeability of a de-mineralised fracture in shale. *Marine and Petroleum Geology*, Vol. 17, 895-907.

HEFFER, K, and LEAN, J. 1993. *Earth stress orientation - a control on, and guide to, flooding directionality in a majority of reservoirs*. Reservoir Characterization III. (Tulsa: PennWell Books.)

IKARI, M J, and KOPF, A J. 2011. Cohesive strength of clay-rich sediment. *Geophys. Res. Lett.*, Vol. 38, L16309.

ITO, T, and ZOBACK, M D. 2000. Fracture permeability and in situ stress to 7 km depth in the KTB Scientific Drillhole. *Geophysical Research Letters*, Vol. 27, 1045-1048.

JAEGER, J C, COOK, N G W, and ZIMMERMAN, R W. 2007. *Fundamentals of rock mechanics*. (Wiley-Blackwell.) ISBN 0632057599

LAUBACH, S E, OLSON, J E, and GALE, J F W. 2004. Are open fractures necessarily aligned with maximum horizontal stress? *Earth and Planetary Science Letters*, Vol. 222, 191-195.

MARRY, V, ROTENBERG, B, and TURQ, P. 2008. Structure and dynamics of water at a clay surface from molecular dynamics simulation. *Physical Chemistry Chemical Physics*, Vol. 10, 4802-4813.

MATILLA, J. and TAMMISTO, E. 2012. Stress-controlled fluid flow in fractures at the site of a potential nuclear waste repository, Finland. Geology, 40, No.4, pp.299-302.

MOGI, K. 2007. *Experimental rock mechanics*. No. 3. (CRC.) ISBN 0415394430

REEVES, H. 2002. The effect of stress and fractures on fluid flow in crystalline rocks, Cumbria, UK. PhD thesis, University of Durham.

ROGERS, S F. 2003. Critical stress-related permeability in fractured rocks. *Fracture and in-Situ Stress Characterization of Hydrocarbon Reservoirs*, Vol. 209, 7-16.

RUTQVIST, J, BÖRGESSON, L, CHIJIMATSU, M, HERNELIND, J, JING, L, KOBAYASHI, A, and NGUYEN, S. 2009. Modeling of damage, permeability changes and pressure responses during excavation of the TSX tunnel in granitic rock at URL, Canada. *Environmental Geology*, Vol. 57, 1263-1274.

RUTQVIST, J, and STEPHANSSON, O. 2003. The role of hydromechanical coupling in fractured rock engineering. *Hydrogeology Journal*, Vol. 11, 7-40.

TALBOT, C J, and SIRAT, M. 2001. Stress control of hydraulic conductivity in fracture-saturated Swedish bedrock. *Engineering Geology*, Vol. 61, 145-153.

TSANG, C F, BERNIER, F, and DAVIES, C. 2005. Geohydromechanical processes in the Excavation Damaged Zone in crystalline rock, rock salt, and indurated and plastic clays - in the context of radioactive waste disposal. *International Journal of Rock Mechanics and Mining Sciences*, Vol. 42, 109-125.

WALTHAM, A.C. (1994) *Foundations of Enginnerring Geology*. Blackie Academic & Professional, 88pp.

ZOBACK, M D, MOOS, D, MASTIN, L, and ANDERSON, R N. 1985. Well bore breakouts and in situ stress. *Journal of Geophysical Research-Solid Earth*, Vol. 90(B7), 5523-5530.

9 Appendix I

Test	Fracture angle	+/-	Method 1			Method 2		
			Gas entry pressure (kPa)	Average entry pressure	+/-	Gas entry pressure (kPa)	Average entry pressure	+/-
0degs(5)	0°	0.5°	*5000*	8440	413	4772	4920	193
0degs(6)			8000			4610		
0degs(7)			9000			4590		
0degs(11)			7500			5475		
0degs(12)			9250			5170		
15degs(8)	15°	0.5°	7500	7580	72	4850	4840	48
15degs(9)			7500			4732		
15degs(10)			7750			4922		
30degs(1)	30°	0.5°	*5200*	7670	289	4373	4640	120
30degs(2)			8000			*7380*		
30degs(3)			7000			4700		
30degs(4)			8000			4839		
45degs(15)	45°	0.5°	8500	8000	354	5046	4980	212
45degs(16)			7500			5373		
45degs(17)			*5000*			4531		
0hi(13)	0°#	0.5°	7000	7500	354	4845	5420	408
0hi(14)			8000			6000		
0Shear(18)	0°@	0.5°	5500	5750	177	4620	4660	28
0Shear(19)			6000			4700		
30Shear(20)	30°@	0.5°	7000	7000	100	4700	4700	100
45Shear(21)	45°@	0.5°	5000	5000	100	4450	4450	100
15Shear(22)	15°@	0.5°	5250	5200	100	4830	4830	100

Table 17 – Results for gas entry pressure for all gas injection experiments. # high pressurisation rate; @ with shear; Method 1 = gas entry determined from STP gas flow into the fracture; Method 2 = entry pressure inferred from comparing pressure curve with ideal gas law.